t8

DOKTORSAVHANDLINGAR
VID
CHALMERS TEKNISKA HÖGSKOLA
Nr 104

RUTILE TRAVELING-WAVE MASER SYSTEMS FOR THE FREQUENCY RANGE 1.3-6.2 GHz AND RADIO ASTRONOMY APPLICATIONS

BY

ERIK L. KOLLBERG

GÖTEBORG
ELANDERS BOKTRYCKERI AKTIEBOLAG
1970

RUTILE TRAVELING-WAVE MASER SYSTEMS FOR THE FREQUENCY RANGE 1.3 - 6.2 GHz AND RADIO ASTRONOMY APPLICATIONS

AKADEMISK AVHANDLING
SOM MED TILLSTÅND AV CHALMERS TEKNISKA HÖGSKOLA
FÖR TEKNOLOGIE DOKTORSGRADS VINNANDE TILL
OFFENTLIG GRANSKNING FRAMLÄGGES Å PALMSTEDTSALEN
INOM KANSLIBYGGNADEN, SVEN HULTINS GATA, GÖTEBORG,
FREDAGEN DEN 29 MAJ 1970 KL. 10

AV

ERIK L. KOLLBERG

Teknologie licentiat

Avhandlingen försvaras på engelska och svenska språket

GÖTEBORG
ELANDERS BOKTRYCKERI AKTIEBOLAG
1970

The present paper serves as an introduction and summary to a doctoral thesis which includes the following papers:

A. E. L. Kollberg, "Rutile Traveling-Wave Maser Systems for the Microwave Range 1.3–6.2 GHz", Research Report No 98, Research Laboratory of Electronics, Chalmers University of Technology, (1970).

B. E. L. Kollberg, "A Dielectrically Loaded Slow-Wave Structure for Traveling-Wave Maser Applications", Research Report No. 72, Research Laboratory of Electronics, Chalmers University of Technology (1966).

C. E. L. Kollberg, "Conductor Admittance in Transverse TEM Filters and Slow-Wave Structures", Electronics Letters, *3*, 294–296, (1967).

D. E. L. Kollberg, "Measurements of Noise in Traveling-Wave Maser Systems, Theory and Experiments", Research Report No. 95, Research Laboratory of Electronics, Chalmers University of Technology (1969).

E. O. E. H. Rydbeck, J. Elldér, and E. L. Kollberg, "OH and Formaldehyde Radiation Properties of the W75 Region", The Astrophysical Journal, (letters), *156*, L141–L146, (1969).

F. O. E. H. Rydbeck, E. L. Kollberg, and J. Elldér, "OH Excited State Emissions from W75B and W3, OH", Research Report No. 97, Research Laboratory of Electronics, Chalmers University of Technology (1970). Accepted for publication in Astrophysical Journal.

G. K. I. Kellerman, B. G. Clark, C. C. Bare, O. E. H. Rydbeck, J. Elldér, B. Hansson, E. Kollberg, B. Höglund, M. H. Cohen, D. L. Jauncey, "High-Resolution Interferometry of Small Radio Sources using Intercontinental Base Lines", Astrophysical Journal (letters), *153*, L209–L214 (1968).

Introduction

The recent increase of activities in the field of satellite communications, telemetry, deep space probes, and radio astronomy, has had a catalytic effect on the development of ultra-low-noise amplifiers. A number of different principles for the amplification have been investigated and amplifiers such as traveling wave tube amplifiers, tunnel diode amplifiers, parametric amplifiers, and masers are currently used in low noise receivers. However, any method of amplification of the electromagnetic field ultimately reverts to the fundamental principles of energy transfer from some energy reservoir to the electromagnetic field, a transfer which can only be done in discrete steps (photons) since the field is quantized.

As early as 1917, Albert Einstein (Einstein 1917) introduced the basic concepts of stimulated emission, stimulated absorption, and spontaneous emission, to describe the interaction processes between matter and the electromagnetic field. The stimulated emission and absorption processes are both proportional to the Einstein B-coefficient, which gives the probability per unit time per unit energy density and radiation mode for a stimulated transition. In the stimulated process, the emitted photons are exactly in phase with the stimulating electromagnetic field.

The spontaneous emission process is proportional to the Einstein A-coefficient, which gives the probability per unit time and radiation mode for spontaneous emission of radiation. Since the photons emitted by the spontaneous emission process are completely uncorrelated with any present electromagnetic field, this process creates electromagnetic noise power. It does not matter what kind of amplification principle is utilized, the spontaneous emission process can never be avoided; i.e., no noise free amplifier can ever be built.

The maser principle can be directly understood from the concepts introduced by Einstein. Most microwave masers utilize transitions between the electron spin levels in paramagnetic single crystals, as originally proposed by Bloembergen (1956).

A typical maser crystal consists of a diamagnetic host crystal (e.g. rutile, TiO_2), doped with a small amount of paramagnetic ions (e.g. chromium ions, Cr^{3+}). In thermal equilibrium, the different ions are statistically distributed among the ground state levels (four levels for Cr^{3+}) as determined by the Boltzmann distribution law.

If the frequency f_s of an electromagnetic field exposing the maser crystal is determined from

$$f_s=(E_n-E_m)/h, \tag{1}$$

where h is Planck's constant and E_m and E_n are the energies of two of the paramagnetic ground state levels ($E_n>E_m$), interaction between the field and the ions may occur. Amplification is obtained if there are more ions with the higher energy than with the lower (population inversion), since for this case the stimulated emission processes becomes more frequent than the stimulated absorption processes. Hence amplification can never occur when the paramagnetic spin system is in thermal equilibrium. However, by exposing the maser crystal to a strong electromagnetic pump field with a frequency corresponding to a different transition, the thermal equilibrium state may be disturbed in such a way as to obtain population inversion at the signal frequency transition. Usually the pump frequency is much higher than the signal frequency.

The most widely used maser material is ruby, i.e. chromium-doped single crystal α-alumina. For the frequency range 1–5 GHz, however, chromium-doped rutile is the most efficient maser material known to date. Chromium-doped rutile ($Cr-TiO_2$) has been used in masers described by a number of authors (e.g. Gerritsen 1959, Yin *et al.* 1963, Morris and Miller 1964, Yngvesson and Kollberg 1965). The maser properties of $Cr-TiO_2$ have been extensively investigated for the frequency range 1–4 GHz (Yngvesson 1968). In paper A, measurements of 5 GHz $Cr-TiO_2$ maser properties are presented.

Iron-doped rutile ($Fe-TiO_2$) is probably the most efficient maser material from about 5 GHz to about 7.5 GHz. The use of $Fe-TiO_2$ in microwave masers has been reported by Morris and Miller (1965). In paper A the maser properties of $Fe-TiO_2$ are investigated in some detail. It is shown that heat treatment is essential for optimum maser properties.

One of the most essential parts in a maser is the electromagnetic circuit utilized for the interaction between the electromagnetic field and the paramagnetic spin system. The intensity of the interaction is proportional to the rf magnetic energy density, which can be increased either by using a feedback circuit (e.g. a cavity resonator) or a low group velocity transmission line (slow-wave structure). A maser in which a slow-wave structure (SWS) is used, is called a traveling-wave maser (TWM).

A TWM is usually preferred to a cavity type maser, since it offers such advantages as greater bandwidth, higher gain stability and easier tuning. The first successfully operated TWM, in which a comb-type SWS was used, was built at the Bell Telephone Laboratories (De Grasse *et al.* 1959). The comb SWS as well as a number of other SWS:s (e.g. the meander line, the interdigital line, the Karp-structure) all utilize an array of transverse parallel conductors. The *rf* magnetic fields in such transverse-conductor SWS:s are predominantly circularly polarized, yielding a method for isolation (backward wave attenuation) by using ferrimagnetic resonance absorption in a ferrimagnetic material (see e.g. Chen 1964*a*).

In papers A, B and C a new SWS utilizing transverse parallel conductors is described and theoretically analyzed. An exploded view of the SWS is shown in Fig. 1. Among the main advantages of this SWS are the mechanical stability of the construction and the high efficiency of the interaction between the maser crystal and the electromagnetic field.

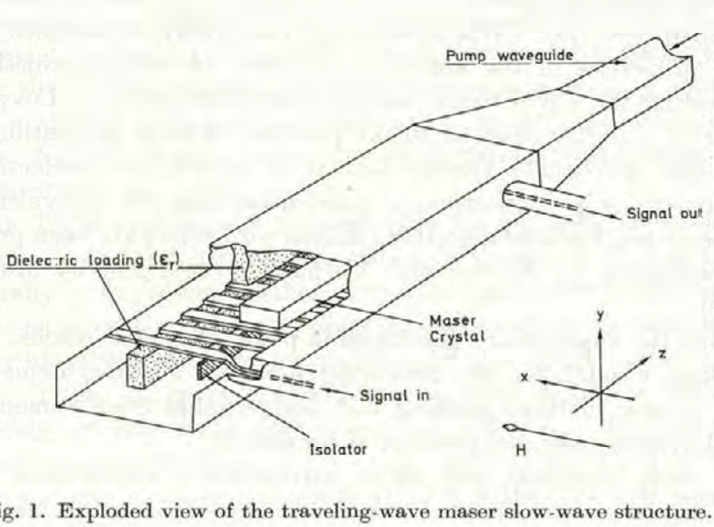

Fig. 1. Exploded view of the traveling-wave maser slow-wave structure.

The theoretical calculation of a transverse conductor SWS dispersion characteristic involves calculation of the conductor admittance vs the phase shift per period. In papers B and C a new method is presented for numerical calculation of the mutual admittances entering the formula proposed by Leblond and Mourier (1952) (see paper C below). We obtain an expression for the conductor admittance which is very accurate and is much easier to use in a SWS design procedure than expressions obtained from space harmonic analysis (see e.g. Fletcher 1952, Kovalenko and Kovalenko 1963,Chen 1964*b*).

In paper A we discuss the design and the amplifying characteristics of nine different traveling wave masers. Particularly interesting is a TWM design in which an unusually small (.5 mm) and nearly optimum pitch (Kollberg 1966) is used, yielding an almost doubled efficiency, compared to earlier designs with a 1 mm pitch.

Special design problems concerning the maser package and the installation in the 84-foot radio telescope at the Onsala Space Observatory are also discussed in paper A. Particular attention is paid to the rf transmission line design, the cryogenics, and to a special type of superconducting magnet with a "dc-transformer" tuning circuit.

In practice, the maser yields the lowest equivalent noise temperature attainable today. Typically, the amplifying SWS of a TWM contributes an equivalent noise temperature lower than 1°K, which is negligible in most practical receiving systems. Hence, the noise properties of a complete receiving TWM system are essentially determined by the noise properties of the antenna and those of the transmission line connecting the TWM to the antenna feed horn (see e.g. Levy 1968). Paper D is partly devoted to the problem of noise generation in the front-end waveguide system and it is shown that reflecting discontinuities (e.g. connectors) in general increase the equivalent noise temperature. Theories describing similar problems have been presented independently by Fischer and Ziermann (1967) and by Mukaihata (1968).

Using the basic theory developed in paper D we also discuss various well-known methods for measuring noise in TWM systems. Moreover, a new method yielding fast and reliable measurements of a TWM system noise temperature is presented.

In such technical and radio astronomical applications, where radio telescopes are directed towards the "cold" sky, full use may be made of the extreme low noise properties and high gain stability of the TWM. The weakest detectable signal is determined by the noise fluctuations at the receiver output. The rms value of the fluctuations, ΔT, is given by

$$\Delta T = \alpha \cdot \frac{T_S}{\sqrt{B\tau}} \tag{2}$$

where α is a constant (of order unity) depending on the particular backend receiver used, T_S is the receiver system noise temperature, B the receiver noise bandwidth and τ the integration time, proportional to the observation time. In such radio astronomical applications, where the bandwidth B is fixed for technical (as in very long baseline interferometry) or other reasons, the sensitivity of the system is determined only by T_S and τ. Moreover, the integration time τ, which is always chosen in such a way that a required value of ΔT is obtained, becomes proportional to $(T_S)^2$. Hence, a low system noise temperature is extremely useful, not only from a scientific point of view but also from the point of view of hourly operational costs.

The TWM system for the Onsala 84-foot radio telescope, described in paper A, was originally developed for research on molecular spectral emission and absorption lines. Hence, the TWM bandwidths are moderate and vary from about 4 MHz at 1400 MHz to about 20 MHz at 6000 MHz.

In order to demonstrate the over-all efficiency of the TWM system, we depict in Fig. 2 OH excited state features, as recorded at Onsala using the TWM equipped 84-foot telescope and make a comparison with a similar recording obtained with the 140-foot radiotelescope at the National Radio Astronomy Observatory Green Bank, W. Va (Zuckerman *et al.* 1968).

The TWM system was indispensable for the success of the radio astronomy research projects described in Papers E, F, and G. Quite naturally the present author found it particularly interesting to participate in the research programs devoted to investigations of maser-like emission from interstellar OH gas clouds (see e.g. Moran 1969). These enormous natural masers emit radiation in the OH molecule ground state transitions, i.e. the $^2\pi_{3/2}$, $J=3/2$, $F=2\rightarrow1$ transition at 1612 MHz, $F=1\rightarrow1$ at 1665 MHz, $F=2\rightarrow2$ at 1667 MHz and the $F=1\rightarrow2$ transition at 1720 MHz. The OH sources are

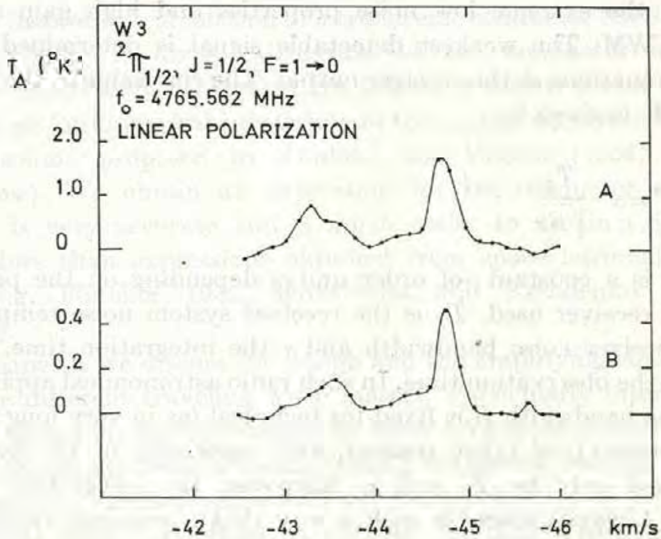

Fig. 2. Comparison between OH excited spectra of W3, OH obtained using A: the NRAO 140-foot radio telescope and a cooled parametric amplifier yielding a system noise temperature of about 110°K, and B: the Onsala 84-foot radio telescope equipped with the TWM system yielding a system noise temperature of about 45°K. Both recordings were obtained with an equivalent filter bandwidth of 3 kHz and a 6 hour integration time. Note the different temperature scales.

quite often found near young red stars and/or near HII-regions, and they have been observed to have apparent substructures comparable in size with the orbit of Jupiter or Saturn. These facts lend support to the idea that these OH masers are related to stars in their earliest stages of formation.

Various methods for obtaining population inversion in the interstellar OH masers have been suggested, such as chemical, infrared, and ultraviolet pumping (see eg. Litvak 1969). Since any pumping mechanism most likely populates and even inverts Λ-doublets in excited rotational states, it is extremely important to look for excited-state OH emission. Recently excited-state OH radiation has been detected from the $^2\pi_{1/2}$, $J=1/2$, $F=1\to 0$ transition at 4765 MHz in W3 (Zuckerman *et al.* 1968), from the $^2\pi_{3/2}$, $J=5/2$, $F=2\to 2$ and $F=3\to 3$ transitions at 6030 and 6035 MHz in W3, OH (Yen *et al.* 1969) and from the $^2\pi_{1/2}$, $J=5/2$, $F=2\to 2$ transition at 8135 MHz in W3 (Schwartz and Barret 1969).

Today about 60 regions emitting maser-like OH radiation have been discovered. At Onsala we have devoted much of our attention to two OH-regions, one in the continuum source W3 called W3, OH and the other in the continuum source W75 (or DR21).

In paper E we have shown that the OH emission from the W75 region emanates from two sources, denoted W75A and W75B respectively, separated by 13 minutes of arc. This discovery most probably means that the earlier reported time variations in W75 (Palmer and Zuckerman 1967, Raimond and Eliasson 1969) are not real, but are caused by inaccurate antenna pointing.

In paper F we report the discovery of a second source, W75B, emitting excited-state OH radiation at 6035 MHz. We also found time variations at 6035 MHz correlated with time variations of one feature in the 1667 MHz spectrum. Detailed recordings of features both in the excited-state and ground-state spectra of W75 and W3 made it possible for the first time to seriously test different models for the physical properties of the OH emitting regions.

When the brightness distributions and the positions of small radio astronomical objects, such as quasars and regions emitting maser-like OH radiation, are to be studied in detail, on can use interferometers with very long baselines. A technique has been developed recently in which separate, highly stable atomic frequency standards are used as LO:s instead of having a single common LO fed to the two antennas by means of cables, microwave links, etc., as in conventional microwave interferometers (see, e.g., Burke 1969). With this technique, it is possible to have any distance between the antennas if only the times at the antennas can be synchronized to within a few microseconds. The very long base line interferometer technique (VLB I) was developed independently and almost simultaneously by two groups (Broten *et al.* 1967, Bare *et al.* 1967).

In paper G, the first successful transatlantic VLBI experiment is described. The measurements were made January 27 to February 3, 1968, using the 84-foot radio telescope at the Onsala Space Observatory in Sweden and the 140-foot telescope at NRAO in Green Bank, W.Va., USA. One strong argument for choosing Onsala as the European station was the very high sensitivity of the 18 cm traveling wave maser receiver used in the Onsala telescope and described in paper A.

Paper A

A Rutile Traveling Wave Maser System for the Microwave Range 1.3–6.2 GHz

In this paper almost every aspect concerning construction of a practical traveling wave maser system for a large telescope is discussed in detail. Both theoretical design considerations and important practical experiences of particular problems, such as the manufacturing of different parts of the system, are presented. Minor parts of the material presented in paper A have been published earlier (Yngvesson and Kollberg 1965, Kollberg 1966, Kollberg and Yngvesson 1966, Rydbeck and Kollberg 1968).

A short presentation of the theory of the slow wave structure (SWS), which is discussed in detail in papers B and C, is given. A number of graphs that will facilitate the SWS design procedure are included. By introducing fairly accurate approximations, formulas are derived from which one can easily learn how to design an optimum dispersion characteristic. We believe that the present SWS theory is unsurpassed by any other theory for the understanding of the SWS and its practical design.

Using the finite difference method (Green 1965) computer calculations of the conductor admittance $Y(\pi)$ have been made (see eqn. 3) for conductors with finite thickness and a cross section equal to that of the dielectric loading region (Fig. 1) at the open end of the conductors.

We also discuss in some detail the maser properties of $Cr-Ti0_2$ and $Fe-Ti0_2$ for frequencies between 4.0 and 7.5 GHz. $Cr-Ti0_2$ has earlier been investigated by, e.g., Schollmeier and Roth (1966) at 4 GHz and quite extensively for frequencies between 1 and 4 GHz by Yngvesson (1968). $Fe-Ti0_2$ has been investigated around 4 GHz by Schollmeier and Roth (1967) and around 5 GHz by Morris and Miller (1965).

We have investigated the maser properties of $Fe-Ti0_2$ for different iron-doping. It is shown that at 4.2°K $Fe-Ti0_2$ and $Cr-Ti0_2$ are almost equally efficient, while at 2°K $Cr-Ti0_2$ is about 50% more efficient than $Fe-Ti0_2$. The maximum signal frequency is determined by the maximum splitting of the signal transitions in moderate magnetic fields, and is 5.4 GHz for $Cr-Ti0_2$ and 7.6 GHz for $Fe-Ti0_2$. It is known that heating of $Fe-Ti0_2$ to more than 800°C, followed by a rapid cooling, dissolves iron precipitates (Johnson *et al.* 1968). In paper A we show that the heat treatment not only increases the number of substitutional ions (in one case by as much as 87%) but also increases the inversion ratio. It is also shown that heat treatment of $Cr-Ti0_2$ yields similar results.

The isolator performance was investigated for different geometries as well as for different placings of the isolator material in the SWS, yielding new data for the TWM isolator design.

Experiments on maser SWS:s are discussed in terms of the theory presented in papers B, C and A. We also discuss in detail the design of nine TWM:s for field use, and present their characteristics, such as gain (typically 30 dB), bandwidth (from 4 to 20 MHz), tunability (from 200 MHz to 1000 MHz), and gain stability (typically ± 0.06 dB).

It is pointed out that there exists an optimum pitch (published separately by Kollberg, 1966). A TWM (5.1–6.1 GHz) was constructed with an optimum pitch for an operating temperature of 4.2°K. This maser had a net gain of more than 20 dB over the SWS passband with a SWS length of only 50 mm, and a pitch as small as .5 mm. The efficiency of this SWS is probably unsurpassed by any design published so far.

The superconducting magnet is a modified Cioffi type magnet (Cioffi 1962). It is furnished with a "dc-transformer" used for small changes of the magnetic field. This transformer is designed for frequency-switched VLBI experiments, and can re-tune an L-band TWM by 30 MHz within 0.1 seconds (a C-band TWM can be changed by as much as 80 MHz). The transformer is also used when frequent retuning is required, e.g., when recording nearby molecular lines or when searching for molecular lines with unknown frequencies.

The practical design of the TWM package is also discussed. Particular attention is paid to the rf transmission line design, the cryogenic design and to practical aspects on the telescope TWM system. It is shown that with a careful cryogenic design, an operation time of more than 25 hours at 2°K is obtained (helium gas pressure of 24 torr; the liquid helium boiling point is 4.2°K at atmospheric pressure). Only about five liters of 4.2°K liquid helium are necessary.

Finally, the convenience of the TWM system is illustrated by mentioning various radio astronomical projects, for which the TWM system has been indispensable.

Paper B

A Dielectrically Loaded Slow-Wave Structure for Traveling-Wave Maser Applications

The most common SWS for the microwave frequency range is the comb structure, which has been used with ruby as the maser material by a number of authors (e.g. de Grasse *et al.* 1959, Chen 1964*b*). Due to the high and anisotropic dielectric constant of rutile ($\epsilon_{\parallel}=240$, $\epsilon_{\perp}=120$), it is much more complicated to design a comb-structure with this material (Solovyev *et al.* 1966, Abazadze and Solovyev 1968). As an alternative SWS, the meander line has been used together with rutile (Morris 1964), although no detailed theory has been published for the rutile loaded meander line. Yngvesson (1963) has proposed a dielectrically loaded Karp-structure to be used with rutile, and Haddad (1966) has made a theoretical investigation (1966) of the dispersion properties of this SWS.

The SWS described in this paper may be considered as a modified comb-structure. An exploded view is shown in Fig. 1. This structure has been utilized in a number of traveling wave masers using rutile as the active material (Kollberg and Yngvesson 1965; Rydbeck and Kollberg 1968). The main features of the SWS may be summarized in the following way:

1. very good mechanical stability, even for small cross sectional dimensions, because the conductors are clamped between the dielectric rods,
2. high filling factor since the dielectrically loaded region contains only a small part of the rf magnetic field energy,
3. high filling factor also in the upper part of the passband since the conductors can be made very thin,
4. since most of the rf electric field energy is contained in the dielectric loading at the open end of the fingers, the SWS is extremely useful with rutile as the maser crystal,

5. the center frequency of the passband can be changed within wide limits merely by changing the dielectric material, or its position along the conductors, and
6. the risk of obtaining a double-valued dispersion characteristic when designing a SWS with a high slowing factor is almost negligible.

The theory developed for this SWS has features in common with the theory developed by Leblond and Mourier (1954) for electron tubes. However, in the present theory not only interaction between nearest neighbours can be numerically considered, but also the interaction with the second and third neighbours (see paper C below). Furthermore, the theory makes it possible to discuss an equivalent circuit for the SWS, which is particularly useful when the coupling to the SWS is treated.

A detailed discussion of the slowing and bandpass properties of the SWS is carried out. We have theoretically and numerically considered the effect of a ridge, similar to the ridge of a Karp structure. This is necessary when the relative dielectric constant of the dielectric loading is close to unity. Moreover, electrolytic tank measurements have made it possible to consider conductors that are not long enough to cover the dielectric loading material. The variation of this extra capacitance over the passband is shown to be non-linear. From an approximate expression for the dispersion characteristics, much is revealed about the influence of the SWS geometry on the slowing factor and pass band.

It is shown that the filling factor of the SWS is quite high even though the maser crystal cannot occupy the space of the dielectric loading material. Furthermore, one method is recommended which may yield an increased filling factor, especially in the lower part of the passband.

Experiments on SWS:s yield a fairly good agreement with theory. However, it is shown that the fit between the dielectric loading material and the conductors, as well as the ground planes, must be extremely good. This is especially so when such materials as polycrystalline rutile ($\epsilon_r = 85$) are used.

Paper C

Conductor Admittance in Transverse TEM Filters and Slow-Wave Structures

In this paper we present an extension of the method discussed in paper B for numerical calculation of the conductor admittance, as expressed in the form originally proposed by Leblond and Mourier (1954). Assume a TEM wave propagating along the conductors and the fields at $z=z_0$ (see Fig. 1) differ from those one period away by a factor $e^{-j\varphi}$ (Floquets theorem, lossless case). Then the conductor characteristic admittance becomes

$$Y(\varphi)=2y_{00}+4\sum_{n=1}^{\infty} y_{0n}\sin^2\left(\frac{n\varphi}{2}\right), \tag{3}$$

where y_{0n} are the mutual admittances to the ground planes (y_{00}) and to the neighbouring conductors (y_{0n}, $n\neq 0$), respectively. Leblond and Mourier retained only rough approximations for y_{00} and y_{01}.

Using a conformal mapping technique and elliptical integrals of the first kind (Harris *et al.* 1964), we have calculated $Y(0)$, $Y(\pi/2)$ and $Y(\pi)$ for conductors with zero thickness (paper B). In paper C it is shown that the field configuration for $\varphi=\pi/3$, using a conformal mapping technique, can be transformed to a configuration with $\varphi=0$. Hence, $Y(\pi/3)$ of the original geometry becomes equal to $Y(0)$ of the transformed geometry.

Using $Y(0)$, $Y(\pi/3)$, $Y(\pi/2)$ and $Y(\pi)$, the mutual admittances y_{00}, y_{01}, y_{02} and y_{03} have been tabulated for various geometries.

For conductors with finite thickness, a contribution to y_{01} is obtained. This contribution has been derived using data for rectangular coaxial lines published by Cruzan and Carver (1964). The over-all accuracy obtained for $Y(\varphi)$ is excellent, with an error of only about 1%.

Paper D

Measurements of Noise in Traveling-Wave Masers, Theory and Experiments

In this paper we discuss how noise power is generated in the antenna front-end transmission line system, connecting a TWM to the antenna feed horn. Various methods for noise measurements are discussed in detail, and a new method for measuring the noise of a TWM system is presented.

The fundamental discussion of the noise generation in a transmission line system containing lossless discontinuities is somewhat similar to the independently developed theory published by Fischer and Ziermann (1967). However, the theory presented in this paper is adapted to cases where both the losses and the temperature vary along the transmission line. Moreover, we point out that for a correct treatment of the noise generation, one must consider the noise generation mechanisms related to the ohmic losses separately from those related to the dielectric losses. This is particularly important when, e.g., a short circuit or an open circuit is connected at the input, creating different types of standing waves in the transmission line.

It is shown that for a transmission line with n discontinuities, each characterized by a reflection coefficient Γ_{va}, and with n sections, each with the attenuation L_v, the equivalent input noise temperature T_t becomes

$$T_t \approx T_0 \textstyle\sum_{v=1}^{n} \left(1 - \dfrac{1}{L_v}\right) \dfrac{1+|\Gamma_{va}|^2}{1-|\Gamma_{va}|^2} \qquad (4)$$

where T_0 is the physical temperature of the transmission line.

Equation (4) clearly demonstrates the influence of reflections in the transmission line. E.g., for $|\Gamma_{va}|=0.3$ (SWR=1.5) one obtains almost 20% increase in the thermal noise from this particular section.

The equivalent noise temperature of a TWM system is carefully defined. In the proposed definition the system noise temperature is referred to the terminating load in such a way that any mismatch in this load (e.g. the antenna) is referred to the amplifier system. Using this definition several different methods for measuring the noise temperature are discussed. E.g. the common hot-cold body method is shown to yield a measured noise temperature referred to the hot termination with a maximum error of

$$\delta T = \pm \frac{2Y}{Y-1} \,|\,\Gamma_t\,|\,|\Gamma_C - \Gamma_H|\,(T_C + T) \tag{5}$$

where Y is the measured "Y"-factor, Γ_t the reflection coefficient of the maser system, Γ_H and Γ_C the reflection coefficients of the hot and cold loads respectively and T the maser input transmission line noise temperature. The theory of hot-cold body measurements has been discussed by other authors, e.g., Otoshi (1968). However, the theory outlined in paper C is particularly useful for applications in TWM noise temperature measurements.

A theory for the methods of TWM noise temperature measurements proposed by Tabor and Sibilia (1963) and Shteinschleiger *et al.* (1966) is presented for the first time. A detailed discussion of the theory for the two methods reveal the expected accuracy under various conditions.

A new and simple method for measurements of the second stage amplifier noise contribution is proposed. A matched, room-temperature (T_0°K) termination is connected to the TWM input. The ratio Y_x of the detected noise power with maximum maser gain to the noise power with no maser gain (zero microwave pump power) is measured. The noise temperature contribution from the second amplifier then becomes

$$T_{\text{sec.amp.}} = \frac{T_0 + T_{\text{maser}}}{Y_x - 1} \tag{6}$$

where T_{maser} is the equivalent noise temperature of the maser amplifier, and which can usually be neglected when compared to T_0.

A new method for noise temperature measurements on a TWM is discussed. In this method, the noise power from the maser is measured when the input line is terminated with a short circuit and with an open circuit. Experiments using two different S-band TWM:s yielded a mean measured noise temperature for the specially made input transmission line of 5 ± 1°K.

Paper E

OH and Formaldehyde Radiation Properties of the W75 Region

One of the most interesting regions where anomalous maserlike OH radiation has been discovered is in W75. This region has been extensively examined using the maser system (paper A) on the Onsala 84-foot radio telescope.

It is shown in this paper that the W75 OH-radiation emanates from two sources separated by as much as 13 minutes of arc. The two sources are denoted W75A and W75B with the positions $\alpha = 20^h37^m12^s$, $\delta = 42^\circ.20$ (1950) and $\alpha = 20^h36^m58^s$, $\delta = 42^\circ\,43$ (1950), respectively. It is believed that some of the time- variations observed earlier by Palmer *et al.* (1967) and Raimond *et al.* (1969) were due to inadequate antenna pointing accuracy.

Since the antenna half power width was 29' the two sources could not be separated directly, and an elaborate beam-subtraction and -addition technique was used. This technique is rather time consuming, and the low noise temperature of the receiving system was a necessity for the final success of the observations.

The radial velocity of the W75 region, as expected from Galactic rotation, is about 2.5 km/sec. Only the velocity of the strongest feature of W75A is compatible with this model. Since a small absorption feature could be seen in the OH spectra of W75A, a search for formaldehyde emission or absorption at 4830 MHz was performed. A maximum absorption was found in the radio source DR 21, positioned only 4' from the W75A OH source. The formaldehyde and OH absorption features in the direction of DR 21 are almost identical in shape, and are symmetrical around 2.5 km/s. This symmetry can be explained by a model where the OH and formaldehyde cloud has the shape of a ring. These findings also indicate that the minimum distance to DR 21 is 0.7 or 2.2 kpc.

Finally, some measurements were performed in the direction of the continuum source W51. Also for this source, a close resemblance was found between OH absorption and formaldehyde absorption. This probably means that the ratio between the number of OH and H_2CO molecules is constant in W51 as well as in DR 21.

Paper F

OH Excited-State Emissions from W75B and W3, OH

A search for the 6 GHz excited-state emission was made early in August 1969 using the Onsala 84-foot radio telescope, equipped with a rutile traveling wave maser receiving system (paper A). Besides the W3, OH, $F=3\rightarrow3$ (6035 MHz) OH emissions, first detected by Yen *et al.* (1969) using the 150 foot Algonquin radio telescope, OH emission was only found from the $F=3\rightarrow3$ transition in W75B. In Table I, the negative results of the search are shown. The search was performed with one hundred 10 kHz filters covering a 1 MHz band. The polarization was linear and the root mean square noise fluctuations 0.1°K.

Table I

Source and transition ($F_1\rightarrow F_2$)	Radial velocity range km/s	Source and transition ($F_1\rightarrow F_2$)	Radial velocity range km/s
ON 1		W49	
$2\rightarrow2$	−11 to +39	$2\rightarrow2$	−10 to +40
		$3\rightarrow3$	−10 to +40
ON 2			
$2\rightarrow2$	−25 to +25	W51	
		$2\rightarrow3$	+35 to +85
DR 21		$2\rightarrow2$	+35 to +85
$2\rightarrow2$	−25 to +25	$3\rightarrow3$	+35 to +85
$3\rightarrow3$	−25 to +25		
		W75A	
NML Cyg.		$2\rightarrow3$	−19 to +31
$2\rightarrow3$	−46 to +4	$2\rightarrow2$	−19 to +31
$2\rightarrow2$	−46 to +4	$3\rightarrow3$	−19 to +31
$3\rightarrow3$	−46 to +4	$3\rightarrow2$	−19 to +31
$3\rightarrow2$	−46 to +4		
		W75B	−19 to +31
W 3	−69 to −19	$2\rightarrow3$	−19 to +31
$2\rightarrow3$	−69 to −19	$2\rightarrow2$	−19 to +31
$3\rightarrow2$	−69 to −19	$3\rightarrow2$	−19 to +31

The 6035 MHz W75B emission was found to vary considerably with time. Moreover we discovered that the 1667 MHz emission also varies in time and, as far as can be judged at present, in phase with the 6035 MHz emission variations. Hence, it is very likely that these emissions originate from the same source component.

Observations of the W3, OH 6030 and 6035 MHz emissions did not reveal any time variations.

Since the observed features in both W75B and W3, OH are extensively circularly polarized, magnetic fields within the source, causing Zeeman-splittings, may be present. It is pointed out that the Zeeman-splitting on a velocity scale, is almost 10 times smaller for the 6030 and 6035 MHz transitions than for the 1665 and 1667 MHz transitions. This fact emphasizes the importance of having 6 GHz excited-state emission profiles as well as ground-state emission profiles for the interpretation of the OH emission mechanisms. It is shown that the observed W75B ground-state and excited-state features fit into a Zeeman-model, with a magnetic field of about $5 \cdot 10^{-3}$ Gauss. The absence of lower frequency Zeeman-components in the ground state is proposed to be caused by a Cook-type mode selection mechanism (Cook 1966).

An assumed Zeeman-splitting of W3, OH 6030 and 6035 MHz emissions, implies a magnetic field of about $5 \cdot 10^{-3}$ Gauss (as in W75B) to be present in the source. 1665 MHz features, corresponding to the assumed 6035 Zeeman-components, were examined in detail using 250 Hz resolution. A close resemblance between 1665 and 6035 MHz features was found, although a higher frequency 1665 MHz Zeeman-component may be missing. Even now this can be explained by the presence of a mode selection mechanism.

Furthermore, a rotating ring configuration containing a magnetic field is discussed. In such a configuration a Shklovskii-type mechanism (Shklovskii 1969) may eliminate the higher frequency 1665 MHz Zeeman-component. Recordings with 250 Hz resolution of the relevant 1665 MHz feature lends support also to this model. Hence, so far we cannot rule out any of the models. Further detailed studies using 250 Hz resolution and VLBI experiments are required for a better understanding of the nature of the W3, OH source.

Paper G

High-Resolution Interferometry of Small Radio Sources Using Intercontinental Base Lines

In this paper the first transatlantic very long base line interferometry (VLBI) measurements are reported. In the experiment we used the 140-foot radio telescope at the National Radio Astronomy Observatory in Green Bank, W.Va and the 84-foot telescope of the Onsala Space Observatory, Sweden. A digital system was used for the observations and it was essentially the same as described by Clark *et al.* (1968).

The measurements were performed between January 27 and February 3, 1968, at frequencies near 1670 and 5010 MHz, corresponding to baselines of 35×10^6 and 105×10^6 wavelengths, respectively. One condition necessary for the success of the measurements was the use of the extremely low noise traveling wave maser receiver of the Onsala telescope for the 18 cm measurements.

Fringes were obtained for thirteen extragalactic objects. Most of the sources were found to contain two or more components of different angular size. This means that the observed fringe visibilities cannot be simply converted into a brightness distribution or an angular size. However, on the basis of the radio spectra of the sources, an approximate division into distinct components could be made, and this was utilized in the interpretation of the interferometric observations. The simplest model consistent with available data was always used, which might be an oversimplification for complex sources.

Particularly interesting are the optically thick sources, since the brightness temperature for these sources is determined only by the magnetic field (synchrotron radiation). The present measurements support a magnetic field of the order of 10^{-4} gauss for some sources, although higher fields seem to be present in many of the smaller sources.

The measurements also confirm the small dimensions predicted from observed intensity variations

Acknowledgements:

I wish to express my sincere gratitude to Professor O. E. H. Rydbeck for his support and encouragement which has been an inspiration for the entire work described in this thesis. My warm thanks are also due to Mr C. O. Lindström for his invaluable assistance for many years. Furthermore I would like to thank Dr. S. Yngvesson for proposing $Cr-Ti0_2$ as the maser material and for much encouragement and support, especially during the initial part of the research described in this thesis. To Mr P. O. Andersson I am grateful for performing many experiments.

I am also indebted to my co-authors in papers E and F, Prof. O. E. H. Rydbeck and Dr. J. Elldér, for pleasant cooperation and many discussions. To Drs. K. I. Kellerman, B. G. Clark, the late C. C. Bare, O. E. H. Rydbeck, J. Elldér, B. Hansson, B. Höglund, M. H. Cohen and D. L. Jauncey I am grateful for the stimulating collaboration during the first successful transatlantic VLBI experiments.

I also wish to acknowledge helpful comments on several of the manuscripts from Prof. B. Höglund, Mr. P. O. Andersson, Mr. C. O. Lindström and Mr. P. Wrane.

Finally, I would like to acknowledge the financial support from the Swedich Board for Technical Development, from the Wilhelm och Martina Lundgrens Vetenskapsfond and from Chalmers University of Technology.

References

ABAZADZE, Y. V., and SOLOVYEV, Y. G., 1968, Radio Eng. and Electron Physics, *13*, 246.

BARE, C., CLARK, B. G., KELLERMAN, K. I., COHEN, M. H., and JAUNCEY, D. L., 1967, Science, *157*, 189.

BLOEMBERGEN, N., 1956, Phys. Rev., *104*, 324.

BROTEN, N. W., LEGG, T. H., LOCKE, J. L., MCLEISH, C. W., RICHARDS, R. S., CHRISHOLM, R. M., GUSH, H. P., YEN, J. L., and GALT, J. A., 1967, Science, *156*, 1597.

BURK, B. F., July 1969, Physics Today, *27*, 54.

CHEN, F. S., and TABOR, W. J., 1964*a*, Bell Syst. Techn. J., *43*, 1005.

CHEN, F. S., and TABOR, W. J., 1964*b*, Bell Syst. Techn. J., *43*, 1035.

CIOFFI, P. P., 1962, J. Appl. Phys., *33*, 875.

CLARK B. G., KELLERMAN, K. I., BARE, C. C., and JAUNCEY, D. L., 1968, Ap. J., *153*, 705.

COOK, A. H., 1966, Nature, *211*, 503.

CRUZAN, O. R., and GARVER, R. V., 1964, IEEE Trans. on Microwave Theory and Techniques, *MTT-12*, 488.

DE GRASSE, R. W., SCHULTZ-DUBOIS, E. O., and SCOVIL, H. E. D., 1959, Bell Syst. Techn. J., *38*, 305.

EINSTEIN, A., 1917, Phys. Z., *18*, 121.

FISHER, K., and ZIERMANN, A., 1967, Archiv Electrischen übertragung, *21*, 464.

FLETCHER, R. C., 1952, Proc. IRE, *40*, 951.

GERRITSEN, H. J., and LEWIS, H. R., 1961, J. Appl. Phys., *31*, 608.

GREEN, H. E., 1965, IEEE Trans. on Microwave Theory and Techniques, *MTT-13*, 676.

HADDAD, G. I., 1966, IEEE Trans. on Microwave Theory and Techniques, *MTT-14*, 120.

HADDAD, G. I., 1963, Tech. Rept. 65, Electron Physics Lab., Electrical Eng. Dept., The University of Michigan, Ann Arbor, Mich.

HARRIS, S. E., DEGRASSE, R. W., and SCHULZ-DUBOIS, E. O., 1964, *43*, 437.

JOHNSON, O. W., OHLSEN, W. D., and KINGSBURY, P. I., 1968, Phys. Rev., *175*, 1102.

KOLLBERG, E. L., and YNGVESSON, K. S., 1966, Proc. IEE 6th Internat'l Conf. on Microwave and Optical Generation, vol. 27, p. 384.

KOLLBERG, E. L., 1966, IEEE Trans. on Microwave Theory and Techniques, *MTT-14*, 212.

KOVALENKO, Y. S., and KOVALENKO, V. S., 1963, Radio Eng. and Electronic Physics, *8*, 1327.

LEBLOND, A., and MOURIER, G., 1954, Ann de Radioélect., 9, 180 and 811.

LEVY, G. S., BATHKER, D. A., HIGA, W., and STELZRIED, C. T., 1968, IEEE Trans. on Microwave Theory and Techniques, *MTT-16*, 596.

LITVAK, M. M., 1969, Science, *165*, 855.

MORAN, J. M., 1969, Science Journal, Aug. 1969, *5A*, 60.

MORRIS, L. C., and MILLER, D. J., 1964, IEEE Trans. on Microwave Theory and Techniques, *MTT-12*, 421.

MORRIS, L. C., and MILLER, D. J., 1965, IEEE J. Quantum Electronics, *QE-1*, 164.

MUKAIHATA, T., 1968, IEEE Trans. on Microwave Theory and Techniques, *MTT-16*, 699.

OTOSHI, T. Y., 1968, IEEE Trans. on Microwave Theory and Techniques, *MTT-16*, 675.

PALMER, P., and ZUCKERMAN, B., 1967, Ap. J., *148*, 727.

RAIMOND, E., and ELIASSON, B., 1969, Ap. J., *155*, 817.

RYDBECK, O. E. H., and KOLLBERG, E. L., 1968, IEEE Trans. on Microwave Theory and Techniques, *MTT-16*, 799.

SCHOLLMEIER, G., and ROTH, D., 1966, Z. Angew. Phys., *21*, 187.

SCHOLLMEIER, G., and ROTH, D., 1967, Z. Angew. Phys., *22*, 471.

SCHWARTZ, P. R., and BARRET, A. H., 1969, Ap. J. (Letters), *157*, L109.

SHKLOVSKII, I. S., 1969, Soviet Astronomy—A.J., 13, 1.

SHTEINSHLEIGER, V. B., AFANASEV, O. A., MISIZHNIKOV, G. S., and ROSENBERG, Y. I., 1966, Cryogenics, *6*, 47.

SIEGMAN, A. E., 1964, Microwave Solid State Masers. New York: McGraw-Hill.

SOLOVYEV, Y. G., ABAZADZE, Y. V. ISAYEV, Y. G., STEPANOVA, Y. G., and KRYNETSKIY, I. B., 1966, Radio Eng. and Electronic Physics, *11*, 1047.

TABOR, W. J., and SIBILIA, J. T., 1963, Bell Syst. Techn. J., *42*, 1863.

YEN, J. L., ZUCKERMAN, B., PALMER, P., and PENFIELD, H., 1969, Ap. J. (letters), *156*, L27.

YIN, H. B., MORRIS, L. C., and MILLER, D. J., 1963, Proc. IEEE, *51*, 225.

YNGVESSON, K. S., 1963, 3rd Internat'l Conf. on Quantum Electronics, p. 899, Paris: Dunod.

YNGVESSON, K. S., and KOLLBERG, E. L., 1965, Proc. IEEE, *53*, 1737.

YNGVESSON, K. S., 1968, Research Report no. 54, Research Laboratory of Electronics, Chalmers University of Technology.

ZUCKERMAN, B., PALMER, P., PENFIELD, H., and LILLEY, A. E., 1968, Ap. J. (Letters), *153*, L69.

GÖTEBORG
ELANDERS BOKTRYCKERI AKTIEBOLAG
1970

RUTILE TRAVELING-WAVE MASER SYSTEMS FOR THE MICROWAVE RANGE 1.3-6.2 GHz

BY
E.L. KOLLBERG

RESEARCH REPORT NO 98
1970

RESEARCH LABORATORY OF ELECTRONICS

CHALMERS UNIVERSITY OF TECHNOLOGY

GIBRALTARGATAN 5 G

GOTHENBURG S, SWEDEN

Research Laboratory of Electronics
CHALMERS UNIVERSITY OF TECHNOLOGY
Gothenburg, Sweden

RESEARCH REPORT No. 98

RUTILE TRAVELING-WAVE MASER SYSTEMS FOR THE MICROWAVE RANGE 1.3 - 6.2 GHz

By

E. L. KOLLBERG

Gothenburg, April 1970

TABLE OF CONTENTS

		Page
1.	Introduction	4
2.	Slow-wave structure theory for the design procedure	
2.1.	Introduction	6
2.2.	The SWS theory	6
2.3.	The special case, when $W_1 = W_2$, $x = 0$	14
2.4.	The case $W_1 \neq W_2$ and $x \neq 0$	17
3.	Isolation of the TWM	
3.1.	Introductory remarks	20
3.2.	The isolator material	25
3.3.	Experimental investigation of the isolator performance	26
4.	Rutile as a maser material in the frequency range 1-7 GHz	
4.1.	Introduction	31
4.2.	Introductory remarks	31
4.3.	Maser properties as a function of iron-concentration for Fe-TiO_2 at 5 GHz.	34
4.4.	Rutile as a maser material in the frequency range 1-7 GHz	39
5.	Further traveling-wave maser design-considerations	
5.1.	Introduction	48
5.2.	Insertion loss in a transverse conductor slow-wave structure	48
5.3.	Optimum pitch of traveling-wave masers	50
6.	Experimental slow-wave structures for traveling-wave masers	
6.1.	Introduction	55
6.2.	Determination of the SWS dispersion characteristics	55
6.3.	Properties of experimental SWS:s	57
6.4.	The influence of the rutile maser crystal on the SWS dispersion characteristic	64
6.5.	Passband vs. the minimum slowing factor	67

Page

6.6. Manufacturing considerations for the SWS:s 68

7. Properties of some operational traveling-wave masers

7.1. Introduction 71
7.2. General remarks 71
7.3. Traveling-wave maser data 72
7.4. Gain stability 79

8. The superconducting magnet

8.1 Introduction 83
8.2. Design and performance of the superconducting magnet 83
8.3. The tuning circuit 90
8.4. Frequency switching 92

9. The maser package

9.1. Introduction 96
9.2. Cryogenic design considerations 96
9.3. The rf-transmission lines 100
9.4. The TWM system arrangements in the 25.6 m radiotelescope at the Onsala Space Observatory 101

10. The performance of the Onsala TWM system and radio astronomical applications

10.1. Introduction 105
10.2. Noise properties and operational experience of the Onsala 25.6 m telescope TWM system 106
10.3. Radio astronomical measurements performed with the TWM system 107

Acknowledgements 114
Appendix A 115
References 119

1. INTRODUCTION AND SUMMARY

Although many different types of low noise amplifiers have been designed, the maser yields the lowest possible equivalent noise temperature. When a slow-wave circuit is used for the interaction between a maser material and the electromagnetic field, we have a traveling wave maser (TWM). The TWM design is advantageous, since no feed-back is used, and this permits greater bandwidth, higher gain stability and easier tuning.

The very low equivalent noise temperature and the high gain stability of TWM:s are essential in applications such as satellite and deep space probe communications, and radio astronomy. The weakest detectable signal is determined by the noise fluctuations at the receiver output. The rms value of these fluctuations, ΔT , is given by

$$\Delta T = \alpha \cdot \frac{T_S}{\sqrt{B \tau}} \qquad (1.1)$$

where α is a constant (of the order unity) depending on the particular back-end receiver used , T_S the receiver noise temperature, B the receiver noise bandwidth, and τ the integration time, proportional to the observing time. In many radio astronomical applications the bandwidth B is fixed (e.g. in spectral line multichannnel receivers or in very long baseline systems) and the sensitivity of the system is only determined by T_S and τ. Since the integration time τ is always chosen to give a certain required value of ΔT, the observation time is proportional to $(T_S)^2$. Hence, a low system noise temperature is extremely useful, not only from a maximum sensitivity point of view but also from hourly operational costs.

This report describes the development and practical application of a series of extremely compact TWM:s using chromium-doped or iron-doped rutile as the active material. They are especially built for microwave emission line studies, for example of anomalous OH radiation, with the 84-foot equatorially mounted Cassegrainian radio telescope at the Onsala Space Observatory in Sweden. The system noise temperature ranges from about $34^{o}K$ at 1500 MHz to about $50^{o}K$ at 6000 MHz.

Our goal is to describe, as completely as possible, the design of the TWM system for the 84-foot telescope. Both theoretical design considerations (chapter 2-5) and important experimental experiences of particular problems (chapter 6-9) are presented. Some details reported in this paper have been published earlier (Yngvesson and Kollberg 1965, Kollberg 1966 a and b, Kollberg and Yngvesson 1966, Rydbeck and Kollberg 1968).

The particular slow wave structure (SWS) used in the TWM:s reported in chapters 1 and 6 is of the type using transverse conductors. Although it might be regarded as a novel design, it is in many respects similar to the comb-type SWS, first introduced by de Grasse et al. (1959). The theory of the SWS, which was first discussed by Kollberg (1966 a), is briefly presented in chapter 2. The practical design considerations are emphasized and a number of new and useful graphs are presented. In order to obtain a more accurate design, we have also calculated by computer the characteristic admittance ($Y(\pi)$) of the conductors in the SWS when an inhomogeneous dielectric loading is present.

In chapter 3 we discuss the ferrimagnetic isolator used in transverse conductor SWS:s. Experimental data of the isolator performance for different geometries as well as for different positions of the isolator material in the SWS, are presented and yield new information for the TWM isolator design.

We also discuss chromium-doped and iron-doped rutile for use in TWM:s. In particular we have investigated their maser properties for frequencies between 4 and 7.5 GHz. It is shown that at 4.2^{o}K and 5 GHz, iron-doped rutile (Fe-TiO_2) and chromium-doped rutile (Cr-TiO_2) are almost equally efficient, while at 2^{o}K Cr-TiO_2 is about 50% more efficient than Fe-TiO_2. The maximum signal frequency is determined by the maximum splitting of the signal transitions in moderate magnetic fields, and is 5.4 GHz for Cr-TiO_2 and 7.6 GHz for Fe-TiO_2.

It is shown that heating Fe-TiO_2 to more than 800^{o}C, followed by a rapid cooling, dissolves iron precipitates and increases the number of substitutional ions. Since the inversion ratio is increased too, it is concluded that the heat treatment of iron-doped rutile is very essential. Preliminary results on Cr-TiO_2 indicate improved maser performance due to heat treatment.

In chapter 5 ohmic losses are discussed, and it is shown that an optimum pitch can be found, effecting a compromise between ohmic losses and electronic gain. For optimum pitch, the TWM noise temperature becomes $1.5 \times T_o$ where T_o is the liquid helium bath temperature.

Measurements on SWS:s for the TWM are presented in chapter 6. The measured properties are discussed using the theoretical framework of chapter 2. We also give information on such practical aspects as tolerance problems and the manufacturing procedure.

A complete presentation of data for nine TWM:s is given in chapter 7. One of the TWM:s was designed for optimum pitch.

The design of the superconducting magnet, which is a modified Cioffi type magnet (Cioffi 1962), is presented in chapter 8. The magnet is furnished with a "dc transformer" that is used for small changes of the magnetic field. This transformer is designed for frequency switched very long baseline interferometer (VLBI) experiments, and is also very useful when frequent retuning of the TWM is required, e.g. when searches for new spectral lines are made or when nearby spectral lines are recorded.

In chapter 9 the design of the maser package is discussed. Particular attention is paid to the rf transmission line design and to the cryogenic design.

Finally, in chapter 10, the over-all performance of the TWM system in the 84-foot radio telescope at the Onsala Space Observatory is discussed. The TWM system has been used in a number of different radio astronomical projects, mentioned in chapter 10, and the accumulated running time is today about 5000 hours.

2. SLOW-WAVE STRUCTURE THEORY FOR THE DESING PROCEDURE

2.1 Introduction.

In this chapter we present a brief review of the SWS theory discussed earlier by the present author (Kollberg 1966 a). The SWS design offers a number of advantages, such as mechanical rigidity, a high filling factor and simplicity in the design. Furthermore, since the maser crystal is placed in a region with minor electric field components, it is extremely useful when a maser material with a high dielectric constant e.g. rutile ($\varepsilon_{\perp} = 120$, $\varepsilon_{11} = 240$) is used. We also present a number of graphs that will facilitate the design of a SWS. New numerical data for the admittance and for the wave propagation constant in the dielectrically loaded region have been obtained using a computer program.

2.2. The SWS theory.

An exploded view of the SWS is shown in Fig. 2.1, and the dimensions to be considered in the design procedure are shown in Fig. 2.2. The dispersion characteristic is obtained by matching the fields at the boundary between region 1 and 2. Using the equivalent circuit approach described by Kollberg (1966 a) one obtains the following characteristic equation for the SWS (eqn. 4.1.7 in Kollberg, 1966 a):

$$-Y_1(\varphi)\cot(\ell_1\beta_1(\varphi)) + \frac{\omega C_f(\varphi) + Y_2(\varphi)\tan(\ell_2\beta_2(\varphi))}{1 - \dfrac{\omega C_f(\varphi)}{Y_2(\varphi)}\tan(\ell_2\beta_2(\varphi))} + p\,\frac{\omega}{v_o}\,\frac{2C_d}{\varepsilon} = 0 \qquad (2.1)$$

where

φ is the phase-shift per period,

$Y_1(\varphi)$, $Y_2(\varphi)$ are the characteristic conductor admittances in region 1 and 2, respectively,

ℓ_1, ℓ_2 are the conductor lengths of region 1 and 2, respectively. (see Fig. 2.2),

$\beta_1(\varphi)$, $\beta_2(\varphi)$ are the TEM-wave propagation constants of region 1 and 2, respectively,

ω is the angular frequency,

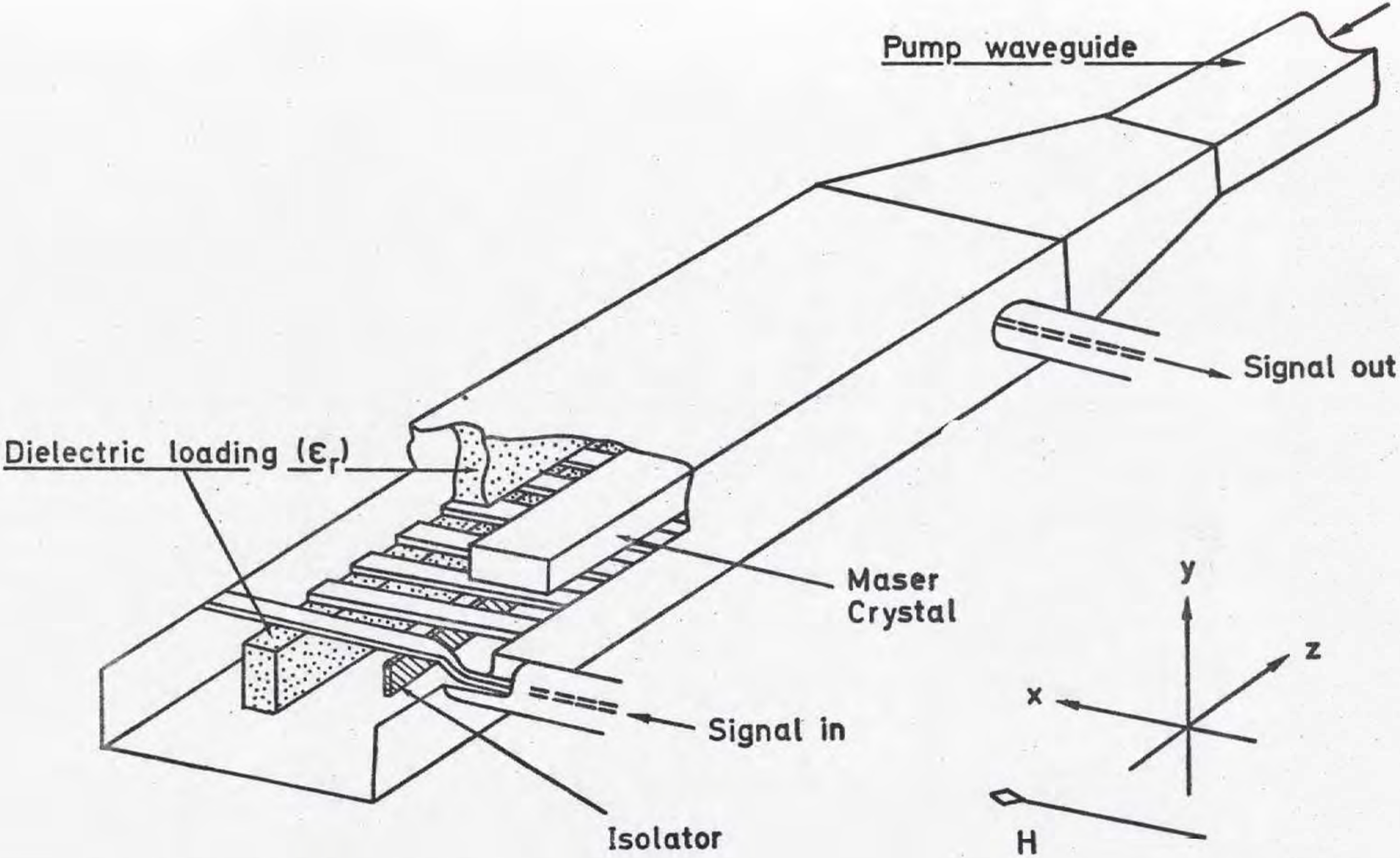

Fig. 2.1 Exploded view of the traveling-wave maser structure.

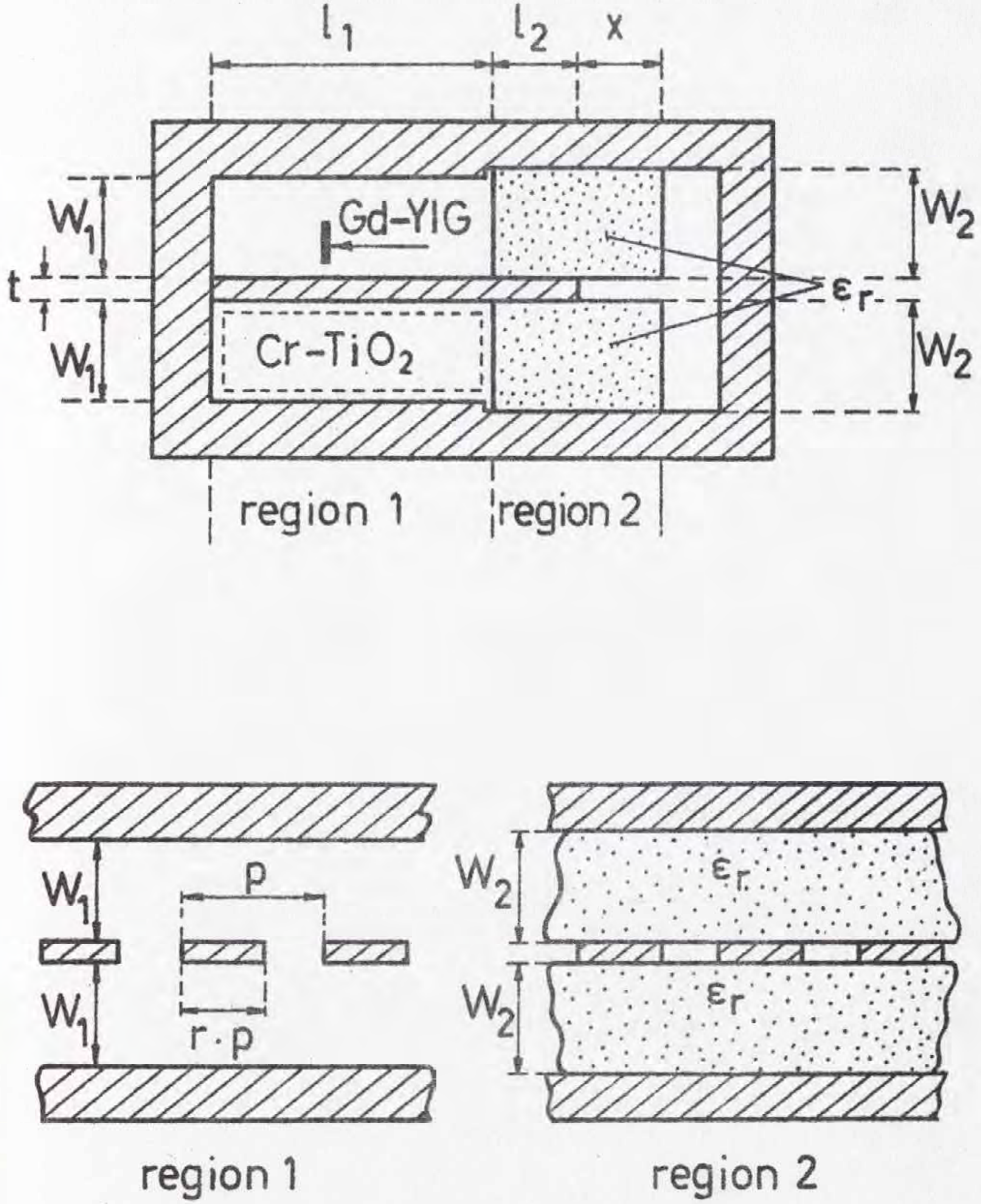

Fig. 2.2 Cross sections of the SWS.

$C_f(\varphi)$ is the stray capacitance at the open end of the conductors in region 2

p is the pitch

v_o is the velocity of light in vacuum.

C_d is the stray capacitance from the conductor to the wall of the ridge at the boundary between region 1 and 2, and

ε is the dielectric constant of the material related to C_d.

Moreover, we have, neglecting terms C_{fon}, $n = 2, 3, ..$ (Kollberg 1966 a)

$$C_f(\varphi) = 2\, C_{foo} + 4\, C_{fo1} \sin^2(\varphi/2) \tag{2.2}$$

where C_{foo} and C_{fo1} are certain fringing capacitances at the finger end in region 2, depicted by Kollberg (1966 a) Fig. 4.3.

A convenient approximation of eqn. (2.1) may be obtained in the following way. First assume $W_1 = W_2$ and $x = 0$. For this case one is allowed to put

$$C_f = C_d = 0 \tag{2.3}$$

It is not quite true that $C_f = 0$ for $x = 0$. However, for a reasonable high ε_r ($\varepsilon_r \gtrsim 10$) and $x = 0$, the influence of C_f is radically reduced, and may be neglected. Hence one obtains

$$\tan[\ell_1 \beta_1(\varphi)] \cdot \tan[\ell_2 \beta_2(\varphi)] = \frac{Y_1(\varphi)}{Y_2(\varphi)} \tag{2.4}$$

Since the fields are assumed to closely resemble TEM fields, we get for

region 1:

$$\beta_1(\varphi) = \frac{\omega}{v_o}\sqrt{\varepsilon_1(\varphi)} \tag{2.5}$$

$$Y_1(\varphi) = \sqrt{\varepsilon_1(\varphi)} \cdot Y_{10}(\varphi) \tag{2.6}$$

region 2:

$$\beta_2(\varphi) = \frac{\omega}{v_o}\sqrt{\varepsilon_2(\varphi)} \tag{2.7}$$

$$Y_2(\varphi) = \sqrt{\varepsilon_2(\varphi)}\; Y_{20}(\varphi) \tag{2.8}$$

where v_o is the velocity of light in vacuum, $\varepsilon_1(\varphi)$ and $\varepsilon_2(\varphi)$ are the relative dielectric constants, $Y_{10}(\varphi)$ and $Y_{20}(\varphi)$ are the characteristic admittances for $\varepsilon_1(\varphi) = \varepsilon_2(\varphi) = 1$.

Equations (2.5) to (2.8) are only true for low frequencies when the rf electric fields are almost independent of the rf magnetic fields.

Hence, the electric field configuration is equal to that obtained for the electrostatic case, and the magnetic field configuration is only determined by the current distribution on the conductor surface.

Eqn. (2.4) may now be transformed to

$$\tan\left[\ell_1 \frac{\omega}{v_o}\sqrt{\varepsilon_1(\varphi)}\right] \cdot \tan\left[\ell_2 \frac{\omega}{v_o}\sqrt{\varepsilon_2(\varphi)}\right] = \frac{Y_{10}(\varphi)\cdot\sqrt{\varepsilon_1(\varphi)}}{Y_{20}(\varphi)\sqrt{\varepsilon_2(\varphi)}} \qquad (2.9)$$

The cut-off frequency ω_o for $\varphi = 0$ is obtained from

$$\frac{\tan\left[\ell_1 \frac{\omega}{v_o}\sqrt{\varepsilon_1(0)}\right]}{\sqrt{\varepsilon_1(0)}} \cdot \tan\left[\ell_2 \frac{\omega}{v_o}\sqrt{\varepsilon_r}\right] = \frac{1}{\sqrt{\varepsilon_r}} \frac{Y_{10}(0)}{Y_{20}(0)} \qquad (2.10)$$

where we have used $\varepsilon_2(0) \approx \varepsilon_r$.
Let us define the following quantities:

$$x_1 = \ell_1 \frac{\omega}{v_o}\sqrt{\varepsilon_1(0)} \qquad (2.11)$$

$$x_2 = \ell_2 \frac{\omega}{v_o}\sqrt{\varepsilon_r} \qquad (2.12)$$

and for the SWS without the maser crystal,

$$x_{10} = \ell_1 \cdot \frac{\omega}{v_o} \qquad (2.13)$$

Thus, eqn. (2.10) becomes

$$\tan x_1 \cdot \tan x_2 = \frac{\sqrt{\varepsilon_1(0)}}{\sqrt{\varepsilon_r}} \quad \frac{Y_{10}(0)}{Y_{20}(0)} \qquad (2.14)$$

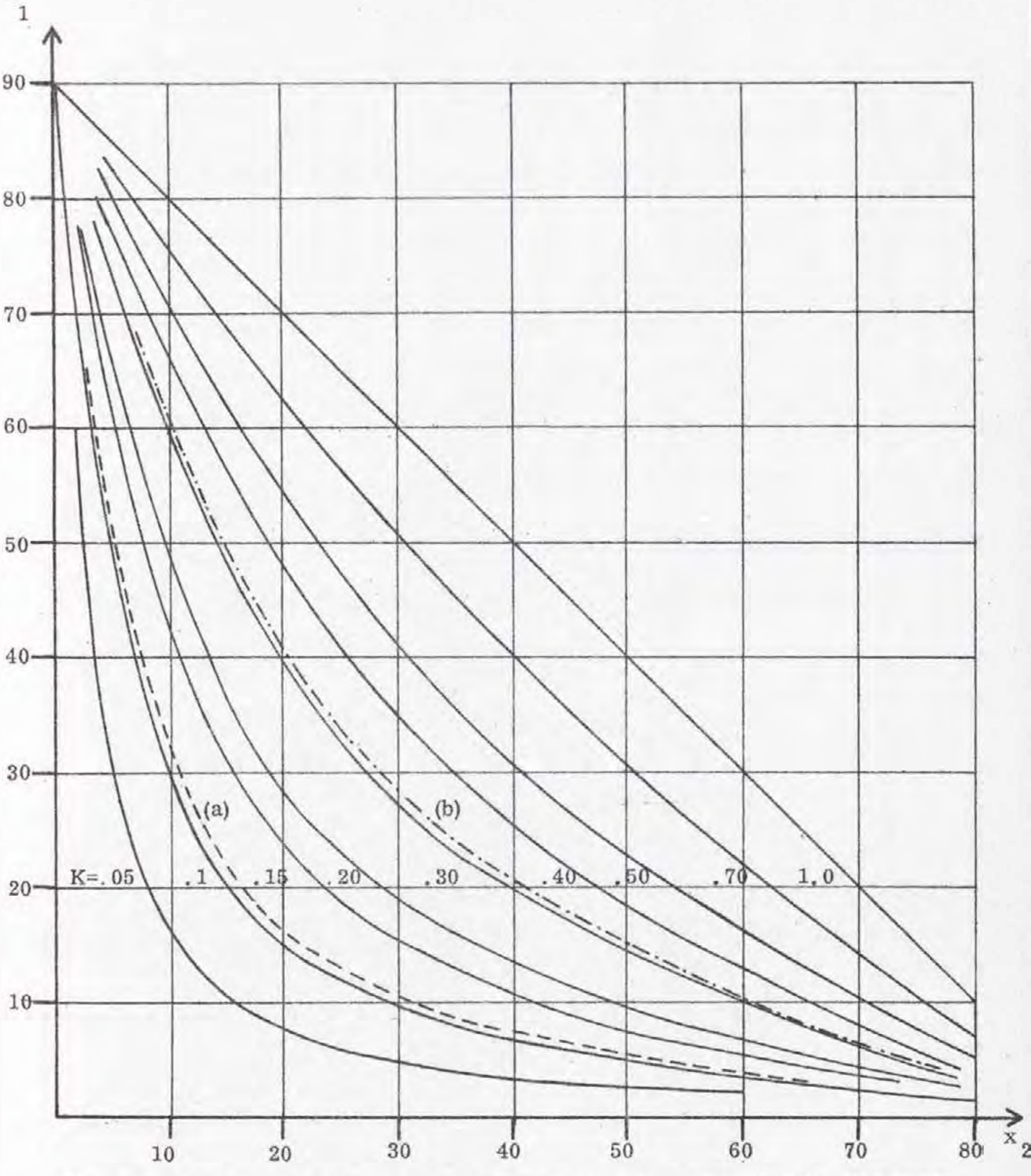

Fig. 2.3 x_1 vs x_2 for $\tan x_1 \cdot \tan x_2 = K$ = constant (see eqn. (2.14)). For curve (a), $K = 1 / \sqrt{85}$ and for curve (b), $K = 1 / \sqrt{10}$.

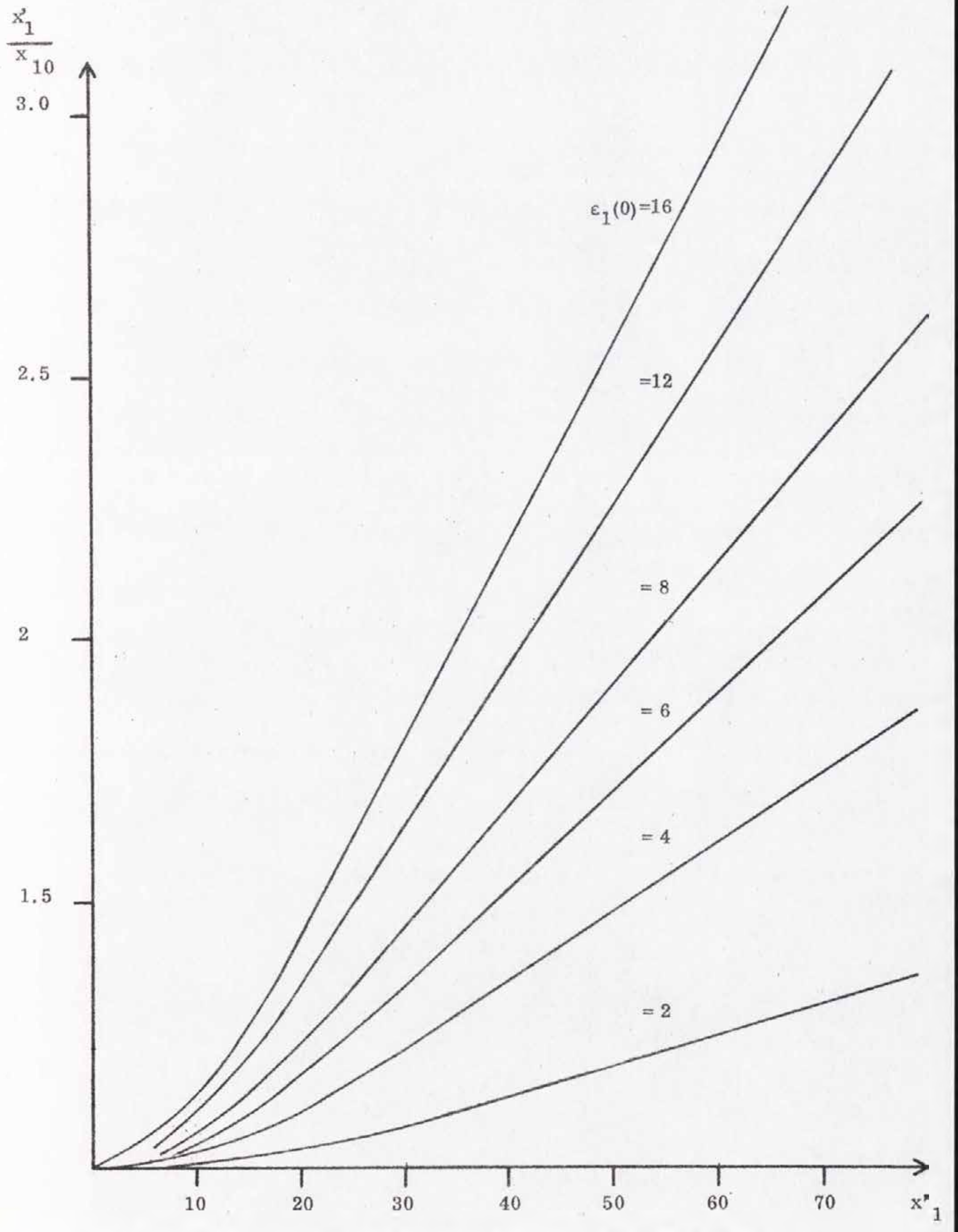

Fig. 2.4 x'_1/x_{10} vs. x'_1 for $\tan x'_1 = \tan\ (x_{10}\sqrt{\varepsilon_1(0)})/\sqrt{\varepsilon_1(0)}$
See eqn. (2.15).

In Fig. 2.3 we may find the values for x_1 and x_2 satisfying eqn. (2.14), when $\varepsilon_1(0)$, ε_r, $Y_{10}(0)$ and $Y_{20}(0)$ are known. However, it is often convenient to define an equivalent argument x_1' from

$$\tan x_1' = \frac{\tan x_1}{\sqrt{\varepsilon_1(0)}} = \frac{\tan\left(x_{10} \cdot \sqrt{\varepsilon_1(0)}\right)}{\sqrt{\varepsilon_1(0)}} \tag{2.15}$$

This argument can be used in eqn. (2.14), yielding a right hand side value, smaller by a factor $1/\sqrt{\varepsilon_1(0)}$. In Fig. 2.4 the relation between x'_1 and x_{10} is depicted for various values of $\varepsilon_1(0)$. Fig. 2.4 may be used when the effect of inserting the maser crystal into the SWS is considered, and to predict the lower cut-off frequency vs the position of the maser crystal in the SWS (section 6.4).

In order to show how different parameters affect the SWS dispersion characteristics, let us use a Taylor series expansion for the tangent functions, and neglect terms of the second order. Hence we obtain approximately

$$\tan\left(\ell_1 \frac{\omega}{v_o} \sqrt{\varepsilon_1(\varphi)}\right) = \tan x_1 + \frac{\Delta\left(\ell_1 \frac{\omega}{v_o} \sqrt{\varepsilon_1(\varphi)}\right)}{\cos^2 x_1} \tag{2.16}$$

$$\tan\left(\ell_2 \frac{\omega}{v_o} \sqrt{\varepsilon_2(\varphi)}\right) = \tan x_2 + \frac{\Delta\left(\ell_2 \frac{\omega}{v_o} \sqrt{\varepsilon_2(\varphi)}\right)}{\cos^2 x_2} \tag{2.17}$$

A measure of the accuracy of eqn. (2.16) and (2.17) is obtained from a calculation of the ratio between the third and the second term, which becomes

$$(\tan x_{\substack{1\\2}})^2 \cdot k_{\substack{1\\2}} \quad \frac{\Delta\left(\ell_{\substack{1\\2}} \frac{\omega}{v_o} \sqrt{\varepsilon_{\substack{1\\2}}(\varphi)}\right)}{x_{\substack{1\\2}}}$$

where

$$k_1 = \frac{2\,x_1}{\sin 2\,x_1} \tag{2.18}$$

$$k_2 = \frac{2\,x_2}{\sin 2\,x_2} \tag{2.19}$$

Here, k_1 and k_2 are constants depicted in Fig. 2.5. In TWM:s discussed in this paper, $\Delta(\ell\omega/v_o\sqrt{\varepsilon(\varphi)})/x$ is less than 0.2 and $(\tan x)^2$ is in most of the TWM:s less than 0.5 (see Table 6.I), i.e. eqn. (2.16) and (2.17) yield very good approximations and the values for k_1 and k_2 are of order unity.

Using eqn. (2.9) and (2.16) - (2.19) we obtain the following approximation for the dispersion characteristic:

$$\frac{\omega}{\omega_o} = \sqrt{\frac{\varepsilon_2(0)}{\varepsilon_2(\varphi)}}\left\{1 - \frac{k_1 - 1}{k_1 + k_2}\left(\sqrt{\frac{\varepsilon_1(\varphi)\cdot\varepsilon_2(0)}{\varepsilon_1(0)\cdot\varepsilon_2(\varphi)}} - 1\right) + \right.$$

$$\left. + \frac{1}{k_1 + k_2}\left(\frac{y_1(\varphi)}{y_2(\varphi)} - 1\right)\sqrt{\frac{\varepsilon_1(\varphi)\,\varepsilon_2(0)}{\varepsilon_1(0)\,\varepsilon_2(\varphi)}}\right\} \tag{2.20}$$

where

$$\frac{y_1(\varphi)}{y_2(\varphi)} = \frac{Y_1(\varphi)}{Y_1(0)}\cdot\frac{Y_{20}(0)}{Y_{20}(\varphi)} \tag{2.21}$$

2.3 The special case $W_1 = W_2$, $x = 0$

When $W_1 = W_2$, one has $y_1(\varphi)/y_2(\varphi) - 1 = 0$. For small arguments x_1, $k_1 - 1 \approx 0$ (see Fig. 2.5) and the dispersion relation simplifies to

$$\frac{\omega}{\omega_o} = \sqrt{\frac{\varepsilon_2(0)}{\varepsilon_2(\varphi)}} \tag{2.22}$$

From the "equal-charge approximation" (Kollberg 1966) we obtain

$$\frac{\omega}{\omega_o} = \sqrt{\frac{C_{20}(\varphi)}{C_2(\varphi)}} \tag{2.23}$$

where $C_{20}(\varphi)$ is the conductor capacitance per unit length for a cross section equal to that of region 2, but completely filled with dielectric material, and

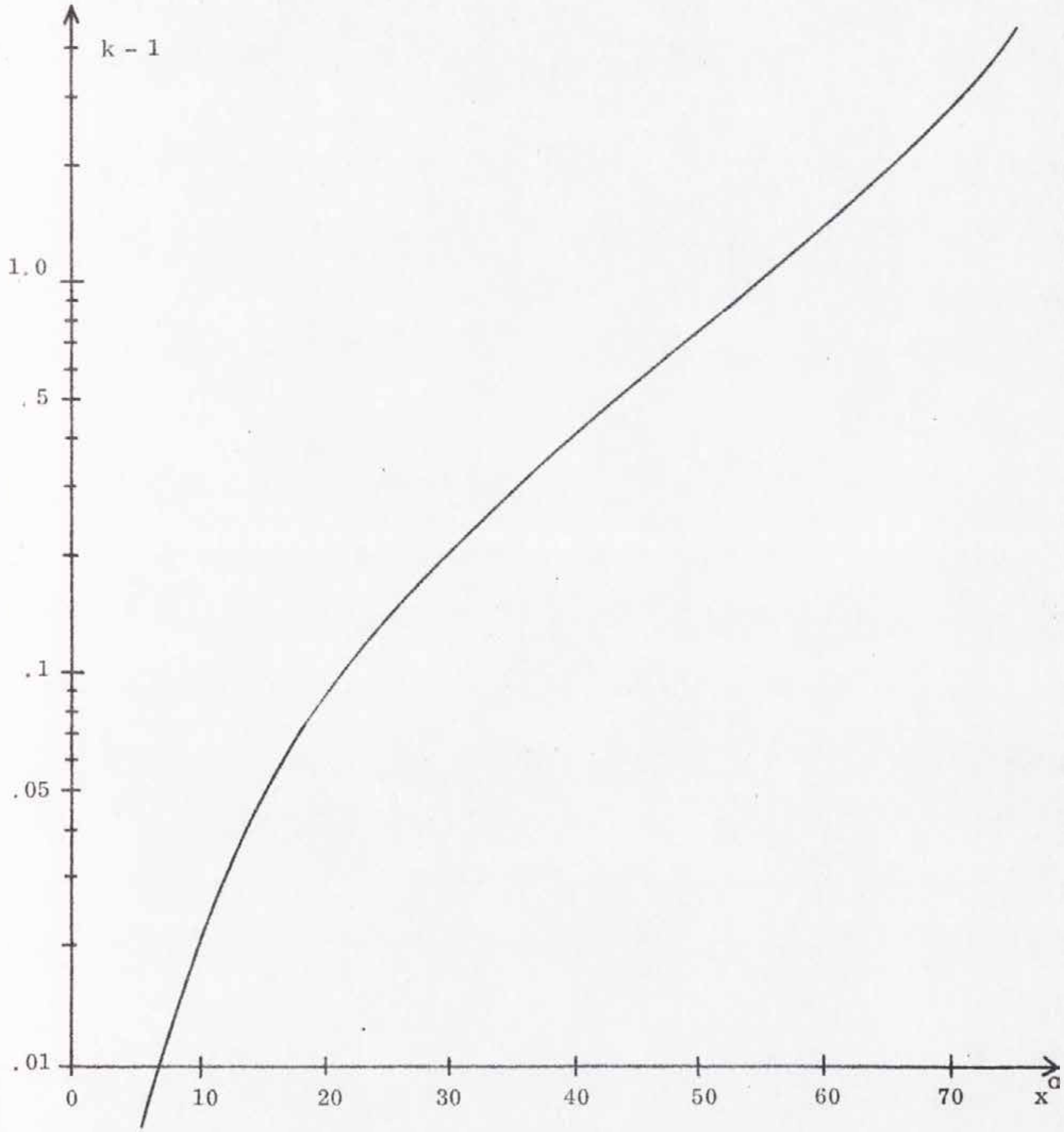

Fig. 2.5 Depicts k - 1 vs. x, where $k = \frac{2x}{\sin 2x}$. See eqn. 2.18 and 2.19.

$C_2(\varphi)$ is the conductor capacitance per unit length when the dielectric material between the conductors is removed. We now obtain

$$\frac{C_{20}(\varphi)}{C_2(\varphi)} = \frac{Y_{20}(\varphi)}{Y_{20}(\varphi) - 4\,y_t\,(1 - \frac{1}{\varepsilon_r})\sin^2 \varphi/2} \tag{2.24}$$

Using eqn. (2.23) and (2.24) we obtain approximately

$$\frac{\omega}{\omega_o} \approx 1 + \frac{4\,y_t\,(1 - \frac{1}{\varepsilon_r})}{2} \; \frac{\sin^2 \varphi/2}{Y_{20}(\varphi)} \tag{2.25}$$

Neglecting the terms y_{on}, $n = 2, 3 \ldots$ we obtain for $Y_{20}(\varphi)$ the following relation,

$$Y_{20}(\varphi) = Y_{20}(0) + [\,Y_{20}(\pi) - Y_{20}(0)\,]\,\sin^2 \varphi/2 \tag{2.26}$$

This relation is exact for $\varphi = 0$ and $\varphi = \pi$, and the maximum error for $W/p < 1.5$ is less than 10 % (see Kollberg 1967).

Using

$$a = \frac{Y_{20}(\pi) - Y_{20}(0)}{Y_{20}(0)} \tag{2.27}$$

together with eqn. (2.25) and (2.26), we may calculate the slowing factor

$$S = \frac{v_o}{p \cdot \frac{d\omega}{d\varphi}} = \frac{\lambda_o}{p} \cdot \frac{2\,Y_{20}(\pi)}{\pi \cdot 4\,y_t\,(1 - \frac{1}{\varepsilon_r})} \cdot F(a, \varphi) \tag{2.28}$$

where

$$F(a, \varphi) = \frac{(1 + a \sin^2(\varphi/2))^2}{(1 + a)\sin\varphi} \tag{2.29}$$

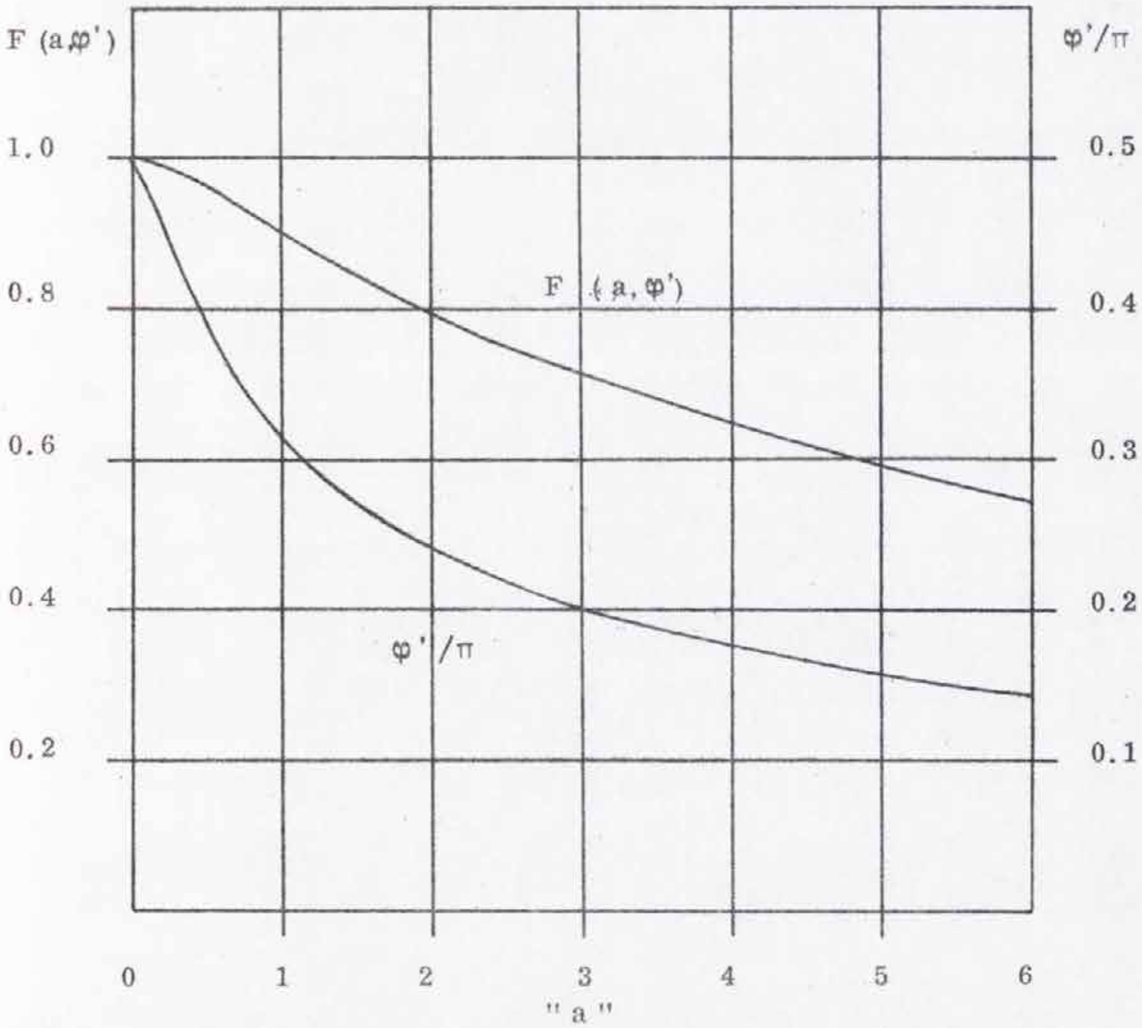

Fig. 2.6 F (a, φ') and φ'/π vs. "a" is depicted.
The minimum slowing factor S_{min} is proportional to F (a, φ') and is obtained at the phase angle φ'.

The minimum slowing factor is obtained for $\varphi = \varphi'$, where φ' satisfies

$$a \cos^2 \varphi' + (2 + a) \cos \varphi' - 2a = 0 \tag{2.30}$$

In Fig. 2.6 F (a, φ') and φ' vs. a is shown.

From eqn. (2.25) and (2.28) we notice that y_t is an extremely important quantity. From eqn. (2.24) it is seen that

$$\frac{4 y_t \left(1 - \frac{1}{\varepsilon_r}\right)}{Y_{20}(\pi)} = \frac{C_{20}(\pi) - C_2(\pi)}{C_{20}(\pi)} \tag{2.31}$$

In order to obtain more reliable numerical values for $4 y_t \left(1 - \frac{1}{\varepsilon_r}\right)$ we decided to compute $C_{20}(\pi)$ and $C_2(\pi)$ by using the Laplace equation, the finite difference method (Green 1965) and a digital computer. Since the computer time required turned out to be quite long we made the computation only for one SWS geometry $t/p = 0.06$, $r = 0.5$, $W/p = 1.52$ and for $\varepsilon_r = 85$ and 10 with the following result:

	$\frac{C_{20}(\pi)}{\varepsilon_o \cdot \varepsilon_r}$	$\frac{C_2(\pi)}{\varepsilon_o \varepsilon_r}$	$\frac{4 y_t (1-1/\varepsilon_r)}{2 Y_{20}(\pi)}$	$\frac{2 Y_{20}(\pi)}{\pi \cdot 4 y_t (1-1/\varepsilon_r)}$
$\varepsilon_r = 85$	4.85	4.23	0.064	4.97
$\varepsilon_r = 10$	4.85	4.29	0.057	5.54

Since $Y_{20}(\pi)$ is almost a constant for $W/p > 1$, and since y_t for a certain ε_r and r is almost only dependent on t/p, we may, for $t/p > 0.06$ and $r = 0.5$, add a homogeneous field contribution for y_t,

$$\Delta \left(\frac{4 y_t}{Y_o}\right) = 8(t/p - 0.06) \tag{2.32}$$

2.4 The case $W_1 \neq W_2$ and $x \neq 0$

The effect of having $W_2 \neq W_1$ and $x = 0$ is shown in Fig. 2.7. Making $W_2 < W_1$ decreases the lower cut-off frequency and leaves the upper part of the dispersion relation almost unaffected. Hence the slowing factor becomes smaller and is less

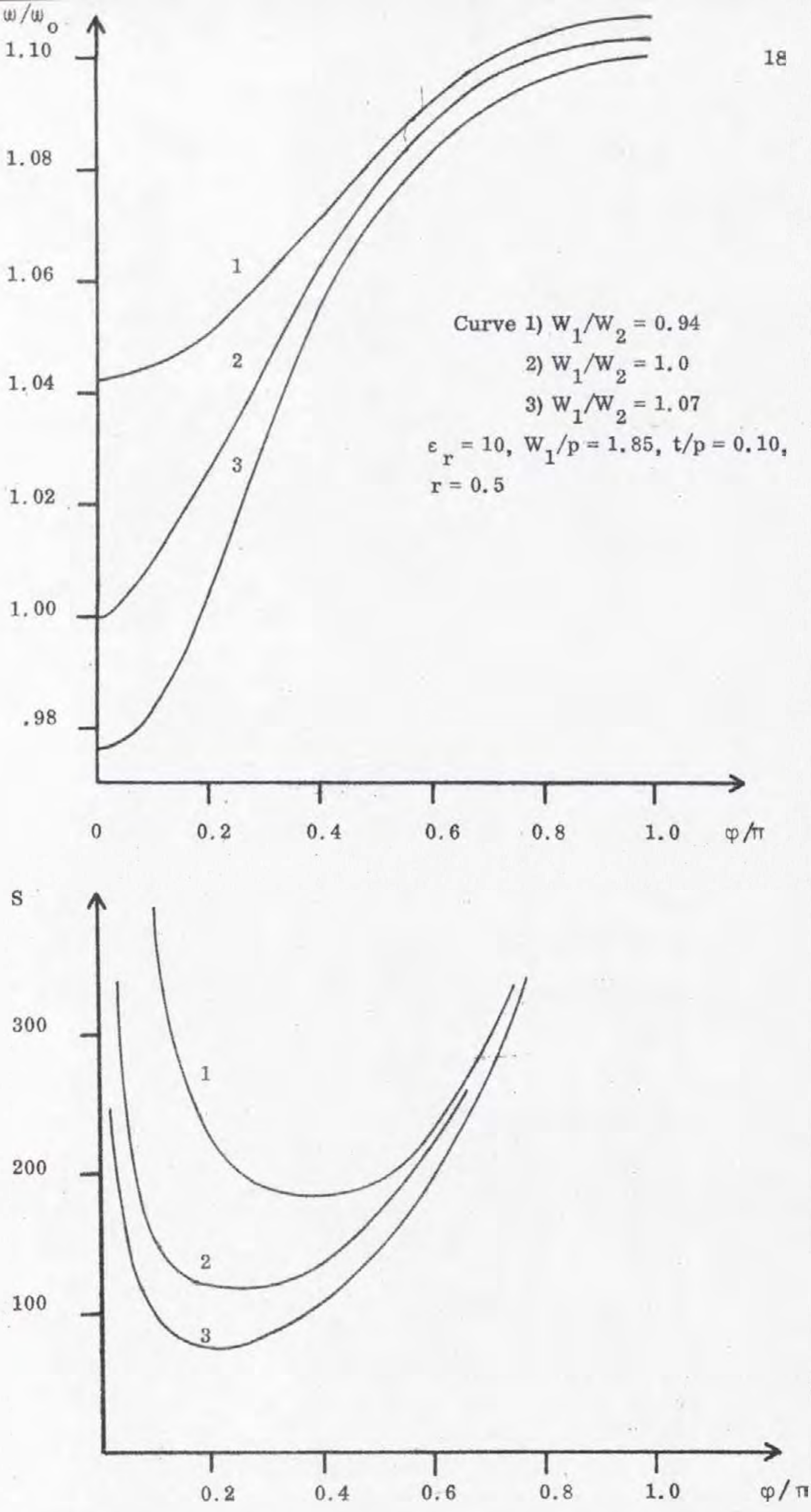

Fig. 2.7 Dispersion characteristic and the slowing factor vs. φ/π for different W_1/W_2.

constant with frequency than for $W_1 = W_2$. On the other hand, making $W_2 > W_1$ increases the lower cut-off frequency and still leaves the upper part of the frequency band unchanged. Hence the slowing factor increases and also becomes more constant with frequency than for $W_1 = W_2$.

It is evidently favorable to make $W_2 > W_1$, since one obtains a more effective form of the $\omega - \varphi$ diagram, which yields a higher slowing factor for a given frequency band or a larger frequency band for a given slowing factor.

Equations (2.20) and (2.14) are extremely useful for the understanding and the design of a SWS with $x = 0$ but $W_1 = W_2$. However, when $x \neq 0$, $C_f(\varphi)$ must be considered. Re-arranging eqn. (2.1) yields

$$\tan \phi_1 \cdot \tan \phi_2 = \frac{Y_1(\varphi)}{Y_2(\varphi)} \left\{ 1 - \frac{\omega \varepsilon_r C_f(\varphi)}{\mathrm{tg}\, \phi_2 \cdot Y_2(\varphi)} \left(\tan^2 \phi_2 + \frac{Y_2(\varphi) \cdot \tan \phi_1 \cdot \tan \phi_2}{Y_1(\varphi)} \right) \right\} \tag{2.33}$$

where

$$\phi_1 = \ell_1 \frac{\omega}{v_o} \sqrt{\varepsilon_1(\varphi)} \tag{2.34}$$

$$\phi_2 = \ell_2 \frac{\omega}{v_o} \sqrt{\varepsilon_2(\varphi)} \tag{2.35}$$

For $C_f(\varphi) = 0$ the second term in the large parenthesis of eqn. (2.33) disappears. Moreover we have approximately

$$\frac{\omega \varepsilon_r C_f(\varphi)}{\mathrm{tg}\, \phi_2 \cdot Y_2(\varphi)} \approx \frac{p}{\ell_2} \cdot \frac{C_f(\varphi) / p\, \varepsilon_o}{Y_{20}(\varphi)/Y_o} \tag{2.36}$$

where $C_f(\varphi)/p\, \varepsilon_o$ is obtained from Kollberg (1966 a, Fig 4.3) It can be seen from eqn. (2.33) and from Fig. 4.3 in Kollberg (1966 a) that for ℓ_2 constant and increasing x, one obtains a larger decrease of the $\varphi = 0$ cut-off frequency than of the $\varphi = \pi$ cut-off frequency. Hence, the SWS band-width increases and the slowing factor decreases.

3. ISOLATION OF THE TWM

3.1. Introductory remarks

The rf magnetic fields in a SWS utilizing parallel conductors (see Fig. 3.1) are to a great extent circularly polarized with the sense of polarization different above and below the conductors. When the wave propagation direction changes, the sense of polarization also changes. By placing a ferrimagnetic material on one side of the conductor array and applying a certain magnetic field parallel to the conductors, reflected waves in the SWS will be attenuated by ferrimagnetic absorption. The forward wave will not be affected by the ferrimagnetic material if the rf magnetic fields are perfectly circularly polarized.

However, at the metallic boundary surfaces the rf magnetic field is linearly polarized in a direction parallel to the surface. Hence the maximum circular polarization is obtained some distance away from the conductors and the ground planes.

The amount of absorption of the backward and the forward wave, A_B and A_F respectively, is determined by

$$A_{\substack{B\\F}} = 27.3 \cdot \frac{L}{\lambda_o} S(\varphi) \cdot \frac{1}{Q_{\substack{B\\F}}} \qquad \text{(dB)} \tag{3.1}$$

where λ_o is the freee space wavelength, $S(\varphi)$ is the slowing factor, Q_F and Q_B are the quality factors associated with the ferrimagnetic resonance absorption for the forward and backward waves, respectively, and L is the length of the isolated region. Furthermore, assuming the backward wave to have a predominantly positive circular polarization and d to be small compared to ℓ_1, we obtain

$$\frac{1}{Q_B} = \frac{d}{\ell_1} \cos^2\left(\frac{y_o}{\ell_1}\beta_1\right) \eta_1 \cdot \eta_+ \chi''_+ \tag{3.2}$$

$$\frac{1}{Q_F} = \frac{d}{\ell_1} \cos^2\left(\frac{y_o}{\ell_1}\beta_1\right) \eta_1 \cdot \eta_- \chi''_+ \tag{3.3}$$

where

d is the thickness of the ferrite slab

ℓ_1 is the conductor length in region 1 (Fig. 5.2),

y_o is the position of the ferrite slab, measured from the shorted end of the conductors

β_1 is the TEM wave propagation constant of region 1 (Fig. 5.2),

η_1 is the ratio of rf magnetic energy in region 1 (Fig. 5.2) to the total rf magnetic energy (see Kollberg 1966, Chapter 7)

η_+, η_- are the ratios of the energy of the rf magnetic field due to the positive and negative circularly polarized components, respectively, over the area occupied by the ferrite slab to the total rf magnetic field energy contained in the area in the x - z plane (Fig. 3.1).

χ''_+ is the imaginary part of ferrimagnetic susceptibility for positive circularly polarized fields.

It is assumed that χ''_-, the susceptibility for negative circularly polarized fields, can be neglected, which is strictly true only if the isolator material is completely saturated and if the ferrimagnetic resonance line is not homogeneously broadened.

Using the space harmonic analysis one may calculate η_+ and η_- in eqn:s (3.2) and (3.3). Chen (1964) has published a number of useful graphs showing the variation of η_+ and η_- with the phase angle per period φ for various SWS geometries and small rectangular ferrite samples. However, Chen's calculations rely on some approximations, yielding results with an unknown accuracy.

According to the ideal conducting sheet approximation for the conductor array (t=0), (Siegman 1964), the rf magnetic fields are everywhere perfectly circularly polarized and the amplitude of the field away from the conductor array varies as $e^{-\varphi\frac{|x|}{p}}$ (see Fig. 3.1). Since the attenuation of the backward (and forward) wave is proportional to the rf magnetic energy density, the attenuation due to a ferri-magnet at $x = x_o$ is proportional to $e^{-2\varphi\frac{x_o}{p}}$

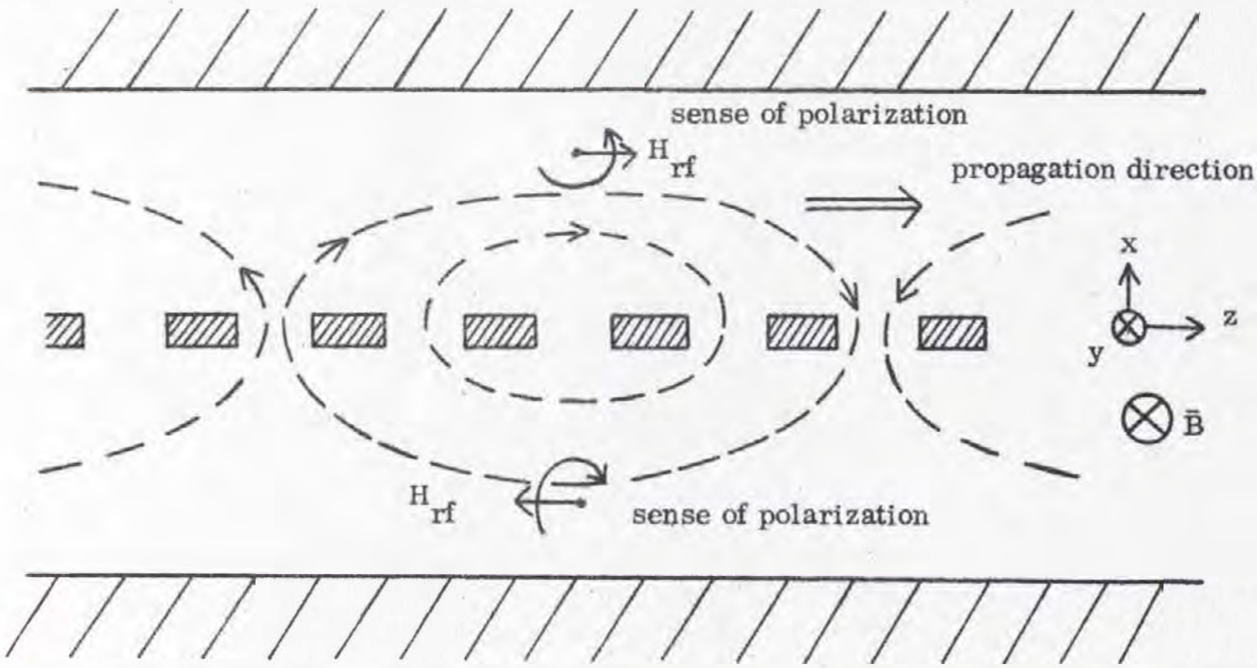

Fig. 3.1. The rf-magnetic field in a transverse conductor SWS. The phase shift per period is $\pi/8$.

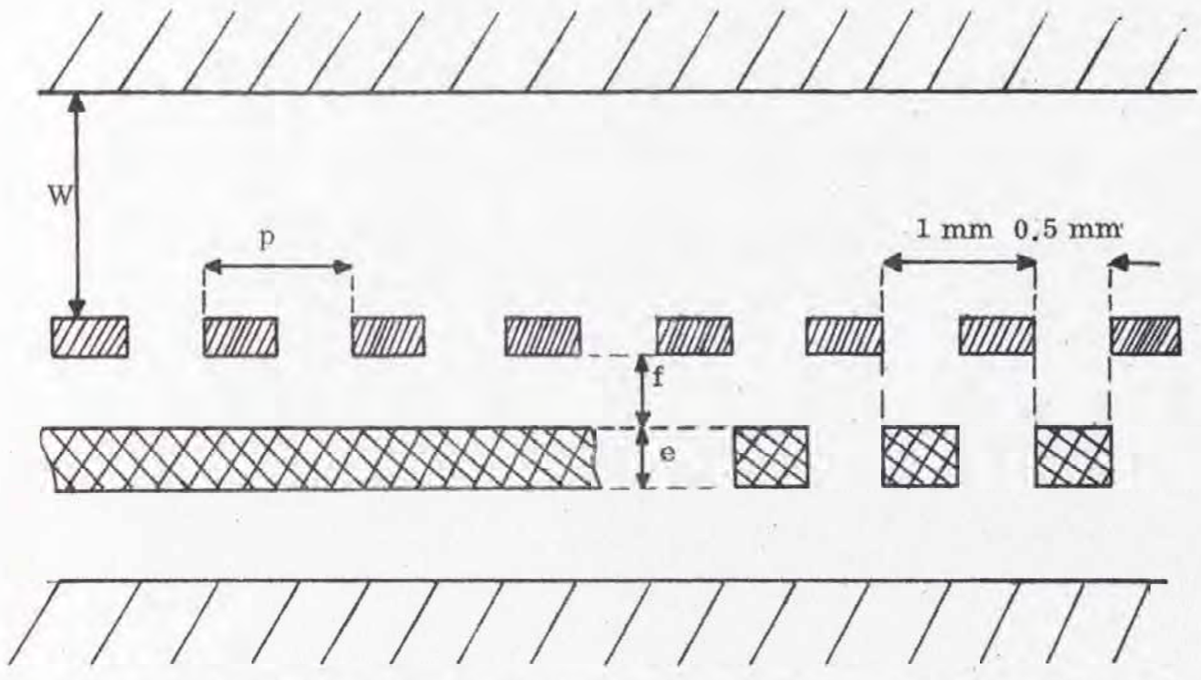

Fig. 3.2 The SWS isolator configuration (see also Fig. 6.4). The right part of the figure shows divided ferrite bar configuration.

The magnetic field required for ferrimagnetic resonance absorption to occur at a certain frequency depends on the geometry of the ferrite sample. For small ellipsoidal samples, the resonance frequency ω_o is given by the Kittell formula (Kittell 1948)

$$\left(\frac{\omega_o}{\gamma\mu_o M_s}\right)^2 = \left[\frac{H_o}{M_s} + (N_x - N_z)\right]\left[H_o/M_s + (N_y - N_z)\right] ,$$

where

$$N_x + N_y + N_z = 1,$$

and

ω_o is the angular frequency,
γ is the gyromagnetic ratio ($\gamma / 2\pi = 2.8$ MHz/Gauss).
μ_o is the free space permeability ($4\pi \cdot 10^{-7}$ H/m),
M_s is the saturation magnetization of the ferrite,
H_o is the external magnetic field, and
N_x , N_y , N_z are the demagnetizing factors.

The dc magnetic field is applied along the z-axis. The demagnetizing factors may be calculated only for ellipsoidal samples (Osborn 1945) since the internal magnetic field is not homogeneous for any other shape. However, useful results are obtained for discs and cylinders if they are considered as ellipsoids of revolution, and for rectangular bars if they are treated as very slender ellipsoids.

The shapes of the ferrimagnetic materials used in the maser reported in the present paper are "infinitely long" bars with rectangular cross-section, extended along the whole SWS, and cubical pieces placed periodically along the SWS. The "infintely long" bar with the cross-section dimensions d and e ("d" is along the magnetic field) may be treated as an infinitely long ellipsoid with the transverse axis equal to d and e, respectively. One obtains (Osborn 1945):

$$N_x = 0 \qquad\qquad N_z = 1 - N_y = \frac{e}{d+e}$$

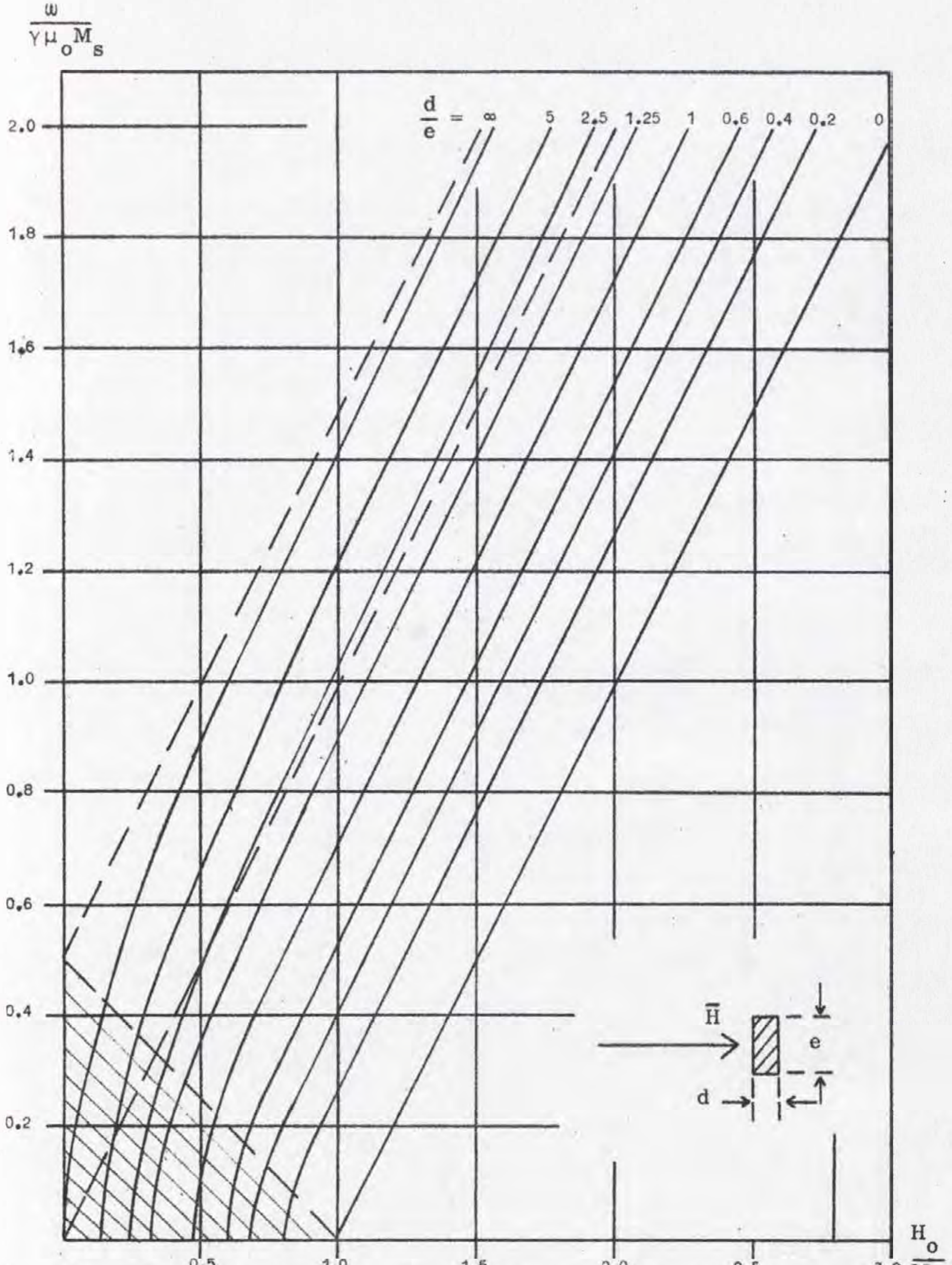

Fig. 3.3 Normalized resonance frequency vs the normalized magnetic field for various bar cross section dimensions.

yielding the resonance frequency

$$\left(\frac{\omega_o}{\gamma\mu_o M_s}\right)^2 = \left(\frac{H}{M_s} - \frac{e}{d+e}\right)\left(\frac{H}{M_s} + \frac{d-e}{d+e}\right)$$

In Fig. 3.3 the resonance frequency vs the external magnetic field has been plotted using the Osborn theory and helpful graphs given by P. Hlawiczka et al. (1963). When the bar is divided into a number of cubical pieces (Fig. 3.2, right part) having a width equal to their spacing (equal to half the pitch), one obtains a change in the resonance frequency, equivalent to a decreased value for d (see Fig. 3.3)

There are two circumstances that lead to a departure from the ideal theoretical situation:

a) the geometry of the sample is not ellipsoidal

b) the rf magnetic field is not constant in polarization and amplitude over the sample.

Point a) means that no homogeneous dc magnetic field can exist within the sample, thus causing a broadened resonance, line absorption.
Point b) means that magnetostatic modes (Lax and Button, 1962) will be excited. This might in practice be considered as a helpful broadening of the resonance line.

3.2 Isolator Material

When the Cr-TiO_2 c-axis operating point is used for L-band TWM:s (see chapter 4), the appropriate magnetic field requires a ferrimagnetic material with a low saturation magnetization for the isolator operating point not to be in the unsaturated region (shaded area in Fig. 3.3). An investigation made by Yngvesson (1965) has shown that aluminium-doped yttrium-iron garnet (Al-YIG) (aluminium substitutes for iron). made from extremely pure Y_2O_3 powder (99,999 % pure Y_2O_3) is efficient for isolating TWM:s using Cr-TiO_2 down to frequencies of about 1000 MHz. The material used in Yngvesson's investigation (and used in the MAL 1 TWM discussed in section 7.3) was supplied by dr. P. E. Ljung, Swedish Defence Research Institute. The composition of the material is

$$3\,Y_2O_3\;[5-x]\;Fe_2O_3\cdot[x]\;Al_2O_3$$

The best material had $x = 0.72$, and the room temperature saturation magnetization was 680 Gauss (see Yngvesson 1965). At 4.2^{o} K the saturation magnetization increases. A similar commercial material (Trans-Tech Inc., G - 610) had $\mu_o M_s$ = 680 Gauss at room temperature and about 1200 Gauss at 4.2^{o}K (Yngvesson 1965). However, at 4.2^{o} K Yngvesson found an anomalous unsaturated resonance absorption with the peak absorption frequency decreasing with increasing magnetic field. Moreover, he also found that the resonance absorption rapidly disappears when the frequency is lowered towards 1000 MHz.

For $x = 0$, i.e. pure YIG, the saturation magnetization is 1800 Gauss at room temperature and around 2 500 Gauss at 4.2^{o}K. Hence, for frequencies lower than 1800 MHz and using the c, 1-2 transition of $Cr\text{-}Ti0_2$, operation takes place in the unsaturated region. For the c, 3-4 transition of $Fe\text{-}Ti0_2$ this lower frequency is about 2 400 MHz.

Gadolinium doped YIG was reported by Morris and Miller (1964) to be another ferrimagnetic material useful in TWM:s using $Cr\text{-}Ti0_2$ as a maser material. The composition of this material is

$$3\,[\,(1-x)\,Y_2 0_3 \cdot x\,Gd_2 0_3] \cdot 5\,Fe_2 0_3$$

With only 5 % Gd substituted for Y, the 4.2^{o}K saturation magnetization decreased from 2 500 Gauss to about 1700 Gauss. Low-field losses using $Cr\text{-}Ti0_2$ should disappear with this material at 1250 MHz and for $Fe\text{-}Ti0_2$ at 1650 MHz. Walker (1965) noticed a decrease in the ratio of backward wave absorption to forward wave absorption for frequences below 1 400 MHz. We have used Gd-YIG in a number of TWM:s (see section 7.3).

3.3 Experimental investigation of the isolator performance.

The shape of an "infinitely long" bar was considered for the isolator, since this shape is easy to fabricate and mount on a substrate. The behaviour of an isolator with such a geometry cannot be predicted from the graphs given by Chen (1964), since they were calculated for small samples (square cross section in the xz-plane with $e/p \approx 0.25$). Moreover, those graphs are restricted to SWS geometries with $W/p \lesssim 1$. (Fig. 3.2).

Experiments with a bar shaped garnet were made at L-band in a SWS with $r = 0.5$, $p = 1$ mm and $W/p = 2.0$. By measuring the dispersion characteristic of the SWS, the isolator attenuation can be presented vs the phase shift per period "φ", rather than vs frequency. Hence, the results may be used for any SWS with the same relative cross-section and the same relative e/p value.

In Fig. 3.4 the backward wave attenuation vs φ is depicted. For $\varphi \to 0$ we expect $A_B \to \infty$, since theoretically $S(\varphi) \to \infty$ when $\varphi \to 0$. We can see that the variation with x and φ somewhat resembles the expected behaviour from the conducting sheet approximation. In Fig. 3.5 the ratio A_B/A_F vs φ is depicted. Quite high ratios A_B/A_F are obtained for $f = 0.25$ mm with the peak at $\varphi/\pi = 0.4$. For increasing values of f, the maximum ratio becomes smaller and the maximum moves to higher values of φ.

For φ/π smaller than 0.25, the A_B/A_F ratio is less than 10. As $\varphi'/\pi = 0.25$ is equivalent to a comparatively small b-value (section 2.3, Fig. 2.6) another shape of the garnet should be investigated. Since the circular polarization of the fields for low values of φ/π evidently is more pronounced midway between adjacent conductors, a better performance should be obtained if the garnet material below the conductors were removed.

An experimental investigation was performed in a SWS for 4.5 - 5.2 GHz. An "infinitely" long garnet bar glued on an aluminium substrate and with $d = 0.18$ mm and $e = 0.35$ mm was investigated in a SWS with $p = 1$ mm and $W/p = 1.50$. When the measurements on the long bar were finished, 0.5 mm garnet material in each period was removed as indicated in the right part of Fig. 3.2. In Fig. 3.6 and 3.7 the effect of dividing the garnet bar is described. In Fig. 3.6 it is seen that (as expected) the sum of A_B for the garnet positioned midway between adjacent conductors and A_B for the garnet position exactly below the conductors is equal to A_B for the undivided bar.

In Fig. 3.8 and 3.9 A_B and A_B/A_F are investigated for a divided bar with the pieces midway between adjacent fingers and for different distances "f" between the isolator and the conductor plane. It is seen that the A_B/A_F ratio is quite high over a wide range of "f"-values. Hence "f" should be chosen to yield the required amount of backward isolation.

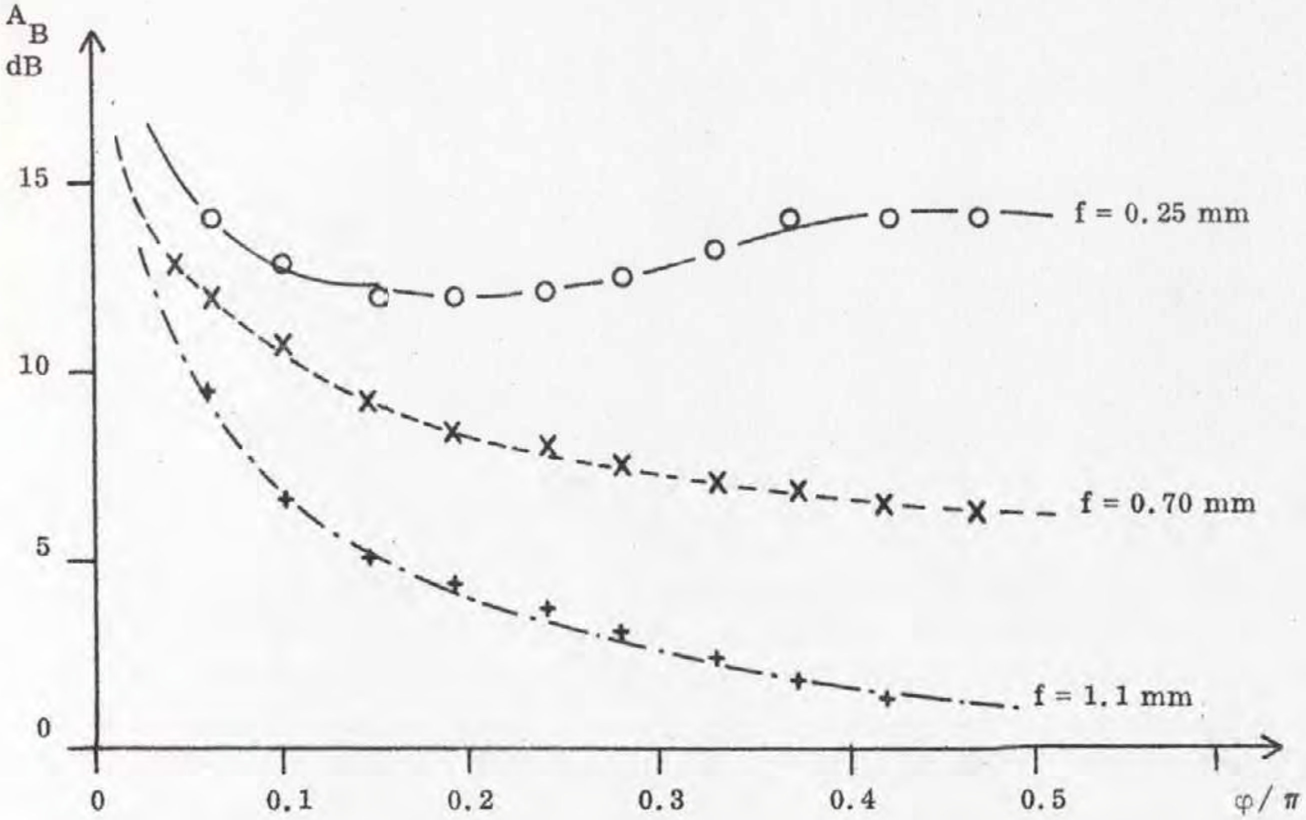

Fig. 3.4 Performance of the backward wave attenuation for an "infinitely" long isolator bar. d = 0.22 mm, e = 0.70 mm, W/p = 2 and p = 1 mm.

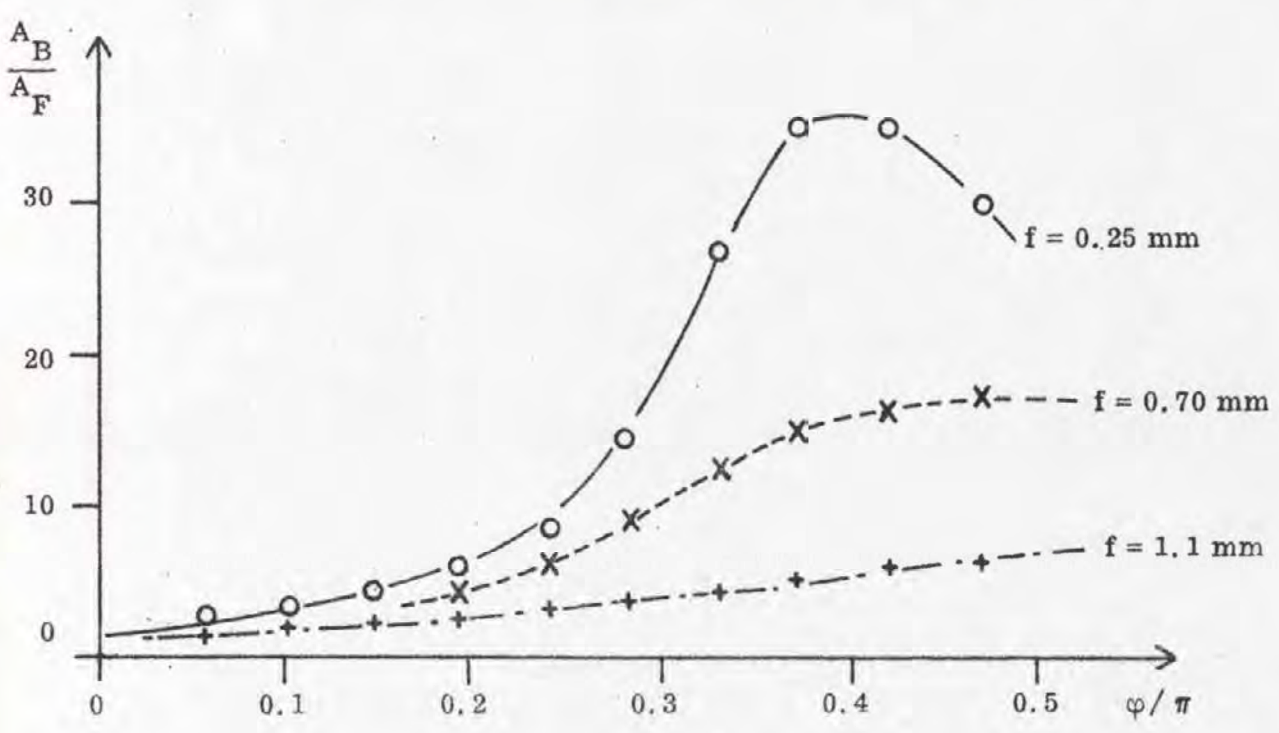

Fig. 3.5 Performance of the ratio backward wave attenuation (dB) to forward wave attenuation (dB) as a function of φ/π. d, e and W/p as in Fig. 3.4.

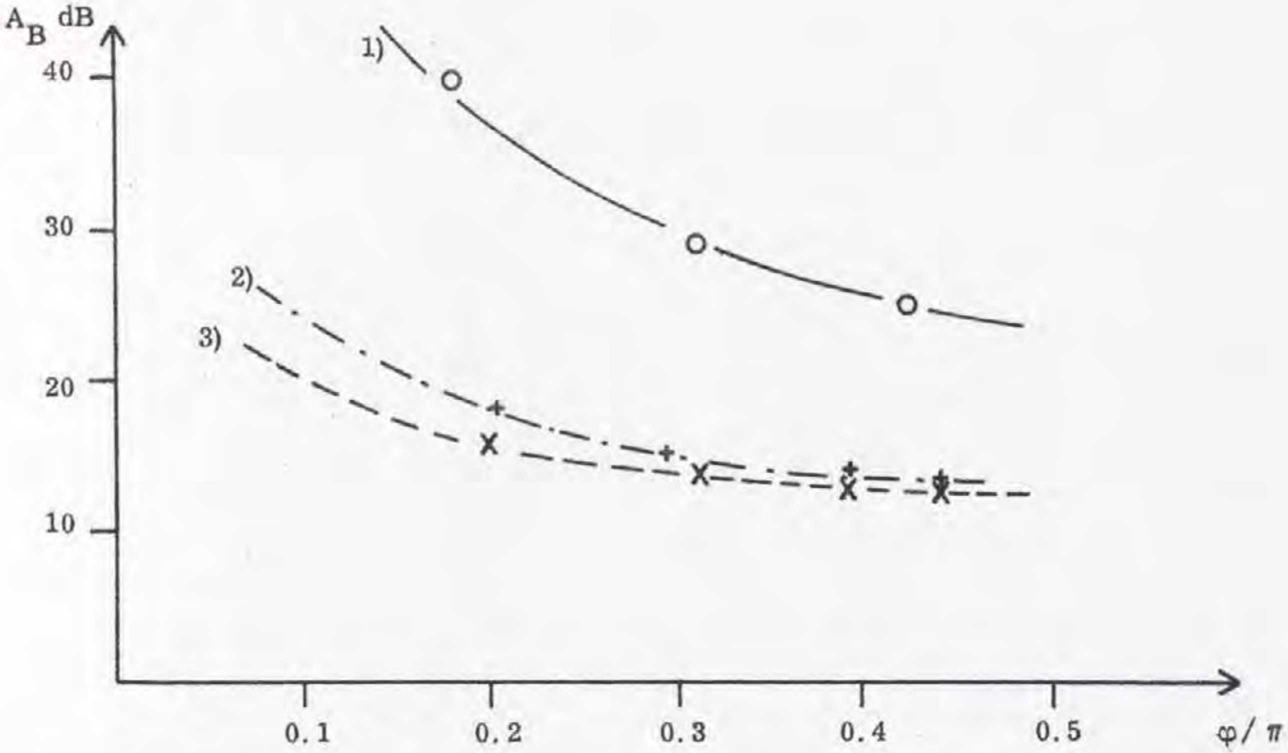

Fig. 3.6 Effects of dividing the isolator bar. The figure depicts the attenuation for the backward wave as a function of φ/π. 1): "infinitely" long garnet bar, 2): divided bar, isolator pieces below the conductors, 3): divided bar isolator pieces midway between adjacent conductors. For 1), 2) and 3), f = 0.57 mm, d = 0.18 mm, e = 0.35 mm, W/p = 1.5 and p = 1 mm.

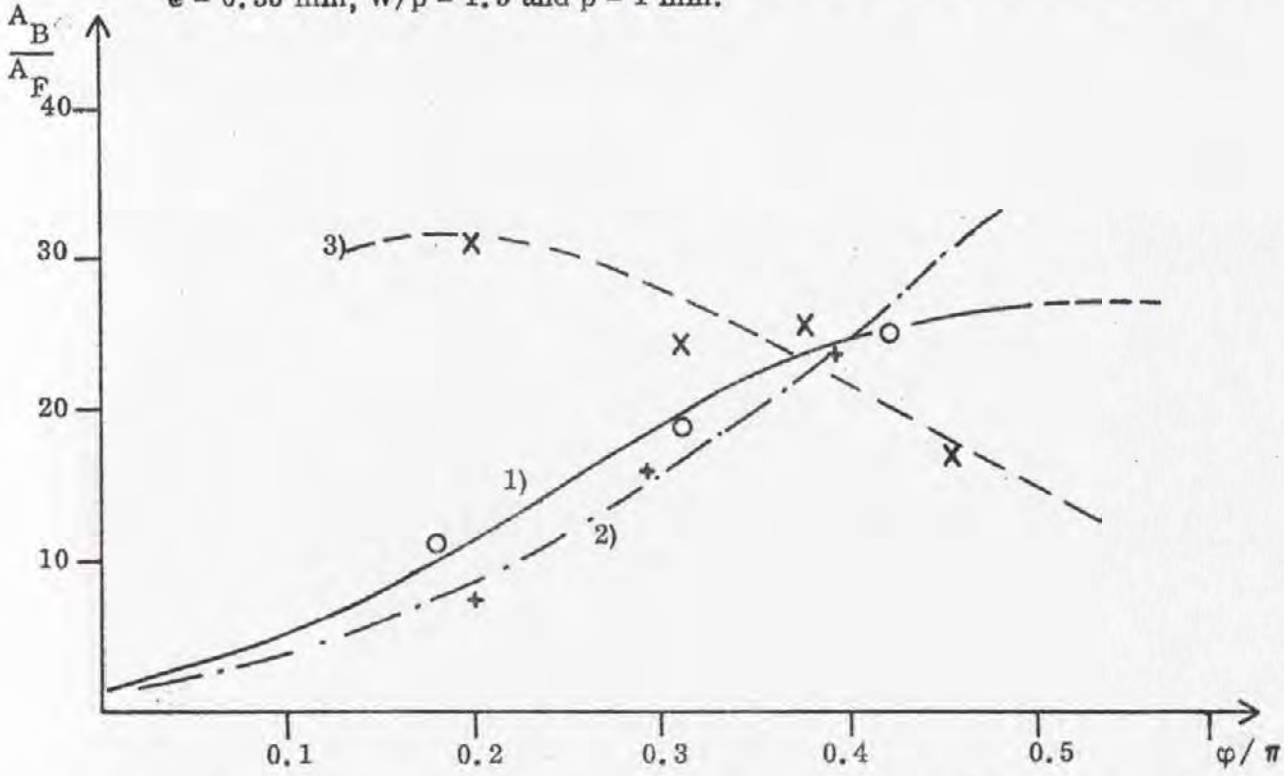

Fig. 3.7 Effects of dividing the bar. The figure depicts the ratio of the backward wave attenuation (dB) to the forward wave attenuation (dB) as a function of φ/π. 1), 2) and 3) as in Fig. 3.6.

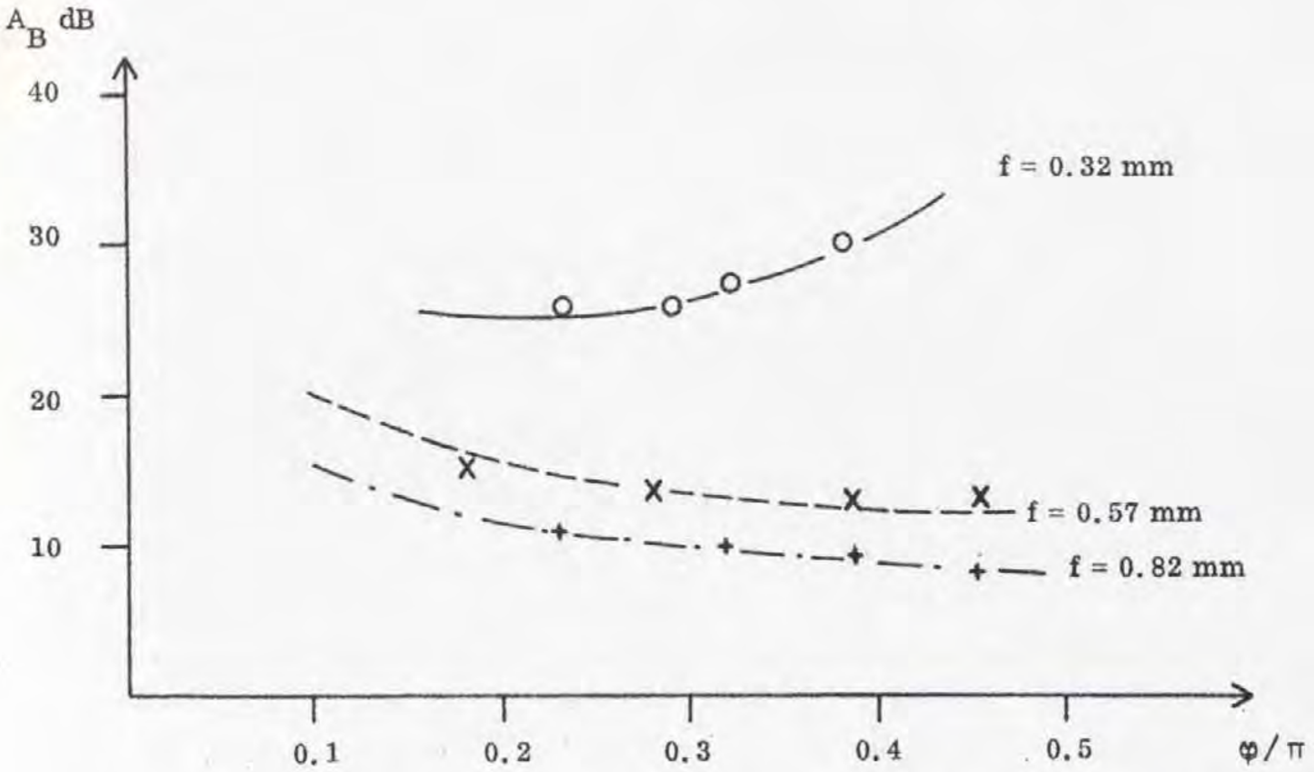

Fig. 3.8 Backward wave attenuation for a divided bar at different distances "f" from the conductor plane vs φ/π. The pieces are placed midway between adjacent conductors. d, e, W/p and p as in Fig. 3.2.

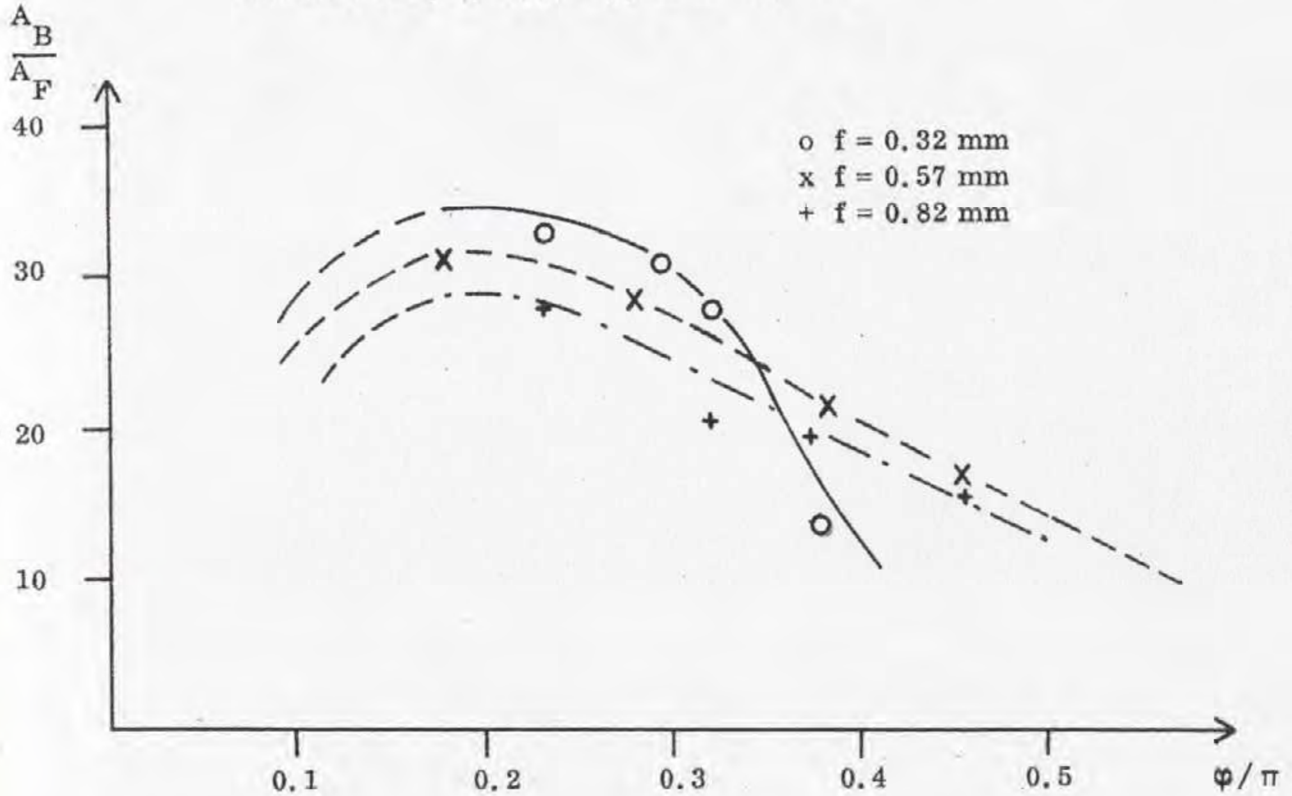

Fig. 3.9 The ratio backward wave attenuation to forward wave attenuation for a divided bar at different distances "f" from the conductor plane vs φ/π. Position and dimensions are as in Fig. 3.8.

4. RUTILE AS A MASER MATERIAL IN THE FREQUENCY RANGE 1 - 7 GHz.

4.1 Introduction

In this chapter we shall discuss chromium-doped and, in particular, iron-doped rutile for maser applications. We have experimentally investigated the maser properties of Fe-TiO_2 near 5 GHz. It was found that heat treatment of the crystals is essential for optimum performance. We also discuss the advantage of using $\chi'' \cdot \Delta f_L$ as a quality factor of the maser material rather than χ'' (χ'' is the imaginary part of the paramagnetic susceptibility and Δf_L is the half-power line width). Finally, we compare the maser properties of Cr-TiO_2 and Fe-TiO_2 at 5 GHz. It is demonstrated that Cr-TiO_2 is the superior material at this frequency.

4.2 Introductory remarks

Since the rf magnetic fields are to a large extent circularly polarized in transverse conductor SWS:s, the quality factor of the maser material can be expressed in the following way (Siegman 1964):

$$\frac{1}{Q_m} = \chi''_+ \cdot \eta_+ \qquad (4.1)$$

where the inverted susceptibility for circularly polarized fields, χ''_+, is given by (assuming a Lorentzian line shape),

$$\chi''_+ = K \cdot I \cdot (\Delta n_s)_o \cdot \frac{N}{\Delta f_L} \cdot |M_+|^2 \qquad (4.2)$$

In this formula K is a constant with the dimension $cm^3 \cdot$ MHz and with a numerical value of $3.25 \cdot 10^{-19}$. Furthermore, in eqn. (4.2) we have

I , the inversion ratio for the signal transition

Δf_L , the equivalent Lorentzian half power linewidth

$(\Delta n_s)_o$, the fractional population difference at the signal transition in thermal equilibrium

N , the number of active ions per unit volume and

$|M_+|^2$, the normalized transition probability for the signal transition

The filling factor η_+ in eqn. (4.1) is given by

$$\eta_+ = \frac{\int_{V_c} |H_+|^2 \, dv}{\int_{V_p} (|H_+|^2 + |H_-|^2) \, dv} \tag{4.3}$$

where V_c is the maser crystal volume over one period, V_p the total volume for one period in the SWS, and H_+ and H_- are the positive and negative circularly polarized rf magnetic field components, respectively. η_+ has been calculated earlier (Kollberg 1966 a) using results obtained from a space harmonic analysis of the fields in a SWS with square fingers (Chen 1964 a). Since no material is placed in the space between the fingers, one obtains a higher filling factor for thin tapes. The SWS:s described in this report all have fingers with a thickness - to - pitch ratio t/p equal to or less than 0.1.

When different operating points are examined for maximum gain, $I \cdot N$ (the inversion ratio I depends on N), Δf_L, $(\Delta n_s)_o$ and $|M|^2$ must be determined. The product $I \cdot N$ and Δf_L are determined experimentally, while $(\Delta n_s)_o$ and $|M|^2$ are obtained theoretically.

Initially, two different operating points in Cr- and Fe- TiO_2 were considered: the c-axis operating point with the dc magnetic field along the crystal c-axis and the a - axis operating point with the dc magnetic field along the a-axis.

In Fig. 4.1. we show the energy levels of Cr-TiO_2 and Fe-TiO_2 for the dc-magnetic field along the rutile c-axis and the a-axis. Yngvesson (1968) has shown that for Cr-TiO_2 and the frequency range 1400-4000 MHz, the best maser performance is obtained when the dc-magnetic field is along the c-axis and the 1-2 transition (c, 1-2 transition) is used for the signal frequency and the 1-4 transition (c, 1-4 transition) is used for the pump frequency. We shall therefore discuss only this operating scheme for Cr-TiO_2

Chromium-doped rutile

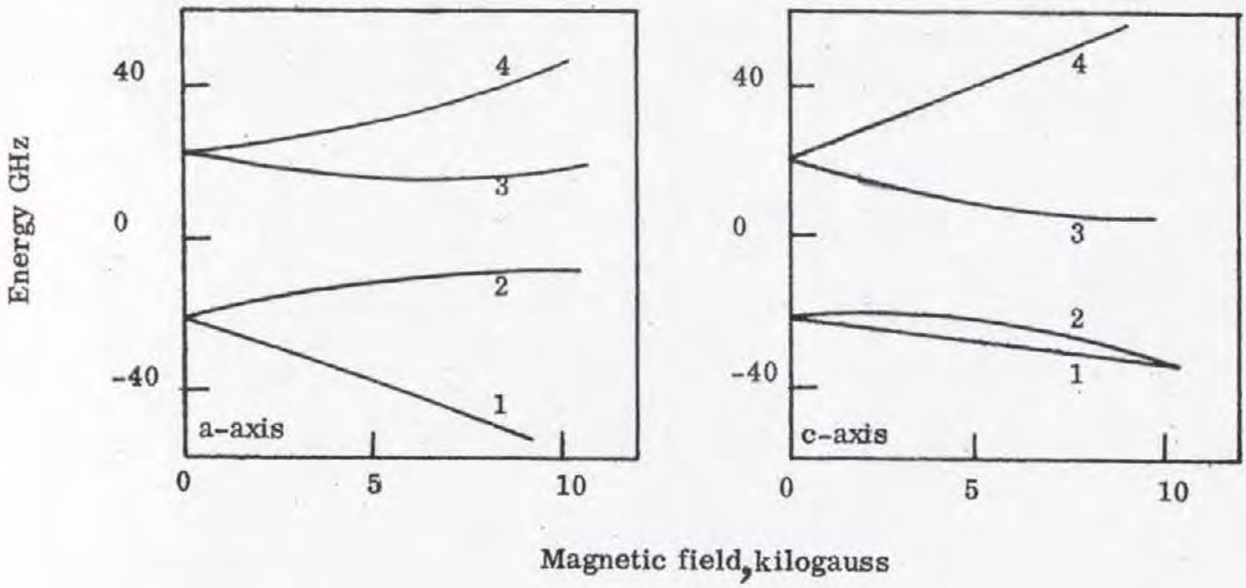

Iron-doped rutile

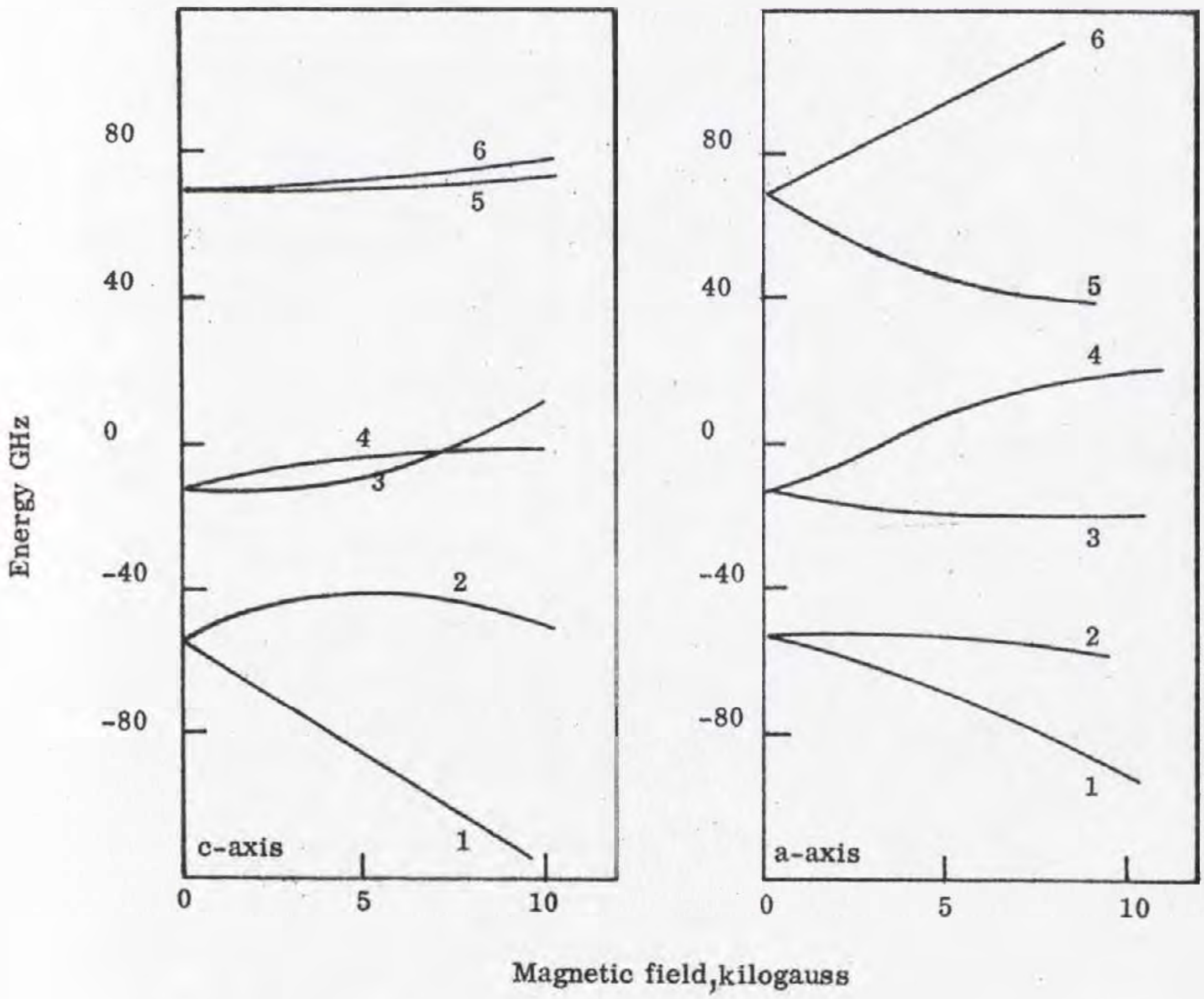

Fig. 4.1 Energy level diagrams for chromium- and iron-doped rutile.

Early measurements at 5 GHz on $Fe\text{-}TiO_2$ with the dc-magnetic field along the a-axis, and using the a, 1-2 transition for the signal and pumping at the a, 1-4 transition, gave inversion ratios of -2.5 at 4.2°K and -3.5 at 1.5°K for an iron concentration of 0.027 % Fe^{3+} by weight. Morris and Miller (1965) have reported an inversion ratio at 5 GHz of -4 at 4.2°K in a sample with about 0.020 % Fe^{3+} b.wt., while Schollmeier and Roth (1967) at 4 GHz have measured I = -5 for 0.015% Fe^{3+} b.wt.

In Section 4.3 we report an extensive investigation of the maser properties of $Fe\text{-}TiO_2$ using the c-axis operating point.

4.3 Maser properties as a function of iron-concentration for $Fe\text{-}TiO_2$ at 5 GHz.

Some experimental data for the maser properties of $Fe\text{-}TiO_2$ at C-band, when the c-axis operating point is utilized, have been published by Morris and Miller (1965) and Schollmeier and Roth (1967). At 4 GHz Schollmeier and Roth (1967) report a measured inversion ratio of -11 in a sample with 0.015 % Fe^{3+} b.wt. and a somewhat degraded inversion ratio in a sample with 0.046 % Fe^{3+} b.wt.(no figure is mentioned). At 5 GHz Morris and Miller (1965) report a measured inversion ratio of -10 in a sample with about 0.03 % Fe^{3+} b.wt.

In order to investigate the inversion ratio vs. the concentration for $Fe\text{-}TiO_2$, we bought three small Verneuil grown iron-doped rutile boules with the c-axis along the boule-axis from the National Lead Company, South Amboy, N.J., with the nominal concentrations 0.014, 0.028 and 0.050 % Fe^{3+} b.wt. We also bought from the same supplier two large boules with the nominal concentrations 0.025 and 0.035 % Fe^{3+} b.wt., but with one a-axis along the boule axis. The iron-content of a sample from the middle of the boule with nominally 0.035 % Fe^{3+} b.wt. was determined using chemical analysis to be 0.045 ± 0.002% Fe^{3+} b.wt.

Rather curious results were obtained in the first measurements, and no clear relation between concentration and inversion ratio in samples from the different boules were obtained. Moreover, the color of the rutile boules varied from (dark) red in one end to (light) yellow in the other. Different inversion ratios were also obtained for samples from the same boule.

Recently Johnson et al. (1968) mention that the reddish coloration, which has usually been assumed to be characteristic of Fe-doped specimens, results from precipitates of a second phase. By heating the crystal to a temperature above 800° C, keeping it in an oxygen atmosphere for a couple of hours, and then rapidly cooling the crystal to room temperature, the crystal colour becomes light yellow.

In order to check if the heat treatment increased the number of Fe^{3+} -ions substituting for Ti^{4+}, a method was developed for determining the concentration of substitutional ions by measuring their contribution to the paramagnetic absorption. In Fig. 4.2 the microwave resonator used in the experiments is shown. The Cr-TiO_2 crystal (0.135 % Cr^{3+} b.wt.) was the same in all the experiments and served as a reference for the measured paramagnetic absorption in the Fe-TiO_2 crystals. Using a microwave spectrometer and a modulated magnetic field, the derivative of the paramagnetic power absorption line vs the magnetic field was recorded. Integrating these curves twice, we obtained a measure of the number of paramagnetic ions. The Fe-TiO_2 samples were similar in shape, eliminating effects due to non-uniform rf magnetic fields.

Paramagnetic absorption measurements were performed on a number of different samples. Some results are shown in Table 4.I, where the substitutional concentration is related to the relative concentration after heat treatment (A) and is calibrated using the sample with nominally 0.035 % Fe^{3+} b.wt., which was analysed chemically to have 0.045 % Fe^{3+} b.wt.

Table 4.I

Nom conc Fe^{3+} % b.wt.	axis along boule axis	Relative conc.		Inversion ratio at 4.2° K		Substit. conc. % Fe^{3+} b.wt.
		B	A	B	A	
0.014	c	1.00	1.13	9.2	-	0.027
0.028	c	1.64	1.97	3.2	5.6	0.047
0.050	c	2.12	2.36	2.3	2.3	0.057
0.025	a	1.38	1.78	8.0	-	0.043
0.035	a	1.42	1.88	7.0	-	0.045

B: before heat treatment.

A: after " "

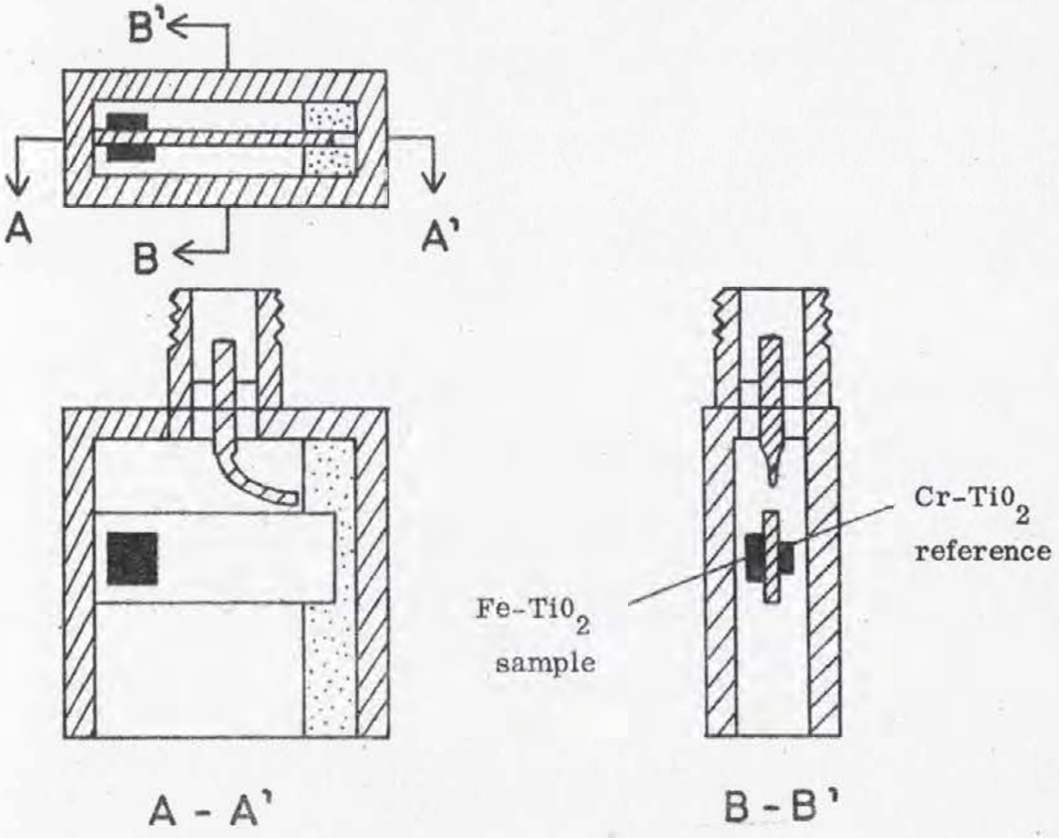

Fig. 4.2 Depicts cross sections of the microwave resonator used for determination of the substitutional paramagnetic ion concentration in Fe-TiO_2.

Less complete measurements have been made on samples from $Fe-TiO_2$ Verneuil-grown boules bought from Hrand Djevahirdjian in Switzerland and on diffusion doped samples (Andersson 1968). For one Verneuil-grown sample (nom. conc. 0.04 % $Fe-TiO_2$ b.wt) the number of substitutional ions increased by as much as 87 %.

From these experiments we conclude that heat treatment is essential for optimum and reproducible maser properties. After heat treatment, the half-power linewidth was measured to be about 19 MHz for 0.020 - 0.040 % Fe^{3+} b.wt. and about 23 MHz for 0.05 % Fe^{3+} b.wt. These linewidths are much smaller than those reported by Schollmeier and Roth (1967) and Morris and Miller (1965). The measured line shape was close to Lorentzian.

The heat treatment not only increased the number of substitutional Fe^{3+} - ions, but in most cases it also increased the inversion ratio (see Table 4.I). We believe this is (at least partly) due to a more homogeneous Fe^{3+} doping throughout the crystal. Yngvesson (1968) has shown that the concentration-dependent inversion ratio in $Cr-TiO_2$ can be explained in terms of relaxation times decreasing with increasing concentration. The concentration dependent term of the relaxation time is probably explained by a model in which a single ion relaxes in two steps to the lattice via pairs, triads or even clusters of exchange coupled ions. Yngvesson measured in $Cr-TiO_2$ a relaxation time dependent on the concentration "c" as $c^{-4} \to c^{-5}$. Hence, an inhomogeneous doping may effectively yield short mean relaxation times and lower inversion ratios.

In Fig. 4.3 we show the inversion ratio vs. the substitutional concentration after heat treatment, calibrated by means of a sample from the boule containing 0.045 % Fe^{3+} b.wt. according to the chemical analysis.

Early experiments on heat treatment of $Cr-TiO_2$ yielded increased inversion ratios near 3 GHz. On a diffusion doped sample (Andersson 1968) with about 0.03 % Cr^{3+} b.wt. we measured the following inversion ratios at 1.5 ^{o}K:

Original sample : $I = -8$

Annealed sample : $I = - 5.8$

Heat treated (quenched) sample: $I = -9.5$

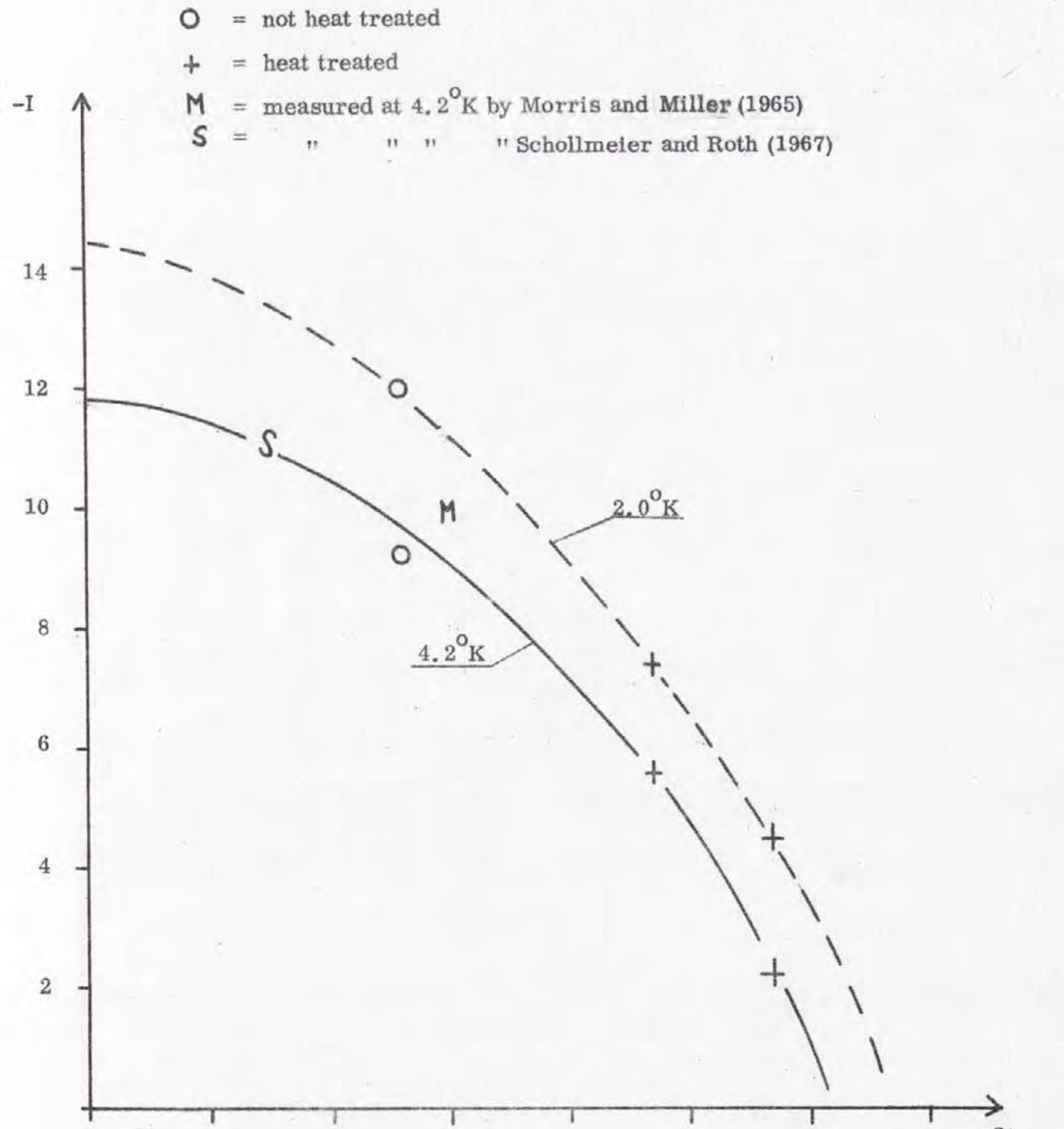

Fig. 4.3 Inversion ratio vs. the substitutional iron concentration for $Fe\text{-}TiO_2$ at 5 GHz.

The paramagnetic absorption before and after the heat treatment was not measured in these experiments. No change in coloration could be seen. However, since the $Cr-TiO_2$ is black and not transparent to light, a color change is not expected. It is quite possible that the number of substitutional Cr^{3+} - ions does increase by the heat treatment, and further experiments may be rewarding.

4.4 Rutile as a maser material in the frequency range 1-7 GHz

When the maser properties vs the concentration of paramagnetic ions are considered, maximum gain is obtained for maximum χ''_+ (eqn. (4.2)). The concentration dependent parameters of eqn. (4.2) are N, I, and Δf_L. Hence, for maximum gain, the expression $(N \cdot I)/\Delta f_L$ has to be maximized, i.e. the lower the value of Δf_L, the higher the gain. However, in most practical TWM:s one obtains line-broadening for various reasons: the isolator material perturbes the dc-magnetic field, or in a long TiO_2 single crystal the crystal axes are twisting, or even worse the crystal may have a mosaic structure (see Fig. 4.4). In many applications one also needs an amplifier with a broader bandwidth than can be obtained from a perfect single crystal in a homogeneous field. Hence, there are strong reasons to consider the maser material optimum when $\chi'' \cdot \Delta f_L$ is maximum, i.e. one has to look for a maximum in the product $I \cdot N$.

Using data published by Yngvesson (1968) we have in Fig. 4.5 and 4.6 depicted $c \cdot I$ for $Cr-TiO_2$ at 1.5 and 3.4 GHz, where c is the concentration Cr^{3+} % b.wt. ($N \sim c$). It is seen that the maximum product $c \cdot I$ is obtained at quite high values for the concentration compared with the concentration for maximum χ''_+. Moreover, if a concentration of 0.06 % Cr^{3+} b.wt. is chosen, we are close to the optimum concentration for any temperature between 1.8 and 4.2 $^{\circ}$K and any frequency between 1.5 and 3.5 GHz.

In Fig. 4.7 we have depicted $I \cdot c$ for $Fe-TiO_2$. The optimum concentration is near 0.037 % Fe^{3+} b.wt. (substitutional) and is more critical than for Cr^{3+} in TiO_2

From Fig. 4.1 it is seen that for the $Cr-TiO_2$, c, 1-2 transition and for the $Fe-TiO_2$, c, 3-4 transition there is a maximum transition frequency for moderate magnetic fields. We have made careful measurements of these transition frequencies vs the magnetic field as shown in Fig. 4.8. From Fig. 4.8 we find the maximum

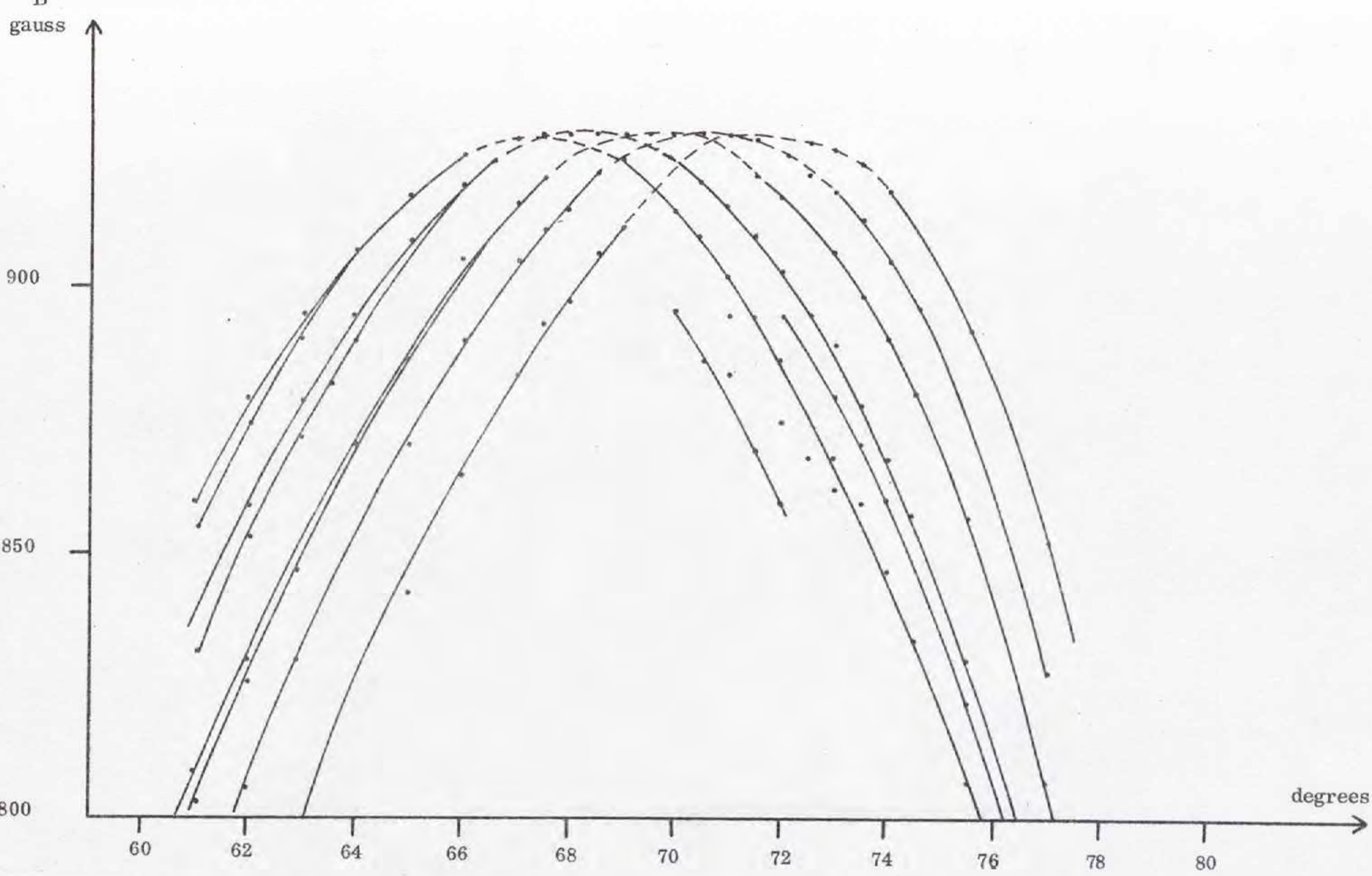

Fig 4.4 Resonance magnetic field vs orientation at 1365 MHz in the ac-plane, close to the c-axis, for a $Cr\text{-}TiO_2$ sample taken from a boule grown with an a-axis along the boule axis.

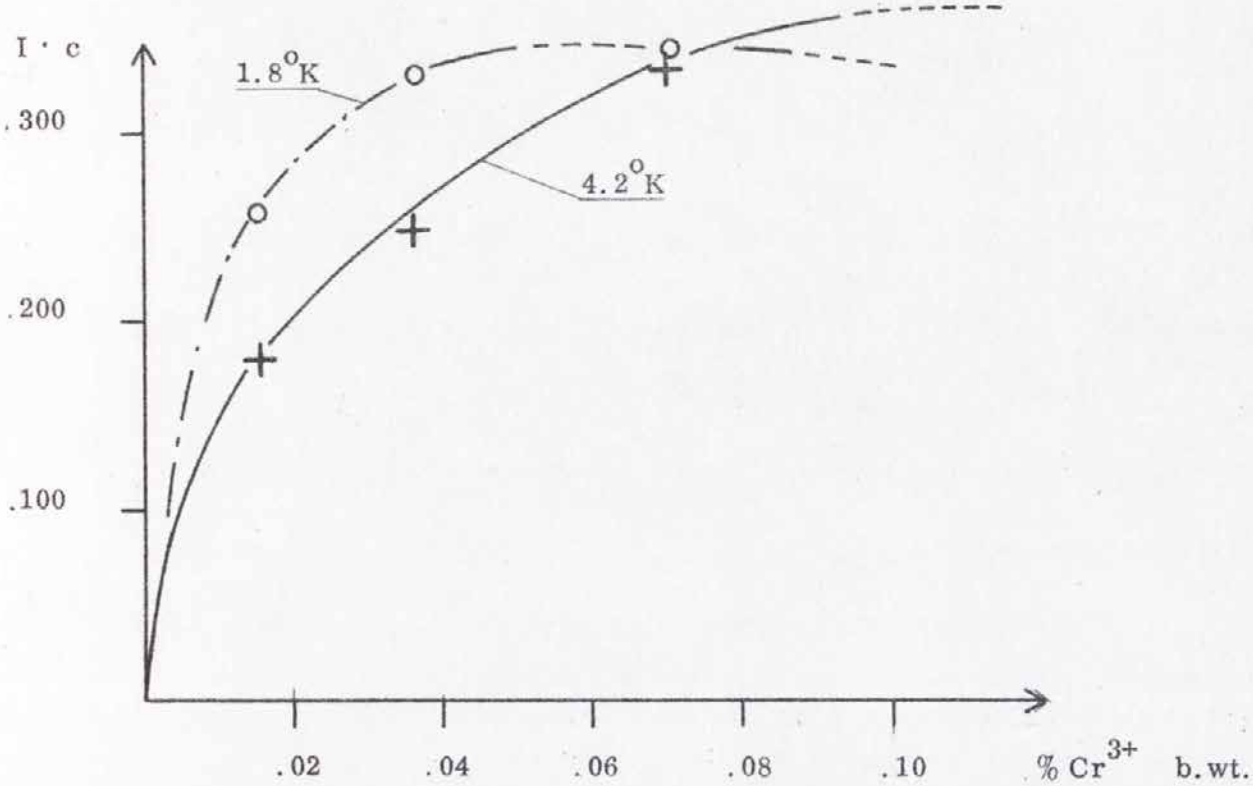

Fig. 4.5 Inversion ratio times ion concentration at 1.5 GHz for $Cr-TiO_2$ as obtained using data published by Yngvesson (1968).

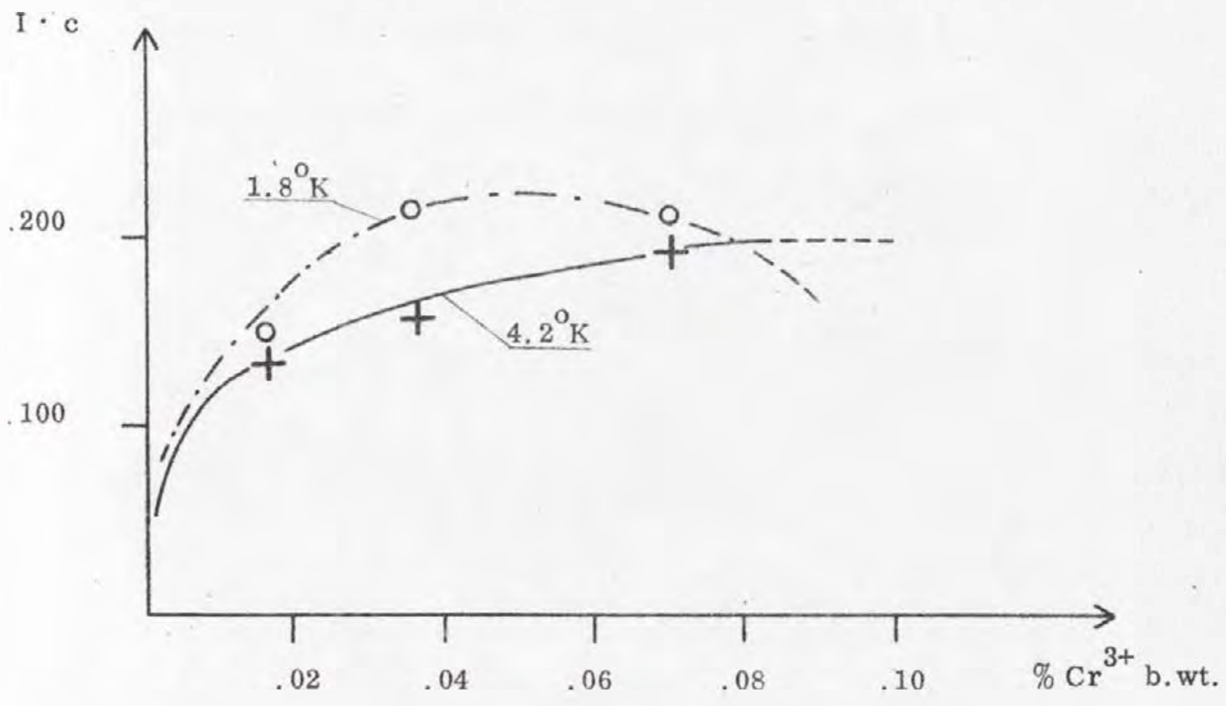

Fig. 4.6 Inversion ratio times ion concentration at 3.4 GHz for $Cr-TiO_2$ as obtained using data published by Yngvesson (1968).

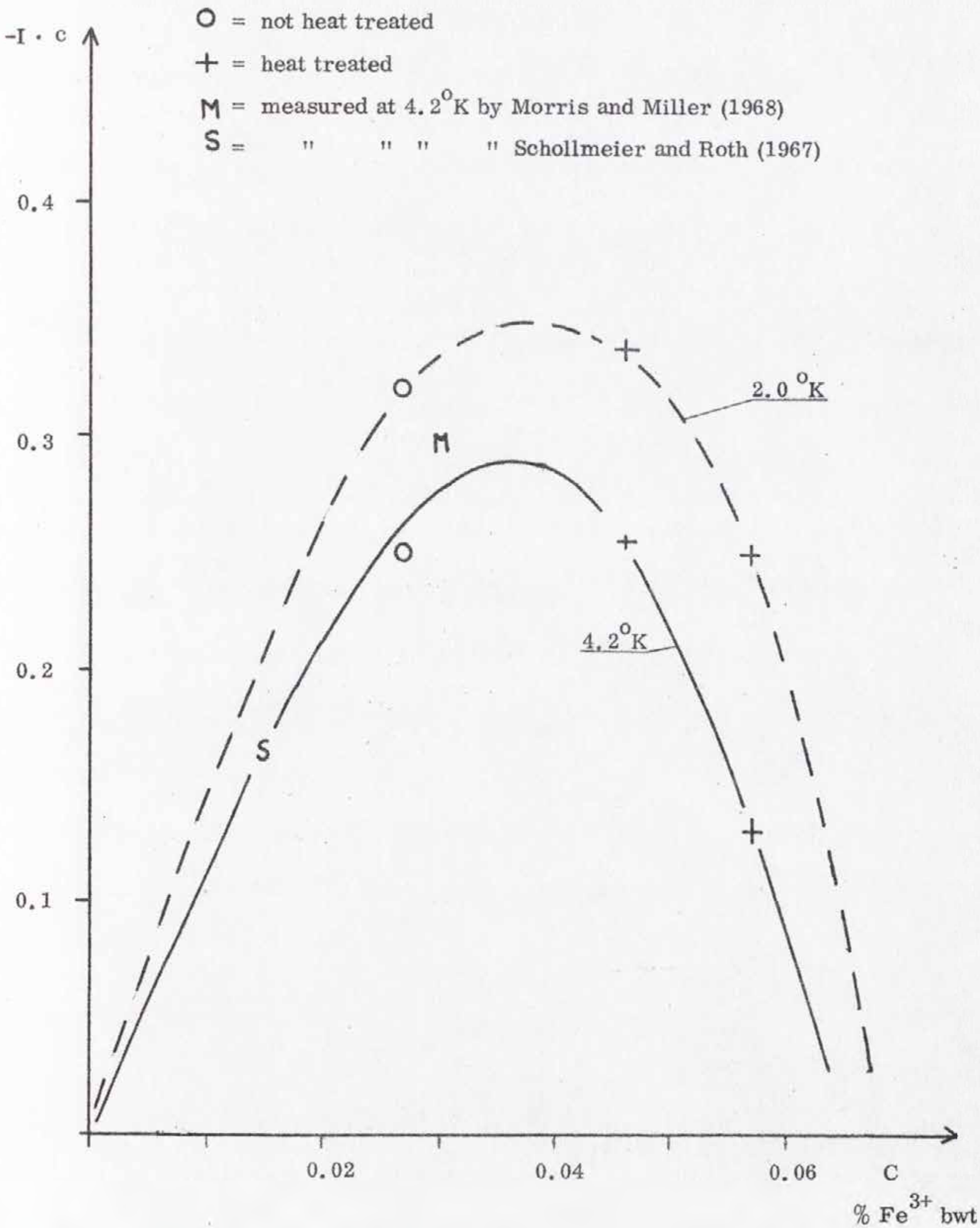

Fig. 4.7 Inversion ratio times substitutional iron concentration for Fe-TiO_2 vs concentration at 5 GHz.

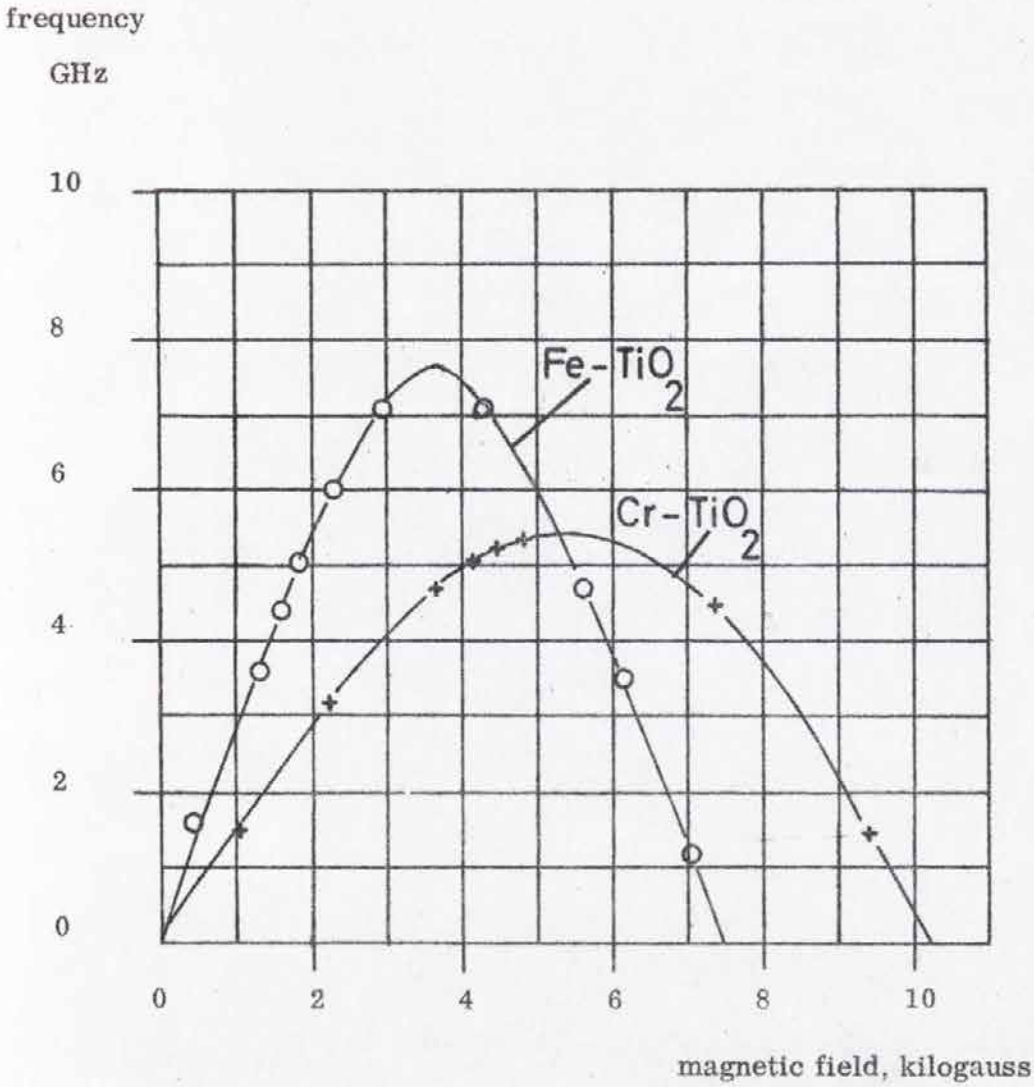

Fig. 4.8 Transition frequency vs. magnetic field for the c, 1 - 2 transition in Cr-TiO_2 and the c, 3 - 4 transition in Fe-TiO_2.

Since Fe^{3+} has the spin S = 5/2 while Cr^{3+} has a spin S = 3/2 , we might expect higher transition probabilities in $Fe\text{-}TiO_2$ than in $Cr\text{-}TiO_2$. In Fig. 4.9 we have depicted the normalized c, 1-2 and c, 3-4 transition probabilities for $Cr\text{-}TiO_2$ and $Fe\text{-}TiO_2$, respectively, using data published by Devor (1960) for $Cr\text{-}TiO_2$ and by Lin and Haddad (1966) for $Fe\text{-}TiO_2$. It is noticed that $Fe\text{-}TiO_2$ does have higher transition probabilities for positive circularly polarized fields.

It is interesting to compare $Fe\text{-}TiO_2$ and $Cr\text{-}TiO_2$ near 5 GHz. In order to do this, we measured the inversion ratio for $Cr\text{-}TiO_2$ (with 0.036 % Cr^{3+} b.wt.) at 5 GHz. Comparing these measured data (Table 4.II) with those measured by Yngvesson (the same sample was used) we notice that the inversion ratio is almost a constant between 4 and 5 GHz. In Table 4.II, the relevant data are given for a comparison of $\Delta f_L \cdot \chi''_+$ for $Cr\text{-}TiO_2$ and $Fe\text{-}TiO_2$ at 4.2°K and 2°K, assuming the same number of substitutional ions to be present.

Table 4.II

ion	% b.wt.	$\lvert M_+\rvert^2$	4.2°K			2°K		
			$(\Delta n_s)_o$	-I	$(\Delta n_s)_o I \lvert M_+\rvert^2$	$(\Delta n_s)_o$	-I	$(\Delta n_s)_o I\lvert M_+\rvert^2$
Fe^{3+}	0.038	3.50	.0092	8.0	-2.58	.0145	11.5	-5.84
Cr^{3+}	0.035	2.60	.0192	5.5	-2.74	.044	6.8	-7.77

Although one must be aware of the uncertainty of this comparison, it is seen in Table 4.II that at 4.2°K, $Cr\text{-}TiO_2$ is somewhat better than $Fe\text{-}TiO_2$ (assuming no errors in the inversion ratios), while at 2°K, $Cr\text{-}TiO_2$ is much superior to $Fe\text{-}TiO_2$. Since the ratio $\lvert M_-\rvert^2$ is smaller for $Fe\text{-}TiO_2$ than for $Cr\text{-}TiO_2$, the latter material in a real SWS may be even more favorable to use, especially if the SWS is loaded with maser material on both sides of the array.

A comparison was made of the $1/Q_m$ value obtained in an S-band TWM (MAS 2, Table 7.II) with that obtained in a C-band TWM (MAC 2, Table 7.II). Assuming the same linewidths, we obtain relative measures that agree within about 10 % with the values for $(\Delta n_s)_o \cdot I \cdot \lvert M_+\rvert^2$ in Table 4.II.

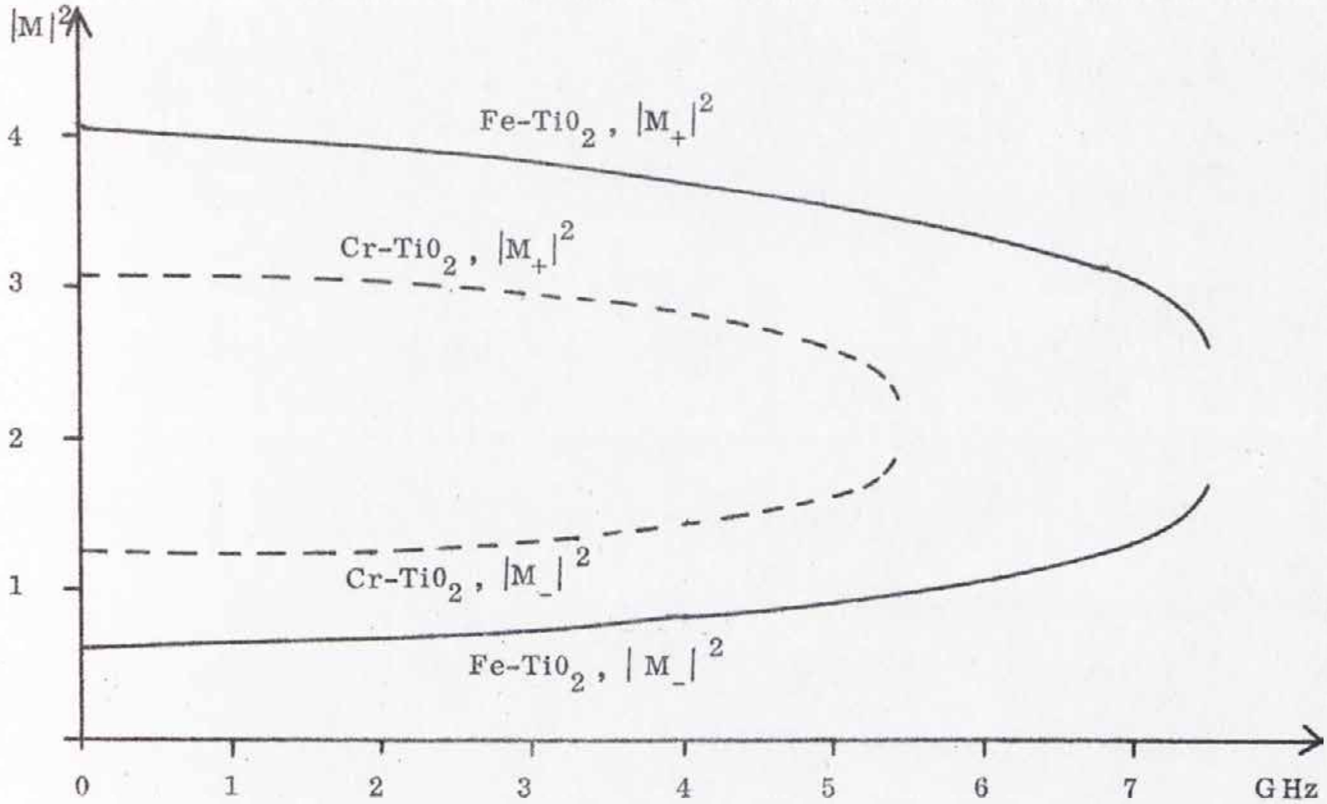

Fig. 4.9 Normalized signal transition probabilities for the c, 1-2 transition Cr-Ti0_2 and the c, 3-4 transition in Fe-Ti0_2 .

For completeness, we have in Fig. 4.10 depicted measured pump frequencies, i.e. the c, 1-4 transition, vs the signal frequency for $Cr-TiO_2$ and $Fe-TiO_2$.

Finally, we would also like to mention that the a, 1-2 transition in $Fe-TiO_2$ has not been carefully investigated during the course of this research. It might be rewarding to reconsider this operating point using heat treated $Fe-TiO_2$ -crystals. The transition probabilities are quite high ($|M_+|^2 = 4.25$ and $|M_-|^2 = 4.16$ at 5 GHz) and, since the 1-2 transition is used, this operating point should be quite useful at lower temperatures and when maser crystals are placed at both sides of the conductor array.

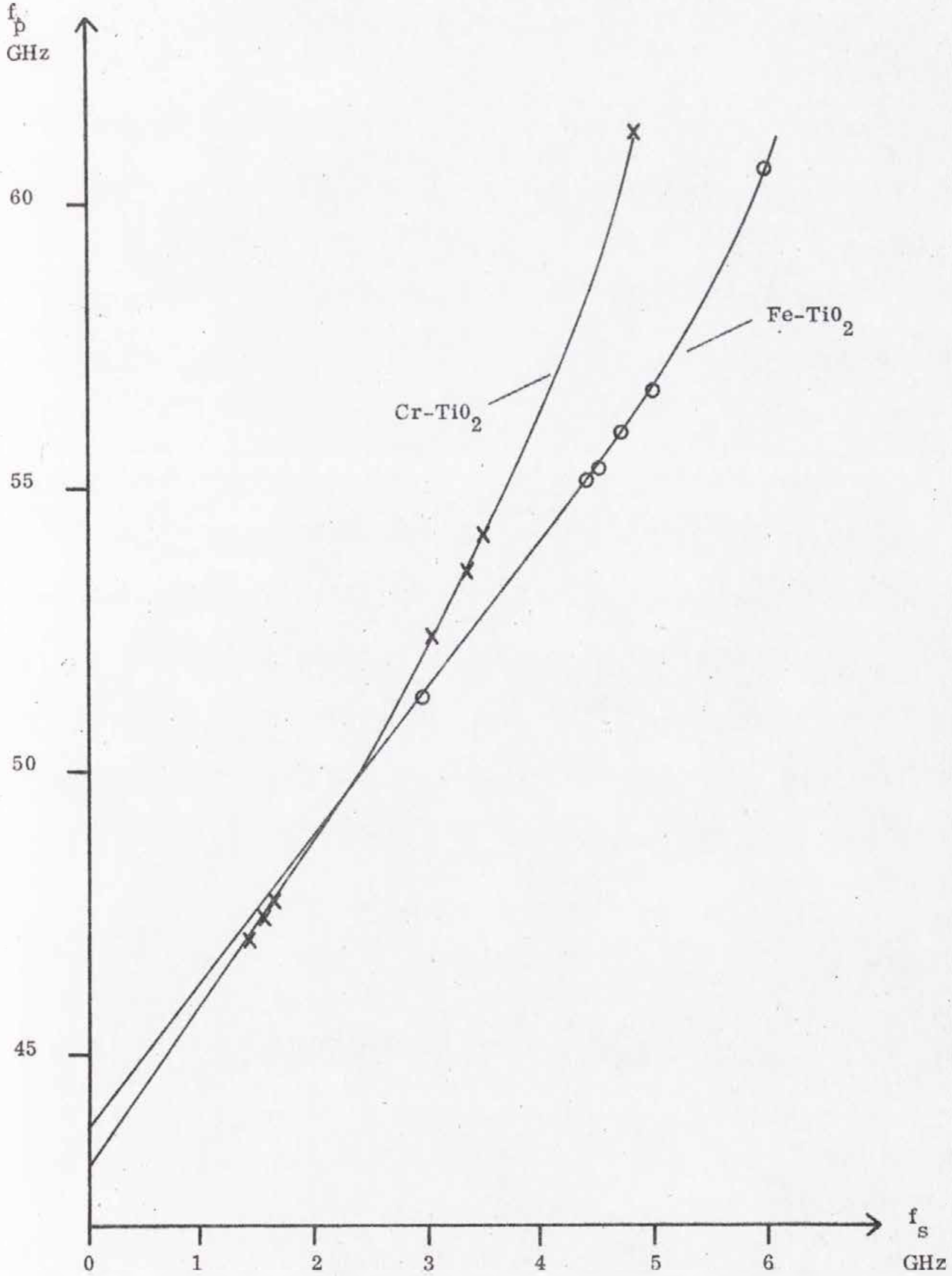

Fig. 4.10 The c, 1 - 4 pump frequency transition for Cr-Ti0$_2$ and Fe-Ti0$_2$.

5. FURTHER TRAVELING WAVE MASER DESIGN-CONSIDERATIONS

5.1 Introduction

When the net gain of a traveling wave maser is calculated, one must know not only the electronic gain produced by the maser crystal, but also the losses caused by the garnet isolator, the ohmic losses in the metal boundary surfaces and the dielectric losses in the dielectric loading material and the maser crystal itself. In this chapter we will discuss the problem of ohmic losses and show that there exists an optimum pitch yielding maximum net gain. The existence of an optimum pitch has been reported separately in an earlier paper by the present author (Kollberg 1966 b).

5.2 Insertion loss in a transverse conductor slow-wave structure

The net gain in dB of a TWM may be expressed as

$$G = 27.3 \cdot \frac{L}{\lambda_o} \cdot S \left[\frac{1}{|Q_m|} - \frac{1}{Q_F} - \frac{1}{Q_o} \right] \tag{5.1}$$

where L is the length of the SWS, λ_o the free space wavelength, S the slowing factor, Q_m the negative Q-factor of the maser material, Q_F the Q-factor related to the forward losses in the isolator material and Q_o a Q-factor related to losses caused by the finite conductivity of the metallic boundaries.

Q_m and Q_F have already been extensively discussed in chapters 3 and 4. Losses in the SWS may also be due to dielectric losses. However, in most materials used in maser SWS:s, the Q-factor related to dielectric losses is larger than 10^4 at liquid helium temperatures, and may therefore be neglected in equation (5.1).

In order to discuss Q_o, let us discuss the Q-factor of one resonator in a simple structure where $W_1 = W_2$ and $\varepsilon_r = 1$ (Fig. 2.2). Assuming that the ohmic attenuation can be treated as a small perturbation, the power dissipation due to the currents at the surface of the conductor boundaries, becomes

$$P_o = \frac{1}{2} R_s(\varphi) \int_0^{\ell} i_o^2(x)\, dx \tag{5.2}$$

where $R_s(\varphi)$ is the skin effect resistance of the circuit (notice that $R_s(\varphi)$ is defined in such a way that ohmic losses in the ground planes are included in eqn. (5.2)), ℓ is the length of the resonator, $i_o(x)$ is the maximum current at the conductor related to one period. The energy stored, W_s, related to the period containing the conductor resonator becomes

$$W_s = \frac{1}{2} \; L(\varphi) \int_o^{\ell} i_o^{\,2}(x)\, dx \tag{5.3}$$

where L is the inductance per unit length of the conductor. This inductance can be related to the capacitance per unit length, $C(\varphi)$ and the conductor admittance $Y(\varphi)$, through the following relation

$$Y(\varphi) = v_o \; C(\varphi) = \sqrt{\frac{C(\varphi)}{L(\varphi)}} \tag{5.4}$$

where v_o is the phase velocity of the TEM wave.

Hence, we obtain by definition

$$\frac{1}{Q_o} = \frac{P_o}{2\pi f\, W_s} = \frac{R_s(\varphi) \cdot v_o^{\,2} \cdot C(\varphi)}{2\pi f} \tag{5.5}$$

where f is the frequency. However, $R_s(\varphi)$ depends on the current distribution on the metallic boundary surfaces. Let us consider a certain cross-section, with all geometrical dimensions normalized using the pitch p. Then one has

$$R_s(\varphi) = \frac{r(\varphi)}{\delta \cdot p} \tag{5.6}$$

where $r(\varphi)$ is a factor depending on the current distributions and δ is the skin depth. Since $\delta \propto 1/\sqrt{f}$ where f is the frequency, we obtain

$$\frac{1}{Q_o} = K \cdot \frac{r(\varphi) \cdot Y(\varphi)}{p \cdot \sqrt{f}} \tag{5.7}$$

where K is a factor only depending on the metal used in the structure. At least for thin conductors, we expect $r(\varphi)$ to increase with φ. Hence, for ordinary slow wave structures, we expect $1/Q_o$ to increase faster with φ than does $Y(\varphi)$. Notice the similarity of the φ- dependence for $1/Q_o$ obtained by Siegman (1964, page 355) for the conducting sheet approximation and $W/p \to \infty$:

$$\frac{1}{Q_o} \sim \varphi \tag{5.8 a}$$

and the φ- dependence obtained from equation (5.7) for conductors with zero thickness, $r = 0.5$, $W/p = \infty$ [using $Y(\varphi) \sim \sin\varphi$ (Butcher, 1957)]:

$$\frac{1}{Q_o} \sim r(\varphi) \cdot \sin\varphi \tag{5.8 b}$$

5.3 Optimum pitch of traveling-wave masers

We will now show theoretically that there exists an optimum pitch which gives maximum net gain for TWM:s, using transverse conductor SWS:s. For convenience a typical cross section of such a SWS is shown in Fig. 5.1.

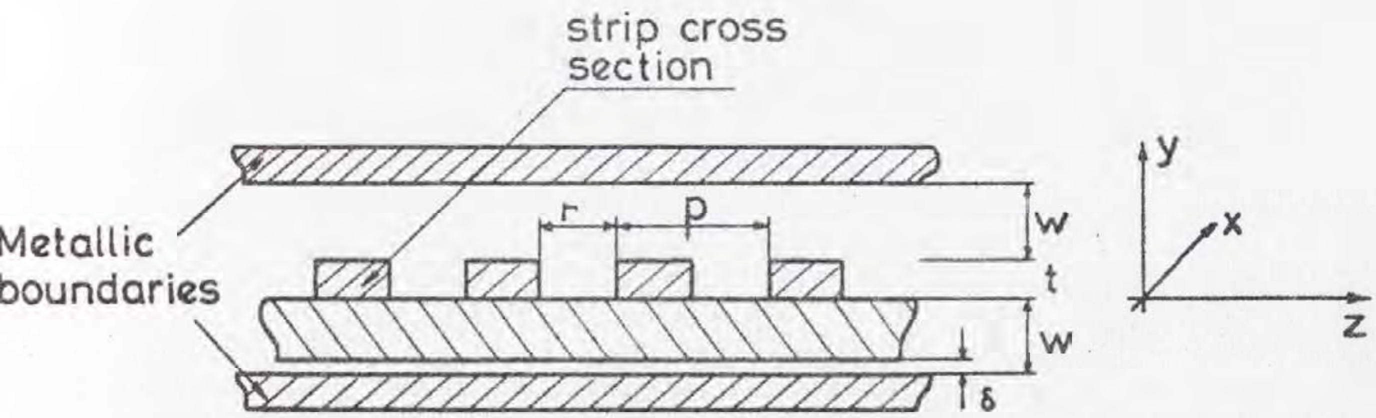

Fig. 5.1 A typical cross section of transverse strip slow-wave structures.

Assume that the pitch of a particular SWS is p_o . The slowing of the structure becomes S_o and the ohmic Q-factor Q_{oo} . A scaling of the cross section is obtained when all cross section dimensions are multiplied by the factor p/p_o . Hence the new pitch becomes p.

In chapter 2 it is shown that the $\omega - \varphi$ characteristic of the structure is determined by the boundary conditions and wave propagation constants of the TEM waves, the length of the conductors and their characteristic admittances, $Y(\varphi)$. We now assume that the boundary conditions, the length of the conductors and the cross section dimensions divided by p are constant during a scaling of the cross section by p/p_o . Hence the $\omega - \varphi$ characteristic is independent of p. The group velocity v_g and the slowing S of the wave traveling in the z-direction becomes

$$v_g = \frac{d\omega}{d\beta} = p \cdot \frac{d\omega}{d\varphi}$$

$$S = \frac{c_o}{v_g} = \frac{c_o}{p_o \cdot \frac{d\omega}{d\varphi}} \cdot \frac{p_o}{p} = S_o \cdot \frac{p_o}{p} \tag{5.9}$$

where c_o is the velocity of light in vacuum.

The ohmic quality factor Q_o is proportional to V/A for constant relative cross section dimensions, where V is the volume and A is the metal boundary surface area of one period of the structure. One obtains (compare eqn. (5.7))

$$Q_o = Q_{oo} \cdot \frac{p}{p_o} \tag{5.10}$$

The magnetic quality factor Q_m is independent of p for constant relative cross section dimensions. Since the isolator Q-factor Q_F is also independent of p, we can write

$$\frac{1}{Q_F} = \alpha \cdot \left| \frac{1}{Q_m} \right| \tag{5.11}$$

where $\alpha < 1$ and typically $\alpha < 0.2$. Using the equations (5.9) - (5.11) we now obtain the net gain

$$G(p) = G(p_o) \frac{\frac{p_o}{p} - \frac{|Q_m|}{(1-\alpha)Q_{oo}} \left(\frac{p_o}{p}\right)^2}{1 - \frac{|Q_m|}{(1-\alpha)Q_{oo}}} \tag{5.12}$$

The net gain G(p) has a maximum for

$$p = p_{opt} = p_o \frac{2\,|Q_m|}{(1-\alpha)Q_{oo}} \tag{5.13}$$

i.e.

$$\frac{1}{Q_{o,opt}} = \frac{1-\alpha}{2\,|Q_m|} \tag{5.14}$$

The optimum net gain becomes

$$G(p_{opt}) = G(p_o) \frac{p_o/p_{opt}}{2 - p_{opt}/p_o} = 27 \frac{L \cdot S}{\lambda_o} \frac{1-\alpha}{2\,|Q_m|} \tag{5.15}$$

In Fig. 5.2 $G(p_{opt})/(G(p_o)$ is plotted for different values of p_o/p_{opt}. The optimum pitch represents a compromise between the ohmic losses and the slowing factor, and the optimum gain is obtained when the electronic gain (the gain obtained for $Q_i = Q_o = \infty$) is approximately twice the ohmic losses (see equation (5.14)).

For $p_o < \frac{1}{2}\, p_{opt}$ the ohmic losses becomes so high that no net gain is obtainable. It may be advisable to choose $1 < p_o/p_{opt} < 1.5$.

The noise temperature for the pitch p_o of the TWM (Siegman 1964) becomes using equations (5.10) and (5.14):

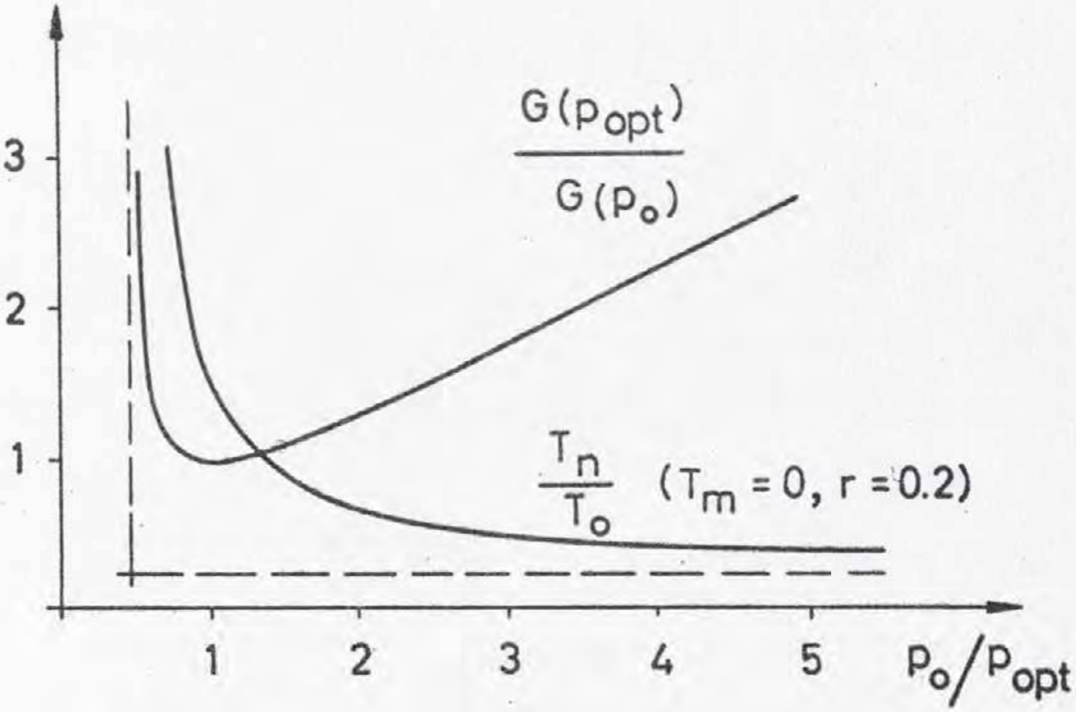

Fig. 5.2 $G(p_{opt})$ / $G(p_o)$ with G in dB and T_n/T_o with $T_m = 0$ and $r = 0.2$ as a function of p_o/p_{opt} .

$$T_n = \frac{G-1}{G}\left[\frac{1/|Q_m|}{1/|Q_m| - 1/Q_i - 1/Q_{oo}} \; T_m + \frac{1/Q_i + 1/Q_{oo}}{1/|Q_m| - 1/Q_i - 1/Q_{oo}} \; T_o\right] =$$

$$= \frac{G-1}{G}\left[\frac{p_o/p_{opt}}{2p_o/p_{opt} - 1} \cdot \frac{2T_m}{1-\alpha} + \frac{\alpha + 1/(2p_o/p_{opt} - 1)}{1-\alpha} \; T_o\right] \ldots \quad (5.16)$$

where T_m is the spin temperature and T_o the liquid helium bath temperature. For $p_o = p_{opt}$, $\alpha = 0.2$, $T_m \ll T_o$ one obtains $T_n = 1.5 \cdot T_o$, a reasonable noise temperature for liquid helium cooled masers. For high temperature masers it may be wiser to choose a pitch larger than the optimum pitch in order to obtain a lower noise temperature (see Fig. 5.2).

It may be emphasized that the scaling procedure proposed here does not change the frequency characteristic of the passband, i.e. the tunable bandwidth of the maser remains constant. Further the coupling to the structure is also unchanged since the impedance levels are constant. The saturation power at the signal frequency of the maser is changed by a factor of p/p_o.

Since Q_m, Q_F and Q_o all depend on the phase shift φ per period, the optimum pitch should in practice be chosen somewhat larger than the minimum value obtained when p_{opt} vs φ is calculated. Hence, we obtain a frequency band over which the TWM equivalent noise temperature is lower than $1.5 \cdot T_o$. In practice it is probably necessary first to design a "trial TWM" where the pitch is larger than the minimum optimum pitch. Measurements on this TWM will give data necessary for a determination of the practical optimum pitch.

The amount of isolation in the final optimum pitch TWM should be chosen in such a way that the backward wave attenuation exceeds the forward wave gain by a certain factor (see eqn. (7.1) and (7.2)). From the measured properties of the trial TWM a suitable value of α can be determined, which might depart from the value of α for the trial TWM.

Investigations of published data of several traveling-wave masers reveal that the net gain could have been considerably increased by optimizing the pitch. Very often the optimum pitch is shorter than the design pitch by a factor of 2 to 3, leading to a loss in net gain (L unchanged) by a factor of 1.33 to 1.80. A substantial decrease of the pitch and a scaling down of the cross section dimensions correspondingly may of course in some cases lead to fabrication difficulties.

Care has to be taken in applying the above results to longitudinally stagger-tuned masers, since in that case $|Q_m|$ becomes different in different sections of the TWM. If the stagger-tuning is performed transverely, i.e. the paramagnetic line is broadene identically for each period, the results are very well applicable. Using superconducting materials in the SWS in such a way that the magnetic field is not severely perturbed, we will get an increased value of Q_{oo} and a larger gain per unit length at optimum pitch. Since a perturbed magnetic field more easily can be tolerated in staggertuned TWM:s, the use of superconducting material may facilitate the design of broad band TWM:s.

6. EXPERIMENTAL SLOW-WAVE STRUCTURES FOR TRAVELING-WAVE MASERS

6.1. Introduction

In this chapter we will discuss the properties of slow-wave structures used in actual TWM:s. A method for determining the SWS dispersion characteristic even when an isolator is present in the SWS, is described. The properties of a number of different SWS:s are discussed using the theory presented in chapter 2. It is shown that airgaps between the conductors and the high-dielectric-constant loading material in region 2, Fig. 2.2, are present and cause deviations between the theoretically predicted and experimentally determined dispersion characteristics.

The influence of the dielectric properties of the rutile maser crystal ($\varepsilon_{\perp} \approx 120$, $\varepsilon_{11} \approx 250$) on the SWS dispersion characteristic is interpreted in some detail.

6.2 Determination of the SWS dispersion characteristic

All measurements of the SWS passband and slowing factor were made using swept frequency techniques. The slowing factor for an empty SWS was measured using the resonant method (see e.g. Kollberg 1966). However, in SWS:s with an isolator, the backward wave is heavily attenuated. Another method was developed in which the phase shift of the transmitted wave in the SWS was measured. The experimental set-up is shown in Fig. 6.1.

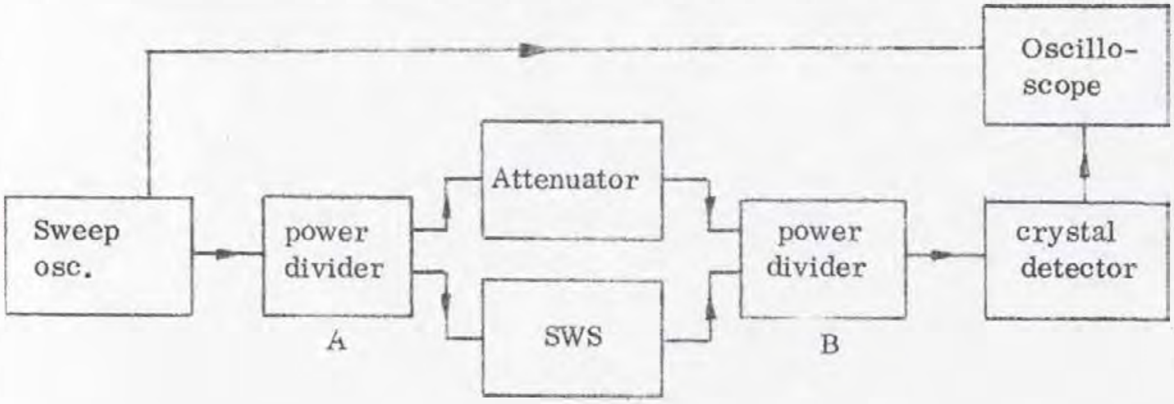

Fig. 6.1 Experimental set-up for measurements of the dispersion characteristic.

At B the wave going through the SWS and the wave going through the attenuator via the power dividers are added. Depending on the phase shift experienced by the two different waves, one obtains positive or negative interference at B. In practice one chooses the electrical length of the attenuator branch equal to that of the feed lines between the SWS and the power dividers. Hence, one obtains

$$\varphi = \frac{p}{L} \cdot n\pi \tag{6.1}$$

where n is an integer related to the detected maxima and minima and L is the physical length of the SWS.

An example of the interference pattern obtained in an experiment on the MAC2 TWM (see Table 6.I and 6.II) is shown in Fig. 6.2. Also notice the gradually decreased transmitted power through the SWS at the high-frequency part of the passband. This decrease is caused by the increased ohmic attenuation, discussed in chapter 5 (eqn. (5.6)).

The method described here has been independently used at the Jet Propulsion Laboratories, Calif. (B. Clauss, private communication).

6.3 Properties of experimental SWS:s

In Table 6.I and 6.II we give data for a number of SWS used in actual TWM:s. They are all loaded with rutile maser crystals and isolator materials, as indicated in Fig. 6.4. Measurements on empty SWS:s yielded, with no exceptions, wider passbands and smaller slowing factors than predicted by the theory described in chapter 2. The most probable explanation of this phenomenon is that small airgaps are present between the conductors and the dielectric loading (see Kollberg 1966, Fig. 9.3). Since the ceramic materials are soldered to the ground planes,no airgaps can be present at those surfaces. However, the fit between the conductors and the dielectric material must be perfect over the whole length ℓ_2 (Fig. 6.4). In Fig. 6.3, we show a recording of the surface of an unpolished dielectric loading material (polycrystalline rutile, $\varepsilon_r = 85$), as used in the SWS:s. We believe that a mean airgap of 1 μm , which is only of the order of 1 % of the conductor thickness, may very well be present. When such a high dielectric constant as $\varepsilon_r = 85$ is used, we find that an airgap of 1 μm considerably affects the SWS dispersion characteristic (Kollberg 1966, Fig. 9.3).

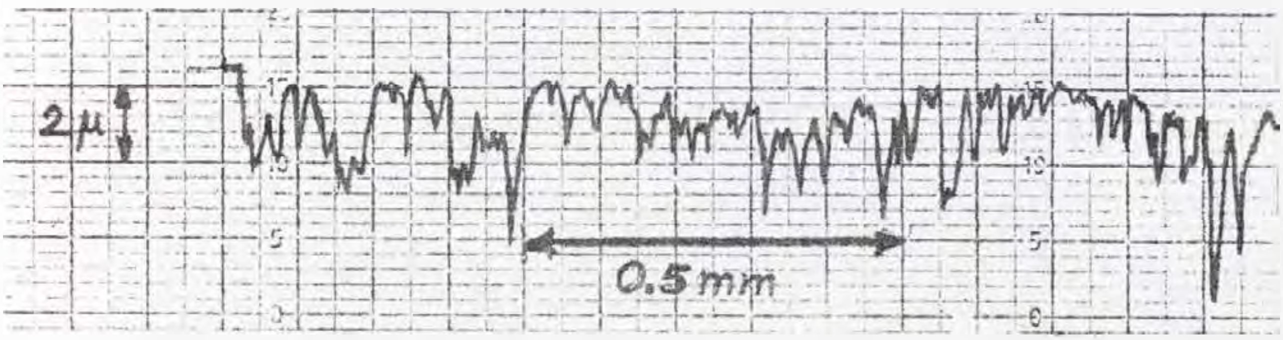

Fig. 6.3 Depicts the surface of a piece of polycrystalline rutile, used as a dielectric loading in region 2 (see Fig. 2.2) of an L-band SWS. The recording has been obtained by using a "Talysurf" apparatus from the Rank-Taylor-Hobson Division of the Rank Organisation in Leicester, England.

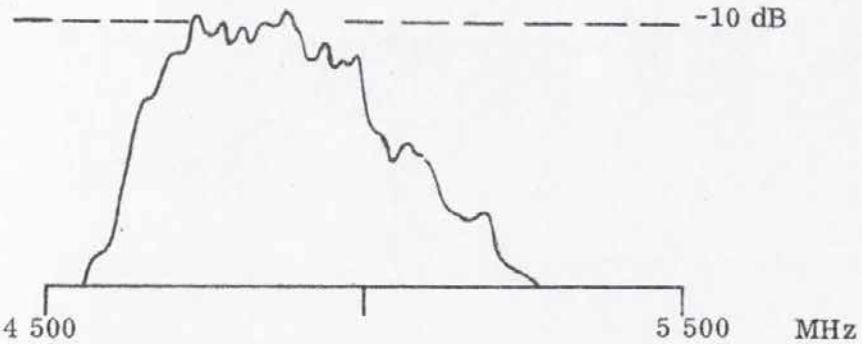

(a)

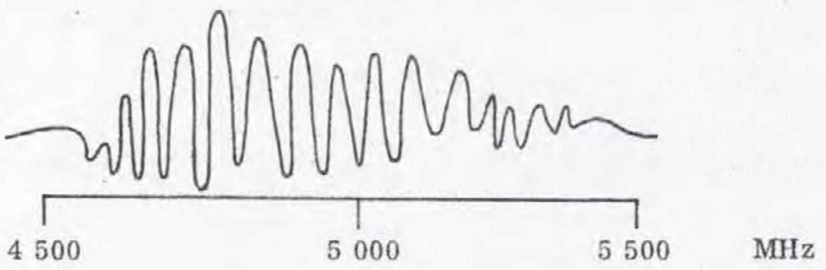

(b)

Fig. 6.2 Passband (a) and interference pattern for detemination of the slowing factor (b) for the TWM MAC 2.

Table 6.1 Dimensions for TWM SWS:s.

Maser	p mm	W_1/p	W_2/p	t/p	x/p	ℓ_1 mm	ℓ_2 mm	ε_r	b mm	a mm	δ mm
MAL 2	1.0	1.75	1.75	0.10	0.4	6.0	1.1	85	1.55	6.0	0.01
MAS 2	1.0	1.75	1.75	0.06	0	5.1	1.37	25	1.55	4.9	0.20
MAC 2	1.0	1.58	1.85	0.10	0	5.3	1.57	10	1.35	4.25	0.10
MAC 3	1.0	1.50	1.80	0.06	0	4.1	1.0	10	1.40 1.18	3.8 2.0	0.10 0.3
MINIMAC	0.5	0.8	1.0	0.06	0	3.50	1.40	10	0.7 0.7	3.20 2.50	0.15 0.10

The dimensions are defined in Fig. 6.4 and 2.2. The last letter in the notations for the masers indicate the waveguide-band corresponding to the TWM frequency band.

Table 6.II. Performance of TWM SWS:s

	MEASURED DATA				CALCULATED DATA							
MASER	f_o MHz	f_π MHz	Δf_t MHz	S_{min}/f_m	$\varepsilon_1(0)$	$\varepsilon_1(\pi)$	E	$\frac{f_\pi - f_o}{\Delta f_t}$	f_o Empty MHz	f_π Empty MHz	$x_1(0)$ degrees	$x_2(0)$ degrees
MAL 2	1719	2160	350	155/1850	4.0	-	7.0	1.3	1710	1950	13.0	
MAS 2	3100	3850	650	91/3450	4.5	-	6.8	1.15	3370	3570	22.5	25.5
MAC 2	4550	5325	650	97/4800	4.0	-	7.5	1.08	5000	5130	37.3	26.3
MAC 3	4900	6350	1360	52/5600	9.5	2.3	7.5	1.03	7280	7130	48.3	18.6
MINIMAC	5250	6550	1100	108/5800	8.0	1.5	7.0	1.18	6710	6650	28.3	35.6

f_o = lower cut-off frequency

f_π = upper cut-off -"-

Δf_t = TWM tunable bandwidth

S_{min} = minimum slowing factor

f_m = frequency for minimum slowing

$\varepsilon_1(0)$ = rel. diel. const. of region 1 for $\varphi = 0$

$\varepsilon_1(\pi)$ = " " " " " 1 " $\varphi = \pi$

$x_1(0)$ = phase shift for the TEM wave in region 1, $\varphi = 0$

$x_2(0)$ = " " " " " " " " 2, $\varphi = 0$.

E = $(f_\pi - f_o) \cdot S_{min} \cdot p$ (GHz · mm)

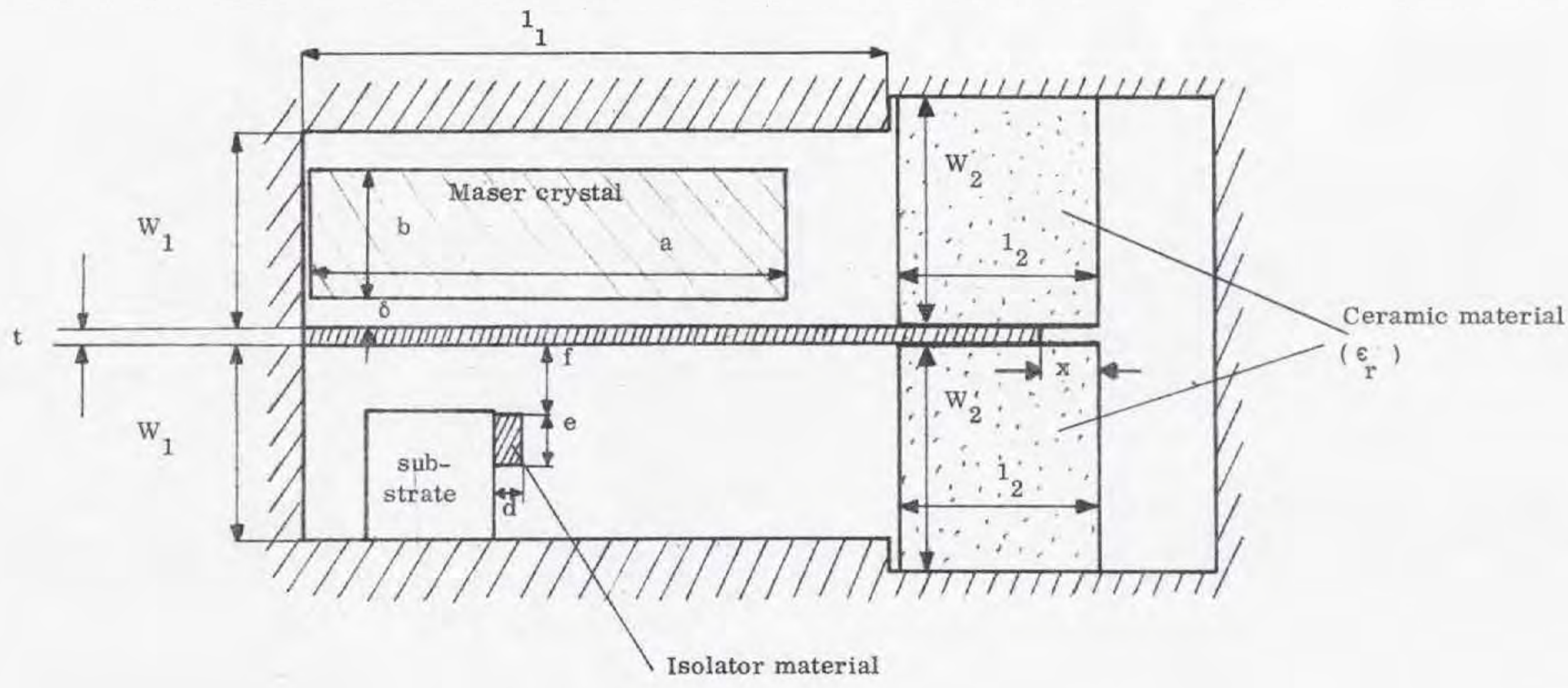

Fig. 6.4 Cross-section of a traveling wave maser.

The highest slowing factor was obtained with an experimental SWS, containing no maser crystal, and with the following dimensions in mm

$p = 1.0$ $\qquad W_1 = 1.95$ $\qquad W_2 = 2.00$

$t = 0.10$ $\qquad \ell_1 = 6.3$ $\qquad \ell_2 = 1.35$

The relative dielectric constant of the dielectric loading was 85. The following parameters were measured and calculated theoretically

	lower cut off frequency MHz	passband MHz	minimum slowing factor
Measured	1460	170	405
Theoretical	1380	80	755

A SWS with such a small passband as this one is of course particularly sensitive to airgaps of the kind discussed above.

Another evidence for airgaps being the cause of the discrepancy between the theoretical predicted and experimentally measured data, was obtained from experiments on the MAL2 SWS. In these experiments we changed the value of x (see Fig. 6.4), as described in Fig. 6.5. For small values of x, the measured slowing factor is again much smaller than the theoretically predicted one. However, when x increases, the theoretical slowing factor rapidly approaches the experimental one, since for large x-values $C_f(\varphi)$ (section 2.3) dominates the shape of the dispersion characteristic. The close resemblance in shape between theory and experiment for the lower cut - off freqeuency supports the idea of airgaps. Furthermore, it is interesting to observe that the measured lower cut-off frequency is higher than the theoretical, although the passband is lowered about 3 % due to the maser crystal.

In this context it is appropriate to ask whether the approximate eqn:s (2.5) - (2.8) are accurate enough or if a more exact theory (assuming no airgaps) will be in better agreement with the measurements. For higher frequencies the rf magnetic field becomes more tightly coupled to the rf electric field and hence deviates from the field configuration satisfying the Laplace eqn. Also the amplitude of the field components

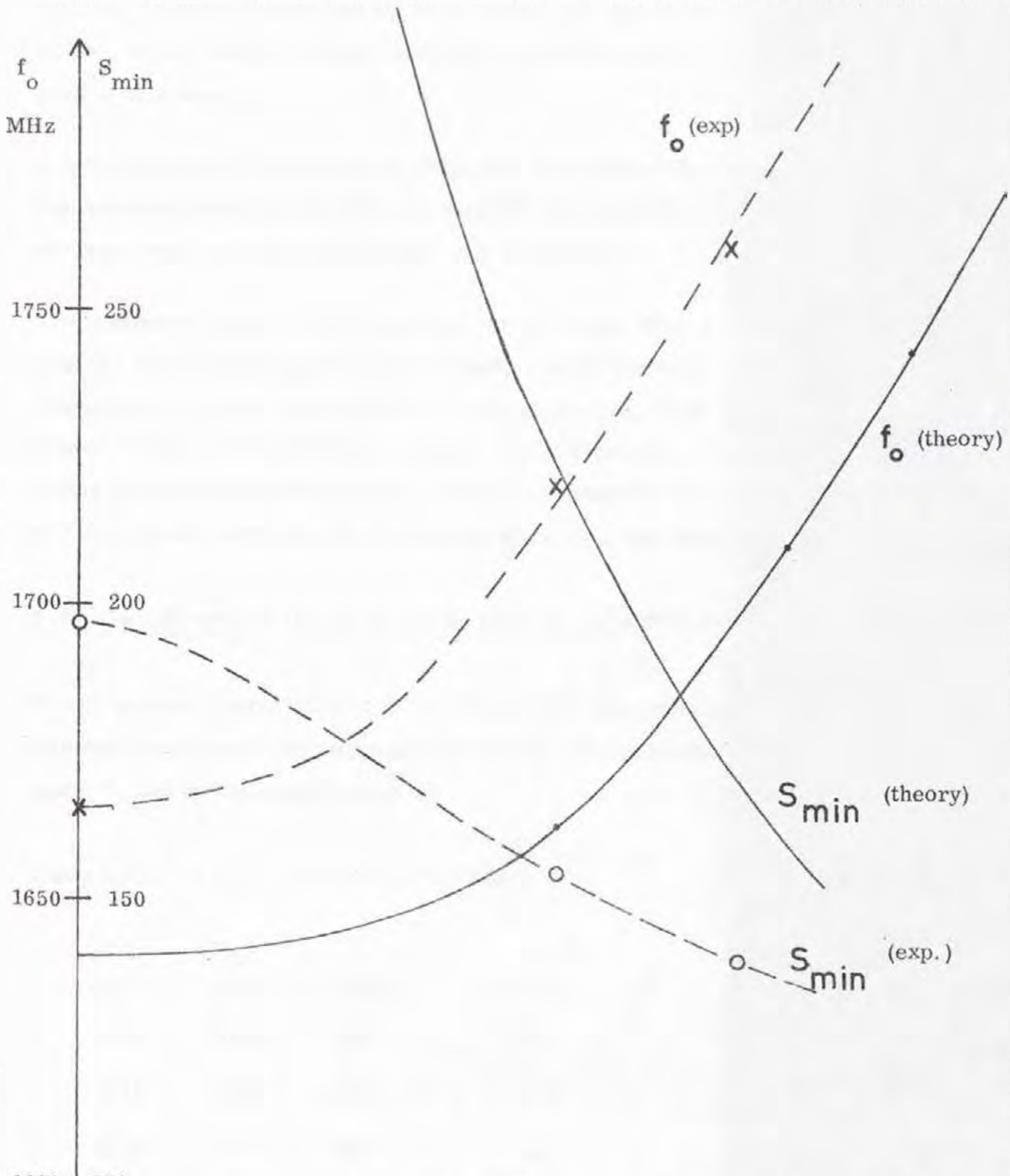

Fig. 6.5. Properties of an L-band SWS vs. x/p, where $(x + \ell_2)/p = 1.5$, $\ell_1/p = 6.0$, $t/p = 0.10$, $p = 1$ mm and $\varepsilon_r = 85$.

along the conductors (these field components are related to a surface wave) increase roughly proportionately to frequency, causing a change of the field configurations. An exact theory has not been worked out, but in the opinion of the present author, it will not give results deviating noticeably from the approximate theory used in this paper.

The upper cut-off frequencies in Table 6.II are obtained from measurements of the reflected power of the SWS. As expected this value for the upper cut-off frequency is higher than the highest frequency of the passband.

The measured upper cut-off frequency for the maser MAS 2 is appreciably higher than the theoretical upper cut-off frequency, most certainly due to air-gaps. Such airgaps also exist in the TWM MAC 2. Theoretically, when this SWS contains no maser crystal, it should have a double-valued dispersion characteristic. However, it was single-valued and yielded a minimum slowing factor of 240. The measured and theoretical lower cut off frequencies were 5160 and 5000 MHz, respectively.

6.4 The influence of the rutile maser crystal on the SWS dispersion characteristic

The dispersion characteristic of the MAC 2 SWS was experimentally determined for different positions of the rutile maser crystal. The experiment is described in Fig. 6.6 and 6.7, and in Table 6.III and 6.IV.

Table 6.III . ($\delta_1 = 0$ mm , $\delta_2 = 1.0$ mm)

w_1 mm	w_2 mm	f_o MHz	$\varepsilon_1(0)$ exp.
0.05	0.18	4550	3.9
0.18	0.05	4485	4.2
0.23	0	4330	5.0

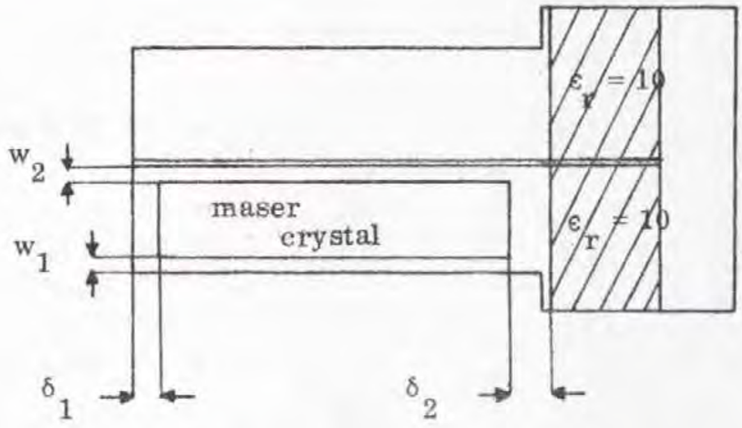

Fig. 6.6 Cross section of the MAC 2 TWM. The position of the rutile crystal (4.25 x 1.35 mm) was changed and the SWS performance described in Fig. 6.7 was measured. For MAC 2, W_1 = 1.58 mm, ℓ_1 = 5.3 mm (see Fig. 6.4).

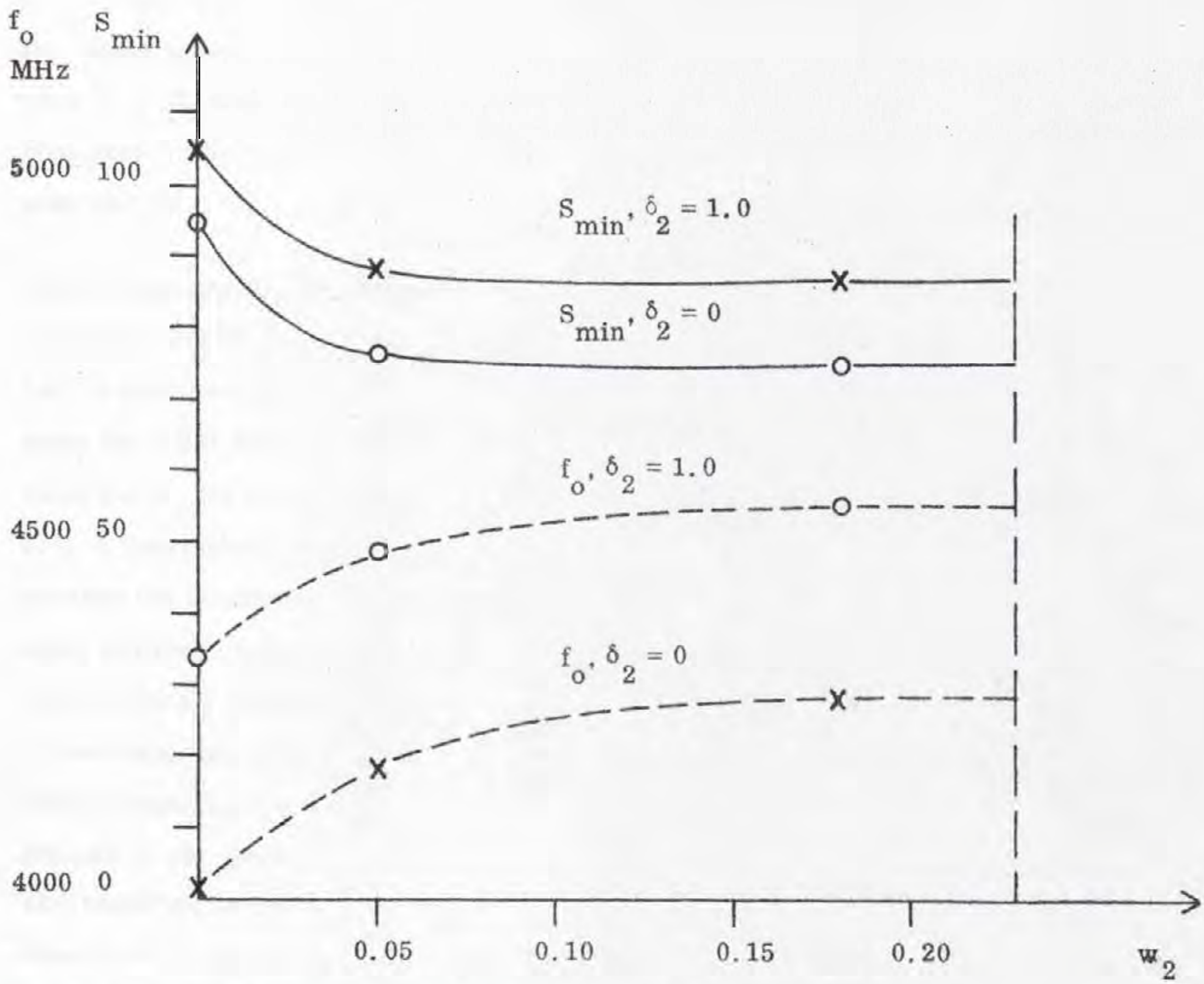

Fig. 6.7 The minimum slowing factor S_{min} and the lower cut-off frequency f_o vs. the position of the rutile crystal (see Fig. 6.4).

Table 6.IV ($\delta_1 = 1.0$ mm, $\delta_2 = 0$ mm)

w_1 mm	w_2 mm	f_o MHz	$\varepsilon_1(0)$ exp.	$\varepsilon_1(0)$ theory
0.05	0.18	4270	5.3	4.3
0.18	0.05	4170	5.8	6.6
0.23	0	4000	6.8	7.1

The distances w_1 and w_2 are determined by using glassfiber-armed teflon sheets with a relative dielectric constant of 2.1. Due to the high dielectric constant of rutile ($\varepsilon_\perp = 120$, $\varepsilon_{11} = 250$), the maser crystal strongly interacts with the electric field. Hence the maser crystal affects the SWS dispersion characteristic most strongly when $\delta_2 = 0$, and by changing δ_1 and δ_2 the passband can be moved in frequency (compare Table 6.III and 6.IV). The determination of $\varepsilon_1(0)$ is described in the subsequent text.

The measurements performed with $\delta_2 = 0$ and $\delta_1 = 1.0$ mm are especially interesting, since they evidently yield results almost equal to those expected for $\delta_1 = \delta_2 = 0$. Let us discuss whether the influence of the rutile maser crystal can be accounted for using the TEM approximation (eqn. (2.5) - (2.8) and eqn. (2.23)). An experimental value for $\varepsilon_1(0)$ is obtained in Table 6.III and 6.IV using the graphs in Fig:s 2.3 and 2.4. A theoretical value is calculated (Table 6.IV), assuming that the capacitance between the conductor and the ground plane, by influence of the rutile crystal, is equal to three capacitances in series: the first one between the conductor and the rutile crystal, proportional to $2.1 \cdot (1-r) \cdot p/w_2$, the second one related to the fields within the rutile crystal ($\varepsilon_r = 120$), obtained from table 1 published by Kollberg (1967) assuming $r = 0.5$, and $W/p = 1.35$ (= the thickness of the rutile maser crystal divided by the pitch), and finally the third capacitance proportional to $2.1 \cdot p/w_1$ The resulting capacitance is coupled in parallel to the capacitance related to the other side of the conductor array, which is equal to half the value obtained from table 1 (Kollberg 1967).

Considering the accuracy in the determination of the relevant parameters (w_1, w_2 and f_o), the agreement between the theoretical and experimental values for $\varepsilon_1(0)$ is very good. This result also means that the rf magnetic field pattern is not noticeably perturbed in shape and therefore closely resembles the field pattern of a homogeneously loaded region 1.

In Fig. 6.5 the lower cut-off frequency and the minimum slowing factor are depicted as functions of w_2 and $\delta_2 = 0$. It is noticed that the influence of the maser crystal changes rapidly for small values of w_2 and is almost constant for $w_2 > 0.05$ mm. The substantial increase in slowing factor for $w_2 \rightarrow 0$ means that $\varepsilon_1(\pi)$ increases, lowering the upper cut-off frequency more rapidly than the lower cut-off frequency.

For the other SWS:s presented in Table 6.II, $\varepsilon_1(0)$ and $\varepsilon_1(\pi)$ have been computed assuming that the cut-off frequencies when the rutile crystal is removed from the SWS can be correctly calculated from theory. In these calculations the graphs in Figs. 2.3 and 2.4 were very useful. It can be seen from Table 6.II that the calculated $\varepsilon_1(0)$ agrees very well with the results obtained in the experiments on MAC 2 (Table 6.III and 6.IV). The high values obtained for $\varepsilon_1(0)$ in MAC 3 and MINIMAS are due to the fact that these SWS:s are loaded by rutile maser crystals on both sides of the conductor array. In the latter two masers, a noticeable effect of the dielectric properties of the maser crystal on the upper cut-off frequency is observed. Notice that such a moderate value for $\varepsilon_1(\pi)$ as 2.5 is enough to lower the upper cut-off frequency of MAC 3 from 7130 MHz to 6300 MHz. This is explained by the fact that $\ell_1\sqrt{\varepsilon_1(\pi)}$ is of considerable length compared with $\lambda_o/4$ (compare $x_1(0) = 48.3^o$).

6.5 Passband vs. the minimum slowing-factor

The product $(f_\pi - f_o) \cdot S_{min}$ is a measure of the SWS contribution to the tunability and the gain of a TWM. Assuming that the form of the dispersion characteristic is at least approximately described by eqn. (2.25) - (2.27) (compare Kollberg 1966, chapter 5), we obtain

$$(f_\pi - f_o) \cdot S_{min} \cdot p \approx 100 \;\; F(a, \varphi')$$

where $F(a, \varphi')$ is obtained from Fig. 2.6 . f_π and f_o are expressed in GHz, and p in mm. From Table 6.II and Fig. 2.6 we can see that the experimental SWS:s fit a-values between a = 3.5 and a = 2.5. By making a design with lower a-values, a larger product $(f_\pi - f_o) \cdot S_{min} \cdot p$ is obtained. The a-value can be decreased, e.g., by using lower ratios W/p. However, this would mean that S_{min} is obtained for higher values of φ and that the degree of circular polarization decreases in most parts of the SWS. We then get difficulties in the design of the isolator (see Chapter 3) and a lower gain from the maser crystal (see Kollberg 1966 a, chapter 7). Other means of improving the SWS performance can be found in section 2.3 and 2.4.

The TWM called MINIMAC is an attempt to build an "optimum pitch" TWM (Kollberg 1966 b). The expected improved performance of the SWS is demonstrated in Fig. 6.8. The improved amplifier characteristics are discussed in chapter 7. Tolerances in the manufacturing process for the transverse dimensions had to be improved by a factor of two in order to obtain the same rf performance as that of MAC 3.

6.6. Manufacturing considerations for the SWS:s

The manufacturing process for the SWS:s was improved with time (the TWM:s were built in the chronological order listed in Tables 6:I and 6.II). In order to avoid airgaps between the dielectric loading and the ground planes, and in order to obtain a mechanically strong and stable construction, the dielectric pieces were soldered to the ground planes. This was done using a special silver paint ("poliersilber 242 L" manufactured by Degussa, Frankfurt, W. Germany) and common solder alloyed with 2 % silver. The following dielectric materials were used for the loading (region 2, Fig. 2.2):

Dielectric Material	Relative dielectric const.	Coeff. of Expansion at 300 °K	Manufacturer	Trade name
Polycrystalline rutile (TiO_2)	85	$8 \cdot 10^{-6}$	3M Corporation	AlSiMag 192
Mixed composition (unknown)	25	$7 \cdot 10^{-6}$	Emmerson and Cumming, Inc.	Eccoceram HiK
Alumina (Al_2O_3)	10	$6 \cdot 10^{-6}$	3 M Corporation	AlSi Mag 772

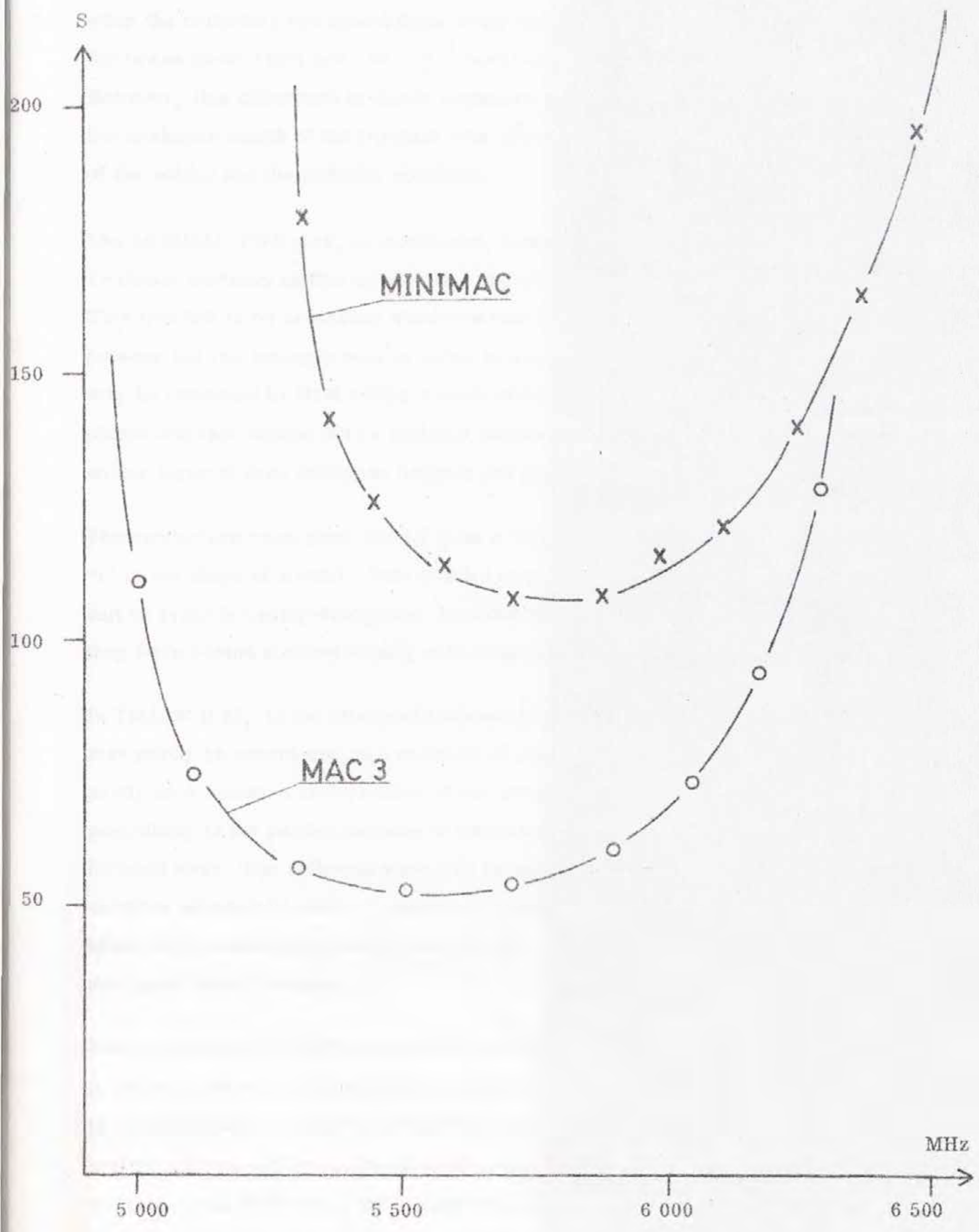

Fig. 6.8 The slowing factor vs.frequency for the TWM:s MAC 3 (p = 1 mm) and MINIMAC (p = 0.5 mm).

The metallic structure was manufactured from brass (58 % Cu, 39 % Zn and 3 % Pb) and was subsequently silver plated. The total relative change in linear dimensions when the materials are cooled from room temperature to near $0^{\circ}K$ is $400 \cdot 10^{-5}$ for brass (Scott 1959) and $100 \cdot 10^{-5}$ (estimated) for the dielectric materials. However, this difference in linear expansion did not cause any trouble, due to the moderate length of the ceramic rods (65 mm) and to the elastic properties of the solder and the metallic structure.

The MINIMAC TWM was, as mentioned, manufactured with still greater care. To obtain surfaces as flat as possible, the whole SWS was polished on a flat board. This was felt to be necessary since one requires a constant gap (t, see Fig. 2. 2) between the two ceramic rods in order to avoid airgaps. The soldering procedure may be improved by first letting a thick string of solder be attached to the ground planes and then cutting it to a suitable thickness. This will ensure a homogeneous solder layer of even thickness between the ceramic and the ground planes.

The conductors were photo etched from a copper sheet of the correct thickness "t" in the shape of a comb. This yielded conductors without burrs, which are difficult to avoid in cutting processes. In order to protect the conductors from oxidation, they were coated electrolytically with a thin layer of gold.

In Table 6. II Δf_t is the observed transmission pass band. The ratio $(f_\pi - f_o)/\Delta f_t$ may partly be considered as a measure of the "mechanical quality" of the TWM:s and partly as a measure of the quality of the design (compare S_{min} $(f_\pi - f_o) \cdot p$). If the periodicity is not perfect because of tolerance problems, reflections will occur for the forward wave. The reflected wave will be quickly absorbed by the isolator and no regenerative effects will show up. Hence, reflections will cause a decreased gain. This effect will be most pronounced close to the cut-off frequencies, and particularly at the upper cut-off freqeuncy.

The couplings to the SWS:s are of the type described by Kollberg (1966 a) fig. 6. 3. In order to obtain a good performance the distance between the first resonator and the coupling strip, as well as the width of the coupling strip, were changed until the best match was obtained. This technique made it possible to obtain a broad-band coupling to the SWS with a VSWR less than 2. 0. This is quite sufficient, since the equivalent noise temperature of the TWM is raised by a negligible amount (see Kollberg 1969) and the equivalent gain loss is equal to or less than 0. 5 dB.

7. PROPERTIES OF SOME OPERATIONAL TRAVELING-WAVE MASERS

7.1 Introduction

In this chapter we shall give data for TWM:s built for the receiver system of the Onsala 25.6 m radio telescope. At the time of writing, TWM:s have been built for frequencies between 1.3 and 6.2 GHz. With the present technique we believe that TWM:s with rutile as the active material can be built for frequencies between about 1 GHz and 15 GHz. The lower frequency limit is determined by the isolator material, while the upper frequency limit is determined by tolerances and dimensions (at 15 GHz and $\epsilon_r = 10$, a quarter wavelength is equal to 1.6 mm).

7.2. General remarks

For frequencies below 4 GHz, $Cr-TiO_2$ with a nominal concentration of 0.025 % Cr^{3+} b.wt. was used as the maser material. The crystal was bought from National Lead Co., South Amboy, N.J. and had the c-axis perpendicular to the boule axis. Paramagnetic absorption measurements indicated that the crystal was not a perfect single crystal, but rather consisted of a number of subcrystals (see Fig. 4.4).

In TWM:s for the C-band (MAC 1-3 and MINIMAC in Table 7.I), $Fe-TiO_2$ was used as the maser material. The iron concentration was nominally 0.025 or 0.035 % Fe^{3+} b.wt. (see Table 7.II and 4.I). These two boules were also grown by National Lead Co. with one of the a-axes along the boule axis. However, the boules were considerably larger and also better single crystals than the $Cr-TiO_2$ boules.

The main reason for using $Fe-TiO_2$ at C-band was that the superconducting magnets available could not deliver the magnetic field required for $Cr-TiO_2$ at the c-axis operating point (see Fig. 4.8 and 8.3). Moreover, the c-axis operating point in $Fe-TiO_2$ can be used up to 7.6 GHz while the maximum signal frequency for $Cr-TiO_2$ is 5.4 GHz (see Fig. 4.8).

The isolator material used in the TWM:s discussed below (except for MAL 1) was Gd-YIG (5 % Gd) made by Sperry Microwaves Electronics Co. In MAL 1 we utilized Al-YIG with a saturation magnetization of 680 Gauss made by the Trans-Tech Inc. No difference in performance was noticed for these materials at L-band frequencies.

The operating temperature of the TWM:s is below the liquid helium lambda point (2.18 ^{o}K), offering the following advantages:

a) the heat conductivity of liquid helium at temperatures below 2.18 ^{o}K (Helium II) is extremely high (see e.g. Scott 1959). Hence, the cooling is extremely efficient and gain instabilities due to rapid heat fluctuations or boiling are negligble,

b) the spin lattice relaxation time of the pump transition is approximately proportional to 1/T, which means that the pump transition can be saturated with less pump power at 2^{o}K than at 4.2^{o}K, and

c) the gain can be increased by lowering the temperature, thus decreasing the contribution of the second amplifier to the system noise.

When the temperature is lowered, the liquid helium volume is reduced. However, this does not reduce the operating time considerably, as will be shown in chapter 9.

7.3 Traveling wave maser data

In Table 7.I, amplifier data and SWS data are given for all TWM:s built by us. The first successfully working TWM was MAL 1. (Kollberg and Yngvesson 1965). All masers but the recently finished MINIMAC have been in operation in the 25.6 m radio telescope at the Onsala Space Observatory. The net gain of all masers except MAL 1 and MAC 1 can be raised above 30 dB when the temperature is lowered below the operating temperature (see Table 7.I and Fig. 7.2).

Fig. 7.1 shows the electronic gain vs the frequency for MAL 2. The solid line represents the theoretical slowing factor in arbitrary units. The close agreement between the frequency dependence of the slowing factor and the electronic gain means that the filling factor is almost constant in the observed frequency interval (equivalent to $0.10 \lesssim \varphi/\pi \lesssim 0.35$). This is consistent with the facts that the maser crystal

Table 7.I

MASER	Tunable frequency range, MHz	T ^{o}K	G_{net} dB	B_{3dB} MHz	A_b dB	A_F dB	$G_{e\ell}$ dB	f_p GHz
MAL 1	1300-1500	1.8	20	5	-	8	34	47
MAL 2	1550-1780	1.9	30	6	>80	13	50	48
MAL 3	1560-1740	2.1	30	4	>80	13	52	48
MAS 1	2850-3250	1.8	30	10	>70	7	45	53
MAS 2	3100-3600	2.0	30	12	>70	8	42	55
MAC 1	4300-5150	1.7	20	12	~60	11	36	56
MAC 2	4550-5200	2.2	33*)	12	~60	3	42	56
MAC 3	5100-6250	1.7	27	20	~45	2	34	60
MINIMAC	5250-6100	4.2	24	~20	~60	3	33	60

*) 8 dB net gain at 4.2 ^{o}K

G_{net} = the minimum net gain over the passband at the operating temperature.

T = the operating temperature.

B_{3dB} = the -3dB bandwidth.

A_B = the backward wave isolator attenuation.

A_F = the forward wave isolator attenuation.

$G_{e\ell}$ = the electronic gain related to G_{net}.

f_p = the pump frequency.

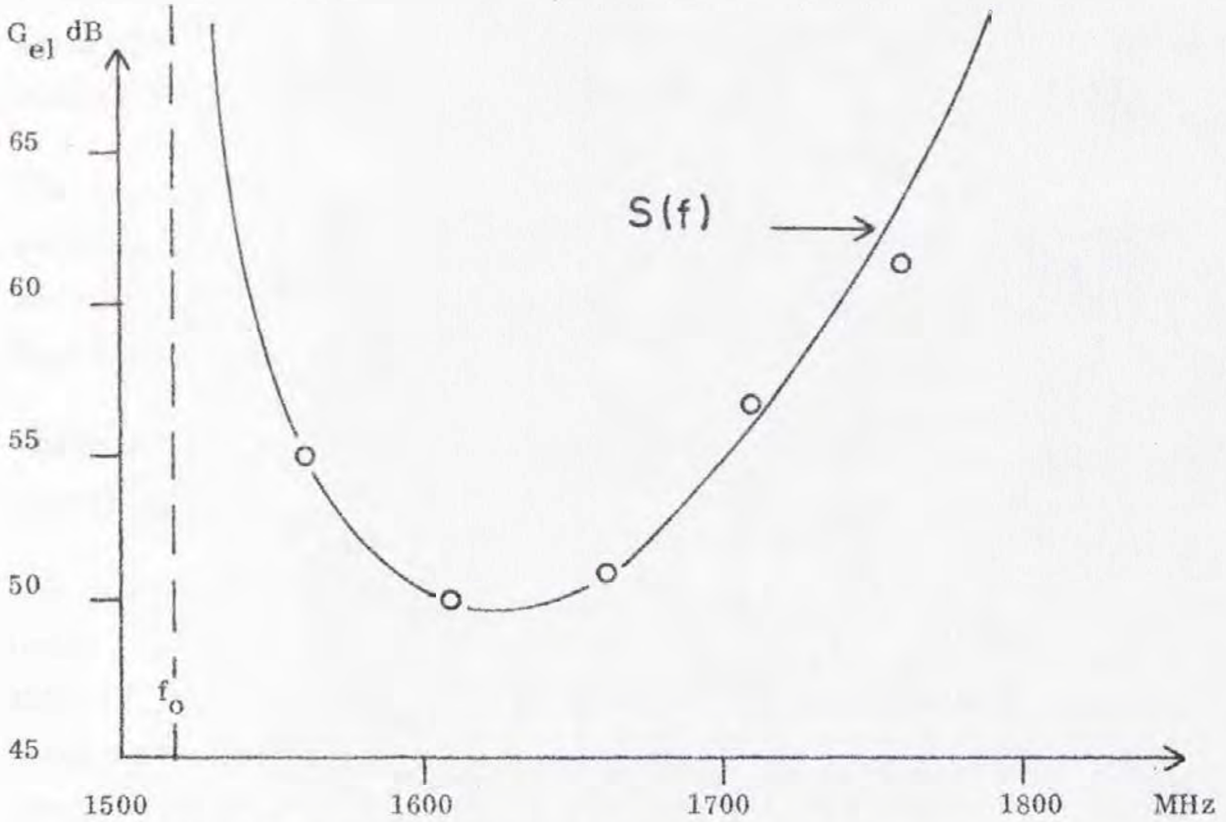

Fig. 7.1. Measured electronic gain (circles) vs. frequency for MAL 2.
The solid line represents the theoretical slowing factor vs. frequency.

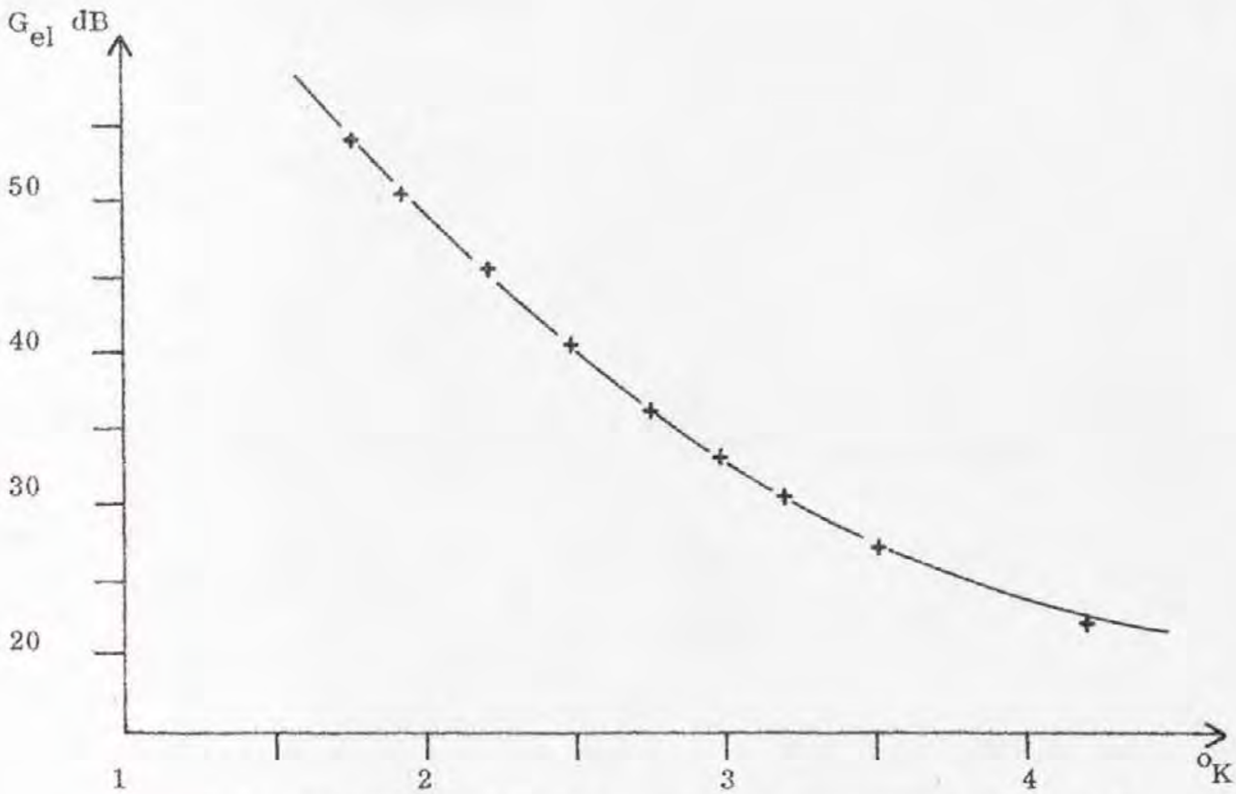

Fig. 7.2 The electronic gain (G_{el}) vs. the temperature for MAC 3.

is mounted very close to the conductor array (see Table 6.I) and that the transition probabilities for positive circularly polarized fields are approximately 2.5 times greater than the transition probabilities for negative circular polarization (Fig. 4.9).

The amplifier data vs. frequency for the different TWM:s listed in Table 7.I are in principle similar. As an example, data for the MAC 2 are depicted in Figs. 7.2 and 7.3. The temperature dependence for G_{el} is more pronounced for Cr-TiO_2 than for Fe-TiO_2 (see Table 7.II).

The 3-dB bandwidth of the TWM:s is determined by crystal quality and line broadening caused by the isolator rather than by the natural paramagnetic linewidth.

The isolator of MAC 2 consists of one cubic garnet piece per period, i.e. the isolator is of the divided type, described in section 3.3. The TWM:s listed above MAC 2 in Table 7.I have an isolator in the shape of a long slab, while the TWM:s listed below MAC 2 all have divided isolators. This is readily seen in Table 7.I, since the forward wave isolator losses (A_F) for the TWM:s with divided isolators are much lower than for the others.

The required isolator attenuation can be found from the following equation for the net gain (see e.g. Kollberg 1969, Appendix A),

$$g_{net} = \frac{(1-|\Gamma_{in}|^2)(1-|\Gamma_{out}|^2)10^{0.1(G_{e\ell}-L_{ins}-A_F)}}{|1-\Gamma_{in}\Gamma_{out}e^{-j2\phi}\cdot 10^{0.1\cdot A}|^2} \qquad (7.1)$$

where

$$A = G_{e\ell}(1+\gamma) - L_{ins} - A_F - A_B \qquad \text{(dB)} \qquad (7.2)$$

and

Γ_{in} = the reflection coefficient at the SWS input,

Γ_{out} = " " " " " " output,

ϕ = the phase shift from the input to the output of the SWS,

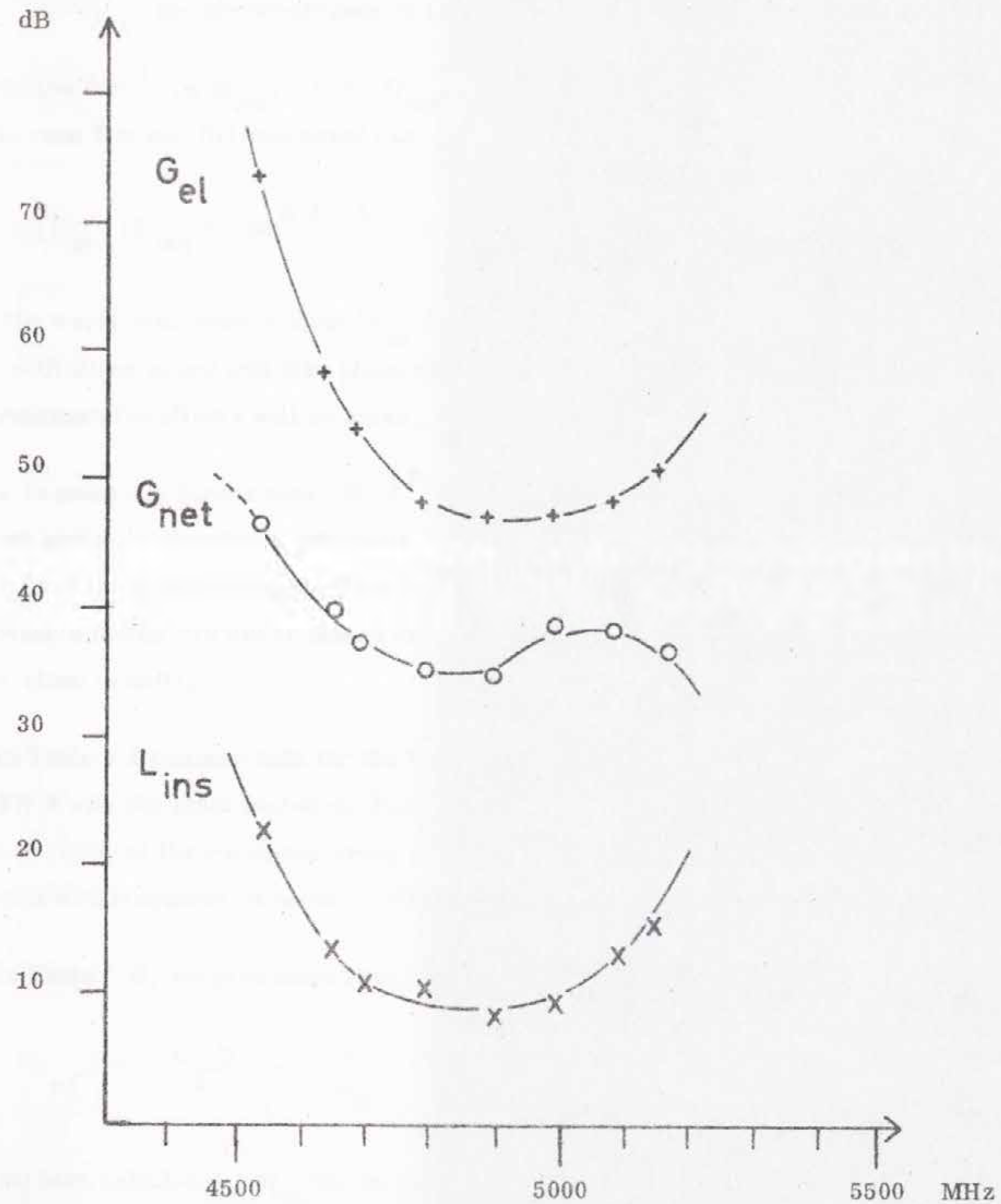

Fig. 7.3 The electronic gain (G_{el}), the net gain (G_{net}) and the insertion loss (L_{ins}) vs. frequency at T = 2.1 ^{o}K for MAC 2.

L_{ins} = insertion losses due to ohmic losses, and

$\gamma \cdot G_{e\ell}$ = the electronic gain of the backward wave.

Notice that ${}^{10}\log(g_{net}) = 0.1 \cdot G_{net}$ with G_{net} expressed in dB. From eqn. (7.1) it is seen that oscillations never can occur if

$$|\Gamma_{in}|\,|\Gamma_{out}| \cdot 10^{0.1 \cdot A} < 1 \tag{7.3}$$

The worst case occurs when $|\Gamma_{in}| = |\Gamma_{out}| = 1$. Hence, to be quite certain that oscillations never will take place and that the frequency variations of G_{net} due to regenerative effects will be small, the value for A in eqn. (7.3) has to be negative.

γ is generally larger than $|M_-|^2/|M_+|^2$, since the SWS rf magnetic fields are not perfectly circularly polarized. Typically, when a maser crystal is placed only on one side of the conductor array, we measured $\gamma = 0.5$ for Cr-$Ti0_2$ and $\gamma = 0.4$ for Fe - $Ti0_2$. When a maser crystal is placed on both sides of the conductor array, we obtain a γ close to unity.

In Table 7.I isolator data for the TWM:s are listed. It is seen that MAC 3 is the TWM with the least isolation. Furthermore, since the SWS is loaded with Fe-$Ti0_2$ on both sides of the conductor array (see Table 6.I), yielding $\gamma \approx 0.75$, a variation of the gain with frequency of about $\pm$ 3 dB is noticed.

In Table 7.II, we give some data for the SWS. Using the formula

$$G_{e\ell} = 27 \cdot \frac{L \cdot S}{\lambda} \cdot \eta \cdot \frac{1}{Q_m} \tag{7.4}$$

we have calculated $1/Q_m$ for the various TWM:s. The filling factor η, is an estimated value for the volume filling factor (see Kollberg 1966 a, chapter 7).

The nominal concentration percentages are given in Table 7.II. $(dG/dp) \cdot \Delta p$ gives the increase in gain for a decrease in the helium vapour pressure of Δp torr at the operating temperature $T^{o}K$.

MASER	p mm	L mm	S_{min}	η	$1/Q_m$	T ^oK	Doping agent % b.wt.nom.	$\frac{dG}{dp}$ ($\frac{dB}{torr}$)
MAL 1	1.0	40	170	0.40	0.100	1.8	.025 Cr	1
MAL 2	1.0	56	155	0.40	0.096	1.9	.025 Cr	1
MAL 3	1.0	56	195	0.40	.080	2.1	.025 Cr	1
MAS 1	1.0	56	90	0.40	.083	1.8	.025 Cr	.5
MAS 2	1.0	56	91	0.40	.067	2.0	.025 Cr	.5
MAC 1	1.0	56	83	0.40	.046	1.7	.025 Fe	.25
MAC 2	1.0	56	97	0.35	.052	2.2	.025 Fe	.25
MAC 3	1.0	56	52	0.45	.052	1.7	.035 Fe	.25
MINIMAC	0.5	50	108	0.45	.028	4.2	.025 Fe	.25

Finally, a few words should be said about the MINIMAC TWM, which is an attempt to build an optimum pitch TWM (section 5.3). Although the SWS-dimensions are not related to those of MAC 3 as required in section 5.3, the increased performance of MINIMAC can be seen from Table 7.I when it is compared with the MAC 3 TWM. The pitch of the MINIMAC SWS is 0.5 mm while it is 1 mm for the MAC 3 SWS. The slowing properties of the two SWS:s are depicted in Fig. 6.8.

At 4.2^oK the MINIMAC TWM has a net gain of 24 dB at 5.560 MHz. The frequency range for which the pitch is larger than the optimum pitch, extends from almost the lower cut-off frequency 5250 MHz to about 5 900 MHz, where the net gain equals the forward wave losses (see eqn. 5.15).

Calculations from the MINIMAC TWM data at 5560 MHz (Table 7.I) give an optimum pitch of 0.2 mm and a net gain of 39 dB at 4.2^oK.

7.4 Gain stability

Since the TWM does not use feed-back to increase the gain, it is an inherently stable amplifier. The relative gain fluctuations due to fluctuations in $1/Q_m$ is readily obtained as

$$\frac{dG_{e\ell}}{G_{e\ell}} = \frac{d(1/Q_m)}{1/Q_m} \qquad (7.5)$$

where $G_{e\ell}$ is expressed in dB. The possible sources of fluctuations in $1/Q_m$ are variations in the temperature and the pump power.

Since the temperature T depends on the liquid helium vapour pressure, the pressure must be kept constant. From Table 7.I we can see that for a pressure change of 1 torr, the gain changes by approximately 1 dB for an L-band maser. Hence, for the gain to fluctuate less than 0.05 dB, the pressure must be constant within 0.05 torr. This is readily obtained with a mechanical manostat of the type described by Sommers (1954).

The pump transition in a maser is always nearly saturated. Typically, the gain of the TWM:s discussed in this chapter changes by 0.1 dB for a 1 dB pump power change. Hence, to get gain fluctuations less than 0.05 dB, the pump power must be constant to within 0.5 dB (approximately 10 %). This is usually easily obtained.

Moreover, the influence of any changes in the klystron reflector voltage is virtually eliminated since the reflector voltage is modulated (Ray 1965). The modulation frequency f_m is such that $1/f_m << T_1$, where T_1 is the spin-lattice relaxation time of the pump transition (of the order of milliseconds). The gain increases appreciably (by about 2 dB) when modulation is used. The maximum increase in gain is obtained when the modulation amplitude is just as large as the klystron mode. Hence, more gain may be obtained if one could modulate the pump frequency over a larger frequency range.

One reason for the increased gain is that the pump transition line-width is quite large, and in order to saturate all spins one must spread the pump power over a certain frequency band. This is essentially what is done when the frequency is modulated. Another reason for the increase in gain is that the rutile crystal is a very high Q resonator with

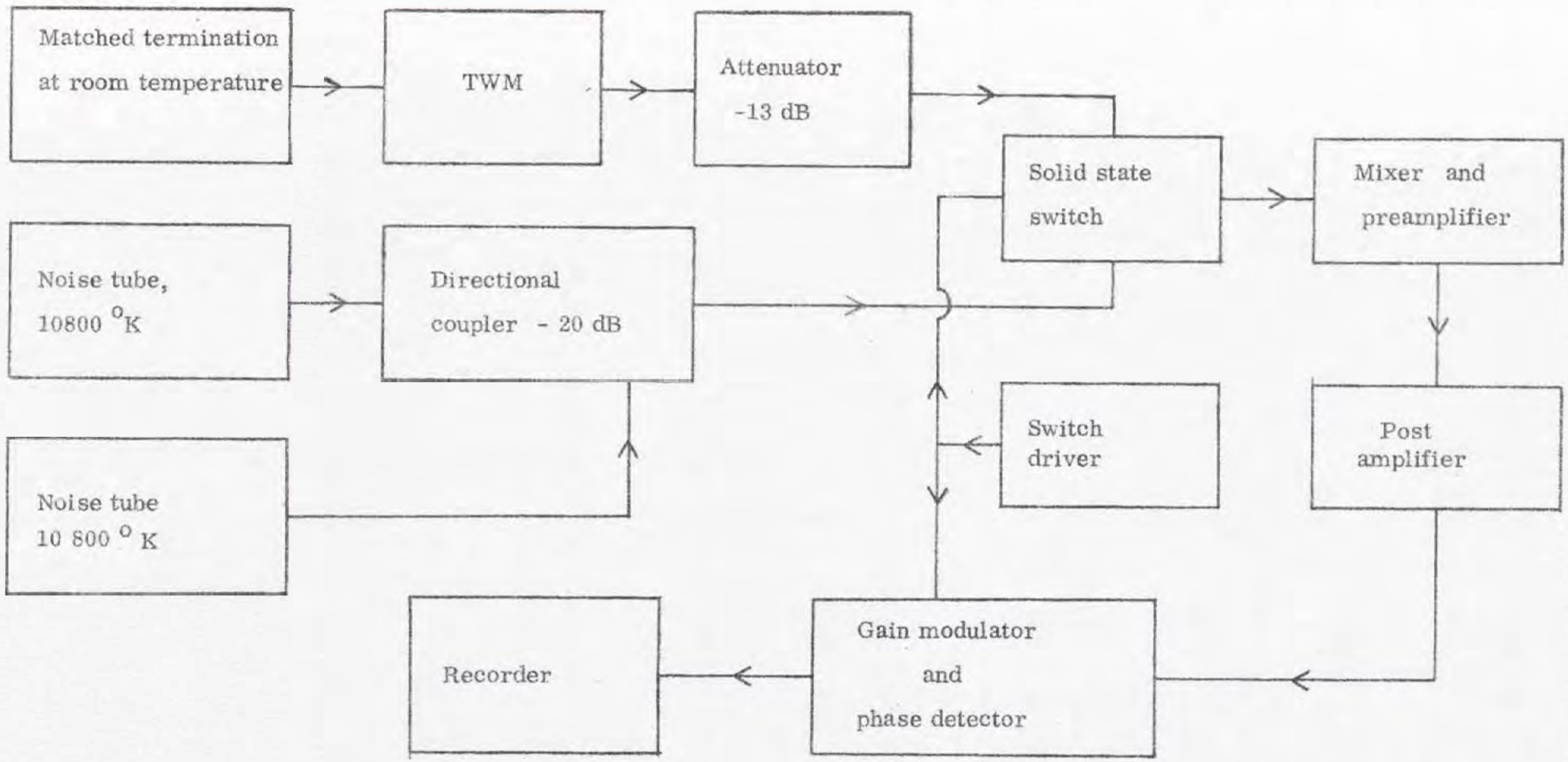

Fig. 7.4. Experimental set up for gain stability measurements.

many resonant modes within the klystron mode. When pump power is delivered into a single resonant mode, there will be regions within the crystal where the rf magnetic field intensity is zero. When the frequency is modulated, the power will be delivered into a number of different modes, and this yields a more homogeneous distribution of the pump frequency magnetic field energy density within the rutile crystal.

An experimental set-up for gain stability tests is shown in Fig. 7.4. The resolution, using a time constant of 2 seconds after the detector, is about 0.01 dB. A slow drift in the set-up of the order of 0.01 dB was measured when the TWM was replaced by a noise tube. A test result for MAL 2 is shown in Fig. 7.5. The long term gain fluctuations are within $\pm$ 0.06 dB. In parallel with the recording of the gain stability the resistance of a carbon resistor mounted just outside the TWM-SWS was monitored. The resistance depends on the bath temperature. However, since pump power was leaking out from the SWS and detected by the carbon resistor (which acts as an extremely sensitive bolometer), the observed changes in resistance are mainly due to changes in pump power. The change in resistance for 1 dB change in pump power is indicated in Fig. 7.5. The strong correlation between the pump power and gain fluctuations is evident. Notice that if the carbon resistor rather indicated temperature variations, we should instead obtain anticorrelation.

To obtain an even more stable gain, the pump power delivered to the rutile crystal must be kept constant. The changes in the detected pump power do not necessarily mean that the klystron output power varies. It could be a matching problem, caused by the changing liquid helium level. The output power of the klystron was not detected in this experiment.

The whole maser package was also tilted about 35 degrees (equal to the maximum tilting angle when the maser package is mounted in the telescope). The maximum changes in gain obtained during this test was 0.1 dB.

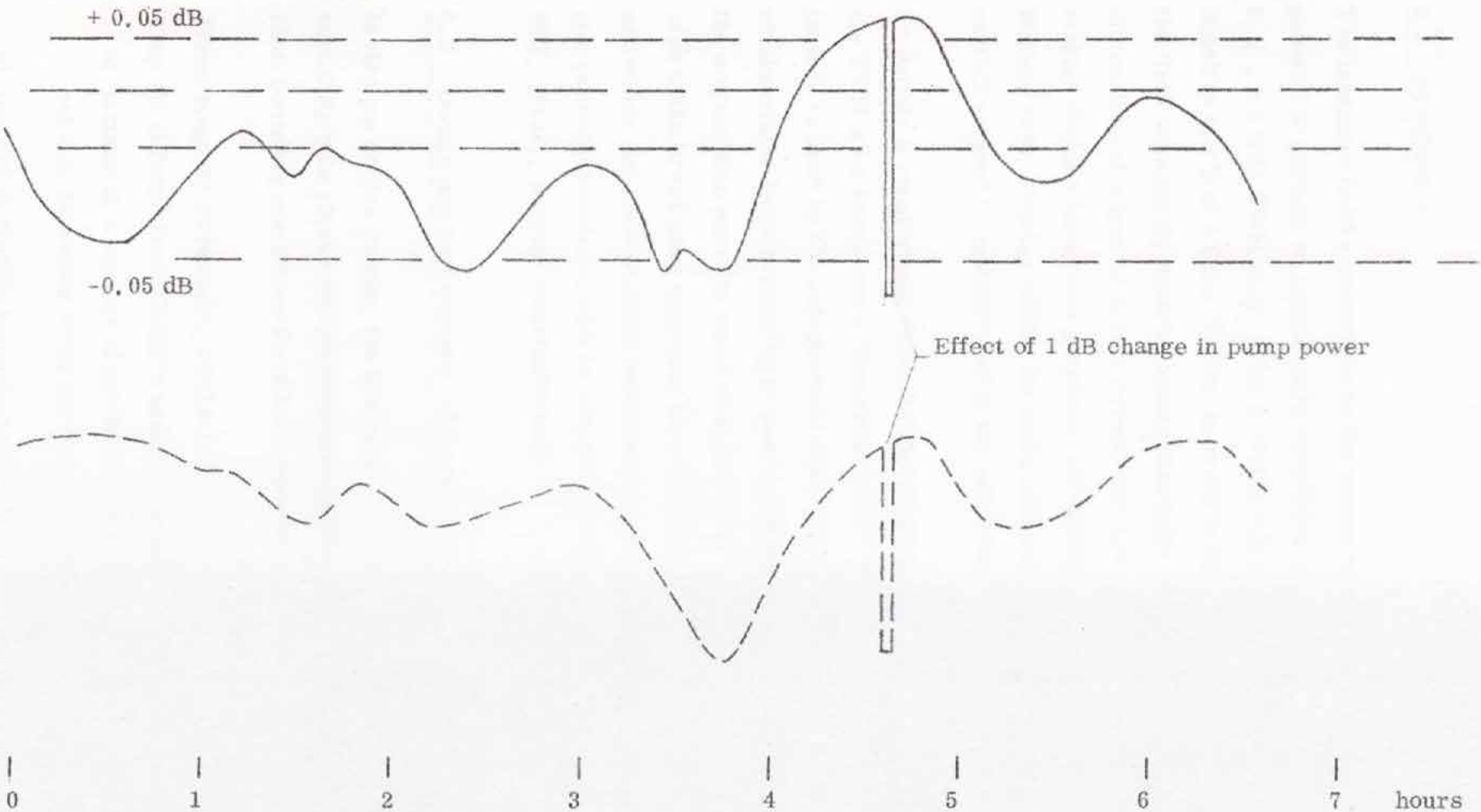

Fig. 7.5 Stability test on the TWM MAL 2. The upper curve depicts the gain variations vs time and the lower curve depicts the resistance of a carbon resistor vs time (see the text).

8. THE SUPERCONDUCTING MAGNET

8.1 Introduction

The magnetic field experienced by the maser crystal must be extremely homogeneous to prevent an undesirable broadening of the paramagnetic resonance line. E.g., a 5 GHz TWM (e.g. MAC 2, Table 7.I) has a half-power bandwidth of 12 MHz, which is 0.2 % of 5 GHz. Hence, in order to avoid an appreciable line broadening, the field homogenity must be better than a few parts in ten thousand. The geometrical dimensions of a typical maser crystal are 1.5 x 5 x 60 mm. Different superconducting magnet designs have been proposed, all fulfilling these requirements (Cioffi 1962, Walker 1966, Hentley 1967). We early adopted the Cioffi design and modified it in certain respects, as described in the subsequent text (section 8.2).

To satisfy a requirement from the radioastronomers for a simple method of tuning the TWM:s we developed a "dc-transformer" for tuning the magnetic field. This facility is used by the astronomers when they search for new molecular emission or absorption lines arising from poorly determined transition frequencies. Since the magnet also permits rapid changes of the TWM amplifying frequency, one can also make broad band very long base line interferometer (VLB I) measurements for extremely accurate position determination of radio sources and determination of transatlantic baselines with an accuracy of a few decimeters (Hans Hinteregger, MIT, Mass., private communication).

8.2 Design and performance of the superconducting magnet

In this particular design, the homogenity of the field is ensured by using high permeability pole pieces and superconducting shields that together constitute almost ideal boundary conditions for a homogeneous magnetic field.

Three magnets were built, SUMA I (1964), SUMA II (1967) and SUMA III (1969). They all differed from Cioffi's original design in the following respects:

a) instead of a number of cylindrical coils behind each pole piece, only one elliptical coil extending along the pole piece was utilized (see Fig. 8.1)

b) instead of shields consisting of many layers of superconducting material, solid shields were used.

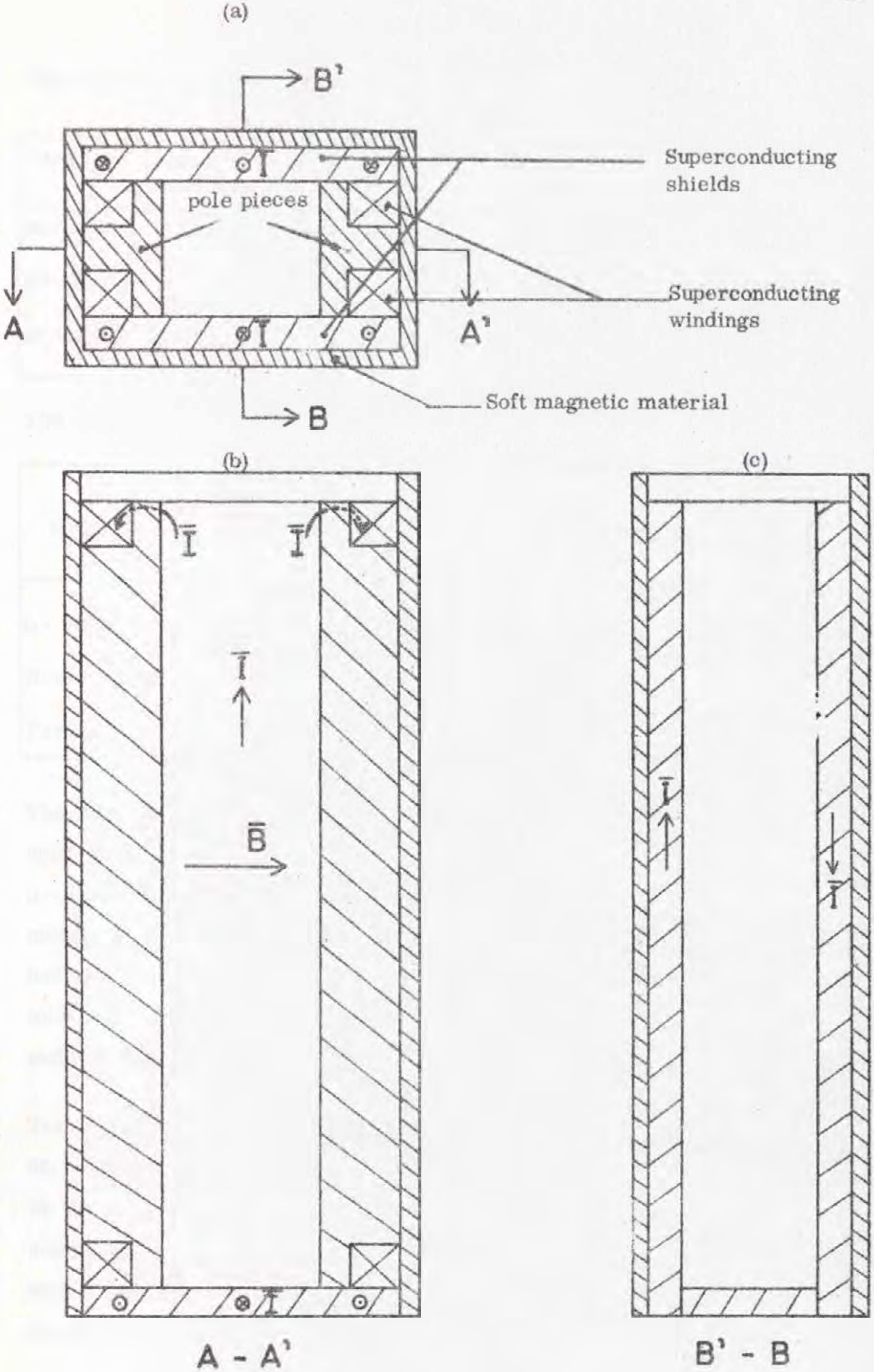

Fig. 8.1 The figure shows different cross-sections of the superconducting magnet SUMA III (see the text). $\bar{I}$ is the current in the super-

The materials used for the three magnets were:

Magnet	Magnetic circuit	Pole pieces	Windings
SUMA I	Permendur	μ-metal	Nb, 0.12 mm
SUMA II	"	radio-metal	Nb Zr, 0.25 mm
SUMA III	"	permendur	Nb Ti, 0.12 mm

The main properties of the magnetic materials are

Material	Saturation magnetization Gauss	Maximum permeability
μ- metal	8 000	120 000
Radio metal	16 000	30 000
Permendur	23 600	7 000

The optimum magnetic circuit is designed in such a way that saturation occurs approximately at the same time everywhere. This was one reason for exchanging μ- metal for radiometal and permendur in the pole pieces. From homogeneity measurements of the magnetic field (Fig. 8.2) it was realized that the pole pieces became saturated in the ends due to flux-loss, as discussed below. Notice that the total flux in the electromagnet cores is equal to the sum of the flux in the air gap and the flux leakage, e.g. from the pole piece through the windings.

The material in the superconducting shields is euthetic lead-bismuth (43.5 % Pb, 56.5 % Bi). This material is cheap and easy to machine. An alternative material is Nb Ti alloy (Walker, 1966), which is considerably lighter than Pb Bi and also allows somewhat higher current densities before it goes normal (about 10^5 A/cm^2 compared with 10^4 A/cm^2 for PbBi, at 5 kGauss.) However, NbTi is also a considerably more expensive material and was therefore not used.

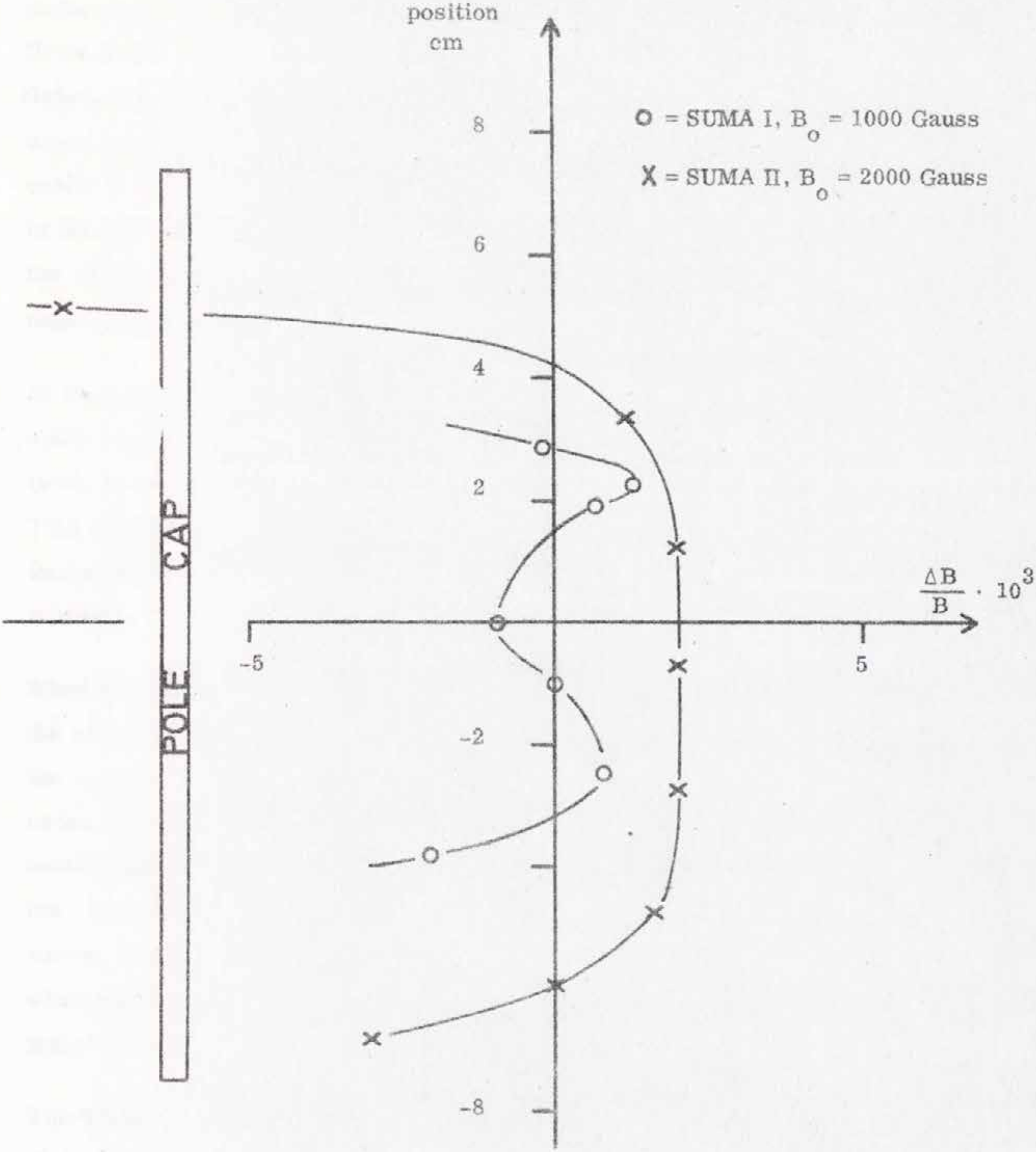

Fig. 8.2 The magnetic field vs. vertical position in the middle of the air gap for SUMA I and II.

One problem that must be consiuered in the design of the superconducting shields is the possibility of obtaining quenched fields in the shields. A qualtitative discussion of the current flow in the shields has been given by Schulz - DuBois (1969). A current flows in the shields perpendicular to the magnetic field lines, as indicated in Fig. 8.1. Hence, for the current to be continuous, it is closed in a path as indicated in the upper part of Fig. 8.1 b. It was found that quenching of a magnetic field occurs more easily if the shields were extended beyond the pole pieces. The price one has to pay in the present design for avoiding quenching is a flux loss over the edge and through the shield which causes an earlier saturation of the pole-piece material and/or magnetic circuit material (see Fig. 8.3).

At the time of the construction of SUMA I, II and III respectively, the best commercially available superconducting wires were chosen. Hence, the best present choice is Nb Ti-wire. The Nb Zr and Nb Ti-wires are coppercoated and formvar isolated. This allows measurements of the coil resistance (see Fig. 8.4), which varies with temperature and disappears when the superconducting transition temperature is reached.

When the magnet is energized, the closed superconducting circuit is broken by heating the wire as indicated in Fig. 8.4. Since the time constant of an LR-circuit is $\tau = L/R$, the copper coating of the superconducting wire had to be removed at the switch. In order to minimize the heating power, the heating wire is wound on a solid teflon core, outside the superconducting wire. Moreover, the switch is contained in a closed teflon structure, which will to some extent prevent the liquid helium from cooling the wires. A change in the necessary heating power is noticed at the λ - point (2.18 $^{\circ}$K) when the liquid helium becomes a superfluid. The power necessary at 4.2°K is typically 120 mW, and 300 mW at 2°K.

The TWM has to be oriented very carefully in order to get the magnetic field closely aligned along the rutile c-axis. This is done by turning the maser around the vertical axis, which is equivalent with turning the magnetic field approximately in the rutile ac-plane. When maximum gain has been obtained, the TWM structure is lifted. A carefully made "male" conical construction on the pump wave-guide will then fit into a "female" conical structure on the magnet, lifting the magnet and inter-locking the TWM and superconducting magnet. When the maser has reached room temperature, two screws are tightened in order to prevent any movements in the conical structure.

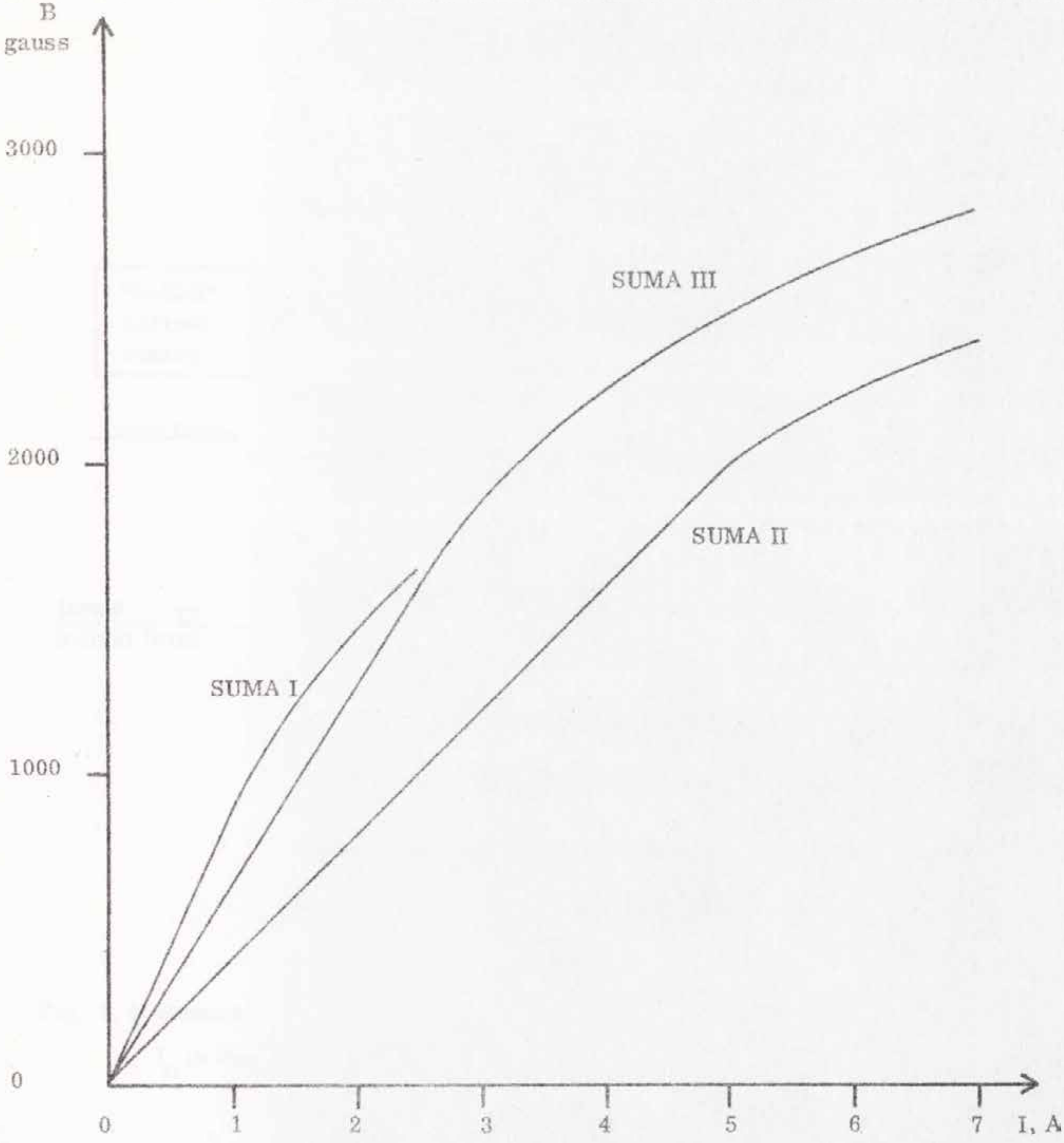

Fig. 8.2 Depicts measured magnetic field vs current for the superconducting magnets SUMA I, II and III.

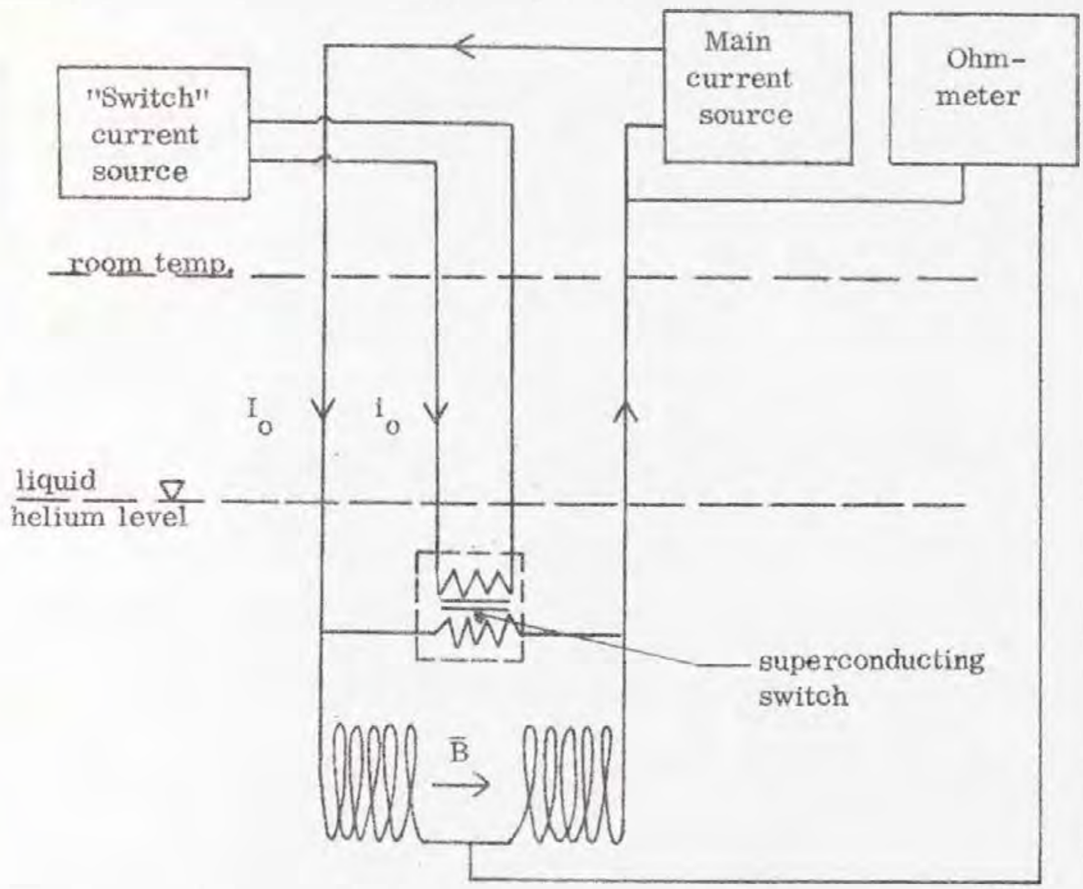

Fig. 8.4 Schematic diagram of the current circuit for the superconducting magnet. I_o is the energizing current and i_o the switch current.

8.3 The tuning circuit

In Fig. 8.5 the modified current circuit which includes the tuning circuit is shown. With the tuning current i_t, the flux φ in the permendur circuit can be changed. However, since the total flux enclosed by a superconductor remains constant, the flux in the magnet will also change. Using the following notations

	Main Magnet	Tuning circuit Magnet	Tuning circuit Tuning
Number of turns	N_m	n_m	n_t
Area	A_m	a_m	a_t
Magnetic field strength	B_m	b_m	b

we obtain (assuming the fields to be homogeneous):

$$N_m A_m B_m + n_m a_m b_m = \text{constant} \tag{8.1}$$

or

$$\Delta B_m = - \frac{n_m a_m}{N_m A_m} \cdot \Delta b_m \tag{8.2}$$

ΔB_m is slightly larger than the change in magnetic field strength over the maser crystal due to flux leakage, e.g. through the coil region. The maximum for Δb is two times the saturation magnetization of permendur, or 47 000 Gauss.

For $\varphi = 0$ one has $i_t = i_{to}$ where

$$i_{to} = \frac{n_m}{n_t} \cdot I_o \tag{8.3}$$

Hence, in order to avoid excessively large currents i_t, causing extra heating in the leads down to the liquid helium and possibly creating stability problems, n_m should not be too large.

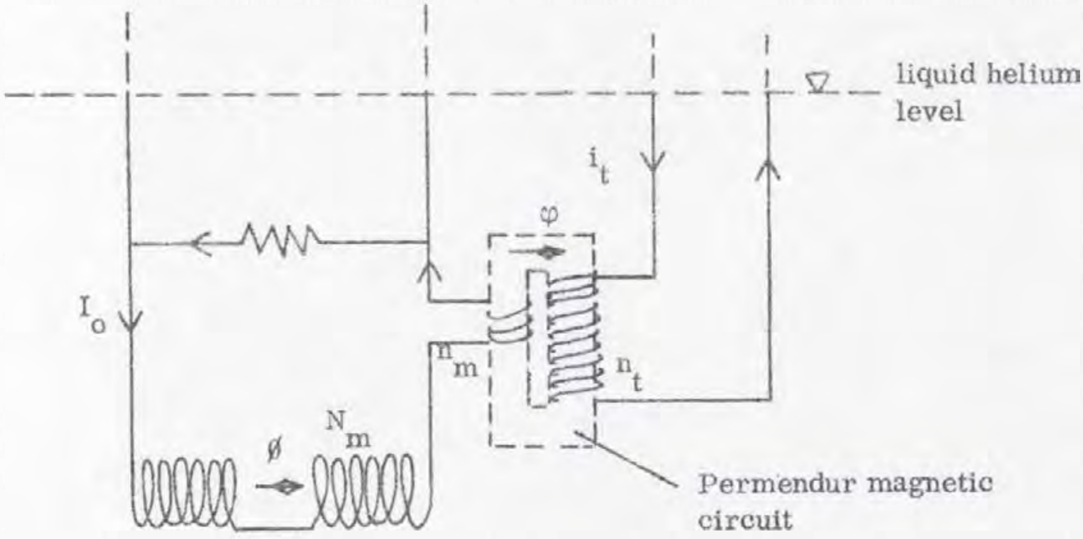

Fig. 8.5 The modified superconducting magnet current circuit.

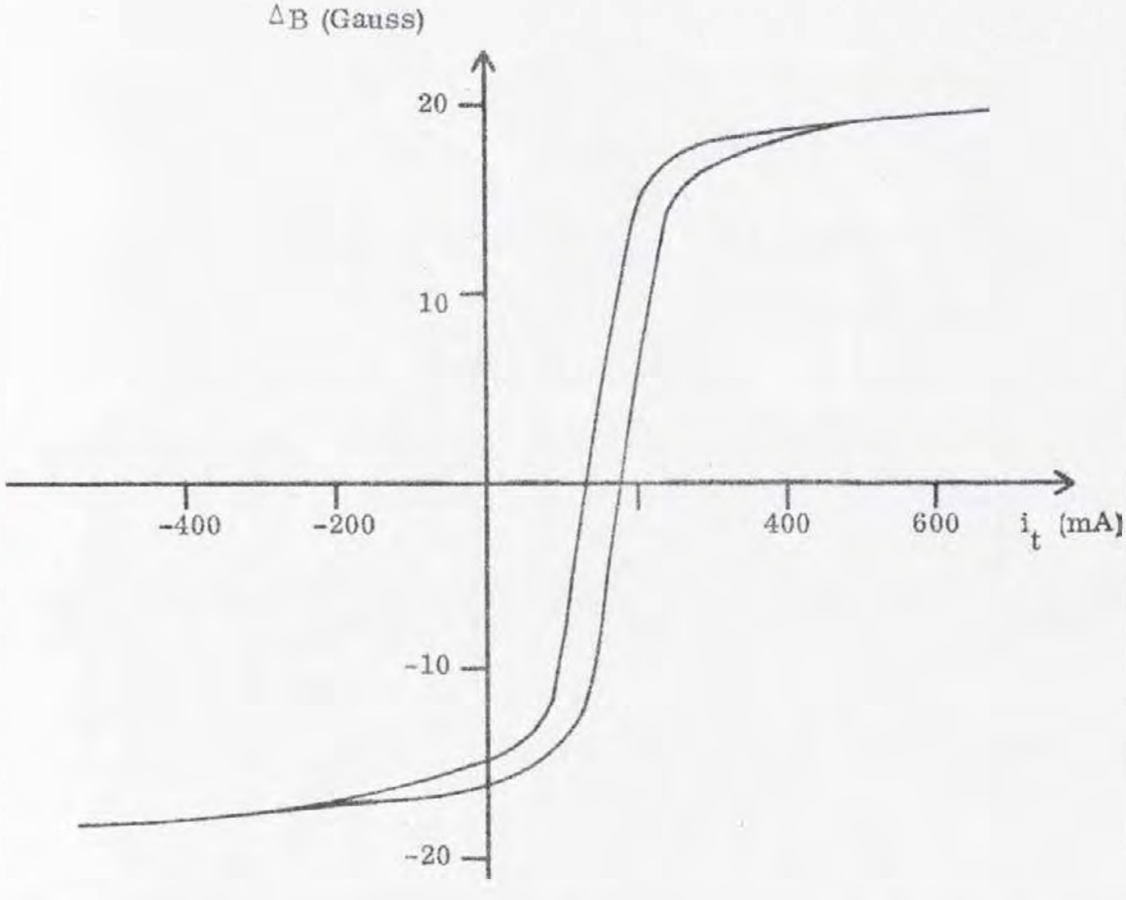

Fig. 8.6 Change of the magnetic field vs. the tuning current (B_o = 2 400 Gauss).

SUMA II and III are both equipped with tuning circuits. The SUMA II permendur circuit is, however, not heat treated for optimum performance. For SUMA III we have the following data:

$N_m = 1515$ $\qquad n_m = 36$ $\qquad n_t = 1000$

$A_m = 9.9\ cm^2$ $\qquad a_m = 1.5\ cm^2$ $\qquad a_t = 1.5\ cm^2$

However, the pole gap area ($36\ cm^2$) should be used rather than $9.9\ cm^2$, since the magnetic flux change in the pole gap is less than the change in the core by approximately a factor 36/9.9. Hence we obtain a theoretical maximum change in ΔB of 47 Gauss.

Measurements were performed at 2.4 kGauss. From Fig. 8.6 we can see that ΔB_{max} was 36 Gauss. This low value is explained by the fact that flux is leaking through the superconducting windings and over the edge of the superconducting shields.

A swing in B of 36 Gauss is equivalent to a frequency swing of approximately 50 MHz for $Cr\text{-}Ti0_2$ at 1660 MHz and about 80 MHz for $Fe\text{-}Ti0_2$ at 5 GHz. Notice that to achieve the lowest possible value for i_t, one can use the left part of the hysteresis curve in Fig. 8.6. Also notice that i_{to} in Fig. 8.6 is proportional to I_o as shown in eqn. (8.3).

The heating power produced in the leads to the tuning circuit is 5.5 mW for $i_t = 250$ mA. However, most of this power is dissipated in the upper part of the dewar.

8.4 Frequency switching

By changing the current i_t in steps, the magnetic field will also change in steps. However, for a current step with zero rise time the magnetic field response has a finite rise time due to hysteresis and eddy-current losses in the magnetic circuit. To check the frequency switching properties of the magnet the following experiment was carried out.

In Fig. 8.7 the experimental set-up is described. The signal going through the maser (V_m) and the signal going through the phase shifter (V_s) are added at the mixer receiver. The resultant amplitude squarred at the mixer becomes

$$|A|^2 = |V_m|^2 + |V_s|^2 + 2|V_m| |V_s| \cos\alpha \tag{8.4}$$

where α is the relative phase difference between the two signals. When the maser is switched in frequency, the signal through the maser exhibits a changed phase and amplitude. Hence, we want to examine $|V_m|$ and α of eqn. (8.4).

In the experiment we chose $|V_m| = |V_s|$ and

$$\cos\alpha = - \frac{|V_s|}{2|V_m|} = -0.5 \tag{8.5}$$

Hence $|A| = |V_m|$. The detector was used in the square law region and hence the recorded amplitudes were proportional to $|A|^2$.

The current through the tuning magnet was pulsed as depicted in curve E of Fig. 8.8. The experiment is summarized in Fig. 8.8. The different curves are:

Curve A: depicts $|A|^2$ for $V_s = 0$, $f_s = 1660$ MHz. Hence, $|A|^2$ is maximum for $i_t = 0$ and is proportional to the maser gain which has almost reached its final value after 0.1 sec.

Curve B: depicts $|A|^2$ for $|V_s| = |V_m|$, $f_s = 1660$ MHz. Since the maser gain is close to its final value at 0.1 sec., the curve B depicts the change in phase $\Delta\alpha$. Approximately, $\Delta\alpha$ is linearly dependent on $[\,|A|^2 - 1]$ and is about 30° at the maximum. $\Delta\alpha$ is almost zero after 0.2 seconds.

Curve C: depicts $|A|^2$ for $V_s = 0$, $f_s = 1690$ MHz. The maser gain at 1690 MHz is maximum for $i_t = 150$ mA and has almost reached its final value after 0.1 second.

Curve D: depicts the change in phase for the 1690 MHz signal. The peak is close to 40° and $\Delta\alpha$ is almost zero after 0.2 seconds.

Curve E: depicts the current i_t (t)

The results of these experiments show that the tuning magnet can be used quite satisfactorily in frequency-switched VLB I experiments where a switching time of 0.2 seconds (equivalent to one sampling block) is required.

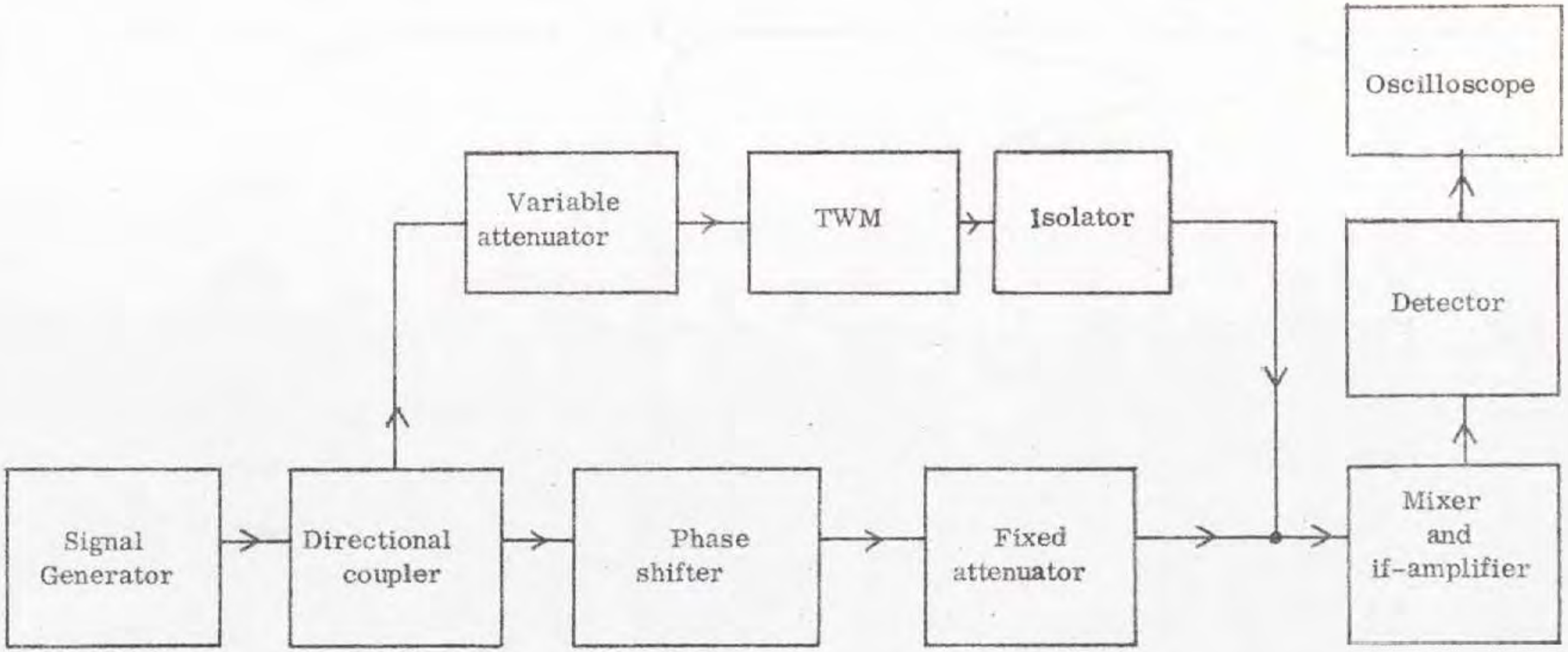

Fig. 8.7 Experimental set up for test of the gain and phase shift variations in switched frequency experiments.

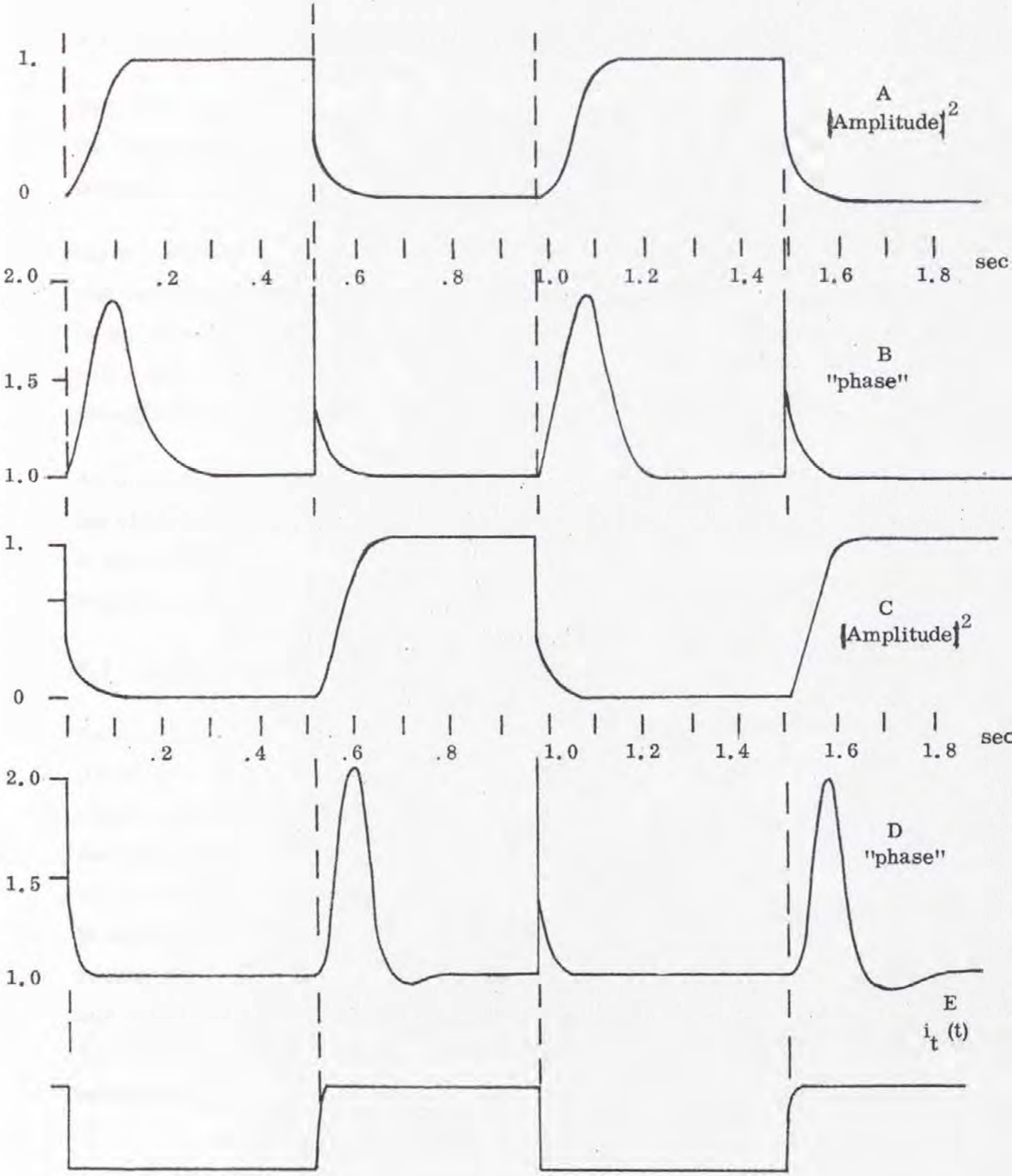

Fig. 8.8 The gain and phase shift performance of MAL 2. in a switched frequency experiment. The two frequencies are 30 MHz apart. The different curves are explained in the text.

9. THE MASER PACKAGE

9.1 Introduction

The maser package consists of the SWS, the rf input and output transmission lines, the superconducting magnet, the dewar assembly and the arrangements necessary for mounting the package at the vertex of the antenna.

We now have in operation nine TWM amplifying units (Table 7.I), three superconducting magnets (Suma I, II and III, chapter 8), and two complete sets of transmission lines, wave guides and dewars (see Fig. 9.1). All these parts are interchangeable. However, Suma I can only be used for the L-band TWM:s due to the limited magnetic field strength (Fig. 8.3).

We discuss some problems concerning the cryogenic design and some useful formulas which have been derived in Appendix A. Some details concerning the construction of the rf transmission lines are presented. We also show how the TWM system is applied to the 25.6 m radio telescope.

9.2 Cryogenic design considerations

An open cycle dewar system is used for cooling the TWM:s. From a practical operational point of view, it is essential to make a cryogenic design which decreases the liquid helium boil-off rate, i.e., one must minimize the heat power radiated and conducted to the liquid helium bath. The use of radiation shields will almost eliminate the heat radiation. The heat conduction can be reduced by a careful choice of material in the design of the different cryogenic parts (see e.g. Scott 1959) and by utilizing the cooling capacity of the evaporated helium gas (see Appendix A). From the thermodynamic properties of helium (Scott 1959) we can calculate the heat exchange capability of the helium gas. Hence, for a liquid helium bath at 2°K and for a complete heat exchange, we obtain (see Appendix A, eqn. (A.3)),

$$\Delta P = 0.23 \cdot \Delta T \cdot P_{he} \qquad \text{(mW)} \tag{9.1}$$

where P_{he} (mW) is the heat power transferred to the liquid helium bath and ΔT ($^{\circ}$K) is the change in gas temperature. Formula (9.1) underestimates the maximum heat exchange capability for temperatures below 10°K.

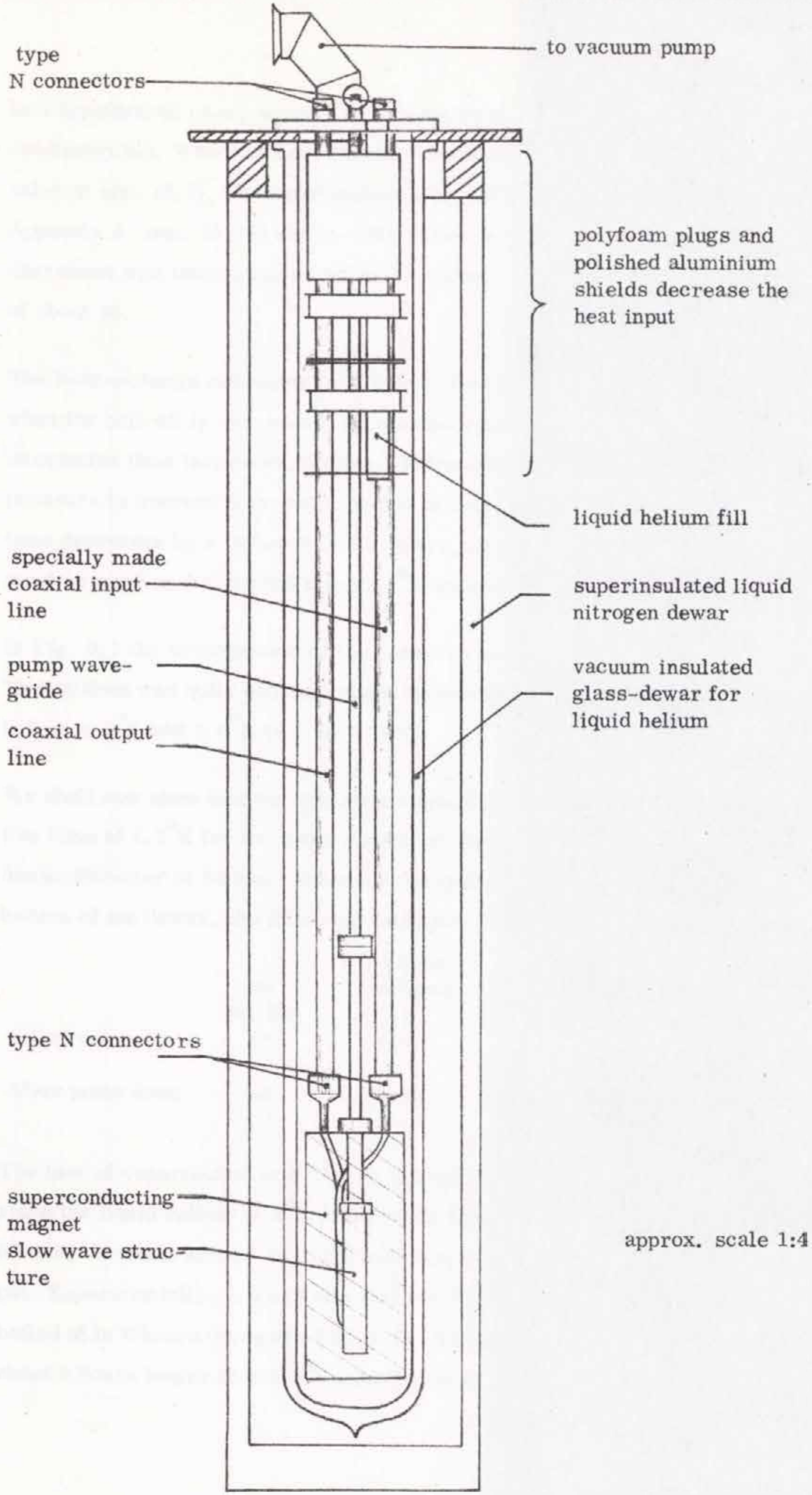

Fig. 9.1 The maser package

In a hypothetical case, we may have materials with temperature-independent heat conductivities. When the heat exchange is increased from zero to the maximum value of eqn. (9.1), the liquid helium boil off is reduced by a factor of 17.2 (see Appendix A, eqn. (A.12) and (A.13)). Since the heat conductivity for most materials decreases with temperature, we might expect a decrease in the boil off by a factor of about 20.

The heat-exchange efficiency is of course dependent on a number of factors. E.g., when the boil-off is decreased, the escape velocity of the gas decreases and the interaction time increases, yielding a more efficient heat exchange. When the gas pressure is lowered from atmospheric pressure to a low value P_1, the interaction time decreases by a factor $P_1/760$. Hence, the design of the heat-exchanging shields must be much more careful at, e.g., $2^{\circ}K$ where $P_1 = 24$ torr.

In Fig. 9.1 the arrangement of the radiation and heat-exchange shields is shown. This system was quite efficient since we measured the same boil-off rate (see Fig. 9.2) at $4.2^{\circ}K$ and $1.8^{\circ}K$ ($P = 12.5$ torr).

We shall now show that the operation time at $2^{\circ}K$ is almost equal to the operation time at $4.2^{\circ}K$ for the same amount of liquid helium transferred. Since the helium dewar diameter is 80 mm, and since the upper part of the SWS is 14 cm above the bottom of the dewar, the following data are valid:

	cm liq. He	liq. He Volume ℓ	Useful liq. He Volume ℓ
Filled dewar	80	4.0	3.3
After pump down	45	2.25	1.55

The heat of vaporization at $4.2^{\circ}K$ is 715 mWh/ℓ and at $2.0^{\circ}K$, 935 mWh/ℓ. Hence, since the liquid helium at $2^{\circ}K$ lasts for 25 hours (equivalent to a mean boil-off power of 58 mW) the same amount at $4.2^{\circ}K$ will last only 19 hours for the same heat power input. Experimentally, it was found that the first 1.75 litres (from 80 cm to 45 cm) boiled of in 8 hours (compare Fig. 9.2). Hence, a $4.2^{\circ}K$ maser can only be operated about 2 hours longer than a $2^{\circ}K$ maser in our dewar system.

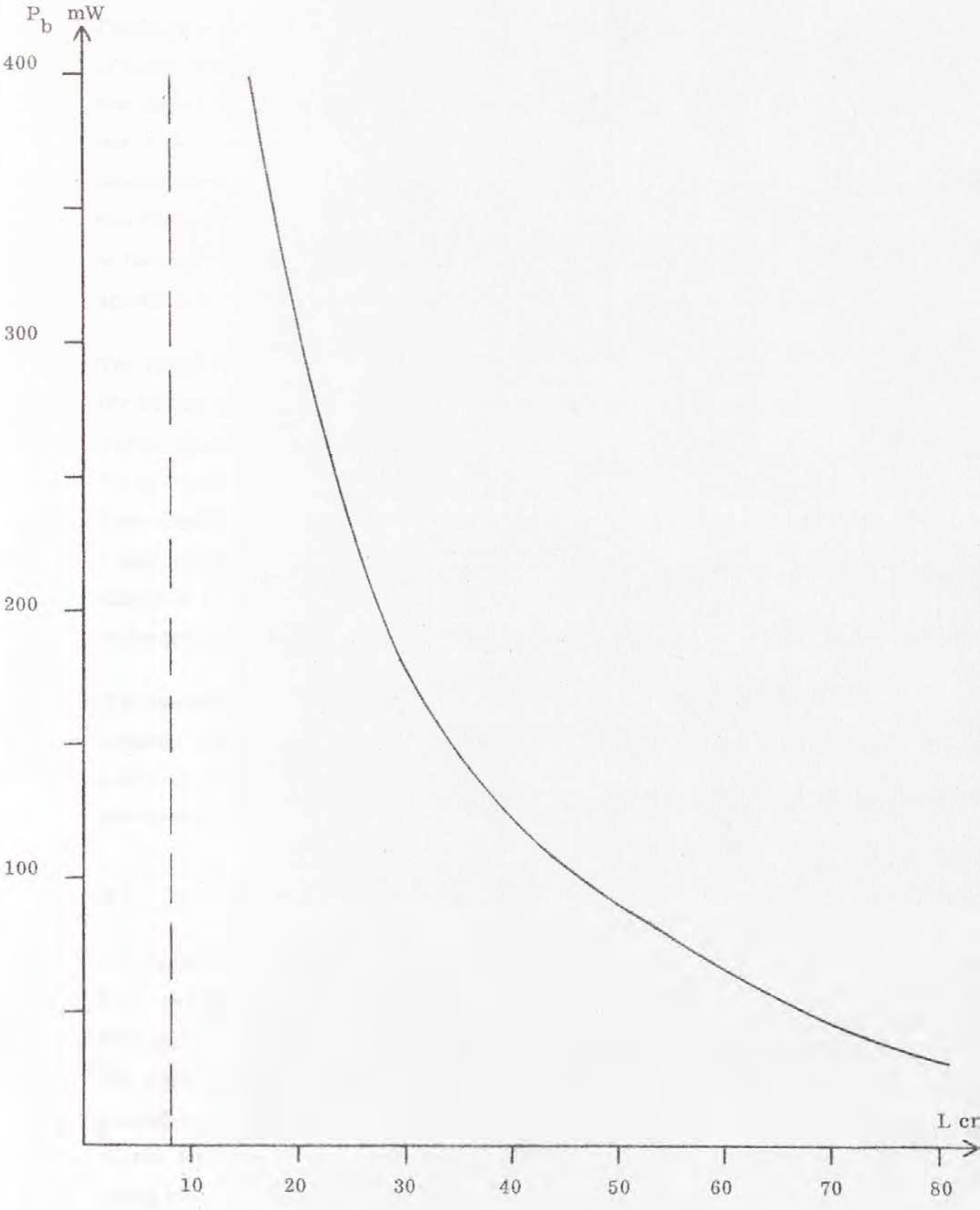

Fig. 9.2 Measured heat power dissipation in the liquid helium bath, vs. the distance from the room temperature cover at the top of the cryostat to the liquid helium level. The total depth of the dewar is 90 cm. The upper SWS input coupling is located 76 cm:s from the top of the dewar.

Furthermore, the pump power required for saturation of the pump transitions decreases almost inversely proportionally to the temperature T, since the pump transition spin-lattice relaxation time is proportional to 1/T. However, the extra boil-off due to the pump power dissipation will increase the cooling of the materials that are conducting heat power to the liquid helium bath. In fact, assuming again that the heat conductivities are independent of temperature, an equivalent increase in the boil-off power of only one-fourth of the applied pump power is obtained (see appendix A, eqn. (A.17)).

The liquid helium dewar is fabricated from a special type of glass, nonpermeable for helium gas (MONAX-Glass from John Moncrieff Ltd., North British Glassworks, Perth, Scotland). Our experience has shown that these dewars can be used regularly for at least one year without repumping being necessary. The liquid nitrogen dewar is a commercial superinsulated stainless steel dewar (Hoffman Division, Minnesota Valley Eng. Inc., New Prague, Minnesota). The dewar assembly is shown schematically in Fig. 9.1. The depth of the liquid helium dewar is 90 cm, and the total height of the package is 100 cm.

The introduction of radiation shields and a careful design for utilizing the cooling capacity of the cold helium gas extended the operation time from about 13 hours to nearly 26 hours. This operating time is quite convenient, since only one refilling is necessary every 24 hours.

9.3 The rf-transmission lines

The rf transmission lines (see Fig. 9.1) are 70 cm long, 50 Ω coaxial lines made from two thin-walled (0.2 mm) German silver tubes (the inner diameter of the outer tube is 12.5 mm and the outer diameter of the inner tube is 5.4 mm). The tubes of the input transmission lines are electrolytically coated with approximately 0.01 mm copper in order to obtain low rf losses. To prevent the copper layer from oxidation, a very thin layer of gold is applied electrolytically. The transmission lines are terminated in both ends by type N female connectors. In the top connector a vacuum-tight teflon window (5 mm thick) and a tapered section are inserted (see Kollberg 1969, Fig. 5.5).

The noise contribution to the system noise temperature from the input transmission line has been carefully measured at 3.5 GHz, using the conventional HOT-COLD body technique and a new more accurate technique described by Kollberg (1969). We measured an input transmission line noise temperature of $5 \pm 1^{\circ}K$. If the noise temperature is determined entirely by the dielectric losses of the teflon window, the maximum equivalent noise temperature at 7 GHz is $10^{\circ}K$. On the other hand, the maximum noise temperature at 1 GHz is obtained if the losses are related to ohmic losses, yielding an equivalent noise temperature of $5/\sqrt{3.5} = 2.9$ $^{\circ}K$.

9.4 The TWM system arrangements in the 25.6 m radio telescope at the Onsala Space Observatory

In the radio telescope, the TWM package is mounted in a cradle as indicated in Fig. 9.3. The cradle can rotate about one axis which is horizontal when the antenna is directed towards north or south. Since the telescope is equatorially mounted at a latitude of 57° 23' 18", the maser package will be tilted at most through an angle of 33° (see Fig. 9.4).

The numbers indicated in Fig. 9.3 refer to the following items:

1) waveguide to coaxial transition from the multi-frequency horn
2) 3/8" Flexwell coaxial cable
3) coaxial rotary joint
4) right angle transition
5) coaxial output cable to mixer
6) larger bearing
7) smaller bearing
8) cradle
9) vacuum pipe
10) vacuum rotary joint
11) flexible vacuum pipe
12) mechanical manostat of the type described by Sommer (1954)

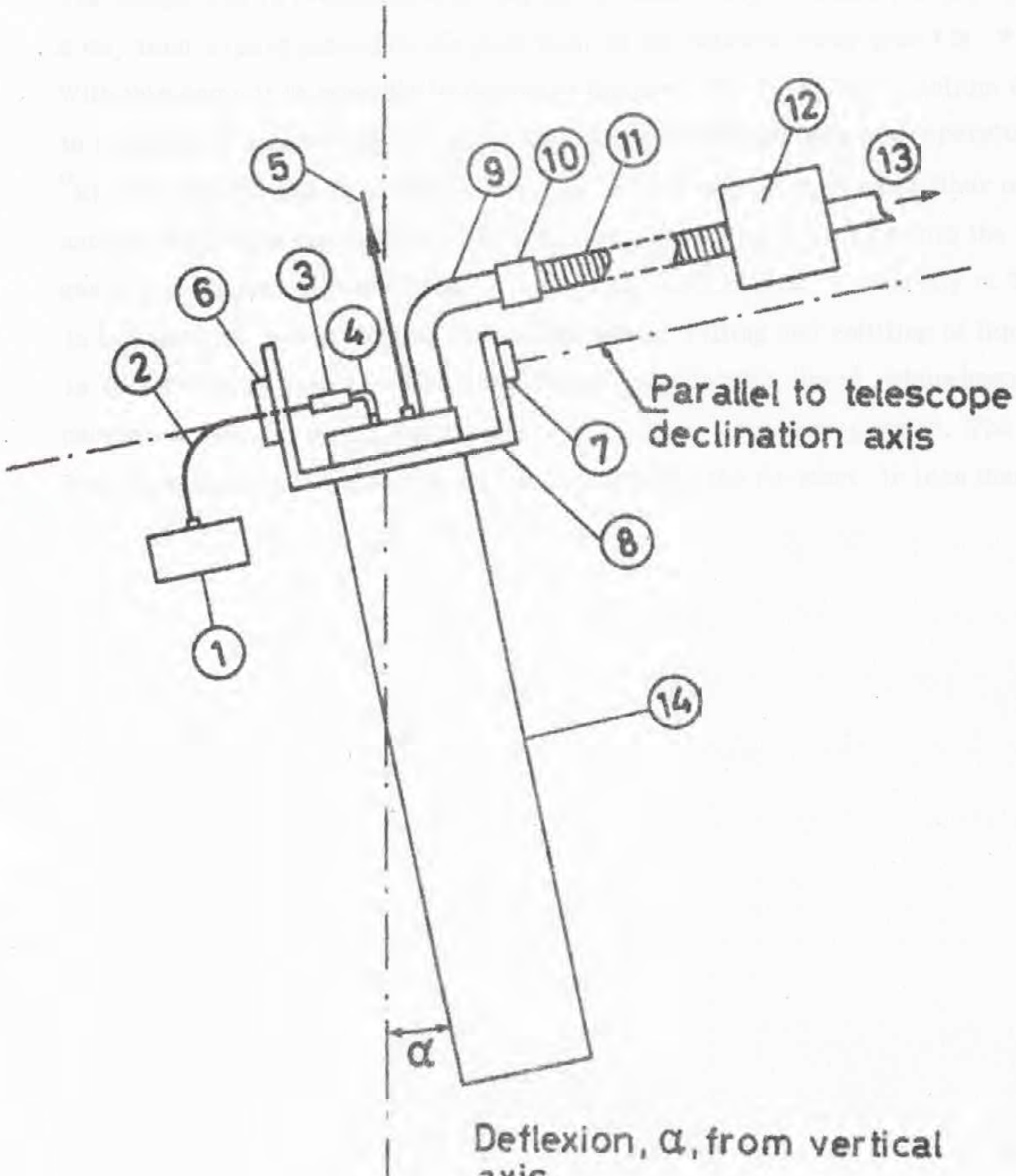

Fig. 9.3 Detailed mechanical arrangement of maser package in receiver housing.

13) pipe to vacuum pump

14) dewar package

The helium gas is evacuated from the dewar with a large vacuum pump (Leybold S 60, 1000 ℓ/min) placed on the 4-th floor in the antenna tower (see Fig. 9.4). With this pump it is possible to decrease the pressure in the liquid helium dewar to a minimum value of about 4 torr (equivalent to a liquid helium temperature of 1.54 ^{o}K). The helium gas is collected in a 1 m^3 rubber bag in the ground floor of the antenna tower and compressed into steel cylinders. The cylinders with the recovered gas are transported to the Physics Department of Chalmers University of Technology in Gothenburg, where the gas is liquified again. Filling and refilling of liquid helium is done every 24 hours in the ground floor of the antenna tower, whereupon the maser package is brought to the focus cabin (Fig. 9.4) by a "cherry-picker". The time elapsing from the interruption of the measurements to the re-start is less than one hour.

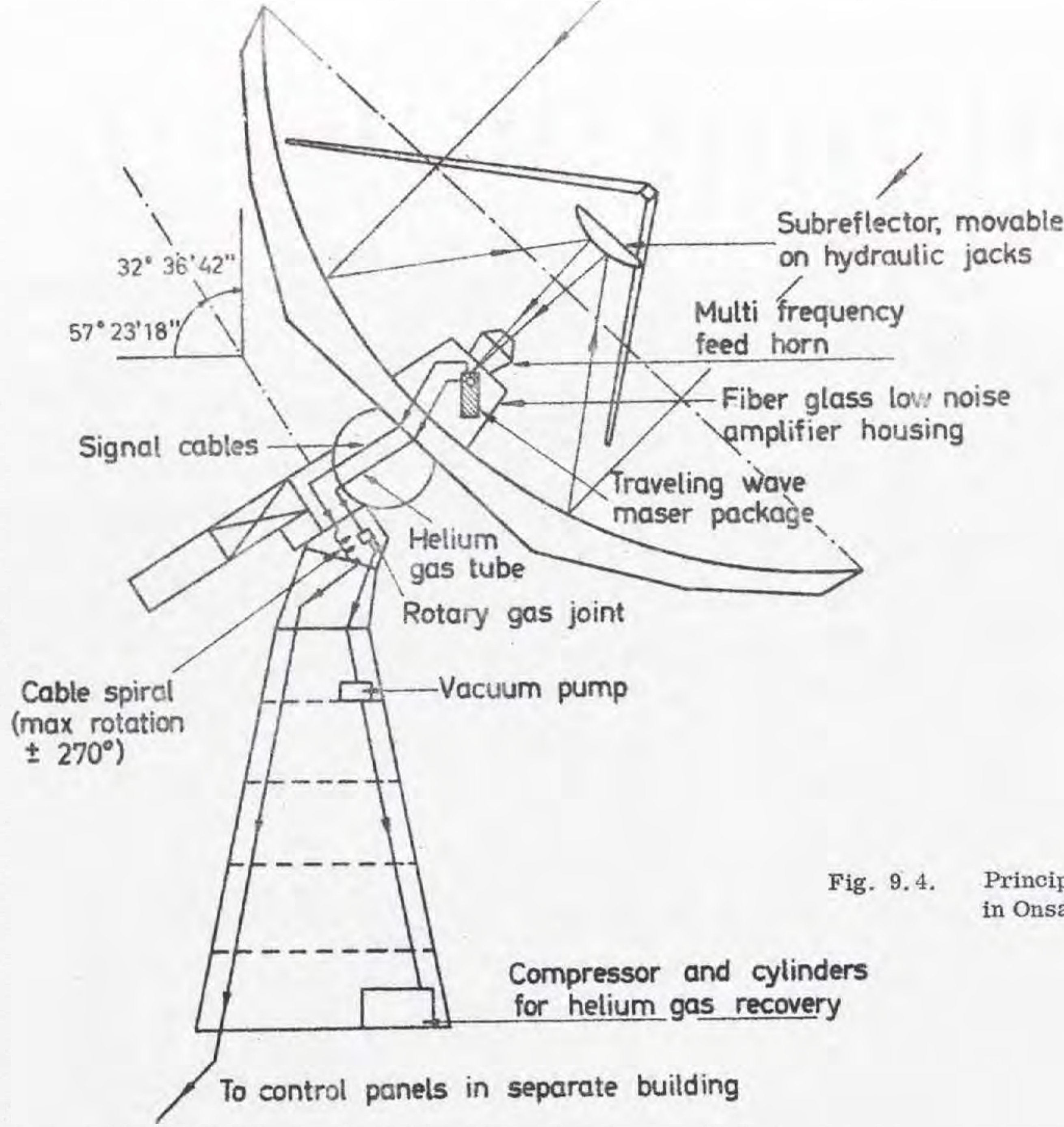

Fig. 9.4. Principal TWM arrangement in Onsala 84 foot telescope.

10. THE PERFORMANCE OF THE ONSALA TWM SYSTEM AND RADIO ASTRONOMICAL APPLICATIONS

10.1 Introduction

The first TWM, MAL 1, was first mounted in the 25.6 m radio telescope in 1966. The original installation yielded a system noise temperature of about 65 ^{o}K. Since then all masers (except for MINIMAC) listed in Table 7.I, have successfully been used in radio astronomical observations. In fact, for about 90% of the observing time, TWM:s have been used instead of other amplifiers (parametric amplifiers). Most of the observing time has been devoted to investigations of molecular emission or absorption lines. These observations require low noise amplifiers with moderate bandwidths (a few MHz) tunable over large frequency bands. The TWM:s described in this report have been ideal for this kind of radio astronomical research.

The development of the MAL 2 and MAL 3 TWM:s was initially motivated by investigations of maser-like radio emission from interstellar OH gas clouds (see, e.g., Moran 1969). These enormous natural masers emit radiation in the ground-state transitions of the OH molecule, i.e. the $^{2}\pi_{3/2}$, J = 3/2, F = 2→1 transition at 1612 MHz, F = 1→1 at 1665 MHz, F = 2→2 at 1667 MHz and the F = 1→2 transition at 1720 MHz. Since these OH masers are pumped in one way or another, most likely even the excited states are inverted. Hence some of the masers were built for excited-state OH emission line investigations (MAC 1-3).

MAL 2 and MAC 2 were also used in the first successful transatlantic very long baseline interferometer (VLB I) measurements. The VLB I technique is used in investigations of the brightness distributions and the positions of small radio astronomical objects, such as quasars and regions emitting maser-like OH - radiation. The VLBI technique was developed independently and almost simultaneously by two groups in North America (Broten et al. 1967, Bare et al. 1967).

10.2 Noise properties and operational experience of the Onsala 25.6 m telescope TWM system

The equivalent noise temperature (T_s) of the TWM-equipped 25.6 m radio telescope at Onsala has been measured carefully at 1665 MHz and 6035 MHz using a well known noise calibration injected through a directional coupler. (J. Elldér, private communication). In Table 10.I we present a noise catalogue with the telescope pointing towards zenith.

Table 10.I

Component	1665 MHz		6035 MHz	
	T_n °K	Error °K	T_n °K	Error °K
Zenith directed antenna with horn and calibration directional coupler	18	± 5.5	20	± 9
Waveguide to coaxial transition 1)	2	± 0.5	4	± 1
3/8" Flexwell cable 2)	4	± 0.5	-	-
Rotary joint 3)	3	± 0.2	-	-
Right angle transition 4)	1	± 0.3	-	-
Flexible waveguide	-	-	10	± 2
Maser package 5)	5	± 1.0	10	± 2
Mixer contribution	2	-	5	-
System noise temperature (T_s)	34	± 3	49	± 4

1) - 4) the numbers refer to the numbered items in Fig. 9.3.

5) This figure includes the maser package input transmission line and the SWS noise (Kollberg 1969).

In the 6035 MHz system, the Flexwell cable and the rotary joint were replaced by a two-foot flexible C-band waveguide.

The noise temperature contribution from the individual parts of the TWM system were partly measured using a special technique (the SHOP-technique) described by Kollberg (1969) and partly with the more common Hot-Cold Body Technique. At 3 GHz the total system noise was less carefully measured, but the noise temperature is close to 50°K. At this frequency exactly the same arrangement with the Flexwell cable and the rotary joint as indicated in Fig. 9.3 was used.

The noise temperature at the zenith of the antenna plus horn and calibration directional coupler is assumed equal to the measured system noise temperature minus the noise temperature of the remaining parts of the system (see Table 10.I). Hence, the maximum error in this temperature is fairly large.

The accumulated operating times for the different masers in the telescope are (as of April 3, 1970).

TWM	hours	TWM	hours
MAL 1	100	MAS 2	90
MAL 2	1717	MAC 1	130
MAL 3	1017	MAC 2	580
MAS 1	345	MAC 3	521

Thus the total operating time for the TWM system is no less than 4400 hours. Most of the down time has been caused by klystron trouble. However, these troubles radically decreased after the pump klystron was mounted on a separate plate which is never removed from the low-noise fiberglass housing, allowing uninterrupted running of the klystron. Another fault (which has occurred five times) is interrruption in the soldered connection between the SWS coupling strip conductor and the coaxial input cable.

10.3 Radio astronomical measurements performed with the TWM system

So far the TWM system has been used for research on interstellar molecular emission and absorption lines and for very long baseline interferometry (VLB I).

A block diagram of the spectral line receiver is shown in Fig. 10.1 (B. Hansson, private communication). The i.f. signal at 6 MHz is fed to the multi-channel units (see lower part of Fig. 10.1) for the analysis of the noise spectrum. Four different channel banks can be connected:

Bank	Number of units	Filter bandwidth kHz	Covered bandwidth MHz
A	40	0.25	0.01
B	100	1.0	0.1
C	100	10.0	1.0
D	24	100.0	2.4

When the MAL 2 TWM (Table 7.I) was finished,measurements were performed in order to test the system (Rydbeck and Kollberg 1968). In Fig. 10.2 a recording shows the stability and reproducibility of the system.

Fig. 10.3 shows the excited state emission at 4765 MHz (the $^2\pi_{1/2}$, $J = 1/2$, $F = 1 \rightarrow 0$ transition) in the source W3, OH recorded by the TWM system (feature B) and by the National Radio Astronomy Observatory (Green Bank, W.Va) 140-foot radio telescope with a cooled parametric amplifier yielding a system noise temperature of 110°K (Zuckerman et al. 1968). Since the system noise temperature of the Onsala system is about 45°K (using MAC 2), the features look similar in spite of the smaller antenna at Onsala (84-foot). Note the different temperature scales in Fig. 10.3.

The MAL 2 and MAL 3 TWM:s have been used in an OH ground-state emission survey (Elldér et al. 1969, Winnberg 1970 to be published) in which four new OH sources (about sixty sources are known at present) were discovered. In this partioular research program the low system noise was essential, since the area of sky covered to the required sensitivity and within a given time is proportional to the sqaure of the system noise temperature, T_s^2.

A substantial part of the research has been devoted to detailed investigations of the OH emissions from W3, OH and W75B (Rydbeck et al 1969, Rydbeck et al 1970). From these research programs, where MAL 2 and 3 and MAC 2 and 3 were used, we show in Fig. 10.4 the right circular features from W3, OH, at all the emission frequencies discovered so far. Rydbeck et al (1970) discovered W75B to be the second source to emit radiation from the exited state $^2\pi_{3/2}$, $J = 5/2$, $F=3 \rightarrow 3$ transition at 6035 MHz.

Searches for new molecular lines have been made. Using MAS 1 the frequency range 3000 to 3075 MHz was covered in a few sources in a search for emission or absorption from the CH molecule. The MAS 2 TWM has been used in an unsuccessful search for the first OH harmonic at 2 x 1665 = 3330 MHz. Formic acid was searched for at 1639 MHz using the MAL 2 (Cato et al 1970).

Finally, very long baseline interferometer measurements have been performed at L-band using the MAL 2 TWM (Kellerman et al. 1968, Rönnäng 1970, to be published) and at C-band using the MAC 1 and MAC 2 TWM(Kellerman, to be published). In these measurements the low system noise is valuable, since the over-all sensitivity is proportional to $\sqrt{T_{s_1} \cdot T_{s_2}}$, where T_{s_1} and T_{s_2} are the system noise temperatures of the two receiving stations involved in the measurements.

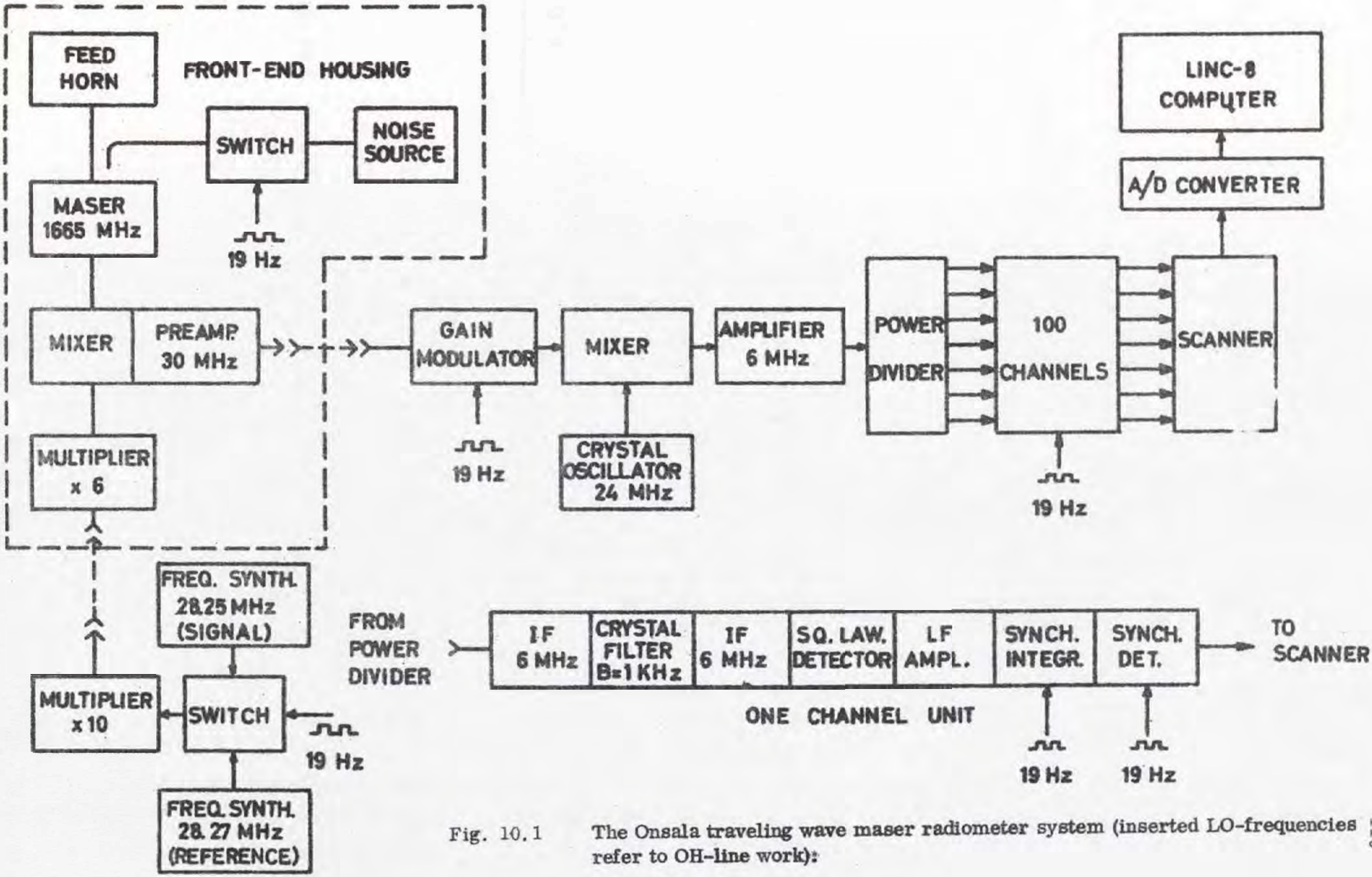

Fig. 10.1 The Onsala traveling wave maser radiometer system (inserted LO-frequencies refer to OH-line work):

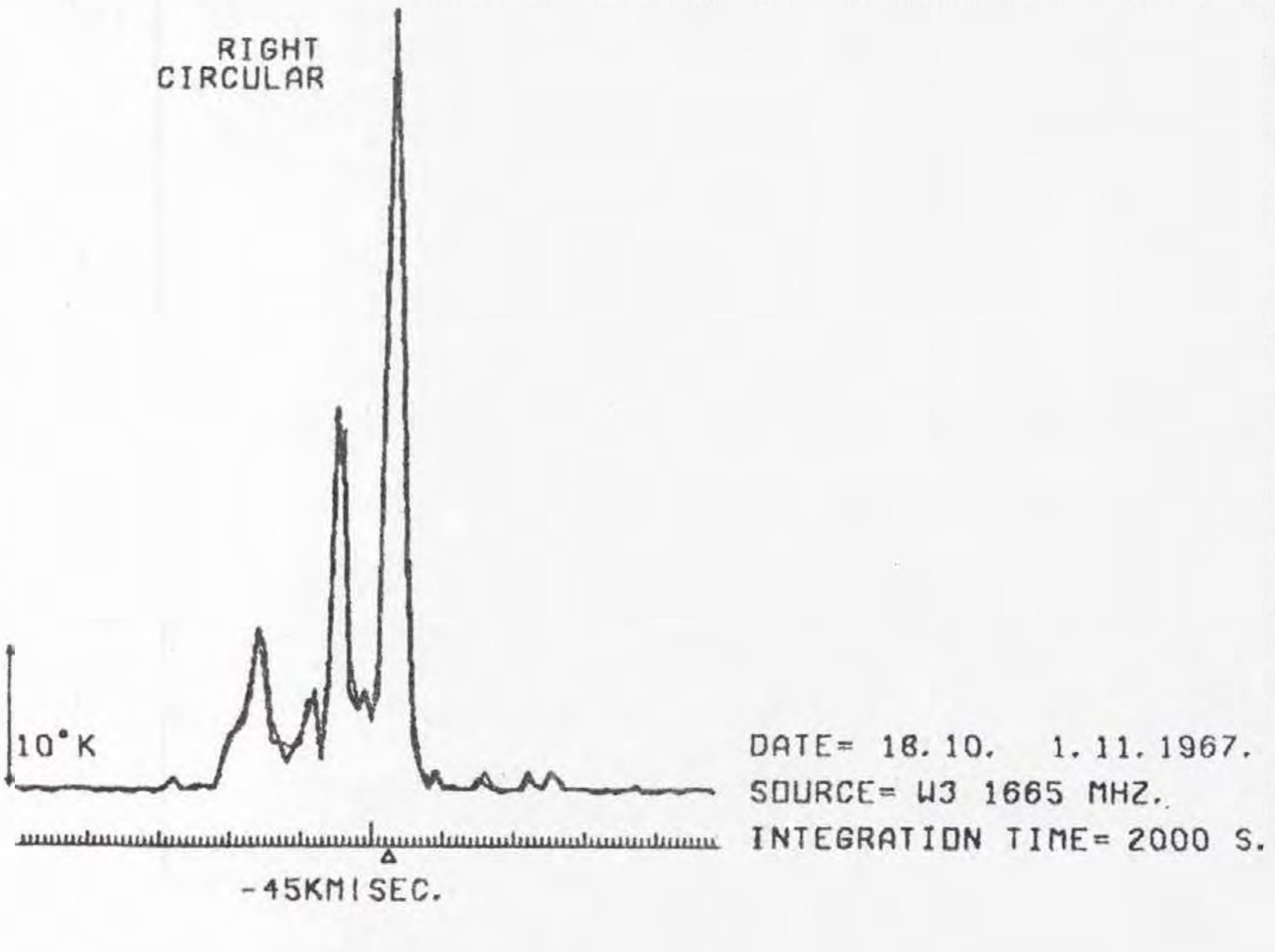

Fig. 10.2 Depicting superimposed W3 OH 1665 MHz spectra taken with about three weeks time difference. No significant change in the emission features is detectable.

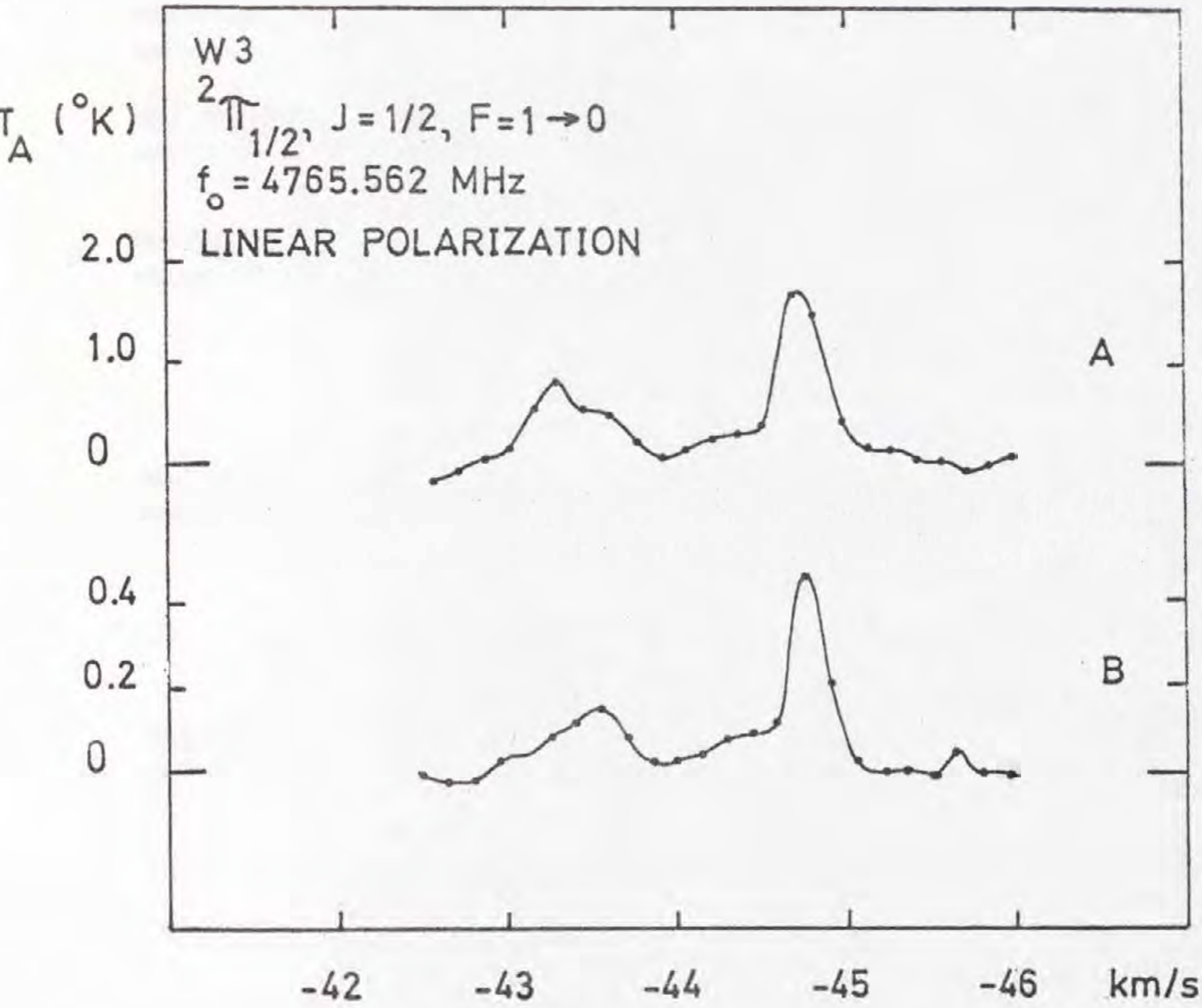

Fig. 10.3 Comparison between OH excited spectra of W3, OH obtained using A: the NRAO 140-foot radio telescope and a cooled parametric amplifier yielding a system noise temperature of about 110°K, and B: the Onsala 84-foot radio telescope equipped with the TWM system yielding a system noise temperature of about 45°K. Both recordings were obtained with an equivalent filter bandwidth of 3 kHz and a 6 hour integration time. Note the different temperature scales.

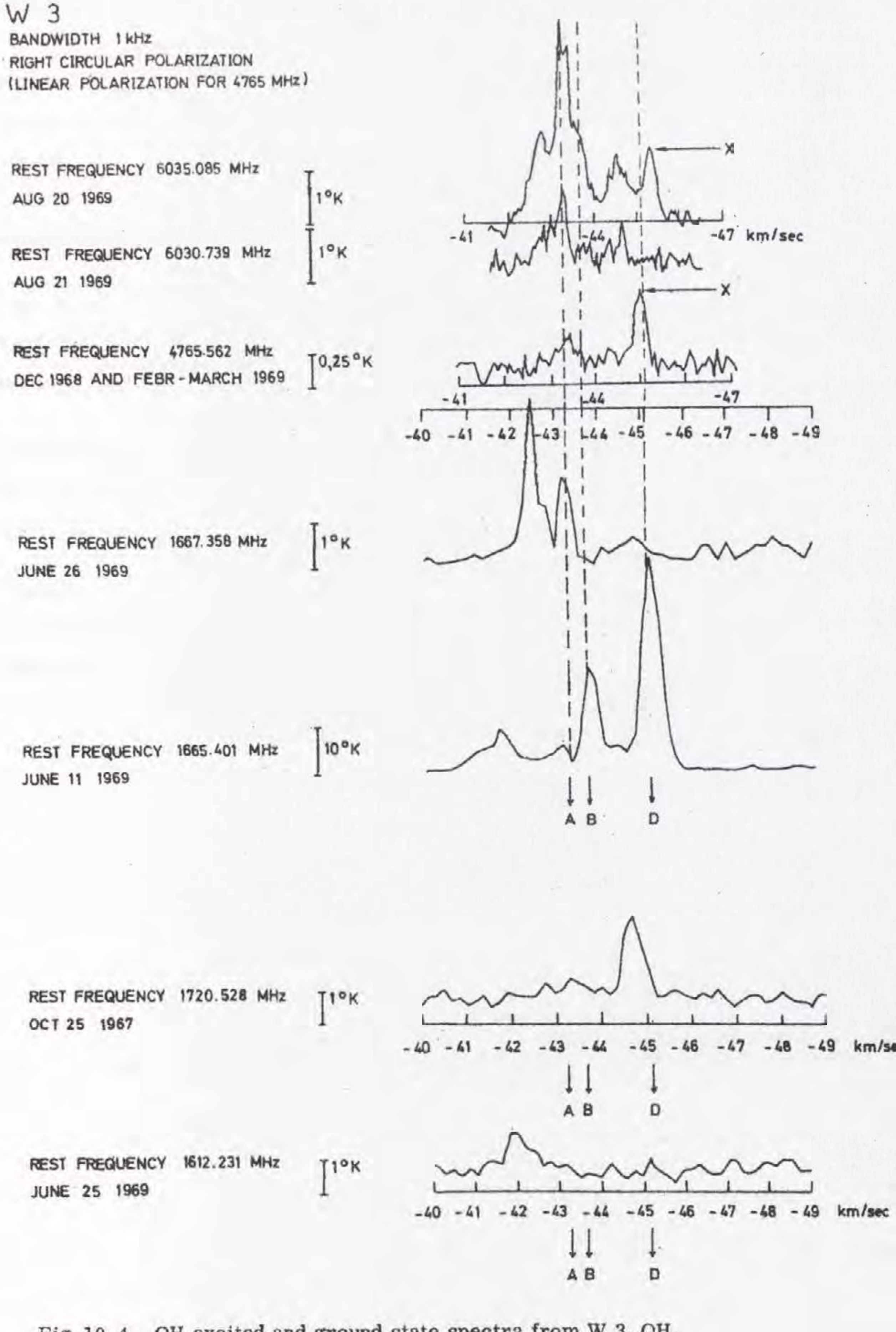

Fig. 10.4 OH excited and ground state spectra from W 3, OH.

ACKNOWLEDGEMENTS:

I wish to express my sincere gratitude to professor O. E. H. Rydbeck for his inspiration and support during the course of the research described in the present report. I am indepted to mr C. O. Lindström for his assistance during the development of the entire TWM-system and to mr P. O. Andersson for performing many experiments, particularly on the iron-doped rutile.

I am also very grateful to the members of the workshop for their skilful work on various mechanical parts of the TWM system. In particular, I would like to thank mr A. Gustafsson for his devoted work on many difficult mechanical problems.

Furthermore I wish to acknowledge the assistance of professor B. Höglund and dr G. Seielstad in correcting the manuscript and the help of miss M. Hansen, who typed the entire report.

Finally, I would like to acknowledge the financial support from the Swedish Board for Technical Development, from the Wilhelm och Martina Lundgrens Vetenskapsfond and from Chalmers University of Technology.

APPENDIX A

The liquid helium boile-off problem

Consider the following figure:

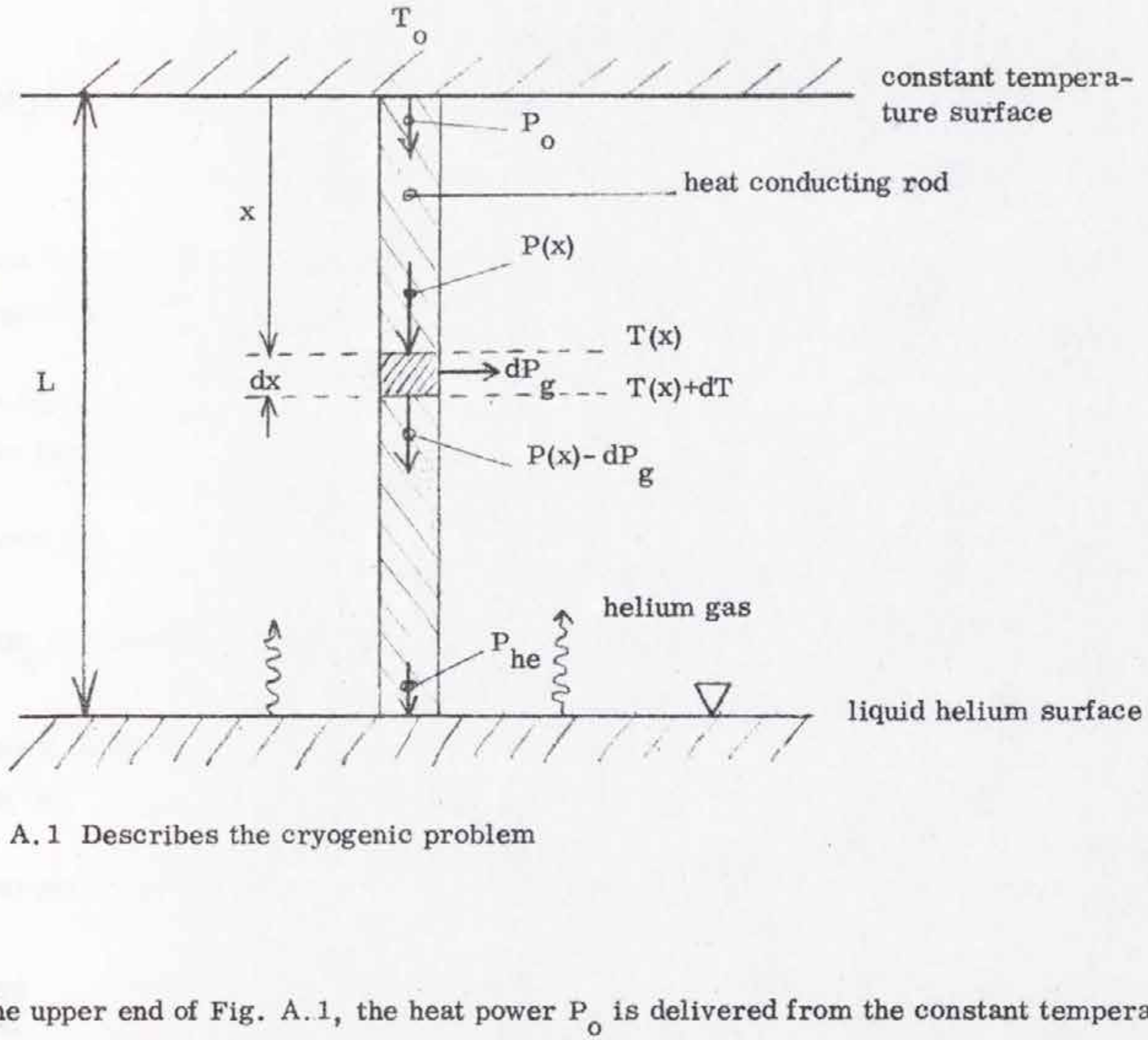

Fig. A.1 Describes the cryogenic problem

At the upper end of Fig. A.1, the heat power P_o is delivered from the constant temperature T_o (room temperature) to the heat conducting rod. We assume that the rod has the cross-section area A and the length L. At x, the heat power dP_g leaves the interval dx of the rod and heats the cold helium gas. We have

$$P(x) = -A\,\sigma \cdot \frac{dT}{dx} \tag{A.1}$$

where σ is the heat conductivity of the rod, dependent on T(x). dP_g is the heat flow from the rod to the helium gas. The heat capacity of helium gas (Scott 1959) for temperatures between $10^{o}K$ and $300^{o}K$ is

$$\frac{dQ}{dT} \approx 5.23 \ (\mathrm{Ws/g,\ ^oK}) \tag{A. 2}$$

Since the heat of vaporization is 20.6 Ws/g at 4.2^{o}K and 23.0 Ws/g at 2^{o}K, the maximum cooling capacity of the helium gas becomes

$$dP_g = \begin{cases} 0.25 \ dT \cdot P_{he} & \mathrm{mW\ at\ 4.2^oK} \\ 0.23 \ dT \cdot P_{he} & \mathrm{mW\ at\ 2^oK} \end{cases} \tag{A. 3}$$

where P_{he} is the heat power transferred to the liquid helium bath and dT is the change in gas temperature (see Fig. A. 1).

This formula underestimates the gas cooling capacity somewhat for temperatures lower than 10^{o}K.

We now put

$$dP_g = dP(x) = k \cdot dT \cdot P_{he} \tag{A. 4}$$

where k depends on the efficiency of the heat exchange and has a maximum value of 0.25 $^oK^{-1}$ at 4.2^{o}K and 0.23$^oK^{-1}$ at 2^{o}K.

From eqn:s (A. 1) and (A. 4) we get

$$\frac{dP}{dx} = - \frac{k \cdot P_{he}}{A \ \sigma(T)} \cdot P \tag{A. 5}$$

Assuming $\sigma(T) = \sigma_o$ independent of temperature, (A. 5) is easily integrated with respect to x, yielding (see Fig. A. 1),

$$P(x) = P_o \cdot e^{-\frac{k P_{he}}{A \sigma_o} x} \tag{A. 6}$$

Hence (see Fig. A. 1):

$$P_{he} = P_o \, e^{-\frac{k P_{he}}{A \sigma_o} L} \tag{A. 7}$$

and the total amount of heat received by the gas is

$$P_g = P_o \left(1 - e^{-\frac{kP_{he}}{A\,\sigma_o} \cdot L}\right) \tag{A.8}$$

When the heat exchange is zero, eqn. (A.6) yields

$$P_{he} = P_o = (T_o - T_{he}) \; \frac{A\,\sigma_o}{L} \tag{A.9}$$

Assuming some heat exchange, we get by integrating eqn. (A.4)

$$P_g = k\, P_{he}\, (T_o - T_{he}) \tag{A.10}$$

Combining eqn:s (A.7) and (A.10) to derive P_g , and putting the result equal to P_g from eqn. (A.8) , we obtain

$$P_{he} = \ell n \left[1 + k\,(T_o - T_{he})\right] \cdot \frac{A\,\sigma_o}{L \cdot k} \tag{A.11}$$

Hence, with maximum heat exchange the boile-off power is reduced by a factor γ , where from (A.9)

$$\gamma = \frac{(T_o - T_{he})\, k}{\ell n \left[1 + k(T_o - T_{he})\right]} \tag{A.12}$$

This factor becomes for $T_o = 300^{\circ}K$

$$\gamma = \begin{cases} 17.2 & \text{for } T_{he} = 4.2^{\circ}K \\ 16.4 & \text{for } T_{he} = 2^{\circ}K \end{cases} \tag{A.13}$$

From eqn:s (A.7) and (A.11) we get

$$P_o = P_{he} \left[1 + k\,(T_o - T_{he})\right] \tag{A.14}$$

When the pump power P_p is dissipated in the liquid helium bath, we get, using eqn:s (A. 10) and (A. 7)

$$P_g = k \cdot (T_o - T_{he})(P_o e^{-\frac{k P_{he}}{A \sigma_o} L} + P_p) \qquad (A.15)$$

This value for P_g must still be equal to P_g in eqn. (A. 8). Hence, the total power P_{he} heating the liquid helium bath becomes

$$P_{he} = P_o e^{-\frac{k P_{he}}{A \sigma_o} L} + P_p = \ell n \left[\frac{1 + k(T_o - T_{he})}{1 - k(T_o - T_{he}) \frac{P_p}{P_o}} \right] \frac{A \sigma_o}{L k} \qquad (A.16)$$

For $k(T_o - T_{he}) \frac{P_p}{P_o} \ll 1$ we have approximately P_o as in eqn. (A. 14) and we obtain from eqn. (A. 16)

$$P_{he} \approx P_{he}^o + \frac{P_p}{\ell n \left[1 + k(T_o - T_{he}) \right]} \qquad (A.17)$$

where P_{he}^o is the heat power input for $P_p = 0$. Hence for small pump powers, the increased boile-off is equivalent to an extra heat input power equal to about one fourth of the pump power.

References:

Abazadze, Y.V., and Solovyev, Y.G., 1968, Radio Eng. and Electronic Physics, 13, 346.

Andersson, P.O., 1968, "Diffusionsdopning av rutil", thesis, Research Laboratory of Electronics, Chalmers Univ. of Technology, Gothenburg, Sweden (in Swedish).

Bare, C., Clark, B.G., Kellerman, K.I., Cohen, M.H., and Jauncey, D.L., 1967, Science, 157, 189.

Broten, N.W., Legg, T.H., Locke, J.L., Mc Leish, C.W., Richards, R.S., Chrisholm, R.M., Gush, H.P., Yen, J.L., and Galt, J.A., 1967, Science, 156, 1597.

Butcher, P.N., 1957, Proc. Instn. Elect.Eng. (London), 104 pt B, 177.

Cato, T., Cato, M., Landgren, P., and Sume, A., 1970, Ap.J. (in print).

Chen, F.S., and Tabor, W.J., 1964, Bell Syst. Techn. J., 43, 1005.

Cioffi, P.P. 1962, J.Appl. Phys., 33, 875.

De Grasse, R.W., Schultz-DuBois, E.O., and Scovil, H.E.D., 1959, Bell Syst. Techn. J., 38, 305.

Devor, D.P., 1960, Research Report No. 148, Hughes Research Laboratories, Malibu, Calif.

Elldér, J., Rönnäng, B., and Winnberg, A., 1969, Nature, 222, 67.

Green, H.E., 1965, IEEE Trans. on Microwave Theory and Techniques, MTT-13, 676.

Hentley, E.L., 1967, Cryogenics, 7, 33.

Hlawiczka, P., and Mortis, A.R., 1963, Proc. IEE, 110, 665.

Johnson, O.W., Ohlsen, W.D, and Kingsbury, P.I., 1968, Phys. Rev., 175, 1102.

Kellerman, K.I., Clark, B.G., Bare, C.C., Rydbeck, O.E.H., Elldér, J., Hansson, B., Kollberg, E., Höglund, B., Cohen, M.H., Jauncey, D.L., 1968, Ap.J. (Letters), 153, L209.

Kollberg, E.L., 1966 a, Research Report No 72, Research Laboratory of Electronics, Chalmers University of Technology, Gothenburg, Sweden.

Kollberg, E.L., 1966 b, IEEE Trans. on Microwave Theory and Techniques, MTT-14, 1327.

Kollberg, E.L., and Yngvesson, K.S., 1966 Proc. IEE 6th Internat'l Conf. on Microwave and Optical Generation, vol. 27, p. 384.

Kollberg, E.L., 1967, Electronics Letters, 3, 294.

Kollberg, E.L., 1969, Research Report No. 95, Research Laboratory of Electronics, Chalmers University of Technology, Gothenburg, Sweden.

Lax, B., and Button, K.J., 1962, Microwave Ferrites and Ferrimagnetics, New York: McGraw-Hill.

Lin, M.S., and Haddad, G.I., 1966, Technical Report No. 89, Department of Electrical Eng., The University of Michigan, Ann Arbor, Mich.

Moran, J.M., 1969, Science Journal, Aug. 1969, 5A, 60.

Morris, L.C., and Miller, D.J., 1964, IEEE Trans. on Microwave Theory and Techniques, MTT-12, 421.

Morris, L.C., and Miller, D.J., 1965, IEEE J. Quantum Electronics, QE-1, 164.

Osborn, J.A., 1945, Phys. Rev., 67, 351.

Ray, R.D., 1965, Proc. IEEE, 53, 318.

Rydbeck, O.E.H, Elldér, J., and Kollberg, E.L., 1969, Ap.J. (Letters), 156, L141.

Rydbeck, O.E.H., Kollberg, E.L., and Elldér, J., 1970, Research Report No. 97, Research Laboratory of Electronics, Chalmers University of Technology, Gothenburg, Sweden.

Rydbeck, O.E.H., and Kollberg, E.L., 1968, IEEE Trans. on Microwave Theory and Techniques, MTT-16, 799.

Rönnäng, B., 1970, to be published.

Schollmeier, G., and Roth, D., 1967, Z.Angew. Phys., 22, 471.

Schulz - DuBois, E.O., 1969, Cryogenics, 9, 194.

Scott, R.B., 1959, "Cryogenic Engineering", D.Van Nostrand Company Inc., Princeton, N.J.

Siegman, A.E., 1964, Microwave Solid State Masers, New York: McGraw-Hill.

Sommers, H.S., 1954, Rev. Sci. Instr., 25, 793.

Walker, B.J., 1965, Proc. IEEE, 53, 1661.

Walker, B.J., 1966, Proc. IEEE, 54, 96.

Winnberg, A., 1970, to be published.

Winnberg, A., and Lundahl, L., 1970, to be published.

Yngvesson, K.S., 1965, Research Report No. 54, Research Laboratory of Electronics, Chalmers University of Technology, Gothenburg, Sweden.

Yngvesson, K.S., 1968, Research Report No. 84, Research Laboratory of Electronics, Chalmers University of Technology, Gothenburg, Sweden

Yngvesson, K.S., and Kollberg, E.L., 1965, Proc. IEEE, 53, 1737.

Zuckerman, B., Palmer, P., Penfield, H., and Lilley, A.E., 1968, Ap.J. (Letters), 153, L69.

Earlier publications from the Research Laboratory of Electronics:

O.E.H.Rydbeck: A theoretical survey of the possibilities of determining the distribution of the free electrons in the upper atmosphere; Trans. Chalmers Univ. of Techn., No. 3, 1942.

O.E.H.Rydbeck: On the propagation of radio waves; Trans. Chalmers Univ. of Techn., No. 34, 1944.

O.E.H.Rydbeck: On the spherical and spheroidal wave functions; Trans. Chalmers Univ. of Techn., No. 43, 1945.

O.E.H.Rydbeck: A simple Kerr modulator for ionospheric recording; Trans. Chalmers Univ. of Techn., No. 44, 1945.

O.E.H.Rydbeck: Chalmers solar eclipse ionospheric expedition 1945; Trans. Chalmers Univ. of Techn., No. 53, 1946.

Reports from the Research Laboratory of Electronics:

1. O.E.H.Rydbeck: The theory of the travelling-wave tube. 1947 x).
2. J.S.A.Tomner: The experimental development of travelling-wave tubes; Trans. Chalmers Univ. of Techn., No. 67, 1948.
3. S.I.Svensson: Pulser and water load for high power magnetrons; Trans. Chalmers Univ. of Techn., No. 68, 1948.
4. U.Ingård: On the radiation of sound into a circular tube with an application to resonators; Trans. Chalmers Univ. of Techn., No. 70, 1948.
5. D.Strantz: A study of impressive wave formation in the atmosphere; Trans. Chalmers Univ. of Techn., No. 71, 1948.
6. D.Strantz: Ozonradiosonde; Trans. Chalmers Univ. of Techn., No. 72, 1948.
7. O.E.H.Rydbeck: On the propagation of waves in an inhomogeneous medium, I; Trans. Chalmers Univ. of Techn., No. 74, 1948.
8. O.E.H.Rydbeck and D.Strantz: Ionospheric effects of solar flares. Preliminary report No. 1, Trans. Chalmers Univ. of Techn., No. 83, 1949.
9. O.E.H.Rydbeck: On the forced electro-magnetic oscillations in spherical resonators. 1948 x).
10. J.S.A.Tomner: Experimental investigation of a long electron beam in an axial magnetic field; Trans. Chalmers Univ. of Techn., No. 92, 1949.
11. O.E.H.Rydbeck: The ionospheric and radio wave propagation observatory at Kiruna, 67° 50' N, 20° 14,5' E. 1949 x).
12. R.Lindquist: The panoramic ionospheric recorder. 1949 x).
13. R.Lindquist: Ionospheric effects of solar flares. Preliminary reports Nos. 2 and 3; Trans. Chalmers Univ. of Techn., No. 95, 1950.
14. O.E.H.Rydbeck: The theory of magneto ionic triple splitting; Trans. Chalmers Univ. of Techn., No. 101, 1951.
15. O.E.H.Rydbeck and S.K.H.Forsgren: On the theory of electron wave tubes; Trans. Chalmers Univ. of Techn., No. 102, 1951.
16. R.Lindquist: Polar blackouts recorded at the Kiruna Observatory; Trans. Chalmers Univ. of Techn., No. 103, 1951.
17. S.K.H.Forsgren: Some calculations of ray paths in the ionosphere; Trans. Chalmers Univ, of Techn., No. 104, 1951.
18. B.N.Agdur: Experimental observations of double-stream amplification. Preliminary notes; Trans. Chalmers Univ. of Techn., No. 105, 1951.

---

x) Not published in the Chalmers Transactions.

19. B.N.Agdur and C-G.L.Åsdal: Noise measurements on a travelling wave tube; Trans. Chalmers Univ. of Techn., No. 106, 1951.

20. S.K.H.Forsgren and O.F.Perers: Vertical recording of rain by radar; Trans. Chalmers Univ. of Techn., No. 107, 1951.

21. O.F.Perers, B.K.E.Stjernberg and S.K.H.Forsgren: Microwave propagation in the optical range; Trans. Chalmers Univ. of Techn., No. 108, 1951.

22. R.Lindquist: A survey of recent ionospheric measurements at the ionospheric and radio wave propagation observatory at Kiruna. 1951 x).

23. R.Lindquist: A 16 kW panoramic ionospheric recorder; Trans. Chalmers Univ. of Techn., No. 109, 1951.

24. B.-A.Lindblad: A radar investigation of the delta aquarid meteor shower of 1950; Trans. Chalmers Univ. of Techn., No. 129, 1952.

25. G.Hellgren: The propagation of electromagnetic waves along a conical helix with variable pitch; Trans. Chalmers Univ. of Techn., No. 130, 1953.

26. G.Hellgren and J.Meos: Localization of aurorae with 10 m high power radar technique, using a rotating antenna. 1952 x).

27. O.E.H.Rydbeck: On the excitation of different space charge wave modes in travelling wave tubes; Trans. Chalmers Univ. of Techn., No. 131, 1953.

28. O.E.H.Rydbeck and B.N.Agdur: The propagation of electronic space charge waves in periodic structures; Trans. Chalmers Univ. of Techn., No. 138, 1954.

29. B.N.Agdur: Experimental investigation of noise reduction in travelling wave tubes; Trans. Chalmers Univ. of Techn., No. 139, 1954.

30. B.N.Agdur: Amplification measurements on a velocity step tube; Trans. Chalmers Univ. of Techn., No. 140, 1954.

31. O.E.H.Rydbeck and H.Wilhelmsson: A theoretical investigation of the ionospheric electron density variation during a solar eclipse; Trans. Chalmers Univ. of Techn., No. 149, 1954.

32. H.Wilhelmsson: The interaction between an obliquely incident plane electromagnetic wave and an electron beam. Part I; Trans. Chalmers Univ. of Techn., No. 155, 1954.

33. S.Olving: Electromagnetic wave propagation on helical conductors imbedded in dielectric medium; Trans. Chalmers Univ. of Techn., No. 156, 1955.

34. S.Olving: Amplification of the travelling wave tube at high beam current. Part I; Trans. Chalmers Univ. of Techn., No. 157, 1955.

35. H.Wilhelmsson: On the reflection of electromagnetic waves from a dielectric cylinder; Trans. Chalmers Univ. of Techn., No. 168, 1955.

36. B.-A.Lindblad: Combined visual and radar observations of Perseid meteors. I: Observations in 1953 x)

37. S.Olving: A new method for space charge wave interaction studies. Part I; Trans. Chalmers Univ. of Techn., No. 175, 1956.

38. V.Westberg: Measurements of noise radiation at 10 cm from glow lamps; Trans. Chalmers Univ. of Techn., No. 180, 1956.

39. S.I.Svensson, G.Hellgren and O.Perers: The swedish radioscientific solar eclipse expedition to Italy, 1952; Trans. Chalmers Univ. of Techn., No. 181, 1956.

40. N.Wax: A note on design considerations for proposed auroral radar; Trans. Chalmers Univ. of Techn., No. 182, 1957.

41. N.Wax: On the ring current hypothesis; Trans. Chalmers Univ. of Techn., No. 171, 1956.

---

x) Not published in the Chalmers Transactions.

42. G.H.Joshi: The electromagnetic interaction between two crossing electron streams. Part I; Trans. Chalmers Univ. of Techn., No. 183, 1957.

43. J.Meos and S.Olving: On the origin of radar echoes associated with auroral activity; Trans. Chalmers Univ. of Techn., No. 196, 1958.

44. G.H.Joshi: The electromagnetic interaction between two crossing electron streams. Part II; Trans. Chalmers Univ. of Techn., No. 197, 1958.

45. H.Wilhelmsson: The interaction between an obliquely incident plane electromagnetic wave and an electron beam. Part II; Trans. Chalmers Univ. of Techn., No. 198, 1958.

46. H.Wilhelmsson: On the properties of the electron beam in the presence of an axial magnetic field of arbitrary strength; Trans. Chalmers Univ. of Techn., No. 205, 1958.

47. H.Wilhelmsson: The interaction between an obliquely incident plane electromagnetic wave and an electron beam. Part III; Trans. Chalmers Univ. of Techn., No. 206, 1958.

48. B.Höglund and V.Radhakrishnan: A radiometer for the hydrogen line; Trans. Chalmers Univ. of Techn., No. 223, 1959.

49. S.Olving: Electromagnetic and space charge waves in a sheath helix; Trans. Chalmers Univ. of Techn., No. 225, 1960.

50. H.Wilhelmsson: A survey of radio-frequency and microwave resonance lines of interest to radio astronomy. 1960 x).

51. S.Olving: A new method for space charge wave interaction studies. Part II; Trans. Chalmers Univ. of Techn., No. 228, 1960.

52. Papers presented at the fourth international conference on ionization phenomena in gases at Uppsala, August 17-21, 1959. 1960 x).

53. H.Wilhelmsson: Two problems concerning the electron ring current. 1960 x).

54. T.Orhaug: The variation of electron density in the ionosphere during a solar eclipse. 1960 x).

55. H.Wilhelmsson and M.Fischer: On the force-free magnetic fields. 1960 x).

56. O.E.H.Rydbeck: On the coupling between waves in inhomogeneous systems. 1961 x).

57. H.Wilhelmsson: The scattering of an electromagnetic wave by a dielectric-coated metallic cylinder. Reprint from Arkiv för Fysik, Band 23, nr 41 x).

58. H.Wilhelmsson: Accounting for smoothing effects in 21 cm observations. Reprint from Arkiv för Astronomi, Band 3, nr 15 x).

59. B.Höglund: 21 cm Observations in the Galactic Anti-centre. Reprint from Arkiv för Astronomi, Band 3, nr 16 x).

60. H.Gerritsen: Recent Developments in Maser Devices and Materials. Reprint from Applied Optics, Vol. 1, No 1 x)

---

x) Not published in the Chalmers Transactions.

Research Reports from the Research Laboratory of Electronics:

1. O.E.H.Rydbeck and K.H.B.Wilhelmsson: The influence of the electron velocity distribution on space charge waves. 1959.
2. K.H.B.Wilhelmsson: Oscillatory properties of gyromagnetic electronic cold plasmas with drift motion. 1959.
3. H.B.Hvatum: Solar radio noise measurements during the 1954 solar eclipse. 1959.
4. T.Aa.Orhaug: Ionospheric observations during the solar eclipse June 30, 1954. 1959.
5. K.H.B.Wilhelmsson: The electromagnetic coupling between an electron beam and incident plane waves for an axially finite interaction domain. 1960.
6. Research notes communicated at the radio scientific conference in Stockholm, February 29 - March 2, 1960. 1960.
7. O.E.H.Rydbeck: The propagation and coupling of waves in inhomogeneous media with applications to electromagnetic and space charge waves. (On the propagation of waves in an inhomogeneous medium II).
8. O.E.H.Rydbeck: Electromagnetic and space charge waves in inhomogeneous structures with applications to ionized media and microwave tubes. 1960.
9. K.H.B.Wilhelmsson: On the geometrical theory of diffraction with application to the electron beam. 1960.
10. O.E.H.Rydbeck: The Doppler effect in dispersive, inhomogeneous media with applications to electromagnetic waves in ionized media. 1960.
11. S.Olving and A.Ots: An experimental investigation of the propagation of space charge waves along radially inhomogeneous electron beams. 1960.
12. A.V.Stomberg: The rotatron - an electron tube for shift and multiplication of frequencies. 1960.
13. O.E.H.Rydbeck and M.H.Fischer: Space charge waves in an electron beam of Gaussian cross section. 1960.
14. O.E.H.Rydbeck: The integral equation of travelling wave tubes with electron beams of arbitrary cross section. 1960.
15. O.E.H.Rydbeck and A.R.Thomasson: Low frequency waves in inhomogeneous magneto ionic media. 1960.
16. T.Aa.Orhaug: Observations of radio star scintillations at high latitudes. 1960.
17. T.Aa.Orhaug: Observations of solar radio noise at 150 Mc/s. 1960.
18. O.E.H.Rydbeck and J.Askne: Whistler mode - ionized stream interactions. Part I, 1963.
19. K.H.B.Wilhelmsson: On the problem of overtaking in a velocity distributed electron stream. 1960.
20. O.E.H.Rydbeck: On the coupling between waves in inhomogeneous systems. 1960.
21. O.E.H.Rydbeck: Research in the field of propagation and interaction of electromagnetic waves and space charge type waves in homogeneous and inhomogeneous media. 1960.
22. D.T.Farley, J.P.Dougherty and D.W.Barron: A theory of incoherent scattering of radio waves by a plasma in a uniform magnetic field. 1961.
23. L.F.Eastman: Coherent non-linearities in a mangeto-ionic medium. 1961.
24. D.T.Farley: Artificial heating of the electrons in the F-region of the ionosphere. 1961.
25. K.H.B.Wilhelmsson: Scattering of electromagnetic waves by an anisotropic medium. 1961.
26. K.H.B.Wilhelmsson: The interaction between an obliquely incident plane electromagnetic wave and an electron beam in the presence of a static magnetic field of arbitrary strength. 1961.
27. O.E.H.Rydbeck: Dynamic non-linear wave propagation in ionized media. 1. The isotropic medium. 1961.
28. O.E.H.Rydbeck: Dynamic non-linear wave propagation in ionized media. 2. The magneto-ionic medium. 1962.

29. O.E.H.Rydbeck: Dynamic non-linear wave propagation in ionized media. 3. Electromagnetic non-linear wave interaction and reflection from a plane ionized medium. 1963.

30. O.E.H.Rydbeck: Dynamic non-linear wave propagation in ionized media. 4. Non-linear electromagnetic wave propagation and harmonic radiation in magneto-ionic media. 1963.

31. K.H.B.Wilhelmsson: Dynamic non-linear wave propagation in ionized media. 5. Reflection of electromagnetic waves from an ionized stream in the presence of a high power primary wave. 1962.

32. K.H.B.Wilhelmsson: Dynamic non-linear wave propagation in ionized media. 6. Scattering of electromagnetic waves by an anisotropic medium with an harmonically time-varying dielectric tensor. 1962.

33. O.E.H.Rydbeck: Dynamic non-linear wave propagation in ionized media. 7. Non-linear plasma waves in a streaming homogeneous, cold ionized medium. 1962.

34. A.R.Thomasson: Dynamic non-linear wave propagation in ionized media. 8. Reflection of electromagnetic waves from a dielectric plane layer varying periodically in space and time. 1962.

35. K.H.B.Wilhelmsson: Dynamic non-linear wave propagation in ionized media. 9. A non-linear coupling mechanism for generation of very low frequency waves. 1963.

36. K.H.B.Wilhelmsson: Dynamic non-linear wave propagation in ionized media. 10. Non-linear interaction between an obliquely incident plane electromagnetic wave and an electron beam. 1963.

37. S.Olving: On the non-linear theory of the plane travelling wave tube. 1963.

38. K-O.Yngvesson: Observations of the Venus probe Mariner R-2 at the Onsala Space Observatory. 1963.

39. K.H.B.Wilhelmsson: Dynamic non-linear wave propagation in ionized media. 11. Non-linear excitation of hydromagnetic waves and hybrid resonances by two interacting high power primary waves. 1963.

40. S.Olving and O.Nilsson: Propagation of nonlinear Hahn-Ramo waves along an annular electron current sheath. 1963.

41. S.Olving and M.Fischer: Small-signal nonlinear klystron waves. 1964.

42. S.Olving and S.Wallander: Nonlinear space charge wave theory of the hydrodynamic disc-electron beam. 1964.

43. O.E.H.Rydbeck: Dynamic non-linear wave propagation in ionized media. 12. Electromagnetic wave reflection from an oscillating, collision free magneto-ionic medium. 1964.

44. A.R.Thomasson: Dynamic non-linear wave propagation in ionized media. 13. Microscopic treatment of the interaction between a plane electromagnetic wave and an oscillating medium. 1964.

45. K.H.B.Wilhelmsson: Dynamic non-linear wave propagation in ionized media. 14. Generation of longitudinal plasma waves by non-linear coupling of two high-power circularly polarized transverse waves. 1964.

46. K.H.B.Wilhelmsson and A.R.Thomasson: Dynamic non-linear wave propagation in ionized media. 15. Čerenkov effect in a pre-oscillating medium. 1964.

47. K.H.B.Wilhelmsson: The magneto-ionic theory for mass-anisotropic electrons. 1964.

48. O.E.H.Rydbeck: Research in the field of propagation of high power waves in ionized media. 1964.

49. R.Tengblad: Concentration effects in a maser material. 1964.

50. O.Nilsson: Some frequency and power conversion properties of cyclotron waves. 1965.

51. O.Nilsson: Anomalous noise peak in Adler tubes. 1965.

52. In preparation.

53. J.Askne: Stimulated scattering from a semi-infinite dispersive medium periodic in time and space. 1965.

54. S.Yngvesson: Chromium-soped rutile: Maser properties at 1420 Mc/s and application to a traveling-wave maser, 1965.

55. T.M.Srinivasan: Measurements on nonlinear space charge waves, 1965.

56. O.E.H.Rydbeck: Wave coupling in multi-mode. inhomogeneous, ionized media, with applications to electron stream-whistler mode interactions. 1966.

57. P.McIsaac: Wave propagation in a dispersive medium. 1966.

58. S.Wallander: Nonlinear theory of the planar microwave vacuum diode. 1966.

59. S.Wallander: Nonlinear traveling wave tube analysis with two signal frequencies, 1966.

60. O.Nilsson: Approximate theory of the wire helix slow wave structure. 1966.

61. O.E.H.Rydbeck and Å.Hjalmarson: Coupled wave equations for multi-mode inhomogeneous media. 1966.

62. O.E.H.Rydbeck and Å.Hjalmarson: Coupled waves in magneto-ionic media. Part I. 1966.

63. J.Askne: Reflection and amplification of electromagnetic waves in an oscillating ionized medium, Part I. 1966.

64. J.Askne: Instability properties of an ionized medium periodic in time and space.
B.Rönnäng: Transient wave propagation in symmetric, ionized Epstein layers. 1966.

65. J.I.Lindström: Measurements of nonlinearities in a traveling wave tube. 1966.

66. J.Jäderblom: Cycletron wave amplification using self generated pump power. 1966.

67. O.Nilsson: Nonlinear distortion in traveling wave tubes. 1966.

68. S.Kronlund: Measurements on a beam-plasma microwave amplifier. 1966.

69. P.R.McIsaac: Boundary conditions for ferromagnetic media. 1966.

70. B.O.Rönnäng: Transient wave propagation in inhomogeneous ionized media. 1966.

71. S.Olving: Nonlinear microwave tube studies. 1966.

72. E.L.Kollberg: A dielectrically loaded slow-wave structure for traveling-wave maser applications. 1966.

73. B.O.Rönnäng: Signal distortion in anisotropic homogeneous ionized media. 1967.

74. A.Winnberg: The structure of galactic neutral hydrogen in a region of cygnus. 1967.

75. Å.Hjalmarson: Coupled wave Equations for Multi-Mode Inhomogeneous Media. II. 1967.

76. D.Berkley: Elastic Analysis of the Cornes. 1967.

77. S.Wallander: Large Signal Analytical Theory of Klyctron Waves. 1967.

78. S.Wallander: Large Signal Computer Analysis of Klystron Waves. 1967.

79. O.E.H.Rydbeck: Energy Flow in Multi-Mode Systems. 1967.

80. J.Askne: Reflection and Amplification of Electromagnetic Waves in an Oscillating Ionized Medium. Part II. 1967.

81. L.Hansson: Measurements of the Pointing Error for the Automatic Steering System of the Chalmers 84 Foot Radio Telescope. 1967.

82. E.A.Harris & K.S.Yngvesson: "Spin-Lattice Relaxation in Some Iridium Salts, Part I, 1:23, 1968.

83. E.A.Harris & K.S.Yngvesson: "Spin-Lattice Relaxation in Some Iridium Salts, Part II, 1:26. 1968.

84. K.S.Yngvesson: "Maser Properties of Cr – TiO_2 at L- and S-Band and Their Interpretation in Terms of Crystal Field and Exchange-Coupled Cluster Relaxation Processes, 1968.

85. I.Ewaldz: "Observations of the 159 (966 MHz) Excited Hydrogen Line in Orion A and M 17". 1968.

86. J.I.Lindström & O.Nilsson: Crossmodulation in Traveling Wave Tubes, 1968.

87. J.Elldér: OH Spectral Line Measurements of Radiation from the Galactic H II Regions W 3 and W 49 at 1665 MHz, 1968.

88. O.E.H.Rydbeck: Multi-Mode Wave Coupling in Inhomogeneous, Anisotropic Media – with Some Magneto-Ionic Applications, 1968.

89. O.E.H.Rydbeck and E.L.Kollberg: Rutile Traveling Wave Masers for the Frequency Range 1300 – 3400 MHz and their Application to the Onsala 84 foot Radio Telescope to Galactic Spectral Line Emission Studies, 1968.

90. Jumpol Prompitaka: The performance of a $LiNbO_3$ light modulator at 1.6 GHz, 1968.

91. J.Askne: Energy Considerations and Coupled Mode Analysis. 1969.

92. S.Wallander: Large Signal Computer Analysis of distortion in Traveling Wave Tubes, 1969.

93. S.Wallander: Nonlinear Multi-Signal Traveling Wave Tube Theory, 1969.

94. J.Askne: Reflection and amplification of electromagnetic Waves in an Oscillating Ionized Medium. Part III. Wave Propagation in a bounded time-space periodic plasma medium. 1969.

95. E.L.Kollberg: Measurements at noise in maser systems, theory and experiments. 1969.

96. J.Elldér: Some OH and Formaldehyde Properties of W 3 and W 51 Regions. 1970.

97. O.E.H.Rydbeck et al: Excited State OH Emissions From W 75 B and W 3, OH. 1970.

98. E.L.Kollberg: Rutile Traveling Wave Maser Systems for the Micro wave range 1.3-6.2 GHz. 1970.

99. P.Ingvarson: The Diffraction of an Electromagnetic Wave by Sound. 1970.

Lecture Notes from the Research Laboratory of Electronics:

1. K.H.B.Wilhelmsson: Lectures on the quantum theory of masers. 1962.

2. D.T.Farley: Lectures on the scattering of radio waves from randomly fluctuating media given 1961 at Chalmers University of Technology, Gothenburg. 1961.

3. A.Elvius: Lectures on galactic dynamics given 1961 at Chalmers University of Technology, Gothenburg. 1961

4. K.H.B.Wilhelmsson and A.G.Lieberman: Lectures on superconductivity. 1964.

I:18

Nr. 104

Bil. 2

Tp

A DIELECTRICALLY LOADED SLOW-WAVE STRUCTURE FOR TRAVELING-WAVE MASER APPLICATIONS

BY
E. L. KOLLBERG

RESEARCH REPORT NO 72
1966

RESEARCH LABORATORY OF ELECTRONICS

CHALMERS UNIVERSITY OF TECHNOLOGY

GIBRALTARGATAN 5 G

GOTHENBURG S, SWEDEN

Research Laboratory of Electronics
CHALMERS UNIVERSITY OF TECHNOLOGY
Gothenburg, Sweden

RESEARCH REPORT No. 72

A DIELECTRICALLY LOADED SLOW-WAVE STRUCTURE FOR TRAVELING-WAVE MASER APPLICATIONS

By

E. L. KOLLBERG

TABLE OF CONTENTS

LIST OF SYMBOLS

SUMMERY

Chapter 1: INTRODUCTION

Chapter 2: THE MASER SWS AND ITS EQUIVALENT CIRCUIT

2.1 Description and features of the SWS

2.2 The equivalent circuit of the SWS

Chapter 3: THE CHARACTERISTIC ADMITTANCE $Y_s(\varphi)$ OF THE TEM-WAVE TRAVELING ALONG THE PARALLEL STRIPS

3.1 The general expression

3.2 Numerical calculation of $Y_s(\varphi)$

3.3 Other methods of calculating $Y_s(\varphi)$. A comparison

Chapter 4: PASSBAND AND SLOWING PROPERTIES OF THE MASER STRUCTURE

4.1 Homogeneous dielectric loading

4.2 Inhomogeneous dielectric loading of region 2

4.3 The effect of inserting the maser crystal into region 1

Chapter 5: APPROXIMATE BEHAVIOR OF THE SWS

5.1 Approximation of the dispersion relation

5.2 The approximate behavior of the slowing factor on the geometrical dimensions

Chapter 6: ON THE COUPLING TO THE SWS

6.1 Introduction

6.2 The characteristic addmittance of the SWS

6.3 Coupling networks

Chapter 7: THE FILLING FACTOR OF THE SWS

7.1 Introduction

7.2 The effect of the dielectric loading in region 2

7.3 A possible method to increase the filling factor η

Chapter 8: DESIGN CONSIDERATIONS FOR THE SWS

8.1 General considerations

8.2 The design procedure

Chapter 9: EXPERIMENTAL SLOW-WAVE STRUCTURES

ACKNOWLEDGEMENTS

Appendix: Asymptotic expressions for Y (0), Y (π/2) and Y (π)

References.

LIST OF SYMBOLS

a, b, d, e	parameters in the SWS dispersion equation (5.5.1)
B_{on}	mutual admittances between strips in the SWS, eq. (2.2.6)
C_t	capacitance per unit length due to the strip thickness, eq. (3.2.9)
C_{on}	capacitance per unit length between strips, eq. (3.1.2)
C_f C_{foo} C_{fo1}	fringing capacitance at the strip ends, eq. (4.1.4)
f_o f_π	cutoff frequencies
Δf	SWS bandwidth $= \lvert f_\pi - f_o \rvert$
G	gain of the TWM in dB, eq. (1.1)
$G_s(\varphi)$	characteristic admittance of the SWS, eq. (2.2.8) and (6.2.3)
$\bar{H}$	magnetic field strength vector
i, i_n	currents related to the equivalent scheme of the SWS, Fig. 2.5
i_{on}	current on a strip due to the interactions on the n-th neighbor strip in an infinite strip array, eq. (3.1.2)
i_s	the total current on a strip in an infinite strip array, eq. (3.1.4)
l_1, l_2	the length of the strip in region 1 and 2 respectively, Fig. 4.1
L	the length of the maser SWS, eq. (1.1)
n	index related to the n-th neighbor strip
p	periodicity length (pitch) of the periodic SWS
p_{opt}	optimum periodicity length, eq. (8.1.5)

Q_o, Q_i, Q_m quality factors, related to the ohmic losses, the forward wave isolator losses and the electronic gain in a TWM

r the ratio of the strip width to the periodicity length p

$\mu = Q_i / |Q_m|$

$S = v_o / v_g$ the slowing factor

t strip thickness, Fig. 4.1

T_o the temperature of the helium bath, eq. (8.1.8)

T_m the spin temperature, eq. (8.1.8)

T_n the noise temperature, eq. (8.1.8)

U_o, U_n the voltages in the equivalent scheme of the SWS, Fig. 2.5, and the voltages on the strips in the infinite strip array, eq. (3.1.1)

v the velocity of the TEM wave

v_o the velocity of light in free space

v_g the group velocity

W_1, W_2 the spacing between the strips and the ground planes in region 1 and 2 respectively, Fig. 4.1

x the distance between the strip end and the boundary of region 2, Fig. 4.1

y_{on} the mutual characteristic admittances, eq. (3.1.3)

y_t the characteristic admittance due to the strip thickness, eq. (3.2.9)

$Y_o = \sqrt{\frac{\varepsilon_o}{\mu_o}}$ the admittance of free space

Y_s	the characteristic admittance of a strip in an infinite strip array, eq. (3.2.8)
Y_{s1}, Y_{s2}	Y_s for region 1 and 2, Fig. 4.1
Y_s^o	Y_s for $t=0$
Y_{in}	the input admittance of the SWS, eq. (6.3.1)
β	the propagation constant, eq. (1.5)
ε_r	the relative dielectric constant
ε_o	the dielectric constant of free space
η	the filling factor, eq. (1.3)
η_1, η_2, η_+	see eq. (7.3.2) and Fig. 7.2
Θ	the gain per period in Neper, eq. (2.2.1)
λ_{oo}	the free space wavelength at the lower cutoff frequency
μ_o	the permeability of free space
$\overline{\sigma}$	the transition probability vector, eq. (1.3)
σ_{nr}	the transition probability vector amplitude for optimum polarization eq. (1.3)
φ	the phase shift per period
$\Delta\varphi$	the shift in φ related to a certain mean slowing factor, eq. (1.6)
ω	the angular frequency

SUMMARY

A slow-wave structure (SWS) which is particularly useful in traveling-wave maser (TWM) applications is introduced in Chapter 2. The SWS resembles the comb-structure, though the analysis and its properties differ from those of the usual comb-structure. The general theory of the SWS is presented in Chapters 2 to 4 and details concerning its properties are derived and discussed in Chapters 5 to 7. Design considerations and experimental data are given in Chapters 8 and 9.

An equivalent circuit, applicable to a class of SWS:s including the one mentioned above and the Karp-structure, is derived and discussed. This circuit is capable of handling a high gain per period, which is out of reach with the usual method.

To be able to calculate the dispersion characteristic and the group velocity for the SWS, the admittance of one particular strip in a strip array guiding TEM waves must be accurately known. The admittance is expressed in the way proposed by Leblond and Mourier. An accurate method for the calculation of the coefficients constituting the admittance is introduced, and numerical values with a maximum error of 3% are tabulated for various SWS geometries. The method of expressing the admittance is particularly suited to the equivalent circuit mentioned above. It is believed that this method, in comparison with other methods, gives a better physical concept and leads to more accurate results.

The method of calculating the dispersion charasteristic for the particular SWS is extensively discussed. Necessary parameters have been measured in an electrolytic tank, and are presented in graphs.

Since the dispersion relations are easy to interpret physically, convenient approximations can be introduced. As a result, it is possible to find geometric requirements for the SWS, leading to a large and constant slowing factor over a maximum frequency band. With a careful design, as much as 30% might be gained in SWS bandwidth or slowing factor.

Using the equivalent circuit of the SWS, the coupling between the input line and the SWS is discussed. The general behavior of the structure impedance level on dimensions and frequency is calculated, and is shown mostly to be higher

than 50 Ω . Two coupling networks, one with transforming properties, will be discussed shortly.

Since the maser crystal cannot fill the entire space of the SWS, a filling factor has to be considered when the gain of the TWM maser is calculated. Calculations show that the degradation of the filling factor due to the lack of maser material at the open end of the strips is less than 10% for practical masers. The thin strips mean that a considerably higher filling factor (of the order 25%) is obtained as compared to square strips (the comb-structure). A method of further increasing the filling with about 25%, utilizes the properties of thin strips.

Measured data show an excellent agreement with the theory. The great flexibility of the design of the SWS is demonstrated by a series of SWS, differing from each other only by the placing of the dielectric loading ($\varepsilon_r = 25$) at the open end of the strips. Hence the lower cut-off frequency is moved in steps from 2660 MHz to 3000 MHz as the bandwidth changes from 600 MHz to 1500 MHz and the slowing factor from about 170 to about 80. By changing the dielectric constant from $\varepsilon_r = 25$ to $\varepsilon_r = 10$, the lower cut-off frequency moves from 2660 MHz to 4000 MHz, the slowing becomes approximately 130 and the passband about 700 MHz.

1. INTRODUCTION

The most convenient type of the extreme low noise maser amplifier is the traveling-wave maser (TWM). The main advantages of the TWM when compared with the cavity maser are

a) lower noise because no circulator is needed.

b) stable amplification due to the isolation between output and input.

The stimulated emission of radiation from the maser crystal is proportional to the magnetic field energy density. The TWM uses a slow-wave structure (SWS) to decrease the group-velocity of the propagating wave, which is equivalent to an increased energy per unit length within the SWS. The gain in dB of the TWM can be expressed as [1]

$$G = 27.3 \, \frac{S \cdot L}{\lambda_o} \cdot \left(\frac{\eta}{Q_m} - \frac{1}{Q_o} - \frac{1}{Q_i} \right) \qquad 1.1$$

L is the active length of the SWS, λ_o the free space wavelength of the amplified signal, Q_m the magnetic quality factor of the maser material for optimum polarization of the rf field. Q_o and Q_i are quality factors related respectively to ohmic losses and forward wave isolator losses. S is the slowing factor, defined as

$$S = \frac{v_o}{v_g} \qquad 1.2$$

where v_o is the velocity of light in vacuum and v_g the group velocity of the wave in the SWS. The filling factor η is defined as [1]

$$\eta = \frac{\int_m \overline{H}^* \; \overline{\delta} \; \overline{\delta}^* \; \overline{H} \, dv}{\delta_{nr}^2 \int_v \overline{H}^* \; \overline{H} \, dv} \qquad 1.3$$

$\overline{\delta}$ is a dimensionless vector characteristic of the particular transition and the particular operating point under consideration. The effective value of $\overline{\delta} \; \overline{\delta}^*$ for the optimum nonreciprocal polarization is indicated by δ_{nr}^2. The integral in the numerator of (1.3) is taken over the volume of the maser crystal and the integral in the denominator is taken over the whole volume of the SWS.

There are essentally four types of slowing used in SWS:s for TWM applications [1]

a) dielectric slowing [2]
b) geometrical slowing, e.g. the helix or the meander-line [1, 3]
c) resonant slowing, e.g. the comb-structure [4, 5],
the Karp-structure [6, 7], coupled cavities [8] and the meander line.
d) dispersive slowing, different to the above mentioned types, e.g. the rectangular waveguide [2].

SWS utilizing geometrical and/or resonant slowing, are usually built in a periodic form with a periodicity length or pitch p. Floquet's theorem is applicable to an infinite, one-dimensional periodic structure [9].

The group velocity v_g of a wave within a periodic structure with moderate dispersion can be expressed as

$$v_g = \frac{d\omega}{d\beta} = p\frac{d\omega}{d\varphi} \qquad 1.4$$

where

$$\varphi = p \cdot \beta \qquad 1.5$$

is the phase shift of the wave over one period.

Structures of the resonant slowing type usually exhibit a relatively small frequency region with a usable slowing factor (see Fig. 1.1.) Let that frequency band be Δf and let the corresponding shift in φ be $\Delta\varphi$. Hence

$$S \approx \frac{v_o}{\frac{\Delta\omega}{\Delta\varphi} \cdot p} \qquad 1.6$$

leading to

$$S \propto \frac{1}{p} \qquad (\Delta f,\ \Delta\varphi \text{ constant}) \qquad 1.7$$

$$\Delta f \propto \frac{1}{p} \qquad (s, \Delta\varphi \text{ constant}) \qquad 1.8$$

These equations show the importance of the pitch. We will return to equation (1.6) in chapter 8. Notice that for the meander line, the distance p/2 between two neighboring strips has to be considered, when the meander line is compared with other types of strip SWS:s (see Fig. 1.1).

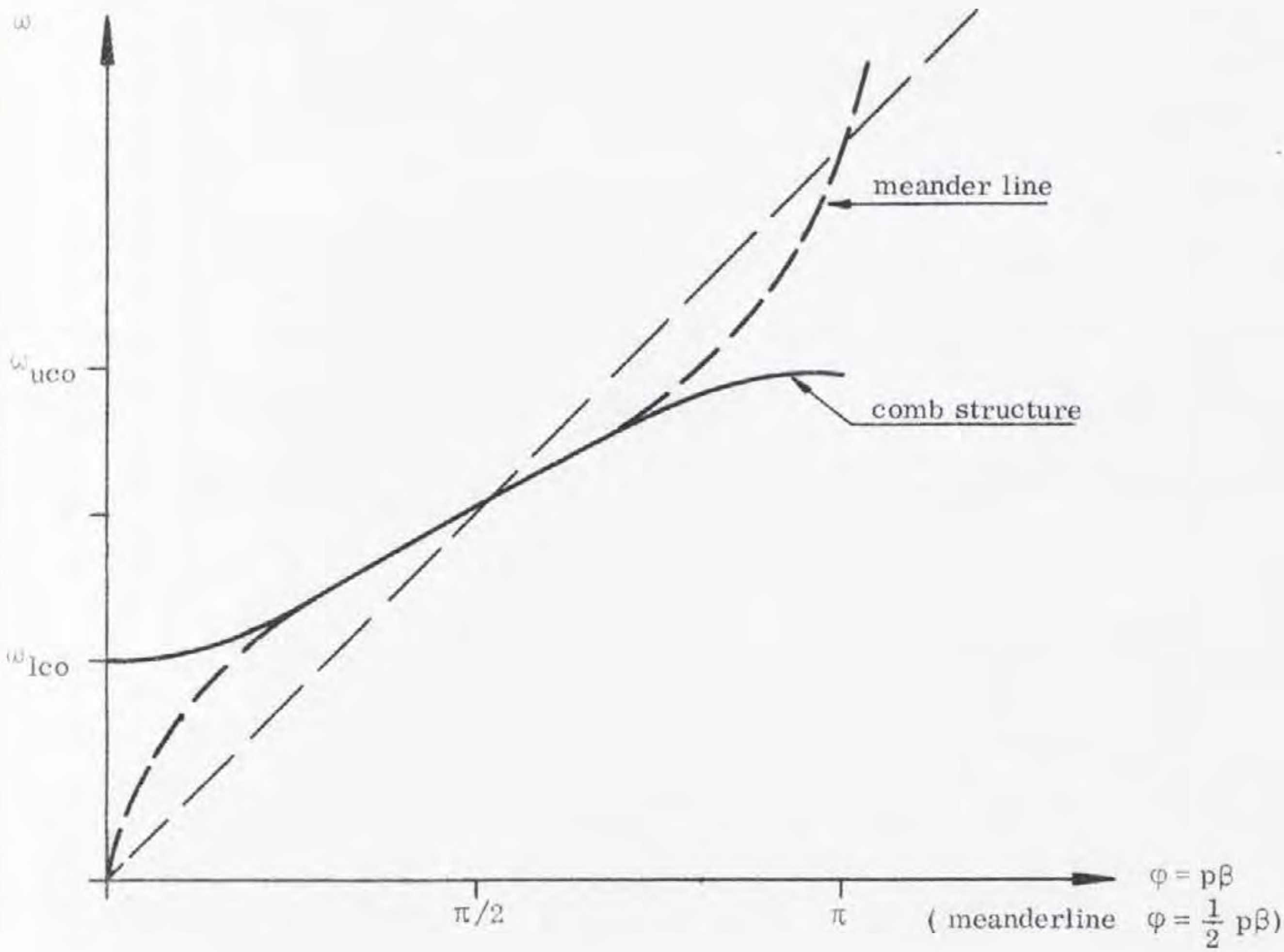

Fig. 1.1 Dispersion relations for SWS exhibiting resonant slowing. Notice that for the meanderline, $\frac{1}{2}$p is the distance between two parallell conductors and $\varphi = \frac{1}{2} p\beta$ is the phase shift over half a period.

2. THE MASER SLOW-WAVE STRUCTURE AND ITS EQUIVALENT CIRCUIT

2.1 Description and features of the SWS.

The particular SWS to be described here, is originally developed from the dielectrically loaded Karp-structure described by S. Yngvesson [6]. In Fig. 2.1, a cross section of the original Karp-structure and the developed SWS are shown. The new structure uses only half as much maser material as the original structure for the same slowing factor bandwidth and structure length. Further work on the SWS has resulted in the structure shown in Fig. 2.2. This structure [10], might be classified as a modified comb-structure. The main features of this structure may be summarized as:

a) mechanical stability because the strip conductors are clamped between the dielectric rods.

b) high filling-factor, since the dielectrically loaded region contains only a small part of the magnetic field energy.

c) high filling factor also in the upper part of the pass-band, since the strip conductors can be made very thin.

d) a maser crystal with a high relative dielectric constant (e.g. rutile) may be inserted into the structure, without noticeably changing its dispersion characteristic.

e) the center frequency of the passband can be changed within wide limits only by changing the dielectric constant of the dielectric load or by choosing its position along the conductors.

f) the design procedure is easy and flexible, since the geometry of the SWS can be kept almost unchanged for different pass-band frequencies and slowing factors.

g) the risk of obtaining a double-valued $\omega - \varphi$ -characteristic when designing a SWS with a very high slowing factor is almost negligible.

A general theory is interpreted in chapters 2 - 4, details concerning the features of the SWS will be given in chapters 5 - 7 and design considerations in chapter 8.

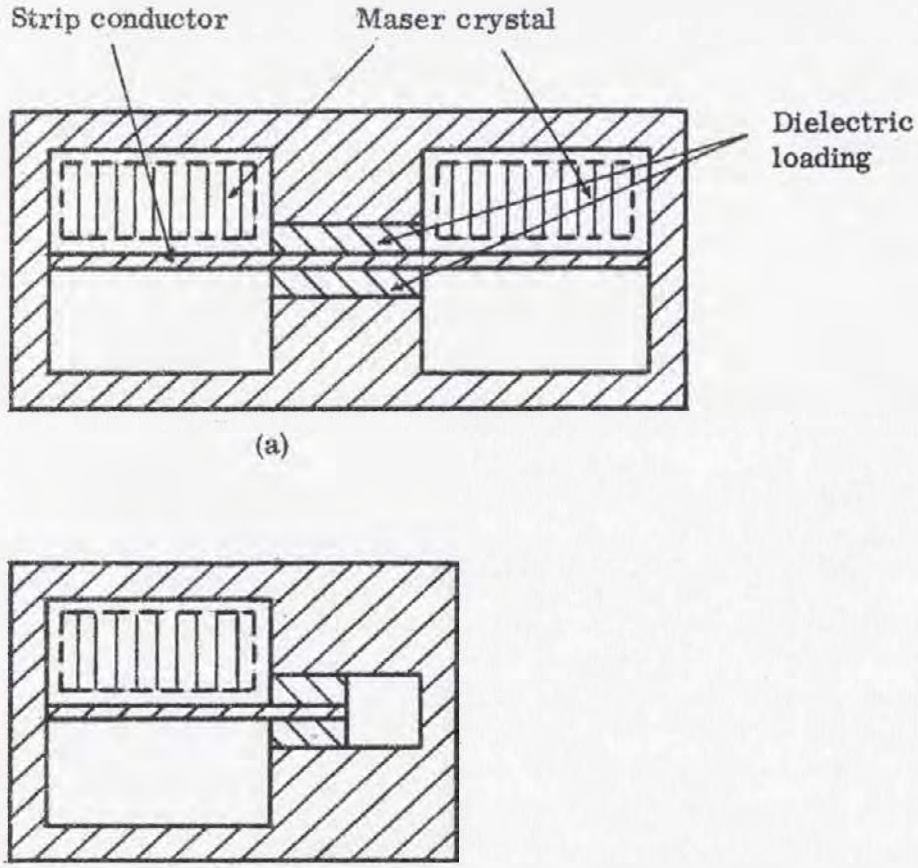

(a)

(b)

Fig. 2.1 (a) Cross-section of the original dielectrically loaded Karp-structure.

(b) Cross-section of the SWS developed from the Karp-structure.

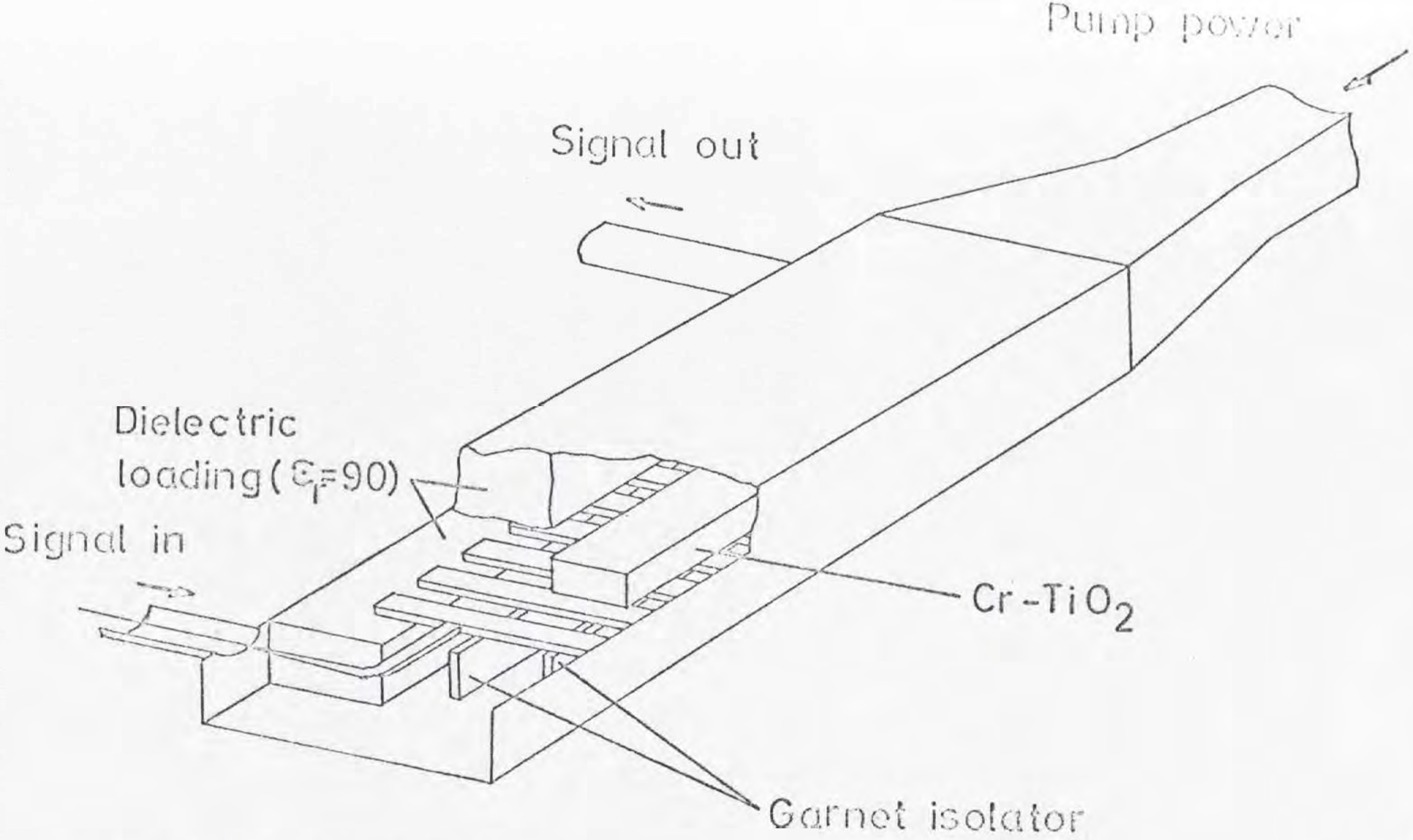

Fig. 2. 2. Exploded view of the SWS.

2.2 The equivalent circuit of the SWS

The need for an equivalent circuit of the SWS is particularly pronounced when one has to develop a coupling network to match the input (50 Ω) line to the SWS. A lot may also be gained in pure understanding of the wave-propagation along the SWS.

We will make use of Fletcher's assumption [20] that the fields in the structure may be approximated by TEM waves running along the parallell conductors (see Fig. 2.2). Since the field of a TEM wave in a plane transverse to its direction of propagation is obtained from the electrostatic solution [11], voltages and currents are easily defined (see also section 3.1).

The SWS under consideration has much in common with microwave filters built from strip-line components guiding TEM waves [12]. The comb-line filter [12, 13] is of particular interest because of its great recemblance to the present SWS (see Fig. 2.3). In the equivalent circuit of the comb-line filter, the reference points are at the open end of the striplines capacitively loaded. Matthaei [13] recomends a coupling network to match the input line to the filter and computes the filter properties. He obtains an excellent agreement between theory and measurements.

The interaction between nonadjacent lines has been omitted in the circuit of Fig. 2.3. This is acceptable since the surrounding ground planes lie close to the strip-lines and thus create an effective shielding. (Fig. 2.3 b). In SWS for TWM applications, however, this is not generally the case (Fig. 2.4 b). A larger ratio W/p will increase the amount of circular polarization (see section 6.1, Fig. 6.2, and reference [14].) which is essential for a good isolator performance in a TWM. Furthermore the dielectric loading at the strip ends (region 2, Fig. 2.4 a) may be inhomogeneous and hence the TEM approximation must be reconsidered. We will return to this question in chapter 4.

A network, similar to that of Fig. 2.3 c taking into account the effect of interaction between any two elements is easily constructed, Fig. 2.5. The reference point on the strip is chosen at the boundary between regions 1 and 2 in Fig. 2.4 a. Assume the SWS to be infinitely long and perfectly periodic. Hence we may apply

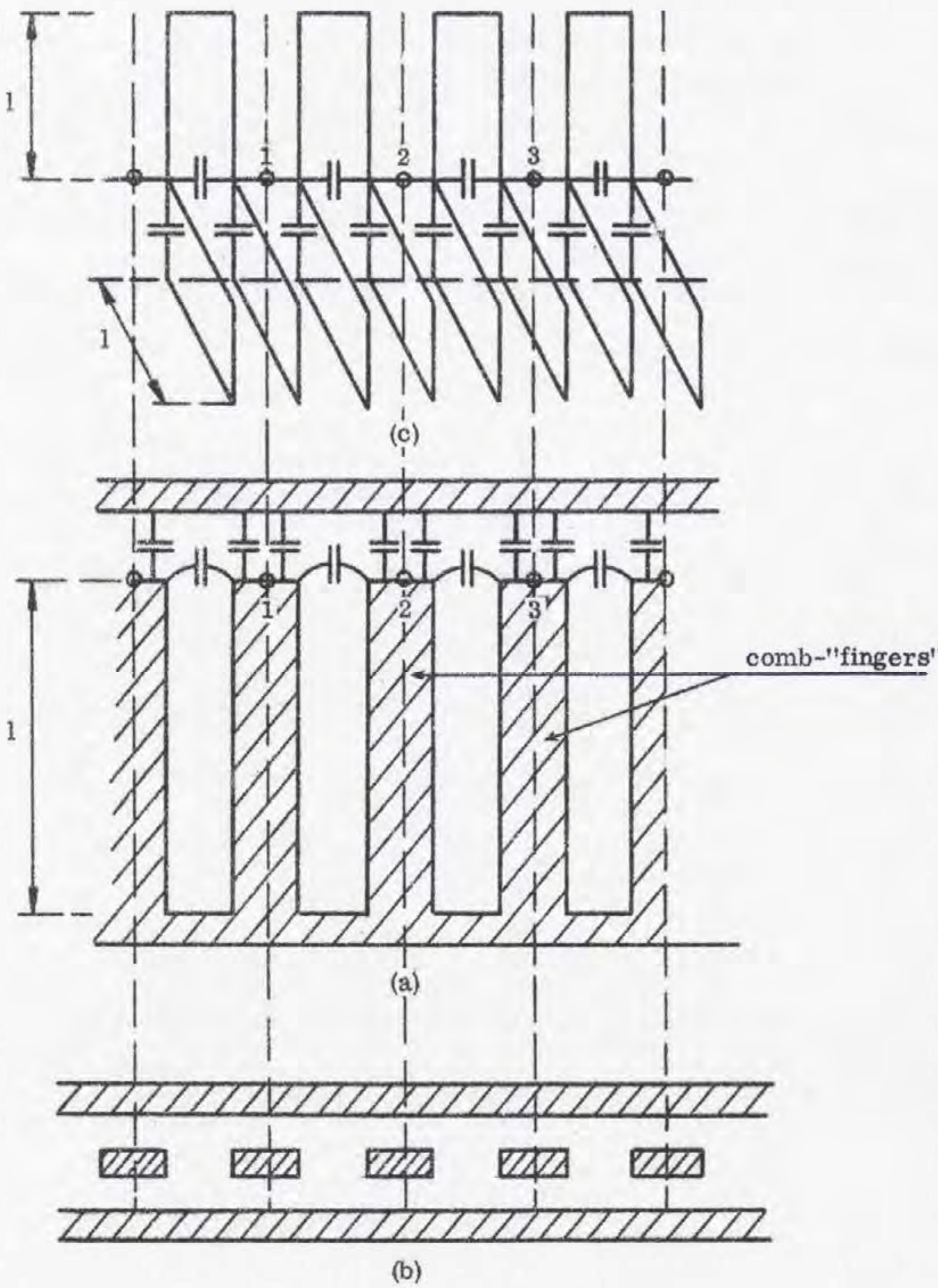

Fig. 2.3 Topview (a), cross section (b) and equivalent circuit (c) of the comb-line band pass filter.

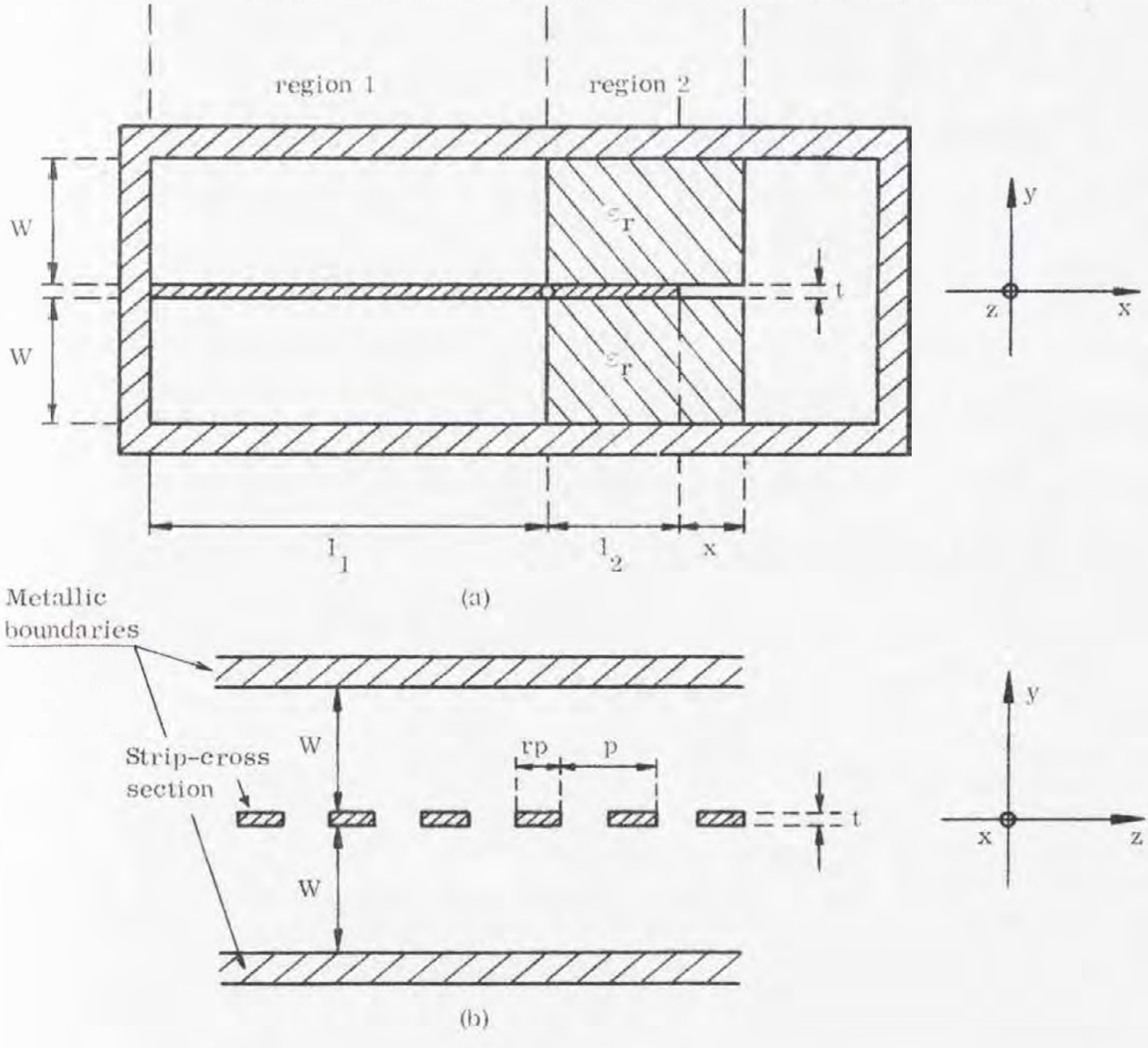

Fig. 2.4. A typical geometry of the SWS

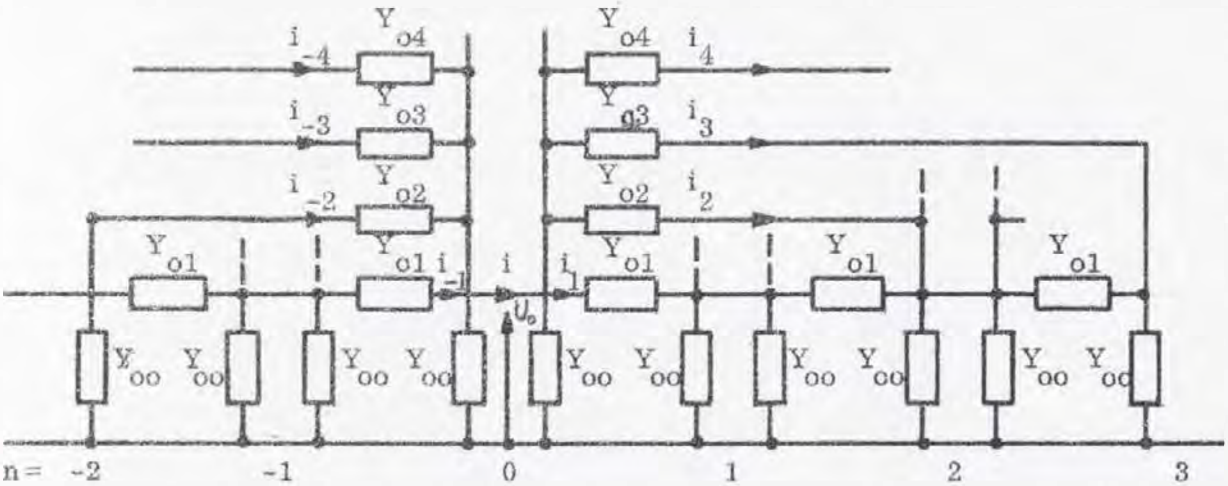

Fig. 2.5 Admittance scheme indicating mutual interactions only to the reference (n = 0) strip.

Floquet's theorem [9] to obtain the voltage at the reference point of the n:th strip,

$$U_n = U_o e^{n(\Theta + j\varphi)} \tag{2.2.1}$$

where U_o is the voltage of the reference strip (n = 0). φ is the phase shift and Θ the voltage gain per period. The current flowing in the Y_{on} admittance is

$$i_n = (U_o - U_n)\, Y_{on} \tag{2.2.2}$$

The characteristic admittance of the wave traveling down the structure may be defined as

$$Y_s = \frac{i}{U_o} = \frac{1}{U_o} \left[U_o Y_{oo} + \sum_{n=1}^{\infty} \left[(U_o - U_n)\, Y_{on} \right] \right] \tag{2.2.3}$$

The current coming to the reference strip from the left must equal the current flowing from the strip to the right. Using equation (2.2.1) this gives

$$2\, Y_{oo} + 2 \sum_{n=1}^{\infty} \left\{ 1 - \cosh n(\Theta + j\varphi) \right\} Y_{on} = 0 \tag{2.2.4}$$

Using equation (2.2.4) the characteristic admittance becomes

$$Y_s = \sum_{n=1}^{\infty} \sinh n(\Theta + j\varphi) \cdot Y_{on} \tag{2.2.5}$$

When energy is propagated along the SWS, $\varphi \neq n\pi$, n = 0, 1, 2..... This is of course the only case of interest for TWM applications.

When the wave propagating along the SWS exhibits gain ($\Theta > 0$) or loss ($\Theta < 0$) the Y_{on} becomes complex:

$$Y_{on} = j\, B_{on} \pm G_{on} \tag{2.2.6}$$

where the plus sign implies $\Theta < 0$ and the minus sign $\Theta > 0$. Hence equation (2.2.4) becomes complex, and hence both φ and Θ can be derived.

Usually, however, $\Theta << 1$, for which case equation (1.1) is applicable:

$$2\Theta = \frac{Sp}{\lambda_o}\left(\frac{\eta}{|Q_m|} - \frac{1}{Q_o}\right) \qquad \text{(Neper)} \qquad 1.1$$

where

$$S = \frac{v_o}{v_g} = \frac{v_o}{p\frac{d\omega}{d\varphi}} \qquad 2.2.7$$

This method of calculation is preferable for other reasons too, namely because

a) the equivalent scheme leading to (2.2.4) is an approximation to the real situation (see chapter 4).

b) the ω-φ-characteristic, and hence the slowing factor S, may be calculated rather accurately by a more direct method than using eq. (2.2.4). See section 4.1.

Furthermore $\Theta << 1$ means that G_{on} is small and may be neglected. (2.2.4) and (2.2.5) are simplified to

$$2\,B_{oo} + 2\sum_{n=1}^{\infty} B_{on}\,(1 - \cos n\varphi) = 0 \qquad (\Theta << 1) \qquad 2.2.8$$

$$G_s = -\sum_{n=1}^{\infty} B_{on}\,\sin n\varphi \qquad (\Theta << 1) \qquad 2.2.9$$

Equation (2.2.8) shows that B_{on} is negative and inductive. Compare the description of a lossless transmission line using series-inductances and parallell capacitances.

In order to design a coupling one must know the characteristic admittance (given by eq. 2.2.8) of the SWS. The coupling will be further considered in Chapter 6.

3. THE CHARACTERISTIC ADMITTANCE $Y_s(\varphi)$ OF THE TEM-WAVE TRAVELING ALONG THE PARALLELL STRIPS

3.1. The general expression.

Let us assume the strips to be infinitely long (x - direction, Figure 2.4), the dielectric material to be homogeneous and a TEM wave to run along the strip conductors. No attenuation or gain is assumed. Consider the current on a reference strip, designated $n = 0$, in an interval x, $x + dx$. The voltage to ground of the n-th strip at x is U_n.

In the SWS under consideration, energy is propagating transversely to the strip array in the z-direction of Figure 2.4. This suggests, as in section 2.2 that the voltage on the n-th conductor is given by

$$U_n = U_o \, e^{jn\varphi} \qquad 3.1.1.$$

where U_o is the voltage on the reference strip and φ is the phase shift per period.

A general treatment of TEM lines involves the capacitance per unit length [13]. If the capacitance per unit length between the n-th strip conductor and the reference strip is C_{on}, the current due to the o-n-th interaction at x becomes

$$i_{on} = (U_o - U_n) \, C_{on} \cdot v \qquad 3.1.2$$

where v is the velocity of the TEM wave. We define the characteristic admittance due to the o-n-th interaction as

$$y_{on} = C_{on} \, v \qquad 3.1.3$$

The total current (i_s) on the reference strip at x, is obtained by summing all currents i_{on}. The total strip admittance is now given by

$$Y_s = \frac{i_s}{U_o} = \frac{1}{U_o} \left[U_o \cdot 2\, y_{oo} + \sum_{n=1}^{\infty} (i_{on} + i_{o-n}) \right] \qquad 3.1.4$$

The term $U_o \cdot 2\, y_{oo}$ is the current due to the interaction between the reference strip and the ground planes. Since $C_{on} = C_{o-n}$, we now obtain, using equation (3. 1. 1)

$$Y_s(\varphi) = 2\, y_{oo} + 4 \sum_{n=1}^{\infty} y_{on} \sin^2\left(\frac{n\varphi}{2}\right) \qquad 3.1.5$$

This equation is well applicable to the analysis of section (2. 2). Equation (3. 1. 5) was obtained by Leblond and Mourier [15]. However, they used a very approximate value for y_{o1} and had to neglect all y_{on}, $n = 2, 3, \ldots\ldots\ldots$ In the next section accurate values of y_{o1}, y_{o2}, y_{o3} and y_{o4} will be derived for various structure geometries.

It may also be pointed out that the calculations here can be made to incorporate gain or losses in the TEM line [13]. If it is assumed that the gain or loss is dependent only on the current on the strips, the propagation constant becomes

$$j\beta = j\frac{\omega}{v} \rightarrow j\beta + \alpha \qquad 3.1.6$$

$$y_{on} \rightarrow y_{on}\left(1 + j\frac{\alpha}{\beta}\right) \qquad 3.1.7$$

where α is the voltage attenuation (gain) constant.

3. 2 Numerical calculation of $Y_s(\varphi)$.

We will first discuss infinitly thin strip conductors ($t = 0$, Fig. 2. 4). It is known that for $t = 0$ and $\varphi = 0,\ \pi/2,\ \pi$, $Y_s^o(\varphi)$ can be derived to any accuracy by conformal mapping technique [16, 28]. Extended calculations have been performed for various W/p and $r = 0.25,\ 0.5,\ 0.75$ and are presented in Table 3. I, 3. II, 3. III. Figure 3. 1 illustrates the degree of accuracy obtained in the calculations.

From equation (3. 1. 5) we now obtain

$$2\, y_{o1} = Y_s^o(0) \qquad 3.2.1$$

$$4\, y_{o1} = Y_s^o(\pi) - Y_s^o(0) - 4 \sum_{n=1}^{\infty} y_{0,\,2n+1} \qquad 3.2.2$$

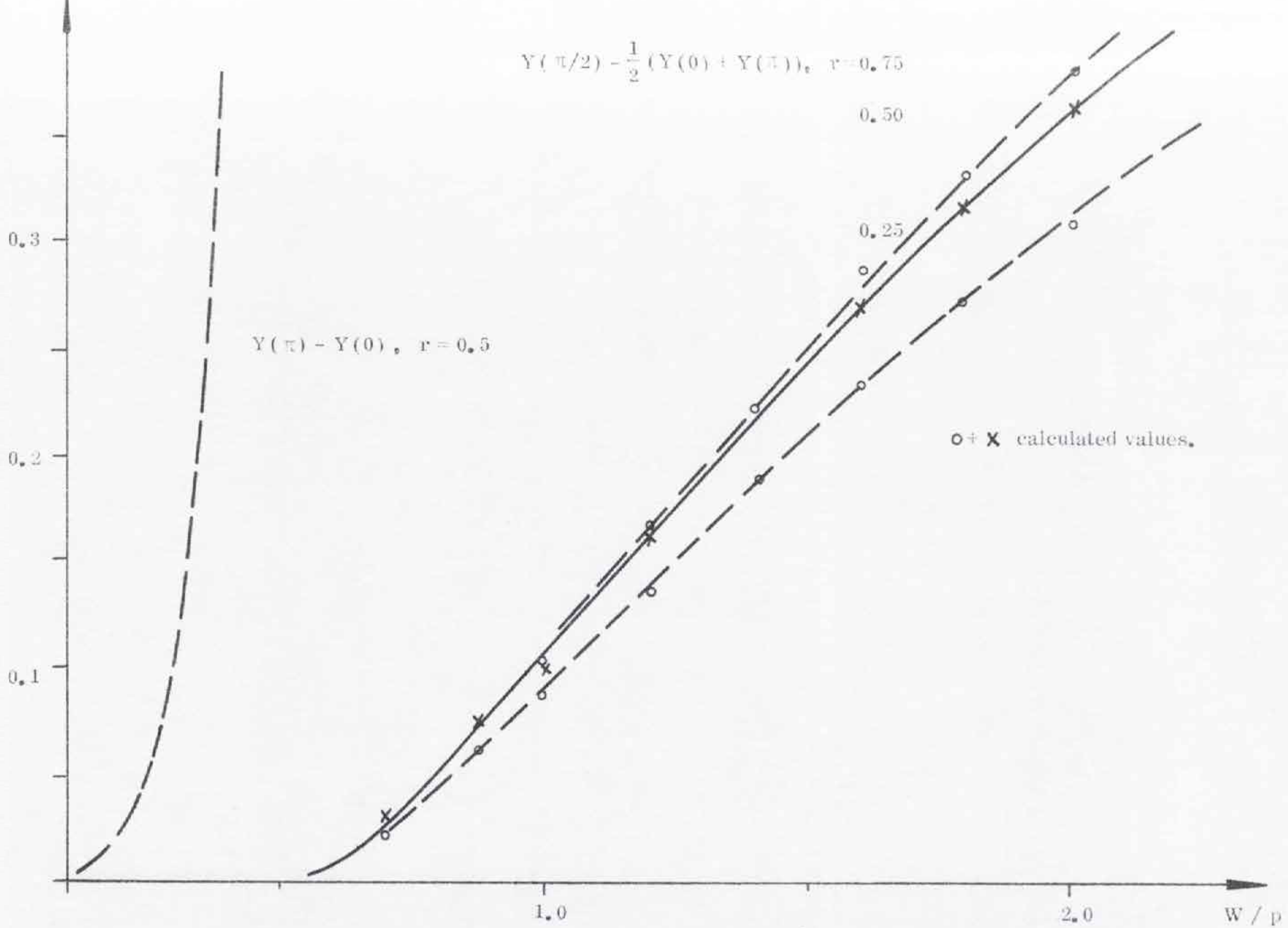

Fig. 3.1. Demonstration of the accuracy in the calculation of $Y(\pi/2) - \frac{1}{2}(Y(0) + Y(\pi))$.

$$4\,y_{o2} = Y_s^o(\pi/2) - \frac{1}{2}\left[\,Y_s^o(\pi) + Y_s^o(0)\,\right] - 4\sum_{n=1}^{\infty} Y_{0,4n+2} \tag{3.2.3}$$

We now intend to derive the series over n in equation (3. 2. 2) and (3. 2. 3). Butcher [7] has calculated an exact formula for $Y_s^o(\varphi)$ when $r = 0.5$ and $W/p = \infty$:

$$\frac{Y_s^o(\varphi)}{Y_o} = 4\sin\varphi/2 \qquad (r = 0.5,\ W/p = \infty) \tag{3.2.4}$$

where Y_o is the space admittance, i. e. $Y_o = \sqrt{\frac{\varepsilon_o}{\mu_o}}$. $Y_s^o(\varphi)$ may be expanded in a Fourier series and compared with equation (3. 1. 5). This leads to

$$\frac{4\,y_{on}}{Y_o} = \frac{32}{\pi}\,\frac{1}{4n^2 - 1} \qquad (r = 0.5,\ \frac{W}{p} = \infty) \tag{3.2.5}$$

and

$$y_{oo} = 0 \qquad (W/p = \infty) \tag{3.2.6}$$

In Table I the first four y_{on} are given, as well as the series of equations (3. 2. 2) and (3. 2. 3).

It is possible to estimate y_{o3} as well as y_{o4}. It is observed that a change of r from $r = 0.5$ to $r = 0.75$ in Fig. 3. 1 only slightly affects the value of

$$Y^o(\pi/2) - \frac{1}{2}\left[\,Y^o(0) + Y^o(\pi)\,\right]$$

which approximately becomes $4\,y_{o2}$. This is so because an increased r narrows strip $n = 2$ to the reference strip at the same time as the shielding effect from strip $n = 1$ increases. Hence a changed r only means a very slight change in y_{o2}. It is further believed that y_{o3} is even more insensitive to changes in r .

In Fig. 3.2, these effects are utilized to calculate $4\,y_{o3}/Y_o$ for $r = 0.5$ and $W/p = 2$. Evidently y_{o3} can be approximated by

$$\left(\frac{4\,y^{o}_{o3}}{Y_o}\right)_{\substack{r=0.5\\ \frac{W}{p_o}}} \approx \left(\frac{Y^{o}(\pi/2) - \frac{1}{2}\left[\,Y^{o}(0) + Y^{o}(\pi)\,\right]}{Y_o}\right)_{\substack{r=0.75\\ \frac{1}{2}\frac{W}{p_o}}} \qquad 3.2.7$$

Through comparing the results presented in Table 3.I with the exact values from Butcher's solution, we have also estimated the value of the series over n in equations (3.2.2) and (3.2.3). The procedure to obtain y_{o1}, y_{o2}, y_{o3} anc y_{o4}, may be found in this table, reading it from left to right. In Table 3.II and 3.III $Y(0)$, $Y(\pi/2)$ and $Y(\pi)$ are given for various W/p and with $r = 0.5$ and 0.75 respectively.

Since y_{on} is fairly independant of r for $n \geq 2$, the series for $r = 0.5$ are also used for $r = 0.25$ and 0.75. The final results for y_{on} are found in Table 3.IV aı Fig. 3.3, 3.4 and 3.5. Note that an error in the estimation of the series Σ_1 in Table I of as much as 20% will affect $Y^{o}_{s}(\varphi)$ by 1% only. It is believed that the maximum error in $Y^{o}_{s}(\varphi)$ for $W/p = 2$, $r = 0.5$ is less than 3%. The error becomes even smaller for lower values of W/p.

For strip conductors with finite thickness ($t > 0$, Fig. 2.4) an extra admittance y_t has to be added to y_{o1} due to the increased interaction on the nearest neigh- bor:

$$Y_s(\varphi) = Y^{o}_{s}(\varphi) + 4\,y_t \sin^2 \varphi/2 \qquad 3.2.8$$

where

$$\frac{4\,y_t}{Y_o} = \alpha \cdot \frac{4\,t}{(1-r)\,p} = \frac{4\,C\,t}{\varepsilon_o} \qquad 3.2.9$$

If the field between the strips is completely homogenous, $\alpha = 1$. Using graphs

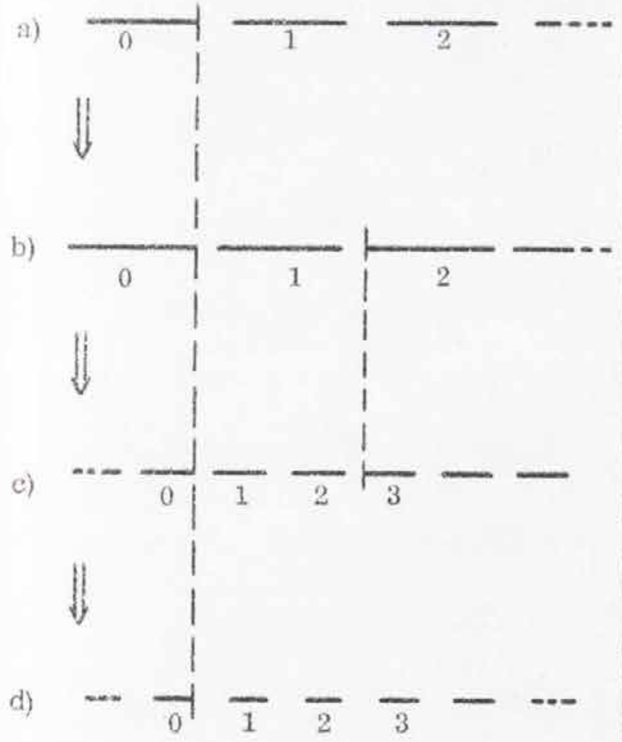

	$\frac{p}{p_o}$	$\frac{W}{p}$	r	
a)	1	1	0.750	$\frac{4\,y'_{o2}}{Y_o} \approx 0.11$
				$\downarrow$ y_{o2} increases
b)	1	1	0.875	$\frac{4\,y''_{o2}}{Y_o} \approx 0.115$
				$\downarrow$ y_{o3} increase very little
c)	0.5	2	0.750	$\frac{4\,y'_{o3}}{Y_o} \approx 0.12$
				$\downarrow$ y_{o3} decreases un-noticable
d)	0.5	2	0.500	$\frac{4\,y_{o3}}{Y_o} \approx 0.12$

Fig. 3.2. Approximate evalution of $\frac{4\,y_{o3}}{Y_o}$ for $r = 0.5$ and $W/p = 2$. Through a) to d), W is kept constant. The surrounding ground planes are not shown in the figure.

Going from a) to b) amounts to an increased r ; b) to c) a very small part is removed from the middle of the strips (p and r changes) ; c) to d) a decrease in r.

given by Cruzan and Garwer [18] for rectangular strip-lines ($\varphi = \pi$) and using Cohn's results [19], it has been possible to find α, see Fig. 3.6. It is believed that $4\, y_{oo}$ and $4\, y_{on}$ for $n \geq 2$ are essentially unaffected by the strip thickness.

$\frac{W}{p}$	$\frac{Y(0)}{Y_o}$	$\frac{Y(\pi/2)}{Y_o}$	$\frac{Y(\pi)}{Y_o}$	$\frac{Y(\pi)-Y(0)}{Y_o}$	$\frac{Y(\pi/2)-\frac{1}{2}[Y(0)+Y(\pi)]}{Y_o}$	$\frac{4\,y_{o3}}{Y_o}$	$\frac{4\,y_{o4}}{Y_o}$	$\frac{4\,y_{o5}}{Y_o}$	Σ_1	Σ_2	$\frac{4\,y_{o1}}{Y_o}$	$\frac{4\,y_{o2}}{Y_o}$
0.357	4.30	4.57	4.85	0.55 ± 0.02							0.55	
0.426	3.74	4.15	4.54	0.80 ± 0.02							0.80	
0.500	3.28	3.81	4.34	1.055 ± 0.02							1.055	
0.587	2.86	3.54	4.19	1.33 ± 0.02	< 0.02						1.33	
0.700	2.47	3.31	4.09	1.62 ± 0.02	0.03 ± 0.02						1.62	0.03
0.867	2.045	3.115	4.035	1.99 ± 0.02	0.075 ± 0.02						1.99	0.075
0.995	1.81	3.02	4.02	2.21 ± 0.02	0.105 ± 0.02						2.21	0.105
1.000	1.80	3.01	4.02	2.22 ± 0.02	0.10 ± 0.02						2.22	0.10
1.2	1.528	2.925	4.000	2.472 ± 0.01	0.161 ± 0.01	~ 0.01					2.46	0.16
1.4	1.323	2.88	"	2.677 ± 0.01	0.218 ± 0.01	~ 0.03			~ 0.05		2.64	0.22
1.6	1.170	2.855	"	2.830 ± 0.01	0.27 ± 0.01	~ 0.05			~ 0.08		2.77	0.26
1.8	1.048	2.84	"	2.952 ± 0.01	0.316 ± 0.01	~ 0.09	~ 0.02		~ 0.12		2.86	0.31
2.0	0.949	2.84	"	3.051 ± 0.01	0.365 ± 0.01	~ 0.12	~ 0.04	< 0.02	~ 0.20	< 0.03	2.90	0.35
10	0.198	2.828	"	3.802 ± 0.01	0.729 ± 0.01							
∞	0	2.825	"	4.000	0.825 ± 0.005	0.29	0.161	0.103	0.60	0.15	3.40	0.68

$$\Sigma_1 = \frac{4}{Y_o} \sum_{n=1}^{\infty} y_{o,\,2n+1} \; ; \quad \Sigma_2 = \frac{4}{Y_o} \sum_{n=1}^{\infty} y_{o,\,4n+2} \; ; \quad \frac{4\,y_{o1}}{Y_o} = \frac{Y(\pi)-Y(0)}{Y_o} - 0.75\cdot\Sigma_1 \, , \quad \frac{4\,y_{o2}}{Y_o} = \frac{Y(\pi/2)-\frac{1}{2}\left(Y(0)+Y(\pi)\right)}{Y_o} - \Sigma_2$$

Table 3.1. Reading this table from left to right describes the way of deriving $4\,y_{on}$, $n = 1, 2, 3, 4, 5$ for $r = 0.5$.

$\frac{W}{p}$	$\frac{Y(0)}{Y_o}$	$\frac{Y(\pi/2)}{Y_o}$	$\frac{Y(\pi)}{Y_o}$	$\frac{Y(\pi) - Y(0)}{Y_o}$	$\frac{Y(\pi/2) - \frac{1}{2}[Y(\pi) + Y(0)]}{Y_o}$
0.357	3.055	3.125	3.225	0.17	
0.626	2.75	2.89	3.05	0.30	
0.500	2.485	2.703	2.92	0.435	
0.587	2.24	2.545	2.84	0.60	<0.01
0.700	1.99	2.403	2.78	0.79	0.018 ± 0.01
0.867	1.702	2.283	2.745	1.043	0.059 ± 0.01
0.995	1.537	2.225	2.74	1.203	0.086 ± 0.01
1.0	1.531	2.225	2.74	1.209	0.086 ± 0.01
1.2	1.329	2.222	2.723	1.394	0.134 ± 0.01
1.4	1.172	2.160	2.723	1.551	0.187 ± 0.01
1.6	1.050	2.135	"	1.673	0.233 ± 0.01
1.8	0.950	2.120	"	1.773	0.273 ± 0.01
2.0	0.867	2.110	"	1.856	0.310 ± 0.01
10	0.1940	2.105	"	2.529	0.642 ± 0.01

Table 3.II. Strip admittances for r = 0.25.

$\frac{W}{p}$	$\frac{Y(0)}{Y_o}$	$\frac{Y(\pi/2)}{Y_o}$	$\frac{Y(\pi)}{Y_o}$	$\frac{Y(\pi) - Y(0)}{Y_o}$	$\frac{Y(\pi/2) - \frac{1}{2}[Y(0) + Y(\pi)]}{Y_o}$
0.357	5.22	6.12	6.97	1.75	0.025
0.426	4.445	5.51	6.58	2.135	0.003
0.500	3.800	5.05	6.31	2.51	0.005
0.587	3.265	4.70	6.14	2.875	0.003
0.700	2.760	4.40	6.00	3.24	0.02
0.867	2.240	4.14	5.92	3.67	0.06
0.995	1.980	4.02	5.90	3.92	0.08
1.0	1.951	4.02	5.876	3.925	0.100
1.2	1.631	3.92	5.876	4.245	0.166
1.4	1.402	3.85	-"-	4.474	0.221
1.6	1.230	3.835	-"-	4.646	0.287
1.8	1.096	3.820	-"-	4.780	0.334
2.0	0.986	3.810	-"-	4.890	0.379
10	0.1995	3.807	-"-	5.676	0.769

Table 3. III. Strip admittances for r = 0.75.

$\frac{W}{p}$	$2y_{oo}/Y_o$			$4y_{o1}/Y_o$			$4y_{o2}/Y_o$			$4y_{o3}/Y_o$	$4y_{o4}/Y_o$
	r = 0.25	r = 0.5	r = 0.75	r = 0.25	r = 0.5	r = 0.75	r = 0.25	r = 0.5	r = 0.75	r = 0.25, 0.5, 0.75	r = 0.25, 0.5, 0.75
0.357	3.055	4.30	5.22	0.17	0.55	1.75					
0.426	2.75	3.74	4.445	0.30	0.80	2.135					
0.500	2.485	3.28	3.800	0.435	1.055	2.51					
0.587	2.24	2.86	3.265	0.60	1.33	2.87	0.01	0.01	0.01		
0.700	1.99	2.47	2.760	0.79	1.62	3.24	0.025	0.025	0.025		
0.867	1.702	2.045	2.240	1.04	1.99	3.67	0.063	0.070	0.070		
1.000	1.533	1.80	1.951	1.21	2.22	3.92	0.090	0.105	0.110		
1.2	1.329	1.528	1.631	1.37	2.46	4.23	0.140	0.162	0.170	~0.01	
1.4	1.172	1.323	1.402	1.51	2.64	4.44	0.185	0.215	0.220	~0.03	
1.6	1.050	1.170	1.230	1.61	2.77	4.59	0.230	0.265	0.275	~0.05	
1.8	0.950	1.048	1.096	1.68	2.86	4.69	0.265	0.310	0.325	~0.09	~0.02
2.0	0.867	0.949	0.986	1.84	2.90	4.74	0.300	0.350	0.370	~0.12	~0.04
∞	0	0	0		3.40			0.68		0.29	0.16

Table 3.IV. The admittances y_{on}, n = 1, 2, 3, 4 for various values of W / p and r = 0.25, 0.5, 0.75.

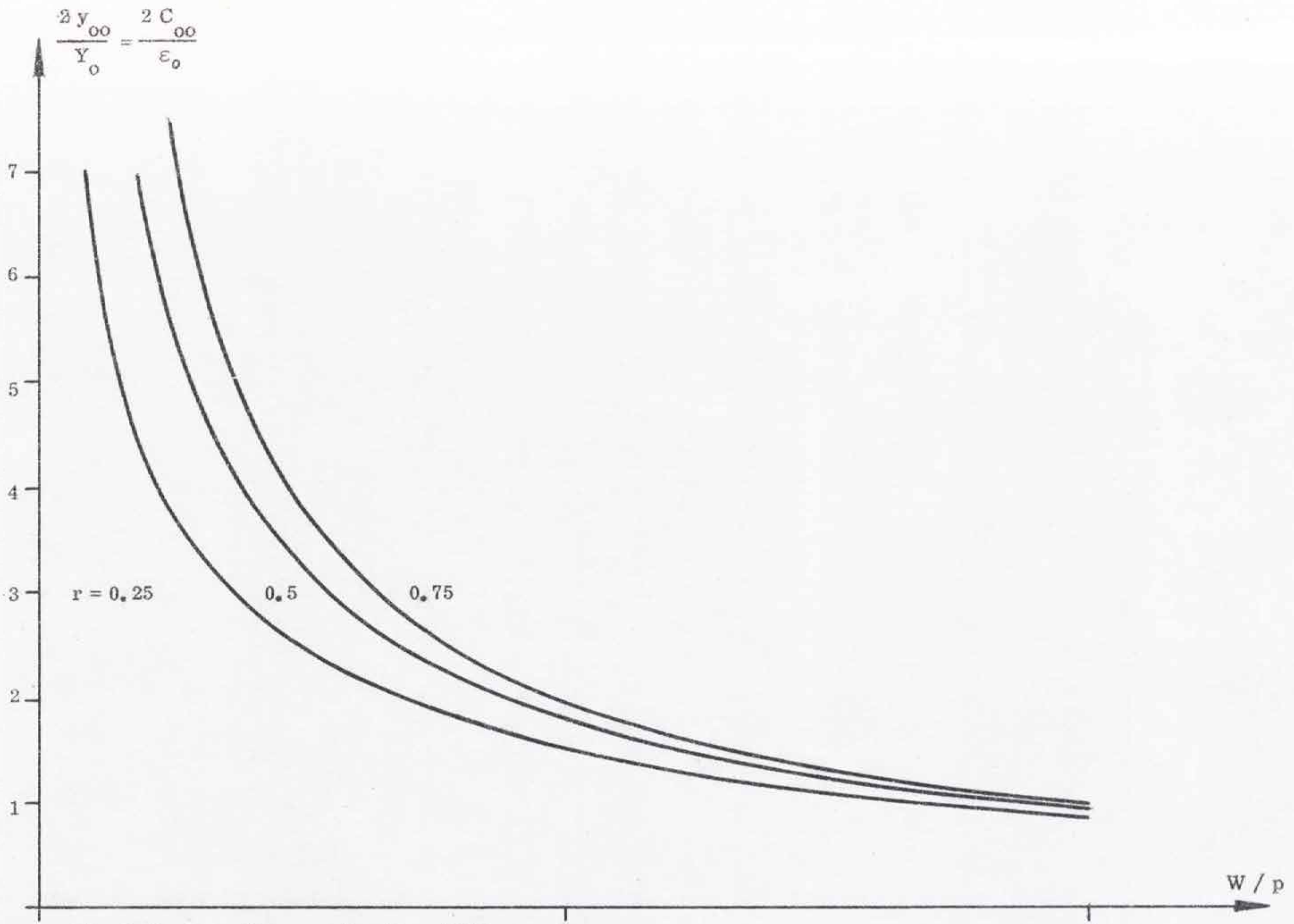

Fig. 3.3. $2\,y_{oo}/Y_o$ as a function of W/p.

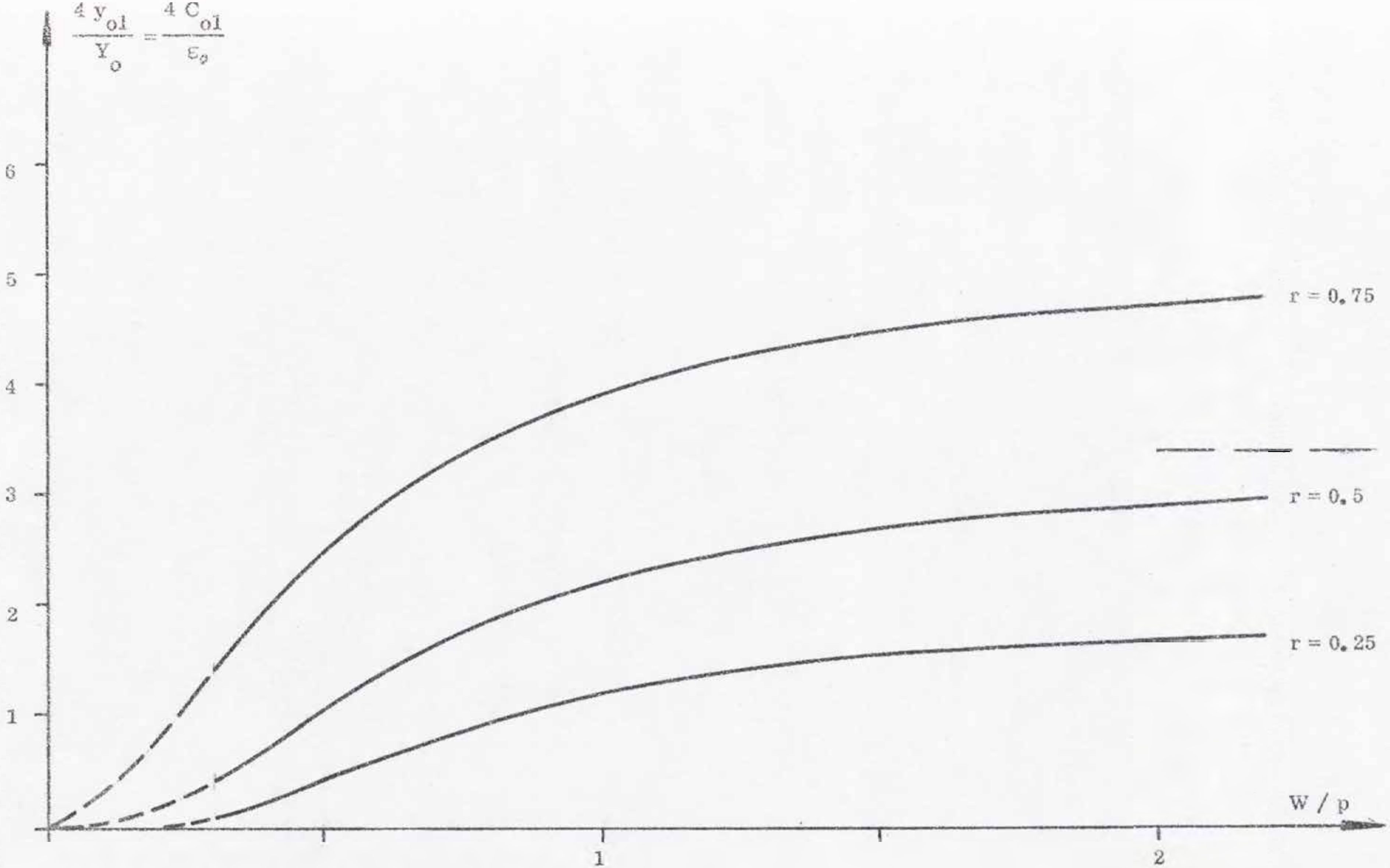

Fig. 3.4. $4\,y_{o1} / Y_o$ as a function of W / p.

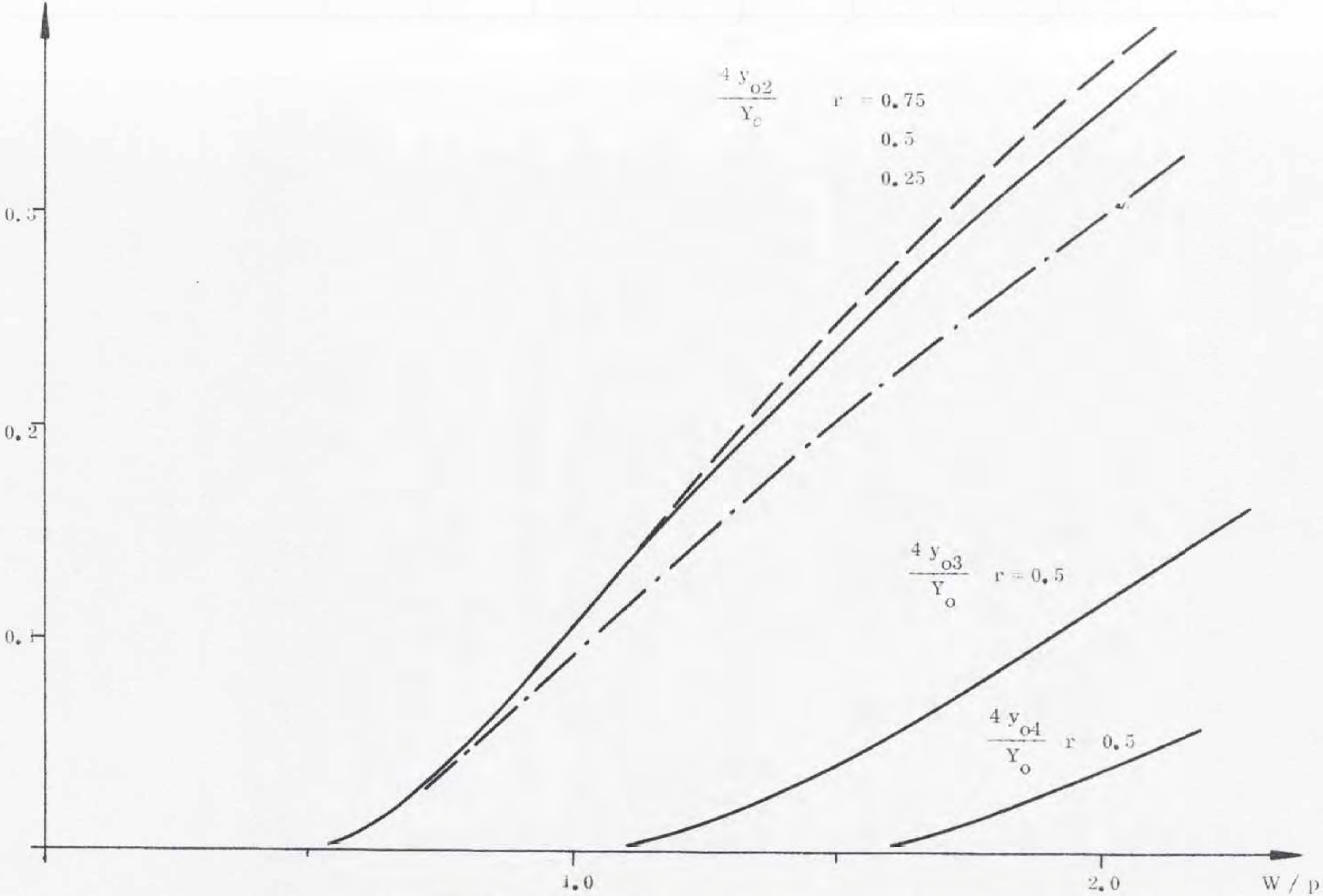

Fig. 3.5. $4\,y_{o2}/Y_o$, $4\,y_{o3}/Y_o$ and $4\,y_{o4}/Y_o$ as a function of W/p.

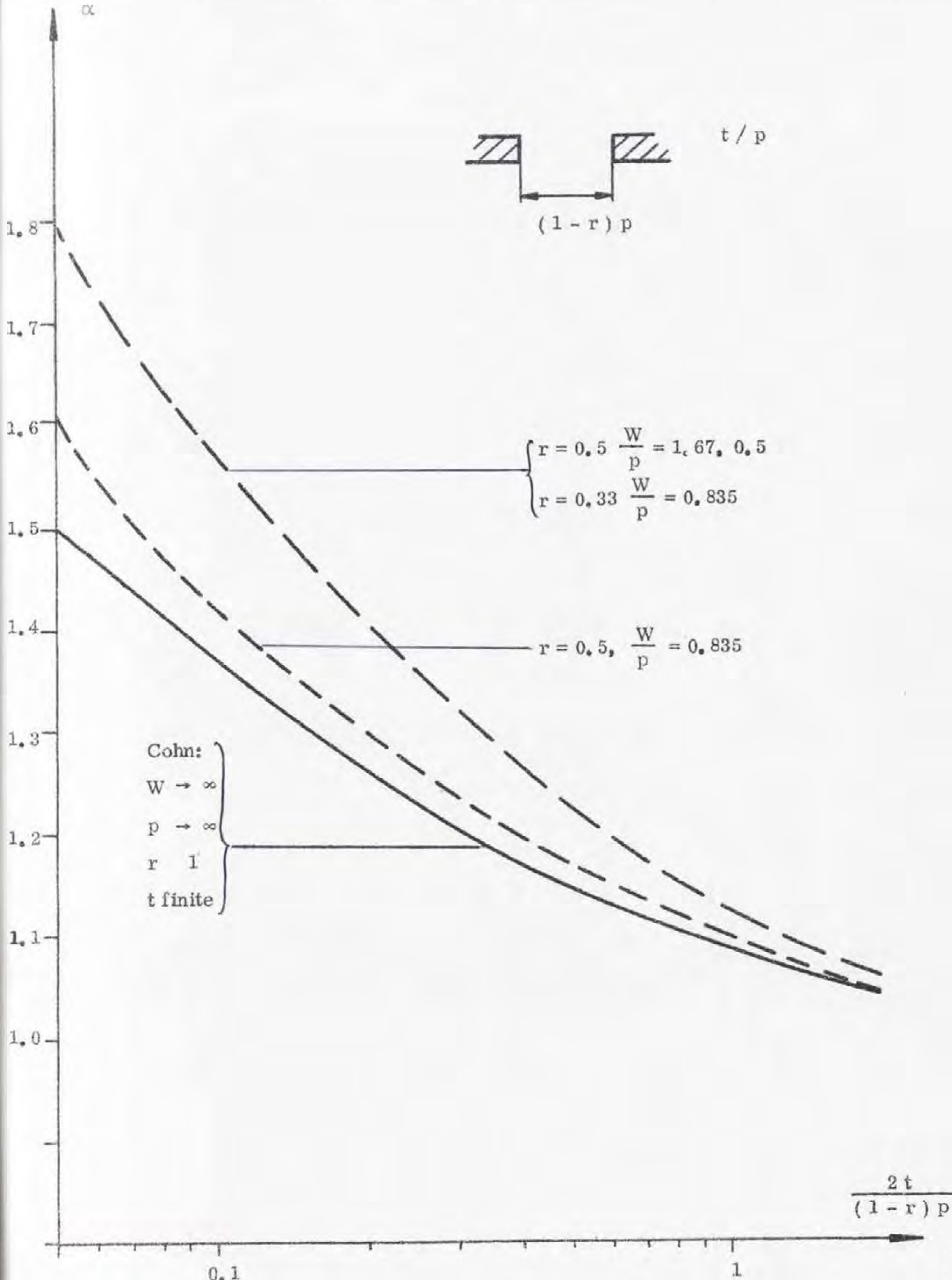

Fig. 3.6. α as a function of the strip thickness t for various geometrical

3.3 Other methods of calculating $Y_s(\varphi)$. A comparison.

The most common method of calculating $Y_s(\varphi)$ has been to use space harmonic analysis [9] to derive the fields, and to find the current on the strip by integrating the magnetic field along a path around the strip. This method was first applied to TEM-structures by Fletcher [20]. In Fletcher's analysis, later also used by other authors [22, 23], the field between the fingers was assumed to be completely homogeneous. This is a rather crude approximation leading to serious errors especially for low values of φ (see Figure 3.7a and b, and Table 3.V).

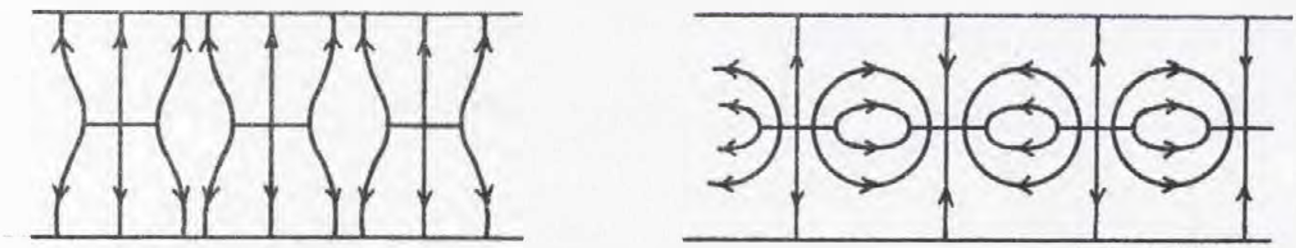

$\varphi = 0$ $\varphi = \pi$

3.7a. The electric fields for the thin tape array.

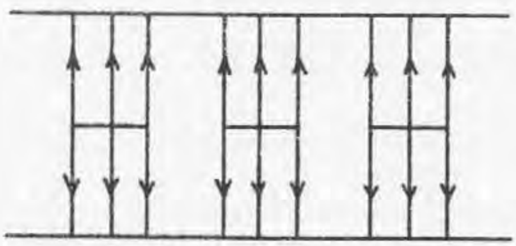

3.7b. The electric fields for $\varphi = 0$ in the "homogenous field approximation".

The most rigorous analysis, by which it is possible to derive $Y_s(\varphi)$ for rectangular strips to any degree of accuracy that is desired, has been carried out by S. Kovalenko and V. S. Kovalenko [21]. Their final equation has the following form

$$\frac{Y_s(\varphi)}{Y_o} = \frac{4t}{(1-r)p} \cdot \sin^2(\varphi/2) +$$

$$+ 4\sin(\varphi/2) \sum_{s=-\infty}^{\infty} A_s \frac{\sin\left[\frac{(1-r)}{2}(\varphi + 2\pi s)\right]}{\frac{(1-r)}{2}(\varphi + 2\pi s)} \coth\left[\frac{W+\frac{t}{2}}{p}(\varphi + 2\pi s)\right] \qquad 3.3.1$$

The coefficients A_s are dependent on φ , and may be determined from an infinite system of equations, which has to be solved by computer methods.

If one assumes the field between adjacent strip to be completely homogeneous, one arrives at

$$A_s = \frac{\sin\varphi/2 \ \sin\left[\frac{(1-r)}{2}(\varphi+2\pi s)\right]}{\frac{\varphi+2\pi s}{2} \ \frac{(1-r)}{2}(\varphi+2\pi s)} \qquad 3.3.2$$

Using (3. 3. 2) in (3. 3. 1) leads to an expression that actually is more exact than Fletcher's original expression, since Kovalenko has improved the convergence of the original series over s in equation (3. 3. 1). J. Walling has arrived at this improved expression for $Y_s(\varphi)$ by evaluating the mean stored energy per unit length of the structure, employing field components derived on the assumption of a constant electric field between adjacent strips. The approximation of equation (3. 3. 2) used in (3. 3. 1) is acceptable for $W/p>1$ (see Table 3. 1). For $\varphi = 0$, the methods lead to

$$Y_s^o(0) / Y_o = 2 \cdot \frac{W}{p} \qquad \text{(Fletcher)}$$

$$Y_s^o(0) / Y_o = 4 \cdot \frac{W}{p} \qquad \text{(equation (3.3.1) + (3.3.2))}$$

which should be compared to the more exact formula obtained from conformal mapping technique (see Appendix A and ref.)

$$Y_s^o(0) = \frac{4}{1+0.11\cdot\frac{p}{W}} \cdot \frac{W}{p} \qquad \frac{W}{p} > 2$$

$$Y_s^o(0) \rightarrow \frac{2W}{p} \qquad \frac{W}{p} \rightarrow 0$$

	$\frac{Y_s^o(0)}{Y_o}$			$\frac{Y_s^o(\pi)}{Y_o}$			
W/p	0. 5	1. 0	2	0. 5	1. 0	2	∞
Conformal mapping (exact)	3. 28	1. 80	0. 95	4. 34	4. 02	4. 00	4. 00
Space harmonics (ref. [21, 29])	4. 00	2. 00	1. 00	4. 76	4. 33	4. 32	4. 32
- " - (ref. [20, 22, 23])	2. 00	1. 00	0. 500	3. 26	2. 98	2. 97	2. 97

Table 3. V. A comparison between different methods of calculating $Y_s^o(\varphi)$.

F. S. Chen [4] has used an improved approximate method which, in accuracy, is superior to the "homogeneous field" approximation technique. Just as we do, he calculates the admittance $Y_s^o(\varphi)$ of the infinitely thin strips and adds an admittance y_t associated with the region between the fingers. He assumes, however, that $\alpha = 1$ in equation (3. 2. 9). For $t = 0$ his result becomes

$$\frac{Y_s^o(\varphi)}{Y_o} = \sqrt{2}\,\frac{Y_s^o(\pi/2)}{Y_o} +$$

$$+\left\{\frac{\sin\frac{\varphi}{4}}{\frac{\varphi}{4}}\coth\left(\varphi\frac{W}{p}\right) - \frac{\sin\frac{\pi}{8}}{\frac{\pi}{8}}\coth\left(\frac{\pi\cdot W}{2p}\right)\right\}\frac{2W}{p}\sin\frac{\varphi}{2}\cdot\frac{Y_s^o(0)}{Y_o} +$$

$$+\frac{\sin\frac{\varphi}{4}}{\frac{\varphi}{4}}\coth\left(\varphi\frac{W}{p}\right)\left(\frac{\varphi}{2}\cos\frac{\varphi}{2} - \sin\frac{\varphi}{2}\right)\frac{4}{p^2}\int g'\cdot z\cdot dz \qquad 3.3.3$$

where g' in the last term of equation (3. 3. 3) describes the potential distribution between two strips for $\varphi = 0$ and has to be integrated numerically. It should be noticed in this connection that Chen [4] has derived an equation which contains a factor $\cos\varphi/2 - \sin\varphi/2$, which differs from the one appearing in (3. 3. 3). The reason for this discrepancy is obscure for the present author. The exact values of $Y_s^o(0)$ and $Y_s^o(\pi/2)$ are obtained by conformal mapping technique. Therefore $Y_s^o(\varphi)$ is exact for $\varphi = 0, \pi/2$. Comparing $Y_s^o(\varphi)$ from equation (3. 3. 3) with exact value thus obtained from conformal mapping technique, Chen argues that equation (3. 3. 3) gives a value 10% too small for $\varphi = \pi$ and $W/p = 1$.

If we compare Chen's result, which is superior previous results obtained by "the homogeneous field" approximation, with our results from section 3. 1 and 3. 2 we find that

a) the accuracy of our method is about 1%, compared to 10% for Chen's method when $W/p = 1$ and $t = 0$.

b) an improved accuracy is obtained in y_t when $\alpha > 1$ (Fig. 3. 6) .

c) the graphs given in reference [4] Fig. 2 do not show an extremum in

$Y(\varphi)$ for $\varphi = 0$, as it should (compare equation (3. 1. 6)).

Experimental data on comb-structures [4] do not differ considerably from what is predicted by theory and equation (3. 3. 3). The explanation may be due to the use of square strips, $t = 0.5\ p$, which means $\chi \approx 1.00$ and that $4\ y_t$ dominates $Y_s(\varphi)$ in the upper part of the pass-band. It is expected that thin fingers will lead to a more significant deviation between computed and measured data.

Another method of calculating $Y_s^o(\varphi)$ has been presented by Cromack [24]. This method is an extention of Butcher's analysis [17] i.e. W/p is finite and $r = 0.5$. Cromack's analysis makes extensive use of the Jacobian elliptic functions, and their associated Theta functions. He arrives at the following expression for $Y_s^o(\varphi)$:

$$\frac{Y_s^o(\varphi)}{Y_o} = 4 \sin(\varphi/2) \frac{\Delta v}{\Delta u} \qquad 3.3.4$$

where Δv and Δu are gradient functions depending on φ and the geometry of the structure. For $W/p \to \infty$ and $r = 0.5$, $\Delta v = \Delta u$, equation (3. 3. 4) becomes equal to Butcher's solution, equation (3. 2. 4). Cromack approximates Δv and Δu by introducing the known solutions for $\varphi = 0$, $\pi/2$ and π.

The conclusions drawn from the present discussion of this section, are that our method of section 3. 1 and 3. 2, is :

a) equal to or more accurate than other methods, except Kovalenko's [21]

b) but superior to them all from a computional and practical design point of view.

Furthermore the y_{on} can be understood in terms of mutual interaction between the strips. The graph of Fig. 3. 5 indicates that for $W/p \leq 0.5$, y_{o2} may be neglected, a knowledge of great value for TEM filter designation [12].

4. PASS-BAND AND SLOWING PROPERTIES OF THE MASER STRUCTURE

4.1. Homogeneous dielectric loadings.

In order to find the $\omega - \varphi$-characteristic of the SWS, we shall adopt the following approximations viz. 1) there is no current flowing transversly to the strips in the structure and 2) that the strips are guiding pure TEM waves. This approximation is commonly believed to be close to the real situation even when the dielectric loading of region 1 and 2 becomes inhomogeneous. In this section we will, however, stick to the situation of homogeneous loading in region 1 and 2.

The types of maser structures which can be analysed by the methods in the present section are described in Figure 4.1. Let C_s be the discontinuity capacitance in the step between regions 1 and 2. Approximately, one has

$$2\,C_s \approx p \cdot 2\,C_d \tag{4.1.1}$$

where $2\,C_d$ is the discontinuity capacitance per unit length [25]. This capacitance closely approaches the fringing capacitance in a constricted conductor, which is obtained by means of the Schwarz-Christoffel transformation [25].

$$\frac{1}{\varepsilon}\,C_d = \frac{1}{\pi}\left[\frac{x^2+1}{x}\ \operatorname{arc\,cosh}\left(\frac{1+x^2}{1-x^2}\right) - 2\ln\frac{4x}{1-x^2}\right] \tag{4.1.2}$$

where $x = W_2 / W_1$. In Figure 4.2 $2\,C_d / \varepsilon$ versus W_2 / W_1 is plotted.

At the end of the strips (Figure 4.1 region 2) there are fringing fields that can be represented by a fringing capacitance $C_f(\varphi)$. Hence the susceptance B_2 (Figure 4.1) may be written as follows

$$j\,B_2 = j\,\frac{\omega\,C_f(\varphi) + \tan(\beta_2 l_2)\;Y_{s2}(\varphi)}{1 - \dfrac{\omega\,C_f(\varphi)}{Y_{s2}(\varphi)}\,\tan(\beta_2 l_2)} \tag{4.1.3}$$

where $Y_{s2}(\varphi)$ is the strip admittance and β_2 the wave propagation constant of region 2.

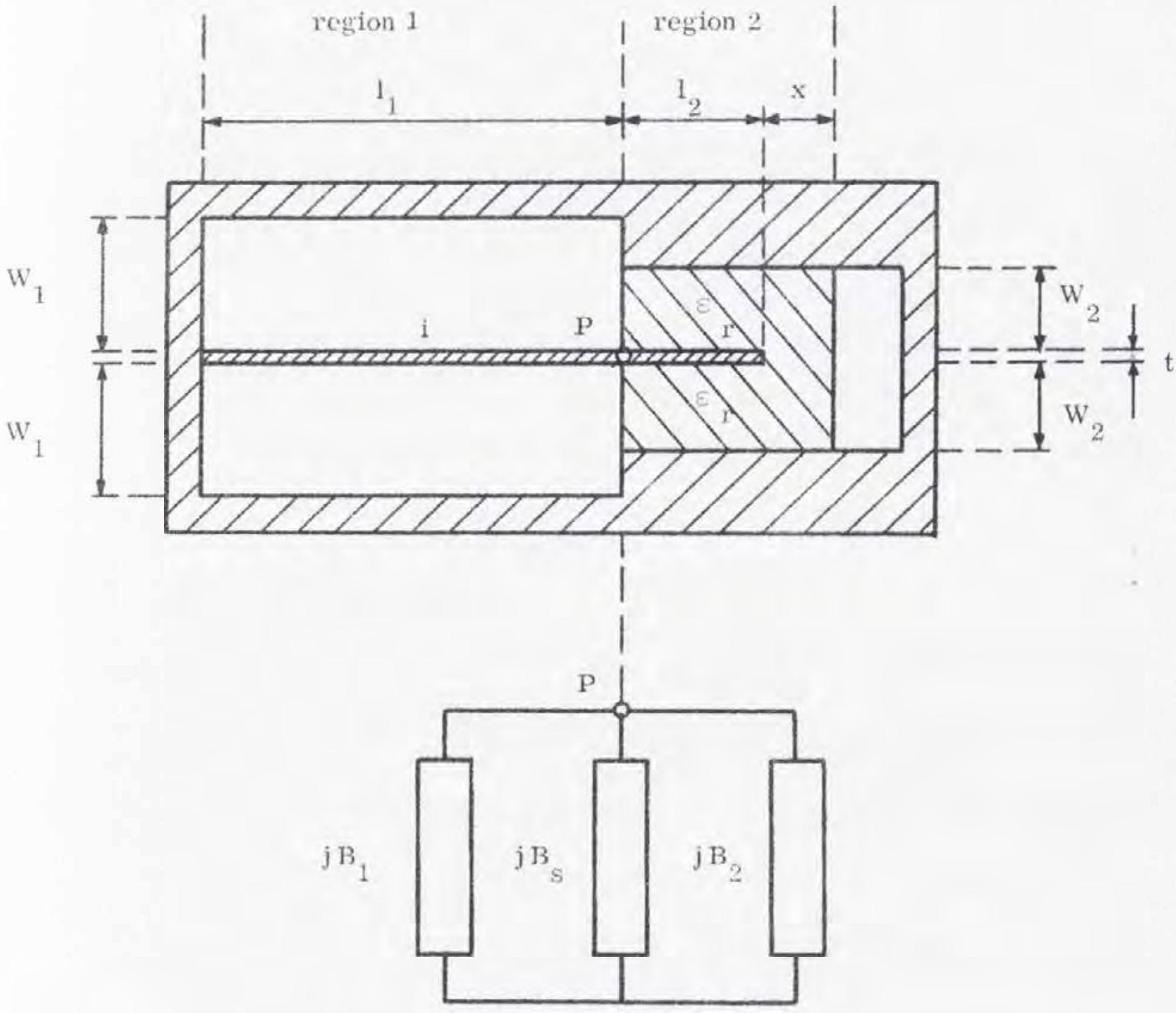

$jB_1 = -j\cot(\beta_1 l_1)\cdot Y_{s1}(\varphi)$

jB_2 see the text

$jB_s = j\omega\cdot 2C_s$

Fig. 4.1. The maser slow wave structure and the equivalent scheme referred to the boundary between region 1 and 2 (the point P).

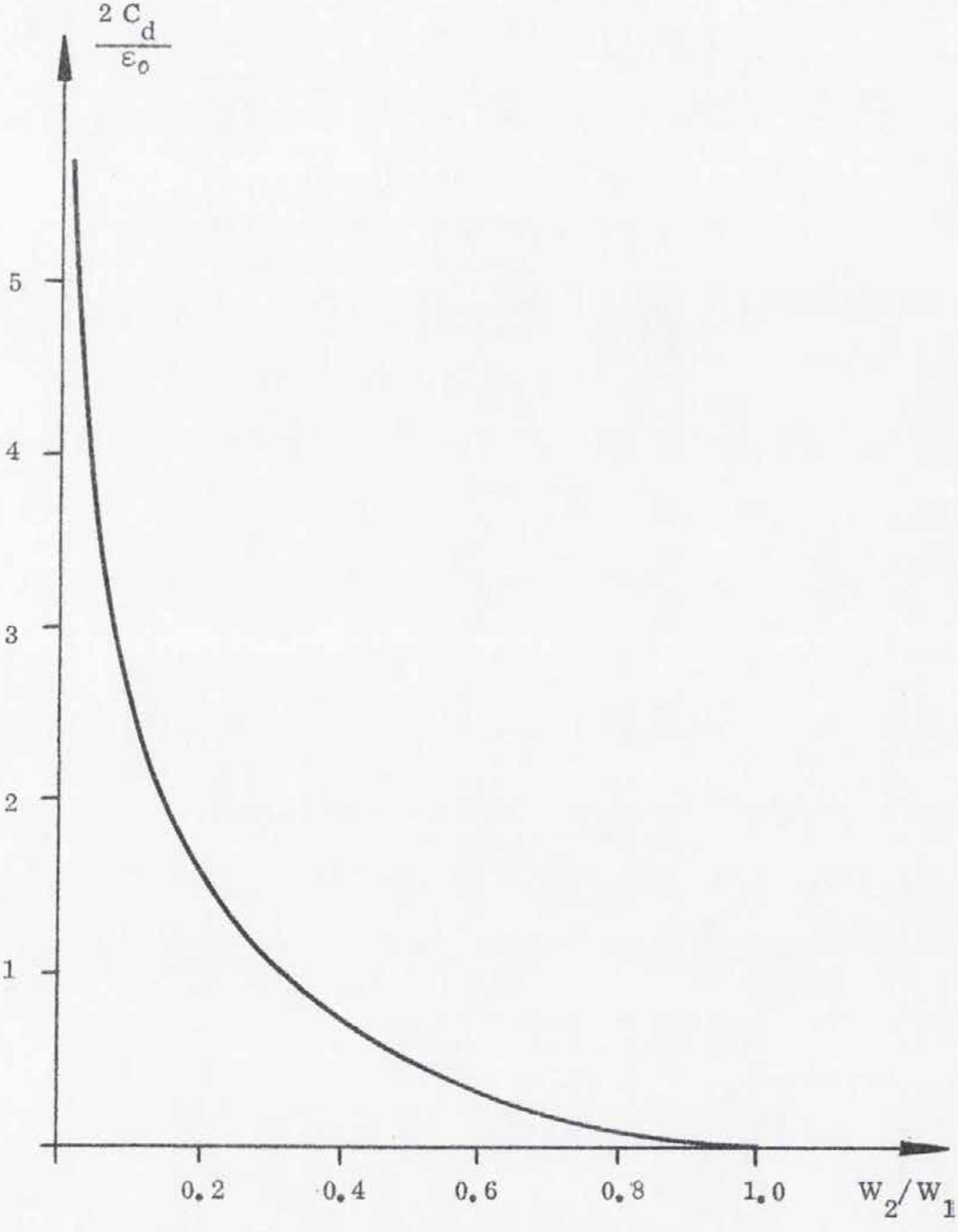

Fig. 4.2. The discontinuity capacitance per meter (C_d) versus W_2/W_1.

Using the same arguments as in section 2.1 one obtains

$$C_f(\varphi) = 2\,C_{foo} + 4 \sum_{n=1}^{\infty} C_{fon} \sin^2 \frac{n\varphi}{2} \qquad 4.1.4$$

The fringing capacitances $2\,C_{foo}$ and $4\,C_{fo1}$ for strips with $t/p = 0.05$ have been determined from electrolytic tank measurements. $2\,C_{foo}$ and $4\,C_{fo1}$, normalized with respect to $p \cdot \varepsilon$ are presented in Figure 4.3 as a function of x/p (Figure 4.1) and with W/p as a parameter. It is assumed that no electric field enters into the space to the right of the dielectric material (Figure 4.1). This approximation becomes better the greater ε_r is.

Note the amazing decrease of C_{fo1} for $x/p > 0.5$. In fact electrolytic tank measurements for square fingers, performed at the Bell Telephone labaratories [4], show that $C_f(\pi) < C_f(0)$, when the waveguide wall comes close to the finger ends in a comb-structure. According to equation (4.1.4) this would imply $C_{fo1} < 0$, which is of course physically impossible.

The true solution of the problem is based on the fact that the fields between the fingers are perturbed some distance from the strip ends. Actually C_{fo1} becomes positive if a small length of the strip is included when deriving $C_f(\varphi)$. Since this part of the strip length in all practical cases is very much smaller than the wavelength, a positioning of $C_f(\varphi)$ at the end of the strip and using negative C_{fo1} does not mean any significant error in the computed dispersion relation

When deriving the $\omega - \varphi$-characteristic of the comb-structure, Chen [4] uses a linear variation of $C_f(\varphi)$ between $C_f(0)$ and $C_f(\pi)$. In the light of equation (4.1.4) this is obviously a rough approximation.

The susceptance B_1 of Figure 4.1 becomes

$$j B_1 = -j\, Y_{s1}(\varphi) \cdot \cot(l_1\, \beta_1) \qquad 4.1.5$$

where $Y_{s1}(\varphi)$ is the strip admittance and β_1 the wave propagation constant of region 1. Realizing that the total current to the point P (Figure 4.1) is zero, one now obtains

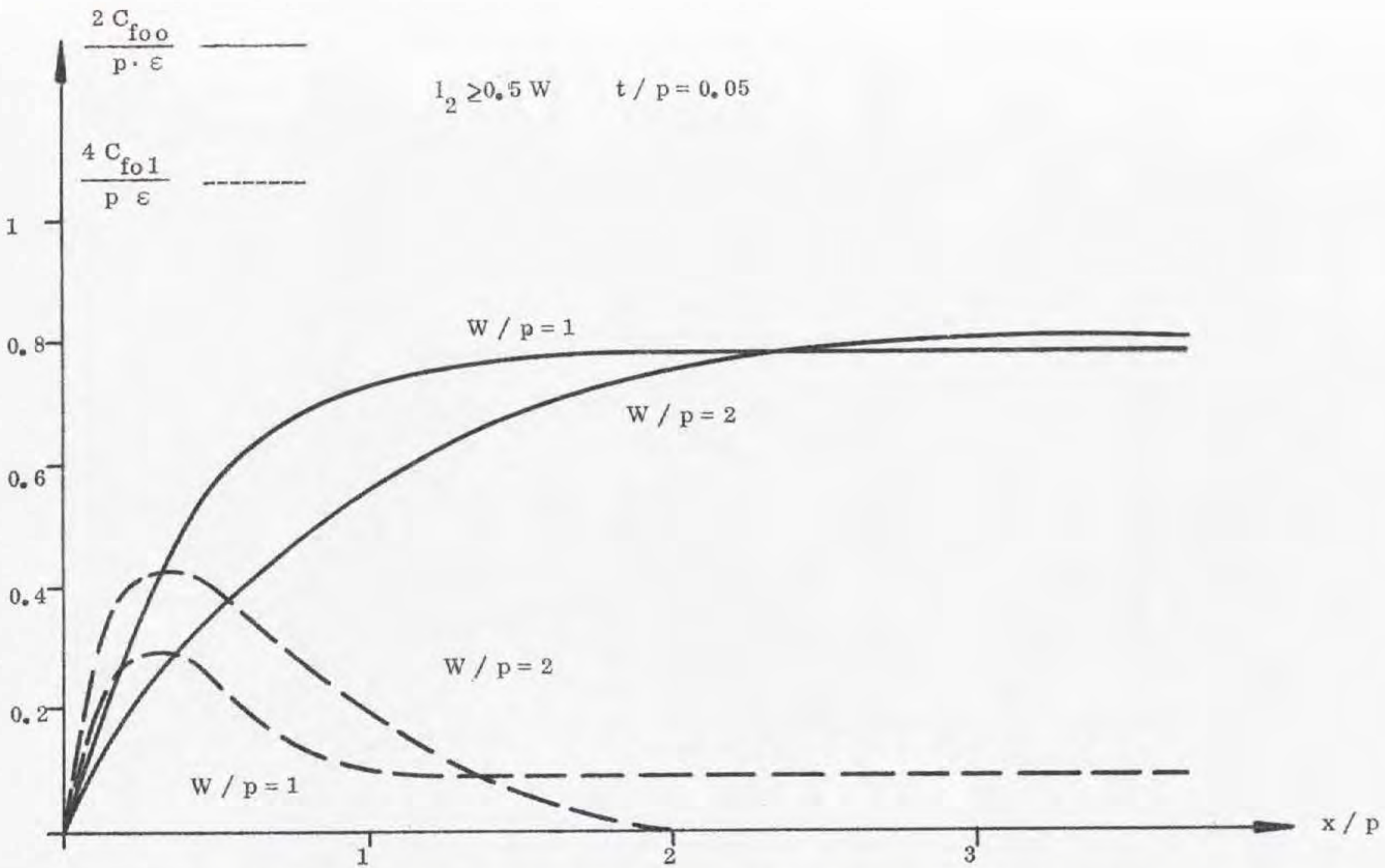

Fig. 4.3. The fringing capacitances per period length (p) at the strip end vs x / p as determined from electrolythic tank measurements.

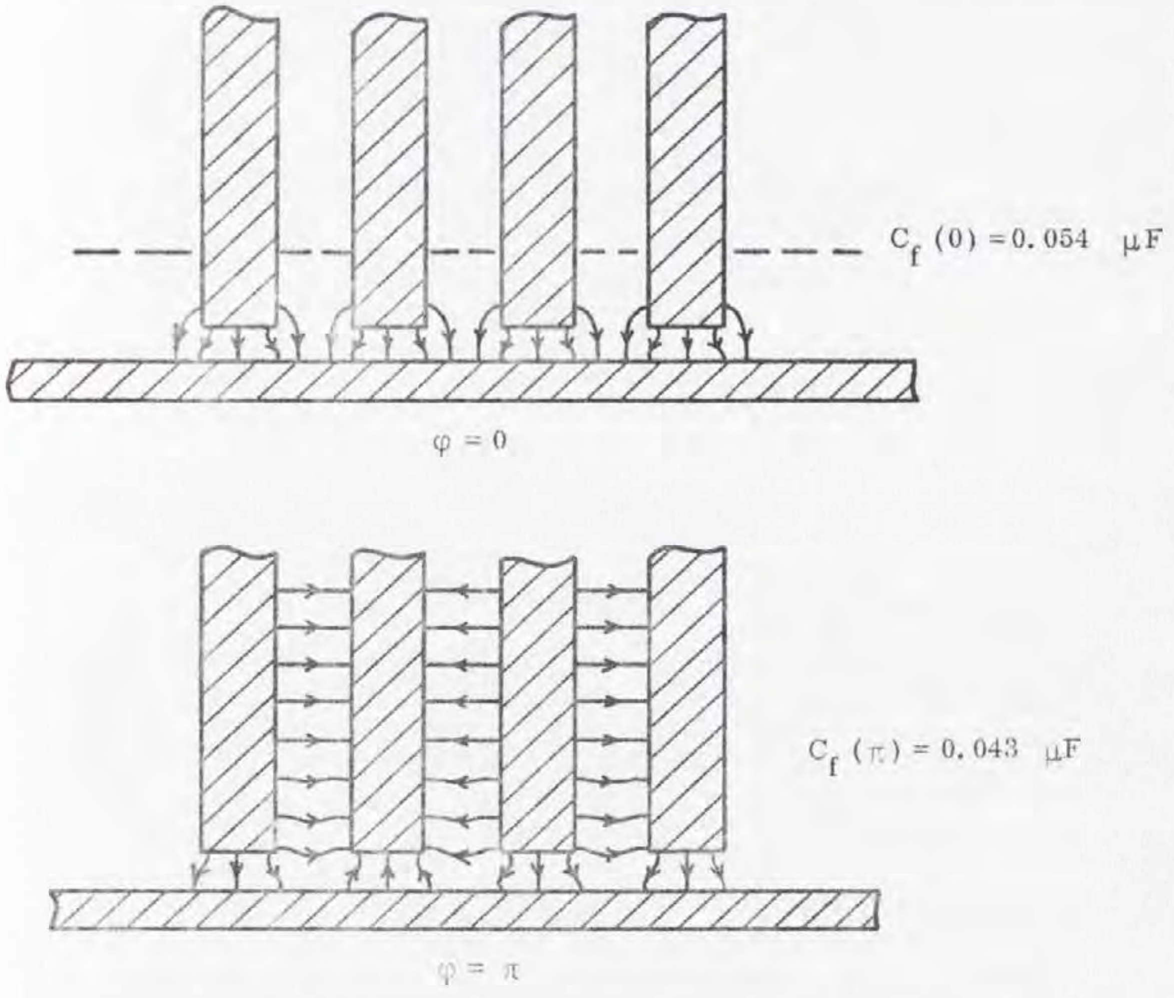

Fig. 4.4. The fringing capacitance of square fingers (0.040×0.040 inch) and the perturbed fields between the fingers for $\varphi = \pi$. The numerical values of $C_f(\varphi)$ are from the reference [2].

$$B_1 + B_2 + B_s = 0 \qquad 4.1.6$$

or by using equations (4. 1. 1), (4. 1. 3) and (4. 1. 5)

$$-Y_{s1}(\varphi)\cdot\cot(l_1\beta_1) + \frac{\omega C_f(\varphi) + Y_{s2}(\varphi)\cdot\tan(l_2\beta_2)}{1 - \frac{\omega C_f(\varphi)}{Y_{s2}(\varphi)}\tan(l_2\beta_2)} + p\cdot\frac{\omega}{v_o}\cdot\frac{2C_d}{\varepsilon} = 0$$

4. 1. 7

Since

$$\beta_1 = \frac{\omega}{v_o} \qquad \beta_2 = \frac{\omega}{v_o}\sqrt{\varepsilon_r} \qquad 4.1.8$$

equation (4. 1. 7) has to be solved in order for us to obtain the $\omega - \varphi$-characteristic of the structure.

When $C_f(\varphi) = 0$, equation (4. 1. 7) is identical to the dispersion equation of the Karp-structure [22], [23]. On the other hand, if $\tan(l_2\beta_2) \approx l_2\beta_2$, and $\omega C_f(\varphi)\tan(l_2\beta_2)/Y_{s2}(\varphi) \ll 1$, the susceptance B_2 is equivalent to a lumped capacitance. Then equation (4. 1. 7) becomes identical with the dispersion equation of the comb-structure [4, 21].

The term

$$\frac{\omega C_f(\varphi)}{Y_{s2}(\varphi)}\tan(l_2\beta_2)$$

usually decreases as φ increases. Hence this term will decrease the center frequency of the pass-band and increase the width of the pass-band , i. e. decrease the slowing factor.

When $W_2/W_1 = 1$, the discontinuity capacitance C_d becomes zero. The main effect of a finite C_d is to decrease the whole pass-band. It is interesting to notice that C_d has been neglected in the literature [22, 23] although it has a considerable effect for small values W_2 / W_1 and for $\varepsilon_r = 1$ (region 2, Figure 4.1). For the maser slow wave structures discussed in the present treatise, $\varepsilon_r >> 1$ and C_d can be neglected.

In order for us to apply the lumped circuit of Figure 2.5 and the equations (2.2.7) and (2.2.8), we must require that

$$\frac{\omega C_f(\varphi)}{Y_{s2}(\varphi)} \tan(\beta_2 l_2) \ll 1 \qquad 4.1.9$$

Hence

$$B_{on} = - y_{on1} \cot(\beta_1 l_1) + \omega \varepsilon_r C_{fon} + \sqrt{\varepsilon_r}\, y_{on2} \tan(\beta_2 l_2) \qquad 4.1.10$$

where y_{on} are the susceptances for the strip in vacuum (see Chapter 3).

It is obvious that the equivalent circuit must be used with care. If we try to adapt this circuit to the particular case, when equation (4.1.9) is not valid, the extreme simplicity of the equations (2.2.7) and (2.2.8) disappears. Fortunately, equation (4.1.9) holds for many practical maser structures, e.g. the comb-structure and the Karp-structure.

In the following sections the practical cases of inhomogeneous dielectric loading in the regions 1 and 2 will be discussed. The properties of the dispersion equation (4.1.7) will be interpreted in more detail in chapter 5.

The property of the structure as a backward one will not be discussed in this connection. It should be mentioned, however, that equation (4.1.7) also covers the backward wave case.

4.2. Inhomogeneous dielectric loading of region 2.

In practice it is very diffcult to arrange a completely homogeneous dielectric loading of region 2 (Figure 4.1). A more realistic situation is shown in Figure 4.5, where the dielectric is clamped between the ground planes and the strips, leaving a space with $\varepsilon_r = 1$ between the strips.

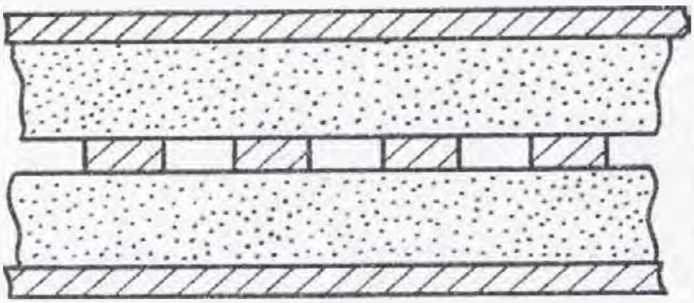

Fig. 4.5. Cross section of the strip array in region 2.

This configuration will not allow pure TEM-waves running along the strips, since the phase velocity of the wave in region B (Figure 4.5) is different to that of region A and C. Let us assume, however, that the TEM field is not severely perturbed by the region B. The wave propagation constant and the strip characteristic admittance will change:

$$\beta_2 \rightarrow \beta_2(\varphi) \qquad Y_{s2}(\varphi) \rightarrow Y'_{s2}(\varphi) \tag{4.2.1}$$

The principal task is to evaluate $\beta_2(\varphi)$ and $Y'_{s2}(\varphi)$ and replace β_2 and $Y_{s2}(\varphi)$ in eqn. (4.1.7). The TEM wave approximation allows for a definition of an effective relative dielectric constant $\epsilon_{r\,eff}$ from the following relation:

$$\frac{\epsilon_{r\,eff}}{\epsilon_r} = \left(\frac{\beta_2(\varphi)}{\beta_2}\right)^2 = \left(\frac{Y'_{s2}(\varphi)}{Y_{s2}(\varphi)}\right)^2 \tag{4.2.2}$$

Let us now define the capacitances C_A and C_C, associated with the charges bound to the strip surfaces of region A and C. We assume that C_A and C_C are almost equal to the infinite thin strip capacitances per unit length (see chapter 3):

$$C_A = C_C = \frac{1}{2}\,\epsilon_r C_o(\varphi) = \frac{1}{2}\,\epsilon_r \epsilon_o \frac{Y_s^o(\varphi)}{Y_o} \tag{4.2.3}$$

where $Y_s^o(\varphi)$ is as before the strip characteristic admittance for $t = 0$.

The capacitance C_B is associated with the charges at the strip surfaces of region B. As an approximation one may use

$$C_B = 4\,C_t \cdot \sin^2 \varphi/2 = \epsilon_o \cdot \frac{4y_t}{Y_o} \sin^2 \varphi/2 \tag{4.2.4}$$

Haddad [23] has discussed two possible approximations for the calculation of $\epsilon_{r\,eff}(\varphi)$. One of the approximations he has called the "equal current" approximation, where he assumes the charges on the center conductor in region A and C to move with a velocity $v_o/\sqrt{\epsilon_r}$, and the charges facing region B to move with the vacuum velocity of light, v_o. Hence one obtains

$$Y'_{s2}(\varphi) = \sqrt{\epsilon_r}\; Y_s^o(\varphi) + 4\, y_t \sin^2 \varphi/2 \qquad 4.2.5$$

which yields an effective dielectric constant

$$\sqrt{\frac{\epsilon_{reff}(\varphi)}{\epsilon_r}} = \frac{Y_s^o(\varphi) + \frac{1}{\sqrt{\epsilon_r}}\, 4\, y_t \sin^2 \varphi/2}{Y_s^o(\varphi) + 4\, y_t \sin^2 \varphi/2} \qquad 4.2.6$$

In the other approximation, the "equal charge" approximation, a material with a relative dielectric constant $\epsilon_{r\,eff}$ is assumed to fill the entire region 2, and the charge induced on the strips is the same as when the region is partially filled with dielectric material. Consequently we obtain

$$\frac{\epsilon_{r\,eff}(\varphi)}{\epsilon_r} = \left[\frac{\beta_2(\varphi)}{\beta_2}\right]^2 = \frac{Y_s^o(\varphi) + \frac{1}{\epsilon_r}\, 4\, y_t \sin^2 \frac{\varphi}{2}}{Y_s^o(\varphi) + 4\, y_t \sin^2 \frac{\varphi}{2}} \qquad 4.2.7$$

Since the difference in the results from the two approximations is not appreciable, [23] , we will adopt the "equal charge" approximation. Calculations using pertubation technique seems to support this assumption. Haddad [23] and Chen [4] , use the "equal charge approximation".

Since C_{foo} is almost independent of the pertubation between the strips, and since C_{fol} is small compared with C_{foo} , it is reasonable to assume that $C_f(\varphi)$ is unaffected by the lack of dielectric material between the strips. If furthermore $C_d = 0$, the ω - φ- characteristic is determined from

$$Y_{1s}(\varphi)\cdot\cot(\beta_1 l_1) = \frac{\omega\varepsilon_r C_f(\varphi) + Y'_{s2}(\varphi)\cdot\tan(l_2\beta_2(\varphi))}{1 - \frac{\omega\varepsilon_r\cdot C_f(\varphi)}{Y'_{s2}(\varphi)}\tan(l_2\beta_2(\varphi))} \qquad 4.2.8$$

The next step is to apply the equivalent scheme of Figure 2.5 if possible. Again the first requirement is that

$$\frac{\omega\varepsilon_r C_f(\varphi)}{Y'_{s2}(\varphi)}\tan(l_2\beta_2(\varphi)) \ll 1 \qquad 4.2.9$$

It is still difficult to know how to define the mutual susceptances B_{on}, since the propagation constant β_{on} vary with n. It is believed that it is best to assume $\beta_2(\varphi)$ to be valid for every interaction o-n. Hence if equation (4.2.9) can be applied for $n \neq 1$

$$B_{on} = -y_{on1}\cot(l_1\beta_1) + \omega\varepsilon_r C_{fon} + \sqrt{\varepsilon_r}\, y_{on2}\tan(l_2\beta_2(\varphi)) \qquad 4.2.10$$

For $n = 1$, $y_t\cdot\frac{1}{\varepsilon_r}$ has to be added to the thin strip admittance y_{o12} and y_t to y_{o11}. See equation (3.1.8).

An interesting situation comes about as $l_1 \to 0$. The circuit of Figure 2.5 is not applicable to this case. The ω - φ-characteristic is determined from

$$l_2\cdot\beta_2(\varphi) = \frac{\pi}{2} \qquad 4.2.11$$

where $\beta_2(\varphi)$ is obtained from equation (4.2.6). Of course, the choice of C_B (equation (4.2.3)) now becomes much more critical in determining the ω - φ-characteristic. The "equal current approximation" may also be too crude to allow for a substantial agreement with experiments.

For TWM applications a SWS with $l_1 = 0$ offers large filling as well as slowing factor. It may, however, be difficult to obtain a good coupling to this structure.

4.3. The effect of inserting the maser crystal into region 1.

The maser crystal may be inserted into the slow-wave structure as indicated in Figure 4.6. Sometimes it is advisable to introduce a second maser crystal symmetrically on the other side of the strip array.

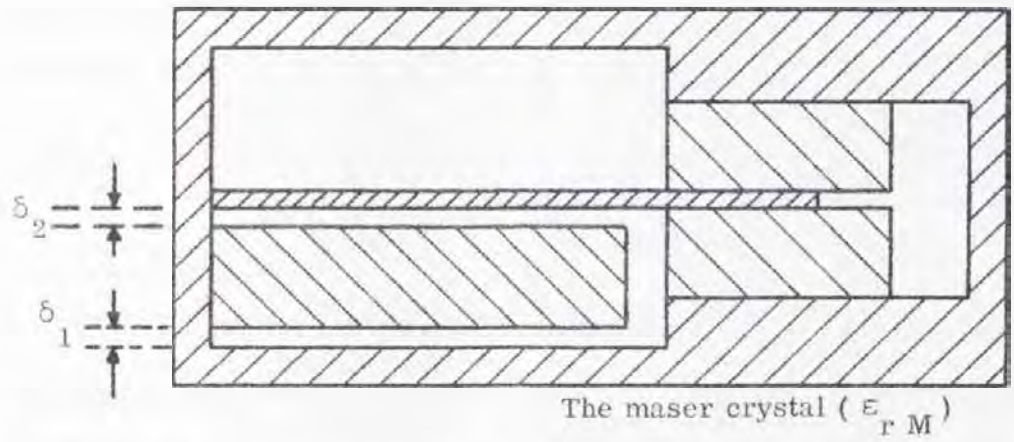

Fig. 4.6. The maser crystal in the slow wave structure.

Let there be a small spacing between the maser crystal and the ground plane (δ_1) and between the maser crystal and strip array (δ_2). Again two things will happen: the admittance changes and the wave propagation constant β_1 changes. Let us assume, as in the last section that the new situation can be described by an effective relative dielectric constant $\varepsilon_{r\,eff}(\varphi)$, then

$$Y'_{s1}(\varphi) = \sqrt{\varepsilon_{r\,eff}(\varphi)} \cdot Y_{s1}(\varphi) \qquad 4.3.1$$

$$\beta_1(\varphi) = \sqrt{\varepsilon_{r\,eff}(\varphi)} \cdot \beta_1 \qquad 4.3.2$$

Calculations using pertubation technique suggest that the equal charge approximation should be the best way to evaluate $\varepsilon_{r\,eff}(\varphi)$ [compare equation (4.2.7)].

The ω - φ-characteristic will only change slightly when the maser crystal is inserted. This can be seen from for example equation (4. 2. 8), if $\cot(l_1 \beta_1(\varphi)) \approx$ $\approx 1/l_1 \beta_1(\varphi)$, in which case

$$Y'_{1s}(\varphi) \cot(l_1 \beta_1(\varphi)) \approx \frac{Y'_{1s}(\varphi)}{l_1 \beta_1(\varphi)} = \frac{Y_{1s}(\varphi)}{l_1 \beta_1} \approx Y_{1s}(\varphi) \cdot \cot l_1 \beta_1 \qquad 4.3.3$$

This situation is quite easy to understand physically, since region 2 contains the shorted end of the strips, leading to a diminishing electric field to interact with the maser crystal .

Because

$$|\cot x| < \frac{1}{x} \qquad (x < \pi/2) \qquad 4.3.4$$

the pass-band will , however, decrease slightly due to the dielectric properties of the maser crystal.

As a first order approximation, the maser crystal only increases the capacitance between the strips and the ground plane slightly. For $\varphi = \pi$, the electric field is stronger between the fingers than for $\varphi = 0$. It is therefore expected that the influence of the maser crystal will be more noticeable for small φ -values and decrease the lower cut-off frequency more than the upper one. Hence the slowing of the structure will decrease slightly when the maser crystal is inserted. This effect has been experimentally verified.

If δ_2 tends to 0 and δ_1 increases, it is possible to reverse the effect due to the maser crystal, i. e. a greater part of the electric field is contained within the crystal for $\varphi = \pi$. These phenomena have been used to increase the slowing of the common comb-structure and are extensively discussed by Chen [4] and Haddad [23]. The latter also discusses the situation when $\varepsilon_M \gg 9$.

In the comb-structure, this effect is fairly difficult to utilize due to the risk of fold-over, i. e. the SWS partly behaves as a backward wave structure and partly as a forward one . The present structure is extremely insensitive to the placing of the maser crystal. It may therefore be advisable to insert the maser crystal close to the strips ($\delta_2 \rightarrow 0$), which will lead to a slight increase of the slowing factor.

5. APPROXIMATE BEHAVIOR OF THE SWS

5.1 Approximation of the dispersion relation.

It is of great interest to find how the geometry of the slow wave structure affects the slowing factor S. We will here derive approximate expressions for the dispersion relation, which will allow us to discuss the behavior of the slowing factor. Since it seems difficult to find an appropriate approximation for the full dispersion relation, equation 4.2.8, the discussion will be limited to two interesting cases: inhomogeneous dielectric material in region 2 with $C_f(\varphi) = 0$, and homogeneous dielectric material in region 2 with $C_f(\varphi) \neq 0$.

The discussion will further assume

$$\frac{\omega \varepsilon_r C_f(\varphi)}{Y'_{s2}(\varphi)} \tan(l_2 \beta_2(\varphi)) << 1 \tag{5.1.1}$$

and

$$W_2 / W_1 = 1 \tag{5.1.2}$$

which allows high slowing factors of the maser structure. With the approximation $\tan x \approx x$ one easily obtains

A. $C_f(\varphi) = 0$, inhomogeneous dielectric material in region 2:

$$\left(\frac{\omega}{\omega_o}\right)^2 = \frac{1 + a \sin^2 \varphi/2}{1 + b \sin^2 \varphi/2} \tag{5.1.3}$$

where

$$a = \frac{4(y_{o1} + y_t)}{2\, y_{oo}} \qquad b = \frac{4(y_{o1} + \frac{1}{\varepsilon_r} \cdot y_t)}{2\, y_{oo}} \tag{5.1.4}$$

B. $C_f(\varphi) \neq 0$, homogeneous dielectric material in region 2.

$$\left(\frac{\omega}{\omega_o}\right)^2 = \frac{1 + d \sin^2 \varphi/2}{1 + e \sin^2 \varphi/2} \tag{5.1.5}$$

where

$$d = \frac{4(y_{o1} + y_t)}{2\, y_{oo}} \qquad e = \frac{4(y_{o1} + y_t + \frac{C_{fo1}}{l_2 \varepsilon_o} Y_o)}{2(y_{oo} + \frac{C_{foo}}{l_2 \varepsilon_o} Y_o)} \tag{5.1.6}$$

For traveling wave maser purposes, a slowing factor as constant as possible is desired. The slowing factor is

$$S = \frac{v_o}{v_g} = \frac{v_o}{\frac{d\omega}{d\beta}} = \frac{v_o}{p\frac{d\omega}{d\varphi}} \tag{5.1.7}$$

One obtains for the two cases

A. $C_f(\varphi) = 0$, inhomogeneous dielectric material in region 2.

$$S = \frac{2\lambda_o}{\pi p} \; \frac{(1 + b \sin^2 \varphi/2)^2}{(a - b) \sin\varphi} \; \frac{\omega}{\omega_o} \tag{5.1.8}$$

The dominating term is

$$a - b = \frac{4 y_t}{2 y_{oo}} \left(1 - \frac{1}{\varepsilon_r}\right) \tag{5.1.9}$$

In the upper part of the pass-band, $b \sin^2 \varphi/2$ will increase the slowing factor. Assuming $y_t / \varepsilon_r << y_{o1}$, b has been computed for various r and W/p in Table 5.I.

Table 5.I

W/p \ r	0.25	0.5	0.75
2.0	1.96	3.06	4.80
1.6	1.52	2.35	3.74
1.2	1.02	1.60	2.58
1.0	0.79	1.23	2.01
0.7	0.35	0.66	1.18

Using $r = 0.25$ and W/p small, the effect of $b \sin^2 \varphi/2$ is decreased.

B. $C_f(\varphi) \neq 0$, homogeneous dielectric material in region 2.

For this case one obtains from equation (5.1.5)

$$S = \frac{2\lambda_o}{\pi p} \frac{\omega}{\omega_o} \frac{(1 + e \sin^2 \varphi/2)^2}{(d - e) \sin \varphi} \tag{5.1.10}$$

The dominant term is (d - e). Since C_{fo1} can usually be neglected, one obtains

$$d - e = \frac{4(y_{o1} + y_t)}{2y_{oo}} \frac{2\frac{C_{foo}}{l_2 \varepsilon_o} Y_o}{2(y_{oo} + \frac{C_{foo}}{l_2 \varepsilon_o} Y_o)} \tag{5.1.11}$$

Hence the slowing becomes inversely proportional to C_{foo}. Again, a small W/p will lead to a small value for e and the ω-φ-characteristic is straightened out.

The φ-dependence on the slowing factor differs from case A through the multiplication by the factor ω/ω_o (equation (5.1.10)). Hence S increases more rapidly with φ.

In Fig. 5.1, we have depicted the ω-φ-characteristic and the slowing factor for large and small values of b, when $C_f = 0$.

For $C_f \neq 0$, things are somewhat more complicated. The term ω/ω_o is usually close to 1, but will increase the slowing as the frequency increases. The coefficient e is usually smaller but of the same order as b.

If a and b are substituted by d and e in Fig. 5.1, at least the correct tendency for different values d and e is obtained.

5.2. Approximate behavior of the slowing factor on the geometrical dimensions.

One might simplify the previous expressions by making use of the following approximate relations for y_{oo} and y_t, by which substitution, one more easily relates the slowing factor S to the basic structure dimensions

Using $r = 0.25$ and W/p small, the effect of $b \sin^2 \varphi/2$ is decreased.

B. $C_f(\varphi) \neq 0$, homogeneous dielectric material in region 2.

For this case one obtains from equation (5.1.5)

$$S = \frac{2\lambda_o}{\pi p} \frac{\omega}{\omega_o} \frac{(1 + e \sin^2 \varphi/2)^2}{(d - e) \sin \varphi} \qquad 5.1.10$$

The dominant term is (d - e). Since C_{fo1} can usually be neglected, one obtains

$$d - e = \frac{4(y_{o1} + y_t)}{2 y_{oo}} \quad \frac{2 \frac{C_{foo}}{l_2 \varepsilon_o} Y_o}{2 (y_{oo} + \frac{C_{foo}}{l_2 \varepsilon_o} Y_o)} \qquad 5.1.11$$

Hence the slowing becomes inversely proportional to C_{foo}. Again, a small W/p will lead to a small value for e and the ω-φ-characteristic is straightened out.

The φ-dependence on the slowing factor differs from case A through the multiplication by the factor ω/ω_o (equation (5.1.10)). Hence S increases more rapidly with φ.

In Fig. 5.1, we have depicted the ω-φ-characteristic and the slowing factor for large and small values of b, when $C_f = 0$.

For $C_f \neq 0$, things are somewhat more complicated. The term ω/ω_o is usually close to 1, but will increase the slowing as the frequency increases. The coefficient e is usually smaller but of the same order as b.

If a and b are substituted by d and e in Fig. 5.1, at least the correct tendency for different values d and e is obtained.

5.2. Approximate behavior of the slowing factor on the geometrical dimensions.

One might simplify the previous expressions by making use of the following approximate relations for y_{oo} and y_t, by which substitution, one more easily relates the slowing factor S to the basic structure dimensions

$$y_{oo} \approx \frac{p}{W} Y_o \qquad y_t \approx \frac{t}{(1-r)p} Y_o \qquad 5.2.1$$

Hence (5.1.8) can be written as

$$S \approx \frac{\lambda_o}{\pi} \frac{(1-r)p\left(1-\frac{1}{\varepsilon_r}\right)}{2\,t\,W} \frac{(1+b\sin^2\varphi/2)^2}{\sin\varphi} \qquad 5.2.2$$

In order to obtain the smallest possible variation of S as a function of φ, it is essential with a small b-value, as is evident from Fig. 5.1. This means W/p as well as r should be made small, which in its turn leads to an over all increase in slowing factor. Furthermore S is inversely proportional to the strip thickness. Finally, it should be noticed that S is almost independant of ε_r when this quantity is large.

For the case B (see equation (5.1.10)) it is difficult to find a convenient approximation, so we limit ourselves to state in this connection that (d - e) increases rapidly with W/p when $C_{foo}/l_2\varepsilon_o$ is kept constant. The same is true as far as the factor e is concerned, i.e. e decreases with W/p.

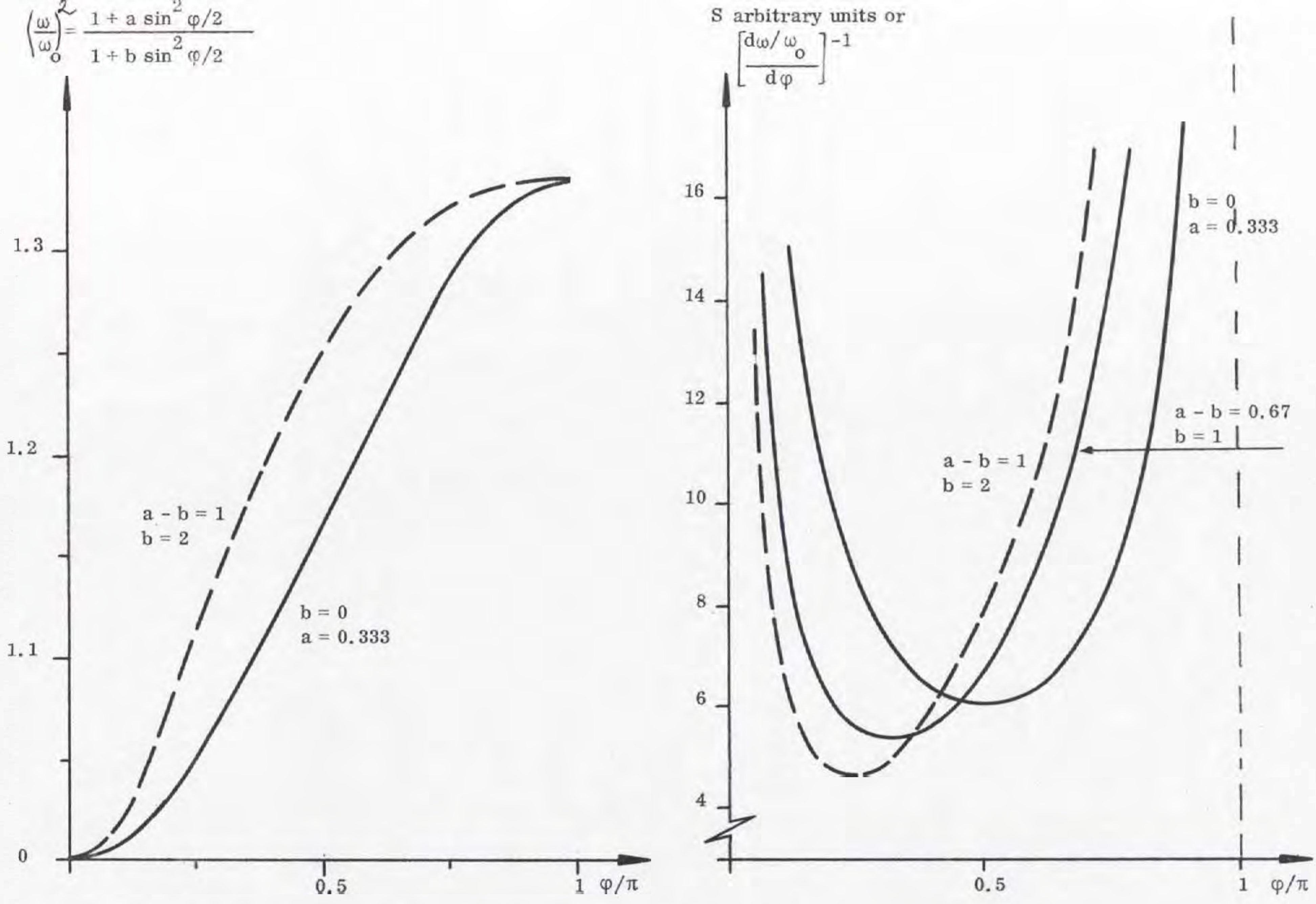

Fig. 5.1 $\omega - \varphi$ and the slowing $S(\varphi)$ for different values a, b with $C_o = 0$ and a constant passband

6. ON THE COUPLING TO THE SWS

6.1. Introduction

Theoretically, the coupling to the SWS is reasonably well understood. The calculations, however, are not very accurate, since the parameters involved are only approximately known. The problem of impedance matching may be separated into the following phases:

a) find the characteristic impedance of the SWS
b) design a network capable of matching the input line to the SWS

The practical problem to perform a perfect match over the whole pass-band of the SWS has not been completely solved. This is mainly due to lack of time and insufficient resources in the workshop. The most critical part in manufacturing the SWS is in fact, the coupling section, since reflections within the SWS are taken care of by the garnet isolator. In practice, a standing wave ratio $s \leq 3$, within a substantial part of the pass-band is readily obtained. This is equivalent to a loss in gain of about 3 dB.

6.2. The characteristic admittance of the SWS.

The first step in the design of the coupling network is to find the characteristic admittance G_s of the SWS. We simplify the problem a great deal by assuming interaction to exist only between the nearest strips within the SWS. Equation (2.2.7) and (2.2.8) are then simplified as follows

$$B_{oo}(\omega) + 2\,B_{o1}(\omega)\sin^2\varphi/2 = 0 \tag{6.2.1}$$

$$G_s = -\,B_{o1}(\omega)\sin\varphi \tag{6.2.2}$$

leading to

$$G_s = B_{oo}(\omega)\cot\varphi/2 \tag{6.2.3}$$

From (6.2.1), (6.2.2) and (6.2.3) it is seen that

a) $B_{oo} = 0$ $\varphi = 0$

b) $B_{oo} > 0$ $\varphi > 0$ (capacitive)

c) $B_{o1} < 0$ $\varphi > 0$ (inductive)

d) $G_s = 0$ $\varphi = 0,\ \varphi = \pi$

e) $G_s = B_{oo}(\omega) = B_{o1}(\omega)$ $\varphi = \pi/2$

Let us estimate $B_{oo}(\omega)$ by assuming $\tan x \approx x$ and $C_f = 0$. Then we get from equation (4.2.8) and (4.2.10).

$$B_{oo} \approx \frac{y_{oo1}\lambda_o}{2\pi l_1} \left(\frac{f}{f_o} - 1\right) \qquad 6.2.4$$

Since $f - f_o$ for a special value of φ roughly is proportional to the structure bandwidth and hence inversely proportional to the slowing factor, one finds that

$$G_s \propto \frac{y_{oo1}}{f_o^2\, l_1\, S} \qquad 6.2.5$$

Normally $l_1 / \lambda_o \leq 1/10$ for our particular SWS. Since $f/f_o - 1 \ll 1/2$,

$$G_s < \frac{1}{2}(2y_{oo1}) \qquad 6.2.6$$

where $2y_{oo1}$ may be found in Fig. 3.3.

Hence the impedance-level in many cases is quite a bit higher than 50Ω, the usual impedance of input and output cables.

6.3. Coupling networks.

Since the treatment of the SWS in chapter 2-5, assumes the SWS to be infinitely long, a finite SWS leads to an interruption of the symmetry. The following discussion is considerably simplified by assuming interaction to exist only between nearest neighbor strips. Hence, the phase-shift between the first and the second strip resonator is φ, i.e. equal to the phase shift between any two strips in the SWS.

These assumptions are rather crude, but helpful in a preliminary design of the coupling network. In Fig. 6.1 the assumed situation is depicted. Notice that the susceptance B'_{oo} is related to the left half of the first strip, since the right half is part of the infinite network, constituting G_s. The susceptance B'_{oo} may differ from B_{oo} (Fig. 2.5) within the SWS, due to the difference in structure geometry to the left and right of the first strip. It will, however, constitute a parallel resonance circuit resonant approximately at the lower cut-off frequency of the SWS.

A simple way of coupling to the SWS is to attach the inner conductor of the 50 Ω cable to the first strip of the SWS at a point close to the boundary between region 1 and 2. The input admittance of the SWS becomes approximately

$$Y_{in} \approx B_{oo}(\omega) \cot \varphi/2 + jB'_{oo} = B_{oo}(\omega) \cot \varphi/2 + j\gamma \qquad 6.3.1$$

where γ is almost frequency independant. If the first strip has the same width as all other strips in the SWS, one may have $\gamma \approx 1.5 - 2$.

It is possible to taper the structure admittance by increasing the width of the strips (increase B_{oo}) and decreasing the spacing between the end strips (increasing B_{o1}). Then φ is approximately unchanged and G_s increased (equation (6.2.1) and (6.2.2)). The width of the first strip may, however, be about half (or even less) of the second strip, which will decrease γ. In this procedure care must be taken to avoid a substantial change of the cut-off frequencies of the end sections.

Due to the low characteristic admittance of the SWS, a coupling network exhibiting transformation characteristics is very useful. In reference [12] two different networks with such properties are discussed, (e.g. page 227 reference [12]) one of which will increase G_s. This network is shown in Fig. 6.2.

It is more convenient to calculate the admittance Y_{in} seen from the SWS, when a 50 Ω impedance is connected to the coupling strip. The properties of the circuit are considerably simplified when the following constraint is used:

$$\frac{1}{2}\left(Y^{a}_{oe} + Y^{a}_{oo}\right) = G_{o} = 1/50\ \Omega^{-1} \qquad 6.3.2$$

where Y^{a}_{oe} and Y^{a}_{oo} are the characteristic admittance of strip a, Fig. 6.2, when the strip b is excited in phase (even excitation) or out of phase (odd excitation) relative strip b. Y^{b}_{oe} and Y^{b}_{oo} are defined in a similar manner.

In Fig. 6.3 the coupling section of the SWS is shown. Y_{in} shall match G_{s} as closely as possible. At the reference point of the first strip, there is added G_{s} and a capacitance C_{o} from dielectrically loaded region. Notice that the coupling strip is not shorted directly to ground as in Fig. 6.2, but small inductance L is connected. This inductance will show up as a capacitance in Y_{in}, and decrease the inductive admittance of Y_{in}. (Fig. 6.2). This technique has been used in comb-structures [26].

In practice, the two coupling methods have been used with some success. Since the design method is far from exact, the "cut- and try method" must also be used to a great extent, which makes the matching procedure relatively time consuming. The coupling is also very sensitive to mechanical imperfections. Very close fit between the strip and the dielectric surfaces is required for best persormance. The irregularities show up as a larger standing wave ratio for certain frequencies at the input cable of the SWS.

Since there are reactive elements in the coupling sections and since G_{s} changes with frequency, it is hard to obtain a true broad-band match without more advanced matching methods. One method has been described [26] which leads to an excellent match. Quite generally one developes a tapered section by decreasing the lower cut-off frequency and increasing the upper cut-off frequency of the first elements in the SWS. Within the SWS pass-band, these sections will exhibit a much smaller change in phase shift and therefore maintain a more constant $G_{s}(\varphi)$, (equation (6.2.2) and 6.2.4)).

It has been outside the scope of the present investigation to taper the end sections of the SWS.

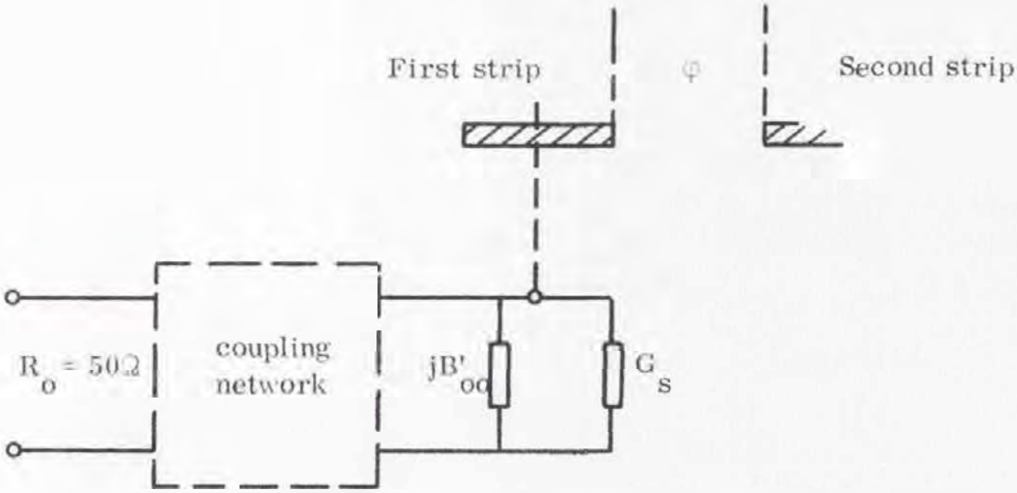

Fig. 6.1. The approximate situation at the ends of the SWS.

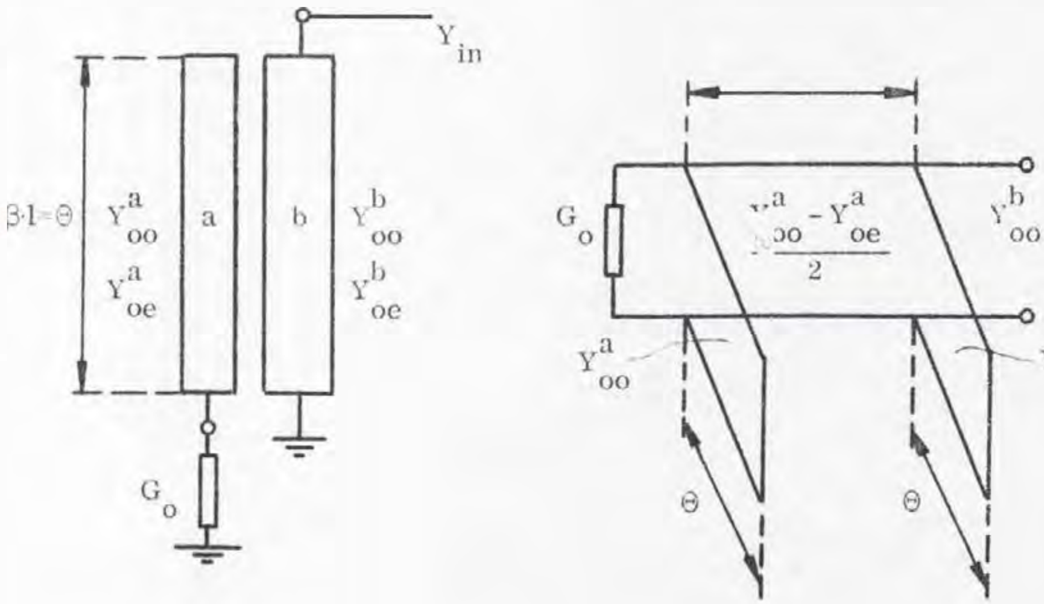

$\frac{1}{2}(Y^a_{oo} - Y^a_{oe}) = \frac{1}{2}(Y^b_{oo} - Y^b_{oe}) = Y_{o1}$ = mutual admittance a - b

With the special constraint $G_o = Y^a_{oo} + Y_{o1}$

$$Y_{in} = \left(\frac{Y_{o1}}{G_o}\right)^2 \cdot G_o - j\left(\frac{Y_{o1}}{G_o} Y^a_{oe} + Y^b_{oe}\right)\cot\Theta$$

Fig. 6.2 Coupling network with transformating properties according to reference [22] and [23].

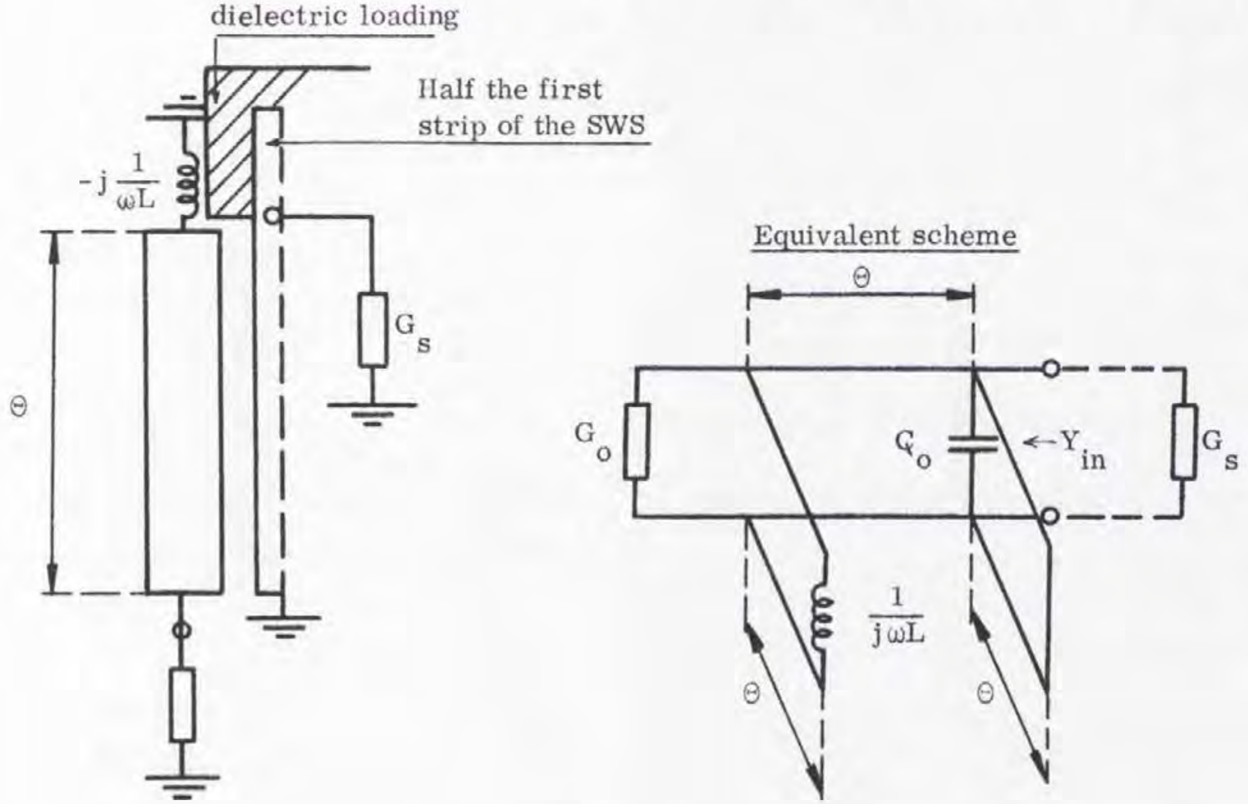

Fig. 6.3 Coupling network to the SWS, using the properties of the circuit in Fig. 6.2.

7. THE FILLING FACTOR OF THE SWS

7.1. Indroduction.

The filling factor was defined in equation (1.3) as

$$\eta = \frac{\int_m \overline{H}^* \overline{\delta}\,\overline{\delta}^* \;\overline{H}\,dv}{\delta_{nr}^2 \int_v \overline{H}^* \;\overline{H}\,dv} \qquad 1.3$$

where the integral in the numerator is taken over the maser crystal volume, and the integral in the denominator is taken over the whole volume of the SWS.

There are two effects that will make $\eta < 1$, namely a) the volume m is only some part of the total structure volume, and b) the polarization of the field does not have its optimum for the transition under consideration.

Let us assume that t = 0 and that the maser crystal almost completely occupies one side of the strip array, as shown in Figure 7.1. Since the SWS is symmetrical to the plane of the strip array, and since there are negligible electric fields available to interact with the maser material, only half the magnetic energy of region 1 can be utilized. Hence $\eta \leq \frac{1}{2}$.

Furthermore the polarization of the fields changes with φ. Usually the maser signal transition is close to being circularly polarized. In Figure 7.2. the ratio of positive to negative circularly polarized field energy, η_+, is shown for different W / p (from reference [14]). The sense of polarization is opposite on different sides of the strip array.

Finally the maser crystal cannot be placed in region 2, which means that the filling factor is further decreased by a factor η_1. If the signal transition of the maser material is perfectly circularly polarized, we obtain:

$$\eta = \frac{1}{2} \cdot \eta_+ \cdot \eta_1 \qquad 7.1.1$$

7.2. The effect of the dielectric loading in region 2.

The ratio of magnetic field energy in region 1, Figure 7.1, to the total magnetic field energy determines η_1 :

$$\eta_1 = \frac{M_1}{M_1 + M_2} = \frac{\left[Y_{s1}(\varphi)\right]^{-1} \int_0^{l_1} i_1^2(x)\,dx}{\frac{1}{Y_{s1}(\varphi)} \int_0^{l_1} i_1^2(x)\,dx + \frac{\sqrt{\varepsilon_r}}{Y_{s2}(\varphi)} \int_0^{l_2} i_2^2(y)\,dy} \qquad 7.2.1$$

where M_1 and M_2 is the magnetic field energies of region 1 and 2 respectively, $i_1(x)$ and $i_2(y)$ the current on the strip in region 1 and 2. See Figure 7.1. Note that $\sqrt{\varepsilon_r}/Y_s$ is proportional to the strip-inductance per unit length.

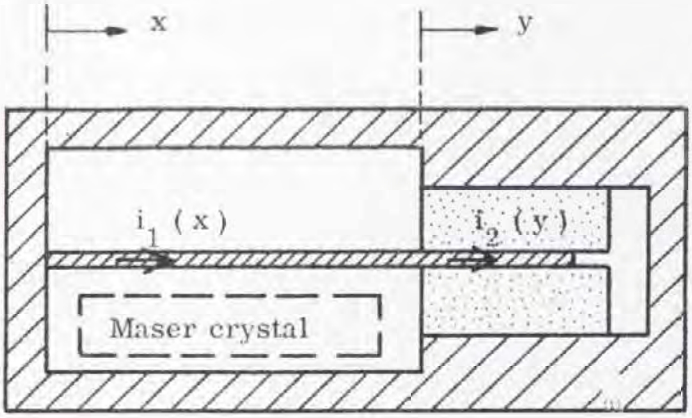

Fig. 7.1

Let $U_1(x)$ and $U_2(y)$ be the voltages on the strips at x and y in region 1 and 2 respectively. Then $i_1(x)$ and $i_2(y)$ may be determined from the following set of equations

$U_1(x) = A\cos\beta_1 x + B\sin\beta_1 x$; $i_1(x) = jY_{s1}(\varphi)\left[-A\sin\beta_1 x + B\cos\beta_1 x\right]$.

$U_2(y) = C\cos\beta_2 y + D\sin\beta_2 y$; $i_2(y) = jY_{s2}(\varphi)\left[-C\sin\beta_2 y + D\cos\beta_2 y\right]$

7.2.2

Using the following boundary conditions,

$U_1(0) = 0 \qquad\qquad i_1(l_1) = i_2(0) \qquad 7.2.3$

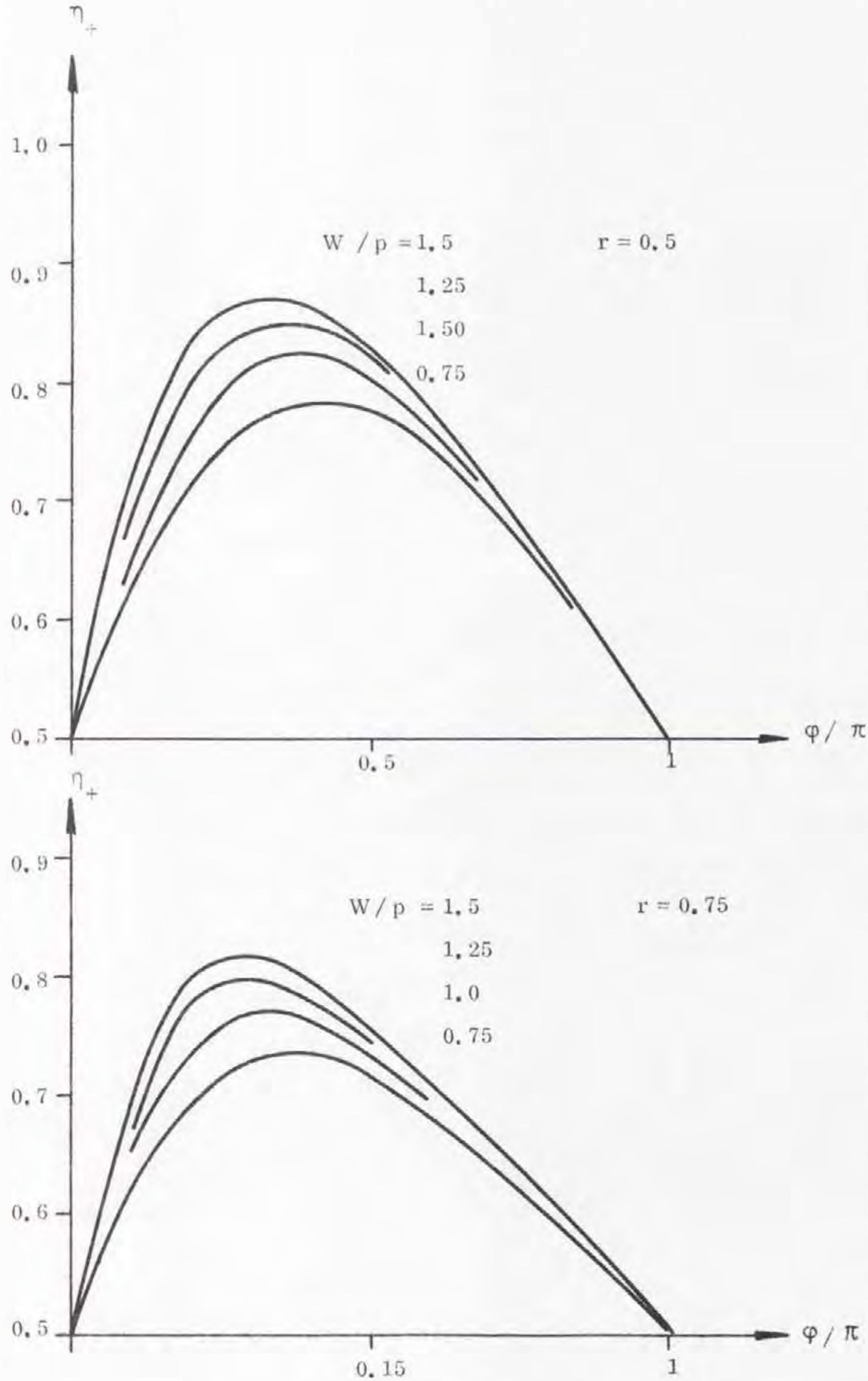

Fig. 7.2. Filling factor for a maser loaded on one side according to reference [14].

$$\frac{i_2(l_2)}{U_2(l_2)} = j\,\omega\,C_f(\varphi) \qquad\qquad U_1(l_1) = U_2(0) \qquad\qquad 7.2.3$$

A, B, C and D can be determined. Then one obtains

$$\eta_1 = \left\{ 1 + \left[\frac{l_2}{l_1} \frac{1}{1 + \frac{\sin 2\beta_1 l_1}{2\beta_1 l_1}} \left[\sin^2 \beta_1 l_1 \left(\frac{Y_{s2}(\varphi)}{Y_{s1}(\varphi)} \right)^2 + \right.\right.\right.$$
$$\left. + \cos^2 \beta_1 l_1 \right] \left(1 - \frac{\sin 2\beta_2 l_2}{2\beta_2 l_2} \right) + 2\cos^2 \beta_1 l_1 \frac{\sin 2\beta_2 l_2}{2\beta_2 l_2} \left[1 - \right.$$
$$\left.\left.\left. - \tan(\beta_1 l_1)\tan(\beta_2 l_2) \frac{Y_{s2}(\varphi)}{Y_{s1}(\varphi)} \right] \right] \frac{Y_{s1}(\varphi)}{Y_{s2}(\varphi)} \sqrt{\varepsilon_r} \right\}^{-1}$$

7.2.4

To calculate η_1, one must know the $\omega - \varphi$-characteristic. Equation (7.2.4) may be simplified considerably if $C_f = 0$, in which case

$$\tan(\beta_1 l_1) \cdot \tan(\beta_2 l_2) = \frac{Y_{s1}(\varphi)}{Y_{s2}(\varphi)}$$

Now

$$\eta_1 = \left\{ 1 + \frac{l_2}{l_1} \frac{\cos^2 \beta_1 l_1}{\sin^2 \beta_2 l_2} \frac{1 - \frac{\sin 2\beta_2 l_2}{2\beta_2 l_2}}{1 + \frac{\sin 2\beta_1 l_1}{2\beta_1 l_1}} \cdot \frac{Y_{s1}(\varphi)}{Y_{s2}(\varphi)} \sqrt{\varepsilon_r} \right\}^{-1} \qquad 7.2.5$$

If $\varepsilon_r \gg 1$, and $l_2 \lesssim \frac{1}{2} l_1$, η_1 is fairly accurately approximated by

$$\eta_1 = \left\{ 1 + 0.3 \frac{l_2}{l_1} \cdot \frac{Y_{s1}(\varphi)}{Y_{s2}(\varphi)} \cdot \sqrt{\varepsilon_r} \right\}^{-1} \qquad 7.2.6$$

As an example, let $W_1 = W_2$ and $l_2 / l_1 = 1/3$ leading to $\eta_1 \approx 0.91$. Hence the decrease in the filling factor due to region 2 is very moderate.

Notice also that in the case of square strips, a large portion of the energy is stored between the strips for $\varphi \to \pi$. This effect appreciably decreases the filling factor. Thin strips evidently offer a higher filling factor.

7.3. A possible method to increase the filling factor.

It was noticed in section 7.1 that $\eta \leq 1/2$ for a symmetric SWS loaded with a maser material on one side of the strip array. For an unsymmetric SWS, Figure 7.3, more than half the total magnetic field energy is stored on one side of the strip array (t = 0). This phenomenon was utilized in early strip cavity masers.

Since the strips are guiding TEM waves, the ratio of magnetic energy in region A to that in region B in equal to the ratio of the electrostatic energies. Hence, instead of the factor 1 / 2 we introduce

$$\eta_2 = \frac{\frac{1}{2} C_A (\varphi) U^2}{\frac{1}{2} (C_A (\varphi) + C_B (\varphi)) U^2} = \frac{Y_A (\varphi)}{Y_B (\varphi) + Y_A (\varphi)} \qquad 7.3.1$$

where it has been assumed that t = 0, i.e. $C_t = 0$ and that no energy is stored between the fingers. Evidently, $\eta_2 \geq 1/2$ for $Y_A (\varphi) \geq Y_B (\varphi)$, and the total filling factor becomes

$$\eta = \eta_1 \cdot \eta_2 \cdot \eta_+ \qquad 7.3.2$$

In Figure 7.4 $\eta_2 / 0.5$ has been plotted for $W_A / p = 0.75$ and $W_B / p = 1.5$. This plot represents the ratio between the gain (in dB) of the unsymmetric SWS to the gain of the symmetrical SWS even for t = 0, if $C_t \ll y_{o1}$. As a consequence the method is not applicable to comb-structures with square fingers.

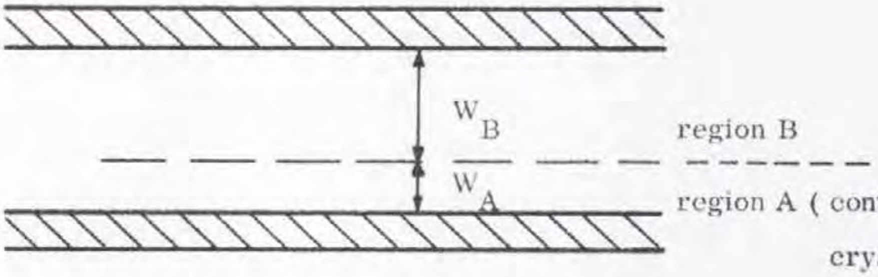

Fig. 7.3. Unsymmetrical SWS with increased filling factor.

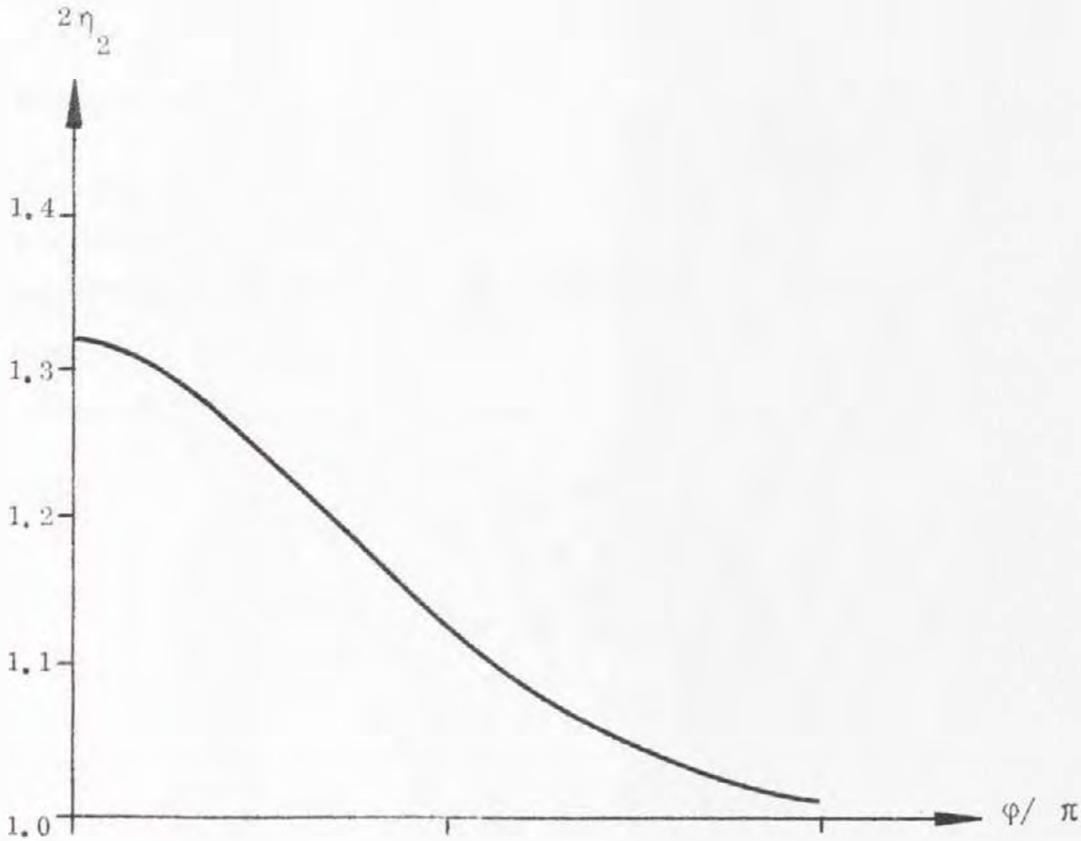

Fig. 7.4. Increase in filling factor for an unsymmetrical SWS with $W_A/p = 0.75$ and $W_B/p = 1.5$.

8. DESIGN CONSIDERATIONS FOR THE SWS

8.1 General considerations.

We will here concentrate on SWS:s for which $C_f = 0$. In chapter 5, the variation of slowing over the SWS pass-band Δf, was rather extensively discussed. In Fig. 5.1 it can be seen that $b = 0$ gives the best performance for Δf = constant. In practice, however, $b = 0$ is not attainable.

In Fig. 8.1, the slowing factor S is shown for different b:s and as a function of the frequency. For an increased b the minimum value of the slowing factor decreases and occurs for lower values of φ. According to equation (5.1.8) and (5.1.10), this variation is almost independant of the absolute amount of slowing.

Let by definition B be the bandwidth of the SWS, determined by $S_{max}/S_{min} = 1.5$. The ratio $B/\Delta f$ where Δf is the total bandwidth, is calculated from Fig. 8.1.1 and is shown in Table 8.I. φ_1 and φ_2 are the phase shift intervals related to B. The change in S and B with b (Δf = constant) is also calculated.

The number $\left(\frac{S}{B}\right)_{b=o}\left(\frac{B}{S}\right)_b$ is a measure of how much better the SWS with $b = 0$ is when compared to a structure for which $b>0$. For obvious physical reasons, b cannot be made too small. One finds that $b = 1$ is a good choice (18% from the ideal case, $b = 0$) and $b \geq 2$ is unfavorable. The numbers to be found in Table 8.I are of course approximate, but the tendencies are certainly correct.

Table 8.I

b	0	1	2
$B/\Delta f$	0.74	0.69	0.61
$\varphi_1/\pi - \varphi_2/\pi$	0.24 - 0.77	0.13 - 0.57	0.10 - 0.45
$S_{b=o}/S$	1	1.10	1.25
$B_{b=o}/S$	1	1.07	1.22
$\left(\frac{S}{B}\right)_{b=0}\left(\frac{S}{B}\right)_b$	1	1.18	1.50

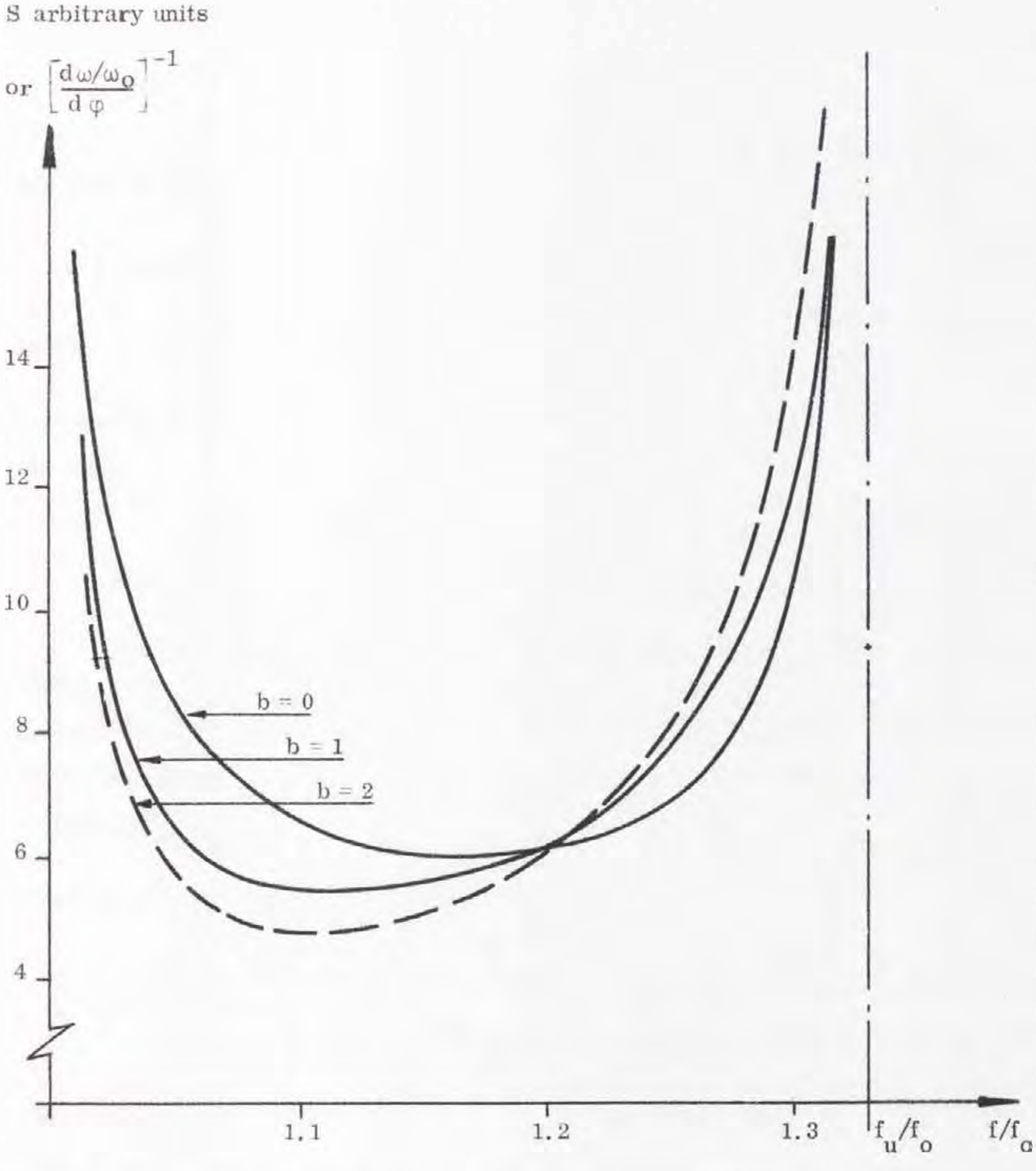

Fig. 8.1. The slowing S as a function of the frequency for different values a and b as obtained from Fig. 5.1.

A relation between the minimum slowing factor S_{min} times the pitch p and the total SWS bandwidth Δf may be found from equation (5.1.3).

$$S_{min}\, p = \frac{1}{\Delta f}\,\frac{v_o}{\pi}\,\frac{(1 + b \sin^2 \varphi'/2)^2}{1 + b} \approx \frac{10^4}{\Delta f_{MHz}}\,\frac{(1 + b \sin^2 \varphi'/2)^2}{1 + b} \qquad 8.1.1$$

where φ' is the φ-value for S minimum, and is determined from

$$b \cos^2 \varphi + (2 + b) \cos \varphi - 2b = 0 \qquad 8.1.2$$

In Fig. 8.2 the relationship between $S_{min} \cdot p$ and Δf is depicted for various b-values.

Concerning the coupling between the input line and the SWS, reference is made to the relation

$$G_s \propto \frac{y_{oo1}}{f_o^2\, l_1\, S} \qquad 8.1.3$$

which shows that the admittance (G_s) decreases with increasing slowing and frequency. This makes it more difficult to obtain a good coupling for higher frequencies and slowing factors. A large slowing and narrow SWS bandwidth also enhances a destructive influence from mechanical imperfections.

The ohmic losses in the SWS are determined by

$$A = 27.3\, \frac{S(\varphi)\, L}{\lambda_o}\, \frac{1}{Q_o(\varphi)} \qquad (dB) \qquad 8.1.4$$

The φ-dependance of Q_o will probably increase the losses when φ increases. Since $1/Q_o \propto \sigma \propto f^{-1/2}$ where σ is the skin depth, one obtains

$$A \propto f^{1/2} \qquad (dB) \qquad 8.1.5$$

when the geometry as well as S and L in equation (8.1.4) are constant.

If the inversion ratio is constant with frequency, it is well known that

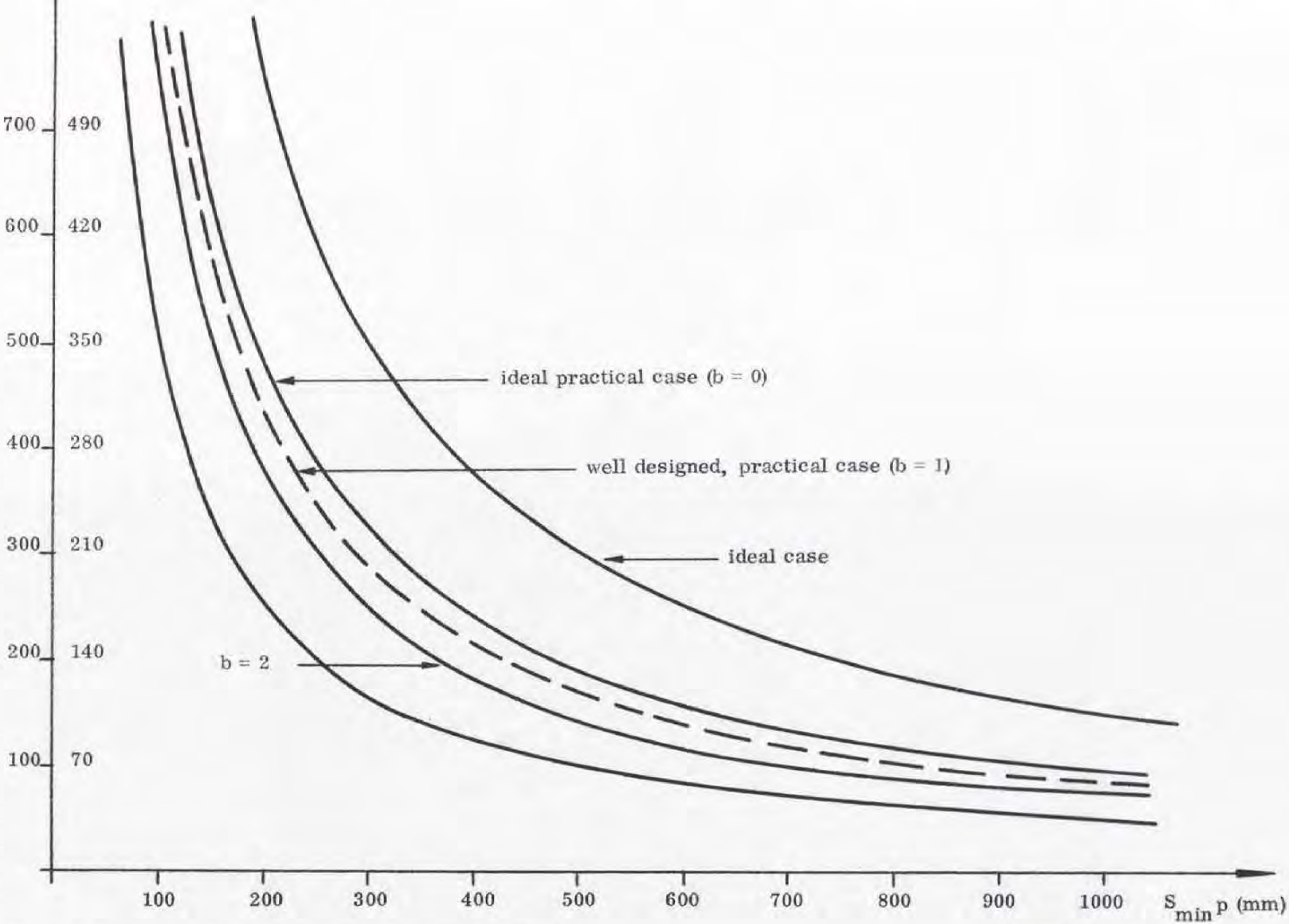

Fig. 8.2. Estimated $S_{min}p$ mm from equation (8.1.1) (Meander line : $S_{min}p/2$ mm)

$$\frac{1}{Q_m} \approx (\text{const.})\, f \qquad 8.1.6$$

Hence it becomes in principle easier to build a TWM for a higher frequency.

Finally, the author has shown that there excists an optimum pitch [27], which represents a compromise between the ohmic losses and the slowing factor, viz.

$$p_{opt} = p_o \frac{2\,|Q_m|}{(1 - \mu Q_{oo})} \qquad 8.1.7$$

where Q_{oo} is the ohmic Q-factor when $p = p_o$,

$$\mu = \frac{Q_i}{|Q_m|} \qquad 8.1.8$$

and Q_i is a Q-factor related to the loss in the isolator material. Under these assumptions the optimum gain becomes

$$G_{popt} = 27 \frac{L\,S}{\lambda_o} \; \frac{1-\mu}{2\,|Q_m|} \qquad (\text{dB}) \qquad 8.1.9$$

The noise temperature of the TWM will increase as the pitch decreases. The author has shown that the noise temperature can be expressed in the following fashion when $p = p_o$

$$T_n = \frac{G-1}{G} \quad \frac{p_o/p_{opt}}{2\,p_o/p_{opt} - 1} \; \frac{2\,T_m}{1-\mu} + \frac{\mu + 1/(2p_o/p_{opt} - 1)}{1-\mu}\, T_o \qquad 8.1.10$$

where T_m is the spin temperature and T_o the bath temperature. For a practical case with $\mu = 0.2$, $p_o = p_{opt}$ and $T_m \ll T_o$, one obtains

$$T_n \approx 1.5\, T_o \qquad 8.1.11$$

8.2 The design procedure.

One possible way to design a particular SWS for a TWM, broadbanded or tunable, is the following:

a) Choose the frequency band over which amplification shall be realized. Multiply this band by a factor 1.5, to obtain the SWS passband Δf.

b) Find the approximate minimum value $S_{min} \cdot p$ from Fig. 8.2.

c) Put $b \approx 1$ (or $e \approx 1$) and choose a (or d) in equation (5.1.3) or (5.1.5) so that the upper cut-off frequency ($\varphi = \pi$) minus the required lower cut-off frequency equals Δf.

d) Choose the structure dimensions to fit a and b (d and e), and find l_1 and l_2 to obtain the correct lower cut-off frequency ($\varphi = 0$).

e) Find Q_{oo}, Q_m and μ (experimentally or if possible theoretically) and find the pitch for optimum performance.

f) Calculate the gain per unit length and find the length L to give the required net gain.

9. EXPERIMENTAL SLOW-WAVE STRUCTURES

The ω-φ-characteristic has been measured for a number of empty slow-wave structures, specified in Table 9.I and Fig. 9.1. The measurements were performed with the SWS acting as a resonator [1]. Resonance is obtained for frequencies when

$$\beta L = \frac{\varphi}{p} L = m\pi \qquad (m = 1, 2, \ldots, \frac{L}{p}) \tag{9.1}$$

or

$$\frac{\varphi}{\pi} = \frac{p}{L} m \tag{9.2}$$

In Fig. 9.2 theoretical and measured ω-φ-characteristics are compared. In order to compare the form of the theoretical and the measured ω-φ-characteristics, the lower cut-off frequencies of the theoretical curves are adjusted to fit the experimental lower cut-off frequencies. In Table 9.I the discrepancy between the theoretical and measured lower cut-off frequencies are given. The discrepancy is only a few per cent, which is probably due to inaccurate values l_1, l_2, ε_r etc. One might also argue that the lower cut-off frequency theoretically becomes too low, since

a) $t > 0$ corresponds to a somewhat larger $Y_{1s}(0)$

b) the effect of $\varepsilon_r = 1$ between the strips in region 2 will decrease $Y_{2s}(0)$ and $\beta_2(0)$.

The lack of measured resonances for $\varphi > \pi/2$ in Fig. 9.2, can be explained by:

a) the length of the SWS, measured in half wavelengths ($\lambda_s = \frac{2\pi}{\varphi} p$), becomes very long when $\varphi \to \pi$, and therefore reflections from mechanical imperfections severely affect the resonant properties.

b) since the ω-φ-characteristic becomes more sensitive to changes in the mecanical dimensions when φ increases (see section 5.1), the reflections due to variations in $G_s(\varphi)$ increase with φ.

c) the slowing factor increases rapidly as φ becomes larger than $\pi/2$ (Fig. 5.1), leading to an increased attenuation of the wave and a very poor coupling to the resonating SWS.

Especially the strip to strip spacing (1 - r)p, affects the upper cut-off frequency considerably more than the lower cut-off frequency.

Much effort must be made to ensure a close fit between the dielectric material of region 2 and the conducting surfaces. In Fig. 9.3 the effect of spacings to the dielectric material is shown. A variation of the spacing along the structure evidently severely perturbs the transmission characteristic of the SWS. Such variation may also cause the lower cut-off frequency to become too high.

It might be advisable to perform measurements on SWS:s with 10 - 15 elements in order to decrease the effect of mechanical imperfections.

SWS No.	l_1 mm	l_2 mm	$\frac{x}{p}$	$\frac{W_1}{p}$	$\frac{W_2}{p}$	ε_r	f_o theor.	$\frac{f_o \text{ meas.}}{f_o \text{ theor.}}$	
1	6.5	1.5	0	2.0	1.0	90	1135	—	Early Karp-structure
2	6.50	1.5	2	2.0	1.0	"	—	—	Halved Karp-structure*)
3	6.25	1.40	1.10	1.75	1.75	"	1385	1.083	Structures as described in the present scientific report
4	6.0	2.0	0	1.50	1.50	25	2570	1.040	
5	6.4	1.6	0.4	"	"	"	2670	1.000	
6	7.3	0.7	1.3	"	"	"	2950	1.042	
7	6.0	2.0	0	"	"	10	4000	1.000	
8	7.2	0.8	1.2	"	"	"	4400	1,030	

For all SWS: p = 1 mm   t/p = 0,12

Table 9.I

*) Karp-structure with $\lambda/4$-resonators

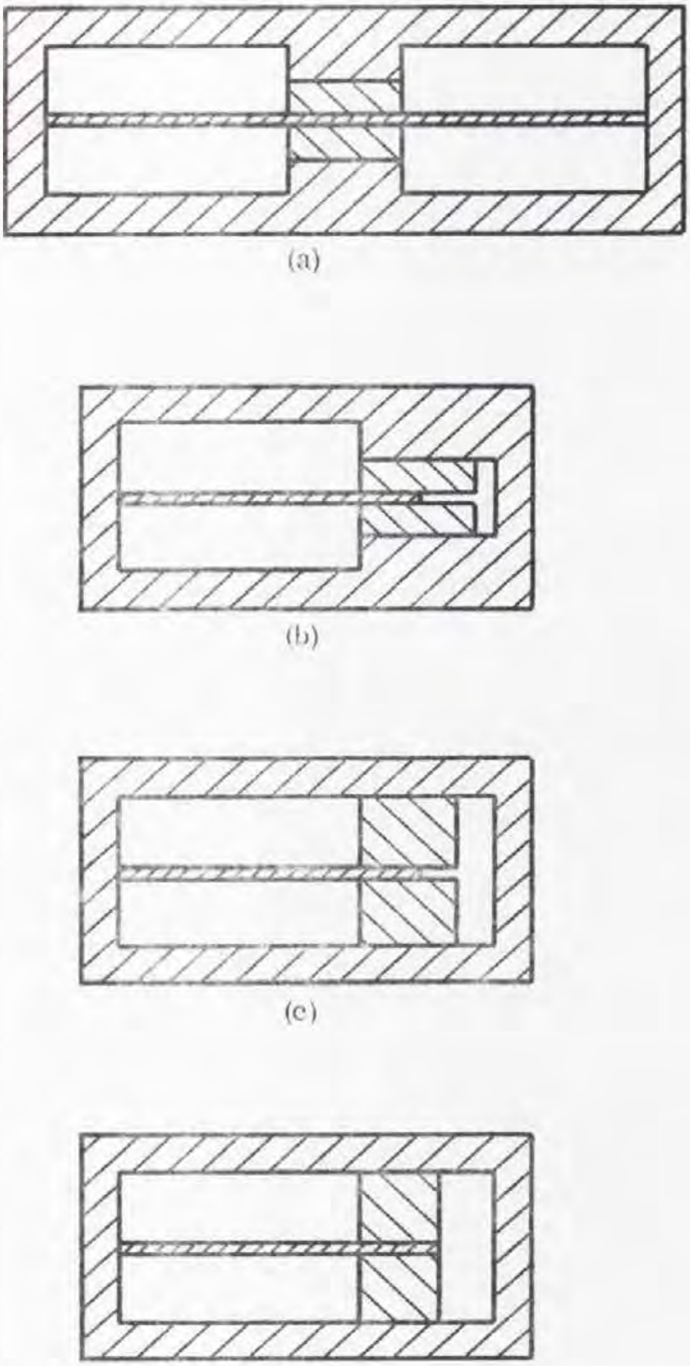

(a)

(b)

(c)

(d)

Fig. 9.1. Cross sections of various experimental slow-wave structures.

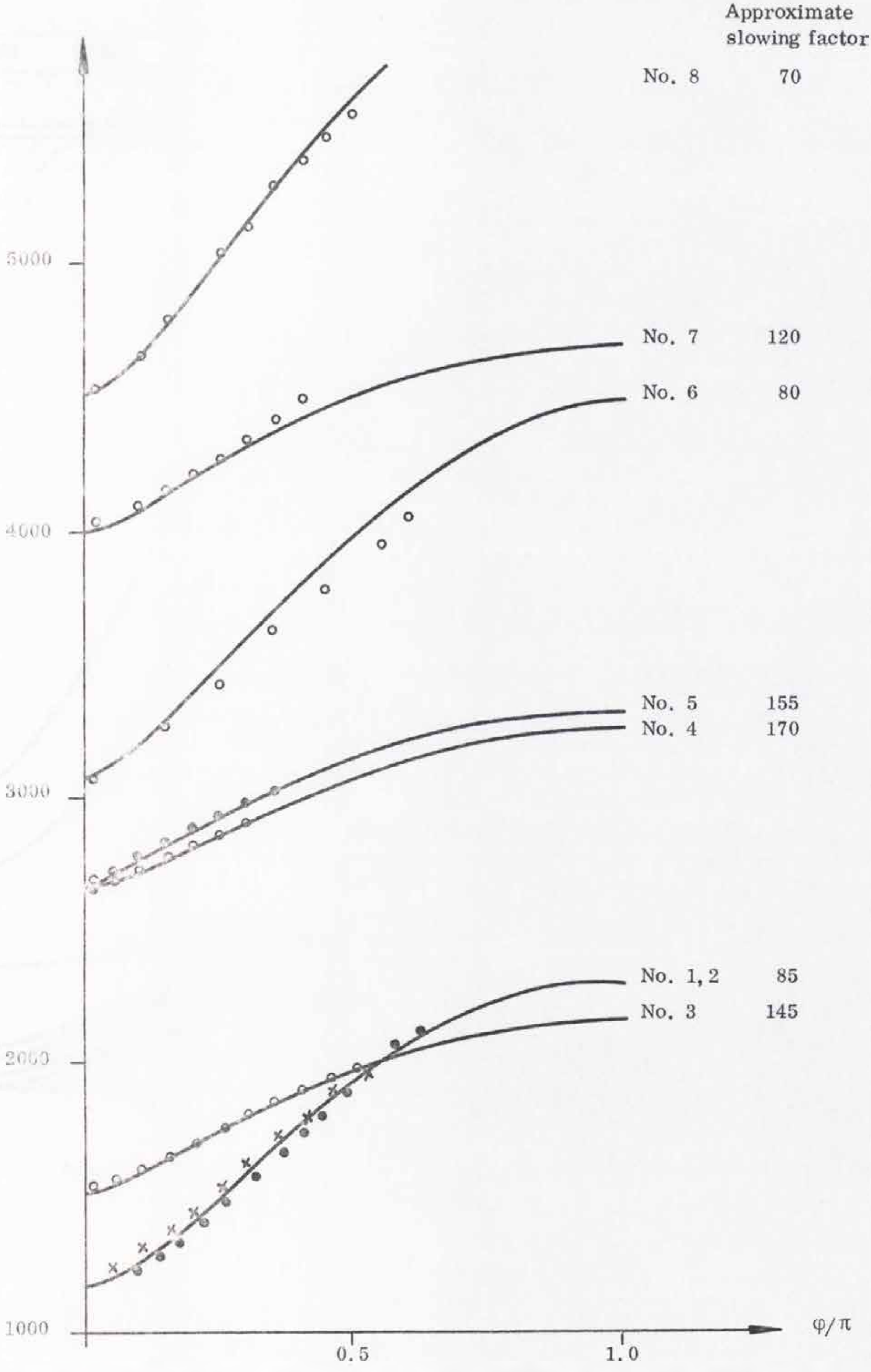

Fig. 9.2. Theoretical (full lines) and measured ω - φ-characteristics for the experimental SWS:s according to Table 9.I. The lower theoretical

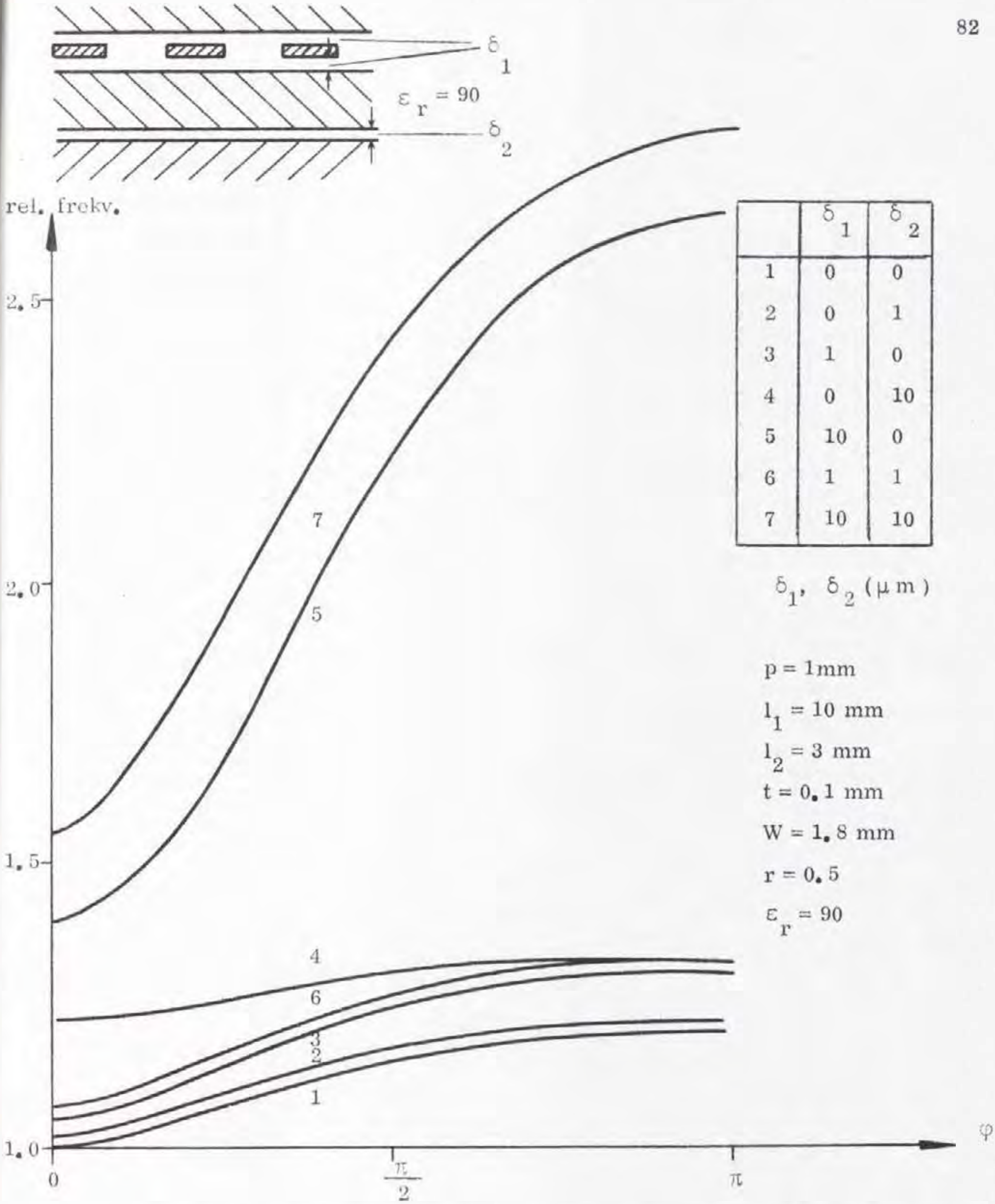

	δ_1	δ_2
1	0	0
2	0	1
3	1	0
4	0	10
5	10	0
6	1	1
7	10	10

δ_1, δ_2 (μm)

$p = 1$mm

$l_1 = 10$ mm

$l_2 = 3$ mm

$t = 0.1$ mm

$W = 1.8$ mm

$r = 0.5$

$\varepsilon_r = 90$

Fig. 9.3. The effect of spacings (δ_1 and δ_2) between the conducting boundaries and the dielectric in region 2. The following approximation is used:

$$\frac{f'_o}{f_o} = \sqrt{\frac{2\,C_{oo}}{2\,C'_{oo}}} \qquad \frac{f_\pi}{f_o} = \sqrt{\frac{2\,C_{oo} + 4\,C_{o1} + 4\,C_t/\varepsilon_r}{2\,C'_{oo} + 4\,C'_{o1} + 4\,C_t/\varepsilon_r}} \qquad \frac{\varepsilon_o}{C'_{oo}\,\varepsilon_r} = \frac{\delta_1}{rp} + \frac{\delta_2}{p} +$$

$$+ \frac{1}{C_{oo}\,\varepsilon_r} \qquad \frac{\varepsilon_o}{C'_{o1}\,\varepsilon_r} = \frac{\delta_1}{rp} + \frac{1}{C_{o1}\,\varepsilon_r}$$

ACKNOWLEDGEMENTS:

The author is indepted to professor O. E. H. Rydbeck for untiring support and inspiration, and to C. O. Lindström for carrying out a large portion of the experiments. The investigations reported in this report were made possible by grants from Swedish Technical Research Council.

Appendix A: Asymptotic expressions for Y (0), Y ($\pi/2$) and Y (π)

Sometimes it might be useful to have asymptotic expressions [16, 29] for the admittances. Hence for $\varepsilon_r = 1$

$$\frac{Y(0)}{Y_o} = \frac{2}{\frac{W}{p} + \frac{1}{\pi} \ln \frac{1}{\sin \frac{r\pi}{2}}} \quad , \quad \frac{W}{p} >> \frac{1}{\pi} \ln \frac{1}{\sin \frac{r\pi}{2}} \qquad \text{A. I. 4}$$

$$\frac{Y(\pi/2)}{Y_o} = \frac{4}{\sqrt{2}} \cdot \frac{K\left[\tan\frac{\alpha_o}{2}\right]}{K\left[\tan\frac{\alpha}{2}\right]} \cdot \frac{\cos\frac{\alpha}{2}}{\cos\frac{\alpha_o}{2}} \qquad \frac{W}{p} > 1.5 \qquad \text{A. I. 5}$$

$$\frac{Y(\pi)}{Y_o} = 4 \cdot \frac{K\left[\sin \alpha_o\right]}{K\left[\sin \alpha\right]} \qquad \frac{W}{p} > 1 \qquad \text{A. I. 6}$$

$$\alpha_o = \frac{\pi}{2} \cdot r \qquad \text{A. I. 7}$$

$$\alpha = \frac{\pi}{2} \cdot (1 - r) \qquad \text{A. I. 8}$$

where K [k] is the complete elliptic integral of the first kind with argument k.

In the graph A. 1 Y (π) / Y_o is shown for $W/p \to \infty$ as a function of r.

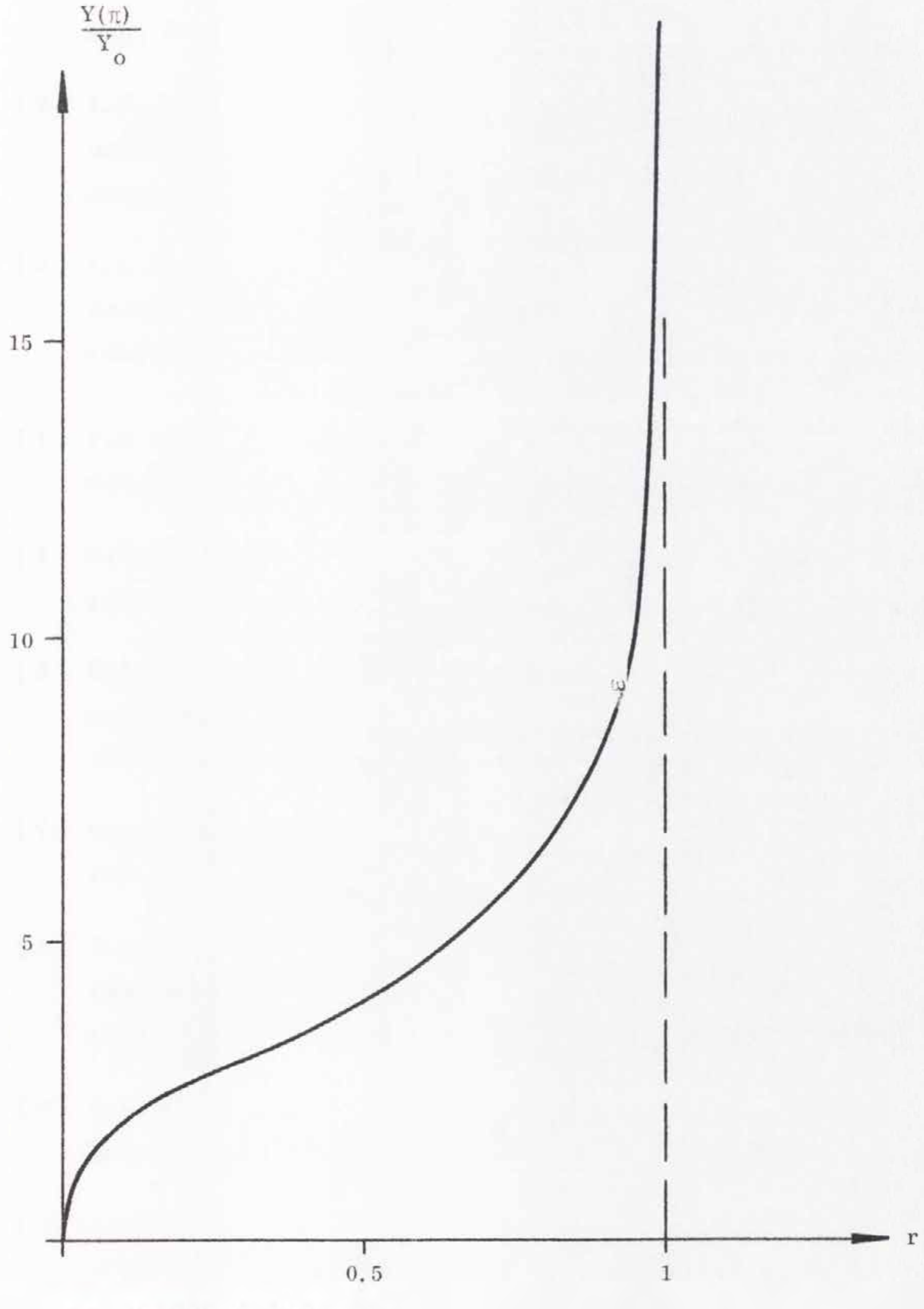

A.1. $Y(\pi)/Y_o$ for $W/p \to \infty$

References.

[1] A. E. Siegman, "Microwave solid state masers." Mc Graw Hill Book Company, New York (1964).

[2] F. R. Arams, B. J. Peyton, "Eight-millimeter traveling-wave maser and maser-radiometer system" IEEE Trans. on Microwave Theory and Techniques, MTT-13, 12-23 (1965).

[3] L. C. Morris, D. J. Miller, "A broad tunable bandwidth traveling-wave maser." IEEE Trans. on Microwave Theory and Techniques, MTT-12, 421-428 (1964).

[4] F. S. Chen, "The comb-type slow-wave structure for TWM applications." Bell Syst. Tech. J. 43, 1035-1066 (1964).

[5] R. W. De Grasse, E. O. Schultz-DuBois, H. E. D. Scovil, "The three-level solid state traveling-wave maser." Bell Syst. Tech. J. 38, 305-334 (1959).

[6] K. S. Yngvesson, "A hydrogen-line traveling-wave maser using chromium-doped rutile." Proc. 3 rd Quantum Electronics Conference, Columbia University Press, New York. pp. 899-911 (1962).

[7] G. I. Haddad, J. E. Rowe, "X-band ladder-line traveling-wave maser." IRE Trans. on Microwave Theory and Techniques, MTT-10, 3-8 (1962).

[8] F. E. Goodwin, J. E. Kiefer, G. E. Moss, "The coupled-cavity transmission maser engineering design." IEEE Trans. on Microwave Theory and Techniques, MTT-12, 349-358 (1964).

[9] D. A. Watkins, "Topics in electromagnetic Theory." John Wiley & Sons, Inc., New York (1958).

[10] E. Kollberg, S. Yngvesson, "An L-band traveling-wave maser using chromium-doped rutile." Proc. IEEE, 53, 1737-1738 (1965).

[11] J. D. Jackson, "Classical Electrodynamics", John Wiley & Sons, Inc., New York (1962).

[12] G. L. Matthaei, L. Young, E. M. T. Jones, "Microwave filters, inpedance-matching nteworks, and coupling structures." Mc Graw-Hill Book Company, New York, San Francisco, Toronto, London (1964).

[13] G. L. Matthaei, "Comb-line band-pass filters of narrow or moderate band-width." The Microwave Journal, Vol. 6, 82-91 (Aug. 1963).

[14] F. S. Chen, W. J. Tabor, "Filling factor and isolator performance of the traveling-wave maser." Bell Syst. Tech. J., 43, 1005-1033 (1964).

[15] A. Leblond, G. Mourier, "Étude des lignes à barraux à structures périodique pour tubes electronique U. H. F." Ann. de Radioélect., 9, 180-192 and 311-328 (1954).

[16] S. Harris, R. W. De Grasse, E. O. Schulz-DuBois, "Cut-off frequencies of the dielectrically loaded comb-structure as used in traveling-wave masers", Bell Syst. Tech. J. 43, 437-484 (1964).

[17] P. N. Butcher, "The coupling impedance of tape structures", Proc. IEE, 104 B, 177-189 (1957).

[18] O. R. Cruzan, R. V. Garver, "Characteristic impedance of rectangular transmission lines", IEEE Trans. on Microwave Theory and Techniques, MTT-12, 488-495 (1964).

[19] S. B. Cohn, "Thickness corrections for capacitive obstacles and strip conductors", IRE Transactions on Microwave Theory and Techniques, MTT-8, 638-644 (1960).

[20] R. C. Fletcher, "A broadband interdigital circuit for use in traveling-wave-type amplifiers", Proc. IRE, 40, 951-958 (1952).

[21] S. Kovalenko, V. S. Kovalenko, "The theory of a maser delay system", Radio Engineering and Electronic Physics, pp. 1327-1336 (Aug. 1963).

[22] J. C. Walling, "Interdigital and other slow-wave structures", J. Electron. Control, 3, 239-258 (1957).

[23] G. L. Haddad, "Characteristics of dielectrically loaded ladder-lines for traveling-wave masers and other applications", Tech. Report no. 65, Electron Physics Laboratory, University of Michigan, Ann Arbor, Michigan.

[24] J. C. Cromack, "A wide tuning range S-band traveling wave maser", Tech. Report No. 155-5, Stanford Electronics Laboratories, Stanford, Calif., (1958).

[25] Tsung-Shan Chen, "Calculation of the parameters of ridge waveguides", IRE Trans. on Microwave Theory and Techniques, MTT-5, 12-17 (1957).

[26] M. L. Hensel, E. O. Schulz-DuBois, "Matching into band-pass transmission structures", IEEE Trans. on Microwave Theory and Techniques MTT-12, 309-315 (1964).

[27] E. Kollberg, "Optimum pitch of traveling-wave masers", IEEE Trans. on Microwave Theory and Techniques, MTT-14, 212-213 (1966).

[28] Bo M. Holmberg, "Admittanser och fältbilder i fördröjningsstrukturer för vandringsvågmasers." Examensarbete, Research Laboratory of Electronics, Chalmers University of Technology, Gothenburg, Sweden (Aug. 1964).

[29] J. Walling, private communication.

Earlier publications from the Research Laboratory of Electronics:

O.E.H.Rydbeck: A theoretical survey of the possibilities of determining the distribution of the free electrons in the upper atmosphere; Trans. Chalmers Univ. of Techn., No. 3, 1942.

O.E.H.Rydbeck: On the propagation of radio waves; Trans. Chalmers Univ. of Techn., No. 34, 1944.

O.E.H.Rydbeck: On the spherical and spheroidal wave functions; Trans. Chalmers Univ. of Techn., No. 43, 1945.

O.E.H.Rydbeck: A simple Kerr modulator for ionospheric recording; Trans. Chalmers Univ. of Techn., No. 44, 1945.

O.E.H.Rydbeck: Chalmers solar eclipse ionospheric expedition 1945; Trans. Chalmers Univ. of Techn., No. 53, 1946.

Reports from the Research Laboratory of Electronics:

1. O.E.H.Rydbeck: The theory of the travelling-wave tube. 1947 x).
2. J.S.A.Tomner: The experimental development of travelling-wave tubes; Trans. Chalmers Univ. of Techn., No. 67, 1948.
3. S.I.Svensson: Pulser and water load for high power magnetrons; Trans. Chalmers Univ. of Techn., No. 68, 1948.
4. U.Ingård: On the radiation of sound into a circular tube with an application to resonators; Trans. Chalmers Univ. of Techn., No. 70, 1948.
5. D.Strantz: A study of impressive wave formation in the atmosphere; Trans. Chalmers Univ. of Techn., No. 71, 1948.
6. D.Strantz: Ozonradiosonde; Trans. Chalmers Univ. of Techn., No. 72, 1948.
7. O.E.H.Rydbeck: On the propagation of waves in an inhomogeneous medium, I; Trans. Chalmers Univ. of Techn., No. 74, 1948.
8. O.E.H.Rydbeck and D.Strantz: Ionospheric effects of solar flares. Preliminary report No. 1, Trans. Chalmers Univ. of Techn., No. 83, 1949.
9. O.E.H.Rydbeck: On the forced electro-magnetic oscillations in spherical resonators. 1948 x).
10. J.S.A.Tomner: Experimental investigation of a long electron beam in an axial magnetic field; Trans. Chalmers Univ. of Techn., No. 92, 1949.
11. O.E.H.Rydbeck: The ionospheric and radio wave propagation observatory at Kiruna, 67° 50' N, 20° 14,5' E. 1949 x).
12. R.Lindquist: The panoramic ionospheric recorder. 1949 x).
13. R.Lindquist: Ionospheric effects of solar flares. Preliminary reports Nos. 2 and 3; Trans. Chalmers Univ. of Techn., No. 95, 1950.
14. O.E.H.Rydbeck: The theory of magneto ionic triple splitting; Trans. Chalmers Univ. of Techn., No. 101, 1951.
15. O.E.H.Rydbeck and S.K.H.Forsgren: On the theory of electron wave tubes; Trans. Chalmers Univ. of Techn., No. 102, 1951.
16. R.Lindquist: Polar blackouts recorded at the Kiruna Observatory; Trans. Chalmers Univ. of Techn., No. 103, 1951.
17. S.K.H.Forsgren: Some calculations of ray paths in the ionosphere; Trans. Chalmers Univ, of Techn., No. 104, 1951.
18. B.N.Agdur: Experimental observations of double-stream amplification. Preliminary notes; Trans. Chalmers Univ. of Techn., No. 105, 1951.

---

x) Not published in the Chalmers Transactions.

19. B.N.Agdur and C-G.L.Åsdal: Noise measurements on a travelling wave tube; Trans. Chalmers Univ. of Techn., No. 106, 1951.

20. S.K.H.Forsgren and O.F.Perers: Vertical recording of rain by radar; Trans. Chalmers Univ. of Techn., No. 107, 1951.

21. O.F.Perers, B.K.E.Stjernberg and S.K.H.Forsgren: Microwave propagation in the optical range; Trans. Chalmers Univ. of Techn., No. 108, 1951.

22. R.Lindquist: A survey of recent ionospheric measurements at the ionospheric and radio wave propagation observatory at Kiruna. 1951 x).

23. R.Lindquist: A 16 kW panoramic ionospheric recorder; Trans. Chalmers Univ. of Techn., No. 109, 1951.

24. B.-A.Lindblad: A radar investigation of the delta aquarid meteor shower of 1950; Trans. Chalmers Univ. of Techn., No. 129, 1952.

25. G.Hellgren: The propagation of electromagnetic waves along a conical helix with variable pitch; Trans. Chalmers Univ. of Techn., No. 130, 1953.

26. G.Hellgren and J.Meos: Localization of aurorae with 10 m high power radar technique, using a rotating antenna. 1952 x).

27. O.E.H.Rydbeck: On the excitation of different space charge wave modes in travelling wave tubes; Trans. Chalmers Univ. of Techn., No. 131, 1953.

28. O.E.H.Rydbeck and B.N.Agdur: The propagation of electronic space charge waves in periodic structures; Trans. Chalmers Univ. of Techn., No. 138, 1954.

29. B.N.Agdur: Experimental investigation of noise reduction in travelling wave tubes; Trans. Chalmers Univ. of Techn., No. 139, 1954.

30. B.N.Agdur: Amplification measurements on a velocity step tube; Trans. Chalmers Univ. of Techn., No. 140, 1954.

31. O.E.H.Rydbeck and H.Wilhelmsson: A theoretical investigation of the ionospheric electron density variation during a solar eclipse; Trans. Chalmers Univ. of Techn., No. 149, 1954.

32. H.Wilhelmsson: The interaction between an obliquely incident plane electromagnetic wave and an electron beam. Part I; Trans. Chalmers Univ. of Techn., No. 155, 1954.

33. S.Olving: Electromagnetic wave propagation on helical conductors imbedded in dielectric medium; Trans. Chalmers Univ. of Techn., No. 156, 1955.

34. S.Olving: Amplification of the travelling wave tube at high beam current. Part I; Trans. Chalmers Univ. of Techn., No. 157, 1955.

35. H.Wilhelmsson: On the reflection of electromagnetic waves from a dielectric cylinder; Trans. Chalmers Univ. of Techn., No. 168, 1955.

36. B.-A.Lindblad: Combined visual and radar observations of Perseid meteors. I: Observations in 1953 x).

37. S.Olving: A new method for space charge wave interaction studies. Part I; Trans. Chalmers Univ. of Techn., No. 178, 1956.

38. V.Westberg: Measurements of noise radiation at 10 cm from glow lamps; Trans. Chalmers Univ. of Techn., No. 180, 1956.

39. S.I.Svensson, G.Hellgren and O.Perers: The swedish radioscientific solar eclipse expedition to Italy, 1952; Trans. Chalmers Univ. of Techn., No. 181, 1956.

40. N.Wax: A note on design considerations for proposed auroral radar; Trans. Chalmers Univ. of Techn., No. 182, 1957.

41. N.Wax: On the ring current hypothesis; Trans. Chalmers Univ. of Techn., No. 171, 1956.

---

x) Not published in the Chalmers Transactions.

42. G.H.Joshi: The electromagnetic interaction between two crossing electron streams. Part I; Trans. Chalmers Univ. of Techn., No. 183, 1957.

43. J.Meos and S.Olving: On the origin of radar echoes associated with auroral activity; Trans. Chalmers Univ. of Techn., No. 196, 1958.

44. G.H.Joshi: The electromagnetic interaction between two crossing electron streams. Part II; Trans. Chalmers Univ. of Techn., No. 197, 1958.

45. H.Wilhelmsson: The interaction between an obliquely incident plane electromagnetic wave and an electron beam. Part II; Trans. Chalmers Univ. of Techn., No. 198, 1958.

46. H.Wilhelmsson: On the properties of the electron beam in the presence of an axial magnetic field of arbitrary strength; Trans. Chalmers Univ. of Techn., No. 205, 1958.

47. H.Wilhelmsson: The interaction between an obliquely incident plane electromagnetic wave and an electron beam. Part III; Trans. Chalmers Univ. of Techn., No. 206, 1958.

48. B.Höglund and V.Radhakrishnan: A radiometer for the hydrogen line; Trans. Chalmers Univ. of Techn., No. 223, 1959.

49. S.Olving: Electromagnetic and space charge waves in a sheath helix; Trans. Chalmers Univ. of Techn., No. 225, 1960.

50. H.Wilhelmsson: A survey of radio-frequency and microwave resonance lines of interest to radio astronomy. 1960 x).

51. S.Olving: A new method for space charge wave interaction studies. Part II; Trans. Chalmers Univ. of Techn., No. 228, 1960.

52. Papers presented at the fourth international conference on ionization phenomena in gases at Uppsala, August 17-21, 1959. 1960 x).

53. H.Wilhelmsson: Two problems concerning the electron ring current. 1960 x).

54. T.Orhaug: The variation of electron density in the ionosphere during a solar eclipse. 1960 x).

55. H.Wilhelmsson and M.Fischer: On the force-free magnetic fields. 1960 x).

56. O.E.H.Rydbeck: On the coupling between waves in inhomogeneous systems. 1961 x).

57. H.Wilhelmsson: The scattering of an electromagnetic wave by a dielectric-coated metallic cylinder. Reprint from Arkiv för Fysik, Band 23, nr 41 x).

58. H.Wilhelmsson: Accounting for smoothing effects in 21 cm observations. Reprint from Arkiv för Astronomi, Band 3, nr 16 x).

59. B.Höglund: 21 cm Observations in the Galactic Anti-centre. Reprint from Arkiv för Astronomi, Band 3, nr 16 x).

60 H.Gerritsen: Recent Developments in Maser Devices and Materials. Reprint from Applied Optics, Vol. 1, No 1 x)

x) Not published in the Chalmers Transactions.

Research Reports from the Research Laboratory of Electronics:

1. O.E.H.Rydbeck and K.H.B.Wilhelmsson: The influence of the electron velocity distribution on space charge waves. 1959.
2. K.H.B.Wilhelmsson: Oscillatory properties of gyromagnetic electronic cold plasmas with drift motion. 1959.
3. H.B.Hvatum: Solar radio noise measurements during the 1954 solar eclipse. 1959.
4. T.Aa.Orhaug: Ionospheric observations during the solar eclipse June 30, 1954. 1959.
5. K.H.B.Wilhelmsson: The electromagnetic coupling between an electron beam and incident plane waves for an axially finite interaction domain. 1960.
6. Research notes communicated at the radio scientific conference in Stockholm, February 29 - March 2, 1960. 1960.
7. O.E.H.Rydbeck: The propagation and coupling of waves in inhomogeneous media with applications to electromagnetic and space charge waves. (On the propagation of waves in an inhomogeneous medium II).
8. O.E.H.Rydbeck: Electromagnetic and space charge waves in inhomogeneous structures with applications to ionized media and microwave tubes. 1960.
9. K.H.B.Wilhelmsson: On the geometrical theory of diffraction with application to the electron beam. 1960.
10. O.E.H.Rydbeck: The Doppler effect in dispersive, inhomogeneous media with applications to electromagnetic waves in ionized media. 1960.
11. S.Olving and A.Ots: An experimental investigation of the propagation of space charge waves along radially inhomogeneous electron beams. 1960.
12. A.V.Stomberg: The rotatron - an electron tube for shift and multiplication of frequencies. 1960.
13. O.E.H.Rydbeck and M.R.Fischer: Space charge waves in an electron beam of Gaussian cross section. 1960.
14. O.E.H.Rydbeck: The integral equation of travelling wave tubes with electron beams of arbitrary cross section. 1960.
15. O.E.H.Rydbeck and A.R.Thomasson: Low frequency waves in inhomogeneous magneto ionic media. 1960.
16. T.Aa.Orhaug: Observations of radio star scintillations at high latitudes. 1960.
17. T.Aa.Orhaug: Observations of solar radio noise at 150 Mc/s. 1960.
18. O.E.H.Rydbeck and J.Askne: Whistler mode - ionized stream interactions. Part I, 1963.
19. K.H.B.Wilhelmsson: On the problem of overtaking in a velocity distributed electron stream. 1960.
20. O.E.H.Rydbeck: On the coupling between waves in inhomogeneous systems. 1960.
21. O.E.H.Rydbeck: Research in the field of propagation and interaction of electromagnetic waves and space charge type waves in homogeneous and inhomogeneous media. 1960.
22. D.T.Farley, J.P.Dougherty and D.W.Barron: A theory of incoherent scattering of radio waves by a plasma in a uniform magnetic field. 1961.
23. L.F.Eastman: Coherent non-linearities in a mangeto-ionic medium. 1961.
24. D.T.Farley: Artificial heating of the electrons in the F-region of the ionosphere. 1961.
25. K.H.B.Wilhelmsson: Scattering of electromagnetic waves by an anisotropic medium. 1961.
26. K.H.B.Wilhelmsson: The interaction between an obliquely incident plane electromagnetic wave and an electron beam in the presence of a static magnetic field of arbitrary strength. 1961.
27. O.E.H.Rydbeck: Dynamic non-linear wave propagation in ionized media. 1. The isotropic medium. 1961.
28. O.E.H.Rydbeck: Dynamic non-linear wave propagation in ionized media. 2. The magneto-ionic medium. 1962.

29. O.E.H.Rydbeck: Dynamic non-linear wave propagation in ionized media. 3. Electromagnetic non-linear wave interaction and reflection from a plane ionized medium. 1963.

30. O.E.H.Rydbeck: Dynamic non-linear wave propagation in ionized media. 4. Non-linear electromagnetic wave propagation and harmonic radiation in magneto-ionic media. 1963.

31. K.H.B.Wilhelmsson: Dynamic non-linear wave propagation in ionized media. 5. Reflection of electromagnetic waves from an ionized stream in the presence of a high power primary wave. 1962.

32. K.H.B.Wilhelmsson: Dynamic non-linear wave propagation in ionized media. 6. Scattering of electromagnetic waves by an anisotropic medium with an harmonically time-varying dielectric tensor. 1962.

33. O.E.H.Rydbeck: Dynamic non-linear wave propagation in ionized media. 7. Non-linear plasma waves in a streaming homogeneous, cold ionized medium. 1962.

34. A.R.Thomasson: Dynamic non-linear wave propagation in ionized media. 8. Reflection of electromagnetic waves from a dielectric plane layer varying periodically in space and time. 1962.

35. K.H.B.Wilhelmsson: Dynamic non-linear wave propagation in ionized media. 9. A non-linear coupling mechanism for generation of very low frequency waves. 1963.

36. K.H.B.Wilhelmsson: Dynamic non-linear wave propagation in ionized media. 10. Non-linear interaction between an obliquely incident plane electromagnetic wave and an electron beam. 1963.

37. S.Olving: On the non-linear theory of the plane travelling wave tube. 1963.

38. K-O.Yngvesson: Observations of the Venus probe Mariner R-2 at the Onsala Space Observatory. 1963.

39. K.H.B.Wilhelmsson: Dynamic non-linear wave propagation in ionized media. 11. Non-linear excitation of hydromagnetic waves and hybrid resonances by two interacting high power primary waves. 1963.

40. S.Olving and O.Nilsson: Propagation of nonlinear Hahn-Ramo waves along an annular electron current sheath. 1963.

41. S.Olving and M.Fischer: Small-signal nonlinear klystron waves. 1964.

42. S.Olving and S.Wallander: Nonlinear space charge wave theory of the hydrodynamic disc-electron beam. 1964.

43. O.E.H.Rydbeck: Dynamic non-linear wave propagation in ionized media. 12. Electromagnetic wave reflection from an oscillating, collision free magneto-ionic medium. 1964.

44. A.R.Thomasson: Dynamic non-linear wave propagation in ionized media. 13. Microscopic treatment of the interaction between a plane electromagnetic wave and an oscillating medium. 1964.

45. K.H.B.Wilhelmsson: Dynamic non-linear wave propagation in ionized media. 14. Generation of longitudinal plasma waves by non-linear coupling of two high-power circularly polarized transverse waves. 1964.

46. K.H.B.Wilhelmsson and A.R.Thomasson: Dynamic non-linear wave propagation in ionized media. 15. Čerenkov effect in a pre-oscillating medium. 1964.

47. K.H.B.Wilhelmsson: The magneto-ionic theory for mass-anisotropic electrons. 1964.

48. O.E.H.Rydbeck: Research in the field of propagation of high power waves in ionized media. 1964.

49. R.Tangblad: Concentration effects in a maser material. 1964.

50. O.Nilsson: Some frequency and power conversion proper ties of cyclotron waves. 1965.

51. O.Nilsson: Anomalous noise peak in Adler tubes. 1965.

52. B.Geidne: Nonlinear analysis of a microwave beamplasma amplifier. 1965.

53. J.Askne: Stimulated scattering from a semi-infinite dispersive medium periodic in time and space. 1965.

54. S.Yngvesson: Chromium-doped rutile: Maser properties at 1420 Mc/s and application to a traveling-wave maser, 1965.

55. T.M.Srinivasan: Measurements on nonlinear space charge waves, 1965.

56. O.E.H.Rydbeck: Wave coupling in multi-mode. inhomogeneous, ionized media, with applications to electron stream-whistler mode interactions. 1966.

57. P.McIsaac: Wave propagation in a dispersive medium. 1966.

58. S.Wallander: Nonlinear theory of the planar microwave vacuum diode. 1966.

59. S.Wallander: Nonlinear traveling wave tube analysis with two signal frequencies, 1966.

60. O.Nilsson: Approximate theory of the wire helix slow wave structure. 1966.

61. O.E.H.Rydbeck:and Å.Hjalmarson: Coupled wave equations for multi-mode inhomogeneous media. 1966.

62. O.E.H,Rydbeck:and Å.Hjalmarson: Coupled waves in magneto-ionic media. Part I. 1966.

63. J.Askne: Reflection and amplification of electromagnetic waves in an oscillating ionized medium, Part. I. 1966.

64. J.Askne: Instability properties of an ionized medium periodic in time and space.
B.Rönnäng: Transient wave propagation in symmetric, ionized Epstein layers. 1966.

65. J.I.Lindström: Measurements of nonlinearities in a traveling wave tube. 1966.

66. J.Jäderblom: Cyclotron wave amplification using self generated pump power. 1966.

67. O. Nilsson: Nonlinear distortion in traveling wave tubes. 1966.

68. S. Kronlund: Measurements on a beam-plasma microwave amplifier. 1966.

69. P.R. McIsaac: Boundary conditions for ferromagnetic media. 1966

70. B.O. Rönnäng: Transient wave propagation in inhomogeneous ionized media. 1966.

71. S. Olving: Nonlinear microwave tube studies. 1966.

Lecture Notes from the Research Laboratory of Electronics:

1. K.H.B.Wilhelmsson: Lectures on the quantum theory of masers. 1962.

2. D.T.Farley: Lectures on the scattering of radio waves from randomly fluctuating media given 1961 at Chalmers University of Technology, Gothenburg. 1961.

3. A.Elvius: Lectures on galactic dynamics given 1961 at Chalmers University of Technology, Gothenburg. 1961.

4. K.H.B.Wilhelmsson and A.G.Lieberman: Lectures on superconductivity. 1964.

Reprinted from *Electronics Letters*, Vol. 3, No. 7, July 1967

CONDUCTOR ADMITTANCE IN TRANSVERSE TEM FILTERS AND SLOW-WAVE STRUCTURES

The admittance $Y(\phi)$ of a single rectangular conductor in a transverse TEM filter or slow-wave structure can be expressed in a series of mutual interaction terms with the neighbouring conductors and with the surrounding ground planes. The first four interaction terms are computed numerically and yield $Y(\phi)$ with about 1% accuracy.

Consider an array consisting of an infinite number of infinitely long parallel rectangular conductors with equal cross-sections between two ground planes (Fig. 1*a*). A TEM wave travels in the *z* direction. For a constant *z*, the voltages of the conductors are assumed to be $U_0 e^{-jn\phi}$. If i is the current flowing in the reference conductor ($n = 0$, Fig. 1a), we may define the admittance of this conductor as $Y(\phi) = U_0/i$.

A number of authors[1-7] have derived formulas for $Y(\phi)$. Usually space-harmonic analysis of the fields has been used,[2-5] but, to obtain useful analytic expressions, one usually makes the approximation that the field between consecutive conductors is homogeneous,[2-4] leading to serious errors in $Y(\phi)$, especially for low values of ϕ. An exact analytic expression, however, has been found by Kovalenko and Kovalenko.[6] The formulas for $Y(\phi)$ derived from space-harmonic analysis are, however, relatively complicated analytic expressions, and consequently difficult to use in practical-filter and slow-wave-structure design.

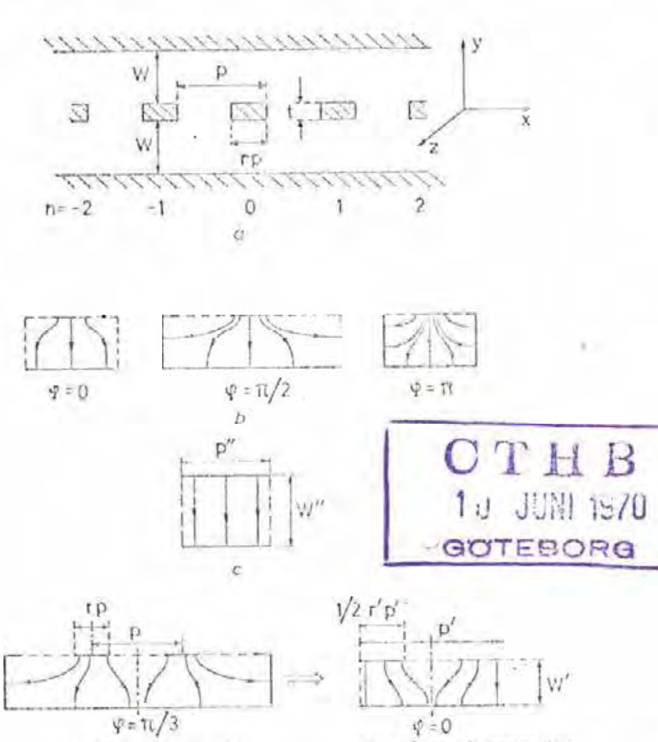

Fig. 1

a Cross-section of the array
b Symmetry properties of the electric field for $\phi = 0$, $\pi/2$ and π
c Simplified geometry for $\phi = 0$, $\pi/2$ and π, derived from the Schwarz–Christoffel transformation
d Symmetry properties of the electric field for $\phi = \pi/3$

Leblond and Mourier[1] have derived $Y(\phi)$, making use of the capacitance per unit length from the reference conductor to earth and to the other conductors. They arrived at a very useful expression for $Y(\phi)$:

$$Y(\phi) = 2y_{00} + 4\sum_{n=1}^{\infty} y_{0n} \sin^2\left(\frac{n\phi}{2}\right) \quad . \quad . \quad . \quad . \quad . \quad (1)$$

where the y_{0n} are the mutual admittances to the ground planes (y_{00}) and to the neighbouring conductors (y_{0n}, $n \neq 0$), respectively. Leblond and Mourier retained only two terms in the expression (y_{00} and y_{01}) and used very approximate values for these. The purpose of this letter is to derive accurate values for y_{00}, y_{01}, y_{02} and y_{03}. The method used is an extension of a previous publication by the author.[8]

First let $t = 0$ in Fig. 1*a*; i.e. we restrict the problem to infinitely thin conductors. For $t = 0$ and $r = 0{\cdot}5$, Harris *et al.*[9] and Chen[5] have given graphs showing $Y(0)$, $Y(\pi/2)$ and $Y(\pi)$ against W/p (Fig. 1*a*), which were derived using conformal mapping techniques.[9] This is possible since, for $\phi = 0$, $\pi/2$ and π, the field solution must have certain simple symmetry properties as shown in Fig. 1*b*. Using the Swarz–Christoffel transformation, the geometries of Fig. 1*b* may be transformed to the simpler geometry of Fig. 1*c*, for which the characteristic admittance is $(p''/W'')Y_0$. Here Y_0 is the admittance of free space.

It has been possible to derive the admittance for $\phi = \pi/3$ as well, using a similar technique. The field for $\phi = \pi/3$ satisfies the simple and symmetric boundary conditions of Fig. 1*d*. This geometry may be transformed using the Schwarz–Christoffel transformation, as illustrated in Fig. 1*d*. The new geometry is equivalent to the case $\phi = 0$, where the original r, W and p are changed to r', W' and p', respectively.

From eqn. 1, one obtains, using $Y(\phi)$ for $\phi = 0$, $\pi/3$, $\pi/2$, $\pi/2$ and π, respectively,

$$2y_{00} = Y(0) \quad . \quad . \quad . \quad . \quad . \quad . \quad . \quad . \quad . \quad . \quad (2a)$$

$$4y_{01} = Y(\pi) - Y(0) - 4y_{03}^0 - \Sigma_1 \quad . \quad . \quad . \quad . \quad (2b)$$

$$4y_{02} = Y\left(\frac{\pi}{2}\right) - \tfrac{1}{2}\{Y(\pi) + Y(0)\} - \Sigma_2 \quad . \quad . \quad (2c)$$

$$4y_{03} = \tfrac{1}{6}\left\{Y(\pi) + 8Y\left(\frac{\pi}{3}\right) - 6Y\left(\frac{\pi}{2}\right) - 3Y(0)\right\} - \Sigma_3 \quad . \quad . \quad . \quad . \quad (2d)$$

where $4y_{03}^0 = 4y_{03} + \Sigma_3$, and

$$\Sigma_1 = 4(-y_{04} + y_{05} + y_{06} + y_{07} - y_{08} + \ldots) \quad . \quad (3a)$$

$$\Sigma_2 = 4(y_{06} + y_{010} + y_{014} + \ldots) \quad . \quad . \quad . \quad (3b)$$

$$\Sigma_3 = 4(y_{04} - y_{06} + y_{08} + y_{09} + \ldots) \quad . \quad . \quad (3c)$$

For $W/p \to \infty$ and $r = 0{\cdot}5$, Butcher[7] has derived an exact formula for $Y(\phi)$, which may be expressed as a Fourier series:

$$\frac{Y(\phi)}{Y_0} = 4\sin\left(\frac{\phi}{2}\right) = \sum_{n=1}^{\infty} \frac{32}{\pi}\, \frac{1}{4n^2 - 1} \sin^2\left(\frac{n\phi}{2}\right) \quad (4)$$

$Y(0)$, $Y(\pi/2)$ and $Y(\pi)$ for $r = 0{\cdot}25$, $0{\cdot}5$ and $0{\cdot}75$ and for various W/p have previously been computed and tabulated by the author.[8] Using the method discussed above, $Y(\pi/3)$ for $r = 0{\cdot}5$ has now also been derived and is presented in Table 1. Hence $4y_{00}$, $4y_{01}^0 = 4y_{01} + \Sigma_1$, $4y_{02}^0 = 4y_{02} + \Sigma_2$ and $4y_{03}^0 = 4y_{03} + \Sigma_3$ can be calculated using eqn. 2. The results are presented in Table 1. For $W/p \to \infty$, Σ_1, Σ_2 and Σ_3 are easily computed from eqn. 4.

In order to evaluate Σ_1, Σ_2 and Σ_3 for finite W/p, an estimate must be made for the general behaviour of y_{0n} as W/p decreases. Table 1 shows that the computed y_{01}^0, y_{02}^0 and y_{03}^0 give decreasing values of the ratio

$$\frac{(y_{0n}^0)_{W/p=2}}{(y_{0n})_{W/p\to\infty}}$$

as n increases. Physically this is expected, since higher-order interactions decrease owing to screening by the ground planes. Thus, the higher is n, the faster y_{0n} decreases with W/p. The entries for Σ_1, Σ_2 and Σ_3 in Table 1 have been obtained in this way.

For $r = 0{\cdot}25$ and $0{\cdot}75$, $4y_{03}^0$ has not been computed. It is seen that $4y_{02}$ is almost independent of r, however, and it is assumed that $4y_{03}$ and the Σ's behave in a similar manner.

When $t \neq 0$ there is an increased interaction, mainly owing to the nearest-neighbour conductors. Hence one may add to $4y_{01}$ a term

$$4y_t = \alpha\,\frac{4t}{(1-r)p}\,Y_0$$

where $\alpha = 1$ if the field is completely homogeneous in the region between the strips.

Cruzan and Garver[10] have computed the admittance for rectangular transmission lines, which is equivalent to $Y(\pi)$

Table 1

$\frac{W}{p}$	$\frac{Y(\pi/3)}{Y_0}$	$3y_{00}/Y_0$ $r=0·25$	$r=0·5$	$r=0·75$	$4y_{01}^0/Y_0$ $r=0·25$	$r=0·5$	$r=0·75$
0·357	—	3·055	4·30	5·22	0·17	0·55	1·75
0·426	—	2·75	3·74	4·45	0·30	0·80	2·14
0·500	—	2·49	3·28	3·80	0·44	1·06	2·51
0·587	—	2·24	2·86	3·27	0·60	1·33	2·88
0·700	—	1·990	2·47	2·76	0·79	1·62	3·24
0·867	—	1·702	2·045	2·240	1·043	1·99	3·67
1·000	2·370	1·533	1·800	1·951	1·209	2·22	3·93
1·200	2·273	1·329	1·528	1·631	1·385	2·464	4·25
1·400	2·174	1·172	1·323	1·402	1·530	2·653	4·45
1·600	2·114	1·050	1·170	1·230	1·630	2·785	4·60
1·800	2·075	0·950	1·048	1·096	1·710	2·883	4·72
2·000	2·049	0·867	0·949	0·986	1·780	2·967	4·81
∞	2·000	0	0	0	—	3·397*	—

$\frac{W}{p}$	$4y_{02}^0/Y_0$ $r=0·25$	$r=0·5$	$r=0·75$	$\frac{4y_{03}^0}{Y_0}$	$\frac{\Sigma_1}{Y_0}$	$\frac{\Sigma_2}{Y_0}$	$\frac{\Sigma_3}{Y_0}$
0·357	—	—	—	—	—	—	—
0·426	—	—	—	—	—	—	—
0·500	—	—	—	—	—	—	—
0·587	0·010	0·010	0·010	—	—	—	—
0·700	0·025	0·025	0·025	—	—	—	—
0·867	0·063	0·070	0·070	—	—	—	—
1·000	0 90	0·100	0·110	—	—	—	—
1·200	0·140	0·161	0·170	0·008	—	—	—
1·400	0·185	0·219	0·220	0·024	—	—	—
1·600	0·230	0·270	0·275	0·045	—	—	—
1·800	0·265	0·316	0·325	0·069	—	—	0·01
2·000	0·300	0·366	0·370	0·084	≃0·01	≃0·01	≃0·02
∞	—	0·679*	—	0·292*	0·095	0·150	0·213

* y_{0n} according to eqn. 4

in our notation. Hence $4y_t = [Y(\pi)]_{t\neq 0} - [Y(\pi)]_{t=0}$ and α may be determined. In Fig. 2, α is plotted against $2t/(1-r)p$.

It is concluded that, for $t = 0$, the method used in this letter yields numerical expressions for $Y(\phi)$ when $W/p < 2$ and $r = 0·25$, 0·5 and 0·75, with an error of about 1%. For $t \neq 0$ the error is probably slightly larger.

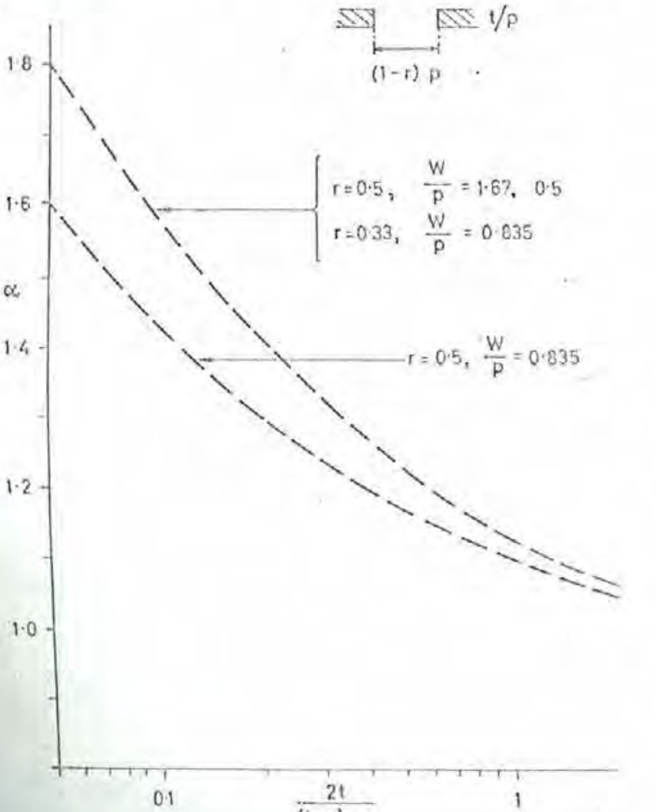

Fig. 2 *α as a function of the conductor thickness t for various geometrical configurations*

The analysis presented here has been used by the author in a slow-wave-structure design for travelling-wave masers[8, 11] with considerable success.

The author is grateful to T. Cato and B. Holmberg for much help with the computations and to O. E. H. Rydbeck for untiring support.

E. KOLLBERG

26th May 1967

Research Laboratory of Electronics
Chalmers University of Technology
Gothenburg, Sweden

References

1 LEBLOND, A., and MOURIER, G.: 'Étude des lignes à barraux à structures periodique pour tubes electronique U.H.F.', *Ann. Radioélect.*, 1954, 9, pp. 311–328

2 FLETCHER, R. C.: 'A broad-band interdigital circuit for use in travelling-wave-type amplifiers', *Proc. Inst. Radio Engrs.*, 1952, 40, pp. 951–958

3 WALLING, J. C.: 'Interdigital and other slow-wave structures', *J. Electronics Control*, 1957, 3, pp. 239–258

4 HADDAD, G. I.: 'Characteristics of dielectrically loaded ladder lines for travelling-wave masers and other applications', *IEEE Trans.*, 1966, MTT-14, pp. 120–129

5 CHEN, F. S.: 'The comb-type slow-wave structure for TWM applications', *Bell Syst. Tech. J.*, 1964, 43, pp. 1035–1066

6 KOVALENKO, S., and KOVALENKO, V. S.: 'The theory of a maser delay system', *Radio Engng. Electronic Phys.*, 1963, 8, pp. 1327–1336

7 BUTCHER, P. N.: 'The coupling impedance of tape structures', *Proc. Inst. Elect. Electronics Engrs.*, 1957, 104B, pp. 177–189

8 KOLLBERG, E. L.: 'A dielectrically loaded slow-wave structure for travelling-wave maser applications', Research Report 72, Research Laboratory of Electronics, Chalmers University of Technology, Gothenburg, Sweden, 1966

9 HARRIS, S., DE GRASSE, R. W., and SCHULZ-DU-BOIS, E. O.: 'Cut-off frequencies of the dielectrically loaded comb-structure as used in travelling-wave masers', *Bell Syst. Tech. J.*, 1964, 43, pp. 437–484

10 CRUZAN, O. R., and GARVER, R. V.: 'Characteristic impedance of rectangular transmission lines', *IEEE Trans.*, 1964, MTT-12, pp. 488–495

11 KOLLBERG, E. L., and YNGVESSON, K. S.: 'An L-band rutile travelling wave maser' *In* '6th international conference on microwave and optical generation and amplification', IEE Conf. Publ., 1966, (27), pp. 384–388

MEASUREMENTS OF NOISE IN TRAVELING WAVE MASER SYSTEMS, THEORY AND EXPERIMENTS

BY

E.L. KOLLBERG

RESEARCH REPORT NO 95

1969

RESEARCH LABORATORY OF ELECTRONICS

CHALMERS UNIVERSITY OF TECHNOLOGY

GIBRALTARGATAN 5 G

GOTHENBURG S, SWEDEN

Research Laboratory of Electronics
CHALMERS UNIVERSITY OF TECHNOLOGY
Gothenburg, Sweden

RESEARCH REPORT No. 95

MEASUREMENTS OF NOISE IN TRAVELING WAVE MASER SYSTEMS, THEORY AND EXPERIMENTS

By

E. L. KOLLBERG

Gothenburg, April 1969

TABLE OF CONTENTS

1. Introduction and summary

2. General discussion of the transmission line noise in a TWM-system.

   2.1. Introduction

   2.2. Calculation of the noise power waves on a transmission line between two mismatched terminations.

   2.3. Power flow per mode.

   2.4. The equivalent noise temperature (T_t) of a lossy transmission line with discontinuities.

   2.5. The equivalent noise temperature of a TWM receiving system.

3. Common methods for noise temperature measurements.

   3.1. Introduction

   3.2. The HOT-COLD-body technique (HC-technique)

   3.3. The Tabor and Sibilia method.

4. Additional methods

   4.1. Introduction

   4.2. The second stage amplifier noise contribution

   4.3. Determination of T_t by "SHOP-technique".

5. Experimental results

   5.1. Introduction

   5.2. Description of the experiments

   5.3. Numerical results

6. Acknowledgements

Appendix A: Properties of a lossy transmission line section between two lossless reciprocal coupling two ports.

Appendix B: Properties of a lossy transmission line with an arbitrary number of lossless reciprocal discontinuities.

Appendix C: The noise power from a lossy transmission line section between two lossless discontinuities.

1. INTRODUCTION AND SUMMARY

During the development of a very low noise traveling wave maser system for the Onsala 25.6 m radio telescope [1, 2], we found it necessary to measure the noise properties of the system. Since the noise contribution from the amplifier itself can be computed with high accuracy from wellknown formulas (see e.g. Siegman ref. [3], page 397) our laboratory investigations were concentrated on measurements of the noise contribution from the input transmission line and from the second stage amplifier.

Early measurements with conventional methods (see e.g. Kraus ref. [4]) gave peculiar results which could not be trusted as a true measure of the noise contribution from the input transmission line. It was readily realized that this phenomenon was due to mismatches in the system [5, 6]. A theory that was independently developed and is described in the text, has made it possible to propose and analyse a new and simple method for fast and fairly reliable measurements of the input line noise temperature (see also various articles in ref. [11]). In the measurements only standard microwave components were used and the result turned out to be accurate within one degree Kelvin.

The fundamental discussion (chapter 2) of the noise generation in a transmission line system containing lossless discontinuities is in its principles similar to the one published by K. Fischer and A. Ziermann (1967, ref. [7]). However, the details in our theory are different, allowing for a correct treatment of a transmission line with the temperature and the losses varying along the line (compare C.T. Stelzried, 1965, ref. [8]). Furthermore, the theory distinguishes between losses due to the currents (ohmic losses) and losses due to the voltages (dielectric losses). To illustrate this, consider a traveling wave maser input transmission line terminated with a short circuit or with an open circuit. Evidently, the ohmic losses of the part at room temperature play a more important role when the short circuit is connected, while the dielectric losses of the room temperature part will be more important when the open circuit is connected. As far as the present author knows these effects have been neglected in the literature, probably because fairly well matched transmission lines have been discussed in most articles on noise in transmission lines.

We have succeeded in deriving (section 2.4) a very simple expression for the noise temperature from a transmission line containing more than two loss-less discontinuities. Let us here consider the special case, when

a) the attenuation "L" per transmission line section is homogeneous along the line and small in the sense that $L = e^{-2\theta} \approx 1 - 2\theta$

b) all parts of the transmission line have a constant temperature T_o,

c) at each discontinuity, the reflection coefficient Γ is small in the sence that $(1 - |\Gamma|^2)/(1 - |\Gamma|^2 e^{-2\theta}) \approx 1$

In this case, the equivalent input noise temperature of the transmission line can be expressed in the following simple way:

$$T_t \approx T_o \sum_{n=1}^{N} (1 - \frac{1}{L_n}) \frac{1 + |\Gamma_{na}|^2}{1 - |\Gamma_{na}|^2} \qquad (1.1)$$

where L_n is the attenuation of the line segment between the n-th and (n+1)-th discontinuity, counted from the antenna primary feed, and Γ_{na} is the reflection coefficient towards the antenna at the n-th discontinuity (see Fig. 2.2). Consider, for instance, the case $|\Gamma_{na}| = 0.3$ (SWR = 1,5). This will cause a 20 % increase in the noise contribution from the n-th line segment.

Chapter 2 is closed by a careful definition of the equivalent noise temperature of a TWM-system.

A few words ought to be said about the definition of the system noise temperature. According to eqn. (1.1) the noise temperature of the input transmission line is dependent on the reflection properties of the terminating load (e.g. the antenna). The system noise temperature will therefore be defined for a selected terminating load (e.g. the antenna) in such a way that a mismatch in the terminating load is referenced to the amplifier system. In practice, this is convenient since it might be very difficult to separate the mismatch of the input transmission line connector and the mismatch of the terminating load.

In chapter 3 two different well-known methods to measure the noise temperature of a TWM-system are discussed in the light of the theoretical treatment of chapter 2. The most common one, the HOT-COLD body technique is shown to give an err neous value of the noise temperature, if different reflection coefficients Γ_C and Γ_H are seen when looking into the cold ($T = T_C$ ^oK) and hot ($T = T_H$ ^oK) terminations respectively (see Fig. 3.1 and compare eqn. (1.1)). Let Γ_t be the reflection coefficient of the maser system, Y_{HC} the Y-factor measured and T_t the noise temperature of the transmission line. For the special case, when there are only two discontinuites, one at the terminating load and another at the amplifier input, we obtain a maximum error of

$$\delta T \approx \pm \frac{2Y_{HC}}{Y_{HC}-1} \; |\Gamma_t| \, |\Gamma_C - \Gamma_H| \, (T_C + T_t) \tag{1.2}$$

The system noise temperature is referenced to the hot termination in this particular case.

The theory of HOT-COLD body measurements has been discussed by a number of other authors (ref. [5], [6], [11], [12]). Their results are not directly applicable to a low noise TWM-system, however, and it is believed that a correct theoretical treatment for this case is published for the first time in the present article.

Another wellknown method for noise temperature measurements on TWM amplifiers was first proposed by W.J. Tabor and J.T. Sibilia [9]. This method, and a modification proposed and used by V.B. Shteinshleiger et. al [10] is theoretically analysed in section 3.3. As far as the present author knows no such analysis has been published earlier. Some approximations involved in these methods, eventually causing serious errors, are pointed out. Furthermore, errors due to the fact that the noise power generated by the current standing waves is different from the noise power generated by voltage standing waves, seems to have been completely overlooked.

In the Tabor and Sibilia method one measures the output noise power from a TWM amplifier, when a movable short circuit is connected to the input. Since we found that the stability of the commersially available movable short circuits frequently are not particularly good, a new method was developed in which we use a fixed open circuit and a fixed short circuit. This method, referred to as the "SHOP-technique", is analysed theoretically in chapter 4.

A new simple method for measurements of the second stage amplifier noise contribution is also discussed in chapter 4. The TWM input is connected to a room-temperature (290°K) matched termination, and the ratio Y_x of the detected noise power with the maser gain maximum to the noise power with no maser gain (no microwave pump power) is measured. Then the noise temperature contribution from the second stage amplifier referred to the TWM input is simply

$$T_{sec.\,amp} = \frac{290 + T_{maser}}{Y_x - 1} \qquad ({}^{\circ}K)$$

This method is very useful when one operates a TWM at temperatures lower than 4.2°K, since one only has to decrease the temperature, i.e. increase the maser gain, until $T_{sec.\,amp.}$ is low enough (usually much smaller than T_{maser}).

In chapter 5 an experimental set up for measuring the [illegible]e temperature of a TWM-system with the SHOP-technique is theoretically analysed. Experimental results obtained with the SHOP-technique and the HOT-COLD-body technique on two TWM:s for the frequency ranges 2.8-3.2 GHz and 3.2-3.7 GHz are presented and discussed.

The noise temperature of the two masers was determined for 12 and 16 frequencies respectively. The 2.8-3.2 GHz maser yielded measured noise temperatures between 6.2 and 3.5 $^{\circ}$K with a mean of 4.9 $^{\circ}$K, while the 3.2 - 3.7 GHz maser yielded measured noise temperatures between 6.7 and 3.5 $^{\circ}$K with a mean of 5.3 $^{\circ}$K. Hence we concluded the equivalent noise temperature of the input line to be $5.0 \pm 1^{\circ}$K. The HC-body measurements yielded noise temperatures of the transmission line between $+12^{\circ}$K and -1.5°K, with a mean of 5.8°K.

The scatter in the measured noise temperatures is explained mainly by errors in the attenuator and errors due to the experimentor, by instabilities in the postamplifiers, the TWM gain, in the open circuit and in the short circuit terminations. A part of the error is probably also due to shortcomings in the theory, as mentioned later in the text.

However, the scatter of the measured noise temperatures indicate that the SHOP-technique is superior to the HC-body technique, using a hot load temperature equal to 373 $^{\circ}$K and the cold load temperature equal to 77 $^{\circ}$K.

2. GENERAL DISCUSSION OF THE TRANSMISSION LINE NOISE IN A TWM-SYSTEM

2.1. Introduction

The main sources of noise generation in a traveling wave maser system are the losses in the transmission line sections between the antenna and the amplifier unit itself. Hence, the emphasis in this chapter is laid upon the theory of noise generation in transmission lines containing several lossless discontinuities scattering the waves. The theoretical treatment makes use of a wave concept for the noise power generated in a transmission line, and is in its main features similar to that of Fisher and Zimmermann [7]. In addition, however, it contains a more detailed analysis of inhomogeneous transmission lines where noise generation related to the currents and to the voltages, respectively, are separated.

To illustrate the theory, the power flow "per mode" is calculated for a transmission line terminated by an open circuit (or a short circuit). The result is shown to be in agreement with that obtained from stastical quantum mechanical considerations.

In practice the theory has been very useful since it gives a simple and powerful method for the analysis of almost any practical problem concerning noise generation in transmission lines.

2.2. Calculation of the noise power waves on a transmission line between two mismatched terminations.

In Fig. 2.1. a lossy, homogeneous transmission line is shown. Both ends of the line are connected to mismatched terminations.

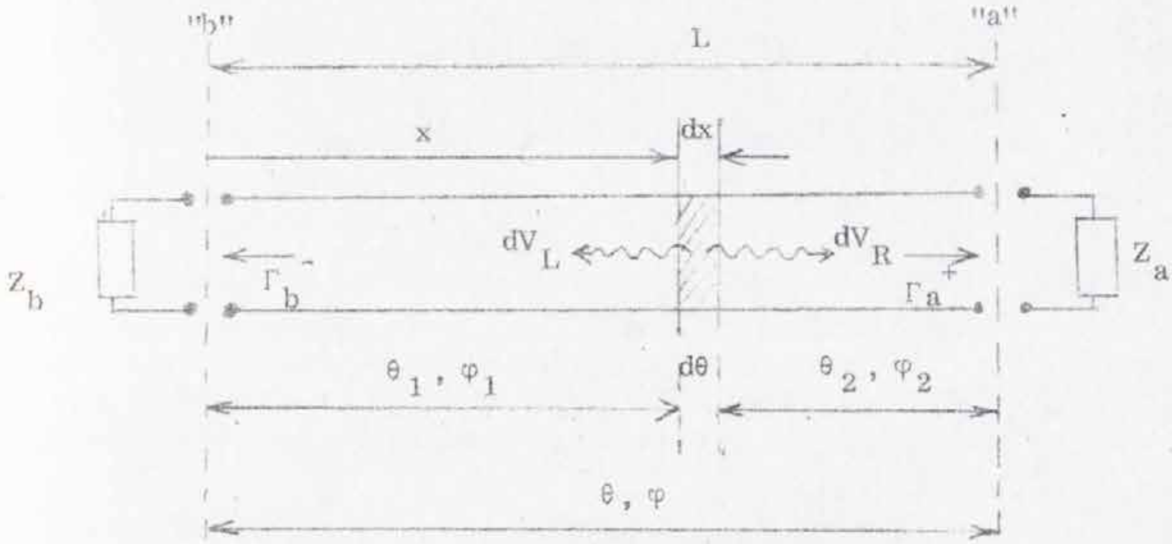

θ_1, θ_2 (nepers) attenuation of the line elements x and L - x respectively

$\theta = \theta_1 + \theta_2$

φ_1, φ_2 (radians) phase shift of the line elements x and L - x respectively

$\varphi = \varphi_1 + \varphi_2$

T (x) (^{o}K) physical temperature at x

Γ_b^-, Γ_a^+ voltage reflection coefficient

Fig. 2.1. A transmission line section terminated in both ends with mismatched loads.

In the line interval dx "noise-waves" traveling to the right and to the left are generated. These waves are completely un-correlated. If we are considering a narrow frequency band Δf, the "noise-waves" may approximately be considered as coherent waves. The complex amplitude of the "noise wave" traveling to the right is denoted by dV_R and that of the one traveling to the left by dV_L. Using common transmission line theory, we can write the associated average noise power as

$$dP_R = d\,P_L = \frac{1}{2}\,\mathrm{Re}\left\{dV_R \cdot dV_r^* \cdot Y_o\right\} = \frac{1}{2}\,\mathrm{Re}\left\{dV_L \cdot dV_L^* \cdot Y_o\right\} \tag{2.1}$$

where Y_o is the complex admittance of the transmission line. Furthermore

$$dP_R = dP_L = k\,T(x)\;2\,\alpha(x)\;dx\;\Delta f \tag{2.2}$$

where k is Boltzmann's constant, T(x) the physical temperature, $\alpha(x)$ the attenuation constant of the transmission line at x. From equation (2. 1) and (2. 2) one readily obtains

$$\left|dV_R\right|^2 \mathrm{Re}\left\{Y_o\right\} = \left|dV_L\right|^2\; \mathrm{Re}\left\{Y_o\right\} = 4\,k\,T(x)\cdot\alpha(x)\;dx\,\Delta f \tag{2.3}$$

At the right end ("a", Fig. 2. 1) the average noise power traveling towards "a" is

$$dP_a = \frac{1}{2}\;\mathrm{Re}\left\{(d\,V_{aR} + dV_{aL})(dV_{aR}^* + dV_{aL}^*)\;Y_o\right\} \tag{2.4}$$

where dV_{aR} and dV_{aL} are the voltage amplitudes of the traveling wave related to dV_R and dV_L respectively. Since dV_{aR} and dV_{aL} also are uncorrelated, we obtain from eqn. (2. 4)

$$dP_a = \frac{1}{2}\,(\left|dV_{aR}\right|^2 + \left|d\,V_{aL}\right|^2)\;\mathrm{Re}\left\{Y_o\right\} \tag{2.5}$$

In this connection a few words should be said about our formalism. It is everywhere assumed that the characteristic admittance of the different line sections are equal. If the characteristic admittances are different, the wave amplitudes are also different for the same power flow. This problem is easily solved by normalizing the wave amplitudes by $\sqrt{\mathrm{Re}\left\{Y_o\right\}}$ (see eqn. (2.3) and (2.5)). This "power wave concept" was first introduced by Penfield [14], and is elegantly discussed by Kurakawa [15].

In the subsequent, however, we will use the usual voltage wave and current wave concept. Since all important formulas will be expressed by using the reflection coefficient (Γ), they are directly applicable to power waves and no attention must be paid to the characteristic admittance of different transmission line sections involved.

Since we in our approximation are treating the noise waves at a certain frequency as a coherent wave, we may consider the element dx to be continuosly transmitting a wave with the output voltage amplitude equal to dV_R. Hence the voltage wave traveling towards "a" becomes at "a":

$$dV_{aR} = dV_R\, e^{-j\varphi_2 - \theta_2} + dV_R\, e^{-j\varphi_2 - \theta_2}\Gamma_a^{\,+}\Gamma_b^{\,-}\, e^{-j2\varphi - 2\theta} +$$

$$+ dV_R\, e^{-j\varphi_2 - \theta_2}\left(\Gamma_a^{\,+}\Gamma_b^{\,-}\, e^{-j2\varphi - 2\theta}\right)^2 + \ldots =$$

$$= \frac{dV_R\, e^{-j\varphi_2 - \theta_2}}{1 - \Gamma_a^{\,+}\Gamma_b^{\,-}\, e^{-j2\varphi - 2\theta}} \tag{2.6}$$

Similarly, dV_L causes a wave traveling towards "a" at "a",

$$dV_{aL} = \frac{dV_L\, \Gamma_b^{\,-}\, e^{-j(\varphi_1 + \varphi) - (\theta_1 + \theta)}}{1 - \Gamma_a^{\,+}\Gamma_b^{\,-}\, e^{-j2\varphi - 2\theta}} \tag{2.7}$$

Using eqn:s (2.5) and (2.3) together with (2.6) and (2.7) we obtain

$$dP_a = \frac{e^{-2\theta_2} + |\Gamma_b^-|^2 e^{-2(\theta_1 + \theta)}}{|1 - \Gamma_a^+ \Gamma_b^- e^{-j2\varphi - 2\theta}|^2} \, k\,T(x) \cdot 2\,\alpha(x)\,dx\,\Delta f \tag{2.8}$$

Since there is no correlation between the noise emitted by different elements dx, the total noise power at "a" traveling to the right, is easily obtained by integration of eqn. (2.8).

$$P_a = \frac{T_a + T_b\,|\Gamma_b^-|^2 e^{-2\theta}}{|1 - \Gamma_a^+ \Gamma_b^- e^{-j2\varphi - 2\theta}|^2} \cdot k\,\Delta f \tag{2.9}$$

where

$$T_a = \int_0^L 2\,\alpha(x)\,T(x)\,e^{-2\theta_2(x)}\,dx \tag{2.10}$$

$$T_b = \int_0^L 2\,\alpha(x)\,T(x)\,e^{-2\theta_1(x)}\,dx \tag{2.11}$$

$$\theta_2(x) = \int_x^L \alpha(x)\,dx \tag{2.12}$$

$$\theta_1(x) = \int_0^x \alpha(x)\,dx \tag{2.13}$$

and as a matter of fact, $\alpha(x)$ and $T(x)$ are constant for a homogeneous transmission line. Hence $T(x) = T_0$ yields

$$T_a = T_b = T_0\,(1 - e^{-2\theta}) \tag{2.14}$$

and eqn. (2.9) becomes identical to eqn. (C.5) in Appendix C, derived from thermodynamic considerations. This fact is a proof for dV_R and dV_L being completely uncorrelated (see also K. Fisher, 1967, ref. [7]).

The noise power delivered to the load Z_a becomes:

$$P_{na} = (1 - |\Gamma_a^+|^2)\, P_a =$$

$$= \frac{1 - |\Gamma_a^+|^2}{|1 - \Gamma_a^+ \Gamma_b^- e^{-j2\varphi - 2\theta}|^2} (T_a + T_b |\Gamma_b^-|^2 e^{-2\theta})\, k\,\Delta f \qquad (2.15)$$

In this section we have so far treated our problem as if the interaction between the lossy material of the transmission line and the electromagnetic field was constant throughout the line, i.e. dV_R and dV_L were assumed to be independent of x. However, since standing waves are created due to the reflections at the ends of the transmission line, we will for example expect less ohmic losses in the current nodes than in the current antinodes. Hence we will get modified expressions for T_a and T_b in eqn. (2.10) and (2.11).

Furthermore the attenuation constants θ, θ_1 (x) and θ_2 (x) will be different when dV_{aR} and dV_{aL} are calculated from eqn. (2.6) and (2.7), since the standing wave pattern and hence the power dissipation of the two modes are not quite alike. However, since the attenuation is small in most low noise applications, this difference is neglected in the following text (see eqn. (2.16) and (2.17)).

It is also necessary to discriminate between losses due to the currents (i) (ohmic losses) and the H-field, α_i (x) on one hand and losses due to voltages (v) and the E-field, α_v (x) on the other hand. We will introduce a filling-factor concept as discussed for example on page 253 in Siegmans book [3] .

The interaction between the electromagnetic field and the waveguide material is proportional to the field amplitude squared. Let $\alpha_i(x)$ and $\alpha_v(x)$ be defined in such a way that the losses are related to $(i)^2$ and $(v)^2$ respectively and that no attention has to be paid to the details in the H- and E-fields. The amplitude at x of the standing wave related to the voltage wave primarily emitted to the right becomes (see eqn. (2.6)):

$$dV_{SR}(x) = \frac{dV_R}{1 - \Gamma_a^+ \Gamma_b^- e^{-j2\varphi - 2\theta}} \left(1 + \Gamma_a^+ e^{-j2\varphi_2 - 2\theta_2}\right)$$

Hence, at a certain point x the interaction is modified through a multiplication by the following energy density ratio:

$$\frac{|dV_{SR}(x)|^2}{\frac{1}{L}\cdot\int_0^L |dV_{SR}(x)|^2\,dx} = \frac{\left|1 + \Gamma_a^+ e^{-j2\varphi_2 - 2\theta_2}\right|^2}{\frac{1}{L}\cdot\int_0^L \left|1 + \Gamma_a^+ e^{-j2\varphi_2 - 2\theta_2}\right|^2 dx}$$

Realizing that for the current $\Gamma \rightarrow -\Gamma$, we may now write down the modified T_a and T_b:

$$T'_a = \int_0^L 2\,T(x)\,e^{-2\theta_2(x)}\left\{\frac{\left|1 + \Gamma_a^+ e^{-j2\varphi_2 - 2\theta_2}\right|^2}{\frac{1}{L}\int_0^L \left|1 + \Gamma_a^+ e^{-j2\varphi_2 - 2\theta_2}\right|^2 dx}\,\alpha_v(x) + \frac{\left|1 - \Gamma_a^+ e^{-j2\varphi_2 - 2\theta_2}\right|^2}{\frac{1}{L}\int_0^L \left|1 - \Gamma_a^+ e^{-j2\varphi_2 - 2\theta_2}\right|^2 dx}\,\alpha_i(x)\right\} dx$$

(2.16)

$$T'_b = \int_0^L 2\,T(x)\,e^{-2\theta_1(x)}\left\{\frac{\left|1 + \Gamma_b^- e^{-j2\varphi_1 - 2\theta_1}\right|^2}{\frac{1}{L}\int_0^L \left|1 + \Gamma_b^- e^{-j2\varphi_1 - 2\theta_1}\right|^2 dx}\,\alpha_v(x) + \frac{\left|1 - \Gamma_b^- e^{-j2\varphi_1 - 2\theta_1}\right|^2}{\frac{1}{L}\int_0^L \left|1 - \Gamma_b^- e^{-j2\varphi_1 - 2\theta_1}\right|^2 dx}\,\alpha_i(x)\right\} dx$$

(2.17)

The fact that θ_1 and θ_2 differ in equation (2.16) and (2.17), as was mentioned before, can evidently be neglected when $2\theta \ll 1$.

It is most interesting to observe that T'_a is not dependent on Γ_b^- and T'_b not dependent on Γ_a^+.

Furthermore $T'_a \rightarrow T_a$ and $T'_b \rightarrow T_b$ for the following special cases

a) $\Gamma_a = \Gamma_b \rightarrow 0$

b) $T(x) = T_o = \text{const}$

$\alpha_v(x) = \text{const}$

$\alpha_i(x) = \text{const}$

$2\,\theta_1\,(x) = 2\,\theta_2\,(x) \to 0$

case a) is selfevident. Case b), however, is true in such practical cases as when one has a homogeneous, low loss transmission line at room temperature.

In the following text we will use the notations T_a and T_b instead of T_a' and T_b' unless otherwise is notified.

2. 3. Power flow per mode

The transmission line including the two discontinuities at "a" and "b" forms an interaction circuit between the electromagnetic field and the lossy material within the transmission line. It is interesting to examine the noise power say at "a" traveling towards "a" when $|\Gamma_b| = |\Gamma_a| = 1$.

$$P_a = k\,T_o\,\Delta f\;\frac{(1-e^{-2\,\theta})\,(1+e^{-2\theta})}{1+e^{-4\theta}-2\,e^{-2\,\theta}\cos 2\,\varphi'} \qquad (2.\,18)$$

For resonance, i.e.

$\varphi' = n\,\pi$

$$P_a = k\,T_o\,\Delta f\,\coth\;\;2\,\theta \qquad (2.\,19)$$

Hence for a small attenuation constant θ i.e. in a high Q resonator, the noise power per frequency interval becomes appreciable.

It is also of some interest to derive the total noise power within one mode defined by

$$(n-\frac{1}{2})\,\pi \leq \varphi \leq (n+\frac{1}{2})\;\pi \qquad (2.\,20)$$

which corresponds to a frequency interval Δf_m in a nondispersive transmission line

$$\Delta f_m = \frac{2c_o}{L} \tag{2.21}$$

one obtains

$$\int_{\Delta f_m} P_a \, df = k\,T_o \cdot \Delta f_m \tag{2.22}$$

in accordance with what is obtained the result for the energy flow per mode using statistical quantum mechanical considerations [3] .

2.4. The equivalent noise temperature (T_t) of a lossy transmission line with discontinuities

Fig. 2.2 schematically shows a transmission line, consisting of N sections and N + 1 discontinuities, connected between the antenna (Z_ℓ) and the receiver. Each section has an attenuation θ_n neper and an electrical length of φ_n radians. The reflection coefficient seen from the line section n towards the receiver is Γ_{nr} and towards the antenna $\Gamma_{n\ell}$.

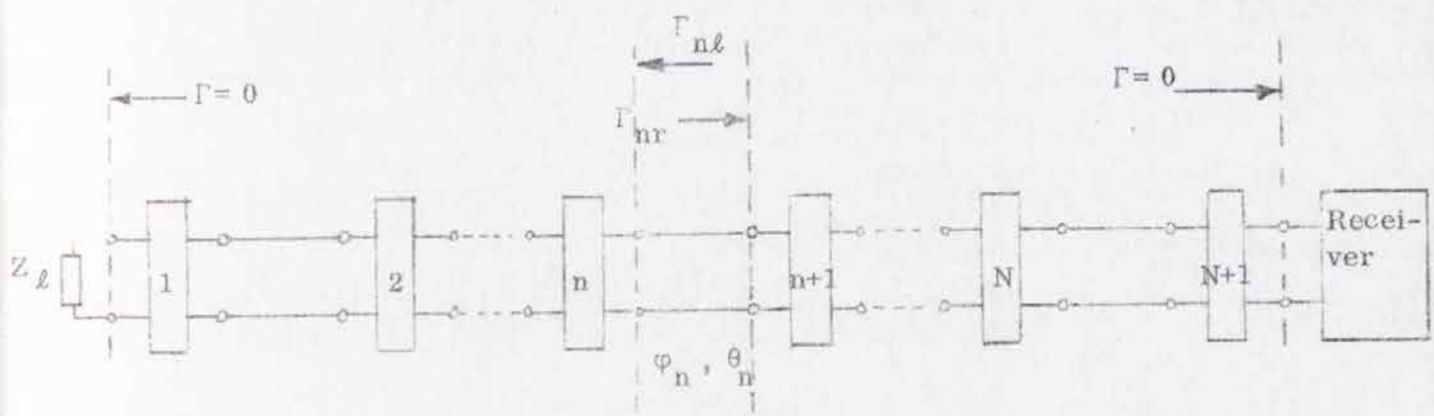

Fig. 2.2. A schematic diagram of a transmission line with N + 1 lossless two-ports between the antenna and the receiver.

To treat this problem we consider a noisy transmission line, b-c, connected to the antenna load Z_ℓ and the receiver Z_r, via reciprocal two port networks described by their scattering matrices [S] and [S'] respectively.

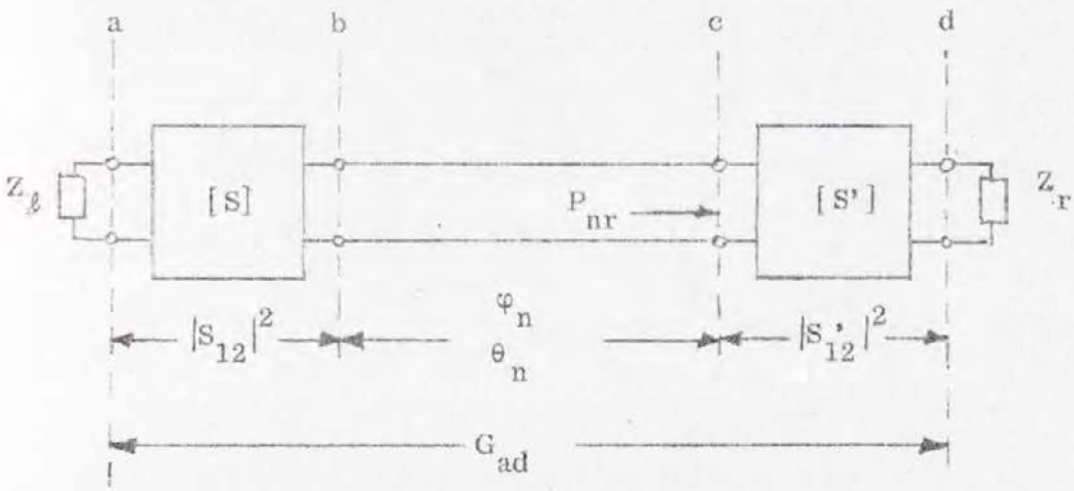

Fig. 2. 3. A transmission line section between lossy two-ports.

$|S_{12}|^2$, $|S'_{12}|^2$ and G_{ad} are the power gains of the respective two-ports assuming the two-ports to be matched at their in and out-put terminals. According to Appendix B,

$$G_{ad} = \frac{|S_{12}|^2 \, |S'_{12}|^2 e^{-2\theta_n}}{\left|1 - S'_{11} \cdot S_{22} e^{-j2\varphi_n - 2\theta_n}\right|^2} \tag{2. 23}$$

Furthermore, the noise power P_{nr} at "c", generated by the lossy line bc and traveling towards the receiver, becomes according to eqn. (2. 9)

$$P_{nr} = \frac{T_{nr} + T_{n\ell} |S_{22}|^2 e^{-2\theta_n}}{\left|1 - S'_{11} \cdot S_{22} e^{-j2\varphi_n - 2\theta_n}\right|^2} \cdot k \Delta f \tag{2. 24}$$

where T_{nr} and $T_{n\ell}$ correspond to T_a and T_b of eqn. (2. 9) - (2. 13).

The noise power P_n delivered to the receiver (Z_r) becomes

$$P_n = P_{nr} \cdot |S_{12}'|^2 \tag{2.25}$$

Hence referring P_n to the input plane "a",

$$P_i = \frac{P_n}{G_{ad}} = \frac{P_{nr}|S_{12}'|^2}{G_{ad}} \tag{2.26}$$

and with eqn. (2.23) and (2.24) the input noise temperature becomes

$$T_n = \frac{T_{nr} + T_{n\ell}|S_{22}|^2 e^{-2\theta_n}}{|S_{12}|^2} \qquad \frac{1}{e^{-2\theta_n}} \tag{2.27}$$

When the two port [S] consists of (n-1) lossy transmission line sections and of n lossless discontinuities, one gets using eqn. (B.9) in Appendix B:

$$T_n = \frac{T_{nr} + T_{n\ell}|\Gamma_{n\ell}|^2 e^{-2\theta_n}}{(1-|\Gamma_{n\ell}|^2)\, e^{-2\theta_{n\ell}}} \prod_{\nu=1}^{n-1} \frac{1-|\Gamma_{\nu\ell}|^2 \cdot e^{-4\theta_\nu}}{1-|\Gamma_{\nu\ell}|^2} \tag{2.28}$$

where $|\Gamma_{\nu\ell}|^2$ and θ_ν are defined in the same way as $|\Gamma_{n\ell}|^2$ and θ_n in Fig. 2.2 and where

$$\theta_{n\ell} = \sum_{\nu=1}^{n} \theta_\nu \tag{2.29}$$

It is realized that the product over ν is very closely equal to 1 when the attenuations and reflection factors are small, i.e.

$$\prod_{\nu=1}^{n-1} \frac{1-|\Gamma_{\nu\ell}|^2 e^{-4\theta_\nu}}{1-|\Gamma_{\nu\ell}|^2} \approx 1 + \sum_{\nu=1}^{n-1} 4\,\theta_\nu |\Gamma_{\nu\ell}|^2 \tag{2.30}$$

Considering the special case when

$$T_{n\ell} = T_{nr} = (1 - \frac{1}{L_n}) T_{on} \tag{2.31}$$

where $L_n = e^{2\theta_n}$ and T_{on} is the physical temperature of the n-th line segment, eqn. (2.28) together with (2.30) and (2.31) yields a second order approximation for T_n:

$$T_n \approx (L_n - 1) T_{on} \frac{1 + |\Gamma_{n\ell}|^2 / L_n}{1 - |\Gamma_{n\ell}|^2} L_{n\ell} (1 + \sum_{\nu=1}^{n-1} 2 (1 - \frac{1}{L_\nu}) |\Gamma_{\nu\ell}|^2) \tag{2.32}$$

where $L_{n\ell} = e^{+2\theta_{n\ell} - 2\theta_n}$. When all $|\Gamma| = 0$, this formula yields the wellknown result $T_n = (L_n - 1) T_{on}$.

Since the terms of the sum over ν are of the second order, they may be neglected in the first order approximation, and (2.32) is simplified to

$$T_n \approx (L_n - 1) T_{on} \frac{1 + |\Gamma_{n\ell}|^2}{1 - |\Gamma_{n\ell}|^2} L_{n\ell} \tag{2.33}$$

The total noise temperature T_t of the line section is, using eqn. (2.33)

$$T_t \approx \sum_{n=1}^{N} (L_n - 1) T_{on} \frac{1 + |\Gamma_{n\ell}|^2}{1 - |\Gamma_{n\ell}|^2} L_{n\ell} \tag{2.34}$$

This formula is very useful in most practical cases. In order to see the influence of reflections in the transmission line, consider a line section in which $(L_n - 1) T_{on} = 25^{\circ}K$. If $|\Gamma_{n\ell}|^2 = 0.09$ (i.e. an equivalent standing wave ratio of $= 1.85$). The increased noise temperature will become $30^{\circ}K$.

2.5. The equivalent noise temperature of a TWM receiving system

In Fig. 2.4 the maser amplifier system including the signal input transmission lines is shown. We want a definition of the system noise temperature referred to the load Z_{ℓ} (the antenna)

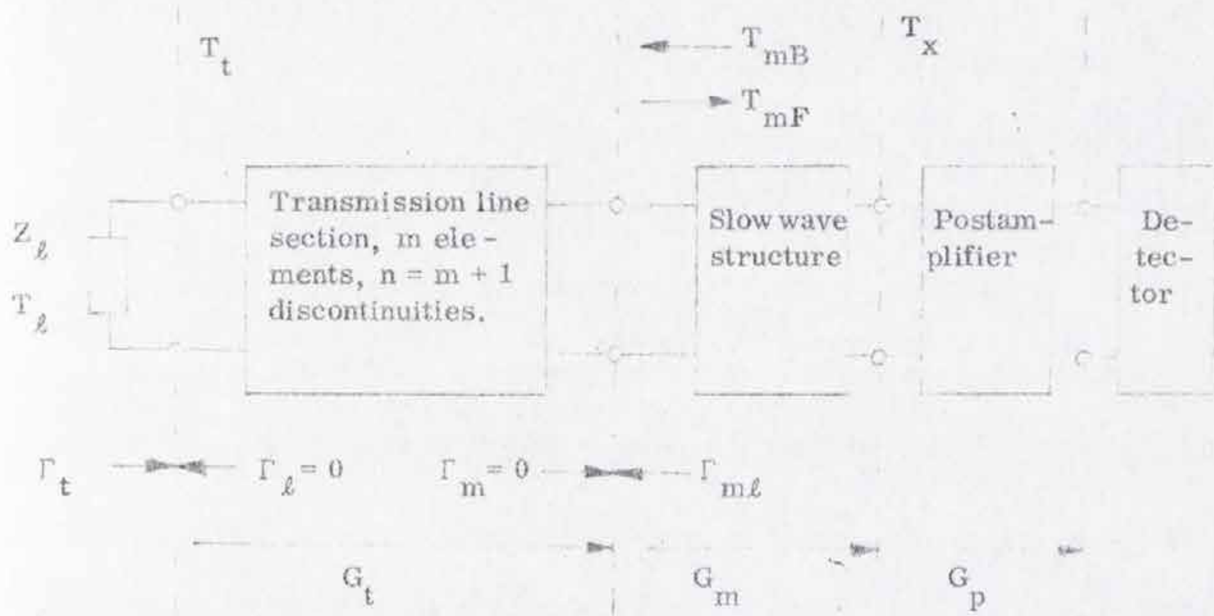

Fig. 2.4 The TWM system.

The transmission line section contains all scattering junctions including the coupling section to the slow wave structure. Hence Z_{ℓ} and the slow wave structure are considered as matched, i.e. no waves are reflected back to the transmission line section, i.e. $\Gamma_m = \Gamma_{\ell} = 0$ in Fig. 2.4. The match of the slow-wave structure is nearly ideal due to the garnet-isolator within the structure, which makes a nonreciprocal gain certain and absorbs any reflected waves.

T_{mF} and T_{mB} are the noise temperatures generated within the slow wave structure in the forward and backward directions. They are referred to the input of the slow wave structure and can be calculated theoretically (ref. [3]):

$$T_{mF} = \frac{G_{e\ell}}{G_{e\ell} - L_A} T_S + \frac{L_A}{G_{e\ell} - L_A} T_o \tag{2.35}$$

$$T_{mB} = \frac{G'_{e\ell}}{L'_A - G'_{e\ell}} T_S + \frac{L'_A}{L'_A - G'_{e\ell}} T_o \tag{2.36}$$

where $G_{e\ell}$ is the electronic gain of the maser material itself in dB, L_A the attenuation in dB due to ohmic losses and losses in the isolator material, T_S the spin temperature of the inverted spin system, T_o the physical temperature of the guiding structure and the isolator material. $G'_{e\ell}$ and L'_A are electronic gain and attenuation in dB measured from the output to the input terminals.

The noise temperature of the transmission line section referred to Z_ℓ can easily be calculated from eqn. (2.28):

$$T_t = \sum_{n=1}^{N} \frac{T_{nm} + T_{n\ell} |\Gamma_{n\ell}|^2 e^{-2\theta_n}}{(1 - |\Gamma_{n\ell}|^2) e^{-2\theta_{n\ell}}} \cdot \prod_{\nu=1}^{n-1} \frac{1 - |\Gamma_{\nu\ell}|^2 e^{-4\theta_\nu}}{1 - |\Gamma_{\nu\ell}|^2} \tag{2.37}$$

For that part of the input transmission line, whose physical temperature is equal to room-temperature, the approximate formula for T_t, eqn. (2.34) may safely be used in most practical cases. For that part of the line that exhibits a temperature gradient from room temperature to the temperature of liquid helium, one must use eqn. (2.10) and (2.11) for T_{nm} and $T_{n\ell}$.

Let $k \cdot T_{tot} \cdot \Delta f \cdot G_p$ be the total noise power from the post-amplifier. Thus

$$T_{tot} = (T_\ell + T_t) G_t \cdot G_m + (T_{mF} + |\Gamma_{m\ell}|^2 T_{mB}) G_m + T_x \tag{2.38}$$

where $\Gamma_{m\ell}$ is the reflection coefficient seen towards the antenna from the interior of the slow-wave structure, and T_x is the noise temperature of the post-amplifier.

Referring T_{tot} to the antenna (Z_ℓ) yields the system noise temperature:

$$T_S = T_\ell + T_t + \frac{T_{mF} + |\Gamma_{m\ell}|^2 T_{mB}}{G_t} + \frac{T_x}{G_m G_t} \tag{2.39}$$

Formulas for G_t may be found in Appendix B.

3. COMMON METHODS FOR NOISE TEMPERATURE MEASUREMENTS

3.1. Introduction

In the light of the theoretical framework of chapter 2 , a critical discussion of common methods for noise temperature measurements on a TWM-system is carried through. The HOT-COLD body method, also discussed by a number of other authors ([6] , [11] , [12]), is fairly sensitive to differences beween the impedance of the hot and the cold loads, and a convenient formula, not given elsewhere, is presented (eqn. (3.14)). The influence on the measured noise temperature from errors in the measured Y-value is shown in a graph (Fig. 3.2.).

Finally the Tabor and Sibilia method for measurements of the traveling wave maser noise temperature is analysed and criticized.

3.2. The HOT-COLD body technique (HC-technique).

In the measuring procedure with the HOT-COLD-body technique (HC-technique), two different loads Z_H and Z_C with different physical temperatures T_H and T_C are connected, one at a time, to the TWM input line. Since in practice one always has $Z_H \neq Z_C$, the power transmission from these loads to the slow wave structure will be different. Let Γ_t be the voltage reflection coefficient of the input transmission line, seen from the terminating load (see Fig. 3.1.). Hence, according to Appendix B the total power gain of the connecting circuit

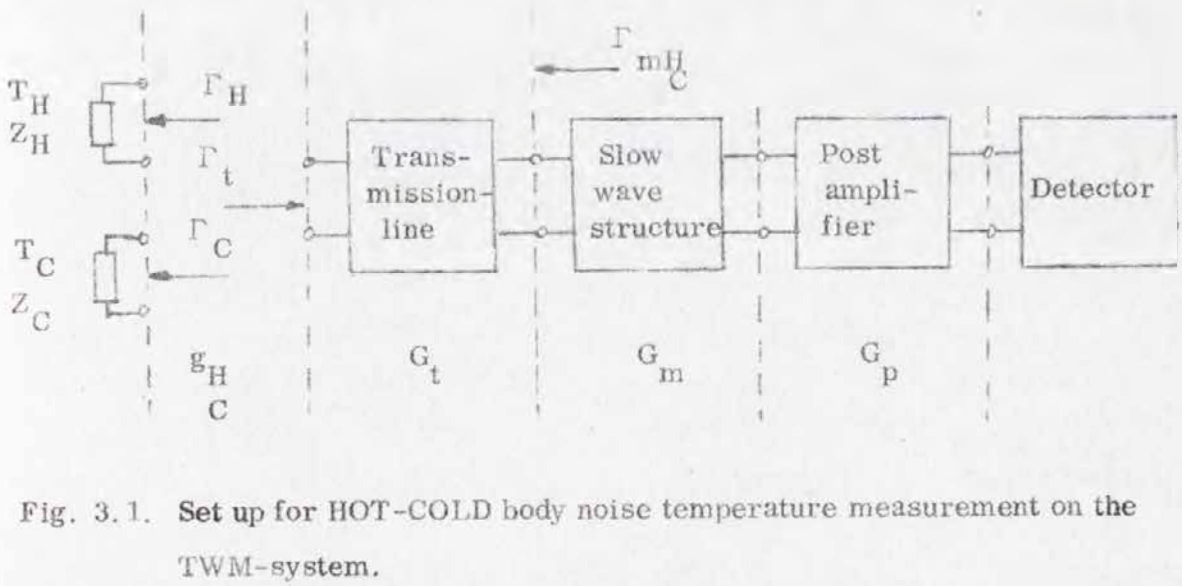

Fig. 3.1. Set up for HOT-COLD body noise temperature measurement on the TWM-system.

between the loads and the SWS is $g_{\substack{H\\C}} \cdot G_t$ where

$$g_{\substack{H\\C}} = \frac{1 - |\Gamma_{\substack{H\\C}}|^2}{|1 - \Gamma_{\substack{H\\C}} \Gamma_t|^2} \tag{3.1}$$

When the hot termination is connected, the noise power at the post amplifier input is proportional to

$$T_{\text{post amp.}} = T_H \cdot g_H \cdot G_t G_m + T_{tH} g_H G_t G_m + (T_{mF} + |\Gamma_{mH}|^2 T_{mB}) G_m + T_x \tag{3.2}$$

where T_{tH} (T_{tC}) is the equivalent noise temperature of the input transmission line at the hot (cold) load.
A similar formula is valid when the cold termination is connected, but

$T_{tH} \rightarrow T_{tC}$ and $\Gamma_{mH} \rightarrow \Gamma_{mC}$

The ratio of the detected noise power with the hot and with the cold termination connected is measured and can be expressed in the following way:

$$Y_{HC} = \frac{(T_{\text{post. ampl.}})_{\text{Hot termination}}}{(T_{\text{post. ampl.}})_{\text{Cold termination}}} =$$

$$= \frac{T_H + T_{tH} + \dfrac{T_{mF} + |\Gamma_{mH}|^2 T_{mB}}{g_H G_t} + \dfrac{T_x}{g_H G_t G_m}}{\dfrac{g_C}{g_H}(T_C + T_{tC}) + \dfrac{T_{mF} + |\Gamma_{mH}|^2 T_{mB}}{g_H G_t} + \dfrac{T_x}{g_H G_t G_m}} \tag{3.3}$$

where g_H and g_C are obtained from eqn. (3.1), which yields

$$\frac{g_H}{g_C} = \frac{1 - |\Gamma_H|^2}{1 - |\Gamma_C|^2} \cdot \left|\frac{1 - \Gamma_C \Gamma_t}{1 - \Gamma_H \Gamma_t}\right|^2 \tag{3.4}$$

In most practical cases, $|\Gamma_H|^2$ and $|\Gamma_C|^2$ are extremely small (for VSWR $<$ 1.22, $|\Gamma|^2 < 0.01$), i.e.

$$\frac{g_H}{g_C} \approx 1 - 2\,|\Gamma_t|\;|\Gamma_C - \Gamma_H|\;\cos\,\emptyset \tag{3.5}$$

where $\emptyset$ is a phase depending on Γ_C, Γ_H and Γ_t.

Since the system noise temperature must be referred to a terminating load (e.g. the antenna in a radio astronomical receiving system) we will in the following discuss the noise temperature referred to the hot termination, which becomes

$$T_{syst.\,H} = T_{tH} + \frac{T_{mF} + |\Gamma_{mH}|^2\, T_{mB}}{g_H\, G_t} + \frac{T_x}{g_H\, G_t\, G_m} \tag{3.6}$$

this yields

$$Y_{HC} = \frac{T_H + T_{syst.\,H}}{\frac{g_C}{g_H}\,(T_C + T_{tC}) - T_{tH} + (1 - \frac{g_C}{g_H})\,T_\Delta + T_{syst.\,H}} \tag{3.7}$$

where for convenience,

$$(1 - \frac{g_C}{g_H})\,T_\Delta = (|\Gamma_{mC}|^2 - |\Gamma_{mH}|^2)\;\frac{T_{mB}}{g_H\, G_t} \tag{3.8}$$

Since eqn. (B.9) yields with a high accuracy

$$\frac{1 - |\Gamma_{mH}|^2}{1 - |\Gamma_{mC}|^2} \approx \frac{g_H}{g_C} \tag{3.9}$$

we obtain for T_Δ,

$$T_\Delta \approx (1 - |\Gamma_{mH}|^2)\;\frac{T_{mB}}{g_H\, G_t} \tag{3.10}$$

Let us now define the calculated system noise temperature ($T_{syst\,O}$) from

$$T_{syst.0} = \frac{T_H - Y_{HC}\,T_C}{Y_{HC} - 1} \tag{3.11}$$

Hence,

$$T_{syst.H} = T_{syst.0} - \delta T \tag{3.12}$$

where

$$\delta T = \frac{Y_{HC}}{Y_{HC} - 1} \left\{ \left(\frac{g_C}{g_H} - 1\right)(T_C - T_\Delta) + \frac{g_C}{g_H}\, T_{tC} - T_{tH} \right\} \tag{3.13}$$

The difficulty in the estimation of δT comes from the term $\frac{g_C}{g_H} T_{tC} - T_{tH}$

This problem is simplified considerably if we assume only two discontinuities to be present, one at the transmission line top connector ($\Gamma_{\substack{H\\C}}$) and the other at the SWS input. For this case we have approximately

$$\frac{T_{tH}}{T_{tC}} = \frac{1 + |\Gamma_H|^2}{1 - |\Gamma_H|^2} \cdot \frac{1 - |\Gamma_C|^2}{1 + |\Gamma_C|^2} \approx 1 + 2\left(|\Gamma_H|^2 - |\Gamma_C|^2\right) \tag{3.14}$$

yielding with (3.13) a maximum error of

$$\delta T = \pm \frac{2Y_{HC}}{Y_{HC} - 1} \left\{ |\Gamma_t|\,|\Gamma_C - \Gamma_H|\,(T_C + T_{tC} - T_\Delta) \mp T_{tC}\left(|\Gamma_H|^2 - |\Gamma_C|^2\right) \right\} \tag{3.15}$$

Notice that $T_{tC}\left(|\Gamma_H|^2 - |\Gamma_C|^2\right)$ gives a systematic error. However, since usually $|\Gamma_t| \gg |\Gamma_{\substack{H\\C}}|$ and $2\,T_{tC}\left(|\Gamma_H|^2 - |\Gamma_C|^2\right)$ is a very small error, we may use the following formula for δT (neglecting T_Δ):

$$\delta T = \pm \frac{2Y_{HC}}{Y_{HC} - 1}\, |\Gamma_t|\,|\Gamma_C - \Gamma_H|\,(T_C + T_{tC}) \tag{3.16}$$

Moreover, $\Gamma_{\substack{H\\C}}$ is dependent on the reflection coefficient from the maser input transmission line connector (Γ_1) and the HOT-COLD-body connector ($\Gamma'_{\substack{H\\C}}$).

Since Γ_1 and $\Gamma'_{\substack{H\\C}}$ are small, we have approximately:

$$|\Gamma_C - \Gamma_H| = |\Gamma'_C - \Gamma'_H| \tag{3.17}$$

i.e. we may use $|\Gamma'_C - \Gamma'_H|$ for $|\Gamma_C - \Gamma_H|$ in eqn. (3.16).

When there are more reflecting discontinuities present in the input transmission line, however, the behaviour of the term $(\frac{g_C}{g_H} T_{tC} - T_{tH})$ in eqn. (3.13) becomes much more complex. Thus we might expect errors greater than those suggested by eqn. (3.16).

The error in $T_{syst.}$ due to inaccurate measurements of Y_{HC} is obtained by derivating $(T_H - Y_{HC} T_C)/(Y_{HC} - 1)$ with respect to Y_{HC}. Hence the error becomes

$$\Delta T_{syst} = - (T_H - T_C) \frac{Y_{HC}}{(Y_{HC} - 1)^2} \frac{\Delta Y_{HC}}{Y_{HC}} \tag{3.18}$$

This error is plotted in Fig. 3.2 for $T_H = 373^0K$, $T_C = 77.3^0K$ and $\Delta Y_{HC}/Y_{HC} =$ $= 0.023$ ($= 0.10$ dB).

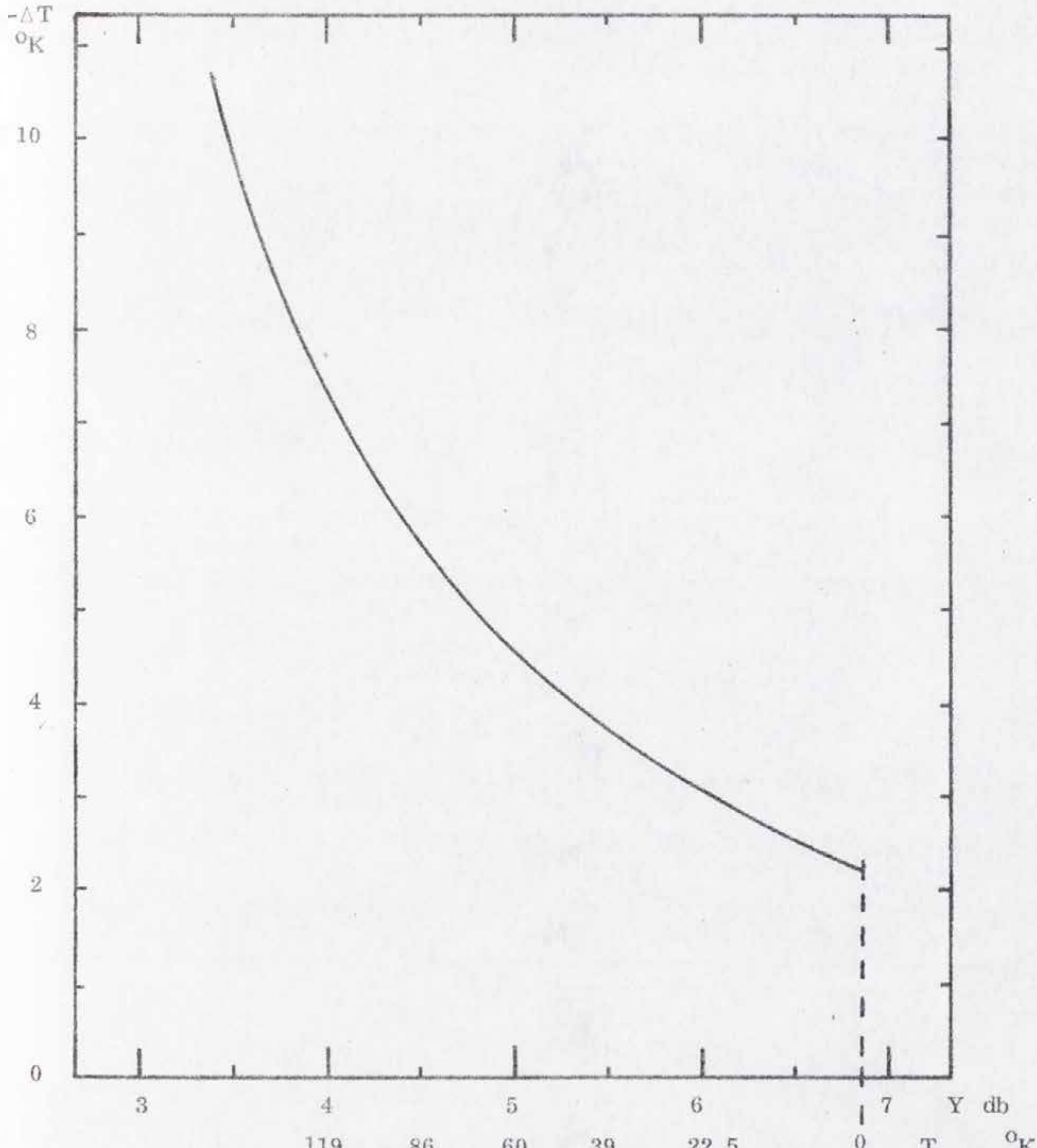

Fig. 3.2. The error ΔT_{syst} is depicted vs the measured Y-factor or T_{syst} for an assumed error of $\Delta Y / Y = 0.023$ ($\approx$ 0.1 db), $T_H = 373\ ^{o}K$ and $T_C = 77^{o}$ K.

3.3. The Tabor and Sibilia method

This method implies a Y-factor to be measured which is the ratio of the detected noise power when the input line is connected to a nearly matched load (Z_ℓ) with its temperature T_ℓ, to the detected noise power when the input line is connected to a movable short circuit ($\Gamma_\ell = -e^{j2\varphi}$). Hence one obtains (see Fig. 3.1 and use $g_{HC} = 1$)

$$Y_{TS} = \frac{T_\ell G_t G_m + T_t G_t G_m + (T_{mF} + |\Gamma_{m\ell}|^2 T_{mB}) G_m + T_x}{(T_{nSH} + T_S) G_m + (T_{mF} + |\Gamma_{mSH}|^2 T_{mB}) G_m + T_x} \tag{3.19}$$

$\Gamma_{m\ell}$ and Γ_{mSH} are the reflection coefficients seen from the interior of the slow-wave structure towards the antenna. T_t is the transmission line noise temperature defined at the load (see eqn. (2.34) or (2.37)). T_{nSH} and T_S are the noise temperatures from the shorted input transmission line (T_{nSH}) and from short circuit itself (T_S). Y_{TS} may be written on the form:

$$Y_{TS} = \frac{T_\ell + T_t + \dfrac{T_{mF} + |\Gamma_{m\ell}|^2 T_{mB}}{G_t} + \dfrac{T_x}{G_t G_m}}{\dfrac{T_{nSH}}{G_t T_t} T_t + \dfrac{T_S}{G_t} + \dfrac{T_{mF} + |\Gamma_{mSH}|^2 T_{mB}}{G_t} + \dfrac{T_x}{G_t \cdot G_m}} \tag{3.20}$$

All terms in this equation except T_{nSH} and T_t are assumed to be known. Hence T_x and $G_t G_m$ are measured separately, allowing $T_x/G_t G_m$ to be derived, T_S, the noise from the movable short circuit, is of the order $1\,^{o}K$ [9]. T_{mF} and T_{mB} can be calculated from eqn. (2.26) and (2.27). Eqn. (3.20) now yields

$$T_t = \frac{T_\ell - (Y_{TS} - 1)\left(\dfrac{T_{mF} + |\Gamma_{m\ell}|^2 T_{mB}}{G_t} + \dfrac{T_x}{G_t G_m}\right) - Y_{TS}\left(\dfrac{T_S}{G_t} + \dfrac{T_{mB}}{G_t}(|\Gamma_{mSH}|^2 - |\Gamma_{m\ell}|^2)\right)}{\dfrac{T_{nSH}}{G_t T_t} Y_{TS} - 1}$$

(3.21)

Tabor and Sibilia approximates this equation by assuming

$$|\Gamma_{m\ell}|^2 = 0 \qquad |\Gamma_{mSH}|^2 = 1$$
$$G_t = 1 \qquad \frac{T_{nSH}}{G_t T_t} = 2 \tag{3.22}$$

These relations are only exact if the slow-wave structure is perfectly matched to the input line and if the input line has "zero losses". If this is not the case, the relations (3.22) will not hold. A qualitative discussion of the errors will now be given.

Since a traveling wave maser usually is a very low noise device, T_ℓ is dominating the numerator of eqn. (3.21) (e.g. $T_\ell = 290^0K$) and $(T_{nSH}/(G_t T_t))\, Y_{TS} \gg 1$. The term $T_{nSH}/(G_t T_t)$ will cause the greatest error in the derivation of T_t. Let us define a term

$$\alpha = \frac{T_{nSH}}{G_t T_t} \tag{3.23}$$

To obtain α expressed in circuit parameters, we will for simplicity assume that the only discontinuities in the system are situated at the terminating load $Z_\ell(\Gamma_\ell)$ and at the coupling between the input line and the slow wave structure (Γ_m). Hence we may use the results of section (2.2) and Appendix A. Equation (2.15) yields for T_{nSH} ($\Gamma_b^- = -1$, Fig. 2.1)

$$T_{nSH} = (1-|\Gamma_m|^2)\,\frac{T_a + T_b e^{-2\theta}}{|1+\Gamma_m e^{-j2\varphi-2\theta}|^2} \approx \frac{(1-|\Gamma_m|^2)(1+e^{-2\theta})}{|1+\Gamma_m e^{-j2\varphi-2\theta}|^2}\, T_a \tag{3.24}$$

Since $G_t T_t$ is the noise temperature from the input line when the matched load is connected, (2.15) can be used directly, i.e.

$$G_t T_t = (1-|\Gamma_m|^2)\,\frac{T_a + T_b|\Gamma_\ell|^2 e^{-2\theta}}{|1-\Gamma_m\Gamma_\ell e^{-j2\varphi-2\theta}|^2} \approx \frac{(1-|\Gamma_m|^2)(1+|\Gamma_\ell|^2 e^{-2\theta})}{|1-\Gamma_m\Gamma_\ell e^{-j2\varphi-2\theta}|^2}\, T_a \tag{3.25}$$

Clearly from (3.24) and (3.25)

$$\alpha = \frac{1 + e^{-2\theta}}{1 + |\Gamma_\ell|^2 e^{-2\theta}} \cdot \left| \frac{1 - \Gamma_m \Gamma_\ell e^{-j2\varphi - 2\theta}}{1 + \Gamma_m e^{-j2\varphi - 2\theta}} \right|^2 \tag{3.26}$$

Usually $|\Gamma_\ell|$ is quite small and $e^{-2\theta} \approx 1$ yielding

$$\alpha \approx \frac{2}{|1 + \Gamma_m e^{-j2\varphi}|^2} = \frac{2}{1 + |\Gamma_m|^2 + 2|\Gamma_m| \cos \phi} \tag{3.27}$$

where ϕ is the phase of $\Gamma_m e^{-j2\varphi}$.

Tabor and Sibilia now suggest that the mean value of the maximum and minimum T_t - values obtained by sliding the movable short circuit is almost correct. Clearly the maximum and the minimum are obtained for $\cos \phi = -1$ and $+1$ in eqn. (3.27). If $\alpha \cdot Y_{TS}$ is dominating the denominator of eqn. (3.21) one obtains:

$$T_t = (1 + |\Gamma_m|^2) \frac{1}{2} (T'_{t\,max} + T'_{t\,min}) \tag{3.28}$$

where T'_t is the value for T_t derived as if $\alpha = 2$.

Shteinshleiger et al suggest that one should use the Y-factor obtained when the movable short circuit is a position $\lambda/8$ from a maximum or minimum T'_t. This is equivalent to make $\cos \phi = 0$ in eqn. (3.27) and yields the same T_t as in eqn. (3.28), if αY_{TS} dominates the denominator.

We observe that neither Tabor and Sibilia nor Shteinshleiger et al do consider effects due to the different noise generation of the current standing waves and of the voltage standing waves. They do not either consider inhomogeneous effects (see section 2.2. eqn. (2.16) and (2.17)). Furthermore, since the equations (3.24)-(3.28) all include approximations, additional errors must be expected when eqn. (3.28) is used for T_t.

4. ADDITIONAL METHODS

4.1. Introduction

In this chapter we will give a simple method for measurement of the second stage amplifier noise contribution, T_x/G_tG_m. This method is very useful when the maser is run at physical temperatures lower than 4.2°K. Then one need only to decrease the temperature until the maser gain (G_m) is high enough to make T_x/G_tG_m small compared to the system noise temperature.

We will also present a new method for measurements of the maser input transmission line noise temperature (T_t). This method was developed merely since we experienced unstable performance of the movable short circuit (Tabor and Sibilia method, section 3.3) available at our laboratory. Another advantage over the Tabor and Sibilia method is obtained by the use of a fixed short circuit and fixed open circuit, leaving the length of the transmission line constant during the measurements. The method is carefully analysed using the theory of chapter 2. The accuracy obtained is at least as good as the accuracy obtained by the methods described in chapter 3.

4.2. The second stage amplifier noise contribution

The gain G_m of a traveling wave maser (see Fig. 2.3) is usually -10 dB or less when the pump power is turned off. The noise power from the slow wave structure then becomes entirely negligible compared with T_x.

The method utilizes a Y-factor which is the ratio of the detected noise power with the pump power on and the pump power off, i.e. using Fig. 2.4:

$$Y_x = \frac{T_\ell G_t G_m + T_t G_t G_m + (T_{mF} + |\Gamma_{m\ell}|^2 T_{mB}) G_m + T_x}{T_x} \tag{4.1}$$

which yields

$$\frac{T_x}{G_t G_m} = \frac{T_\ell + T_t + \dfrac{T_{mF} + |\Gamma_{m\ell}|^2 T_{mB}}{G_t}}{Y_x - 1} \tag{4.2}$$

Since T_ℓ dominates the numerator of eqn. (4.2) ($T_\ell \approx 300^oK$) and since

$T_t + \dfrac{T_{mF} + |\Gamma_{m\ell}|^2 T_{mB}}{G_t}$ is the maser noise temperature which can be measured with an accuracy of about $\pm 3^oK$, $T_x/G_t G_m$ is calculated from (4.2) with an error of only about 1 %.

4.3. Determination of T_t by the "SHOP-technique".

When this method is used, the maser input transmission line is terminated by a short circuit and an open circuit. Y-factors are measured as the ratio of detected noise power with the pump power on (maser gain = G_m) and the pump power off (maser gain $\approx$ 0). Hence, when the input line is shorted, we obtain a Y-factor

$$Y_{SH} = \frac{T_x + (T_{nSH} + T_{mF} + |\Gamma_{mSH}|^2 T_{mB})\, G_m}{T_x} \tag{4.3}$$

where T_{nSH} is a measure of the noise power from the input line injected into the SWS and Γ_{mSH} is the reflection coefficient experienced by the backward SWS "noise power wave" at the SWS input (see Fig. 4.1).

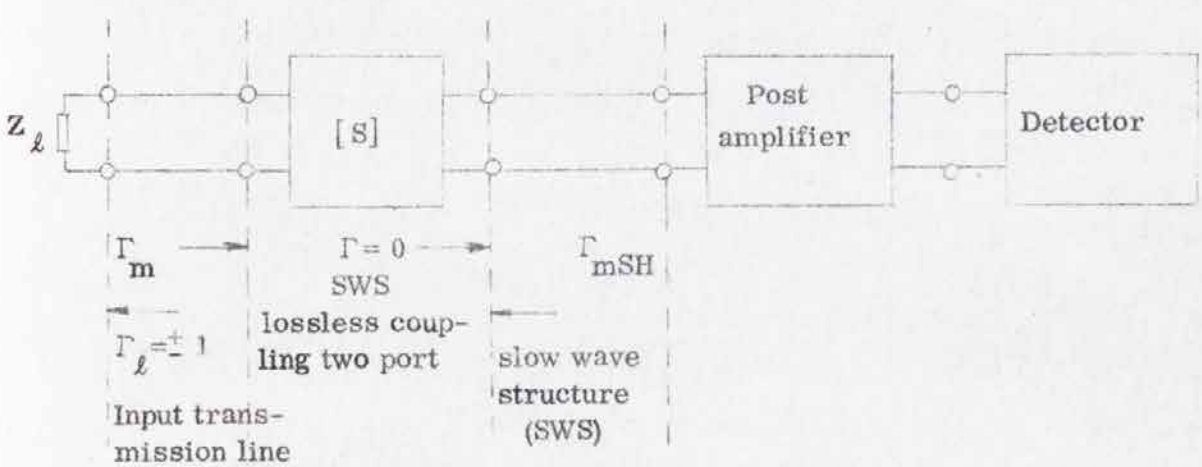

Fig. 4.1. Diagram showing the essential features for the theoretical analyses of the SHOP-technique.

From eqn. (4.3) we obtain for the case with a shorted ($\Gamma_\ell = -1$) input line,

$$\frac{T_{nSH}}{G_t} = (Y_{SH} - 1)\,\frac{T_x}{G_t\,G_m} - \frac{T_{mF} + |\Gamma_{mSH}|^2\,T_{mB}}{G_t} \tag{4.4}$$

where $T_x / G_t\,G_m$ may be accurately measured using the technique described in section 4.1. A formula similar to eqn. (4.4) is obtained when the input line is terminated by an open circuit. According to Appendix A, eqn. (A 8) we have

$$|\Gamma_{\substack{mSH\\OP}}|^2 = \left| \frac{\Gamma_m^* \pm e^{-j2\varphi - 2\theta}}{1 \pm \Gamma_m\, e^{-j2\varphi - 2\theta}} \right|^2 \approx$$

$$\approx e^{-4\theta}\left(1 + \frac{|\Gamma_m|^2 \pm 2\,|\Gamma_m| \cos\phi}{1 + |\Gamma_m|^2 \pm 2\,|\Gamma_m| \cos\phi}\right) \cdot 4\theta \tag{4.5}$$

where ϕ is the phase of the complex quantity $\Gamma_m\, e^{-j2\varphi}$. For those terms with a plus or a minus sign, the plus sign is used with Γ_{mSH} and the minus sign with Γ_{mOP}.

According to eqn. (2.15) and (2.16) the noise temperature injected from the input line into the slow-wave structure is

$$T_{\substack{nSH\\OP}} = \frac{(1 - |\Gamma_m|^2)\,[\,T_a + (T_{bo} \pm \Delta T_b)\, e^{-2\theta}\,]}{|\,1 \pm \Gamma_m\, e^{-j2\varphi - 2\theta}\,|^2} \tag{4.6}$$

where $T_{bo} \pm \Delta T_b = T'_{\substack{bSH\\bOP}}$ according to eqn. (2.12 b) and the plus signs are related to the input line terminated by a short circuit and the minus sign related to the input line terminated by an open circuit. Defining $<T_n>$ from

$$\frac{G_t}{\langle T_n \rangle} = \frac{1}{2} \left(\frac{G_t}{T_{nSH}} + \frac{G_t}{T_{nOP}} \right) \tag{4.7}$$

we obtain

$$T_a = \frac{1 + |\Gamma_m|^2 e^{-4\theta}}{1 - |\Gamma_m|^2} \cdot \frac{G_t}{1 + \frac{T_{bo}}{T_a} e^{-2\theta}} \frac{\langle T_n \rangle}{G_t} \cdot E \tag{4.8}$$

where

$$E = \frac{1 - \frac{2 |\Gamma_m| e^{-2\theta} \cos \phi}{1 + |\Gamma_m|^2 e^{-4\theta}} \cdot \frac{\Delta T_b e^{-2\theta}}{T_a + T_{bo} e^{-2\theta}}}{1 - \frac{(\Delta T_b e^{-2\theta})^2}{(T_a + T_{bo} e^{-2\theta})^2}} \tag{4.9}$$

Use of eqn. (2.28) yields

$$T_t = \frac{T_a + T_b |\Gamma_\ell|^2 e^{-2\theta}}{1 - |\Gamma_\ell|^2} \cdot \frac{1}{e^{-2\theta}} \tag{4.10}$$

where Γ_ℓ is the reflection coefficient when the transmission line is connected to the antenna. With eqn. (4.7) and (4.8) we may now obtain the equivalent noise temperature T_t of the input transmission line:

$$T_t = \frac{1 + \frac{T_b}{T_a} |\Gamma_\ell|^2 e^{-2\theta}}{(1 - |\Gamma_\ell|^2) e^{-2\theta}} \cdot \frac{1 + |\Gamma_m|^2 e^{-4\theta}}{1 - |\Gamma_m|^2} \cdot \frac{G_t}{1 + \frac{T_{bo}}{T_a} e^{-2\theta}} \cdot \frac{\langle T_n \rangle}{G_t} \cdot E \tag{4.11}$$

5. EXPERIMENTAL RESULTS

5.1. Introduction

The noise temperature T_t from the input transmission line of a TWM has been determined by two different methods, Hot-Cold body technique ($T_C = 77.4^{\circ}K$, $T_H = 373.3\ ^{\circ}K$, see section 3.2) and the method which uses a shorted and open input transmission line (SHOP-technique, see section 4.2). Furthermore the power dissipation in the input transmission line at room temperature has been determined and is in good agreement with the noise temperature measurements.

The masers utilized in these experiments had a rather poor match between the input transmission line and the slow wave structure ($S \leq 2.1$) and as a consequence rather strong coherence effects were observed with a short circuit (open circuit) at the input line. A rather good agreement was obtained between the results using the HC-body technique and the SHOP-technique. Both methods have certain sources of error, discussed in the subsequent text. Since the measurements with the SHOP-technique are much less scattered, however, this method is certainly much more reliable than the HC-body technique with the hot load temperature equal to $373^{\circ}K$ and the cold load temperature equal to $77^{\circ}K$.

5.2. Description of the experiments

The system which will be discussed is described schematically in Fig. 5.1. The experiments are devoted to a determination of the noise temperature T_t of the maser input transmission line.

The measurements were performed at a number of discrete frequencies and all noise power ratios (Y-values) were measured with the noise of the mixer receiver as a reference and using a precision attenuator at the if-frequency (30 MHz).

According to section 2.5 and eqn.(2.34) we expect the noise temperature contribution from the input transmission line to be completely independent of a mismatched SWS and almost independent of reasonable small reflections in the input transmission line. The double stub tuner in Fig. 5.1 and 5.2 may be adjusted to any value of the reflection coefficient at the maser input connector, e.g. to a value making $\Gamma_{1\ell} = 0$ in eqn. (2.34). Our aim is to determine T_t as if $\Gamma_{1\ell} = 0$.

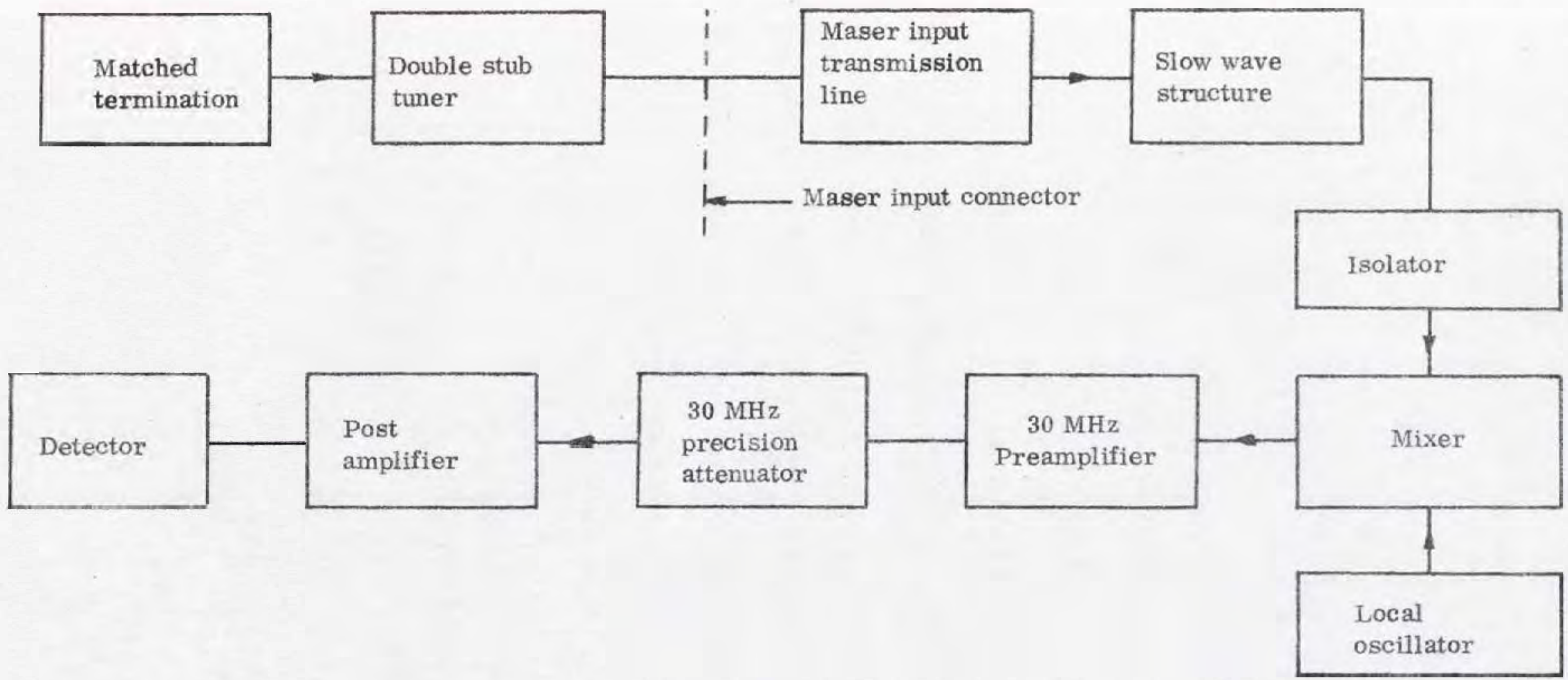

Fig. 5.1. The system used to measure the noise contribution T_t from the maser input transmission line.

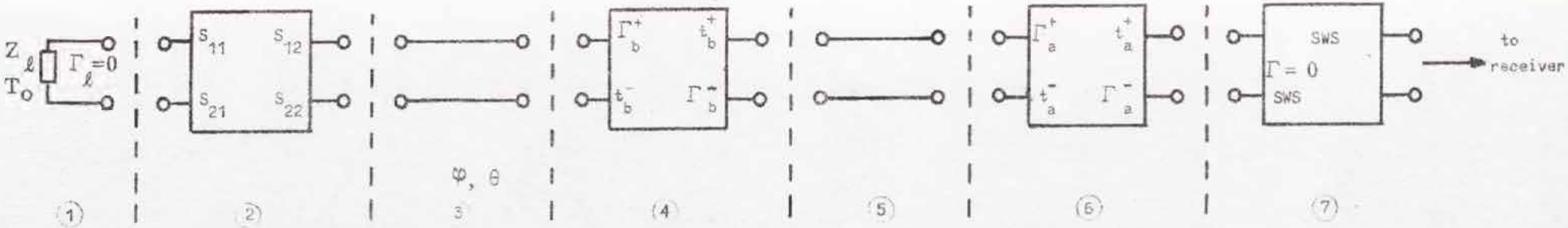

Fig. 5.2 Equivalent circuit of the system in fig. 5.1.

1. Perfectly matched termination
2. Coupling section (including the double stub tuner) between the matched termination 1 and the input transmission line section 3

3.5 Input transmission line section without internal discontinuities

4. Type N male-female connector
6. Coupling section between the input transmission line and the SWS
7. Perfectly matched SWS.

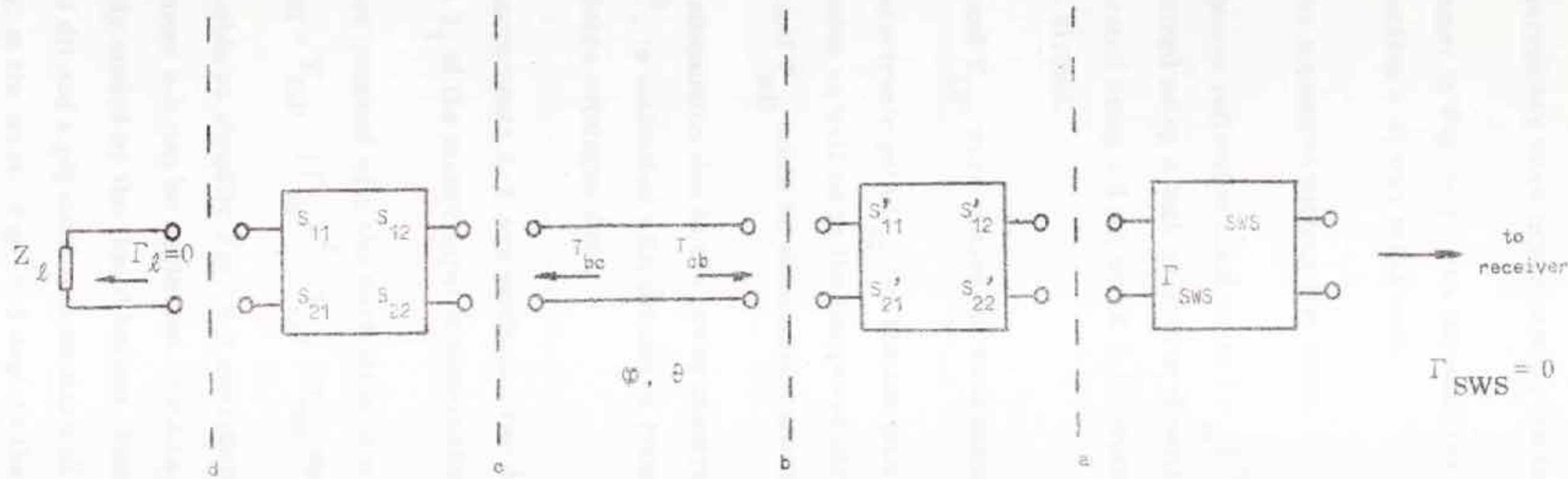

Fig. 5.3 The equivalent circuit of Fig. 5.2 simplified.

The measurements were performed in the following way:

A. The tuner in Fig. 5.1. was adjusted for maximum detected noise power and Y_x (section 4.2) was measured.

B. Y_x was measured without the tuner.

C. The power reflection coefficient $|\Gamma_m|^2$ of the input transmission line was measured using a high precision directional coupler. This set up was calibrated using a 3 dB and a 6 dB precision attenuator terminated with a short circuit.

D. Y_{SH} and Y_{OP} were measured as discussed in section 4.3.

E. The electronic gain G_{el} and the net gain G_{net} were measured in the forward direction as well as in the backward direction. Hence the noise temperatures T_{mF} and T_{mB} could be determined according to eqn. (2.35) and (2.36)

F. The attenuation due to the power dissipation in the input transmission line, $e^{-2\theta}$, is estimated with the aid of room temperature measurements and/or available catalogue data.

The measurements A-F are sufficient for determining the noise temperature contribution T_t of the maser input transmission line.

Let us now proceed with the derivation of a formula for T_t expressed in terms of Y_x, Y_{SH}, Y_{OP}, $|\Gamma_m|^2$, T_{mF}, T_{mB} and $e^{-2\theta}$

It is possible to simplify Fig. 5.2 considerably since the noise contribution of the line segment a-b can be neglected. This is so because this line segment is very effectively cooled by the liquid helium. Hence, since it has an attenuation of maximum 0.3 dB and a physical temperature of 2 ^{o}K, it will cause a noise contribution of 0.1 ^{o}K at the most. Fig. 5.3 depicts the new situation.

Let us now explain step A. The total noise power entering the SWS is

$$T_{SWS} = \frac{T_{cb} + T_{bc} \, |S_{22}|^2 e^{-2\theta}}{|1 - S'_{11} S_{22} e^{-j2\varphi - 2\theta}|^2} \, G_{ba} +$$

$$+ T_o \frac{(1 - |S_{22}|^2) e^{-2\theta}}{|1 - S'_{11} S_{22} e^{-j2\varphi - 2\theta}|^2} \, G_{ba} \tag{5.1}$$

where it has been assumed that $|S_{12}|^2 = 1 - |S_{22}|^2$ (lossless stub tuner). G_{ba} is the power transmission coefficient which is not necessarily equal to $|S'_{12}|^2$ since the characteristic impedance of the SWS is generally not equal to $50\,\Omega$.

Let us now consider the special case when

$$T_{cb} = T_{bc} = T_o (1 - e^{-2\theta}) \tag{5.2}$$

where T_o is room temperature.
Maximum for T_{SWS} is in this case obtained for

$$S_{22} S'_{11} \; e^{-j2\varphi - 2\theta} = |S'_{11}|^2 \tag{5.3}$$

This relation yields zero reflection coefficient seen from the SWS, i.e. the SWS is seeing a matched load of the temperature T_o. Notice that maximum transmitted noise power from the matched termination is obtained when

$$S_{22} S'_{11} \, e^{-j2\varphi - 2\theta} = |S'_{11}|^2 \, e^{-4\theta} \tag{5.4}$$

i.e. the phase is identical to that obtained from eqn. (5.3) but the amplitude is a little lower. Hence even when the line section b-c is partly cooled by the liquid helium and by the helium gas in the dewar, equation (5.3) will hold when the tuner is adjusted for maximum detected noise power.

According to eqn. (5.1) and (5.3) the noise temperature contribution T_t of the transmission line, section b-c (Fig. 5.3), referred to the termination Z_ℓ becomes

$$T_t = \frac{T_{cb} + T_{bc}\,|S'_{11}|^2\, e^{+2\theta}}{(1 - |S'_{11}|^2)^2} \cdot \frac{G_{ba}}{G_{da}} \tag{5.5}$$

where G_{da} is the power transmission coefficient from d to a. From eqn. (4.8) we obtain (using the approximation $E = 1$):

$$T_{cb} = \frac{1 + |S'_{11}|^2\, e^{-4\theta}}{1 - |S'_{11}|^2} \cdot \frac{G_{da}}{1 + \frac{T_{bc}}{T_{cb}}\, e^{-2\theta}} \cdot \frac{\langle T_n \rangle}{G_{da}} \tag{5.6}$$

Using the very good approximation $(T_{bc}/T_{cb})\, e^{-2\theta} = 1$ (note that $T_{bc}/T_{cb} > 1$) and the relation

$$G_{ba} = (1 - |S'_{11}|^2)\, e^{-2\theta_{ab}} \cdot \frac{1 - |\Gamma_a|^2}{1 - |\Gamma_a|^2\, e^{-4\theta_{ab}}} \tag{5.7}$$

obtained from eqn. (A 12)$^{x)}$ in appendix A and Fig. 5.2 we arrive at the expression

$$T_t = e^{-2\theta_{ab}} \cdot \frac{(1 + |S'_{11}|^2\, e^{-4\theta})(1 + |S'_{11}|^2\, e^{+2\theta})}{(1 - |S'_{11}|^2)^2} \cdot \frac{1 - |\Gamma_a|^2}{1 - |\Gamma_a|^2\, e^{-4\theta_{ab}}} \cdot \frac{\langle T_n \rangle}{2\, G_{da}} \tag{5.8}$$

In practice the reflection coefficient at the input connector ("c" in Fig. 5.3) is quite small. Hence, when a matched termination is connected directly to the input connector the influence from the reflection S_{22} becomes negligible. Therefore we may <u>normalize</u> T_t in eqn. (5.8) by dividing it by $(1 + |S_{22}|^2)/(1 - |S_{22}|^2)$ (see eqn. 2.28).

x) Notice that (A.12) will hold in this special case even if the SWS impedance differs from 50 Ω since the factor $(1 - |\Gamma|^2)/(1 - |\Gamma|^2\, e^{-4\theta})$ is related to the extra power dissipation due to the standing waves.

Hence using eqn. (5.3) again, we obtain

$$T_t = e^{-2\theta_{ab}} \frac{(1+|S'_{11}|^2 e^{-4\theta})}{1-|S'_{11}|^2} \cdot \frac{1+|S'_{11}|^2 e^{2\theta}}{1+|S'_{11}|^2 e^{4\theta}} \cdot \frac{1-|S'_{11}|^2 e^{4\theta}}{1-|S'_{11}|^2} \cdot$$

$$\frac{1-|\Gamma_a|^2}{1-|\Gamma_a|^2 e^{-4\theta_{ab}}} \quad \frac{<T_n>}{2\,G_{da}} \tag{5.9}$$

Or approximately

$$T_t \approx \frac{(1+|S'_{11}|^2 e^{-4\,\theta})}{1-|S'_{11}|^2} \cdot \frac{<T_n>}{2G_{da}} \tag{5.10}$$

Notice that (5.10) yields a value for T_t which in every case is larger than the more exact value of eqn. (5.9)

Next $<T_n>/2\,G_{da}$ is calculated as in section 4.3 yielding

$$\frac{2\,G_{da}}{<T_n>} = \frac{G_{da}}{T_{nSH}} + \frac{G_{da}}{T_{nOP}} =$$

$$= \frac{1}{(Y_{SH}-1)\,\frac{T_x}{G_{da}\,G_m} \quad \frac{T_{mF}+|\Gamma_{adSH}|^2\,T_{mB}}{G_{da}}} + \frac{1}{(Y_{OP}-1)\,\frac{T_x}{G_{da}\,G_m} - \frac{T_{mF}+|\Gamma_{adOP}|^2\,T_{mB}}{G_{da}}} \tag{5.11}$$

where according to section

$$\frac{T_x}{G_{da}\,G_m} = \frac{T_o + T_{maser}}{Y_x - 1} \tag{5.12}$$

In this expression T_{maser} consists of T_t and the contribution from the SWS. Furthermore since the stub tuner is adjusted for nearly maximum transmission (eqn. (5.3) and (5.4)) we have with a very high accuracy

$$G_{da} = e^{-2\theta_{ad}} \tag{5.13}$$

For $|\Gamma_{adSH}|^2$ and $|\Gamma_{adOP}|^2$ we may use equation (4.5) as an approximation (we neglect Γ_b). Approximately

$$|\Gamma_{\substack{adSH\\OP}}|^2 \approx \exp\left\{-4\,\theta\left(1 - \frac{2\,(|\Gamma_m|^2 \pm |\Gamma_m|\cos\phi)}{1 + |\Gamma_m|^2 \pm 2\,|\Gamma_m|\cos\phi}\right)\right\} \tag{5.14}$$

From eqn. (5.14) it can be seen that if e.g. $|\Gamma_m| = 0.50$, we get

$$e^{-12\theta} \leq |\Gamma_{\substack{adSH\\OP}}|^2 \leq e^{-1.3\theta}$$

i.e. the noise delivered by the transmission line varies by a factor of 9. In fact, when $|\Gamma_m|$ is close to one, we might get $|\Gamma_{\substack{adSH\\OP}}| = 0$, for some values of ϕ i.e. the transmission line acts like a matched resonator.

As an approximation for $|\Gamma_{\substack{adSH\\OP}}|^2$ we will use

$$|\Gamma_{\substack{adSH\\OP}}|^2 = e^{-4\theta_{ad}} \tag{5.15}$$

Using eqn. (5.12), (5.13) and (5.15), eqn. (5.11) becomes

$$\frac{2\,G_{da}}{<T_n>} = \frac{1}{(Y_{SH} - 1)\dfrac{T_x}{G_{da}\,G_m} - (T_{mF}\,e^{+2\theta_{ad}} + T_{mB}\,e^{-2\theta_{ad}})} +$$

$$+ \frac{1}{(Y_{OP} - 1)\dfrac{T_x}{G_{da}\,G_m} - (T_{mF}\,e^{+2\theta_{ad}} + T_{mB}\,e^{-2\theta_{ad}})} \tag{5.16}$$

T_{mF} and T_{mB} are calculated from eqn. (2.26) and (2.27).

Notice that the errors introduced by the following approximations may be of a significant order of magnitude

1) an error is introduced in equation (5.6) due to the approximation $E = 1$

2) the approximation which gives eqn. (5.10) from (5.9) will give a too large value for T_t .

3) equation (5.15) introduces another approximation, which becomes smaller the smaller T_{mF} and T_{mB} affect the calculation of $\langle T_n \rangle$ out of eqn. (5.16).

5.3. Numerical results

The TWM package is shown schematically in Fig. 5.4. The main input transmission line is a 70 cm long, special made, 50Ω coaxial line. It is made from thinwalled (0.2 mm) german silver tubes (outer diameter 12.5 mm and inner diameter 5.4mm) electrolythically coated with approximately 0.01 mm copper on the wave-guiding surfaces. To prevent the copper layer from oxidation, a very thin layer of gold is applied electrolythically. The line is terminated in both ends with a type N female connector. In the top connector there is a vacuum-tight teflon window (5 mm thick) and a tapered section (Fig. 5.5). The lower connector is immersed in the liquid helium bath and does not contribute to the noise properties.

The noise contribution of this coaxial line was measured with the SHOP-technique and the HC-body technique. Fig. 5.6 and 5.7 summarize the SHOP-technique measurements performed on two S-band TWM:s. The relevant properties of these masers are:

	TWM 1		TWM 2	
	Forward direction	Backward direction	Forward direction	Backward direction
Electronic gain (dB)	43–47	15 ± 3	44–49	15 ± 3
Insertion loss (dB)	12–14	≈ 100	12–14	≈ 100
Frequency range (MHz)	3300 - 3575		3000 - 3200	

The values given in the table vary slightly over the passbands. However, T_{mF} and T_{mB} derived from eqn. (2.26) and (2.27) become accurate enough if the average values are choosen. The insertion loss in the backward direction was measured to be more than 70 dB. The adopted value of 100 dB is estimated but will not be critical for the evaluation of T_{mB}. The electronic gain of 15 ± 3 dB in the backward direction is calculated from the fact that it should be 1/3 of the electronic gain in the forward direction.

The helium bath temperature is 2.0 °K and the measured inversion ratio I = - 11. Hence

$$T_{mF} = 1.04 \pm 0.1\ ^{\circ}K$$

$$T_{mB} = 2.33 \pm 0.1\ ^{\circ}K$$

From Fig. 5.3 it is seen that $e^{-2\theta_{ad}} \approx 0.93$, yielding

$$T_{mF}\, e^{+2\theta_{ad}} + T_{mB}\, e^{-2\theta_{ad}} = 3.2 \pm 0.2\ ^{\circ}K$$

to be inserted into eqn. (5.16).

To get $T_x / G_m\, G_{da}$ we used (eqn. (5.12)):

$$\frac{T_x}{G_{da} \cdot G_m} \approx \frac{300}{Y_x - 1} \tag{5.17}$$

To calculate T_t from eqn. (5.10), we must estimate $|S_{11}'|^2\, e^{-4\theta}$, since this quantity cannot be measured directly. This estimation has been made in two different ways:

a) using a precision directional coupler and measuring the power reflection coefficient $|\Gamma|^2$ of the entire maser input transmission line. This measure will then be used for $|S_{11}'|^2\, e^{-4\theta}$

b) realizing that

$$G_{da} \approx (1 - |\Gamma|^2) e^{-2\theta_{da}}$$

when no double stub tuner is used (Y_{x1} is measured), and

$$G_{da} \approx e^{-2\theta_{da}}$$

with the tuner adjusted for maximum noise power out from the maser (Y_{x2} is measured), we obtain by using eqn. (5.12)

$$1 - |\Gamma|^2 \approx \frac{Y_{x1} - 1}{Y_{x2} - 1} \tag{5.18}$$

In Fig. 5.6 the relevant properties of maser 1, vs frequency are shown. In Fig. 5.6 a is depicted $|\Gamma|^2$, used for $|S'_{11}|^2 e^{-4\theta}$ to calculate T_t (Fig. 5.6 c). A very good agreement between method a) and b), described above, is obtained. Fig. 5.6 b shows T_{nSH}/G_{da} and T_{nOP}/G_{da} vs frequency.

Fig. 5.7 shows the noise properties with maser 2. The experimental procedure was slightly different since no double stub tuner was used. The theoretical treatment is very similar to that of section 5.2, and will not be given here.

Possible sources of error in the calculation of T_t are mainly the approximations 1) - 3) on page 45 . The most serious one is probably nr 1), since it may be assumed that an essential amount (of the order 30 %) of the noise from the input line (T_t ^oK) emanates from the type- N female top connector at the maser package (Fig. 5.5). The losses within the contact are mainly related to the current in the metalic boundaries. Hence T_{nSH} would be too large and T_{nOP} too small. There is no clear tendency, related to this effect in Fig. 5.6. However, the low values for T_t at frequencies around 3020 MHz in Fig. 5.7, may be related to the described effect.

Another possible source of error is the effect of the beeds within the coaxial line which will cause reflections that we have not accounted for in our calculations. These beeds are predicted to cause a SWR of about 1.04 at our particular frequency and hence this influence is not quite negligible. It is probable that this effect is one cause of the spread in the experimental values of T_t.

One must also consider regenerative effects of the gain. In particular, these might arise in the coupling region at the input of the slow wave structure. This effect influences the term

$$T_{mF}\, e^{+2\theta_{ad}} + T_{mB}\, e^{-2\theta_{ad}}$$

in eqn. (5.16). Measurements of the reflection properties of the input line of the TWM revealed only a very small change of the SWS input impedance when the spin system was inverted.

The scatter in the measured noise temperatures is explained mainly by errors caused by the experimentalist and errors in the attenuator reading, by instabilities in the TWM and postamplifier gain and by variations in the connection of the short circuit and open circuit terminations.

However, since the experiments have been performed at a number of different frequencies, and since the value for T_t in the experiments with maser 1 gives 5.3^{o}K and with maser 2, 4.9^{o}K, we believe that a reasonable value for T_t is

$$T_t = 5.0 \pm 1^{o}\mathrm{K}$$

at 3.300 MHz.

The system noise temperature T_S was also measured using a Hot-Cold-body (AIL type 07004). In Fig. 5.8 the experimental set up is shown. T_S is defined from (see Fig. 5.8):

$$T_S = 1.25 + 13.0 + T_t + \frac{1.04 + |\Gamma|^2\, 2.33}{1 - |\Gamma|^2} + \frac{T_x}{G_m\, G_{ca}} \quad (^{o}\mathrm{K}) \qquad (5.19)$$

and is obtained by measuring the Y-factor Y_{HC} and using the formula

$$T_S = \frac{371 - Y_{HC} \cdot 83.2}{Y_{HC} - 1} \qquad (^{o}K) \tag{5.20}$$

Then T_t is evaluated from equation (5.19) . The noise contribution from the RG-8-cable and the connector is measured by using other RG-8 cables in combination with the actual RG-8 cable. Furthermore, 13^{o}K is consistent with the nominal attenuation of 0.17 dB/foot, yielding 12^{o} K for a 30 cm cable without connectors.

In Fig. 5.9 T_t is depicted as obtained with the two methods.

Finally, the attenuation at room temperature of the TWM-input transmission line was measured, yielding an attenuation of 0.13 dB. The temperature distribution along the line was measured in a separate cryogenic experiment (Fig. 5.10). The average temperature is 130^{o} K which yields an equivalent noise temperature of 4.0^{o} K, if the losses are assumed constant along the line. In reality, the losses are lower the lower the temperature and this would yield a still lower noise temperature. However, since the top connector will certainly contribute a considerable amount of the noise, $4.0\,^{o}$ K must be considered to be in reasonable agreement with the measured noise temperature.

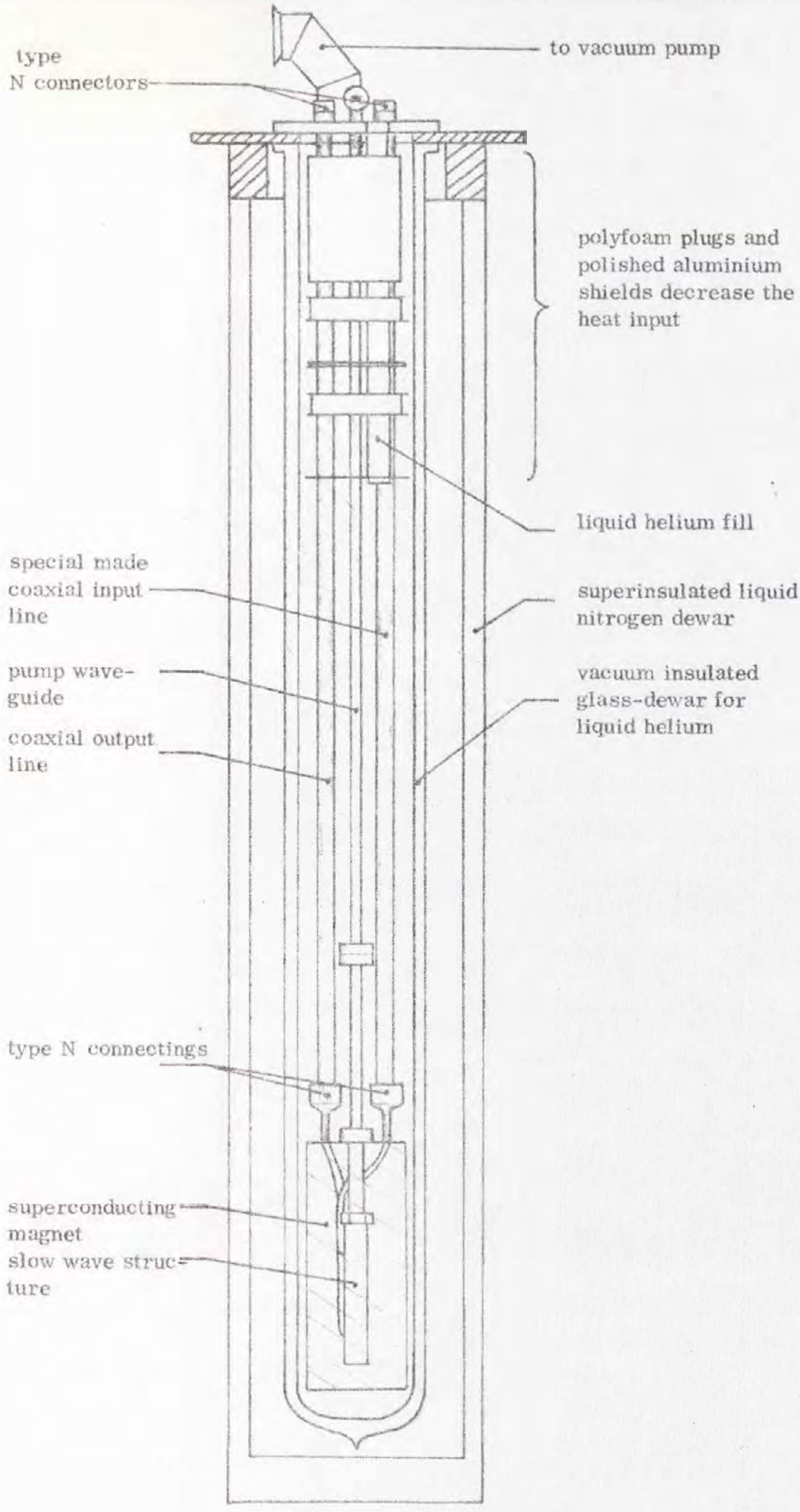

Fig. 5.4. The maser package

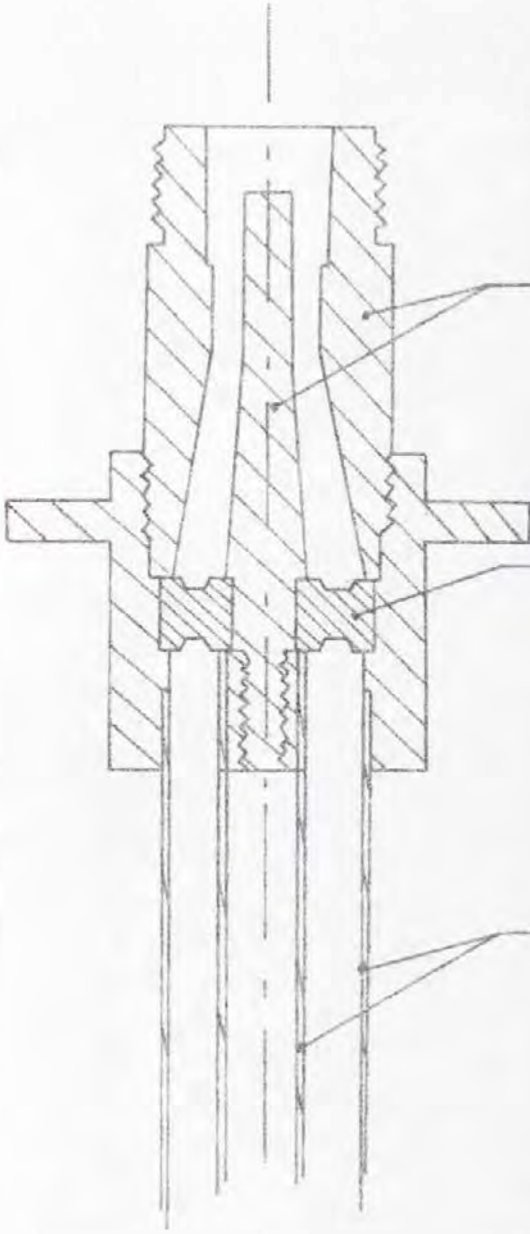

Fig. 5.5. The maser package input connector

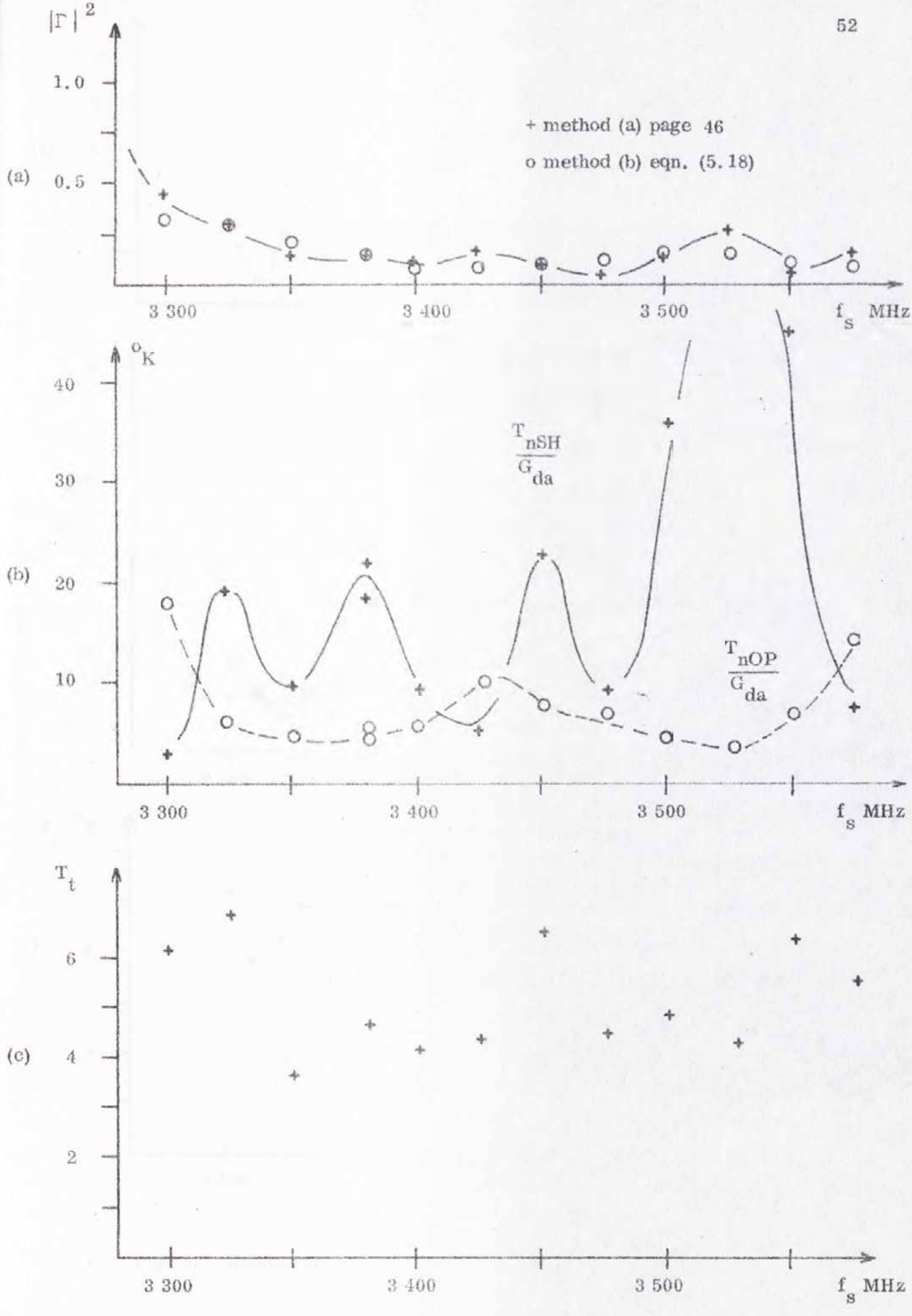

Fig. 5.6 Results from noise temperature measurements on Maser I.

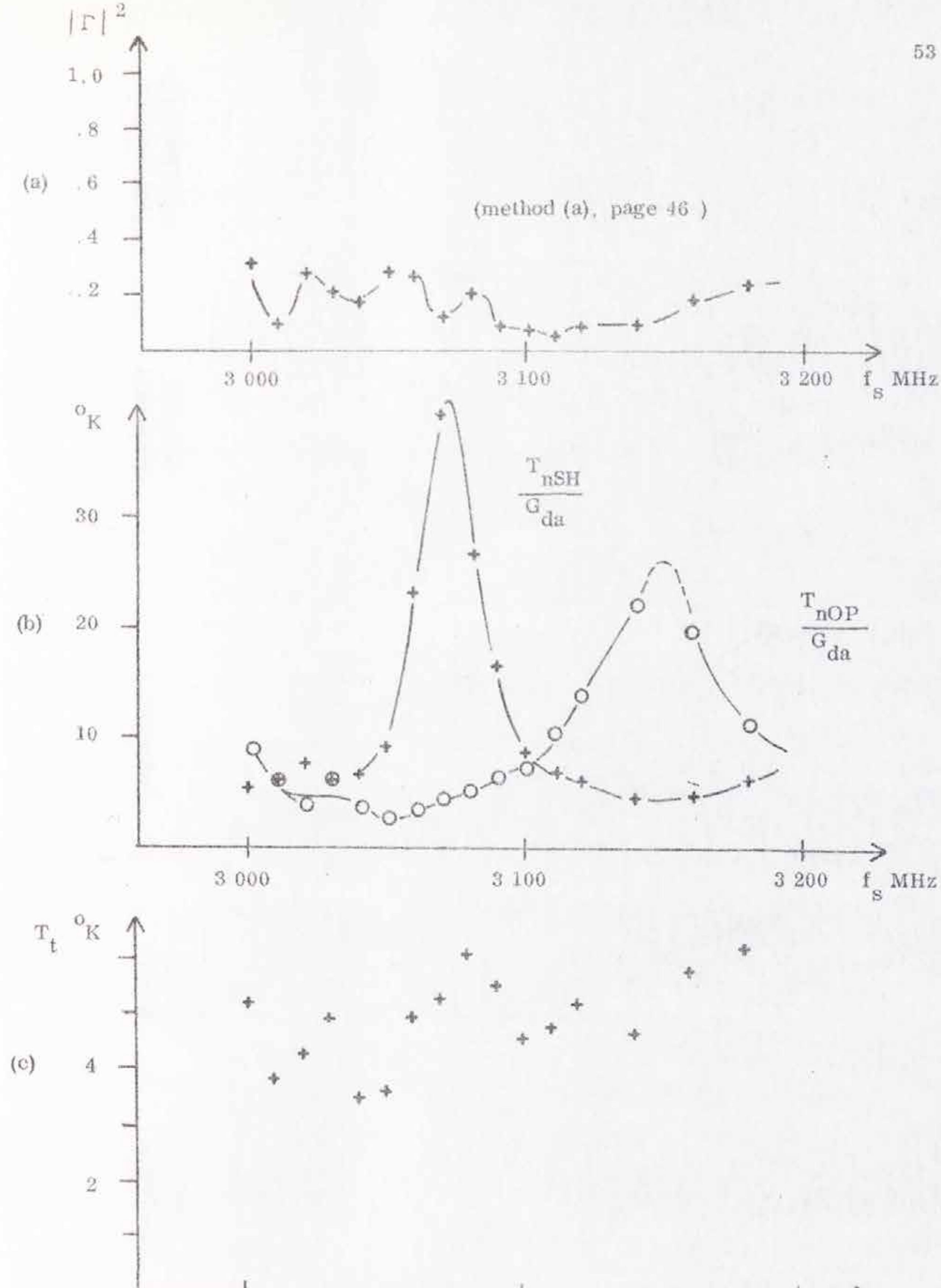

Fig. 5.7 Results from noise temperature measurements on Maser II.

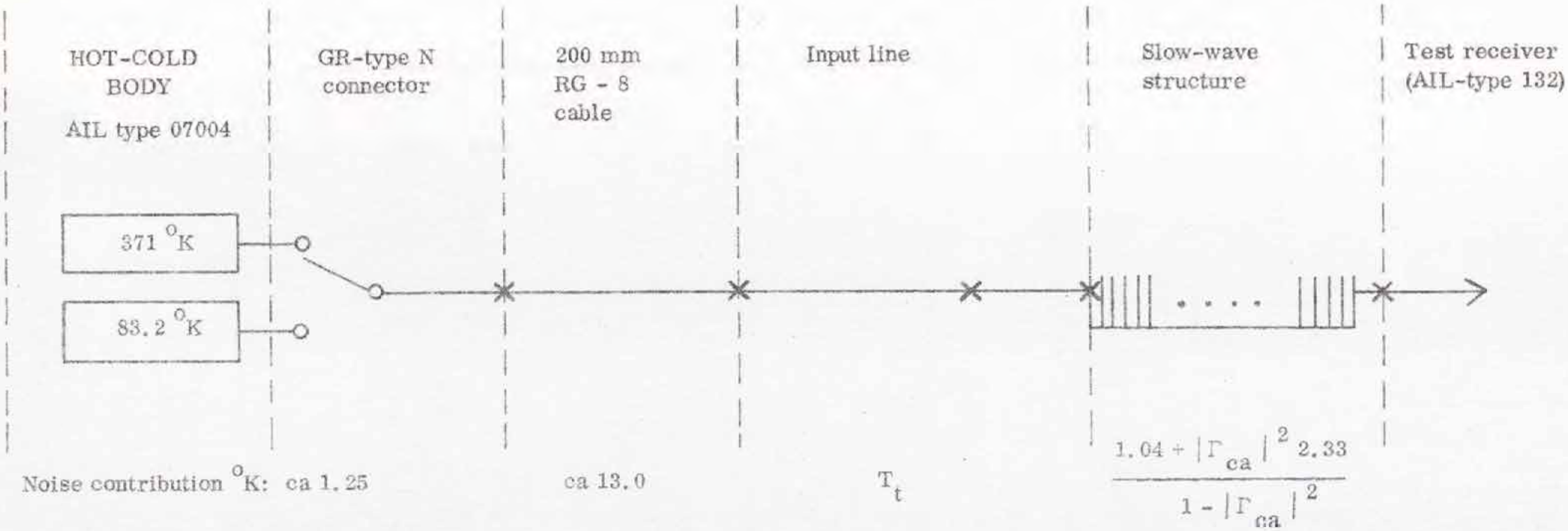

Fig. 5.8 Experimental set up for HC-body measurements.

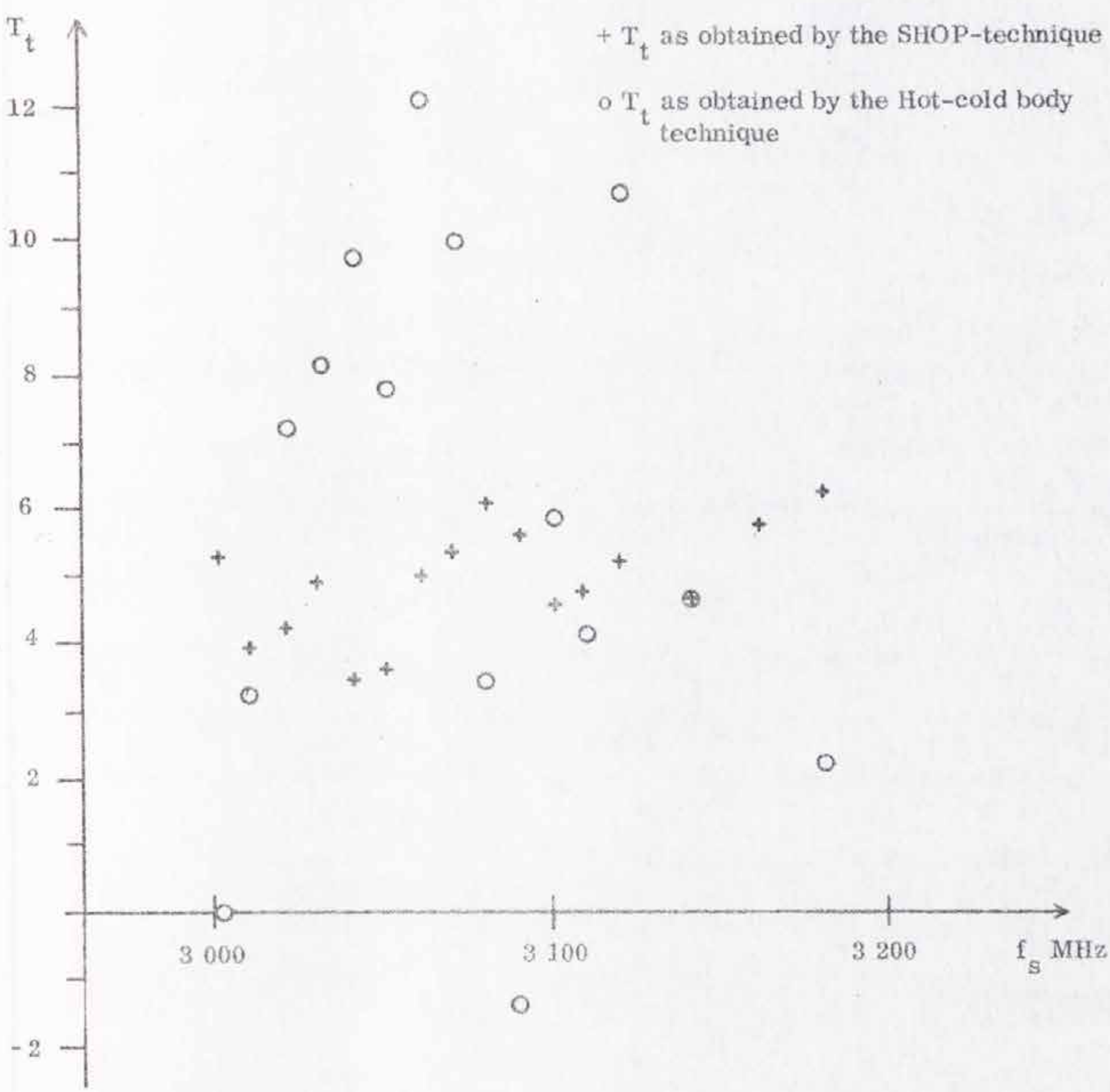

Fig. 5.9 Results from noise temperature measurements on Maser II using the SHOP-technique and the HOT-COLD body technique.

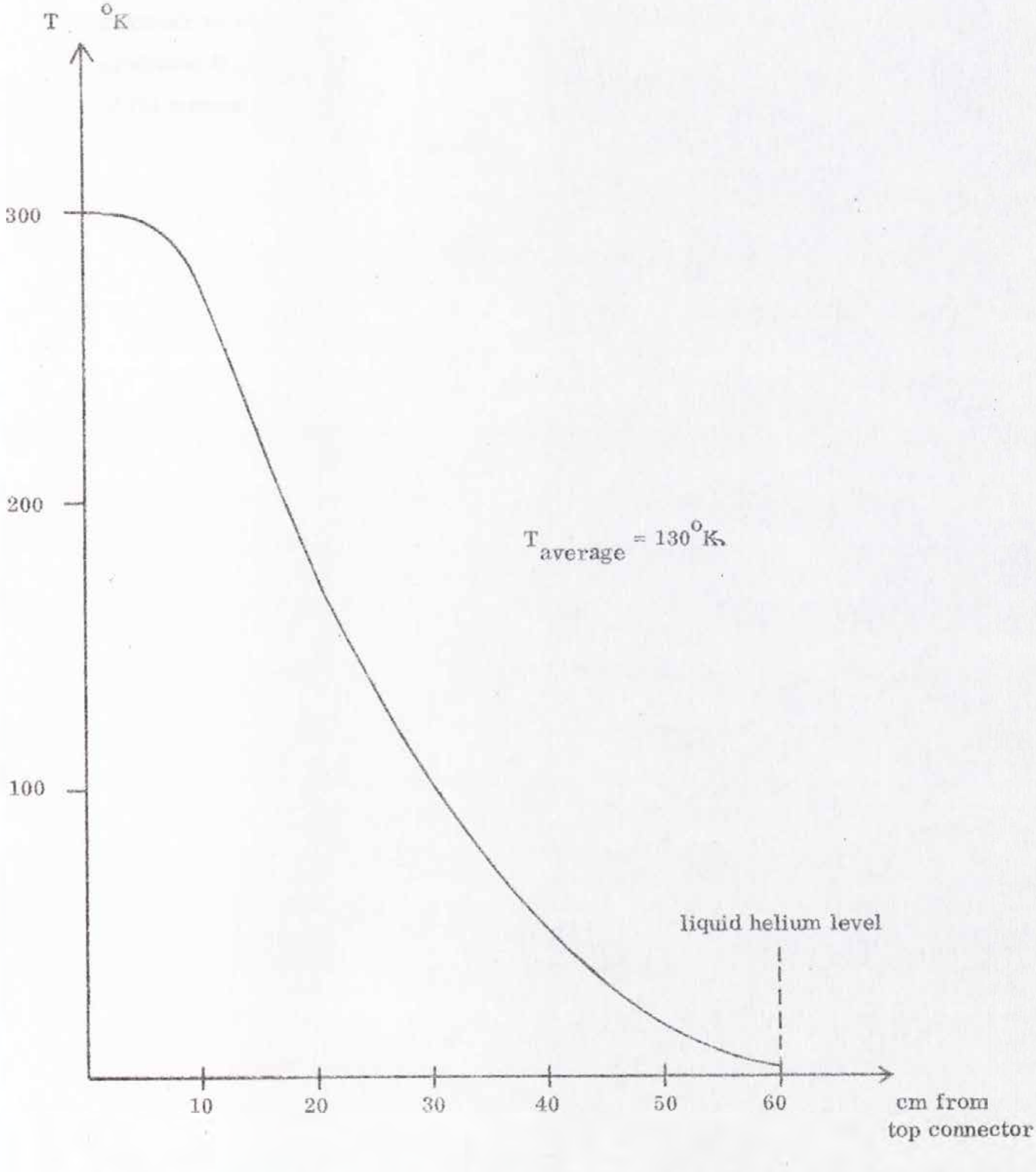

Fig. 5.10 Measured temperature distribution on the maser package input transmission line.

ACKNOWLEDGEMENTS:

I am indebted to professor O. E. H. Rydbeck for much encouragement and inspiration during the course of this research. Furthermore, I would like to express my gratitude to Mr. C. O. Lindström for invaluable help with the experiments and to professor B. Höglund, Mr. P. O. Andersson and Mr. P. Wrane for critical reading of the manuscript.

Appendix A

Properties of a lossy transmission line section between two lossless reciprocal coupling two ports.

The problem considered is illustrated in Fig. A 1.

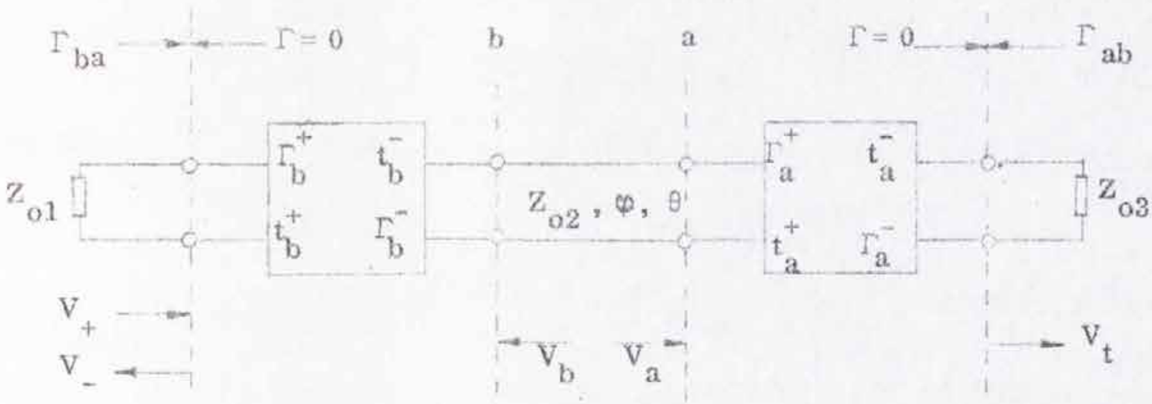

V_+ is the amplitude of the incident "power wave" from the generator. The coupling two-ports are assumed lossless and reciprocal. The properties of the scattering matrix for a lossless two-port yields in our notations (see e.g. ref. [13])

$$|\Gamma_b^+| = |\Gamma_b^-| \qquad |\Gamma_a^+| = |\Gamma_a^-| \tag{A.1}$$

$$t_b^+ t_b^- - \Gamma_b^+ \Gamma_b^- = - \frac{\Gamma_b^+ \Gamma_b^-}{\Gamma_b^2} \tag{A.2}$$

$$t_a^+ t_a^- - \Gamma_a^+ \Gamma_a^- = - \frac{\Gamma_a^+ \Gamma_a^-}{\Gamma_a^2} \tag{A.3}$$

To obtain the reflection coefficient $\Gamma_{ba} = \frac{V_-}{V_+}$, it is convenient to derive the amplitude of the traveling wave V_b

$$V_b = V_a \cdot \Gamma_a^+ e^{-j\varphi - \theta} \tag{A.4}$$

where

$$V_a = V_+ \, t_b^+ \, e^{-j\,\varphi - \theta} + V_b \, \Gamma_b^- \, e^{-j\,\varphi - \theta} \tag{A.5}$$

Since

$$V_- = V_+ \, \Gamma_b^+ + V_b \cdot t_b^- \tag{A.6}$$

the input reflection coefficient Γ_{ba} becomes

$$\Gamma_{ba} = \frac{V_-}{V_+} = \Gamma_b^+ + \frac{t_b^+ \, t_b^- \cdot \Gamma_a^+ \, e^{-j2\,\varphi - 2\,\theta}}{1 - \Gamma_a^+ \, \Gamma_b^- \, e^{-j2\,\varphi - 2\,\theta}} \tag{A.7}$$

or with (A. 2)

$$\Gamma_{ba} = \frac{\Gamma_b^+ - \dfrac{\Gamma_b^+ \, \Gamma_a^-}{|\Gamma_b|^2} \, \Gamma_a^+ \, e^{-j2\,\varphi - 2\,\theta}}{1 - \Gamma_a^+ \, \Gamma_b^- \, e^{-j2\,\varphi - 2\,\theta}} =$$

$$= \frac{\Gamma_b^{-*} - \Gamma_a^+ \, e^{-j2\,\varphi - 2\,\theta}}{1 - \Gamma_a^+ \, \Gamma_b^- \, e^{-j2\,\varphi - 2\,\theta}} \qquad \frac{\Gamma_b^+ \, \Gamma_b^-}{|\Gamma_b|^2} \tag{A.8}$$

where Γ_b^{-*} is the complex conjugate of Γ_b^-.
Similarly, the transmitted wave amplitude $V_t = V_a \cdot t_a^+$ is related to V_+ through

$$t_{ab} = \frac{V_t}{V_+} = \frac{t_a^+ \, t_b^+ \, e^{-j\,\varphi - \theta}}{1 - \Gamma_a^+ \, \Gamma_b^- \, e^{-j2\,\varphi - 2\,\theta}} \tag{A.9}$$

The transmitted power $P_t = |V_t|^2$ is related to the input power $P_i = |V_+|^2$ with a power transmission coefficient G_{ab}

$$G_{ab} = \left| t_{ab} \right|^2 = \frac{(1 - |\Gamma_a|^2)(1 - |\Gamma_b|^2)\, e^{-2\theta}}{\left| 1 - \Gamma_a^+ \Gamma_b^- e^{-j2\varphi - 2\theta} \right|^2} \tag{A.10}$$

From (A.8)

$$1 - \left| \Gamma_{ba} \right|^2 = \frac{(1 - |\Gamma_b|^2)(1 - |\Gamma_a|^2 e^{-4\theta})}{\left| 1 - \Gamma_a^+ \Gamma_b^- e^{-j2\varphi - 2\theta} \right|^2} \tag{A.11}$$

yielding with (A.10)

$$G_{ab} = (1 - |\Gamma_{ba}|^2)\, e^{-2\theta}\, \frac{1 - |\Gamma_a|^2}{1 - |\Gamma_a|^2 e^{-4\theta}} \tag{A.12}$$

Appendix B

Properties of a lossy transmission line with an arbitrary number of lossless discontinuities

In Fig. B.1 a situation is described in which a transmission line with an arbitrary number of lossless discontinuities is given. The section bc is an arbitrarily selected section not containing any discontinuity. The two port junctions I and II are transmission lines containing lossless discontinuities and are represented by their scattering matrixes [S] and [S'].

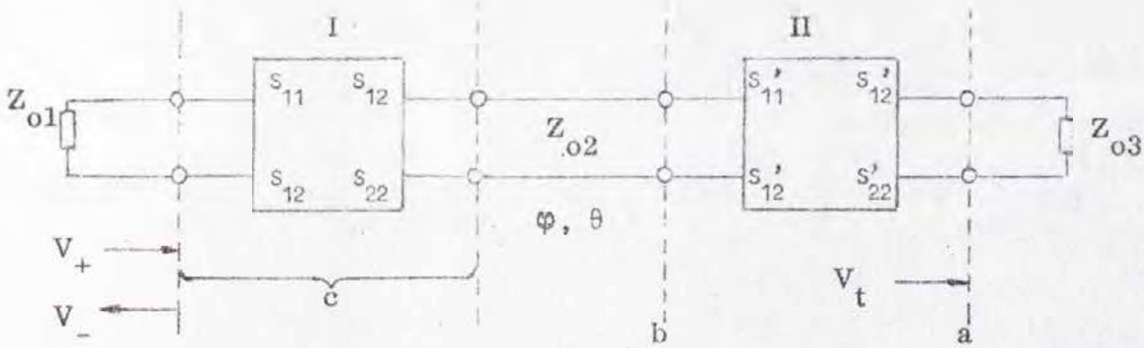

Fig. B.1

The calculations follow exactly the same lines as in Appendix A yielding

$$\Gamma^+ = \frac{V_-}{V_+} = \frac{S_{11} - \frac{S_{11}\,S_{22}}{|S_{11}|^2}\, S'_{11}\, e^{-j2\varphi - 2\theta}}{1 - S'_{11}\, S_{22}\, e^{-j2\varphi - 2\theta}} \tag{B.1}$$

or since $|S_{11}| = |S_{22}|$

$$\Gamma^+ = \frac{S^*_{22} - S'_{11}\, e^{-j2\varphi - 2\theta}}{1 - S'_{11}\, S_{22}\, e^{-j2\varphi - 2\theta}} \cdot \frac{S_{11}\, S_{22}}{|S_{11}|^2} \tag{B.1 a}$$

and

$$t = \frac{V_t}{V_+} = \frac{S_{12} \cdot S'_{12}\, e^{-j\varphi - \theta}}{1 - S'_{11}\, S_{22}\, e^{-j2\varphi - 2\theta}} \tag{B.2}$$

(Compare eqn. (A. 8) and (A. 9))

Consider now the special case when

$$[S] = \begin{bmatrix} \Gamma_c^+ & t_c^- \\ t_c^+ & \Gamma_c^- \end{bmatrix} \tag{B.3}$$

$$[S'] = \begin{bmatrix} \Gamma_{ba} & t_{ab} \\ t_{ba} & \Gamma_{ab} \end{bmatrix} \tag{B.4}$$

where Γ_{ba}, Γ_{ab}, t_{ba} and t_{ab} are obtained from eqn. (A. 8) and (A. 9). The power transmission coefficient G_{ca} can be obtained as

$$G_{ca} = \frac{(1 - |\Gamma_c|^2)\, G_{ab}\, e^{-2\theta_{bc}}}{\left|1 - \Gamma_c^- \Gamma_{ba}\, e^{-j2\varphi_{bc} - 2\theta_{bc}}\right|^2} \tag{B.5}$$

and similarly to eqn. (A. 11) , with eqn. (B. 1):

$$1 - |\Gamma_{ca}|^2 = \frac{(1 - |\Gamma_c|^2)(1 - |\Gamma_{ba}|^2\, e^{-4\theta_{bc}})}{\left|1 - \Gamma_c^- \Gamma_{ba}\, e^{-j2\varphi_{bc} - 2\theta_{bc}}\right|^2} \tag{B.6}$$

thus yielding, together with eqn. (A. 12)

$$G_{ca} = (1 - |\Gamma_{ca}|^2)\, e^{-2\theta_{ac}} \; \frac{1 - |\Gamma_{ba}|^2}{1 - |\Gamma_{ba}|^2\, e^{4\theta_{bc}}} \cdot \frac{1 - |\Gamma_a|^2}{1 - |\Gamma_a|^2\, e^{-4\theta_{ab}}} \tag{B.7}$$

This procedure may be repeated as many times as one wish, yielding a relation between the transmitted and reflected powers. The terms

$$\frac{1-|\Gamma|^2}{1-|\Gamma|^2 e^{-4\theta_{\alpha\beta}}} \tag{B.8}$$

are clearly a measure of the losses due to standing waves in the section $\alpha - \beta$.

If one let a, b, c ... be replaced by 1, 2, 3.... and if n scattering junctions are considered,

$$G_{n1} = (1-|\Gamma_{n1}|^2)\, e^{-2\theta_{n1}} \prod_{\nu=1}^{n-1} \frac{1-|\Gamma_{\nu 1}|^2}{1-|\Gamma_{\nu 1}|^2 e^{-4\theta_{\nu,\nu+1}}} \tag{B.9}$$

Appendix C

The noise power from a transmission line section between two lossless discontinuities.

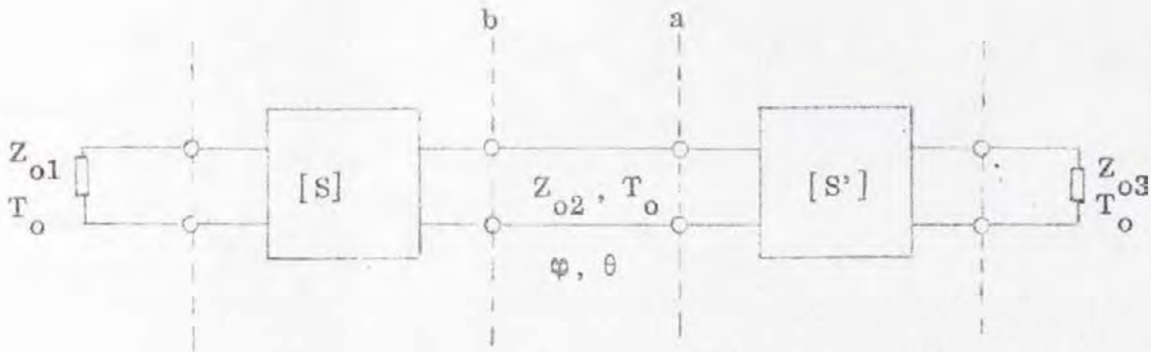

Fig. C.1.

Let all lossy parts of the circuit have the same temperature T_o . Note that the coupling sections are lossless. The lossy parts will emit noise power into the circuit. The noise power delivered by the transmission line a - b, to the terminating resistance Z_{o3} will now be derived. At the reference-plane, Z_{o3} will send a noise power to the left

$$P_3 = k\, T_o\, \Delta f \tag{C.1}$$

The impedance Z_{o1} will contribute a "noise power wave" to the right at the reference plane,

$$P_{t1} = \frac{|S_{12}|^2 |S'_{12}|^2\ e^{-2\theta}}{|1 - S'_{11}\, S_{22}\, e^{-j2\varphi - 2\theta}|^2} \cdot k\, T_o\, \Delta f \tag{C.2}$$

according to equation (B. 2), Appendix B.

The "noise power wave" P_3 emanating from Z_{o3} will be reflected at the reference plane and will contribute a "noise power wave" P_{r3} traveling back to Z_{o3} equal to

$$P_{r3} = \frac{\left| S_{11}'^{*} - S_{22}\, e^{-j2\varphi - 2\theta} \right|^2}{\left| 1 - S_{11}' S_{22}\, e^{-j2\varphi - 2\theta} \right|^2} \; k\, T_o\, \Delta f \qquad \text{(C.3)}$$

according to eqn. (B.1 a), Appendix B. Let the noise power delivered by the transmission line a - b be P_2. Then, considerations of thermodynamic equilibrium at the reference plane, lead to the conclusion that the noise power traveling to the right is equal to the noise power traveling to the left. Hence

$$P_3 = P_{t1} + P_{r3} + P_2$$

Solving for P_2 yields

$$P_2 = \left\{ 1 - \frac{\left| S_{12} \right|^2 \left| S_{12}' \right|^2 e^{-2\theta}}{\left| 1 - S_{11}' S_{22}\, e^{-j2\varphi - 2\theta} \right|^2} - \frac{\left| S_{11}'^{*} - S_{22}\, e^{-j2\varphi - 2\theta} \right|^2}{\left| 1 - S_{11}' S_{22}\, e^{-j2\varphi - 2\theta} \right|^2} \right\} \cdot$$

$$\cdot\, k\, T_o\, \Delta f \qquad \text{(C.4)}$$

or after some manipulation

$$P_2 = \frac{\left| S_{12}' \right|^2 \left(1 + \left| S_{22} \right|^2 e^{-2\theta}\right)}{\left| 1 - S_{11}' S_{22}\, e^{-j2\varphi - 2\theta} \right|^2} \left(1 - e^{-2\theta}\right) k\, T_o\, \Delta f \qquad \text{(C.5)}$$

This result is equivalent with that which can be obtained with the formulas in Appendix I of reference [6] if, in the notations of the reference

$$\left| C_{21} \right| = e^{-2\theta} \qquad \text{(C.6)}$$

$$\Gamma_1 = \Gamma_L\, e^{-j2\varphi - 2\theta} \qquad \Gamma_2 = \Gamma_r\, e^{-j2\varphi - 2\theta} \qquad \text{(C.7)}$$

and if $P_\eta\ (T_a)$ is solved.

References.

[1] E.L.Kollberg, K.S.Yngvesson: "An L-band rutile traveling wave maser". Proc. IEE 6th International Conf. on Microwave and optical Generation", vol. 27, 384 - 388, 1966.

[2] E.L.Kollberg, O.E.H.Rydbeck, "Rutile traveling wave maser system for the Onsala 84-foot radio telescope", IEEE Trans. on Microwave Theory and Technique, MTT-16, 799-803, 1968.

[3] A.E.Siegman, "Microwave solid state masers", Mc Graw Hill Book Co., New York 1964.

[4] J.D.Kraus, "Radio Astronomy", Mc Graw Hill Book Co., New York 1966.

[5] M.M.Brady, "The influence of mismatch error in noise performance measurements", Proc. IEEE, 52, 1075 - 1076, 1964.

[6] J.S.Wells, W.C.Daywitt, K.S.Miller, "Measurements of effective temperatures of microwave noise sources", IEEE Trans. on Instrumentation and Measurement, I - 13, 17 - 28, 1964.

[7] K.Fischer, A.Ziermann, "Zur Beschreibung der homogenen rauschenden Leitung mit Hilfe des Wellenkonzepts", Archiv der Electrischen Ubertragung, 21 , 464 - 470, 1967.

[8] C.T.Stelzried, "Microwave Thermal Noise Standards", IEEE Trans, on Microwave Theory and Technique, MTT-16, 646 - 655, Sept. 1968.

[9] W.J.Tabor, J.T.Sibilia, "Masers for the Telstar satellite communication experiments", Bell Syst. Tech. J., 42, 1863 - 1865, 1963.

[10] V.B.Shteinshleiger, O.A.Afanasev, G.S.Misizhnikov, Ya. I.Rosenberg, "A traveling wave quantum paramagnetic amplifier with enhanced efficiency", Cryogenics, 6 , 47 - 49, 1966.

[11] Noise issue of IEEE Transaction on Microwave Theory and Technique, MTT-16, Sept. 1968.

[12] W.E. Pastori, "New equation analysis mismatch errors in noise measurements", Microwaves, 8, 58 - 63, April 1968.

[13] R.E. Collin, "Foundations for microwave engineering", Mc Graw Hill Book Co. New York, 1966.

[14] P. Penfield, "Noise in Negative resistance amplifiers", IRE Trans. on circuit Theory, CT - 7, 166 - 170, 1960.

[15] K. Kurokawa, "Power waves and the scattering matrix", IEEE Trans. on Microwave Theory and Technique, MTT-13, 194 - 202, 1965.

Earlier publications from the Research Laboratory of Electronics:

O.E.H.Rydbeck: A theoretical survey of the possibilities of determining the distribution of the free electrons in the upper atmosphere; Trans. Chalmers Univ. of Techn., No. 3, 1942.

O.E.H.Rydbeck: On the propagation of radio waves; Trans. Chalmers Univ. of Techn., No. 34, 1944.

O.E.H.Rydbeck: On the spherical and spheroidal wave functions; Trans. Chalmers Univ. of Techn., No. 43, 1945.

O.E.H.Rydbeck: A simple Kerr modulator for ionospheric recording; Trans. Chalmers Univ. of Techn., No. 44, 1945.

O.E.H.Rydbeck: Chalmers solar eclipse ionospheric expedition 1945; Trans. Chalmers Univ. of Techn., No. 53, 1946.

Reports from the Research Laboratory of Electronics:

1. O.E.H.Rydbeck: The theory of the travelling-wave tube. 1947 x).
2. J.S.A.Tomner: The experimental development of travelling-wave tubes; Trans. Chalmers Univ. of Techn., No. 67, 1948.
3. S.I.Svensson: Pulser and water load for high power magnetrons; Trans. Chalmers Univ. of Techn., No. 68, 1948.
4. U.Ingård: On the radiation of sound into a circular tube with an application to resonators; Trans. Chalmers Univ. of Techn., No. 70, 1948.
5. D.Strantz: A study of impressive wave formation in the atmosphere; Trans. Chalmers Univ. of Techn., No. 71, 1948.
6. D.Strantz: Ozonradiosonde; Trans. Chalmers Univ. of Techn., No. 72, 1948.
7. O.E.H.Rydbeck: On the propagation of waves in an inhomogeneous medium, I; Trans. Chalmers Univ. of Techn., No. 74, 1948.
8. O.E.H.Rydbeck and D.Strantz: Ionospheric effects of solar flares. Preliminary report No. 1, Trans. Chalmers Univ. of Techn., No. 83, 1949.
9. O.E.H.Rydbeck: On the forced electro-magnetic oscillations in spherical resonators. 1948 x).
10. J.S.A.Tomner: Experimental investigation of a long electron beam in an axial magnetic field; Trans. Chalmers Univ. of Techn., No. 92, 1949.
11. O.E.H.Rydbeck: The ionospheric and radio wave propagation observatory at Kiruna, 67^{0} 50' N, 20^{0} 14,5' E. 1949 x).
12. R.Lindquist: The panoramic ionospheric recorder. 1949 x).
13. R.Lindquist: Ionospheric effects of solar flares. Preliminary reports Nos. 2 and 3; Trans. Chalmers Univ. of Techn., No. 95, 1950.
14. O.E.H.Rydbeck: The theory of magneto ionic triple splitting; Trans. Chalmers Univ. of Techn., No. 101, 1951.
15. O.E.H.Rydbeck and S.K.H.Forsgren: On the theory of electron wave tubes; Trans. Chalmers Univ. of Techn., No. 102, 1951.
16. R.Lindquist: Polar blackouts recorded at the Kiruna Observatory; Trans. Chalmers Univ. of Techn., No. 103, 1951.
17. S.K.H.Forsgren: Some calculations of ray paths in the ionosphere; Trans. Chalmers Univ. of Techn., No. 104, 1951.
18. B.N.Agdur: Experimental observations of double-stream amplification. Preliminary notes; Trans. Chalmers Univ. of Techn., No. 105, 1951.

x) Not published in the Chalmers Transactions.

19. B.N.Agdur and C-G.L.Åsdal: Noise measurements on a travelling wave tube; Trans. Chalmers Univ. of Techn., No. 106, 1951.

20. S.K.H.Forsgren and O.F.Perers: Vertical recording of rain by radar; Trans. Chalmers Univ. of Techn., No. 107, 1951.

21. O.F.Perers, B.K.E.Stjernberg and S.K.H.Forsgren: Microwave propagation in the optical range; Trans. Chalmers Univ. of Techn., No. 108, 1951.

22. R.Lindquist: A survey of recent ionospheric measurements at the ionospheric and radio wave propagation observatory at Kiruna. 1951 x).

23. R.Lindquist: A 16 kW panoramic ionospheric recorder; Trans. Chalmers Univ. of Techn., No. 109, 1951.

24. B.-A.Lindblad: A radar investigation of the delta aquarid meteor shower of 1950; Trans. Chalmers Univ. of Techn., No. 129, 1952.

25. G.Hellgren: The propagation of electromagnetic waves along a conical helix with variable pitch; Trans. Chalmers Univ. of Techn., No. 130, 1953.

26. G.Hellgren and J.Meos: Localization of aurorae with 10 m high power radar technique, using a rotating antenna. 1952 x).

27. O.E.H.Rydbeck: On the excitation of different space charge wave modes in travelling wave tubes; Trans. Chalmers Univ. of Techn., No. 131, 1953.

28. O.E.H.Rydbeck and B.N.Agdur: The propagation of electronic space charge waves in periodic structures; Trans. Chalmers Univ. of Techn., No. 138, 1954.

29. B.N.Agdur: Experimental investigation of noise reduction in travelling wave tubes; Trans. Chalmers Univ. of Techn., No. 139, 1954.

30. B.N.Agdur: Amplification measurements on a velocity step tube; Trans. Chalmers Univ. of Techn., No. 140, 1954.

31. O.E.H.Rydbeck and H.Wilhelmsson: A theoretical investigation of the ionospheric electron density variation during a solar eclipse; Trans. Chalmers Univ. of Techn., No. 149, 1954.

32. H.Wilhelmsson: The interaction between an obliquely incident plane electromagnetic wave and an electron beam. Part I; Trans. Chalmers Univ. of Techn., No. 155, 1954.

33. S.Olving: Electromagnetic wave propagation on helical conductors imbedded in dielectric medium; Trans. Chalmers Univ. of Techn., No. 156, 1955.

34. S.Olving: Amplification of the travelling wave tube at high beam current. Part I; Trans. Chalmers Univ. of Techn., No. 157, 1955.

35. H.Wilhelmsson: On the reflection of electromagnetic waves from a dielectric cylinder; Trans. Chalmers Univ. of Techn., No. 168, 1955.

36. B.-A.Lindblad: Combined visual and radar observations of Perseid meteors. I: Observations in 1953 x)

37. S.Olving: A new method for space charge wave interaction studies. Part I; Trans. Chalmers Univ. of Techn., No. 178, 1956.

38. V.Westberg: Measurements of noise radiation at 10 cm from glow lamps; Trans. Chalmers Univ. of Techn., No. 180, 1956.

39. S.I.Svensson, G.Hellgren and O.Perers: The swedish radioscientific solar eclipse expedition to Italy, 1952; Trans. Chalmers Univ. of Techn., No. 181, 1956.

40. N.Wax: A note on design considerations for proposed auroral radar; Trans. Chalmers Univ. of Techn., No. 182, 1957.

41. N.Wax: On the ring current hypothesis; Trans. Chalmers Univ. of Techn., No. 171, 1956.

---

x) Not published in the Chalmers Transactions.

42. G.H.Joshi: The electromagnetic interaction between two crossing electron streams. Part I; Trans. Chalmers Univ. of Techn., No. 183, 1957.

43. J.Meos and S.Olving: On the origin of radar echoes associated with auroral activity; Trans. Chalmers Univ. of Techn., No. 196, 1958.

44. G.H.Joshi: The electromagnetic interaction between two crossing electron streams. Part II; Trans. Chalmers Univ. of Techn., No. 197, 1958.

45. H.Wilhelmsson: The interaction between an obliquely incident plane electromagnetic wave and an electron beam. Part II; Trans. Chalmers Univ. of Techn., No. 198, 1958.

46. H.Wilhelmsson: On the properties of the electron beam in the presence of an axial magnetic field of arbitrary strength; Trans. Chalmers Univ. of Techn., No. 205, 1958.

47. H.Wilhelmsson: The interaction between an obliquely incident plane electromagnetic wave and an electron beam. Part III; Trans. Chalmers Univ. of Techn., No. 206, 1958.

48. B.Höglund and V.Radhakrishnan: A radiometer for the hydrogen line; Trans. Chalmers Univ. of Techn., No. 223, 1959.

49. S.Olving: Electromagnetic and space charge waves in a sheath helix; Trans. Chalmers Univ. of Techn., No. 225, 1960.

50. H.Wilhelmsson: A survey of radio-frequency and microwave resonance lines of interest to radio astronomy. 1960 x).

51. S.Olving: A new method for space charge wave interaction studies. Part II; Trans. Chalmers Univ. of Techn., No. 228, 1960.

52. Papers presented at the fourth international conference on ionization phenomena in gases at Uppsala, August 17-21, 1959. 1960 x).

53. H.Wilhelmsson: Two problems concerning the electron ring current. 1960 x).

54. T.Orhaug: The variation of electron density in the ionosphere during a solar eclipse. 1960 x).

55. H.Wilhelmsson and M.Fischer: On the force-free magnetic fields. 1960 x).

56. O.E.H.Rydbeck: On the coupling between waves in inhomogeneous systems. 1961 x).

57. H.Wilhelmsson: The scattering of an electromagnetic wave by a dielectric-coated metallic cylinder. Reprint from Arkiv för Fysik, Band 23, nr 41 x).

58. H.Wilhelmsson: Accounting for smoothing effects in 21 cm observations. Reprint from Arkiv för Astronomi, Band 3, nr 15 x).

59. B.Hoglund: 21 cm Observations in the Galactic Anti-centre. Reprint from Arkiv för Astronomi, Band 3, nr 16 x).

60. H.Gerritsen: Recent Developments in Maser Devices and Materials. Reprint from Applied Optics, Vol. 1, No 1 x)

x) Not published in the Chalmers Transactions.

Research Reports from the Research Laboratory of Electronics:

1. O.E.H.Rydbeck and K.H.B.Wilhelmsson: The influence of the electron velocity distribution on space charge waves. 1959.

2. K.H.B.Wilhelmsson: Oscillatory properties of gyromagnetic electronic cold plasmas with drift motion. 1959.

3. H.B.Hvatum: Solar radio noise measurements during the 1954 solar eclipse. 1959.

4. T.Aa.Orhaug: Ionospheric observations during the solar eclipse June 30, 1954. 1959.

5. K.H.B.Wilhelmsson: The electromagnetic coupling between an electron beam and incident plane waves for an axially finite interaction domain. 1960.

6. Research notes communicated at the radio scientific conference in Stockholm, February 29 - March 2, 1960. 1960.

7. O.E.H.Rydbeck: The propagation and coupling of waves in inhomogeneous media with applications to electromagnetic and space charge waves. (On the propagation of waves in an inhomogeneous medium II).

8. O.E.H.Rydbeck: Electromagnetic and space charge waves in inhomogeneous structures with applications to ionized media and microwave tubes. 1960.

9. K.H.B.Wilhelmsson: On the geometrical theory of diffraction with application to the electron beam. 1960.

10. O.E.H.Rydbeck: The Doppler effect in dispersive, inhomogeneous media with applications to electromagnetic waves in ionized media. 1960.

11. S.Olving and A.Ots: An experimental investigation of the propagation of space charge waves along radially inhomogeneous electron beams. 1960.

12. A.V.Stomberg: The rotatron - an electron tube for shift and multiplication of frequencies. 1960.

13. O.E.H.Rydbeck and M.H.Fischer: Space charge waves in an electron beam of Gaussian cross section. 1960.

14. O.E.H.Rydbeck: The integral equation of travelling wave tubes with electron beams of arbitrary cross section. 1960.

15. O.E.H.Rydbeck and A.R.Thomasson: Low frequency waves in inhomogeneous magneto ionic media. 1960.

16. T.Aa.Orhaug: Observations of radio star scintillations at high latitudes. 1960.

17. T.Aa.Orhaug: Observations of solar radio noise at 150 Mc/s. 1960.

18. O.E.H.Rydbeck and J.Askne: Whistler mode - ionized stream interactions. Part I, 1963.

19. K.H.B.Wilhelmsson: On the problem of overtaking in a velocity distributed electron stream. 1960.

20. O.E.H.Rydbeck: On the coupling between waves in inhomogeneous systems. 1960.

21. O.E.H.Rydbeck: Research in the field of propagation and interaction of electrom[illegible]es and space charge type waves in homogeneous and inhomogeneous media. 1960.

22. D.T.Farley, J.P.Dougherty and D.W.Barron: A theory of incoherent scattering of radio waves by a plasma in a uniform magnetic field. 1961.

23. L.F.Eastman: Coherent non-linearities in a mangeto-ionic medium. 1961.

24. D.T.Farley: Artificial heating of the electrons in the F-region of the ionosphere. 1961.

25. K.H.B.Wilhelmsson: Scattering of electromagnetic waves by an anisotropic medium. 1961.

26. K.H.B.Wilhelmsson: The interaction between an obliquely incident plane electromagnetic wave and an electron beam in the presence of a static magnetic field of arbitrary strength. 1961.

27. O.E.H.Rydbeck: Dynamic non-linear wave propagation in ionized media. 1. The isotropic medium. 1961.

28. O.E.H.Rydbeck: Dynamic non-linear wave propagation in ionized media. 2. The magneto-ionic medium. 1962.

29. O.E.H.Rydbeck: Dynamic non-linear wave propagation in ionized media. 3. Electromagnetic non-linear wave interaction and reflection from a plane ionized medium. 1963.

30. O.E.H.Rydbeck: Dynamic non-linear wave propagation in ionized media. 4. Non-linear electromagnetic wave propagation and harmonic radiation in magneto-ionic media. 1963.

31. K.H.B.Wilhelmsson: Dynamic non-linear wave propagation in ionized media. 5. Reflection of electromagnetic waves from an ionized stream in the presence of a high power primary wave. 1962.

32. K.H.B.Wilhelmsson: Dynamic non-linear wave propagation in ionized media. 6. Scattering of electromagnetic waves by an anisotropic medium with an harmonically time-varying dielectric tensor. 1962.

33. O.E.H.Rydbeck: Dynamic non-linear wave propagation in ionized media. 7. Non-linear plasma waves in a streaming homogeneous, cold ionized medium. 1962.

34. A.R.Thomasson: Dynamic non-linear wave propagation in ionized media. 8. Reflection of electromagnetic waves from a dielectric plane layer varying periodically in space and time. 1962.

35. K.H.B.Wilhelmsson: Dynamic non-linear wave propagation in ionized media. 9. A non-linear coupling mechanism for generation of very low frequency waves. 1963.

36. K.H.B.Wilhelmsson: Dynamic non-linear wave propagation in ionized media. 10. Non-linear interaction between an obliquely incident plane electromagnetic wave and an electron beam. 1963.

37. S.Olving: On the non-linear theory of the plane travelling wave tube. 1963.

38. K-O.Yngvesson: Observations of the Venus probe Mariner R-2 at the Onsala Space Observatory. 1963.

39. K.H.B.Wilhelmsson: Dynamic non-linear wave propagation in ionized media. 11. Non-linear excitation of hydromagnetic waves and hybrid resonances by two interacting high power primary waves. 1963.

40. S.Olving and O.Nilsson: Propagation of nonlinear Hahn-Ramo waves along an annular electron current sheath. 1963.

41. S.Olving and M.Fischer: Small-signal nonlinear klystron waves. 1964.

42. S.Olving and S.Wallander: Nonlinear space charge wave theory of the hydrodynamic disc-electron beam. 1964.

43. O.E.H.Rydbeck: Dynamic non-linear wave propagation in ionized media. 12. Electromagnetic wave reflection from an oscillating, collision free magneto-ionic medium. 1964.

44. A.R.Thomasson: Dynamic non-linear wave propagation in ionized media. 13. Microscopic treatment of the interaction between a plane electromagnetic wave and an oscillating medium. 1964.

45. K.H.B.Wilhelmsson: Dynamic non-linear wave propagation in ionized media. 14. Generation of longitudinal plasma waves by non-linear coupling of two high-power circularly polarized transverse waves. 1964.

46. K.H.B.Wilhelmsson and A.R.Thomasson: Dynamic non-linear wave propagation in ionized media. 15. Čerenkov effect in a pre-oscillating medium. 1964.

47. K.H.B.Wilhelmsson: The magneto-ionic theory for mass-anisotropic electrons. 1964.

48. O.E.H.Rydbeck: Research in the field of propagation of high power waves in ionized media. 1964.

49. R.Tengblad: Concentration effects in a maser material. 1964.

50. O.Nilsson: Some frequency and power conversion proper ties of cyclotron waves. 1965.

51. O.Nilsson: Anomalous noise peak in Adler tubes. 1965.

52. In preparation.

53. J.Askne: Stimulated scattering from a semi-infinite dispersive medium periodic in time and space. 1965.

54. S.Yngvesson: Chromium-soped rutile: Maser properties at 1420 Mc/s and application to a traveling-wave maser, 1965.

55. T.M.Srinivasan: Measurements on nonlinear space charge waves, 1965.

56. O.E.H.Rydbeck: Wave coupling in multi-mode. inhomogeneous, ionized media, with applications to electron stream-whistler mode interactions. 1966.

57. P.McIsaac: Wave propagation in a dispersive medium. 1966.

58. S.Wallander: Nonlinear theory of the planar microwave vacuum diode. 1966.

59. S.Wallander: Nonlinear traveling wave tube analysis with two signal frequencies, 1966.

60. O.Nilsson: Approximate theory of the wire helix slow wave structure. 1966.

61. O.E.H.Rydbeck and Å.Hjalmarson: Coupled wave equations for multi-mode inhomogeneous media. 1966.

62. O.E.H.Rydbeck and Å.Hjalmarson: Coupled waves in magneto-ionic media. Part I. 1966.

63. J.Askne: Reflection and amplification of electromagnetic waves in an oscillating ionized medium, Part I. 1966.

64. J.Askne: Instability properties of an ionized medium periodic in time and space.
B.Rönnäng: Transient wave propagation in symmetric, ionized Epstein layers. 1966.

65. J.I.Lindström: Measurements of nonlinearities in a traveling wave tube. 1966.

66. J.Jäderblom: Cycletron wave amplification using self generated pump power. 1966.

67. O.Nilsson: Nonlinear distortion in traveling wave tubes. 1966.

68. S.Kronlund: Measurements on a beam-plasma microwave amplifier. 1966.

69. P.R.McIsaac: Boundary conditions for ferromagnetic media. 1966.

70. B.O.Rönnäng: Transient wave propagation in inhomogeneous ionized media. 1966.

71. S.Olving: Nonlinear microwave tube studies. 1966.

72. E.L.Kollberg: A dielectrically loaded slow-wave structure for traveling-wave maser applications. 1966.

73. B.O.Rönnäng: Signal distortion in anisotropic homogeneous ionized media. 1967.

74. A.Winnberg: The structure of galactic neutral hydrogen in a region of cygnus. 1967.

75. Å.Hjalmarson: Coupled wave Equations for Multi-Mode Inhomogeneous Media. II. 1967.

76. D.Berkley: Elastic Analysis of the Cornea. 1967.

77. S.Wallander: Large Signal Analytical Theory of Klyctron Waves. 1967.

78. S.Wallander: Large Signal Computer Analysis of Klystron Waves. 1967.

79. O.E.H.Rydbeck: Energy Flow in Multi-Mode Systems. 1967.

80. J.Askne: Reflection and Amplification of Electromagnetic Waves in an Oscillating Ionized Medium. Part II. 1967.

81. L.Hansson: Measurements of the Pointing Error for the Automatic Steering System of the Chalmers 84 Foot Radio Telescope. 1967.

82. E.A.Harris & K.S.Yngvesson: "Spin-Lattice Relaxation in Some Iridium Salts, Part I, I:25, 1968.

83. E.A.Harris & K.S.Yngvesson: "Spin-Lattice Relaxation in Some Iridium Salts, Part II, I:26. 1968.

84. K.S.Yngvesson: "Maser Properties of Cr - TiO_2 at L- and S-Band and Their Interpretation in Terms of Crystal Field and Exchange-Coupled Cluster Relaxation Processes, 1968.

85. I.Ewaldz: "Observations of the 189 (965 MHz) Excited Hydrogen Line in Orion A and M 17". 1968.

86. J.I.Lindström & O.Nilsson: Crossmodulation in Traveling Wave Tubes, 1968.

87. J.Elldér: OH Spectral Line Measurements of Radiation from the Galactic H II Regions W 3 and W 49 at 1665 MHz, 1968.

88. O.E.H.Rydbeck: Multi-Mode Wave Coupling in Inhomogeneous, Anisotropic Media - with Some Magneto-Ionic Applications, 1968.

89. O.E.H.Rydbeck and E.L.Kollberg: Rutile Traveling Wave Masers for the Frequency Range 1300 - 3400 MHz and their Application to the Onsala 84 foot Radio Telescope to Galactic Spectral Line Emission Studies, 1968.

90. Jumpol Prompitaks: The performance of a $LiNbO_3$ light modulator at 1.6 GHz, 1968.

91. J.Askne: Energy Considerations and Coupled Mode Analysis. 1969.

92. S.Wallander: Large Signal Computer Analysis of distortion in Traveling Wave Tubes, 1969.

93. S.Wallander: Nonlinear Multi-Signal Traveling Wave Tube Theory, 1969.

94. J.Askne: Reflection and amplification of electromagnetic Waves in an Oscillating Ionized Medium. Part III. Wave Propagation in a bounded time-space periodic plasma medium. 1969.

95. E.L.Kollberg: Measurements at noise in maser systems, theory and experiments. 1969.

96. J.Elldér: Some OH and Formaldehyde Properties of W 3 and W 51 Regions. 1970.

97. O.E.H.Rydbeck et al: Excited State OH Emissions From W 75 B and W 3, OH. 1970.

98. E.L.Kollberg: Rutile Traveling Wave Maser Systems for the Micro wave range 1.3-6.2 GHz. 1970.

99. P.Ingvarson: The Diffraction of an Electromagnetic Wave by Sound. 1970.

Lecture Notes from the Research Laboratory of Electronics:

1. K.H.B.Wilhelmsson: Lectures on the quantum theory of masers. 1962.

2. D.T.Farley: Lectures on the scattering of radio waves from randomly fluctuating media given 1961 at Chalmers University of Technology, Gothenburg. 1961.

3. A.Elvius: Lectures on galactic dynamics given 1961 at Chalmers University of Technology, Gothenburg. 1961

4. K.H.B.Wilhelmsson and A.G.Lieberman: Lectures on superconductivity. 1964.

THE ASTROPHYSICAL JOURNAL, Vol. 156, June 1969

OH AND FORMALDEHYDE RADIATION PROPERTIES OF THE W75 REGION

O. E. H. RYDBECK, J. ELLDÉR, AND E. KOLLBERG
Onsala Space Observatory, Research Laboratory of Electronics, Chalmers University of Technology, Gothenburg, Sweden
Received May 12, 1969

Possible temporal variations in the anomalous OH ground-state emission features associated with the W75 region were discussed by Palmer and Zuckerman (1967) and more recently also by Raimond and Eliasson (1969). Such variations, carefully recorded over a sufficient period of time, could yield extremely useful information concerning the relaxation times of supposed OH maser mechanisms and the lifespan of such emissions in protostars.

Originally the W75 OH emission was believed to come from the compact H II region DR 21 ($\alpha = 20^h37^m14^s$; $\delta = +42°09'$; Gaussian half-width of main component, 20″ at 1.4 GHz [Ryle and Downes 1967]) or from its immediate neighborhood. There have been various estimates of the distance to this source, ranging from 1.5 kpc, with a velocity with respect to the local standard of rest of 2.3 km sec^{-1} (Mezger *et al.* 1967), to 6 kpc, with -26 km sec^{-1} (Ryle and Downes 1967).

We have been recording the OH ground-state spectra of W75 from time to time since 1967 in order to estimate the magnitude and nature of these variations, using the Onsala 84-foot telescope with a rutile traveling-wave maser radiometer system (Rydbeck and Kollberg 1968). After carefully mapping the W75 region, depicted with the 1414-MHz isophotes of Pike and Drake (1964) on the red-sensitive *National Geographic–Palomar Sky Survey Atlas* plate, we found that it was composed of two sources, which we have temporarily designated W75 A and W75 B, with the following coordinates: W75 A, $\alpha = 20^h37^m12^s$, $\delta = 42.^\circ20$ (1950); W75 B, $\alpha = 20^h36^m58^s$, $\delta = 42.^\circ43$ (1950). These values were established only after an elaborate beam-subtraction and -addition technique had been used, since the antenna beam of the telescope has a half-power width of 29′ at the wavelength in question. Figure 1 (Plate L1) shows an enlargement of the area of interest, with scales and error limits inserted (DR 21 is represented by the small black circle adjacent to W75 A).

The final spectra, at the four OH ground states, at right- and left-circular polarization, are shown for sources A and B in Figures 2 and 3 (frequency resolution, 1 kHz). Both sources have their main (anomalous) emission in the 1665-MHz band, in the case of W75 A in the velocity range 0 to $+6$ km sec^{-1} and in that of W75 B in the more extended range 0 to $+14$ km sec^{-1}. Since the regular (H I) galactic rotation yields a maximum positive velocity of about 2.5 km sec^{-1} in the direction of DR 21, the strongest feature of W75 A is the only one with a velocity compatible with this model. The other velocities must, in one sense or the other, be regarded as peculiar and as characteristic for the various objects, possibly protostars, contributing to the spectrum.

One notices in Figures 2 and 3 the existence of an absorption region, at small negative velocities, in the 1720-, 1667-, and 1665-MHz spectra of W75 A. In order to investigate the position of this absorption, we searched for the 4830-MHz formaldehyde (H_2CO) line, recently reported by Snyder *et al.* (1969). No emission was detected in the area, but a randomly polarized absorption, almost identical in shape with the OH absorption, was

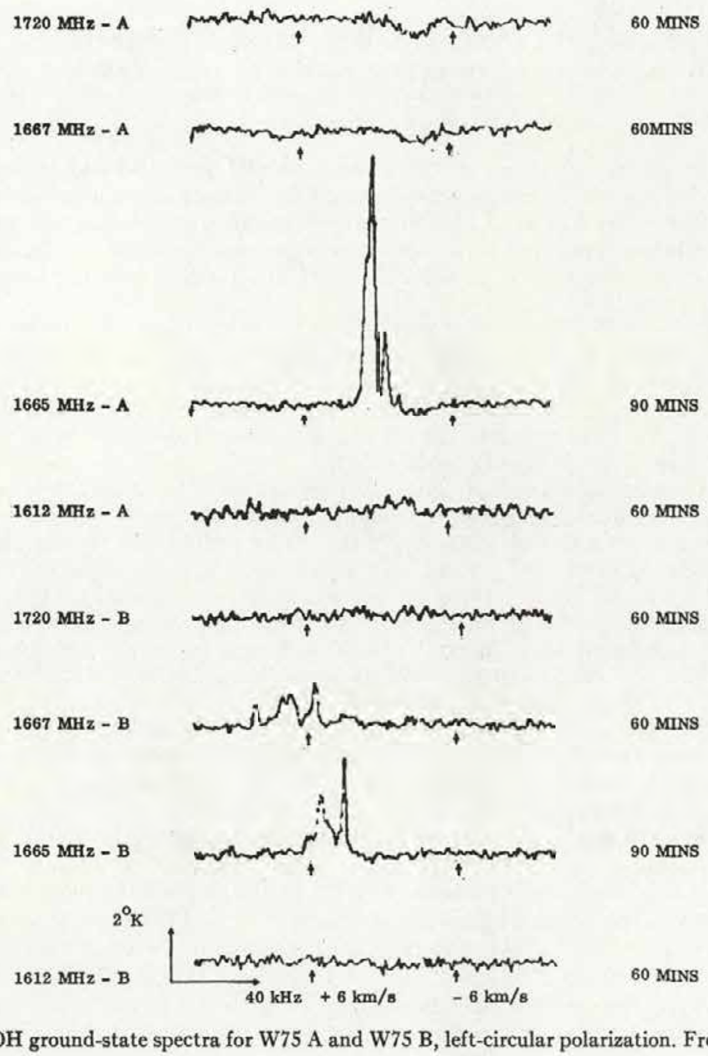

FIG. 2.—OH ground-state spectra for W75 A and W75 B, left-circular polarization. Frequency resolution, 1 kHz.

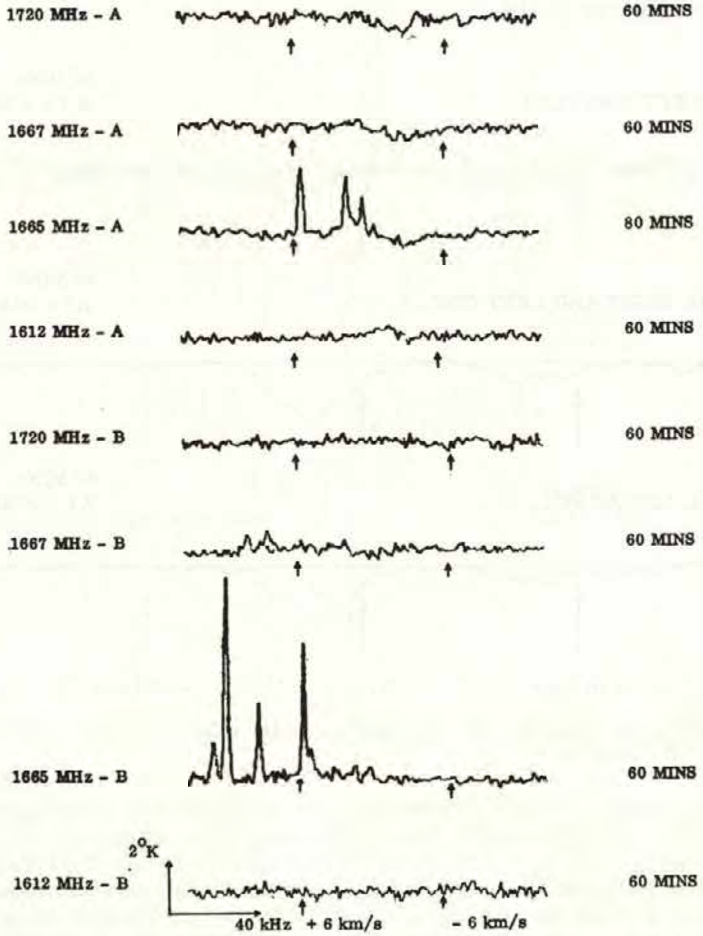

FIG. 3.—OH ground-state spectra for W75 A and W75 B, right-circular polarization. Frequency resolution, 1 kHz.

observed (Fig. 4). At this frequency (4830 MHz) it became easier to analyze the position of this absorption, originally designated W75 C. There is every indication that this is seen against the background of DR 21. Since this two-dip absorption feature could be regarded as emanating from an expanding, contracting, and also rotating gas ring, or cloud, it is interesting to notice that the mean velocity of these double absorption maxima is 1.5 km sec^{-1} for H_2CO as well as for OH. This would correspond to a distance of either 0.7 or 2.2 kpc, assuming that the center of the "absorption complex" moves synchronously with the galactic rotation. These values thus might indicate the minimum expected distance to DR 21.

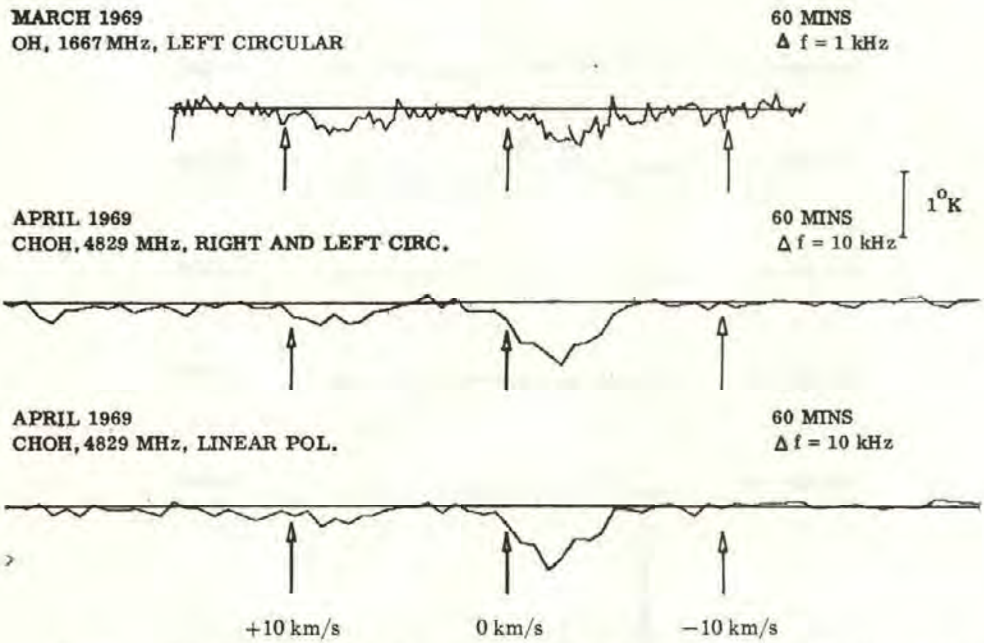

FIG. 4.—W75 C (DR 21) absorption spectra for OH and H_2CO (formaldehyde). Adopted H_2CO rest frequency, 4829.649 MHz.

The almost detailed similarity between the OH and H_2CO absorption spectra is especially interesting. Figure 5 depicts the situation for W51, as recorded at the Onsala Observatory. Apart from the strong anomalous emission feature in the 1612-MHz band, at right-circular polarization (which may be unrelated to the absorption complex), these absorption profiles are also almost identical for OH and H_2CO. As in the case of W75 C (DR 21), this probably indicates a relatively constant ratio between the numbers of OH and H_2CO molecules.

Let us finally return to the problem of the temporal variations of the W75 sources. Some of the earlier "variations" were, quite obviously, due to inadequate pointing accuracy. A slight position offset from W75 A would greatly influence the (later subtracted) contributions from W75 B. A certain temporal variation seems to remain in W75 A, however, at least as far as the main 1665-MHz feature around 0.5 km sec^{-1} is concerned. So far, no conspicuous changes have been found in W75 B, but the time of reliable observation on this source is too short for any definitive conclusions to be drawn. W75 B is

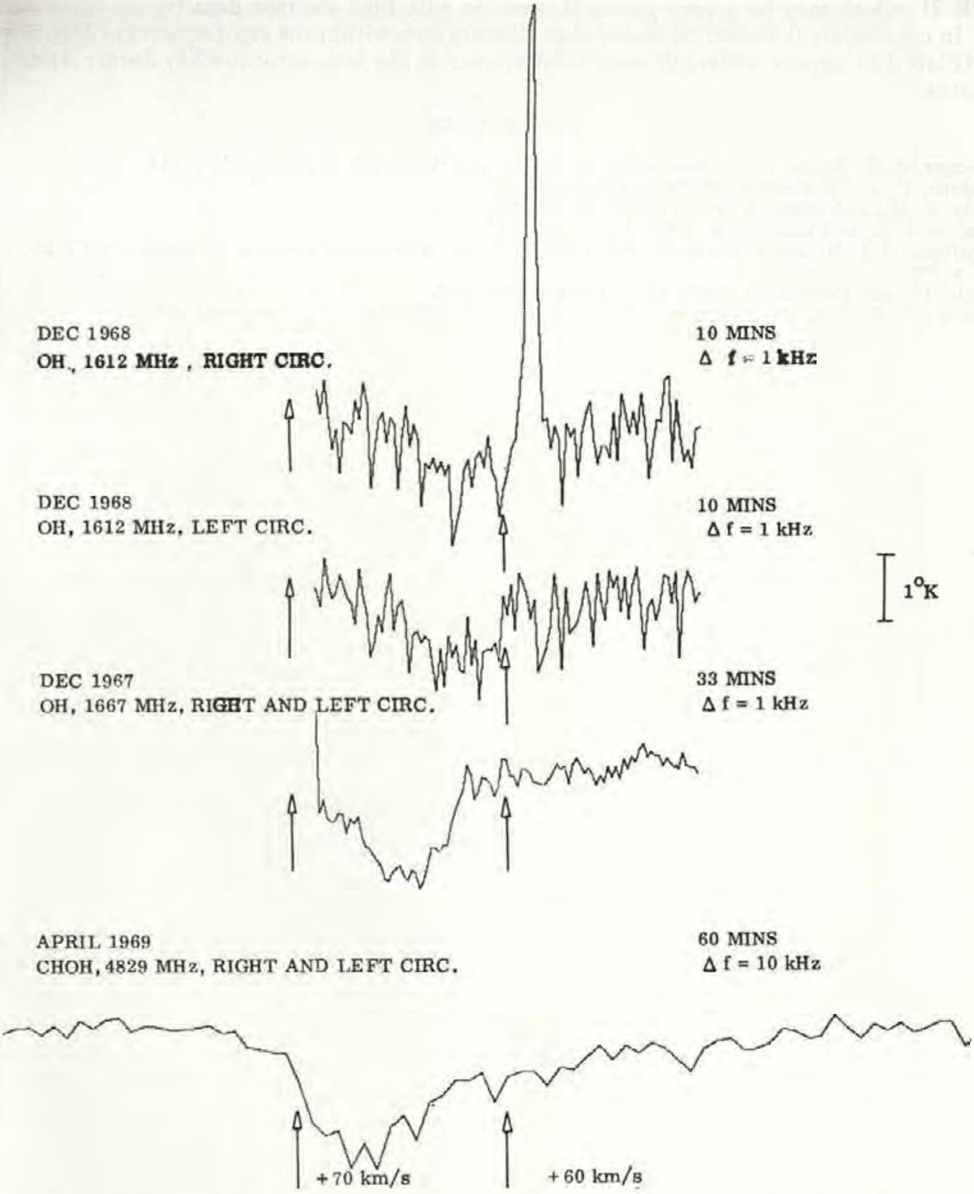

FIG. 5.—OH and H_2CO absorption spectra for the W51 complex. Adopted H_2CO rest frequency, 4829.649 MHz.

located in a "virtually" empty part of the region, whereas W75 A lies much closer to DR 21, which may be a very young H II region with high electron density.

In conclusion, it should be added that all stars seen within the error squares of Figure 1 (Plate L1) appear, although more faintly, even in the blue-sensitive *Sky Survey Atlas* plates.

REFERENCES

Mezger, P. G., Burke, B. F., Reifenstein, E. C., III, and Wilson, T. L. 1967, *A.J.*, **7**, 817.
Palmer, P., and Zuckerman, B. 1967, *Ap. J.*, **148**, 727.
Pike, E. M., and Drake, F. D. 1964, *Ap. J.*, **139**, 545.
Raimond, E., and Eliasson, B. 1969, *Ap. J.*, **155**, 817.
Rydbeck, O. E. H., and Kollberg, E. 1968, *I.E.E.E. Trans. Microwave Theory and Techniques* (MTT-16), **9**, 799.
Ryle, M., and Downes, D. 1967, *Ap. J.* (*Letters*), **148**, L17.
Snyder, L. E., Buhl, D., Zuckerman, B., and Palmer, P. 1969, *Phys. Rev. Letters*, **22**, 679.

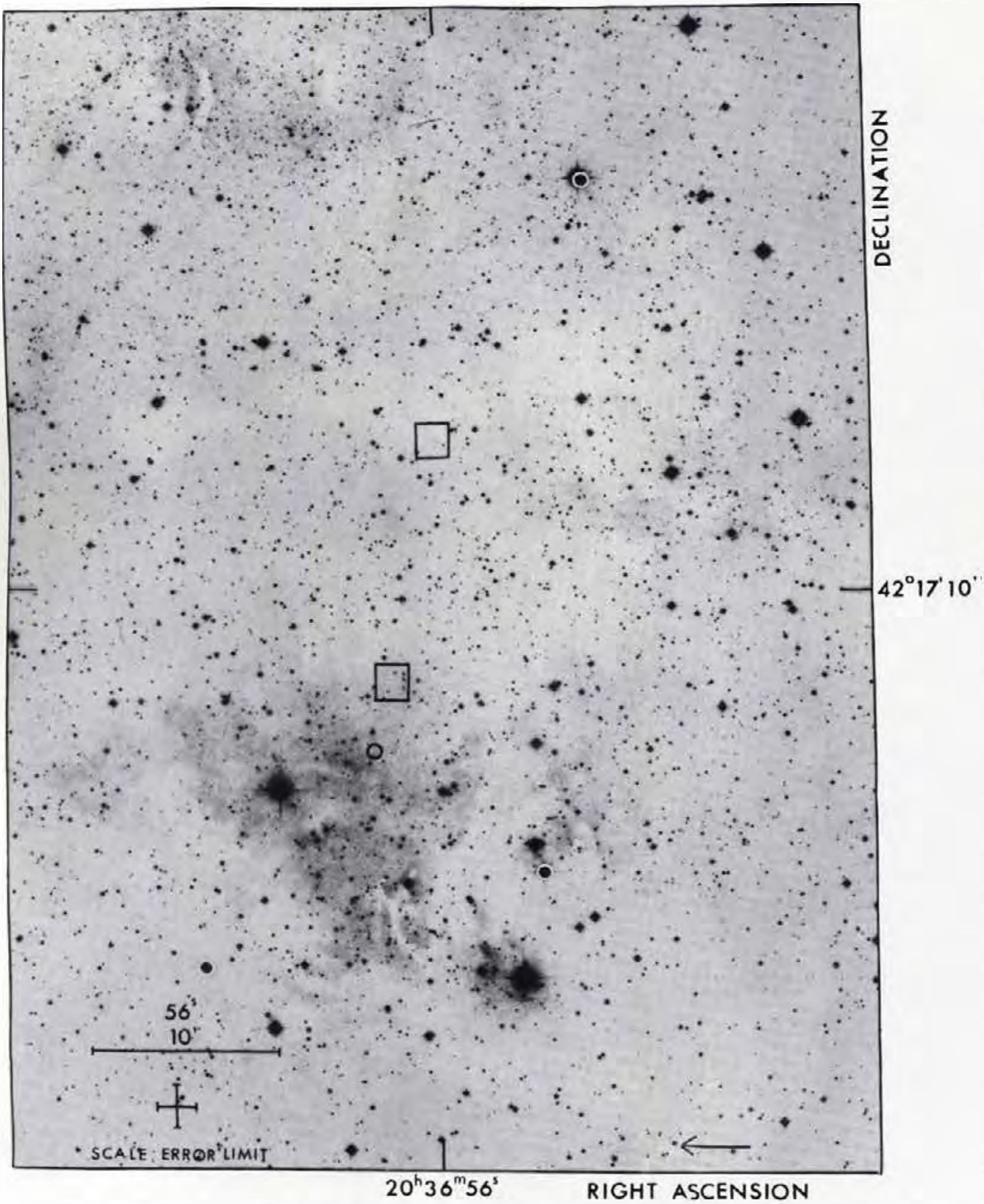

FIG. 1.—Red-sensitive detail of W75 A and W75 B regions, with DR 21 (W75 C) marked with open circle.

RYDBECK *et al.* (*see* page L141)

I:37

Nr. 104
Bil. 6

Tp

OH EXCITED STATE EMISSIONS FROM W 75 B AND W 3, OH

BY
O.E.H. RYDBECK, E. KOLLBERG
AND J. ELLDÉR

RESEARCH REPORT NO 97
1970

RESEARCH LABORATORY OF ELECTRONICS

CHALMERS UNIVERSITY OF TECHNOLOGY
GIBRALTARGATAN 5 G
GOTHENBURG S, SWEDEN

Research Laboratory of Electronics
CHALMERS UNIVERSITY OF TECHNOLOGY
Gothenburg, Sweden

RESEARCH REPORT No 97

OH EXCITED STATE EMISSIONS FROM W 75 B AND W 3, OH

by

O.E.H. Rydbeck, E. Kollberg and J. Elldér

Onsala, February 1970

OH EXCITED STATE EMISSIONS FROM W 75 B, AND W 3, OH.

by

O.E.H. Rydbeck, E. Kollberg, and J. Elldér

Onsala Space Observatory, Research Laboratory of Electronics,

Chalmers University of Technology, Gothenburg, Sweden

Abstract

Strongly varying 6035 MHz emission from the F = 3 → 3 transition of the $^2\Pi_{3/2}$, J = 5/2 state of OH has been detected in W 75 B with the Onsala 84-foot, maser equipped telescope. These variations appear to be well correlated with simultaneously observed temporal variations in the 1667 MHz ground state radiation. The 6035 - emission is split, possibly by rotation of the emitting object or by a magnetic field, into two almost circularly polarized components. None of the remaining three lines of this state were found in W 75 B.

Detailed Onsala observations of the F = 3 → 3, and 2 → 2 lines from W3 - OH, have shown that they are also polarized much like the W 75 B emissions, but lack detectable temporal variations. An effort has been made to relate the W 3- OH excited state emissions to some of the ground state components previously resolved by VLBI-methods.

The Onsala - group has looked for the 6 GHz excited state emission in several other sources including W 75 A, but so far with negative results. Because of the strong intensity variations found in W 75 B, negative results must be received with some caution.

W 75 B ($\alpha = 20^h 36^m 58^s$; $\delta = 42^o.43$; 1950.0)

Early in August 1969 the Onsala 84-foot telescope, equipped with a rutile traveling wave maser radiometer system (Rydbeck, and Kollberg 1968; Kollberg 1970) was used to search for the Λ -doublet transitions of the excited $^2\Pi_{3/2}$, J = 5/2 state of OH in the W 75 B ground state source earlier reported by the authors (Rydbeck et al. 1969). Yen et al. (1969) observed both Δ F= 0 transitions in W 3 - OH, using the 150 foot Algonquin telescope. In W 75 B only one, the F = 3 → 3 transition at 6035.085 ($\pm$ 0.005) MHz, has been found so far.

Its maximum intensity amounts to about 40 % of the corresponding emission from W 3-OH. (The distances to the two sources are comparable). The emission in the two sources has several features in common, except that in W 75 B it varies most remarkably with time (and therefore easily escapes detection).

Fig. 1 demonstrates the spectral shape of this radiation and its temporal variation. The zenith system noise was 45°K. Right and left circular polarizations denote intensities recorded with right and left circular filters in the feed system. All profiles are 3 kHz smoothed versions of the original 1 kHz resolution recordings. Mean integration time of the latter is 120 minutes.

There are four main features in the velocity range + 6 to + 10 km/s. All of them vary strongly with time (not unlike water vapor), but not in phase, which suggests that they originate in different sources. In what follows we will confine our attention to the main components (about + 6.5 km/s) which almost vanished during a brief period in late October.

It appears from Fig. 1 that the $F = 3 \rightarrow 3$ emission is predominantly circularly polarized and looks like Zeeman-doublets (viewed in the direction of the magnetic field). It differs notably from the ground state features in this respect.

A closer inspection of the RC-LC difference, reveals that the right and left polarized components are split around a mean center velocity of 6.45 km/s by about 0.3 km/s (or 6 kHz). Since $\Delta v = \pm 0.28 \times 10^{2} \times H$ (Gauss) km/s for the state in question, magnetic splitting would correspond to a field of $\sim 5.3 \times 10^{-3}$ Gauss. This value is rather high and, if real, indicates that the excited state emission emantes from relatively dense OH - clouds.

Since it is likely that an excited state source is also a strong ground state emitter, one is tempted to look for correlations, or relationships between the 6035 MHz features and the 1665 and/or 1667 MHz ones. This is not very easy because the OH ground state features, though strongly polarized (usually circularly right (RC) or left (LC)), do not display consistent Zeeman patterns. Furthermore, 1665 MHz VLBI measurements (Moran 1968), which ought to be repeated, seem to prove that RC, and LC sources do not coincide in position in W 3 - OH. The situation is perhaps analogous in other OH emitting regions such as W 75 B.

The Zeeman splittings for the Δ F = 0 components of the ground state are Δ v = $\pm$ 1.8 x 10^2 x H, for 1667 MHz, and Δ v = $\pm$ 3.0 x 10^2 x H, for 1665 MHz. Thus, the lower frequency Zeeman components for the ground state lines corresponding to the excited state emission with an assumed center velocity of 6.45 km/s (if at all present), should be found at + 7.4 km/s for the 1667 component, and + 8.0 km/s for the 1665 component if H ~ 5.3 x 10^{-3} Gauss. It appears from Fig. 3 that there are no such features at, or near these velocities (the rest frequency uncertainty is $\pm$ 0.25 km/s for the excited state and $\pm$ 0.36 km/s for the ground state). With the above assumptions the higher frequency Zeeman components for the ground state should fall at 5.5 km/s (1667) and 4.9 km/s (1665). In this case there are discrete, narrow features (both predominantly LC) at the predicted velocities. Moreover, it should be pointed out that the 1667 features are stronger than the 1665 ones, contrary to the situation in W 3 -OH.

If this coincidence is not accidental, it means that at least one of the ground state features is a higher frequency Zeeman component, and is related to the excited state emission. Further evidence for such a relationship with the 1667 component at + 5.5 km/s appeared during the measurements, when it was found that the amplitude of this component varies greatly with time (as is indicated in Fig.3) in approximately the same time phase (with a possible period of about 5 months)as the 6035 MHz feature. This variation is demonstrated in Fig. 4 which also suggests that the ratio of the maximum amplitudes of the RC and LC 6035 components, the ellipticity of the 1667 feature and the 1665 MHz intensity varied but little, if at all, during the measurements. Furthermore, the apparent correlation between the 6035 and 1667 emissions might imply that the maser gains are almost identical for the two; that is, that the " coupling " between these emissions remains approximately constant.

A " coupling " between the 6035 and 1667 transitions is quite plausible. It should, for example, be possible to transfer part of the ground state inversion to the excited state by means of collisional excitation or by far infrared (120 μ) radiation (see Litvak, 1969). Furthermore, overlap of the Doppler-widths of the IR-absorption lines, which connect some hyperfine levels of the ground Λ -doublet with the first excited rotational states ($^2\Pi_{3/2}$ J = 5/2 and $^2\Pi_{1/2}$, J = 1/2), should make 1667 - and 1665 MHz emission possible as a result of IR pumping alone. If for example the 1667- emission varies with time, one might expect the 6035-one to do the same, as (so far) seems to be the case in W 75 B.

We found none of the three $^2\Pi_{1/2}$, J = 1/2 -lines (4660.242 MHz, F = 0 → 1; 4750.656 MHz, F = 1 → 1; 4765.562 MHz, F = 1 → 0) in W 75 B, although the latter line was found in W 3 - OH by Zuckerman et al. 1968. It is also interesting to notice that Meeks et al. found no water vapor in W 75 B, but in W 75 A, where it varies strongly with time (Knowles et al., 1969). We found none of the excited OH-lines in W 75 A, the limit of detection being about 0.1 °K.

Finally, it should be mentioned that the weaker 6035-features in W 75 B also showed a conspicuous variation with time, though not always in phase with the main feature. This proves that these temporal variations are not due to an agency between the receiver, and the emitting regions. Such an agency would most likely also affect the 1665 MHz emission, which lacks temporal variations. Assuming that the weaker 6035-features form a Zeeman-doublet the lowest frequency component is RC polarized, as is the case with the main 6035- feature at + 6.45 km/s.

If the 6035 and 1667 sources (or complexes of sources) are pairwise identical, or very closely related to each other, why is a lower frequency Zeeman component missing in the ground state emission? At the assumed magnetic field strength the ground state Zeeman shifts are larger than the Doppler widths, however, and some type of Zeeman-Doppler shift-compensation (or " shift resonance ") scheme (Cook, 1966) may have to be considered as a mode selection mechanism for the ground state. If it favors a 1667 MHz σ_+ mode, as in the present case (for example in an emitting medium expanding towards us with $\overline{v} \times \overline{H} \sim 0$), it should favor also the 1665 σ_+ mode but, most likely, a little deeper into the medium. So far, this seems to agree with our present ground state results for W 75 B, but the evidence is far from conclusive. The Zeeman shifts for the excited states are much smaller than for the ground state so that both Zeeman components may grow along the ground state path.

A rotating cloud, on the other hand, containing OH in the shape of a ring, could perhaps display velocity dispersion characteristics so that σ_+ and σ_- emissions from diametrically opposite limbs not only experienced shift resonances but were received at the earth at about the same frequency (e.g., Shklovskii 1968). Since the polarization would be the same for both emissions, one might erroneously be lead to assume that the medium emits only one Zeeman mode. But this would be inconsistent with the split shape of the excited state features, unless some kind of non linear mode competition (see e.g., Litvak 1969) is at work for these states. It seems to be difficult to adjust the rotational model to explain the W 75 B data satisfactorily at present.

W 3. OH ($\alpha = 2^h\ 23^m\ 14^s$; $\delta = 61.^o64$; 1950.0)

The variability of the 6035- emissions in W 75 B induced us to study the OH-excited state spectra of W 3-OH (the only other source in which 6035 MHz emission has been found so far) in more detail, and over a sufficient span of time.

In contrast to the 6035-emissions in W 75 B, there are no temporal variations associated with this component, or its left handed counterpart. The same was found to hold for the RC and LC components of the 6030.739 MHz transition ($^2\Pi_{3/2}$, J = 5/2; F = 2 → 2), as well as for the practically unpolarized 4765.562 MHz emission (whose molecular g factor is almost zero). The lack of temporal variations of the excited state emission in W 3, is not too surprising, since the ground state features are known to be practically constant with time.

The 6035 MHz emissions as well as the 6030-ones are predominantly circularly polarized, with a Zeeman-type, longitudinal pattern splitting (for a comparison see also Yen et al, 1969). As in the case of W 75 B, the lower frequency components are RC polarized.

In an effort to relate the W 3-OH excited and ground state spectra to each other, we have in Figs. 6 and 7 plotted all of them as functions of the (radial) velocity. A denotes the velocity (-43.35 km/s), at which the RC 6035 - component has its main maximum; B, the velocity (- 43.75 km/s) of the smallest OH-source component in W 3-OH, (the diameter determined by VLBI between the US and Onsala is 0.0045" corresponding to 7 AU); D (45.1), the strongest feature (RC); and E (45.5) and F (-46.4), two LC sources of about the same magnitude.

The similarity between the RC and LC, 6035 and 6030 spectra is striking. They are most intense near and around the velocity B. But this does not necessarily imply that their peak emission originates in the samllest OH-compound. The 4765 emission, for example, which is unpolarized, bears no resemblance to the 6035/30-features, and has a very pronounced maximum (X) at about the D-velocity.

There is no obvious correlation between the 6035/30-features and those of the ground state. This is to be expected since W 3-OH consists of a complex of discrete sources (which have been VLBI-mapped only at 1665 MHz so far). In view of the results for W 75 B,the strongest 6035/30 emission might be related to one, or perhaps two, of these discrete sources of ground state emission (such fine structure could not be resolved at the ground state frequencies by terrestrial VLBI-experiments).

The striking similarity between the major parts of the RC and LC profiles of the 6035/30 emissions, leads one to shift them in frequency (velocity) by an amount that yields the best possible mutual fit. The results are shown in Fig. 8 (the upper and middle feature groups). The velocity shift, across a center velocity - 43.5 km/s (corresponding frequency, f_0, see Fig. 8), equals about 0.3 km/s for the 6035 - transition (or about the same as in W 75 B), and about 0.5 km/s (10 kHz) for the 6030 transition, for which $\Delta v = \pm 0.40 \times 10^2 \times H$ km/s. If the profile shifts are magnetic, one obtains 5.3×10^{-3} Gauss for the 6035 feature (as in W 75 B), and 6.3×10^{-3} for the 6030 one. The errors, about 10%, are hardly sufficient to explain the field strength differences (the magnitude of the peak-to-peak fluctuations shown in Fig. 8 equals about five times the RMS- value). The 6030 emission may, of course, be generated in a more dense medium.

In passing, it should be mentioned, however, that the ratio of the velocity splittings of the 6035 and 6030 features equals the ratio of the splittings of the ground state 1667 and 1665 features. This might only be a coincidence, but one could perhaps visualize a situation of non linear " coupling ", between the excited and ground state emissions, such that the 6035 splitting equalled that of the 1667 emission, and the 6030 splitting that of 1665. Such a coupling might lead to equal maser gain for the " related " excited and ground state radiations along a common amplification path (see also the previous section on W 75 B).

The wings of the 6035/30 spectra have peculiar maxima T, U, and V, which almost coincide (in velocity) when the RC and LC features are shifted to match each other. These maxima are perhaps related to different emitters within the same complex of sources. The X-features are almost unpolarized and appear, within the frequency error, at the same velocity as the main peak of the 4765 feature. All of them may be related to the RC 1665 MHz feature at about -45.1 km/s. Recent VLBI measurements Haystack - Onsala (Rönnäng et al, 1970) have shown this feature to consist of at least two sources, one at about -45.0 km/s, and the other one, with the highest visibility, at -45.3 km/s.

If we assume that the 6035/30 spectrum is magnetically split by a mean field of the strength 6×10^{-3} Gauss, the corresponding lower frequency Zeeman components (RC) should appear at -41.7 km/s (1665 MHz), and at -42.4 km/s (1667 MHz). It is interesting to notice from Fig. 6 and 7 that there are pronounced RC ground state peaks at these velocities, but no clearly corresponding LC peaks at the higher frequency Zeeman velocities (-45.3 km/s (1665 MHz), and -44.5 km/s (1667 MHz)). Moreover, VLBI measurements do not place the -45.5 km/s (LC) 1665 component at the position of the -41.7 km/s (RC) source. However, recent 250 Hz resolution recordings of the -45.5 km/s feature (Rydbeck et al., 1970) have shown that it can be broken up into three Gaussian components, with the following center velocities, -45.1, -45.3, and -45.5 km/s. Future VLBI structure measurements may perhaps place the -45.3 km/s component at the position of the -41.7 (RC) source.

If the -41.7 km/s 1665 RC feature, and the main 6035 RC complex are related to each other, a detailed comparison between them should be illuminating, provided they are properly shifted in velocity (equal to the difference in Zeeman-splitting) and suitably scaled in amplitude. For this purpose, we have been recording the relevant ground state feature with 250 Hz resolution. The result is shown in the lower part of Fig. 8. There are obvious and interesting similarities in the velocity range -41 to -42 km/s, which suggests that the U- and T-features may be associated with a structure similar to (or possibly the same as) the one indicated by 1665 MHz RC VLBI fringe phase variations across the feature in question.

A Cook-type shift resonance, non linear mode competition, or perhaps, a Shklovskii-type exclusion effect might explain the possible absence of a higher frequency ground state 1665 MHz (LC) Zeeman component, corresponding to the -41.7 km/s feature. This leads us to consider a rotating configuration as an alternate way of relating the ground and excited state features to each other. If we interpret the splitting of the main 6035 complex as a rotational effect (which seems to require that one of the Zeeman modes be suppressed) the velocity of rotation would be about 0.15 and 0.25 km/s respectively for the 6035 and 6030 features. If a Shklovskii-type mechanism eliminates the 1665 LC component, the necessary magnetic field to make both limb contributions

σ_+ and σ_- , appear at about the same velocity, would be about 5 x 10^{-4} Gauss, i.e., about one order of magnitude less than the previous value. This assumes that the major 6035 and 1665 components are radiated at the same (limb) velocity. The 6035 Zeeman splitting is only $\pm$ 0.015 km/s at this field strength, i.e., less than the Doppler widths and the (presumed) velocity of rotation. Therefore, one of the 6035/6030 Zeeman modes must disappear or be deamplified in the medium. If for example the lowest frequency Zeeman mode survives, the center velocity of the rotating system would be -43.52 km/s. This differs by 0.23 km/s from the center velocity, -43.75 km/s, of the smallest ground state component in W 3 -OH.

We have performed a careful measurement of this feature, at 1665 MHz, with a resolution of 250 Hz. It shows that the main peak actually consists of two nearly equal peaks, separated by 0.09 km/s, the saddle-point depression amounting to about 7.5%, counted from the peaks. A very recent analysis of narrow band VLBI data (Rönnäng et al., 1970) lends support to the belief that the feature in question actually consists of two separate components (and thus that the saddle is not a non linear saturation phenomenon). If these components are uncorrelated (a proof of this would require a specific experiment), it is not unlikely that they are diametrically opposite σ_+ and σ_- -components generated in the Shklovskii fashion. With a diameter of 7 AU, and a rotational velocity of 0.15 km/s, the period would be about 700 years. Furthermore considering the fact that the peaks have a velocity separation of about 0.09 km/s, the magnetic field would be reduced to $\sim$ 3.3 x 10^{-4} Gauss. Finally, assuming that the rest frequency of the 1665 transition is correct, the rest frequency of the 6035 transition (and perhaps of the 6030 one) might be about 4 kHz too high.

Since the rotation concept is especially interesting we have in Fig. 9 folded the LC 6035 pattern about the "best possible" velocity axis (f_0 + 0.5 kHz). The similarity between the RC and LC patterns now is much more striking than in the previous case of a regular pattern shift. One wonders if this close resemblance, that the LC feature looks like the RC one mirrored, (somewhat less noticeable at 6030 MHz), is significant.

We have in the lower part of Fig. 9 plotted the RC 1665 MHz feature in the -43.5 km/s velocity region properly displaced and scaled, in order to compare it with the main part of the RC 6035 spectrum. The over all feature correspondance is less striking than in the -41.7 km/s case, but the main peaks are quite similar in appearance, suggesting that the gain for the excited and the ground states might be about the same (the intensity ratio between the " corresponding " 1665 and 6035 emissions is about six, and between 1667/6035 in W 75 B about five).

The F = 2 → 2 line of $^{2}\Pi_{1/2}$, J = 5/2, at 8135.160 MHz was detected by Schwartz and Barrett (1969) in W 3-OH with a radiometer resolution of 10 kHz (about 0.4 km/s). This very weak emission had one pronounced maximum at about -43.15 km/s, which, within the limits of resolution and possible error in rest frequency, might agree with the velocity (-43.75 km/s) of the smallest W 3-OH 1665 source component.

Furthermore it is of interest to notice that the W 3, OH water vapor emission has its strongest peak at a velocity of about -46.7 km/s if one assumes the rest frequency to be 22235.220 MHz. In order to place this emission at a velocity of -45.1 km/s the water vapor frequency would have to be increased to 22235.358 MHz which is outside the water vapor band measured by Bluyssen et al. (1967). However, this does not rule out a relation between the OH features around this velocity and the water vapor emission (there may for example be a systematic velocity difference between the two within the same source compound). Neither the excited OH emission nor the water vapor emission (Buhl et al, 1969) seem to vary noticeably with time in the case of this particular source.

Finally we have looked for the OH, $^{2}\Pi_{3/2}$, J = 5/2-emission, in several other sources, so far with negative result. The search, which included the ON 1, and ON 2 sources in Cygnus found by Elldér et al. (1969) is recorded in table 1. Since the W75 B 6035 -emission has been found to vary greatly and on one occasion to almost disappear, the search recorded in this table should be repeated.

Acknowledgements

The authors would like to thank Messrs. A. Winnberg, T. Cato, A. Sume, P. Landgren, P. Wrane, and G. Netzler who participated in the experiments.

Table 1., Summary of Observational Results
(Root Mean Square Noise < 0.1 ^{o}K)

Source and Transition	Filters (kHz)	Radial Velocity Range covered * (km/sec)	Polarization	Feature Intensity, in ^{o}K
ON 1:				
2 → 2	10	- 11 to + 39 km/s	Linear	< 0.1
ON 2:				
2 → 2	10	- 25 to + 25 km/s	Lin.	< 0.1
W 51:				
2 → 3	10	+ 35 to + 85 km/s	Lin.	< 0.1
2 → 2	10	- " -	Lin	< 0.1
3 → 3	10	- " -	Lin.	< 0.1
W 49:				
2 → 2	10	- 10 to + 40 km/s	Lin	< 0.1
3 → 3	10	-"-	Lin.	< 0 1
DR 21:				
2 → 2	10	- 25 to + 25 km/s	Lin.	< 0.1
3 → 3	10	-"-	Lin.	< 0 1
W 75 A:				
2 → 3	10	- 19 to + 31 km/s	Lin.	< 0.1
2 → 2	10	-"-	Lin.	< 0.1
3 → 3	10	-"-	Lin.	< 0.1
3 → 2	10	-"-	Lin.	< 0.1
W 75 B:				
2 → 3	10	- 19 to + 31 km/s	Lin.	< 0.1
2 → 2	10	-"-	Lin.	< 0.1
3 → 3	10,3,1	-"-	Lin., RC, LC	See text
3 → 2	10	-"-	Lin.	< 0 1
NML Cyg:				
2 → 3	10	- 46 to + 4 km/s	Lin.	< 0.1
2 → 2	10	-"-	Lin.	< 0.1
3 → 3	10	-"-	Lin.	< 0.1
3 → 2	10	-"-	Lin.	< 0 1
W 3, OH				
2 → 3	10	- 69 to - 19 km/s	Lin.	< 0.1
2 → 2	10 3,1	-"-	Lin.,RC LC	See text
3 → 3	10 3,1	-"-	Lin.,RC LC	See text
3 → 2	10	-"-	Lin.	< 0 1

*) With respect to the local standard of rest

REFERENCES

Bluyssen, H., Dymanus, A., and Verhoeven, J. 1967, Phys. Lett., 24 A, 482.

Buhl, D., Snyder, L.E., Schwartz, P.R., and Barrett, A.H. 1969, Ap. J. (Letters) 158, L 97.

Cook, A.H. 1966, Nature, 211, 503.

Elldér, J., Rönnäng, B., and Winnberg, A 1969, Nature, 222, 67.

Knowles, S.H., Mayer, C.H., and Sullivan III, W.T. 1969, Science, 166, 221.

Kollberg, E. 1970, Res. Report No. 98. Res. Lab. of Electronics, Chalmers University of Technology, Gothenburg.

Litvak, M.M. 1969, Ap.J., 156, 471.

Litvak, M.M. 1969, Science, 165, 855.

Meeks. L.M., Carter, J.C., Barrett, L.H., Schwartz, P.R., Waters, J.W., and Brown III, W.E. 1969, Science, 165, 180.

Moran, J.M. 1968, Thesis, Dept. Elec. Eng., MIT.

Rydbeck, O.E.H., and Kollberg, E. 1968, IEEE Trans. on Microwave Theory and Techniques, MTT - 16, 799.

Rydbeck, O.E.H., Ellder, J., and Kollberg, E. 1969, Ap. J. (Letters), 156, L 141.

Rydbeck, O.E.H., Ellder, J., and Rönnäng, B. 1970, Res. Report, Research Lab. of Electronics, Chalmers University of Technology, Gothenburg (to be published).

Rönnäng, B., and Moran, J. 1970, Res. Report, Research Lab. of Electronics, Chalmers University of Technology, Gothenburg (to be published).

Schwartz, P.R., and Barrett, A.H. 1969, Ap.J. (Letters), 157, L 109.

Shklovskii, I.S. 1969, Soviet Astronomy - AJ, 13, 1.

Yen, J.L., Zuckerman, B., Palmer, P., and Penfield, H. 1969, Ap. J. (Letters) 156, L 27.

Zuckerman, B., Palmer, P., Penfield, H., and Lilley, A.E. 1968, Ap. J. (Letters), 153, L 69.

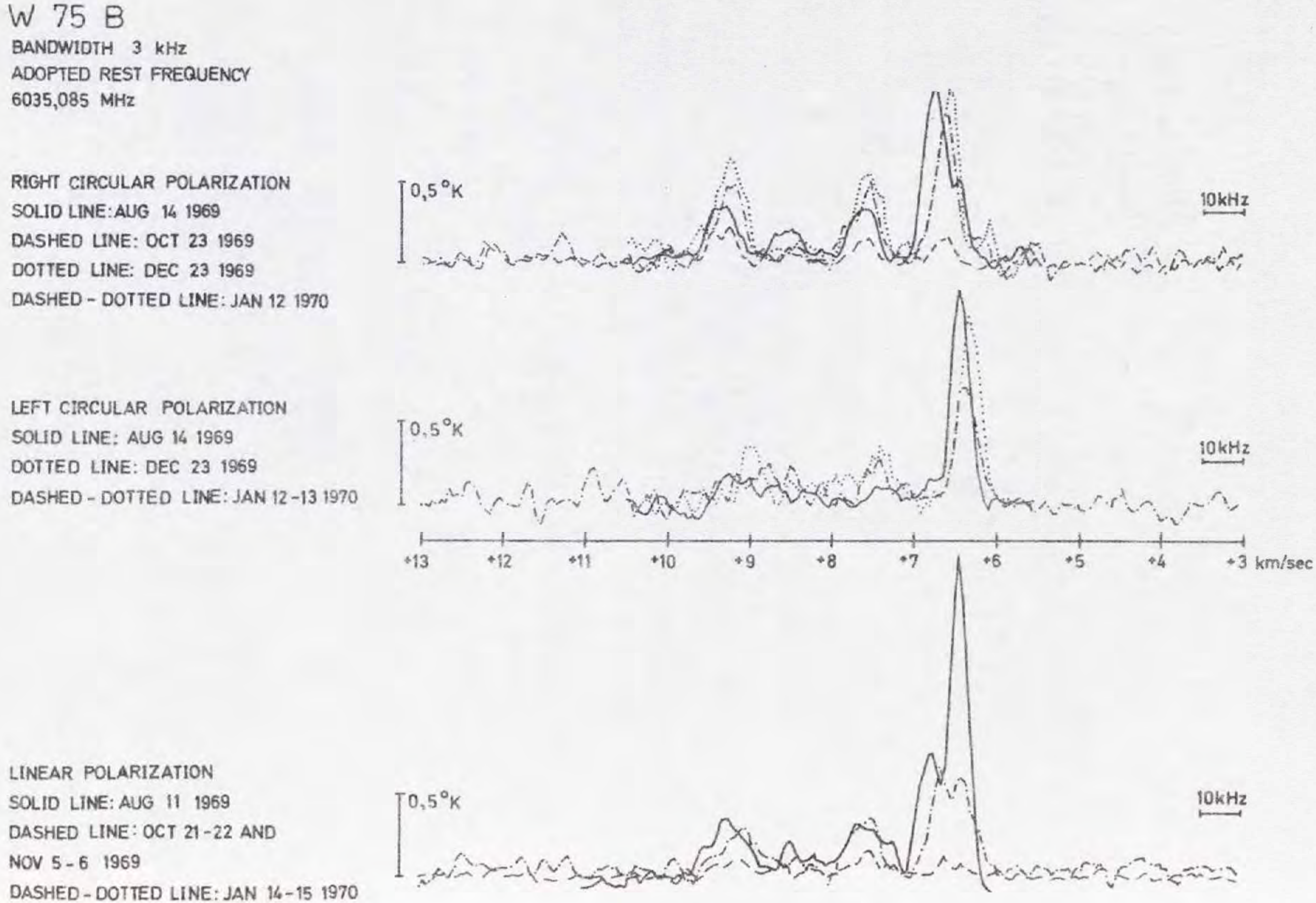

Fig. 1 $^2\Pi_{3/2}$, J = 5/2, F = 3 → 3, 6035 MHz spectra from the OH source W 75 B.

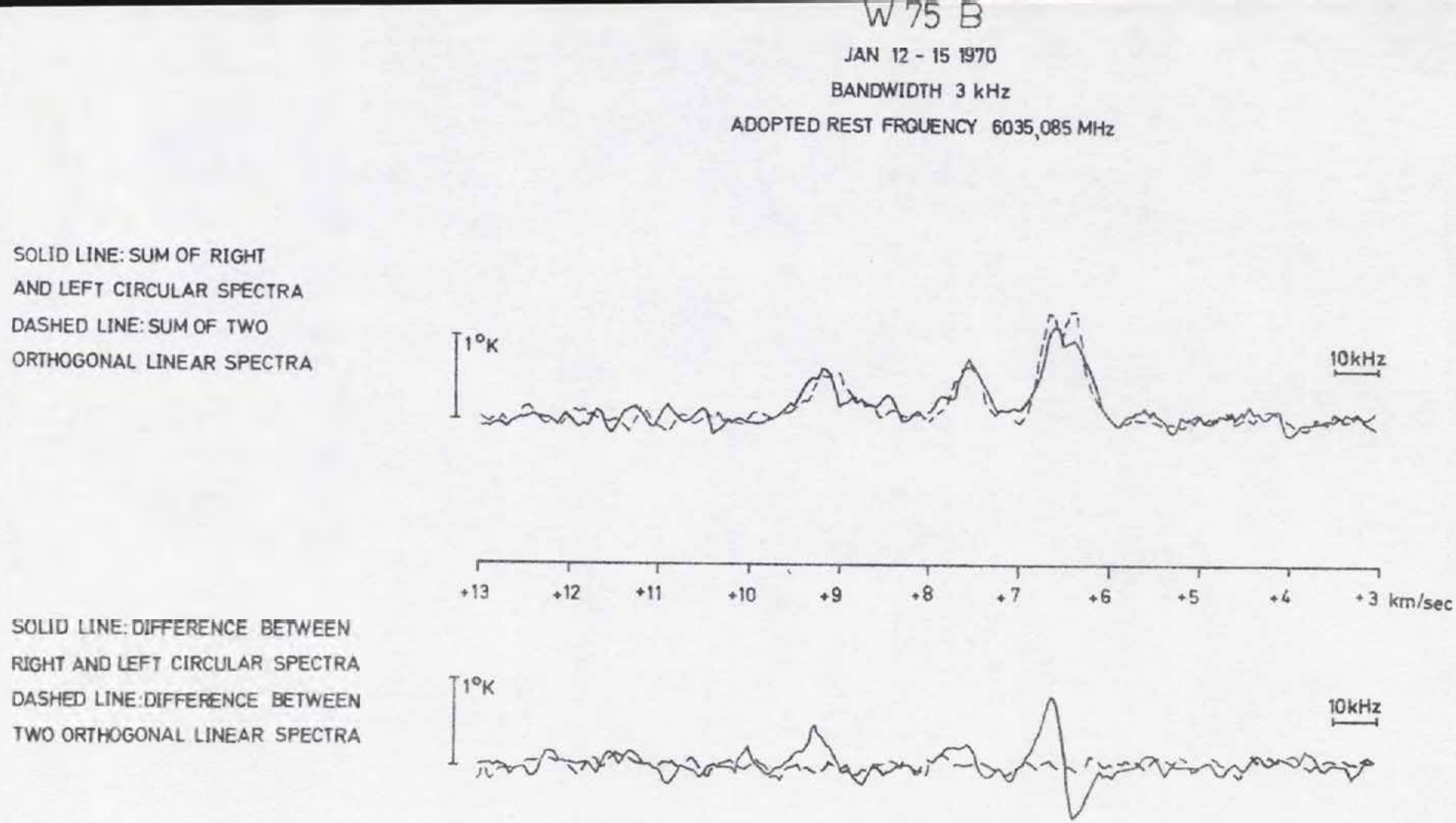

Fig. 2 6035 MHz sum and difference spectra from W 75 B.

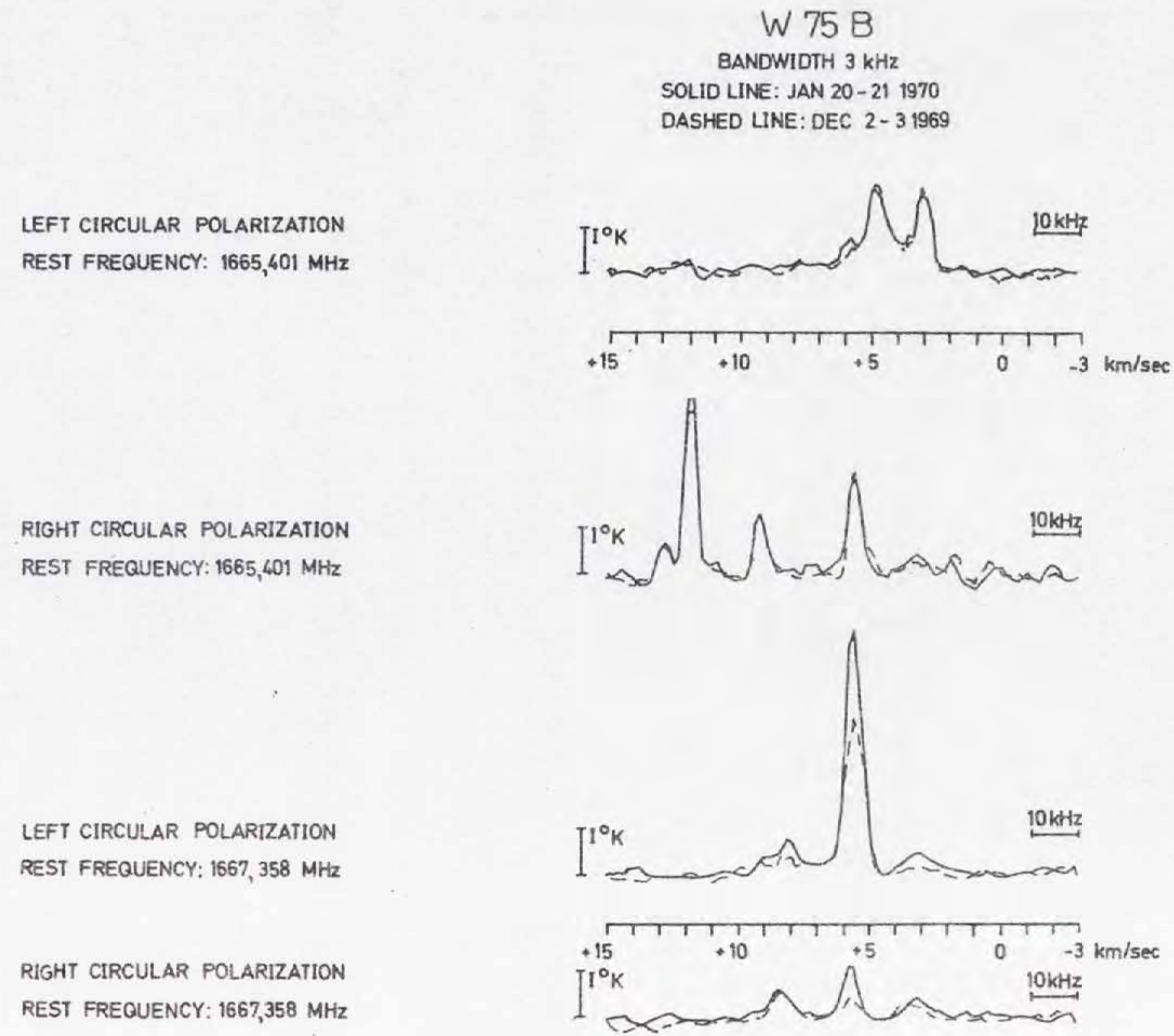

Fig. 3 OH ground state emissions from W 75 B.

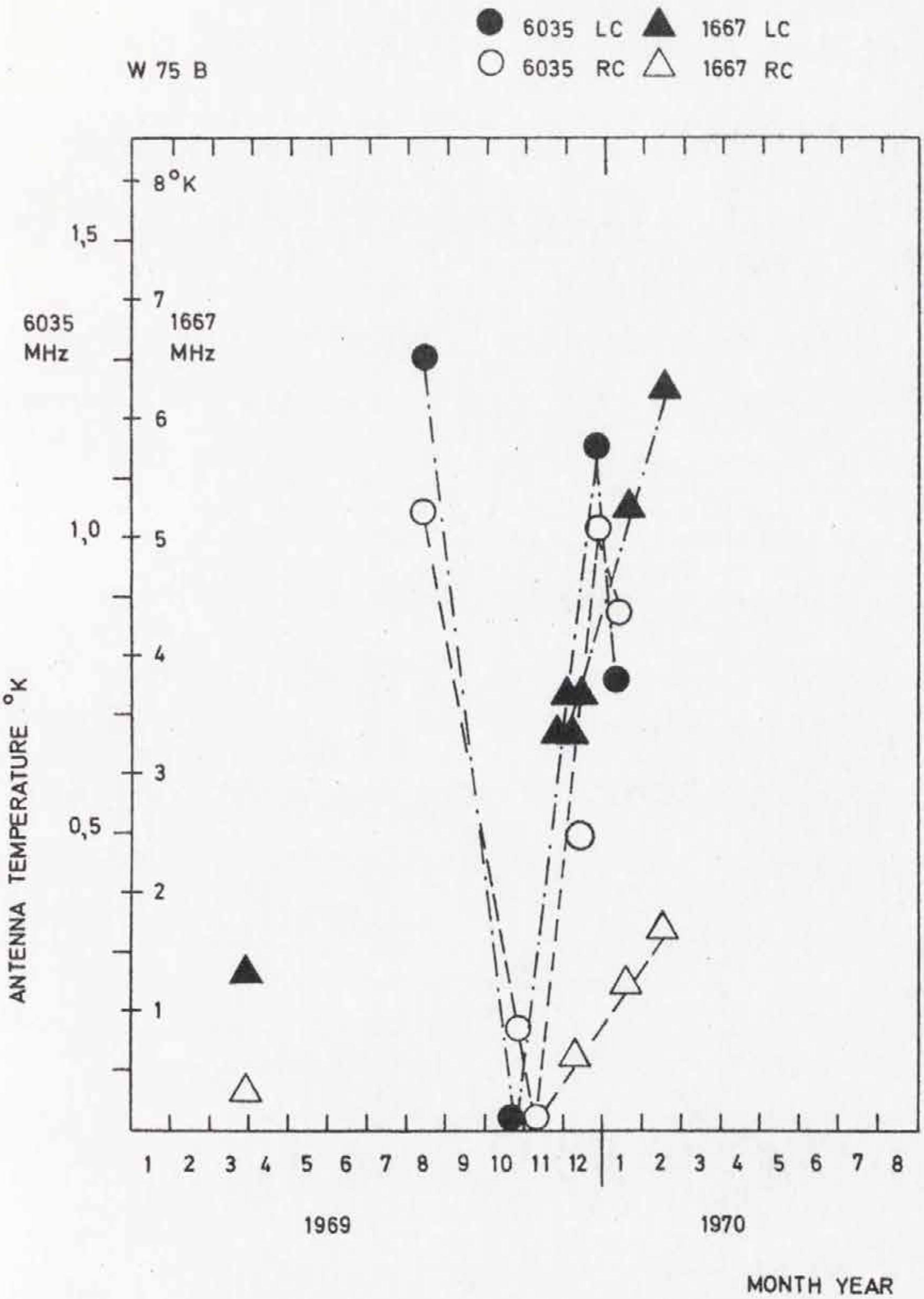

Fig.4. Time variations of 6035 and 1667 MHz emissions from W 75 B.

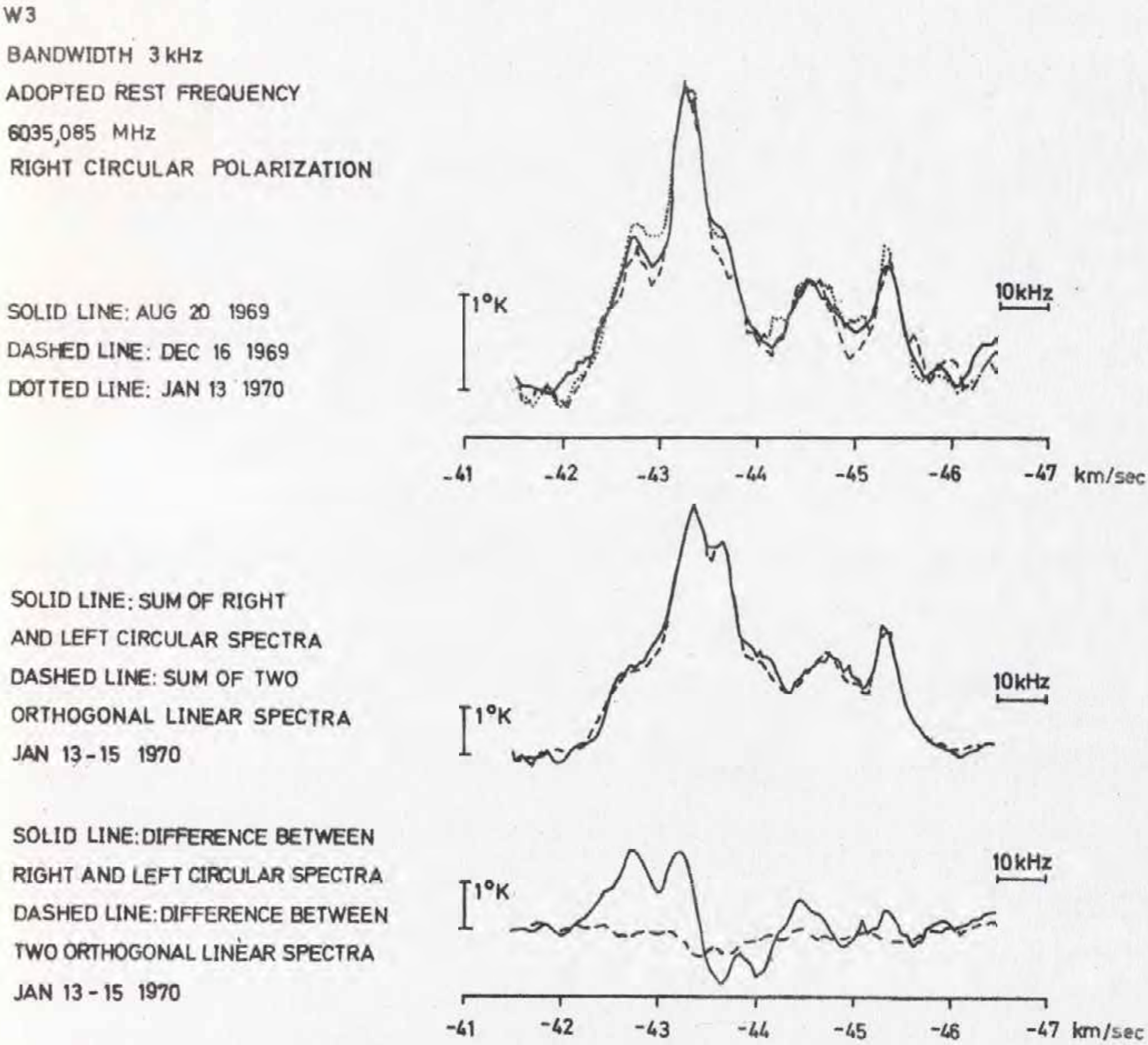

Fig. 5 6035 MHz emissions from W3, OH.

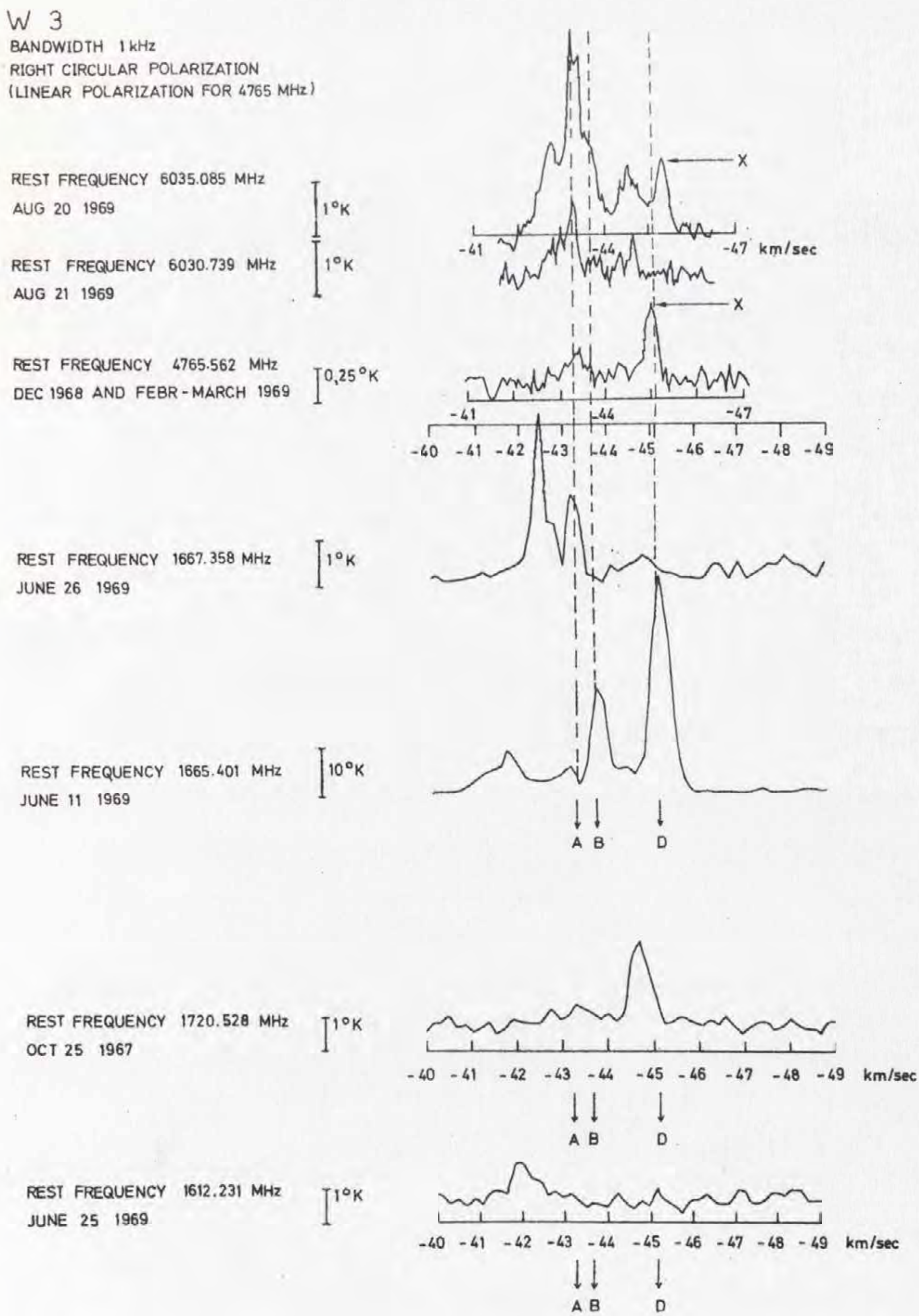

Fig. 6. OH excited and ground state spectra from W 3, OH.

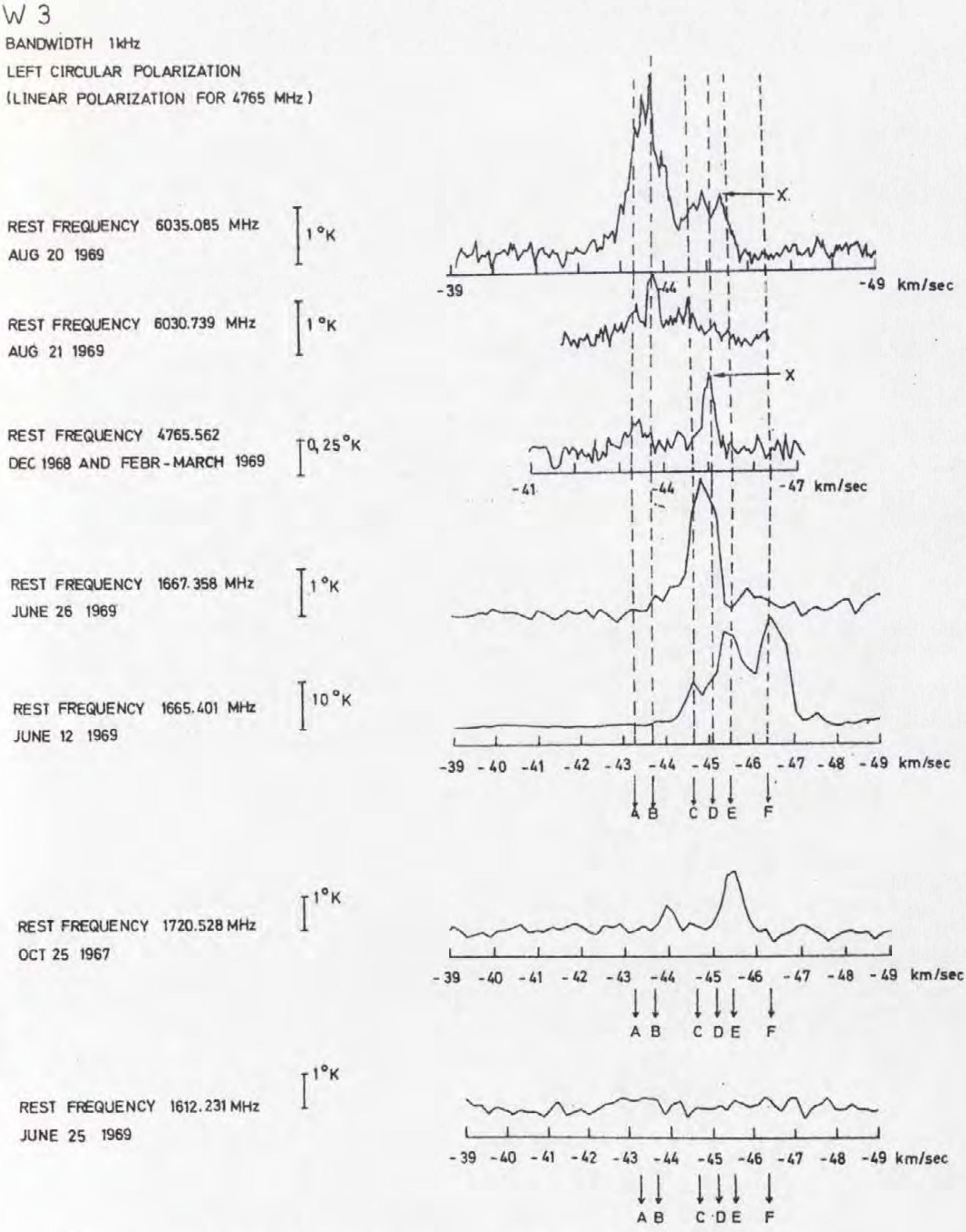

Fig.7. OH excited and ground state spectra from W 3, OH.

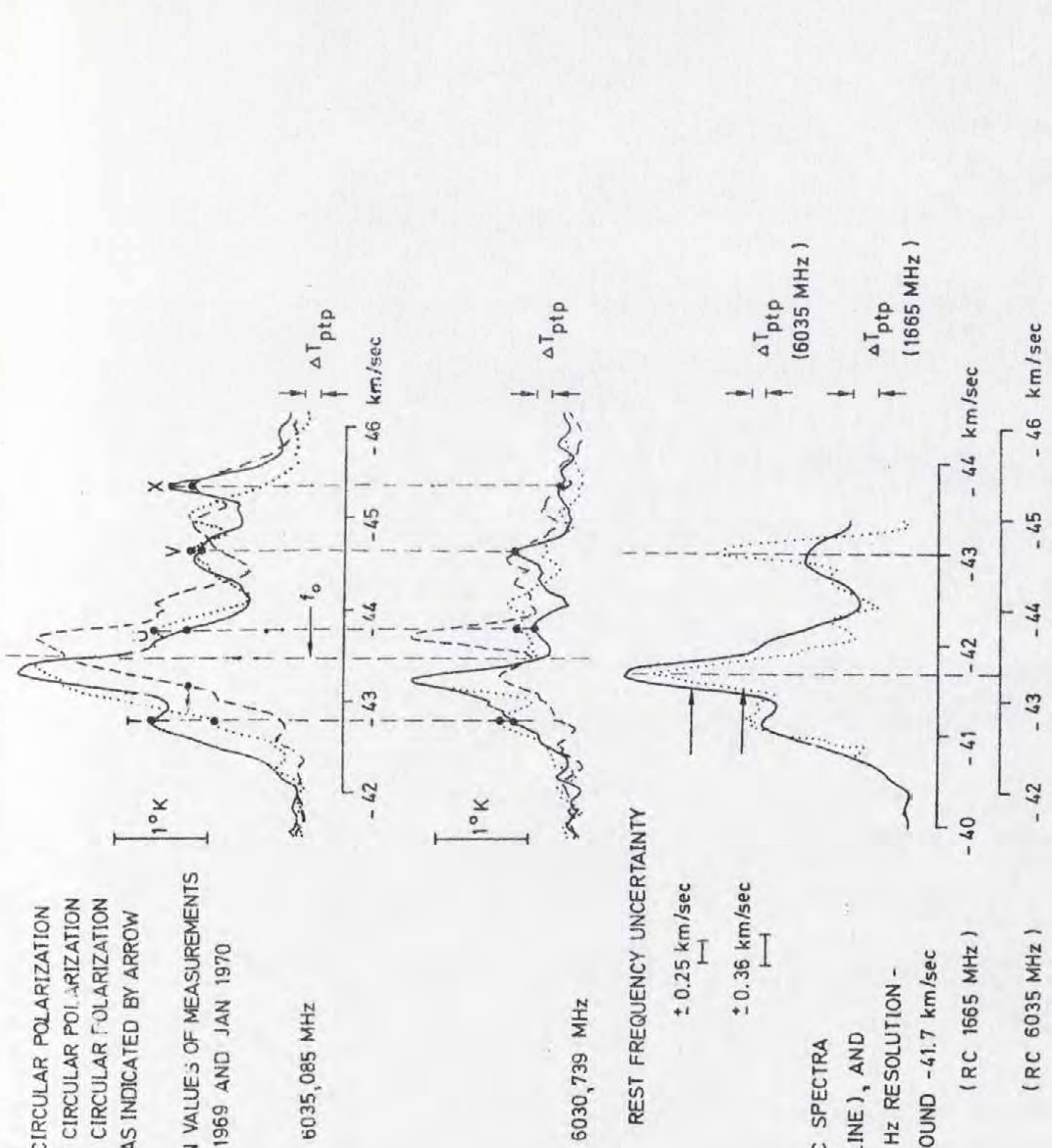

Fig. 8 Spectral shape comparisons for W 3, OH.

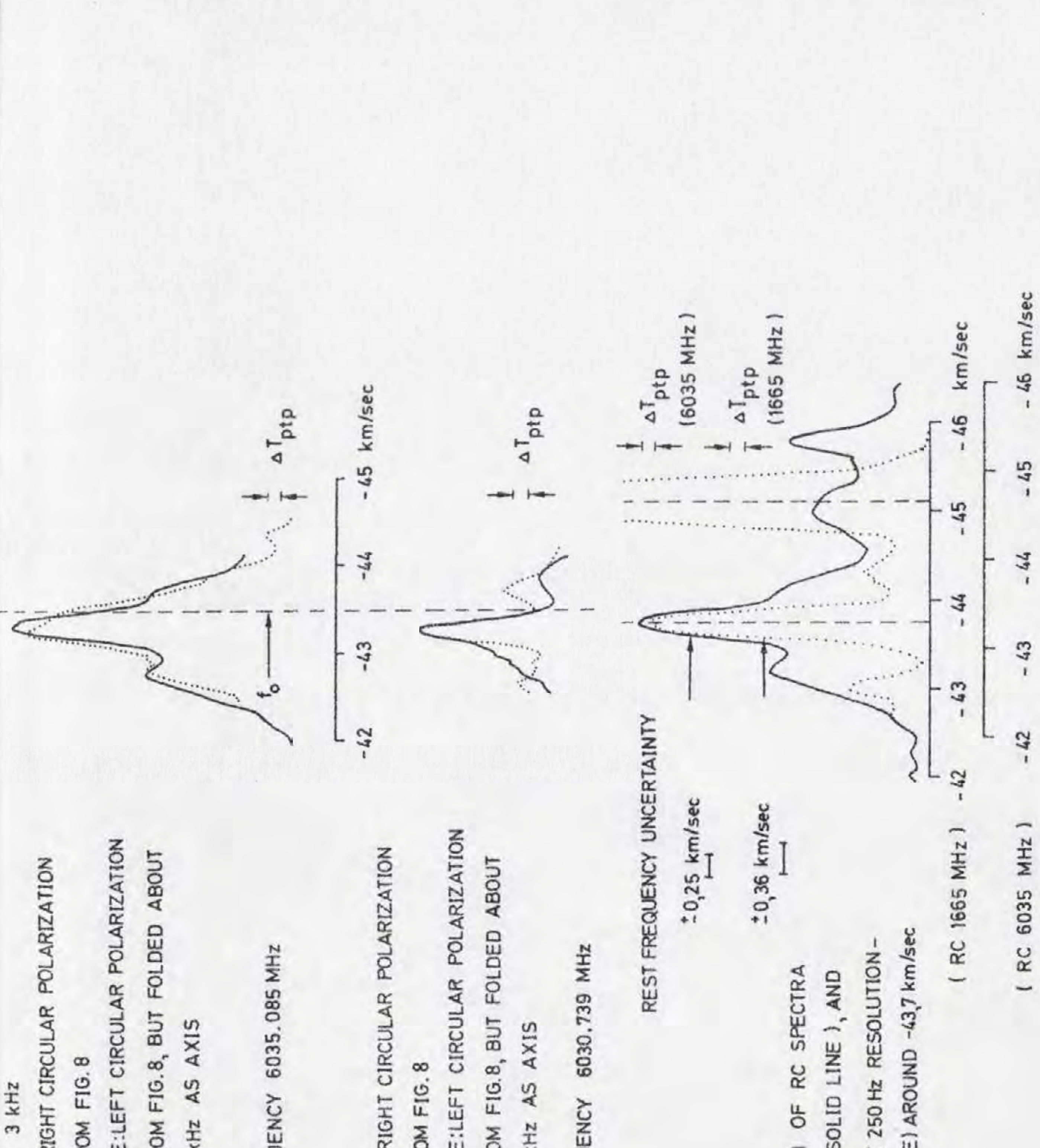

Fig. 9 Spectral shape comparisons for W 3, OH.

THE ASTROPHYSICAL JOURNAL, Vol. 153, September 1968

HIGH-RESOLUTION INTERFEROMETRY OF SMALL RADIO SOURCES USING INTERCONTINENTAL BASE LINES

K. I. KELLERMANN, B. G. CLARK, AND C. C. BARE
National Radio Astronomy Observatory, Green Bank, West Virginia*

O. RYDBECK, J. ELLDER, B. HANSSON, E. KOLLBERG, AND B. HOGLUND
Onsala Space Research Observatory, Chalmers Institute of Technology, Gothenburg, Sweden†

M. H. COHEN‡
University of California, La Jolla

D. L. JAUNCEY
Cornell-Sydney University Astronomy Center, Cornell University, Ithaca, New York§

Received August 19, 1968

ABSTRACT

Radio telescopes located near Green Bank, West Virginia, and Onsala, Sweden, have been used as elements of an interferometer with a base line of 6319 km. Observations at 18 cm (35×10^6 λ base line) and at 6 cm (105×10^6 λ base line) show that a number of radio galaxies and quasi-stellar sources contain components with angular dimensions of the order of 0".001 or less. In two Seyfert galaxies, the upper limits to the sizes of regions of time-varying emission indicate that the sources do not expand with extreme relativistic velocities in the manner suggested by Rees and Simon.

Previous very long base-line interferometer observations have shown that a number of extragalactic radio sources contain unresolved components with angular dimensions under 0".005 (Clark, Cohen, and Jauncey 1967; Clark *et al.* 1968*a*, *b*). Even smaller dimensions are implied by the self-absorption cutoff frequency and by the time scale of the intensity variations.

To study these sources further, we have extended our base line and decreased the operating wavelength. As elements of the interferometer, we used the 140-foot radio telescope at the National Radio Astronomy Observatory in Green Bank, West Virginia, and the 85-foot telescope of the Onsala Space Research Observatory near Onsala, Sweden (base line 6319 km).

The instrumentation, method of observing, and data-processing were essentially as described in the earlier experiments (Clark *et al.* 1968*b*), except that the 30-MHz IF signal was fed to a single side-band converter rather than a double side-band one as used earlier. The IF band width was increased to 350 kHz, the maximum allowed by our 720-kHz data-sampling rate.

Observations were made during the period January 27–February 3, 1968, at frequencies near 1670 and 5010 MHz, corresponding to base-line lengths of 35×10^6 and 105×10^6 wavelengths, respectively.

The observations at 18 cm were made using a rutile traveling-wave-maser receiver on the Onsala telescope and an uncooled parametric amplifier on the NRAO telescope. The

* Operated by Associated Universities, Inc., under contract with the National Science Foundation.

† The Onsala Space Observatory is supported jointly by the Swedish Natural Science Research Council and the Swedish Council for Applied Research.

‡ Supported by AFOSR grant AF-AFOSR-1260-67.

§ Operated by Cornell University with the support of ARPA under a research contract with the AFOSR.

corresponding effective system-noise temperature of the interferometer ranged from 90° to 125° K. With the narrow band widths and short observing times used, only sources with fringe amplitudes greater than about 1.5 flux units could be detected with reasonable certainty. The flux scale of the interferometer was established by (1) setting the measured flux for 3C 279 equal to the 5.5 flux units measured between 10×10^6 and 20×10^6 wavelengths (Clark *et al.* 1968*a*), (2) setting the measured flux for the source P1127−14 equal to the 2.5 flux units expected from the spectrum for the flux of the small component, and (3) calculating the flux scale directly from the system-noise temperature and antenna efficiencies. These three methods give results that are consistent within their internal errors, and the resulting instrumental calibration is believed accurate to ±20 per cent.

The results of the 18-cm observations are given in Table 1. The first column lists the source name; the second, the total flux density (in units of 10^{-26} W m^{-2} Hz^{-1}) of the radio source at 18-cm wavelength (except in the case of 3C 273, where the flux from the large component A is subtracted out). The length of the projected base line is given in the third column in millions of wavelengths. The projected base line in all cases lies within a few degrees of 78° position angle. The fourth column contains the measured correlated flux density, also in flux units. Observations made with approximately the same projected base lines have been averaged together. For most objects the major source of error at 18 cm is the uncertainty in the flux-density scale.

At 6 cm we used a cooled parametric amplifier on the 140-foot telescope and a room-temperature parametric amplifier on the Onsala telescope; the effective system temperature was about 220° K. At this frequency the sensitivity was further degraded by instabilities in the two local oscillators, which led to a mutual coherence time less than our 3-min observation interval. Since the effective sensitivity is determined by the coherence time of the local oscillators at the instant of observation, it is not well known and varies from one observation to the next.

At 6 cm the strongest fringes seen were those from 3C 454.3. The radio spectrum of this source indicates that about 85 per cent of the 6-cm flux density probably comes from a very small component. This component was assumed to be unresolved, and its value was used to establish the flux-density scale of the interferometer. This calibration is consistent with the expected sensitivity determined from the consideration of the individual sensitivities of the two antenna systems and gives values for the fluxes of other small components that are consistent with their source spectra.

The results of the 6-cm observations are given in Table 2. The significances of the columns are the same as in Table 1. It should be noted that although positive values, rather than upper limits, are quoted for the correlated flux densities of 3C 345 and P2134+00, these values are less than twice the rms noise and may thus be only a high noise fluctuation rather than a true detection.

The simple detection of fringes over base lines of 100×10^6 wavelengths is sufficient to show that a significant fraction of the flux density is in one or more components with a diameter smaller than 0"001. Most of the sources in Tables 1 and 2 are complex and contain two or more components of different angular size. The observed fringe visibilities therefore cannot be simply converted into a brightness distribution or an angular size, particularly at 6 cm, where there are no data at short spacings. An approximate division of the total flux at any frequency into distinct components may, however, be made on the basis of the radio spectra of the sources, and this has been used to interpret the interferometer observations.

These results are summarized in Table 3, including results previously derived for these sources (Clark *et al.* 1968*a*, *b*). We list for each component the flux density at 18 cm (third column) and 6 cm (fourth column), the cutoff frequency, f_m (fifth column), and the angular size deduced from the interferometer measurements (sixth column). The optical identification, when available, is shown in the second column. The table is incom-

Table 1

Sources Seen with the NRAO-Onsala Interferometer at 18 cm Wavelength

Source	Total Flux Density 1968.0	Projected Baseline Length	Correlated Flux Density
CTA 21	7.0	34	1.6 ± 0.4
NRAO 150	4.0	34	<1.5
3C 120	4.0	34	1.9 ± 0.4
P1127-14	6.2	35	2.4 ± 0.5
3C 273	31.0	27	10.0 ± 2.0
		34	8.4 ± 1.7
3C 279	11.0	28	5.7 ± 1.2
		35	6.3 ± 1.3
CTD 93	4.2	35	1.6 ± 0.4
3C 345	6.5	34	1.6 ± 0.4
CTA 102	6.4	35	3.5 ± 0.7
3C 454.3	12.0	35	4.0 ± 0.8

Table 2

Sources Seen with the NRAO-Onsala Interferometer at 6 cm Wavelength

Source	Total Flux Density 1968.0	Projected Baseline Length	Correlated Flux Density
3C 84	19.7	84	6.4 ± 3.1
NRAO 150	6.5	100	<5
3C 120	9.0	67	6.2 ± 3.1
		99	4.7 ± 3.1
4C 39.25	7.2	95	6.5 ± 1.8
1127-14	7.1	100	<5
3C 273	31	74	9.8 ± 3.1
		104	8.7 ± 2.2
3C 279	15.4	102	5.9 ± 2.2
3C 345	6.5	90	3.8 ± 2.2
P2134+00	11.3	95	4.5 ± 3.1
3C 454.3	21.8	70	18.2 ± 3.1
		100	17.4 ± 2.2

Table 3

Structure of the Sources

Source	Identification	S_{18}	S_6	f_m	θ	$\log_{10} B$
CTA 21		7.0	3.5		0".008 ± 0".002	−3.5 ± 1
3C 84A	Seyfert Galaxy	2	<1	0.05	~5'*	
B		8	2.5	0.7	0".03 ± 0".01	−1 ± 1
C		2	17	20	0".0012 ± 0".0002	−1 ± 1
3C 120A	Seyfert Galaxy	0.7	0.2	<0.05	10' ± 5'†	
B		~2	2	?	≲0".003	
C		0.7	0.7	0.7	?	
D		0.5	6	9	≲0".0008	<−2
4C 39.25A	QSS	1	0.2	0.1		
B		2	7	8	≲0".0007	<−2.5
P1127-14A	QSS	4	2	0.7	0".007 ± 0".003	−4 ± 1.5
B		2.5	5	7	<0".003	<0
3C 273A	QSS	15	7	<0.05	23" x 2"‡	
B		15	8	0.7	0".020 ± 0".005	−3 ± 1
C		15	15	2.5	0".0025 ± 0".001	−3.5 ± 1
D		1	8	40	≲0".0006	<−2
3C 279A	QSS	3	1.5	<0.05	~10"§	
B		2	~1	~1	0".02 ± 0".01	0 ± 2.5
C		5	6	2	~0".002	−3 ± 2.5
D		~1	7	20	≲0".001	<0
CTD 93	Galaxy	4.2	1.6	1	0".003 ± 0".001	−4 ± 1
3C 345A	QSS	~1	0.2	<0.05	< 2"	
B		5	3	0.8	0".010 ± 0".005	−3 ± 2
C		~1	3	30	<0".001	<−2
P2134+00	QSS	2.7	11.3	4	0".001 ± 0".0005	−4 ± 1.5
CTA 102	QSS	6.4	3.2	1	0".004 ± 0".0015	−4.5 ± 1.5
3C 454.3A	QSS	3	1.4	<0.05	< 2"‖	
B		6	2	0.5	0".007 ± 0".003	−4.5 ± 1.5
C		3.5	17.5	10	≲0".0006	<−3

* Ryle and Windram 1968

† Pomalont 1968

‡ von Hoerner 1966

§ Extended N-S with an overall extent 30" (Gulkis and Sutton 1968)

‖ Clark and Hogg 1966

plete in the sense that the simplest model consistent with all the data was always used, and in some cases the source structure may be more complex than assumed.

Objects 3C 273 and 3C 279 are rather similar in appearance. Each has a large elongated component (A) of 20″ or more in extent, a smaller component (B) $\sim 10^{-2}$″, a yet smaller one (C) $\sim 10^{-3}$″, and a very small component (D) $< 10^{-3}$″. A similar structure is seen in 3C 120. Here the two smallest components, C and D, are related to outbursts that occurred near the end of 1965 and in 1967 (Pauliny-Toth and Kellermann 1968), and it is inferred that the multiple structure found for the other sources may be explained as the remains of expanding components caused by outbursts that occurred at different times.

High-resolution observations of optically thick sources are of particular interest, since for these sources the brightness temperature is determined only by the value of the magnetic field, and so a measure of the flux density and angular size uniquely determines the value of the magnetic field. In terms of the angular size θ in arc seconds, the maximum flux density, S_m in flux units, and the frequency f_m in GHz at which the flux density is a maximum, the magnetic field B (in gauss) is given by

$$B \sim 2.4 \times 10^7 \, \theta^4 \, S_m^{-2} \, f_m^5 \, (1 + z)^{-1} . \tag{1}$$

Since B determined in this way depends on the fifth power of the cutoff frequency and the fourth power of the angular size, it is not well determined. The earlier measurements (Clark *et al.* 1968*b*) indicated that, in the resolved optically thick quasi-stellar sources, the magnetic field was of the order of 10^{-4} gauss. The newer, higher-resolution observations tend to support this value, although for many of the smaller sources the resolution is still only sufficient to put upper limits of 0.01–0.1 gauss on the value of the field. The seventh column of Table 3 gives the logarithm of the magnetic field deduced from the fifth and sixth columns and equation (1). The magnetic fields have been calculated by assuming a uniform circular brightness distribution for each component. Presence of further small-scale structure in individual components will cause the magnetic fields to be less than that given in Table 3.

Only in the case of Seyfert galaxy NGC 1275 (3C 84) is there strong evidence of a magnetic field significantly greater than 10^{-4} gauss. The earlier measurements indicated that the field in component B is at least 10^{-3} gauss, although this result was questionable because of the uncertainty in the cutoff frequency. Component C appears to have a field of about 0.1 gauss, but this may be an overestimate if the source is complex.

The very small dimensions which we have measured directly had been previously inferred from the observations of the intensity variations and the assumption that the linear dimensions divided by the speed of light could not exceed the time scale for the variations. These small sizes lead to an extremely high radiation density, particularly in some of the quasi-stellar objects if they are at cosmological distances. The resultant inverse Compton radiation is then very great. Several authors (Rees and Simon 1968; Morrison and Sartori 1968) have pointed out that the apparent size of a radio source can be very much greater than usually deduced from the flux variations if, for example, the source is expanding with velocities close to that of light.

The observations reported here, however, confirm the predicted small dimensions and, at least in the case of the Seyfert galaxy NGC 1275 (3C 84), show that the expansion velocity is much less than the speed of light. The measured angular size of 3C 84 corresponds to a linear diameter of only 0.8 light-years. From the observations of the flux variations at centimeter wavelengths (Kellermann and Pauliny-Toth 1968), the age of the centimeter-wavelength component is estimated at approximately ten years, so the expansion velocity is of the order of 10 per cent that of light.

In 3C 120, the other variable Seyfert galaxy, the flux at 6 cm at the time of these measurements was near a maximum as a result of an outburst that occurred in April 1967

(Pauliny-Toth and Kellermann 1968). The limit[1] of 0".0008 corresponds to a diameter of less than one light-year at the distance of 3C 120 (100 Mpc) and so, with an apparent age of 0.7 year, again the apparent source size does not exceed that deduced from the age and travel time of light.

We wish to thank the many people who in one way or another contributed to this experiment. These include D. Thacker, G. Jobson, S. Weinreb, and I. Pauliny-Toth at the National Radio Astronomy Observatory; L. Andreasson, T. Cato, I. Ewaldz, A. Hjält, C. O. Lindstrom, L. Lundahl, G. Netzler, L. Gunnarsson, and B. Ronnang at Onsala; and P. Lundbom and C. Abom of the Research Institute of Swedish National Defense. Two of us (K. I. K. and C. C. B.) wish to thank the Onsala Observatory for their hospitality during the period of these observations.

REFERENCES

Clark, B. G., Cohen, M. H., and Jauncey, D. L. 1967, *Ap. J.* (*Letters*), **149**, L151.
Clark, B. G., and Hogg, D. E. 1966, *Ap. J.*, **145**, 21.
Clark, B. G., Kellermann, K. I., Bare, C. C., Cohen, M. H., and Jauncey, D. L. 1968*a*, *Ap. J.* (*Letters*), **153**, L267.
———. 1968*b*, *Ap. J.* (in press).
Fomalont, E. B. 1968, *Ap. J. Suppl.*, **15**, 203.
Gulkis, S., and Sutton, J. 1968 (private communication).
Kellermann, K. I., and Pauliny-Toth, I. I. K. 1968, *Ap. J.*, **152**, 639.
Morrison, P., and Sartori, L. 1968, *Ap. J.* (*Letters*), **152**, L139.
Pauliny-Toth, I. I. K., and Kellermann, K. I. 1968, *Ap. J.* (*Letters*), **152**, L169.
Rees, J. J., and Simon, M. 1968, *Ap. J.* (*Letters*), **152**, L145.
Ryle, M., and Windram, M. D. 1968, *M.N.R.A.S.*, **138**, 1.
von Hoerner, S. 1966, *Ap. J.*, **144**, 483.

[1] The limit of 0".0006 quoted by Pauliny-Toth and Kellermann was based on a preliminary reduction of these data.